Journal of Raman Spectroscopy

WILEY

Journal of RAMAN SPECTROSCOPY

SHORT COMMUNICATION OPEN ACCESS

Time-Domain Raman Spectroscopy: An Emerging Technique in Space Exploration?

Y. Ha[1,2] | S. G. Pavlov[1] | M. D. Rabasovic[3] | A. J. Krmpot[3] | J. Petrovic[4] | J. Woeste[1,2] | D. A. Azih[1,2] | S. Wall[5] | I. Weber[6] | N. Stojanovic[1] | M. Gensch[1,2]

[1]Institute of Space Research, German Aerospace Center, Berlin, Germany | [2]Institute of Physics and Astronomy, TU Berlin, Berlin, Germany | [3]Institute of Physics Belgrade, University of Belgrade, Belgrade, Serbia | [4]Vinča Institute of Nuclear Sciences, Belgrade, Serbia | [5]Department of Physics and Astronomy, Aarhus University, Aarhus, Denmark | [6]Institut für Planetologie, University of Münster, Münster, Germany

Correspondence: M. Gensch (michael.gensch@tu-berlin.de)

Received: 26 March 2025 | **Revised:** 31 March 2025 | **Accepted:** 21 May 2025

Funding: We thank the Deutsche Forschungsgemeinschaft (DFG, German Research Foundation) through the priority program SPP2314 INTEREST (project IDs GE 3288 2-1, GE 3288 2-2, and GE 3288 1-1).

ABSTRACT

The potential of time-domain Raman spectroscopy in space exploration is discussed. This work is motivated by the emergence of robust, space-qualified femtosecond lasers and by the fact that time-domain detection allows the design of very compact instruments. As is shown, time-domain Raman spectroscopy gives access to the same fingerprint spectrum of minerals as conventional Raman spectroscopy, while avoiding problems such as fluorescence or ambient light backgrounds.

1 | Introduction

Since its discovery in 1928 [1], Raman scattering has evolved into one of the most powerful techniques to study the vibrational spectrum of matter (e.g., [2]). The applications have evolved from studying simple gases, liquids, and solids to analyzing biological tissue and planetary materials. Photonic advancements have led to ever more performant and robust instruments. Stand-off Raman instruments are since 2021 operational on rovers on Mars and are under development for operation on moons (e.g., [3, 4]). In this communication, we propose that the emergence of compact, space-qualified femtosecond lasers [5] may enable the detection of Raman-active fingerprints in space research with particularly compact and better-suited instruments based on time-domain Raman spectroscopy (TDRS) (for more details, see Section S6).

In contrast to conventional frequency-domain Raman spectroscopy (FDRS), TDRS detects the modulation of the polarizability directly by transient, stroboscopic measurements of changes in the linear or nonlinear optical properties (see, e.g., [6]). Prerequisite is that a coherent ensemble of the molecular vibrations is prepared, or in other words, that the excited vibrational modes are phase-locked. This can be achieved if appropriately short laser pulses are utilized. The pulse duration limits the detectable spectral bandwidth in time-domain detection as well as the signal strength towards higher frequencies via the time-bandwidth product (TBP) [7]. Non phase-locked photons, such as from fluorescence or ambient light, are not detected.

Meanwhile, the rapid progress of femtosecond lasers provides pulse durations down to sub-10 fs. This enables broadband TDRS over a large part of the spectral range typically utilized for fingerprinting minerals (see Figure 1). Of special interest for space exploration are fiber lasers, as they can be designed to be quite compact and have already been shown to be robust enough to operate in space (e.g., [9]).

TDRS studies have been performed on gases, liquids, and solids, in transmission, reflection, or emission geometries, and exceptional sensitivities to surface or interface properties have been demonstrated [6]. In contrast, TDRS studies on planetary materials are scarce, and there exists no published work on rock-forming minerals, to our knowledge. Here, we show

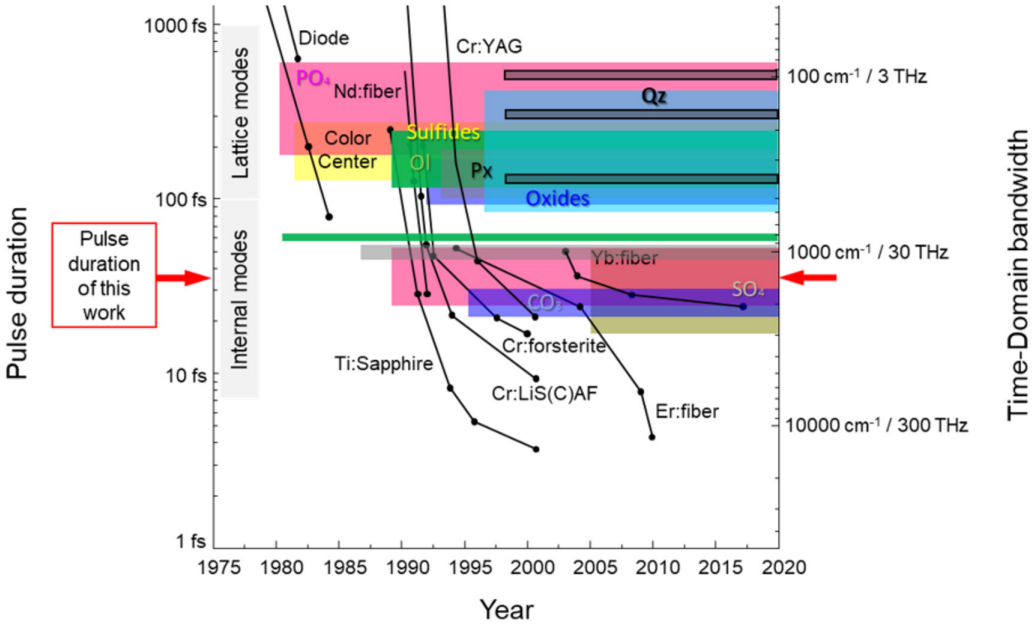

FIGURE 1 | Evolution of pulse durations of solid-state laser systems since 1975 (adapted from [8]). The corresponding spectral bandwidth [7] in time-domain detection is also shown. Ranges of selected relevant vibrational eigenfrequency classes in planetary materials are also displayed (Qz, quartz; PO_4, phosphates; SO_4, sulfates; CO_3, carbonates; Px, pyroxenes; Ol, olivine).

measurements of the vibrational fingerprints of two relevant minerals (for details, see Section S7): quartz (the second-most common Si-bearing mineral) and calcite (the most common carbonate) of the Earth's crust.

2 | Experimental

Both z-cut samples calcite and α-quartz were purchased from Korth Crystals GmbH.

TDRS measurements were performed in transmission with 800-nm femtosecond pump and probe pulses with a duration of 34.4 ± 1.3 fs incident at normal (pump) and near normal (probe) incidence, at a repetition rate of 80 MHz. Pump and probe beams were linearly polarized, in parallel to each other. The pump and probe foci had diameters of 90 and 50 μm (FWHM), respectively. The pump pulse energy of 800 pJ ensured that the fluence stayed orders of magnitude below the damage thresholds of quartz and calcite. The pump pulse-trains were modulated at a frequency of 407 Hz. The detected probe laser signal was then denoised via a lock-in amplifier set to this reference frequency. For calcite, the transient changes of polarization were detected, while for α-quartz, the transient changes in transmission were measured (see insets of Figure 2). For more details on the experimental set-ups, see Section S1.

FDRS measurements were performed utilizing a commercial WITEC alpha-300 confocal microscope (for more details, see Section S2). The wavelength of the Raman laser was 532.2 nm, intensity 3 mW, and probe spot ~1.5 μm. The Stokes intensity was detected in the backscattering geometry with polarization filtering and with intensity calibration.

3 | Results and Discussion

Figure 2 shows a comparison of TDRS and FDRS measurements on calcite and α-quartz. While there is an overall fair agreement, the relative amplitudes of detected modes differ significantly in the as-measured data. In the following, the current understandings for the observed discrepancies shall be discussed (for more details, see Section S4).

The TDRS signal (ΔS) is fundamentally proportional to the first-order Raman tensor $\left(\frac{\partial \chi}{\partial Q}\right)$ [12]:

$$\Delta S \sim \left(\frac{\partial \chi}{\partial Q}\right).$$

The observed intensity of phonons in TDRS is furthermore governed by the TBP, which for a Gaussian intensity profile with frequencies ω and a pulse duration of τ_p takes the following form [7]:

$$\Delta S \sim e^{-\left(4 \ln 2\, t/\tau_p\right)^2}.$$

For calcite, a fair agreement between FDRS and TDRS is found, and the relative amplitudes in the Stokes intensity are well reproduced when including the influence of the TBP (for more details, see Section S3).

The agreement between TDRS and FDRS of α-quartz with the Stokes intensity is also fair. However, only five of the seven modes observed in FDRS are detected. While the missing high frequency E mode at 35 THz/1167 cm^{-1} can be explained by the noise in the measurement, the absence of the E modes at 11.9 THz/397 cm^{-1} and 21 THz/700 cm^{-1} cannot be explained by the TBP alone. The relative amplitudes of the E and A_1 modes at

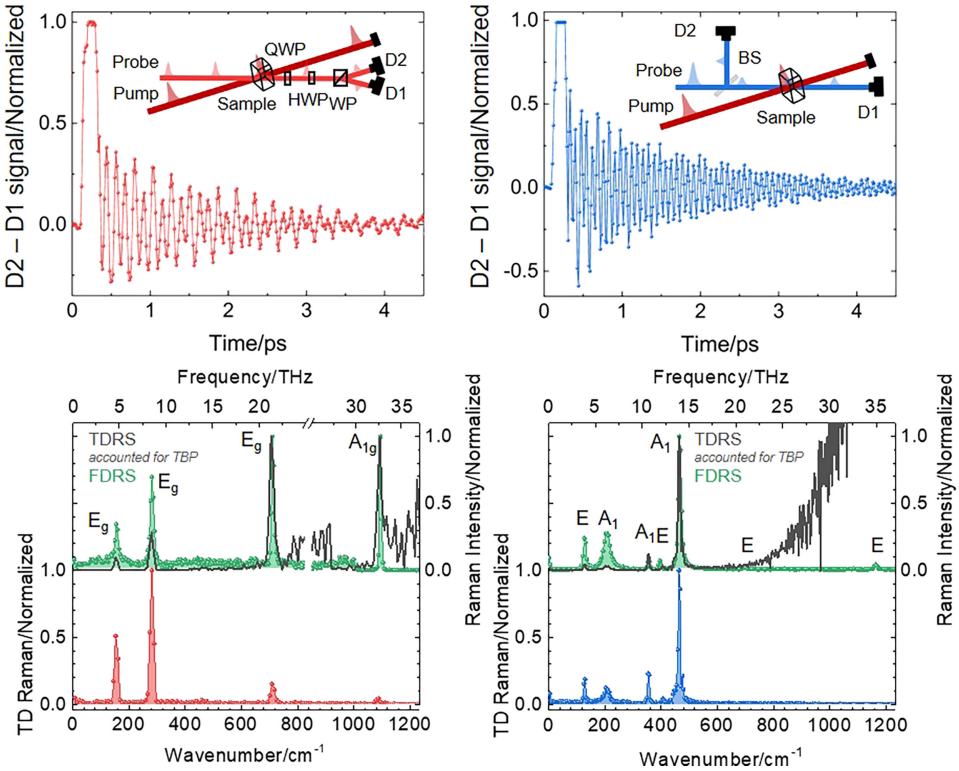

FIGURE 2 | TDRS measurements of changes in birefringence in calcite (left) and changes in transmitted intensity in α-quartz (right). The TDRS signal and the respective measurement geometries are shown in the top panels. The Fourier transform (FT) of the time-domain signals is shown in the bottom panels (red and blue). Note that the so-called coherent artefact [10] in the first 300 fs is omitted and the signal was apodized by the Hamming window [11] function before the FT. The Stokes intensities measured with a conventional FDRS instrument are also shown and the TDRS signal corrected for the convolved TBP of pump and probe pulses is overlaid as a black line. Note that the incident and detected light in all measurements were polarized in parallel (for more details see Sections S1, S2, S3, and S5).

3.8 THz/127 cm^{-1} and 6.2 THz/207 cm^{-1} with respect to the dominant A_1 mode at 13.9 THz/464 cm^{-1} are also underestimated. Future work will focus on gaining a deeper understanding of these discrepancies. It is interesting to note that the TDRS measurements are in better agreement with FDRS measurements on the α-cristobalite phase of quartz [13].

4 | Conclusions and Outlook

TDRS on minerals can be performed with comparatively weak (sub-nJ) near-infrared femtosecond pulses. TDRS and FDRS give comparable results. Differences of relative amplitudes between TDRS and FDRS are not fully understood. Development of a breadboard-level instrument optimized for stand-off detection is in progress, as is research on photonic chip integration of time-domain detection building blocks.

Acknowledgments

We thank the Deutsche Forschungsgemeinschaft (DFG, German Research Foundation) through the priority program SPP2314 INTEREST (project IDs GE 3288 2-1, GE 3288 2-2, and GE 3288 1-1). Open Access funding enabled and organized by Projekt DEAL.

Conflicts of Interest

The authors declare no conflicts of interest.

Data Availability Statement

The data that support the findings of this study are available from the corresponding author upon reasonable request.

References

1. C. V. Raman and K. S. Krishnan, "A New Type of Secondary Radiation," *Nature* 21 (1928): 501–502.

2. L. A. Nafie, "Recent Advances in Linear and Nonlinear Raman Spectroscopy. Part XIV," *Journal of Raman Specroscopy* 51 (2020): 2354–2376.

3. R. Bhartia, L. W. Beegle, L. DeFlores, et al., "Perseverance's Scanning Habitable Environments With Raman and Luminescence for Organics and Chemicals (SHERLOC) Investigation," *Space Science Reviews* 217, no. 4 (2021): 58, https://doi.org/10.1007/s11214-021-00812-z.

4. Y. Cho, U. Böttger, F. Rull, et al., "In Situ Science on Phobos With the Raman Spectrometer for MMX (RAX): Preliminary Design and Feasibility of Raman Measurements," *Earth, Planets and Space* 73 (2021): 232.

5. M. E. Fermann and A. Rolland, "The Impact of Femtosecond Fiber Lasers in Technology and Science," *Optics Communication* 574 (2025): 131197.

6. K. Ishioka and O. Misochko, *Progress in Ultrafast Intense Laser Science*, Vol. 5, ed. K. Yamanouchi, A. Giulietti, and K. Ledingham (Springer, 2010): 23–46.

7. J. C. Diels and W. Rudolph, *Ultrashort Laser Phenomena: Fundamentals, Techniques, and Applications on a Femtosecond Time Scale*, vol. 10, 2nd ed., (Academic Press, 2006).

8. F. X. Kärtner, E. P. Ippen, and S. T. Cundiff, *Femtosecond Optical Frequency Comb: Principle, Operation, and Applications*, eds. J. Ye and S. T. Cundiff (Springer, 2006): 54–77.

9. J. Lee, K. Lee, Y. S. Jang, et al., "Testing of a Femtosecond Pulse Laser in Outer Space," *Scientific Reports* 4 (2014): 5134.

10. F. J. Harris, "On the Use of Windows for Harmonic Analysis With the Discrete Fourier Transform," *Proceedings of the IEEE* 66 (1978): 51–83.

11. M. V. Lebedev, O. V. Misochko, T. Dekorsy, and N. Georgiev, "On the Nature of "Coherent Artifact"," *Journal of Experimental and Theoretical Physics* 100 (2005): 272–282.

12. T. Dekorsy, G. C. Cho, and H. Kurz, *Light Scattering in Solids VIII. Topics in Applied Physics*, vol. 76, eds. M. Cardona and G. Güntherodt (Springer, 2000): 169209.

13. J. Etchepare, M. Merian, and P. Kaplan, "Vibrational Normal Modes of SiO_2. II. Cristobalite and Tridymite," *Journal of Chemical Physics* 68 (1978): 1531–1537.

Supporting Information

Additional supporting information can be found online in the Supporting Information section.

Celebrating 50 years of fluorescence correlation spectroscopy (FCS): Advancing live-cell massively parallel FCS studies with photostable GFPs, mStayGold and StayGold/E138D

Article *in* Biochimica et Biophysica Acta (BBA) - General Subjects · April 2025

DOI: 10.1016/j.bbagen.2025.130809

CITATIONS
0

READS
29

7 authors, including:

Sho Oasa
Karolinska Institutet
38 PUBLICATIONS **223** CITATIONS
SEE PROFILE

Stanko Nikolic
Institute of Physics Belgrade
42 PUBLICATIONS **374** CITATIONS
SEE PROFILE

Akira Kitamura
Hokkaido University
107 PUBLICATIONS **2,161** CITATIONS
SEE PROFILE

Vladana Vukojević
Karolinska Institutet
178 PUBLICATIONS **2,638** CITATIONS
SEE PROFILE

BBA - General Subjects 1869 (2025) 130809

Contents lists available at ScienceDirect

BBA - General Subjects

journal homepage: www.elsevier.com/locate/bbagen

Celebrating 50 years of fluorescence correlation spectroscopy (FCS): Advancing live-cell massively parallel FCS studies with photostable GFPs, mStayGold and StayGold/E138D☆

Sho Oasa [a,*], Borislav Stoyanov [b], Yuta Hamada [c], Stanko N. Nikolić [a,d], Aleksandar J. Krmpot [a,d], Akira Kitamura [e], Vladana Vukojević [a,*]

[a] Department of Clinical Neuroscience, Center for Molecular Medicine, Karolinska Institutet, 17176 Stockholm, Sweden
[b] School of Science, Constructor University, 28759 Bremen, Germany
[c] Laboratory of Cellular and Molecular Sciences, Graduate School of Life Science, Hokkaido University, Sapporo 001-0021, Japan
[d] Institute of Physics Belgrade, University of Belgrade, 11080 Belgrade, Serbia
[e] Laboratory of Cellular and Molecular Sciences, Faculty of Advanced Life Science, Hokkaido University, Sapporo 001-0021, Japan

ARTICLE INFO

Keywords:
Fluorescence correlation spectroscopy (FCS) and massively parallel FCS
mStayGold
Apparent brightness analysis
Glucocorticoid receptor
Homodimerization
Nucleocytoplasmic transport

ABSTRACT

More than 50 years after its inception, fluorescence correlation spectroscopy (FCS) remains a cornerstone technique for quantitative characterization of the cellular dynamics of molecules and their concentration and interactions in live cells. The enhanced green fluorescent protein (eGFP) has long been a preferred tag in live-cell FCS, valued for its brightness, photostability and lack of posttranslational modifications. However, low eGFP photostability limits measurement durations, posing challenges for studying dynamic cellular processes necessitating longer measurement time. Recent advancements in fluorescent protein engineering have yielded mStayGold and StayGold/E138D, two highly photostable monomeric GFP variants. In this study, we evaluate their performance in live cells and utility for FCS by quantifying glucocorticoid receptor (GR) homodimerization and nuclear import/export dynamics in live cells. Our study shows that both mStayGold and StayGold/E138D exhibit twice the brightness of eGFP, significantly enhancing the signal-to-noise ratio (SNR). Using massively parallel FCS (mpFCS) and two-foci cross-correlation to characterize the direction of GR nucleocytoplasmic transport along the nuclear envelope, we also confirm that these proteins show significantly improved photostability over eGFP.

1. Introduction

Fluorescence correlation spectroscopy (FCS), first proposed in 1972 as a method to study translational motion of molecules and measure chemical rate constants in a chemically reactive system at equilibrium through fluorescence intensity fluctuations of the fluorescent reaction product diffusing in and out of the focused laser beam [1], was formalized in 1974 in a series of seminal papers that laid out its theoretical and experimental foundation [2–4]. In 1993, integration of FCS with confocal microscopy revolutionized its potential for applications in biomedical research by enabling precise measurements in femtoliter volumes (in conventional confocal laser scanning microscopes the observation volume is (0.2–1) $\times 10^{-15}$ l) vastly improving the signal-to-noise ratio (SNR) [5] and enabling single-molecule sensitivity [6,7], which is of utmost relevance for measurements in live cells [8]. Over the following decades, innovations such as dual-colour fluorescence cross-correlation spectroscopy (FCCS) [9,10], two-photon FCS [11], scanning FCS [12], Förster resonance energy transfer FCS (FRET-FCS) [13], stimulated emission depletion FCS in sub-diffraction focal volumes (STED-FCS) [14], pin-hole array correlation imaging (PACI) [15], multipoint holographic FCS (MP-hFCS) [16], total-internal reflection FCS (TIR-FCS) [17], single-plane illumination FCS (SPIM-FCS) [18], inverse FCS (iFCS) [19], massively parallel FCS (mpFCS) [20–22], to name but a few, have been developed. These developments extended the FCS-toolbox and its applications for quantitative characterization of important determinants of the kinetics of biochemical reactions: the

☆ This article is part of a Special issue entitled: 'FCS - 50 years & forward' published in BBA - General Subjects.

* Corresponding authors.
E-mail addresses: sho.oasa@ki.se (S. Oasa), vladana.vukojevic@ki.se (V. Vukojević).

https://doi.org/10.1016/j.bbagen.2025.130809
Received 27 December 2024; Received in revised form 26 March 2025; Accepted 16 April 2025
Available online 17 April 2025

concentration of biomolecules and their fast intracellular dynamics in complex biological systems, *i.e.*, in live *ex vivo* organs [23], small organisms [24] and biological fluids for prospective disease diagnosis [25]. These endeavors build on the solid foundation laid by Prof. Rudolf Rigler, whose contribution has been indispensable for growing the FCS field, thereby advancing our understanding of molecular mechanisms underlying basic biological processes, and detailed mechanisms of action of approved [26] and prospective pharmacotherapeutics [27–29].

The application of FCS in biomedical studies is inseparable from the development of fluorescent proteins (FPs), imperative tools for live-cell fluorescence microscopy imaging and FCS. Their relevance is such that in 2008, the Nobel Prize in Chemistry was awarded to three laureates for their seminal work on discovering and developing the green fluorescent protein (GFP) [30], on which the brighter and the more photostable enhanced GFP (eGFP) is based.

FCS applications in biomedical research commonly rely on the use of eGFP as a genetically fused fluorescence tag for proteins of interest in live cells [31–35]. But FCS has also been used to characterize photophysical properties of fluorescent proteins [36–38], revealing their proneness to photobleaching. To account for this shortcoming, mathematical tools were developed to separate the fluorescence intensity fluctuations arising due to translational molecular motion through the observation volume element (OVE) from the steady decay in average fluorescence intensity due to photobleaching, known as the photobleaching correction [39–41]. While this correction method works well, it relies on the use of so-called raw FCS data, *i.e.*, photon counts, which necessitates working with large file sizes and is time consuming. To avoid difficulties arising due to fluorescent proteins' photobleaching, alternative labeling strategies using engineered proteins such as the Halo and SNAP tags, are utilized to allow the use of photostable organic dyes. However, this approach is experimentally more cumbersome as it is necessary to establish the efficiency of organic dye labeling using the Halo/SNAP tags. Otherwise, protein concentration and the extent of protein-protein interactions (*e.g.*, under homo- or heterodimerization) will be underestimated.

Recently, Hirano et al. developed the photostable GFP dimer StayGold from *Cytaeis uchidae* [42]. StayGold is characterized by high photostability ($t_{1/2}^{StayGold} = 12{,}421$ s: the time to reduce emission rate to half in live cells under wide-field illumination is about twenty-five (25) times longer than that of eGFP ($t_{1/2}^{eGFP} = 481$ s), and of about 4-times higher brightness compared to that of eGFP under same conditions [42]. Ando et al. continued to construct the monomeric variant of StayGold, so called mStayGold [43], which retains the high photostability and high brightness of StayGold but is monomeric (molecular weight = 25.6 kDa). With the same aim, Ivorra-Molla et al. have developed the monomeric form of StayGold with a single E138D point mutation (StayGold/E138D) [44], and Zhang et al. developed the monomeric form of StayGold called mBaojin [45]. These bright and photostable GFPs allow for longer signal acquisition during FCS measurements, improving the signal-to-noise-ratio (SNR) and making complicated FCS data analysis redundant.

In this work, we have characterized two monomeric forms of StayGold, mStayGold and StayGold/E138D in live cells and assessed their photostability and brightness, as indicators of suitability for FCS measurements in conventional single-point FCS (spFCS) and massively parallel FCS (mpFCS). We have further quantitatively characterized ligand-stimulated homodimerization and nuclear import/export of the glucocorticoid receptor (GR) genetically fused with mStayGold. GR is a hormone-dependent transcription factor and a target for steroid pharmacotherapeutics [32]. In unstimulated cells, the GR is localized in the cytoplasm, bound into a large complex with other molecules. Upon ligand binding, this complex dissociates and GRs translocate to the cell nucleus [22], where they bind to the glucocorticoid response elements (GREs) in the genomic DNA and exert gene expression regulation function [46–49]. In parallel, ligand binding induces GR homodimerization and heterodimerization with other transcription factors for rewiring gene expression [50].

Our data clearly shows that increased brightnesses of mStayGold and StayGold/E138D allow us to reduce the excitation intensity, achieving the same SNR as when using eGFP, allowing at the same time longer time series data acquisition. This, in turn, improves the precision of autocorrelation curves' fitting, as autocorrelation curves with less noise are obtained.

2. Materials and methods

2.1. Chemical reagents

The GR-specific synthetic ligand dexamethasone (Dex) was purchased from Sigma-Aldrich and used without any further purification. 2 mM stock solution of Dex was prepared by dissolving it in dimethyl sulfoxide (DMSO). The stock solution was dispensed, and aliquots were stored at −20 °C. For cell treatment, the stock solution was warmed to room temperature and diluted to 500 nM using phenol red-free FluoroBrite DMEM (Gibco) cell culture medium.

2.2. Plasmid DNAs

Plasmid DNAs encoding mStayGold (#212020; pcDNA3/mStayGold (c4) = UtrCH) or StayGold/E138D (#211363; pcDNA3-10His-mStayGold (E138D)), were purchased from Addgene. These plasmids were used as templates in the polymerase chain reaction (PCR) to amplify the DNA sequence of mStayGold and StayGold/E138D. The Phusion® High-Fidelity PCR Master Mix with GC Buffer (Thermo Fisher Scientific), a 2× master mix consisting of Phusion Hot Start II DNA Polymerase, deoxynucleotides and optimized reaction buffer with $MgCl_2$, particularly useful for sequences with high GC content, was used to ensure accurate DNA replication. PCR products were purified using the QIAquick PCR purification kit (QIAGEN).

mStayGold for C1 vector

Forward primer: 5'-ATCCACCGGTCGCCACCATGGTGTCTACAGGC-3'.

Reverse primer: 5'-GAGCTCGAGATCTGAGTCCGGACAGGTGGGCC TCCAG-3'.

StayGold/E138D.

Forward primer: 5'-ATCCACCGGTCGCCACCATGGCCAGCACGCCG-3'.

Reverse primer: 5'-GAGCTCGAGATCTGAGTCCGGAAAGATGAGC TTCTAA-3'.

mStayGold for N1 vector.

Forward primer: 5′- ATCCACCGGTCGCCACCATGGTGTCTACAGGC-3'.

Reverse primer: 5'-GTCGCGGCCGCTTTACAGGTGGGCCTCCAG-3'.

Tandem dimer of mStayGold.

Forward primer: 5'-GACGGTACCATGGTGTCTACAGGCG-3'.

Reverse primer: 5'-GCGACCGGTGGCAGGTGGGCCTCCAG-3′.

To swap the DNA sequences encoding eGFP in the peGFP-C1 and the peGFP-GR-C1 plasmids with the sequences for mStayGold or StayGold/E138D, the PCR-amplified sequences for mStayGold and StayGold/E138D and the peGFP-C1 plasmid encoding eGFP in the C1 vector or the peGFP-GR-C1 plasmid encoding eGFP-tagged full-length human glucocorticoid receptor α (GR) in the C1 vector [51], were digested using the restriction enzymes *Age*I-HF (New England Biolabs (NEB)) and *Xho*I (NEB) in the rCutSmart buffer (NEB) at 37 °C for 1 h. To minimize annealing of DNA fragments, the plasmid DNAs were treated with Quick CIP (NEB), followed by the purification using QIAquick nucleotide removal kit (QIAGEN). The PCR-amplified sequences of mStayGold or StayGold/E138D were inserted into the plasmid backbone DNAs (C1 vector or GR-C1 vector) and ligated using the Instant Sticky-end Ligase Master Mix (NEB). The resulting constructs were verified using DNA sequencing to ascertain that pmStayGold-C1 and pStayGold/E138D-C1

contain mStayGold and StayGold/E138D, respectively in the C1 vector, and that pmStayGold-GR-C1 is encoding both mStayGold and GR in the C1 vector.

To construct the tandem dimer of mStayGold, eGFP in the peGFP-N1 plasmid was swapped with mStayGold using the procedure with *Age*I-HF (NEB) and *Not*I (NEB). Another mStayGold was inserted into the pmStayGold-N1 with *Kpn*I-HF (NEB) and AgeI-HF (NEB).

2.3. Cell culture

HEK293 cells (American Type Culture Collection) were maintained in a humidified atmosphere containing 5 % CO_2 at 37 °C in Dulbecco's Modified Eagle Medium (DMEM; Gibco) supplemented with 10 % fetal bovine serum (Gibco) and 1 % penicillin-streptomycin (100 U/ml of penicillin and 100 μg/ml of streptomycin; Gibco). For FCS measurements, the cells were seeded in Nunc Lab-Tek 8-well Chambered Coverglass (Thermo Fisher Scientific) at the density of 2.0×10^4 cells/well in 400 μl of cell culture medium.

24 h after seeding the cells in the 8-well chambered coverglass, the cells were transfected with 100 ng of plasmid DNAs encoding: eGFP, mStayGold, tandem dimer of eGFP [52] or mStayGold, StayGold/E138D, eGFP-GR or mStayGold-GR, using 0.2 μl/well of Lipofectamin 2000 (Thermo Fisher Scientific). Following a 24 h' transfection in a humidified atmosphere containing 5 % CO_2 at 37 °C, the cell culture medium was replaced with the phenol red-free medium FluoroBrite DMEM (Gibco) for live-cell fluorescence microscopy imaging and FCS.

For GR activation, the 2 mM Dex stock solution was thawed at room temperature, diluted to 500 nM using the phenol red-free FluoroBrite DMEM (Gibco) medium and the cell culture medium was replaced. Unless otherwise stated, Dex treatment lasted 30 min at 37 °C and 5 % CO_2 in a humidified atmosphere. In control experiments, sham treatment with the cell culture medium FluoroBrite DMEM (Gibco) was used.

2.4. Confocal laser scanning microscopy and fluorescence correlation spectroscopy

Confocal Laser scanning microscopy (CLSM) imaging and FCS measurements were performed at 25 °C using an LSM880 (Carl Zeiss) microscope system equipped with a 405 nm laser, 488 nm Ar-ion laser, and a water immersion objective lens (C-Apochromat, 40×, 1.2 N.A., Corr, Carl Zeiss), a gallium arsenide phosphide (GaAsP) detector and photomultiplier tube (PMT) detectors. eGFP, mStayGold or StayGold/E138D were excited using the 488 nm laser line of the Ar-ion laser. The pinhole size was adjusted to 1 Airy unit (34 μm). For fluorescence detection, the GaAsP detector was used, and the wavelength range of 500–530 nm was collected. FCS measurements were performed in a series of 10 consecutive recordings, each individual recording lasting 20 s. For fluorophore brightness analysis as a function of excitation laser intensity, the following values were tested: 0.07, 0.11, 0.15, 0.21, 0.26, 0.38, 0.72 and 1.45 μW at the objective lens, corresponding to: 0.05, 0.09, 0.11, 0.15, 0.2, 0.29, 0.54 and 1.1 kW·cm^{-2}. For glucocorticoid receptor measurements in live cells, laser intensity of 0.72 μW (0.54 kW·cm^{-2}) was used.

For transfection efficiency analysis, transfected cells were stained using the cell-permeable nuclear dye NucBlue™ Live ReadyProbes™ Reagent (Hoechst33342; Invitrogen). Hoechst33342 and eGFP, mStayGold or StayGold/E138D were excited using the 405 nm laser and the 488 nm laser line of the Ar-ion laser, respectively. The pinhole size was set to a maximum value (600 μm) to observe all fluorescence. Hoechst33342 fluorescence was detected in the 419–500 nm range using a PMT detector, and in the 500–550 nm range for eGFP, mStayGold or StayGold/E138D using the GaAsP detector. To minimize the signal crosstalk, the multi-track imaging mode was used.

2.5. FCS data analysis

FCS data were analyzed using the ZEN software (Carl Zeiss). Autocorrelation curves (ACCs) were generated by plotting as a function of the lag time (τ) the autocorrelation function ($G(\tau)$) calculated as:

$$G(\tau) = \frac{\langle I(t) \bullet I(t+\tau) \rangle}{\langle I(t) \rangle^2} \tag{1}$$

where $I(t)$ is the fluorescence intensity at time t.

The autocorrelation curves were analyzed by fitting, using for eGFP, mStayGold or StayGold/E138D in live cells a one-component anomalous diffusion model [21]:

$$G(\tau) = G(\infty) + \left(1 + \frac{F_t \bullet e^{-\frac{\tau}{\tau_t}}}{1 - F_t}\right) \bullet \frac{1}{N} \bullet \left[\frac{1}{1 + \left(\frac{\tau}{\tau_D}\right)^{\alpha}}\right] \bullet \left[\frac{1}{1 + \frac{1}{S^2} \bullet \left(\frac{\tau}{\tau_D}\right)^{\alpha}}\right]^{\frac{1}{2}} \tag{2}$$

A two-component free 3D diffusion model was used for eGFP-GR and mStayGold-GR in the cytoplasm in untreated live cells (Eq. (3) with $i = 2$), whereas a three-component free 3D diffusion model (Eq. (3) with $i = 3$) was used for eGFP-GR or mStayGold-GR in the nucleus after treatment with 500 nM Dex:

$$G(\tau) = G(\infty) + \left(1 + \frac{F_t \bullet e^{-\frac{\tau}{\tau_t}}}{1 - F_t}\right) \bullet \frac{1}{N} \bullet \sum_{i=1}^{2\ or\ 3} F_i \bullet \left(\frac{1}{1 + \frac{\tau}{\tau_{D,i}}}\right) \bullet \left(\frac{1}{1 + \frac{\tau}{S^2 \bullet \tau_{D,i}}}\right)^{\frac{1}{2}} \tag{3}$$

In Eq. (2) and Eq. (3), F_t is the average fraction of fluorescent molecules in the triplet state; τ_t is the average relaxation time of the triplet state; N is the average number of fluorescent molecules in the effective volume element; F_i is the relative molar fraction of the i-th component ($F_1 + F_2 = 1$ in the two-component free 3D diffusion model and $F_1 + F_2 + F_3 = 1$ in three-component free 3D diffusion model); $\tau_{D,i}$ is the average diffusion time of the i-th component; S is the structure parameter ($S = z/w$) which is the ratio of the axial (z) to lateral (w) radii of the effective volume element; $G(\infty)$ is the offset at infinite lag time. In Eq. (2), α is the anomalous diffusion exponent that is $\alpha \neq 1$ for translational motion through complex/disordered systems and $\alpha = 1$ for normal, Brownian motion.

Since GRs bind in the cell nucleus to the genomic DNA, we have also performed fitting analysis using the so-called binding models (for details, see Supplementary Information), a two-component free 3D diffusion with one-component binding (Eq. (4)) and the one-component free 3D diffusion with two-component binding (Eq. (5)):

$$G(\tau) = G(\infty) + \left(1 + \frac{F_t \bullet e^{-\frac{\tau}{\tau_t}}}{1 - F_t}\right) \bullet \frac{1}{N} \bullet \left[F_1 \bullet \left(\frac{1}{1 + \frac{\tau}{\tau_{D,1}}}\right) \bullet \left(\frac{1}{1 + \frac{\tau}{S^2 \bullet \tau_{D,1}}}\right)^{\frac{1}{2}} + F_2 \bullet \left(\frac{1}{1 + \frac{\tau}{\tau_{D,2}}}\right) \bullet \left(\frac{1}{1 + \frac{\tau}{S^2 \bullet \tau_{D,2}}}\right)^{\frac{1}{2}} + (1 - F_1 - F_2) \bullet e^{\left(-k_{B,1} \bullet \tau\right)}\right] \tag{4}$$

$$G(\tau) = G(\infty) + \left(1 + \frac{F_t \bullet e^{-\frac{\tau}{\tau_t}}}{1 - F_t}\right) \bullet \frac{1}{N} \bullet \left[F_1 \bullet \left(\frac{1}{1 + \frac{\tau}{\tau_{D,1}}}\right) \bullet \left(\frac{1}{1 + \frac{\tau}{S^2 \bullet \tau_{D,1}}}\right)^{\frac{1}{2}} + F_2 \bullet e^{\left(-k_{B,1} \bullet \tau\right)} + (1 - F_1 - F_2) \bullet e^{\left(-k_{B,2} \bullet \tau\right)}\right] \tag{5}$$

where $k_{B,1}$ and $k_{B,2}$ are rate constants determining the kinetics of GR binding to the genomic DNA [53].

When fitting Eq. (4) or Eq. (5) to the experimental ACCs, diffusion time of the first component ($\tau_{D,1}$) was fixed to the value measured for

eGFP-GR or mStayGold-GR in the cytoplasm before Dex treatment, since this component originates from the free 3D diffusion of these molecules in the cytoplasm/nucleus.

Values of the lateral (w) and axial (z) radii of the effective volume element were determined in calibration measurements using the ATTO488 dye ($D_{ATTO488} = 400\ \mu m^2 s^{-1}$) [54]:

$$w = \sqrt{4 \bullet D_{ATTO488} \bullet \tau_{D,ATTO488}} \tag{6}$$

$$z = w \bullet S \tag{7}$$

$$V_{eff} = \pi^{\frac{3}{2}} \bullet w^2 \bullet z \tag{8}$$

where $D_{ATTO488}$ is the diffusion coefficient of ATTO488, and $\tau_{D,ATTO488}$ is the diffusion time of ATTO488. V_{eff} is the effective detection volume. The diffusion coefficients were calculated from the corresponding experimentally measured diffusion times and the lateral radius determined as described above (Eq. (6)).

The average number of eGFP, mStayGold, StayGold/E138D, eGFP-GR and mStayGold-GR were obtained from the fitting analysis. To compare the apparent brightnesses of eGFP, mStayGold and StayGold/E138D and quantitatively characterize homodimerization of eGFP-GR and mStayGold-GR, counts *per* second *per* molecule (*CPM*) were calculated as:

$$CPM_i = \frac{I_i}{N_i} \tag{9}$$

where i denotes eGFP, mStayGold, StayGold/E138D, eGFP-GR or mStayGold-GR; I_i is the average fluorescence intensity in counts *per* second, and N_i the number of molecules of the corresponding species determined by fitting analysis.

We have furthermore calculated the fraction of monomer (F_m) and homodimer (F_d) from the relative molecular brightness (R) as follows [55]:

$$R = \frac{CPM_j}{CPM_k} \tag{10}$$

$$F_m = \frac{4 - 2R}{3 - R} \tag{11}$$

$$F_d = \frac{R - 1}{3 - R} \tag{12}$$

where j denotes eGFP-GR or mStayGold-GR; k denotes eGFP or mStayGold; *CPM* is the counts *per* second *per* molecule calculated using (Eq. (9)). We confirmed that the brightness of homodimers is twice that of a monomer, $CPM^{norm}_{eGFP\ dimer} = 1.98 \pm 0.08$; and $CPM^{norm}_{mStayGold\ dimer}$: 1.97 ± 0.15 (Fig. S1). The dissociation constant of GR homodimerization is determined by using both linear regression analysis without and with Deming method (Eq. (13)) and histogram analysis of the dissociation constant of GR homodimerization in each single-cell data:

$$K_{d,homo} = \frac{[C_m]^2}{[C_d]} \tag{13}$$

$$[C_m] = F_m \bullet [C_l] \tag{14}$$

$$[C_d] = F_d \bullet [C_l] \tag{15}$$

where $K_{d,homo}$ denotes the dissociation constant of eGFP-GR or mStayGold-GR homodimers; $[C_m]$ and $[C_d]$ are the concentration of monomeric and homodimeric eGFP-GR or mStayGold-GR, respectively; $[C_l]$ is the concentration of eGFP-GR or mStayGold-GR obtained from FCS measurements (with l denoting eGFP-GR or mStayGold-GR).

2.6. Massively parallel FCS integrated with fluorescence lifetime imaging microscopy (mpFCS/FLIM)

The optical setup for mpFCS/FLIM is described in detail in our previous work [21]. Briefly, the instrument was built using an inverted epi-fluorescence microscope Axio Observer D1 equipped with a C-Apochromat 63×/1.2 W Corr objective lens (Carl Zeiss, Germany) and a filter set (Filter Set 38 HE; Ex BP 470/40 nm, long pass dichoric mirror with a cutoff wavelength of 495 nm, Em BP 525/50 nm) for eGFP, mStayGold and StayGold/E138D. A direct current-modulated picosecond 482 nm laser (Laser Diode Head LDH-D-C-485, PicoQuant, Germany) was used as the excitation light source. The laser was driven by a Picosecond Pulsed Diode Laser Driver (PDL 800-D), allowing operation in either continuous wave (CW) mode or pulsed mode. A Diffractive Optical Element (DOE; Holoeye, Germany) was used to precisely create a spot-wise 16 × 16 illumination pattern that matches centrally positioned 16 × 16 single-photon avalanche diodes (SPADs) on the SPC3 camera with 64 × 32 circular SPADs (Micro Photon Devices MPD, Italy). To enable fast sample localization, an 18.0 megapixel digital single-lens reflex (DSLR) camera EOS 600D (pixel size of 18.5 μm^2 and pixel pitch of 4.3 μm; Canon Inc., Japan) was coupled to the side port of the microscope opposite to the SPC3 camera, and the light path between the two camera ports was manually switched.

2.7. mpFCS/FLIM data acquisition and analysis

For mpFCS measurements, 1,048,575 frames were acquired at a temporal resolution of 20 μs/frame. Fluorescent molecules were excited using 2.1 μW (1.43 $kW \cdot cm^{-2}$) laser power *per* spot (total 535 μW), yielding 256 fluorescence intensity fluctuation traces recorded over 20.97 s. For mStayGold-GR measurements, 15 min after treatment with 500 nM Dex, the same number of frames was acquired at a temporal resolution of 40 μs/frame, lasting 41.94 s.

The ACCs were calculated using our home-built dedicated mpFCS software for fast auto- and cross-correlation analysis by parallel signal processing using a graphic processing unit (GPU), allowing temporal autocorrelation across all pixels in the image frame in 1 s and cross-correlation between first- and second-order neighbor pixels in several seconds [21]. Fitting analysis using the one-component anomalous diffusion model (Eq. (2)), was performed for eGFP, StayGold/E138D and mStayGold. To this aim, the Origin Data Analysis and Graphing software (OriginLab) was used. Fitting analysis for mStayGold-GR was performed by two-component free diffusion model (Eq. (3), $i = 2$) in the cytoplasm and the three-component free diffusion model (Eq. (3), $i = 3$) in the nucleus.

For glucocorticoid receptor translocation analysis, we analyzed two-foci cross-correlation curves (tfCCCs) as previously described [22]. A schematic diagram on the tfCCC analysis is drawn in Fig. S2. In brief, the Origin Data Analysis and Graphing software (OriginLab) was used to compute the tfCCCs between foci in the cytoplasm and nucleus. To reduce the calculation cost, the photon count data was integrated into 4 ms bins. Of note, the photobleaching correction before tfCCCs calculation was not needed in the case of mStayGold due to its remarkable photostability!

The arbitrarily assigned as forward $G_c^{c,n}(\tau)$, reflecting molecular transport from the cytoplasm to the cell nucleus, and the backward $G_c^{n,c}(\tau)$, designating the cell nucleus to cytoplasm translocation tfCCCs are defined as follows:

$$G_c^{c,n}(\tau) = \frac{\langle I^n(t) \bullet I^c(t+\tau) \rangle}{\langle I^n(t) \rangle \bullet \langle I^c(t) \rangle} \tag{16}$$

$$G_c^{n,c}(\tau) = \frac{\langle I^c(t) \bullet I^n(t+\tau) \rangle}{\langle I^n(t) \rangle \bullet \langle I^c(t) \rangle} \tag{17}$$

where $I^n(t)$ *and* $I^c(t)$ are time series of fluorescence intensity fluctuations recorded in the selected pixels in the nucleus and cytoplasm,

respectively.

We further calculate the so-called subtracted tfCCC, $G_{c,sub}(\tau)$:

$$G_{c,sub}(\tau) = G_c^{c,n}(\tau) - G_c^{n,c}(\tau) \quad (18)$$

to readily visualize the translocation direction as positive (nuclear import) or negative peaks (nuclear export).

FLIM data acquisition and analysis were performed as previously described [21,56]. In brief, the signal was acquired for 5 min to obtain low-noise FLIM curves necessary to enable precise fitting analysis. By fitting a one-component exponential decay function:

$$I(t) = I_{off} + A exp\left(-\frac{t - t_0}{\tau_f}\right) \quad (19)$$

to the FLIM curves using our dedicated mpFCS software, fluorescence lifetime of eGFP, StayGold/E138D and mStayGold in live-HEK cells were determined. In Eq. (19), $I(t)$ denotes photon cunts at time t, I_{off} is the offset due to background photon counts, A is the amplitude of the FLIM curve, and τ_f is the fluorescence lifetime of eGFP, StayGold/E138D or mStayGold. In each cell, the fluorescence lifetime was calculated as an average from 16 to 100 independent positions in the cell.

3. Results

3.1. Monomeric StayGold variants are twice as bright as eGFP in live HEK cells

To measure the brightness of the different GFP variants in live cells, we transiently expressed eGFP, mStayGold or StayGold/E138D in live HEK cells (Fig. 1A) and used conventional spFCS to measure their brightness (Fig. 1B-D). Our unique mpFCS/FLIM system was used to measure fluorescence lifetime (Fig. S3).

Temporal ACCs in live cells (Fig. 1B), reflecting the diffusion of the investigated GFP variants, overlapped to a very large extent, suggesting that their diffusion is similar. Fitting the one-component anomalous diffusion model to these ACCs (Fig. S4), diffusion times and the average number of molecules were determined, and the diffusion coefficients (Fig. 1C) and CPMs, reflecting on apparent molecular brightness (Fig. 1D) were calculated. As expected, diffusion coefficients and anomalous diffusion exponents were not significantly different between different GFP variants (Fig. 1C, S5A), whereas molecular brightness of both monomeric StayGold variants was twice that of eGFP (Fig. 1D). This may lead to the reduction of chi-square value *per* degree of freedom in the fitting analysis (Fig. S5C).

Apparent molecular brightness measured for all three GFP variants shows linear correlation with the excitation laser intensity at the objective lens (Fig. 2A). Apparent molecular brightness of mStayGold and StayGold/E138D relative to that of eGFP, *i.e.*, relative molecular brightness according to Eq. (10), is $R = (2 \pm 0.07)$, and remains roughly the same in the whole range of laser intensities tested (Fig. 2B), suggesting that mStayGold and StayGold/E138D achieve the same signal-to-noise ratio with half the laser power. Of note, while a downward trend in relative molecular brightness as a function of excitation intensity is apparent in Fig. 2B, the difference is not statistically significant in the range of excitation intensities tested. However, if confirmed for even higher excitation intensities, this downward trend may suggest that

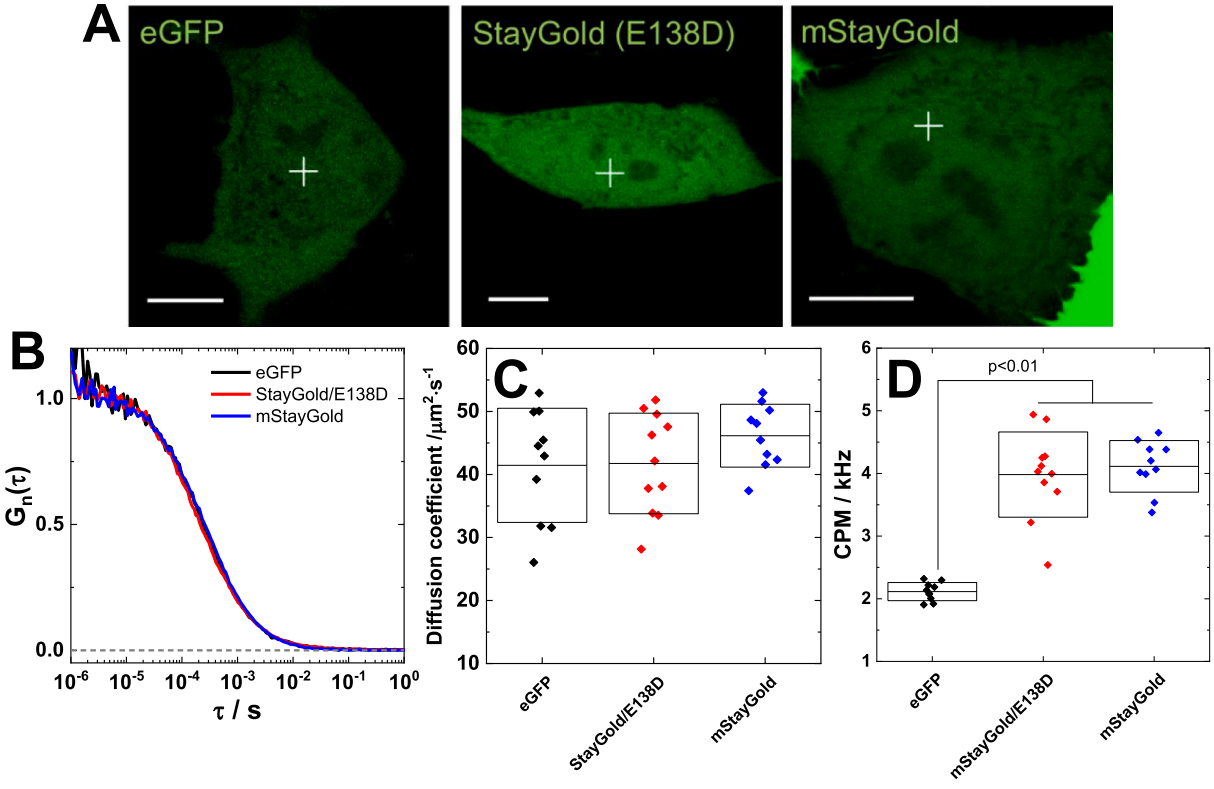

Fig. 1. The intracellular distribution and diffusion of monomeric StayGold variants are indistinguishable from those of eGFP, but they are twice as bright. **(A)** Confocal Laser Scanning Microscopy (CLSM) images of HEK cells expressing eGFP (left), StayGold/E138D (middle) or mStayGold (right). White cross indicates the position at which FCS measurement were performed. Scale bar: 10 μm. **(B)** Autocorrelation curves (ACCs) normalized to the same amplitude, $G_n(\tau) = 1$ at $\tau = 10$ μs, reflecting the dynamics of eGFP (black), StayGold/E138D (red) and mStayGold (blue) in HEK cells. **(C)** Diffusion coefficients of eGFP (black), StayGold/E138D (red) and mStayGold (blue) derived by fitting analysis. **(D)** Apparent molecular brightness of eGFP (black), StayGold/E138D (red) and mStayGold (blue) expressed as counts *per* second *per* molecule (CPM). The middle lines and box edges indicate the mean value and standard deviation, respectively. Data analysis was performed using the one-way ANOVA test with *post hoc* Tukey test. A statistically significant difference was not observed, $p > 0.05$. (For interpretation of the references to colour in this figure legend, the reader is referred to the web version of this article.)

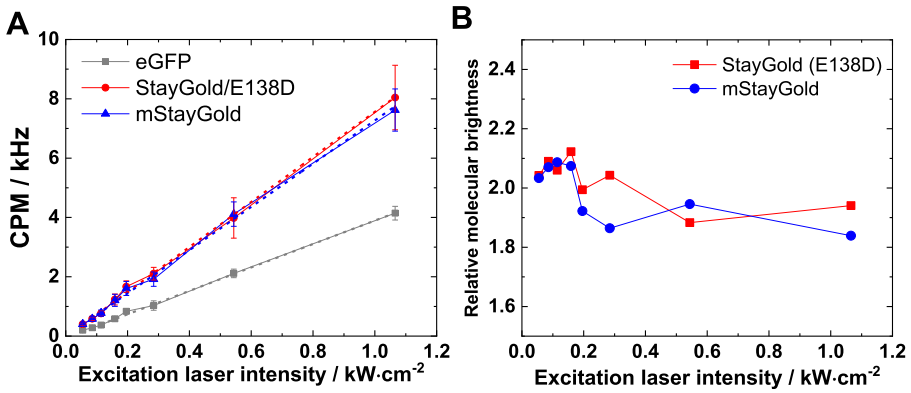

Fig. 2. Excitation-intensity-independent brightness of monomeric StayGold variants compared to eGFP. **(A)** Apparent brightness of eGFP (black), StayGold/E138D (red) or mStayGold (blue) linearly increases as a function of the excitation laser intensity at 488 nm in the range of intensities tested. Average CPM values and corresponding standard deviations were calculated from 10 single-cell data recordings. Linear regression analysis yielded Pearson's correlation coefficient > 0.99. The slopes, reflecting the average apparent molecular brightness across the range of laser intensities tested, were: $slope_I^{eGFP} = 2.95 \pm 0.04$, $slope_I^{StayGold/E138D}$ 5.67 ± 0.09 and $slope_I^{mStayGold} = 5.42 \pm 0.11$. **(B)** Relative molecular brightness as a function of excitation intensity. In the range of excitation laser intensities tested, $R_{StayGold/E138D} = 2.02 \pm 0.08$ and $R_{mStayGold} = 1.98 \pm 0.1$. The two-tailed Student's *t*-test indicated no significant difference between the monomeric StayGold variants. (For interpretation of the references to colour in this figure legend, the reader is referred to the web version of this article.)

subtle differences in saturation kinetics may exist between the monomeric StayGold variants and eGFP.

Fluorescence lifetime (Fig. S3) of both monomeric StayGold variants, $\tau_f^{mStayGold} = (2.90 \pm 0.01)$ ns and $\tau_f^{StayGold/E138D} = (2.88 \pm 0.02)$ ns, is somewhat longer than that of eGFP, $\tau_f^{eGFP} = (2.50 \pm 0.03)$ ns, in good agreement with previous report [43].

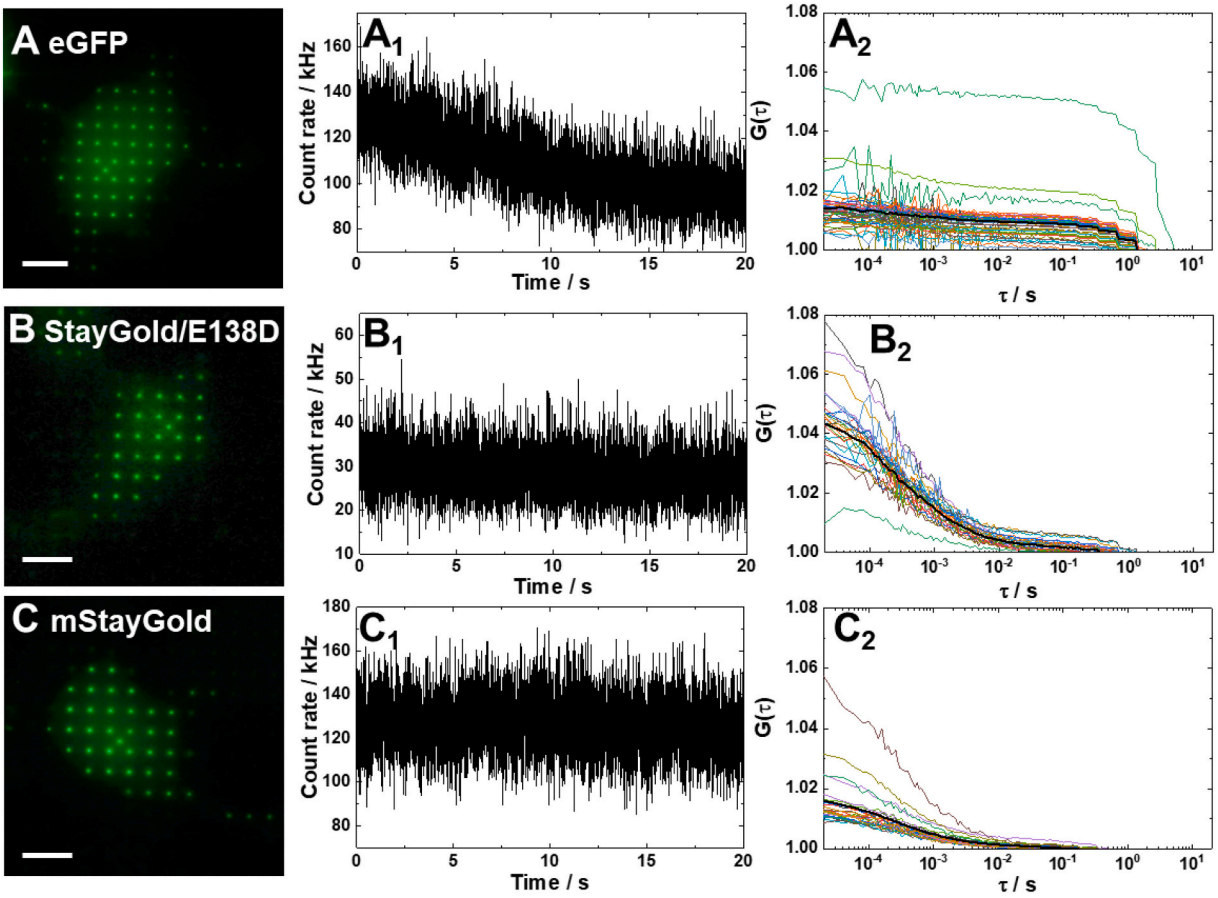

Fig. 3. Monomeric StayGold variants with enhanced photostability facilitate photobleaching-free mpFCS measurements in live cells. **(A, B, C)** Fluorescence microscopy images showing the intracellular localization of eGFP (A), StayGold/E138D (B) and mStayGold (C) in live HEK cells acquired using spot-wise illumination and the DSLR Canon camera coupled to the side port of the mpFCS system. Scale bar: 10 μm. **(A_1, B_1, C_1)** Corresponding fluorescence intensity fluctuation time series showing prominent photobleaching in eGFP-expressing HEK cells (A_1) and photobleaching-free time series acquired in mStayGold- or StayGold/E138D-expressing cells (B_1 and C_1). **(A_2, B_2, C_2)** Corresponding temporal autocorrelation curves (ACCs) derived in all cells from first acquired time series in each cell. Autocorrelation curves of eGFP after the photobleaching are shown in Fig. S7A.

3.2. Enhanced photostability of monomeric StayGold variants enables photobleaching-free mpFCS measurements

Results of mpFCS measurements in live HEK cells transiently expressing eGFP, mStayGold or StayGold/E138D are summarized in Fig. 3. In line with data shown in Fig. 1A, mpFCS shows uniform fluorescence intensity distribution of all three GFP variants in live HEK cells (Fig. 3A-C). However, fluorescence intensity significantly decreased over time for mpFCS measurements in HEK cells expressing eGFP (Fig. 3 A_1), while it remained unchanged in HEK cells expressing StayGold/E138D (Fig. 3 B_1) or mStayGold (Fig. 3 C_1). This was also reflected in the raw ACCs, derived without applying the photobleaching correction (Fig. 3 A_2-C_2). Here, temporal autocorrelation analysis yielded for measurements in eGFP-expressing cells ACCs with two characteristic decay times and a high relative amplitude of the component with the long decay time that is characteristic of photobleaching (Fig. 3 A_2 and S6A). This is markedly different from the ACCs acquired in StayGold/E138D- or mStayGold-expressing cells (Fig. 3 B_2 and Fig. 3 C_2, respectively) that showed a high relative amplitude of the component with the short decay time, which is reflecting protein diffusion within the cells, and a very low relative amplitude, if at all, for the component with the long decay time that is characteristic of drawn-out fluorescence intensity fluctuation from slow processes (Fig. S6B). Photobleaching correction in the fluorescence intensity fluctuation using the 4th-degree polynomial function to account for slow changes in the average fluorescence intensity due to photobleaching, makes it possible to remove these slower decays (Fig. S6C, D).

Of note, following several initial mpFCS measurements in eGFP-expressing cells a more stable fluorescence signal is obtained, yielding ACCs with a short decay time component and a barely visible long decay time component that is characteristic of photobleaching (Fig. S7A). However, the corresponding single-pixel ACCs were noisier than those acquired for monomeric StayGold variants (Fig. S7B). And, the low SNR affected the precision of the curve fitting analysis (Fig. S5C), causing large deviations in the calculated diffusion coefficients and anomalous diffusion exponents (Fig. S5B and S7C).

In addition, eGFP apparent molecular brightness, reflected through CPM, seems to be 4 times lower than that of mStayGold or StayGold/E138D (Fig. S7D). This is possibly due to dynamic quenching of eGFP, presumably by reactive oxygen species (ROS) generated during prebleaching (Fig. S8).

3.3. Enhanced brightness and photostability of mStayGold improve live-cell analysis of glucocorticoid receptor (GR) binding to genomic DNA

Functional proteins with lower mobility such as DNA-bound transcription factors are more easily photobleached than their unbound counterparts that freely diffuse through the nuclear lumen. Using the glucocorticoid receptor (GR) as a transcription factor model, we have characterized in live HEK cells mStayGold-GR binding (Fig. 4) – of note, due to lower transfection efficiency of StayGold/E138D in HEK cells (Fig. S9), we have not proceeded with StayGold/E138D-GR.

CLSM imaging clearly showed the cytoplasmic localization of both GR constructs, eGFP-GR and mStayGold-GR, in untreated HEK cells (Fig. 4A, left). After 30 min treatment with 500 nM Dex, nuclear localization is clearly observed (Fig. 4A, right). FCS measurements reveal slower diffusion in the cell nucleus of both GR constructs, due to GR binding to the genomic DNA (Fig. 4B and C). To characterize GR diffusion properties, we tested several fitting models for both, eGFP-GR and mStayGold-GR in the cytoplasm of untreated cells (Fig. S10A_1 and B_1) and in the cell nucleus of Dex-treated cells (Fig. S10A_2, A_3, B_2 and B_3). In untreated cells, both one-component anomalous diffusion model and two-component free 3D diffusion model could well fit the ACCs. However, the fit residues were larger when in subsequent analyses the diffusion time obtained from the one-component anomalous diffusion model was used. We have therefore decided to apply throughout the two-component free diffusion model. This model is consistent with the notion that the cytoplasmic pool of GRs consists of freely diffusing GRs and GRs bound to other molecules, forming cytoplasmic components of lower mobility. In the nucleus of Dex-treated cells, three-component models (Fig. S10A_3 and B_3) were needed as the agreement with two-component models was poor (Fig. S10A_2 and B_2). Fitting residuals were, however, nearly identical between the free diffusion model (Eq. (3)) and the binding model (Eqs. (4) and (5)). We have therefore decided to proceed using the three-component free 3D diffusion model (Eq. (3)), fixing the diffusion time of the first component to the value determined for free 3D diffusion of GR in the cytoplasm. The second and the third component, related to GR binding to the genomic DNA, were allowed to freely vary. Superior mStayGold brightness and photostability lead to less noisy ACCs and significantly improved chi-squared values (Fig. S11).

The diffusion time of mStayGold-GR is longer than that of eGFP-GR, as evident from the shift of the ACC to longer lag times (Fig. S12A and B), yielding in the cytoplasm of untreated cells $\tau_D^{mStayGold-GR} = (1.8 \pm 0.6)$ ms) and ($\tau_D^{eGFP-GR} = (1.0 \pm 0.3)$ ms (Fig. S12C_1). This apparent difference in diffusion time is likely because of eGFP photobleaching before it exits the effective volume element, due to which it appears as if the molecule has traversed it in a shorter time. Faster eGFP photobleaching compared to mStayGold may also explain why the fraction of bound mStayGold-GR appears to be higher than that of eGFP-GR (Fig. S12D_1 and D_2).

DNA-bound fraction did not show clear concentration dependence (Fig. S13), likely due to the narrow range of GR concentration tested.

3.4. Enhanced brightness and photostability of mStayGold improve the precision of determining the dissociation constant of glucocorticoid receptor homodimerization via molecular brightness analysis

Molecular brightness of fluorescently labelled proteins is sensitive to homo-oligomerization, making molecular brightness analysis a powerful tool for characterizing homo-oligomerization. Classical view on GR activation is that ligand binding to cytoplasmic GR dissociates the heteromolecular complex in which it resides, leading to GR translocation and subsequent homodimerization and possibly also homotetramerization in the cell nucleus, followed by the homo-GR complexes binding to GREs to regulate gene expressions. Given that GR homotetramers were only observed in genetically modified cells containing many GRE sequences on the mouse mammary tumor virus (MMTV) promoter array [47,57,58], and that even in these cells the GR homodimer in the nucleoplasm was significantly more abundant than the homotetramer [47,59], we have, in the first approximation, disregarded GR homotetramerization and used brightness analysis to examine GR homodimerization in the cytoplasm and cell nucleus.

As a first step, we measured the apparent brightness of eGFP and mStayGold in cells expressing these fluorescent proteins only and used these values to determine the relative molecular brightnesses (R) of eGFP-GR and mStayGold-GR against the apparent brightness of the corresponding monomeric GFP variant eGFP or mStayGold, respectively (Eq. (10)). We further calculated the monomeric/homodimeric fractions, F_m and F_d, according to Eq. (11) and Eq. (12), respectively. Linear regression analysis without the Deming method of the relationship $[C_m]^2 = f(C_d)$ according to Eq. (13), yielded the dissociation constant for GR homodimerization ($K_{d,homo}$) (Fig. 4 D and E). In the cytoplasm of untreated HEK cells, the $K_{d,homo}$ values were determined to be $K_{d,homo,cyto}^{eGFP-GR}$ = 11.2 μM ($R^2 = 0.88$) and $K_{d,homo,cyto}^{mStayGold-GR}$ = 8.8 μM ($R^2 = 0.92$) (Fig. 4D_1). Since each measurement enables us to compute the dissociation constant, histogram analysis was applied, yielding $K_{d,homo,cyto}^{eGFP-GR} = (8.2 \pm 6.5)$ μM and $K_{d,homo,cyto}^{mStayGold-GR} = (7.1 \pm 3.6)$ μM (Fig. 4 D_2), which are in good agreement with the values obtained by linear regression analysis.

Following the same procedure, the dissociation constant of eGFP-GR

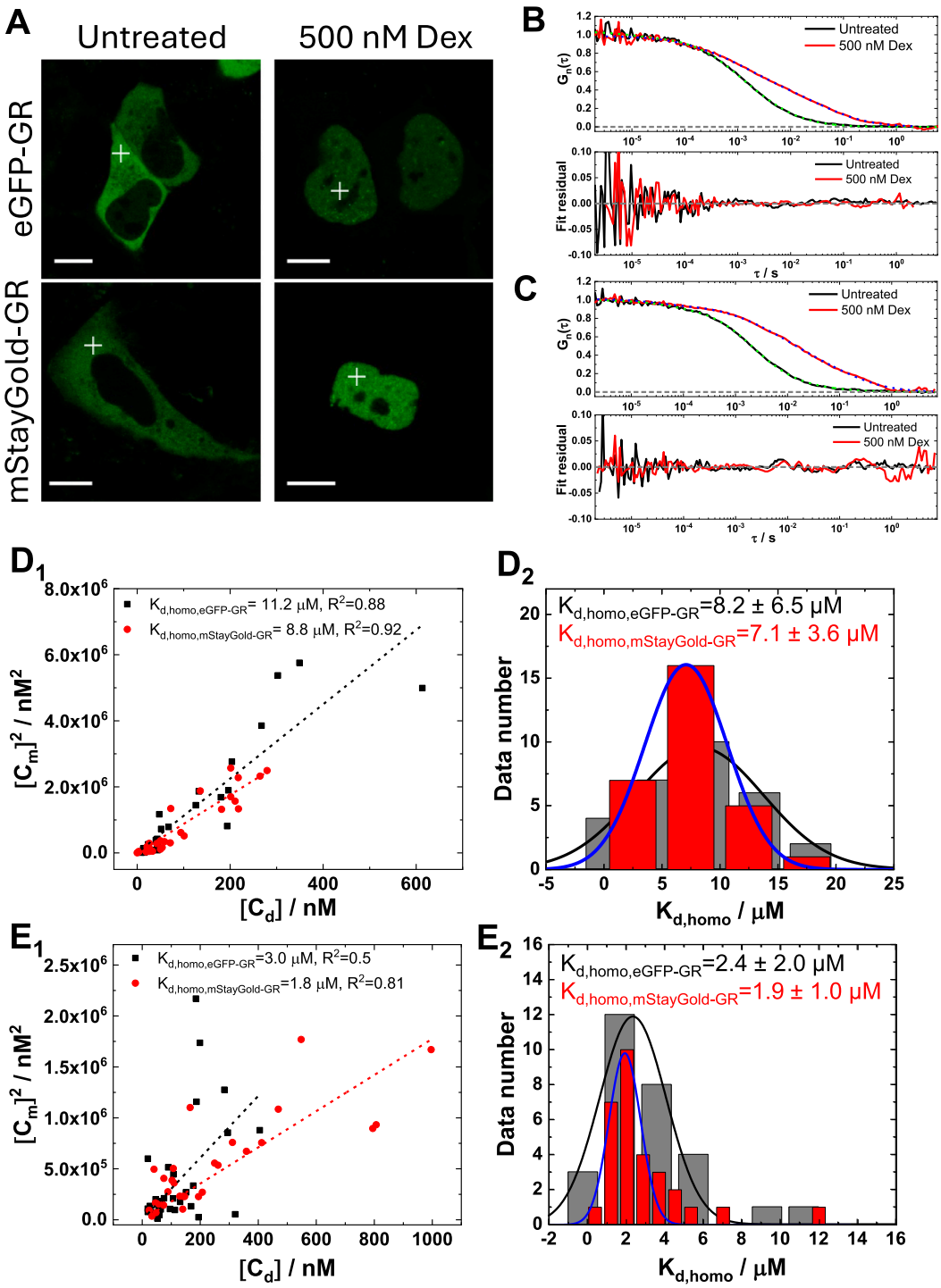

Fig. 4. Enhanced brightness and photostability of mStayGold improve live-cell analysis of glucocorticoid receptor (GR) homodimerization by brightness analysis. **(A)** Confocal fluorescence microscopy images of HEK cells expressing eGFP-GR (top) or mStayGold-GR (bottom) in untreated cells (left) or cells treated with 500 nM Dex (right). White crosses indicate the positions at which FCS measurements were performed. Scale bar: 10 μm. **(B, C)** Autocorrelation curves (ACCs) normalized to the same amplitude, $G_n(\tau) = 1$ at $\tau = 10$ μs, (top) and corresponding fit residuals (bottom), reflecting the dynamics of eGFP-GR (B) and mStayGold-GR (C) in the cytoplasm of untreated HEK cells (black) and the nucleus in cells treated with 500 nM Dex for 30 min (red). Green- and blue-dashed curves represent the best fit of two-component and three-component free diffusion model, respectively. **(D_1, D_2, E_1, E_2)** Apparent dissociation constant of eGFP-GR homodimers (black) and mStayGold-GR homodimers (red) in the cytoplasm of untreated cells (D_1, D_2) and in the nucleus of cells treated with 500 nM Dex for 30 min (E_1, E_2). Linear regression analysis (D_1, E_1) and Gaussian curve fitting applied to histograms (D_2, E_2) determined the dissociation constant, $K_{d,homo}$, for the eGFP-GR and the mStayGold-GR homodimer complexes. (For interpretation of the references to colour in this figure legend, the reader is referred to the web version of this article.)

or mStayGold-GR homodimer complexes in the nucleus of Dex-treated cells were determined to be $K_{d,homo,nuc}^{eGFP-GR}$ = 3.0 μM (R^2 = 0.5) and $K_{d,homo,nuc}^{mStayGold-GR}$ = 1.8 μM (R^2 = 0.81) (Fig. 4 E_1). Similar dissociation constant values were obtained by histogram analysis, yielding $K_{d,homo,nuc}^{eGFP-GR}$ = (2.4 ± 2.0) μM and $K_{d,homo,nuc}^{mStayGold-GR}$ = (1.9 ± 1.0) μM (Fig. 4 E_2). These values are in good agreement with data from live U2OS cells obtained using Fluorescence Cross-Correlation Spectroscopy (FCCS) [32]. We also tested linear regression analysis with the Deming method (Fig. S14), observing that fitting the scattered data of eGFP-GR in cells treated with 500 nM Dex, is not satisfactory. The Deming method required a dataset with small deviations to determine the dissociation constants, and the mStayGold-GR data met these requirements.

As expected, the relative standard deviation (defined as the ratio of the sample standard deviation to the sample average) was smaller for measurements using the brighter and more photostable mStayGold fluorophore than eGFP, as can be seen from the obtained values: 0.79 *vs* 0.51 in the cytoplasm of untreated cells and 0.83 *vs* 0.52 in the nucleus of Dex-treated cells. But, even in measurements where mStayGold was used, the relative standard deviation was rather high, around 0.5, suggesting that other factors such as heterogeneity of chromatin structure for measurements at different positions in the cell nucleus affect the dispersion of the data.

3.5. *mStayGold facilitates spatial mapping of glucocorticoid receptor dynamics and transport*

In our previous work, eGFP-GR nucleocytoplasmic shuttling was characterized in live cells at different positions along the nuclear envelope 15 min after treatment with 500 nM Dex, *i.e.*, at the half time of ligand-induced eGFP-GR nuclear import [22]. Here, we characterized mStayGold-GR nucleocytoplasmic translocation using mpFCS (Fig. 5). Under the same conditions as before, 15 min after initiating the treatment with 500 nM Dex, mStayGold-GR has largely translocated into the cell nucleus (Fig. 5A, left), whereas a comparatively small amount of mStayGold-GR was still present in the cytoplasm, as can be seen in the highly contrasted image (Fig. 5A, right). Using mpFCS, we could simultaneously record fluorescence intensity fluctuations at different locations in the cytoplasm and the cell nucleus, obtaining ACCs at all locations (Fig. 5B). As expected, the average ACC recorded in the cell nucleus was characterized by significantly longer decay time than the one recorded in the cytoplasm (Fig. 5C), consistent with GR binding to the genomic DNA. Spatial mapping of diffusion times (Fig. 5D) clearly showed longer diffusion times, *i.e.*, slower mobility. In the cytoplasm, there was no statistically significant difference between the diffusion coefficients of the two components measured by spFCS in untreated cells and mpFCS in Dex-treated cells (Fig. 5E, left), which is consistent with our previous results showing that the effective volume in the spFCS and mpFCS systems are similar [21]. However, the relative fraction of the second component was significantly higher in treated *vs* untreated cells (Fig. 5E, right), consistent with GR binding to cytoplasmic structures (*e.g.*, microtubles) and/or protein complexes (*e.g.*, transporting machinery). Both spFCS and mpFCS showed that mStayGold-GR diffusion in the cell nucleus is complex, identifying at least three characteristic decay times, *i.e.*, three components. Fixing the diffusion time of the first component as described in the Methods section, diffusion times of the second/third component could be determined, yielding, as in the cytoplasm, similar values for spFCS and mpFCS measurements (Fig. 5F, left). While statistically significant difference was not observed for the fraction of the first component between the spFCS and mpFCS measurements, the relative amplitude of the second/third components were significantly different (Fig. 5F, right). To understand whether this difference is arising due to differences between spFCS, for which the data dispersion is reflecting differences between different cells, and mpFCS, which reflects intracellular differences, we have analyzed mpFCS data acquired on different cells (Fig. S15). This analysis suggests that the stepwise decay observed at long lag times, $\tau \approx 1$ s (red; Fig. 5C), is due to low data sampling at such long lag times in a time series that is acquired for 40 s, may contribute to these differences. In line with this, the difference in relative molar fractions arises due to the offset, the value of which needs to be estimated using the data fitting. Of note, a large spread of measured values is observed, suggesting that heterogeneity in the availability of DNA-binding sites within a single cell or among cells is important.

Two-foci cross-correlation (tfCCC) analysis ($G_c(\tau)$) used to characterize the direction of GR translocation and the passing time between the cytoplasm and the nucleus along the nuclear envelope (Fig. 5G), yielded the so-called subtracted CCCs, $G_{c,sub}(\tau) = G_{c,imp}(\tau) - G_{c,exp}(\tau)$, showing the direction of nuclear import/export as positive/negative peaks, respectively. Importantly, tfCCC with zero amplitude, *i.e.*, no tfCCC, was observed in cells expressing the fluorescent protein mStayGold. Nuclear import of mStayGold-GR was observed at sites: 2, 3, 4, 7, 8, 9, 10, 11, and 13 (Fig. 5H, red), whereas nuclear export of mStayGold-GR was observed at sites: 1, 5, 6, 12, 14, and 15 (Fig. 5H, blue). Integration of the subtracted CCCs clearly showed a curve with a positive peak (Fig. S16, black), indicating that mStayGold-GR is still being imported into the cell nucleus. Peaks in the subtracted CCCs occurred at lag times of (10−20) s, consistent with our previous data for eGFP-GR showing a peak width of (1−20) s. In contrast, mStayGold-GR improved fitting precision (Fig. S17). Also, peaks with extended width or a complex peak structure with multiple components are indicative of transport in both directions or through several nuclear pore complexes concomitantly observed in the same OVE. For example, a random walk characterized by alternating forward and backward motions can produce wider peaks, with peak-width depending on the frequency and extent of the directional changes.

4. Discussion

Photobleaching is a persistent challenge in fluorescence microscopy/correlation spectroscopy experiments. eGFP is widely used in live-cell fluorescence microscopy due to its brightness, photostability, monomeric size and absence of post-translational modifications. However, despite its relative photostability compared to other fluorescent proteins, eGFP still suffers from photobleaching during live-cell microscopy experiments.

To address this issue, brighter variants such as mNeonGreen have been developed [60,61], but photobleaching remained a limitation. Recently, a photostable dimeric GFP known as StayGold was introduced [42]. StayGold offers superior brightness and exceptional resistance to photobleaching. However, as a dimeric fluorescent tag, it can interfere with the functionality of the target protein. Hence, several monomeric variants of StayGold have been developed, including mStayGold, StayGold/E138D, and mBaojin [43–45]. These monomeric variants retain the brightness and photostability of the original dimeric StayGold, while minimizing potential functional disruptions to the protein of interest.

In this study, we have characterized the suitability of mStayGold and StayGold/E138D for conventional spFCS and mpFCS in live cells, which require prolonged recording of fluorescence intensity fluctuations leading likely to photobleaching even under low-intensity illumination. Photobleaching introduces an additional component in the ACC, with a long decay time that is typically in the (1−10) s range, causing underestimation of the number of molecules (due to an artificially large amplitude of the ACC) and "masks" the diffusion of slow-moving molecules.

To mitigate photobleaching effects, pre-bleaching before FCS experiments is typically used and/or photobleaching effects are accounted for in the analysis of fluorescence intensity fluctuations by incorporating photobleaching effects into fitting models. This may be done either by adding an offset for correlation at infinite time or by including photobleaching kinetics by adding an exponential decay curve in the data fitting function, as photobleaching typically follows an exponential

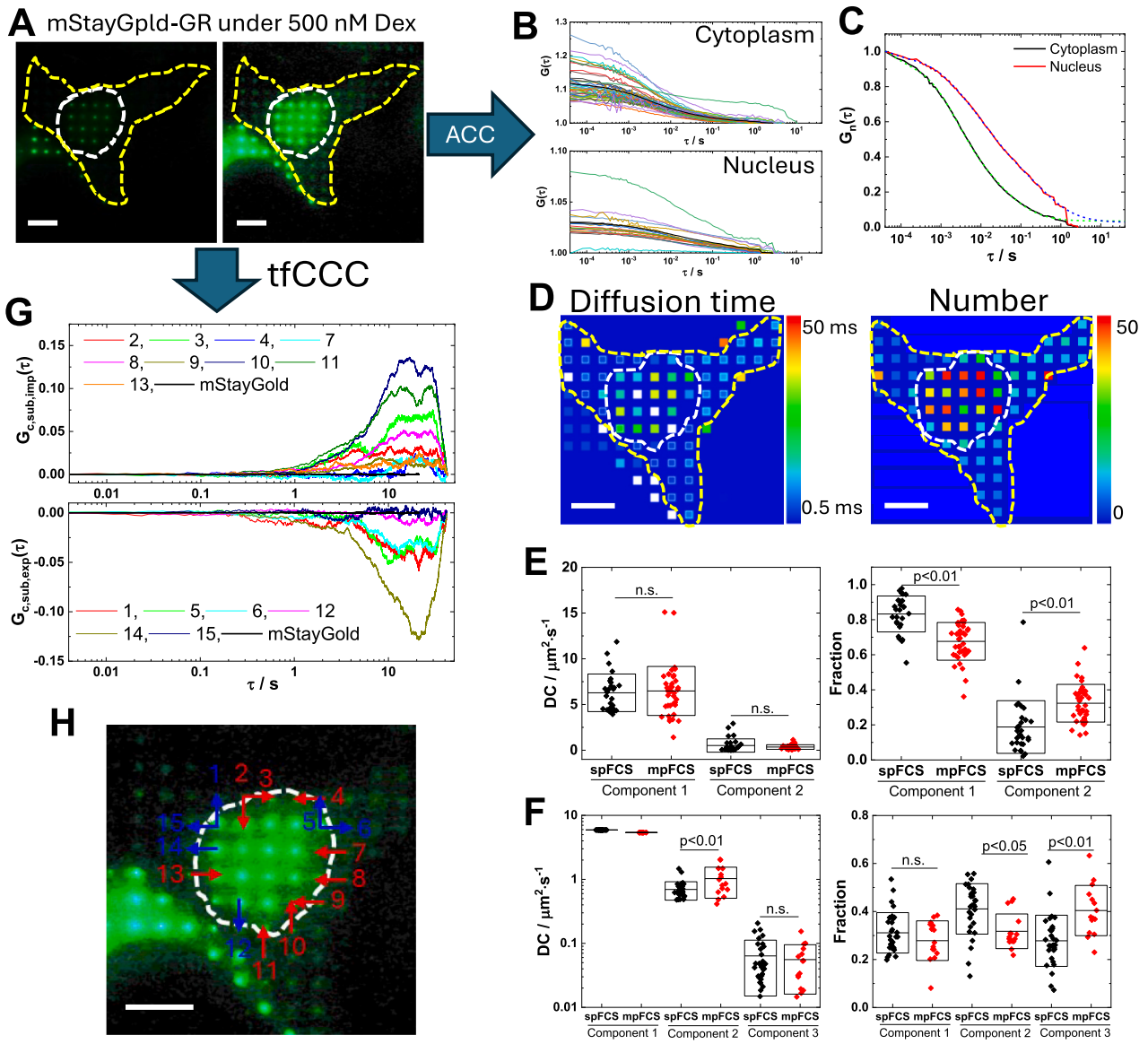

Fig. 5. Enhanced brightness and photostability of mStayGold improve live-cell analysis of GR diffusion and nuclear import/export. **(A)** Fluorescence microscopy images showing mStayGold-GR distribution in a live HEK cell acquired after 15 min incubation with 500 nM Dex using spot-wise illumination and the DSLR Canon camera coupled to the side port of the mpFCS system. *Left image:* Original fluorescence image without any change in brightness and contrast. *Right image:* Image brightness was adjusted to enhance contrast and render the cytoplasmic component visible. The yellow and white dashed lines indicate the positions of the cytoplasm and the nucleus, respectively. Scale bar: 10 μm. **(B)** Autocorrelation curves (ACCs) recorded in the cytoplasm (top) and the cell nucleus (bottom). **(C)** Average ACCs recorded in the cytoplasm (black) and the cell nucleus (red) normalized to the same amplitude, $G_n(\tau) = 1$ at $\tau = 40$ μs. Green-dashed and blue-dashed lines represent the best fit of two-component or three-component free diffusion models, respectively. **(D)** Spatial mapping of mStayGold-GR diffusion time (left; image presented without applying any pixel masking) and average number of molecules (right; pixel masking outside the cell was applied to enhance visibility). Scale bar: 10 μm. **(E)** Comparison of diffusion coefficients (DCs) (left) and relative molar fractions (right) of components 1 and 2 in the cytoplasm of untreated cells acquired using spFCS (black) or cells treated with 500 nM Dex for 15 min acquired using mpFCS (red). **(F)** Comparison of diffusion coefficients (DCs) (left) and relative molar fractions (right) between components 1, 2 and 3 in the nucleus of cells treated with 500 nM Dex for 15 min acquired using spFCS (black) and mpFCS (red). Here, the first component was fixed in the fitting analysis using the first component measured in the cytoplasm as representative of free 3D diffusion of GR. In the boxplots (E and F), the sample mean and standard deviation are represented by the middle line and boxes, respectively. Statistical analysis was performed using the one-way ANOVA test with *post hoc* Tukey test. Lack of statistically significant difference is denoted as n.s., $p > 0.05$. **(G)** The so-called subtracted cross-correlation curves $G_{c,sub,imp}(\tau)$ and $G_{c,sub,exp}(\tau)$ for all analyzed positions along the nuclear envelope shown in H. Briefly, two-foci cross-correlation analysis yields two two-foci cross-correlation curves (tfCCCs), one for each direction of calculation: from focus 1 in the cell nucleus to focus 2 in the cytoplasm, $G_{c,exp}(\tau)$, and conversely, from focus 2 in the cytoplasm to focus 1 in the cell nucleus, $G_{c,imp}(\tau)$. Their difference, the so-called subtracted cross-correlation curve, $G_{c,sub}(\tau) = G_{c,imp}(\tau) - G_{c,exp}(\tau)$, shows a positive amplitude for nuclear import, $G_{c,sub,imp}(\tau)$, and a negative amplitude for nuclear export, $G_{c,sub,exp}(\tau)$. **(H)** Fluorescence image shown in A (right) with numbers designating positions along the nuclear envelope where two-foci cross-correlation analysis was performed, and arrows showing the directions of mStayGold-GR nucleocytoplasmic translocation: nuclear import (red) and nuclear export (blue). Scale bar: 10 μm. (For interpretation of the references to colour in this figure legend, the reader is referred to the web version of this article.)

decay [39,40]. Frequency-domain analysis, leveraging the low-frequency nature of photobleaching can also be used [41]. While these techniques are effective, they require additional processing of fluorescence intensity fluctuation data *post* data acquisition. They carry also significant risks – the possibility to underestimate the number of molecules, *i.e.*, the concentration of molecules of interest, and to lose information about slower diffusion components.

Our results from both spFCS and mpFCS demonstrate that mStayGold and StayGold/E138D are twice as bright as eGFP and exhibit minimal photobleaching during spFCS and mpFCS measurements, enabling measurements with high SNR.

Using mStayGold, we analyzed in live cells the dissociation constant for the homodimerization of wild-type GR genetically fused with eGFP or mStayGold. Molecular brightness measurements yielded values consistent with previous results obtained using fluorescence cross-correlation spectroscopy (FCCS) [32]. Notably, the relative standard deviation was smaller with mStayGold, indicating that its high signal-to-noise ratio enhances the precision of molecular brightness measurements, resulting in reduced variability in the dissociation constant. This improved precision may lower the number of data points required for accurate dissociation constant analysis. Furthermore, better precision in molecular brightness can compensate for variability introduced by heterogeneity in genomic DNA organization in different parts of the same cell and among different cells.

We further demonstrated molecular transport analysis using cross-correlation between two foci: one in the cytoplasm and another in the nucleus. Overall, mStayGold-GR was imported into the nucleus during time-lapse observations under Dex treatment. Interestingly, the translocation of mStayGold-GR at individual positions was location-specific, aligning well with our previous findings using eGFP-GR [22]. Notably, photobleaching correction was unnecessary with mStayGold-GR, streamlining data analysis and saving time and effort.

5. Conclusion

In summary, this work shows that mStayGold and StayGold/E138D are under the conditions relevant for this experiment twice as bright as eGFP and more photostable. This makes it possible to acquire photobleaching-free spFCS and mpFCS data even for longer measurement times, thereby abolishing the need for FCS data pre-processing to account for photobleaching. These advances are crucial for addressing the technical limitations that hinder our understanding of how complex biological functions such as gene expression emerge in live cells through entangled reaction-diffusion networks. The bold vision to create “virtual cells” [62] is constrained by the availability of high-resolution, quantitative tools to capture without disruption the fast cellular dynamics of molecules. mpFCS is a novel dynamic imaging method that eliminates the need for scanning, while retaining the capacity of optical sectioning of confocal laser scanning microscopy. By delivering spatially resolved quantitative maps of molecular concentration, diffusion, local environment, and direction of molecular motion with single-molecule sensitivity in live cells, mpFCS provides critical information needed for understanding the dynamic integration of molecular interactions in live cells. This will enable researchers to progress in their efforts towards emulating *in silico* self-regulation and the emergence of biological functions that are characteristic of the smallest unit of animate matter, the cell.

Moreover, these new tools will enable a more detailed investigation of the cellular dynamics of glucocorticoid receptors and their mechanisms of action, focusing on yet unresolved challenges associated with glucocorticoid pharmacotherapy, such as glucocorticoid insensitivity, whether genetically inherited or acquired through environmental or physiological changes, and treatment side effects, like metabolic disturbances, immune suppression, or tissue-specific resistance.

Data and materials availability

Data supporting this study is included in the article and/or supporting materials. Raw data are available on request.

CRediT authorship contribution statement

Sho Oasa: Writing – review & editing, Writing – original draft, Visualization, Validation, Supervision, Resources, Project administration, Methodology, Investigation, Formal analysis, Data curation, Conceptualization. **Borislav Stoyanov:** Writing – review & editing, Investigation. **Yuta Hamada:** Writing – review & editing, Investigation. **Stanko N. Nikolić:** Writing – review & editing, Software. **Aleksandar J. Krmpot:** Writing – review & editing, Methodology. **Akira Kitamura:** Writing – review & editing. **Vladana Vukojević:** Writing – review & editing, Writing – original draft, Supervision, Resources, Methodology, Funding acquisition, Conceptualization.

Declaration of competing interest

The authors have no competing interests to declare.

Acknowledgements

This work was supported by the Swedish Research Council (VR 2022-03402), Qatar National Research Fund (PPM 04-0131-200019) and Magnus Bergvalls Foundation (2023-877) to VV, the National Institute on Alcohol Abuse and Alcoholism (R01AA028549 to VV) and the Science Fund of the Republic of Serbia (4545) to AJK. The content is solely the responsibility of the authors and does not necessarily represent the official views of the National Institutes of Health. AJK and SNN gratefully acknowledge financial support from the Institute of Physics Belgrade through a grant by the Ministry of Science, Technological Development and Innovation of the Republic of Serbia (25-200024). The funding agencies had no influence on the study design, methods, data collection, analyses, or manuscript writing.

Appendix A. Supplementary data

Supplementary data to this article can be found online at https://doi.org/10.1016/j.bbagen.2025.130809.

Data availability

Data will be made available on request.

References

[1] D. Magde, E. Elson, W.W. Webb, Thermodynamic fluctuations in a reacting system—measurement by fluorescence correlation spectroscopy, Phys. Rev. Lett. 29 (1972) 705–708.
[2] E.L. Elson, D. Magde, Fluorescence correlation spectroscopy. I. Conceptual basis and theory, Biopolymers 13 (1974) 1–27.
[3] D. Magde, E.L. Elson, W.W. Webb, Fluorescence correlation spectroscopy. II. An experimental realization, Biopolymers 13 (1974) 29–61.
[4] M. Ehrenberg, R. Rigler, Rotational brownian motion and fluorescence intensify fluctuations, Chem. Phys. 4 (1974) 390–401.
[5] R. Rigler, Ü. Mets, J. Widengren, P. Kask, Fluorescence correlation spectroscopy with high count rate and low background: analysis of translational diffusion, Eur. Biophys. J. 22 (1993) 169–175.
[6] M. Eigen, R. Rigler, Sorting single molecules: application to diagnostics and evolutionary biotechnology, Proc. Natl. Acad. Sci. 91 (1994) 5740–5747.
[7] V. Vukojević, M. Heidkamp, Y. Ming, B. Johansson, L. Terenius, R. Rigler, Quantitative single-molecule imaging by confocal laser scanning microscopy, Proc. Natl. Acad. Sci. USA 105 (2008) 18176–18181.
[8] J.C. Politz, E.S. Browne, D.E. Wolf, T. Pederson, Intranuclear diffusion and hybridization state of oligonucleotides measured by fluorescence correlation spectroscopy in living cells, Proc. Natl. Acad. Sci. 95 (1998) 6043–6048.
[9] J. Rika, T. Binkert, Direct measurement of a distinct correlation function by fluorescence cross correlation, Phys. Rev. A 39 (1989) 2646–2652.

[10] P. Schwille, F.J. Meyer-Almes, R. Rigler, Dual-color fluorescence cross-correlation spectroscopy for multicomponent diffusional analysis in solution, Biophys. J. 72 (1997) 1878–1886.
[11] K.M. Berland, P.T. So, E. Gratton, Two-photon fluorescence correlation spectroscopy: method and application to the intracellular environment, Biophys. J. 68 (1995) 694–701.
[12] N.O. Petersen, Scanning fluorescence correlation spectroscopy. I. Theory and simulation of aggregation measurements, Biophys. J. 49 (1986) 809–815.
[13] K. Remaut, B. Lucas, K. Braeckmans, N.N. Sanders, S.C. De Smedt, J. Demeester, FRET-FCS as a tool to evaluate the stability of oligonucleotide drugs after intracellular delivery, J. Control. Release 103 (2005) 259–271.
[14] L. Kastrup, H. Blom, C. Eggeling, S.W. Hell, Fluorescence fluctuation spectroscopy in subdiffraction focal volumes, Phys. Rev. Lett. 94 (2005) 178104.
[15] D.J. Needleman, Y. Xu, T.J. Mitchison, Pin-hole array correlation imaging: highly parallel fluorescence correlation spectroscopy, Biophys. J. 96 (2009) 5050–5059.
[16] J. Yamamoto, S. Mikuni, M. Kinjo, Multipoint fluorescence correlation spectroscopy using spatial light modulator, Biomed Opt. Express 9 (2018) 5881–5890.
[17] J. Sankaran, H. Balasubramanian, W.H. Tang, X.W. Ng, A. Röllin, T. Wohland, Simultaneous spatiotemporal super-resolution and multi-parametric fluorescence microscopy, Nat. Commun. 12 (2021) 1748.
[18] T. Wohland, X. Shi, J. Sankaran, E.H.K. Stelzer, Single plane illumination fluorescence correlation spectroscopy (SPIM-FCS) probes inhomogeneous three-dimensional environments, Opt. Express 18 (2010) 10627.
[19] S. Wennmalm, J. Widengren, Inverse-fluorescence cross-correlation spectroscopy, Anal. Chem. 82 (2010) 5646–5651.
[20] A.J. Krmpot, S.N. Nikolić, S. Oasa, D.K. Papadopoulos, M. Vitali, M. Oura, S. Mikuni, P. Thyberg, S. Tisa, M. Kinjo, L. Nilsson, L. Terenius, R. Rigler, V. Vukojević, Functional fluorescence microscopy imaging: quantitative scanning-free confocal fluorescence microscopy for the characterization of fast dynamic processes in live cells, Anal. Chem. 91 (2019) 11129.
[21] S. Oasa, A.J. Krmpot, S.N. Nikolić, A.H.A. Clayton, I.F. Tsigelny, J.-P. Changeux, L. Terenius, R. Rigler, V. Vukojević, Dynamic cellular cartography: mapping the local determinants of oligodendrocyte transcription factor 2 (OLIG2) function in live cells using massively parallel fluorescence correlation spectroscopy integrated with fluorescence lifetime imaging microscopy (mpFCS/FLIM), Anal. Chem. 93 (2021) 12011–12021.
[22] S.N. Nikolić, S. Oasa, A.J. Krmpot, L. Terenius, M.R. Belić, R. Rigler, V. Vukojević, Mapping the direction of nucleocytoplasmic transport of glucocorticoid receptor (GR) in live cells using two-foci cross-correlation in massively parallel fluorescence correlation spectroscopy (mpFCS), Anal. Chem. 95 (2023) 15171–15179.
[23] V. Vukojević, D.K. Papadopoulos, L. Terenius, W.J. Gehring, R. Rigler, Quantitative study of synthetic Hox transcription factor-DNA interactions in live cells, Proc. Natl. Acad. Sci. USA 107 (2010) 4093–4098.
[24] X. Shi, Y.H. Foo, T. Sudhaharan, S.W. Chong, V. Korzh, S. Ahmed, T. Wohland, Determination of dissociation constants in living zebrafish embryos with single wavelength fluorescence cross-correlation spectroscopy, Biophys. J. 97 (2009) 678–686.
[25] A. Tiiman, V. Jelic, J. Jarvet, P. Jaremo, N. Bogdanovic, R. Rigler, L. Terenius, A. Graslund, V. Vukojević, Amyloidogenic Nanoplaques in blood serum of patients with Alzheimer's disease revealed by time-resolved Thioflavin T fluorescence intensity fluctuation analysis, J. Alzheimers Dis. 68 (2019) 571–582.
[26] S. Oasa, E. Sezgin, Y. Ma, D.A. Horne, M.D. Radmilović, T. Jovanović-Talisman, R. Martin-Fardon, V. Vukojević, L. Terenius, Naltrexone blocks alcohol-induced effects on kappa-opioid receptors in the plasma membrane, Transl. Psychiatry 14 (2024) 477.
[27] S. Oasa, V. Vukojević, R. Rigler, I.F. Tsigelny, J.P. Changeux, L. Terenius, A strategy for designing allosteric modulators of transcription factor dimerization, Proc. Natl. Acad. Sci. USA 117 (2020) 2683–2686.
[28] Y. Li, C. Lim, T. Dismuke, D. Malawsky, S. Oasa, Z.C. Bruce, C. Offenhäuser, U. Baumgartner, R.C.J. D'Souza, S.L. Edwards, J.D. French, L.S.H. Ock, S. Nair, H. Sivakumaran, L. Harris, A.P. Tikunov, D. Hwang, C.D.M.A. Pauneto, M. Maybury, T. Hassall, B. Wainwright, S. Kesari, G. Stein, M. Piper, T.G. Johns, M. Sokolsky-Papkov, L. Terenius, V. Vukojevic, L.F. McSwain, T.R. Gershon, B. W. Day, Suppressing recurrence in Sonic Hedgehog subgroup medulloblastoma using the OLIG2 inhibitor CT-179, Nat. Commun. 16 (2025) 1091.
[29] S. Oasa, V.L. Kouznetsova, A. Tiiman, V. Vukojevic, I.F. Tsigelny, L. Terenius, Small molecule decoys of aggregation for elimination of Abeta-peptide toxicity, ACS Chem. Neurosci. 14 (2023) 1575–1584.
[30] M. Zimmer, GFP: from jellyfish to the Nobel prize and beyond, Chem. Soc. Rev. 38 (2009) 2823–2832.
[31] S. Mikuni, C. Pack, M. Tamura, M. Kinjo, Diffusion analysis of glucocorticoid receptor and antagonist effect in living cell nucleus, Exp. Mol. Pathol. 82 (2007) 163–168.
[32] M. Tiwari, S. Oasa, J. Yamamoto, S. Mikuni, M. Kinjo, A quantitative study of internal and external interactions of Homodimeric glucocorticoid receptor using fluorescence cross-correlation spectroscopy in a live cell, Sci. Rep. 7 (2017) 4336.
[33] S. Veerapathiran, C. Teh, S. Zhu, I. Kartigayen, V. Korzh, P.T. Matsudaira, T. Wohland, Wnt3 distribution in the zebrafish brain is determined by expression, diffusion and multiple molecular interactions, eLife 9 (2020) e59489.
[34] A. Fujimoto, M. Kinjo, A. Kitamura, Short repeat ribonucleic acid reduces cytotoxicity by preventing the aggregation of TDP-43 and its 25 KDa Carboxy-terminal fragment, JACS Au 4 (2024) 3896–3909.
[35] J. Buchholz, J. Krieger, C. Bruschini, S. Burri, A. Ardelean, E. Charbon, J. Langowski, Widefield high frame rate single-photon SPAD imagers for SPIM-FCS, Biophys. J. 114 (2018) 2455–2464.
[36] R.M. Dickson, A.B. Cubitt, R.Y. Tsien, W.E. Moerner, On/off blinking and switching behaviour of single molecules of green fluorescent protein, Nature 388 (1997) 355–358.
[37] P. Schwille, S. Kummer, A.A. Heikal, W.E. Moerner, W.W. Webb, Fluorescence correlation spectroscopy reveals fast optical excitation-driven intramolecular dynamics of yellow fluorescent proteins, Proc. Natl. Acad. Sci. 97 (2000) 151–156.
[38] F. Malvezzi-Campeggi, M. Jahnz, K.G. Heinze, P. Dittrich, P. Schwille, Light-induced flickering of DsRed provides evidence for distinct and interconvertible fluorescent states, Biophys. J. 81 (2001) 1776–1785.
[39] J. Ries, P. Schwille, New concepts for fluorescence correlation spectroscopy on membranes, Phys. Chem. Chem. Phys. 10 (2008) 3487–3497.
[40] R. Macháň, Y.H. Foo, T. Wohland, On the equivalence of FCS and FRAP: simultaneous lipid membrane measurements, Biophys. J. 111 (2016) 152.
[41] M. Baum, F. Erdel, M. Wachsmuth, K. Rippe, Retrieving the intracellular topology from multi-scale protein mobility mapping in living cells, Nat. Commun. 5 (2014) 4494.
[42] M. Hirano, R. Ando, S. Shimozono, M. Sugiyama, N. Takeda, H. Kurokawa, R. Deguchi, K. Endo, K. Haga, R. Takai-Todaka, S. Inaura, Y. Matsumura, H. Hama, Y. Okada, T. Fujiwara, T. Morimoto, K. Katayama, A. Miyawaki, A highly photostable and bright green fluorescent protein, Nat. Biotechnol. 40 (2022) 1132–1142.
[43] R. Ando, S. Shimozono, H. Ago, M. Takagi, M. Sugiyama, H. Kurokawa, M. Hirano, Y. Niino, G. Ueno, F. Ishidate, T. Fujiwara, Y. Okada, M. Yamamoto, A. Miyawaki, StayGold variants for molecular fusion and membrane-targeting applications, Nat. Methods 21 (2024) 648–656.
[44] E. Ivorra-Molla, D. Akhuli, M.B.L. McAndrew, W. Scott, L. Kumar, S. Palani, M. Mishima, A. Crow, M.K. Balasubramanian, A monomeric StayGold fluorescent protein, Nat. Biotechnol. 42 (2024) 1368–1371.
[45] H. Zhang, G.D. Lesnov, O.M. Subach, W. Zhang, T.P. Kuzmicheva, A.V. Vlaskina, V. R. Samygina, L. Chen, X. Ye, A.Y. Nikolaeva, A. Gabdulkhakov, S. Papadaki, W. Qin, V. Borshchevskiy, M.M. Perfilov, A.S. Gavrikov, M. Drobizhev, A.S. Mishin, K.D. Piatkevich, F.V. Subach, Bright and stable monomeric green fluorescent protein derived from StayGold, Nat. Methods 21 (2024) 657–665.
[46] E.R. Weikum, M.T. Knuesel, E.A. Ortlund, K.R. Yamamoto, Glucocorticoid receptor control of transcription: precision and plasticity via allostery, Nat. Rev. Mol. Cell Biol. 18 (2017) 159–174.
[47] D.M. Presman, S. Ganguly, R.L. Schiltz, T.A. Johnson, T.S. Karpova, G.L. Hager, DNA binding triggers tetramerization of the glucocorticoid receptor in live cells, Proc. Natl. Acad. Sci. USA 113 (2016) 8236.
[48] S. Belikov, O.G. Berg, Ö. Wrange, Quantification of transcription factor-DNA binding affinity in a living cell, Nucleic Acids Res. 44 (2015) 3045–3058.
[49] T.A. Johnson, V. Paakinaho, S. Kim, G.L. Hager, D.M. Presman, Genome-wide binding potential and regulatory activity of the glucocorticoid receptor's monomeric and dimeric forms, Nat. Commun. 12 (2021) 1987.
[50] D. Alvarez de la Rosa, Z. Ramos-Hernández, J. Weller-Pérez, T.A. Johnson, G. L. Hager, The impact of mineralocorticoid and glucocorticoid receptor interaction on corticosteroid transcriptional outcomes, Mol. Cell. Endocrinol. 594 (2024) 112389.
[51] S. Mikuni, M. Tamura, M. Kinjo, Analysis of intranuclear binding process of glucocorticoid receptor using fluorescence correlation spectroscopy, FEBS Lett. 581 (2007) 389–393.
[52] C. Pack, K. Saito, M. Tamura, M. Kinjo, Microenvironment and effect of energy depletion in the nucleus analyzed by mobility of multiple oligomeric EGFPs, Biophys. J. 91 (2006) 3921–3936.
[53] Z.W. Zhao, M.D. White, Y.D. Alvarez, J. Zenker, S. Bissiere, N. Plachta, Quantifying transcription factor–DNA binding in single cells in vivo with photoactivatable fluorescence correlation spectroscopy, Nat. Protoc. 12 (2017) 1458–1471.
[54] P. Kapusta, Absolute Diffusion Coefficients: Compilation of Reference Data for FCS Calibration, Application Note (PicoQuant), Available at, https://www.picoquant.com/images/uploads/page/files/7353/appnote_diffusioncoefficients.pdf, 2010.
[55] S. Oasa, S. Mikuni, J. Yamamoto, T. Kurosaki, D. Yamashita, M. Kinjo, Relationship between Homodimeric glucocorticoid receptor and transcriptional regulation assessed via an in vitro fluorescence correlation spectroscopy-microwell system, Sci. Rep. 8 (2018) 7488.
[56] A. Kitamura, S. Oasa, H. Kawaguchi, M. Osaka, V. Vukojević, M. Kinjo, Increased intracellular crowding during hyperosmotic stress, Sci. Rep. 13 (2023) 11834.
[57] D.M. Presman, G.L. Hager, More than meets the dimer: what is the quaternary structure of the glucocorticoid receptor? Transcription 8 (2017) 32.
[58] A. Jiménez-Panizo, A. Alegre-Martí, Theophilus T. Tettey, G. Fettweis, M. Abella, R. Antón, Thomas A. Johnson, S. Kim, R.L. Schiltz, I. Núñez-Barrios, J. Font-Díaz, C. Caelles, Annabel F. Valledor, P. Pérez, Ana M. Rojas, J. Fernández-Recio, Diego M. Presman, Gordon L. Hager, P. Fuentes-Prior, E. Estébanez-Perpiñá, The multivalency of the glucocorticoid receptor ligand-binding domain explains its manifold physiological activities, Nucleic Acids Res. 50 (2022) 13063–13082.
[59] D.M. Presman, M.F. Ogara, M. Stortz, L.D. Alvarez, J.R. Pooley, R.L. Schiltz, L. Grøntved, T.A. Johnson, P.R. Mittelstadt, J.D. Ashwell, S. Ganesan, G. Burton,

V. Levi, G.L. Hager, A. Pecci, Live cell imaging unveils multiple domain requirements for in vivo dimerization of the glucocorticoid receptor, PLoS Biol. 12 (2014) e1001813.

[60] N.C. Shaner, G.G. Lambert, A. Chammas, Y. Ni, P.J. Cranfill, M.A. Baird, B.R. Sell, J.R. Allen, R.N. Day, M. Israelsson, M.W. Davidson, J. Wang, A bright monomeric green fluorescent protein derived from Branchiostoma lanceolatum, Nat. Methods 10 (2013) 407–409.

[61] F. Steiert, E.P. Petrov, P. Schultz, P. Schwille, T. Weidemann, Photophysical behavior of mNeonGreen, an evolutionarily distant green fluorescent protein, Biophys. J. 114 (2018) 2419–2431.

[62] C. Bunne, Y. Roohani, Y. Rosen, A. Gupta, X. Zhang, M. Roed, T. Alexandrov, M. AlQuraishi, P. Brennan, D.B. Burkhardt, A. Califano, J. Cool, A.F. Dernburg, K. Ewing, E.B. Fox, M. Haury, A.E. Herr, E. Horvitz, P.D. Hsu, V. Jain, G. R. Johnson, T. Kalil, D.R. Kelley, S.O. Kelley, A. Kreshuk, T. Mitchison, S. Otte, J. Shendure, N.J. Sofroniew, F. Theis, C.V. Theodoris, S. Upadhyayula, M. Valer, B. Wang, E. Xing, S. Yeung-Levy, M. Zitnik, T. Karaletsos, A. Regev, E. Lundberg, J. Leskovec, S.R. Quake, How to build the virtual cell with artificial intelligence: priorities and opportunities, Cell 187 (2024) 7045–7063.

Spectrochimica Acta Part A: Molecular and Biomolecular Spectroscopy 327 (2025) 125420

Contents lists available at ScienceDirect

Spectrochimica Acta Part A:
Molecular and Biomolecular Spectroscopy

journal homepage: www.journals.elsevier.com/spectrochimica-acta-part-a-molecular-and-biomolecular-spectroscopy

Light on abnormal red blood cell subpopulations: Label-free optics-based approach for studying *in vitro* rigidified blood cells

Mihajlo D. Radmilović [a], Vesna Lj. Ilić [b], Dušan D. Vučetić [c,d], Drenka I. Trivanović [b], Mihailo D. Rabasović [a], Aleksandar J. Krmpot [a], Ivana T. Drvenica [b,*]

[a] Institute of Physics Belgrade, University of Belgrade, Belgrade, Serbia
[b] Institute for Medical Research, National Institute of Republic of Serbia, University of Belgrade, Belgrade, Serbia
[c] Institute for Transfusiology and Haemobiology, Military Medical Academy, Belgrade, Serbia
[d] Faculty of Medicine, Military Medical Academy, University of Defence, Belgrade, Serbia

HIGHLIGHTS

- Label-free optics-based approach for studying abnormal RBCs was established.
- Ektacytometry was supplemented by flow cytometry, phase-contrast, and TPEF microscopy.
- Fluorescence peak area effectively revealed oxidized RBC subpopulations.
- TPEF microscopy disclosed spatial location of fluorescence intensity near RBC membrane.

GRAPHICAL ABSTRACT

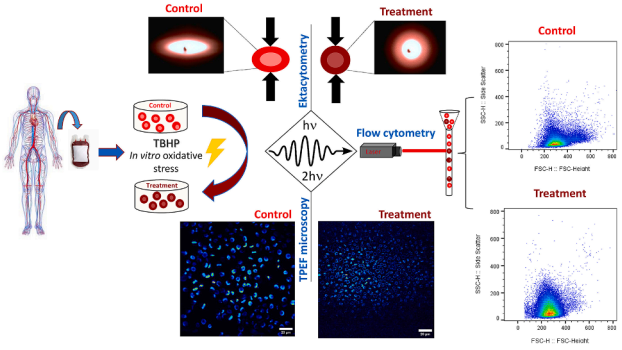

ARTICLE INFO

Keywords:
Red blood cells
Deformability
Oxidation
Ektacytometry
Flow cytometry
Two-photon excitation fluorescence microscopy

ABSTRACT

RBCs deformability plays a crucial role in maintaining proper blood flow and oxygen delivery throughout the body. Conventional ektacytometry fails to differentiate between variations in deformability of RBC subpopulations as the averaging measurement process obscures these differences. In this study, we introduced an approach that integrates label-free optics-based techniques (flow cytometry, phase-contrast, and two-photon excitation fluorescent microscopy) with ektacytometry to evaluate subpopulations that exhibit decreased RBCs deformability upon an *in vitro* oxidation using 0.5 mM TBHP, as a low-level oxidative agent.

We found that flow cytometry can easily detect rigidified and oxidized subpopulations based on FSC/SSC light distribution, as well as RBCs fluorescence intensity and peak area likely originating from hemoglobin photo and/or degradation products. Two-photon excitation fluorescence microscopy proved altered morphology and spatial location of fluorescence intensity signal near the membrane of oxidized RBCs, when compared to control RBCs, indicating a link with the reduced deformability. The proposed label-free optics-based methodology, which combines established techniques with more sophisticated microscopy, emerges as a promising tool for detecting mechano-biological changes in different RBC subpopulations induced by oxidative stress. The findings suggest

* Corresponding author.
E-mail address: ivana.drvenica@imi.bg.ac.rs (I.T. Drvenica).

https://doi.org/10.1016/j.saa.2024.125420
Received 8 May 2024; Received in revised form 17 October 2024; Accepted 7 November 2024
Available online 10 November 2024

potential applications in clinical practice for monitoring pathological conditions influenced by physical or environmental stress and as a quality control measure for stored RBCs.

1. Introduction

Red blood cells (RBCs), during their 120-day life in circulation, play several essential roles [1,2]. Their primary function is transporting oxygen from the lungs to all the body's tissues, thanks to the major intracellular protein-hemoglobin. Nevertheless, ensuring efficient oxygen delivery to tissues [3,4] is also enabled by RBCs membrane deformability, a crucial physiological property that allows RBCs to navigate through the intricate microcirculatory system. The excellent elastic properties of RBCs and resistible integrity during billions of passages through microcapillaries are provided by the specific discoid biconcave shape and proteins and lipids composition and organization in RBCs [5,6]. Besides inevitable RBCs physical trauma due to shear stress during squeezing to narrow capillaries, the proteins and lipid bilayers within RBCs undergo chemical alterations throughout their entire lifespan, by oxidation, metabolic depletion, loss of ions gradients, or cellular aging [7,8]. Therefore, the deformability of the RBCs membrane becomes an important biophysical parameter to be monitored, as well as one of the many that can reflect oxidative stress levels and even hemoglobin degradation [9]. Impaired deformability has been associated with various pathological conditions, including cardiovascular diseases, diabetes, and certain hematological disorders [10,11].

Ektacytometry, a laser diffraction technique, has been the method of the first choice for evaluating the deformability of RBCs in both research and clinical settings [12]. However, ektacytometry measures average deformability in populations of RBCs and does not provide information on the deformability of individual cells. Several studies revealed that some optics-based methods like optical tweezers or newly designed microfluidic devices could supplement and provide a more sensitive assessment of the progressive impairment of RBCs deformability than ektacytometry [12–14]. On the other hand, it is crucial to monitor RBCs with impaired deformability on an individual level since a recent study has demonstrated that the presence of a fraction of rigid RBCs in blood flow can disrupt the adhesion of leukocytes to the vascular wall, which in turn affects the immune response [15]. However, measurement deformability of RBCs should be accompanied with the information's directly associated with it, such as hemoglobin location within RBCs [16] and it's photophysical properties [17]. Based on our latest study on the formation of fluorescent photoproducts from hemoglobin after light interaction and its application for labeling and tracking single human RBCs [17], we were motivated to explore the use of optics-based techniques in combination with ektacytometry to better distinguish between populations of healthy persons' untreated RBCs and those *in vitro* oxidized and rigidified by TBHP (Tert – Butyl – hydroperoxide). Prior studies have demonstrated that exposure to 1 mM TBHP results in the oxidation of fatty acids of membrane phospholipids and hemoglobin [18,19]. This oxidation leads to the transformation of iron ions into higher oxidized states, culminating in methemoglobin formation [20]. Using label-free optics-based methods: ektacytometry, flow cytometry, phase contrast, and Two-photon Excitation Fluorescence (TPEF) microscopy we aimed to expand knowledge on possibilities toward effective monitoring of rigid and/or oxidized RBC subpopulations, since we show that oxidation of RBCs lead to increased rigidification.

The samples of an equal population of RBCs and RBCs oxidized/rigidified by 0.5 mM TBHP (slight oxidation) showed elongation indices in the physiological range, i.e., the effect of the oxidation treatments was annulled when measuring deformability of the sample by ektacytometry. On the other hand, it was possible to differentiate between the oxidized / rigidified subpopulation presences of RBCs based on the difference in FSC (Forward scatter) light distribution by using flow cytometry. Light scattering by human RBSs involves a combination of Rayleigh and Mie scattering mechanisms influenced by their unique shape, refractive index, and interactions with surrounding fluid. This phenomenon is crucial for understanding various physiological processes and developing potentially new diagnostic tools [21,22]. Flow cytometry offers in-depth insights into the optical properties of RBCs by measuring their laser light scattering. This technique elucidates the relationships between RBCs morphology and scattering characteristics, particularly through FSC and side scatter (SSC) light measurements [23]. It is well known that flow cytometry is mainly used for measuring fluorescence intensity [24]; however, measuring fluorescence intensity from samples that are not labeled with specific fluorescent dye is not a standard task in the flow cytometry community. Fluorescence of human RBCs, measured by flow cytometry, was obtained on the samples that were treated with H_2O_2 [25], and based on this research, we introduce a novel approach to utilizing flow cytometry that goes beyond its typical use for labeling and sorting cells with fluorescent dyes. Instead, we showed that it is possible to analyze abnormalities in non-labeled TBHP-oxidized/rigidified RBCs by detecting their autofluorescence properties. Specifically, we demonstrated that fluorescence intensity and fluorescence peak area, often overlooked parameters in flow cytometry of non-labeled cells, can be used to assess these abnormalities. The fluorescence peak area is derived from the total fluorescence intensity over time as the particle passes through the laser. This area is calculated by integrating the fluorescence signal over the duration of the signal, which often corresponds to how long the particle is illuminated by the laser [26,27]. In our study, we have been shown that fluorescence peak area can be used to determine aggregation in oxidized RBCs, probably due to its increased fluorescence upon oxidation with 0.5 mM TBHP. This correlation between fluorescence characteristics and RBCs aggregation underscores the potential for advanced imaging techniques in this area. Moreover, our findings suggest that a proposed label-free optics-based integrated approach, which combines techniques such as ektacytometry, flow cytometry, phase-contrast microscopy, single-photon excitation microscopy with, to some extent, more sophisticated TPEF microscopy, is a highly promising methodology for detecting changes in the mechanobiology of different subpopulations of RBCs induced by oxidation.

2. Material and methods

2.1. Blood samples

Venous blood from three healthy blood donors was collected at the Institute for Transfusiology and Hemobiology, Military Medical Academy, Belgrade, Serbia, by the blood draw protocol, which included informed consent of the participants, approved by the Institutional Ethical Review Board (No 9/2021). The blood was drawn using vacutainer tubes (10 mL plastic vacutainer (BD Vacutainer® EDTA Tubes) with BD Hemogard™ lavender closure, containing 18 mg K_2EDTA). The peripheral blood RBCs parameters (hematocrit, hemoglobin concentration, RBCs concentration and volume distribution width), were in the reference range for healthy people (Supplementary material Table S1).

2.2. RBCs isolation and in vitro oxidation/rigidification

For the RBCs isolation, a centrifugation procedure was employed, wherein 10 mL of whole blood underwent centrifugation at 1811 × *g* for a duration of 20 min at 4 °C, utilizing the Megafuge 1.0R Heraus centrifuge (Langenselbold, Germany). The ensuing supernatant, containing leucocytes and blood plasma, was cautiously aspirated and subsequently discarded. The precipitated RBCs were then reconstituted

in an isotonic saline solution (0.9 % NaCl, specifically Natrii chloridi infundibile 9 g/L, Hemofarm, Serbia) at a volumetric ratio of 1:4, and this suspension was homogenized through a twisting motion applied to the test tube. The residual plasma proteins were separated from the RBCs suspension via 10 min centrifugation at 1257 × g, at 4 °C. These procedures were iterated three times. Ultimately, the packed RBCs were revived by resuspending them in an isotonic phosphate-buffered saline solution (denoted as PBS; comprising 0.8 % saline buffered with 10 mM sodium phosphate and maintaining a pH range of 7.2–7.4) at the same volumetric ratio of 1:4. According to the protocol by Gutierrez et al (2018) [15], the isolated RBCs were treated at 2 % Hct (hematocrit) in PBS with 0.75 or 0.5 mM Tert-butyl hydroperoxide (TBHP, Sigma Aldrich, USA) for 30 min, to induce oxidative damages on cellular membranes and consequent rigidification. The oxidized rigid cells were then washed with PBS and then used separately or reconstituted with healthy RBCs in a volume ratio of 1:1. In order to confirm the oxidation, RBCs were lysed with distilled water, and the absorbance of resulting hemolysate was measured using UltroSpec 3300 pro spectrophotometer (AmershamBioscience, Uppsala, Sweden). Additionally, lipid peroxidation (i.e., thiobarbituric acid reactive species; TBARS) levels in treated RBCs were analyzed according to the method described in Brujić et al. (2021) [28].

2.3. Ektacytometry

Ektacytometry, also known as laser diffraction ektacytometry, utilizes laser light scattering patterns produced by RBCs subjected to controlled shear stress, allowing quantitative deformability assessment. By measuring the changes in the diffraction patterns, ektacytometry provides valuable information about the mechanical properties of RBCs, such as elongation index (EI), deformability index (DI), and other parameters related to cell membrane viscoelasticity [29].

In this study, the RheoSCAN-AnD300 ektacytometer (RheoMeditech Inc, Korea) was used for the RBCs deformability measurement [29]. Specifically, 6 µl of packed RBCs was carefully suspended in the tube containing polyvinylpyrrolidone (PVP, MW 360,000) in PBS (overall viscosity, 30 mPa/s) solution provided by the producer (test kit RSD-K02). A 500 µl volume of the RBCs suspension in PVP was transferred to the designated chamber of the microchannel measurement cuvette for exposure to standardized inputs of increasing shear stress. The microchannel width was 200 µm. Cell deformation was expressed as an EI using Equation (1), originating from the resulting ellipsoid laser diffraction pattern, where the major and minor axes of the elongated RBCs are represented by A and B, respectively. The calculated values for the elongation index were plotted versus shear stress (Pa) to obtain the deformability curve [15].

$$EI = \frac{A - B}{A + B} \tag{1}$$

2.4. Flow cytometry

For the flow cytometric measurements of non-labeled normal or 0.5 mM TBHP treated RBCs, the protocol by Drvenica et al. (2021) [23] was used on BD FACSCalibur flow cytometer (Becton Dickinson, Franklin Lake NJ, USA, [30]. A laser operating on 488 nm was used for the excitation. This protocol was based on determining FSC and SSC parameters of the RBCs, after the short time incubation in a series of solutions with decreasing molarity (155 mM, 139 mM, 124 mM, 93 mM) [23]. As an added value of flow cytometric analysis, we investigated the fluorescence peak area and fluorescence intensity of untreated RBCs, TBHP-treated RBCs and of a mixture of untreated and 0.5 mM TBHP-treated RBCs using spectral channel which corresponds to the following excitation and emission wavelengths: ex = 488 nm / em = 525 (40) nm. The fluorescence peak area was used as an indirect measure of fluorescent particles size [27]. Flow cytometer measure fluorescence intensity which can be represented as a pulse, characterized as the detector's signal output during a fluorescent particle's passage through the laser beam. The signal intensity rises as the cell traverses the laser beam and returns to baseline upon exiting the beam. The fluorescence intensity signal was detected by the PMT (Photomultiplier Tube) which is an integral part of the flow cytometer. PMT measures the current generated from photo-electrons in time. In the next processing stage, the signal is discretized and classified by some parameter such as fluorescence peak area. The fluorescence peak area was calculated by integrating the fluorescence signal over time, which often corresponds to how long the laser illuminates the particle. [26,27]. We assumed that the fluorescence peak area is directly proportional to the fluorescence intensity of the particle/cell size that passes through the laser beam and the time that particle/cells spent in it (Supplementary Material Fig. S1). The data were analyzed using Flow J software (v10.8.1) and Graph Pad Prism 7. At least 100.000 events were recorded per sample.

2.5. Phase contrast microscopy

The morphology and aggregation of RBCs were obtained by an Olympus CKX 41 inverted phase-contrast microscope (Olympus Europa Holding GmbH, Hamburg, Germany) using Quick PHOTO Camera 2.3 software (PROMICRA, Prague, Czech Republic). Images were analyzed using Fiji (an open − source platform for biological-image analysis).

2.6. Two-photon excitation fluorescence (TPEF) microscopy

Prior literature has detailed the experimental arrangement and the home-constructed TPEF microscope [31]. We harnessed a Ti:Sapphire laser (Coherent, Mira 900-F), driven by a frequency-doubled Nd:YVO4 laser (Coherent, Verdi V10), to produce ultrashort laser pulses at a 76 MHz repetition rate and a 160 fs pulse duration. Galvo-scanning mirrors (Cambridge Technology) were employed for raster scanning. Two different microscope objectives were utilized for this research: EC Plan-NEOFLUAR 40× /1.3 N.A. oil (Carl Zeiss) for RBCs imaging and Plan-Apochromat 20× /0.8 N.A. air (Carl Zeiss) for hemoglobin TPEF emission spectra measurement. We expanded the laser beam to match the objective lens's back aperture. A short-pass dichroic mirror was applied to reflect the laser beam toward the objective lens and transmit the signal to both the 15.1-megapixel digital single-lens reflex (DSLR) camera (Canon, EOS 50D) and the Photomultiplier Tube (PMT) (RCA, PF1006). The DSLR camera served the purpose of capturing bright-field images. We removed the camera's infrared filter to enable the observation of the laser beam's back reflection from the cover glass, aiding in system alignment and facilitating the axial positioning of the RBCs, for measuring TPEF emission spectra. Band-pass filters (VIS and/or 450 nm short pass) were positioned in front of the PMT to gather hemoglobin photoproduct fluorescence [17]. A 700 nm long-pass filter was used to eliminate parasitic laser lines shorter than 700 nm. A short-pass 700 nm filter was installed in front of the PMT detector to further eliminate back-scattered laser light. The RBCs and RBCs ghost imaging were carried out using 730 nm ultrashort laser pulses. This wavelength was selected based on the optical setup and the characteristics of the hemoglobin molecule, with further information provided in our earlier investigations [17,32]. Microscopic slides were prepared for RBCs imaging, 10 µL of packed RBCs underwent dilution in isotonic saline solution (0.9 % NaCl, Hemofarm, Serbia) at a 1:30 vol ratio. A 3 µL portion of the diluted whole blood sample was applied to a microscope slide, overlaid with a No. 1.5 coverslip, and sealed.

2.7. Statistical analysis

Statistical analysis of the results was carried out using Graph PadPrism 9 software. According to Drvenica et al. (2021) [23], kurtosis and skewness of FSC distribution were determined for the 400–1000 quantity range with an aim to exclude cell debris and large aggregates,

rarely formed during samples preparation.

The results are expressed as mean ± standard deviation. The statistical significance of differences between the groups was determined with a two-tailed paired *t*-test since the comparison was made between the same donor (control and TBHP treatment). Differences with p values of < 0.05 were considered significant.

3. Results and Discussion

3.1. Measuring RBCs deformability

The impact of TBHP on the integrity of the RBCs membrane was discernible by its response to mechanical stress, as determined by ektacytometry and shown in Fig. 1. Consequently, oxidative crosslinking transpires between methemoglobin and spectrin, resulting in a reduction in membrane flexibility [18,20]. These findings were proven decades ago in the case of hydrogen peroxide treatment of RBCs, where increased rigidity, along with morphological and surface changes in the RBCs, are shown to be mainly a cause of oxidation of heme-protein and in its cross-linking to skeletal proteins, i.e., spectrin and actin [33,34], and in addition, to the cytoplasmic component of Band 3. In this study, we aim to simulate mild oxidative stress in a controllable manner, so we investigated how the influence of a lower concentration of TBHP as a stable oxidant, specifically 0.5 mM TBHP (Fig. 1), manifests in terms of membrane elasticity within the packed RBCs population. This concentration of 0.5 mM TBHP induced an evident decrease in the EI compared to the control. After treating RBCs with 0.5 mM TBHP, it was found that the hemolysate absorbance spectra indicated the presence of methemoglobin (as seen in Supplementary Material Fig. S2a). Moreover, there was a higher level of lipid peroxides in the treated RBCs compared to the control RBCs (as seen in Supplementary Material Fig. S2b), confirming that oxidation had indeed occurred. A more pronounced oxidative impact (Fig. 1) associated with 0.75 mM TBHP led to a reduction in EI (at the beginning of the measurement, small values of shear stress were negligible [35,36]) and ultimately guided the cells toward irreversible lysis, as confirmed by the osmotic fragility test (Supplementary material Fig. S3). It is worth noting that the mixture of control RBCs and those treated with 0.5 mM TBHP (Fig. 1) re-established the EI curve within a range similar to that observed for control RBCs, which is also scenario with mixture of 0.75 mM and control (Fig. 1). This observation underscores one of the limitations of ektacytometry – the calculation of the EI curve as an average across the entire RBCs population, so it does not provide data on altered deformability of individual RBCs or affected subpopulation [37], such as RBCs altered by oxidation in this study.

3.2. Flow cytometry analysis based on FSC (forward scatter) and SSC (side scatter) light distribution

For all samples of RBCs, encompassing both control and those subjected to treatment with 0.5 mM TBHP, flow cytometry analyses were conducted, examining the forward scatter (FSC) and side scatter (SSC) dot plots, cell counts in the FSC/SSC channels, and autofluorescence intensity signals. Alterations in the distribution of light in the FSC and SSC channels were assessed by comparing changes in statistical parameters of the distribution, including skewness and kurtosis.

Incubation of RBCs in isotonic solutions resulted in a multimodal FSC distribution, as outlined in the supplementary information, with two partially overlapping peaks (Supplementary material Fig. S4). The emergence of a multimodal FSC signal distribution was primarily attributed to the random spatial orientation of RBCs within the flow channel and their deformation under hydrodynamic forces [23,21,38].

In the case of RBCs suspended and swelled (i.e., spherized) in a 93 mM phosphate buffer saline (PBS), FSC exhibited a unimodal distribution (Fig. 2), consistent with previous findings [23]. To attenuate the influence of RBCs orientation within the flow channel and individual variations between donors on the FSC and SSC signals [23], both control and treatment samples were subjected to swelling through incubation in a 93 mM hypotonic PBS solution and a distinct relationship between the intensities of forward and scattered light were observed in treated and control samples (Fig. 2a, 2b). Based on the FSC histogram presented in Fig. 2c, it is evident that the oxidized and rigidified RBCs by 0.5 mM TBHP exhibited a slight decrease in size. This decrease in size can be attributed to an increase in the area-to-volume ratio, which is already established to be associated with a reduction in cell deformability [39,40]. The histogram of SSC values obtained from oxidized and rigidified RBCs treated with 0.5 mM TBHP and control RBCs showed a more pronounced difference when compared to the FSC signal (Fig. 2d). The possible reasons for this could be the treatment – triggered changes in the shape and associated intracellular modifications, such as refractive index scattering at the right angle depends on the cell shape and internal properties of the scattering cells [41].

The consequences of RBCs oxidation are multifaceted and can be quantified using the flow cytometry technique across a larger cell population. Our observations indicated that a higher percentage of light was scattered forward in control samples compared to those treated with 0.5 mM TBHP, possibly due to alterations in the hydrodynamic forces acting on RBCs within the flow channel. As evidenced by ektacytometry, the mechanical properties of RBCs differed, with RBCs treated with 0.5 mM TBHP displaying as rigid, i.e., with reduced deformability. Although a direct comparison between ektacytometry and flow cytometry results is challenging, it is highly conceivable that changes in behavior in microfluidics techniques between rigid and deformable cells exist [42]. Based on that, it is realistic to speculate that the altered biomechanical properties of RBCs could induce alterations in FSC light intensity as the results of Gienger et al. (2019) [21] already gave a proof of principle that rheological properties of RBCs can be derived from flow cytometric measurements, however using the custom-made flow cytometric set-up. The use of commercially available flow cytometers for that purpose still

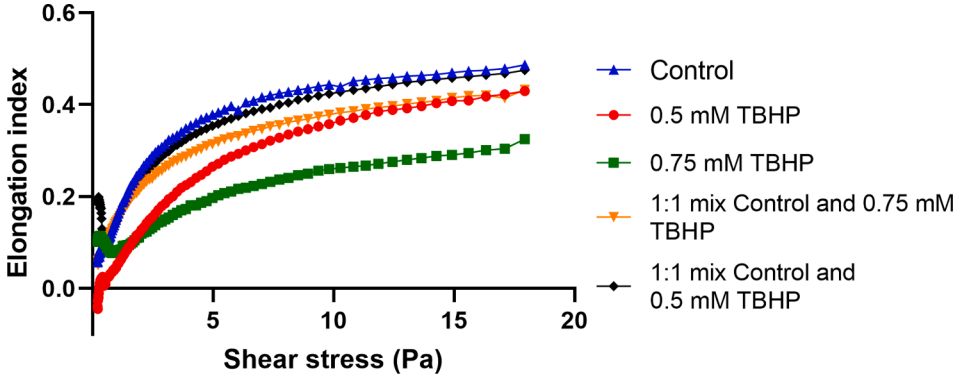

Fig. 1. Change of elongation indices, obtained by ektacytometry, with healthy donor RBCs treatment with 0.5 mM and 0.75 mM TBHP.

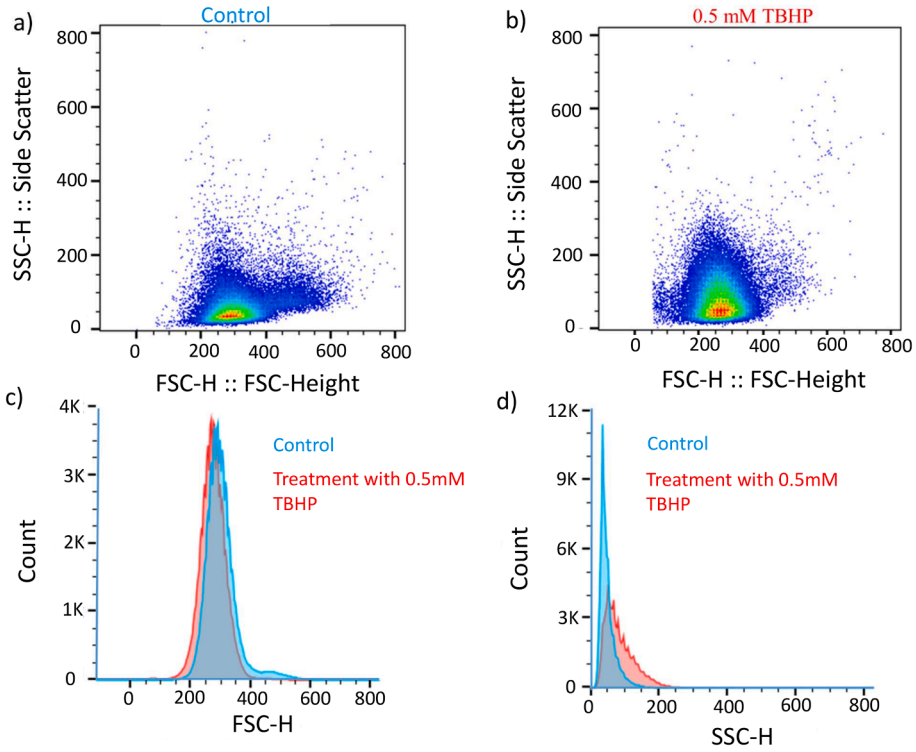

Fig. 2. Representative flow cytometry data of oxidized / rigidified and control RBCs swelled by incubation in 93 mM sodium phosphate buffer: a) SSC/FSC dot plot of control, untreated RBCs, b) SSC/FSC dot plot of RBCs treated with 0.5 mM TBHP, c) Overlapped FSC/Cell count histograms of control and RBCs treated with 0.5 mM TBHP, d) Overlapped SSC/Cell count histograms of control and RBCs treated with 0.5 mM TBHP.

requires the development of a more realistic shape model of elastic properties of RBCs made of several parameters and new mathematical approaches like surrogate modeling or tools of large-scale data analysis [21].

Based on the obtained FSC and SSC distributions in 93 mM hypotonic PBS, we perform an analysis of two statistical parameters related to RBCs sphericity, skewness, and kurtosis. Kurtosis exhibits greater sensitivity to oxidation compared to skewness in the analysis of FSC distribution. It is well-established that hypoosmotic incubation of RBCs leads to decreased kurtosis [23] as RBCs sphericity becomes predominant [43]. Our investigation revealed that oxidative conditions also exerted an influence on kurtosis, with a lesser impact on skewness of the FSC distribution (Fig. 3a, 3b).

One potential reason for the reduced kurtosis in the FSC distribution may be the induced oxidation of hemoglobin and the subsequent relocation of oxidized hemoglobin to the cell membrane [20]. The kurtosis parameter increases with the fourth degree of difference between the mean and specific measurements [44–46] and is more sensitive to deviations from the mean than skewness. Accordingly, kurtosis could serve as a valuable parameter for assessing the effects of oxidation on FSC and

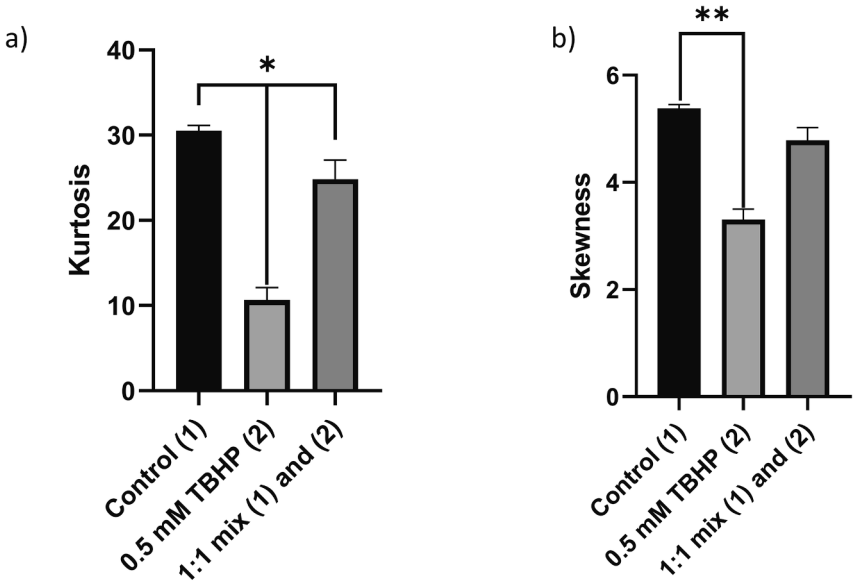

Fig. 3. Statistical parameters of FSC light distribution averaged on three different healthy blood donors: a) Kurtosis and b) Skewness of FSC light distribution of control (1), 0.5 mM treated RBCs (2) and 1:1 mix of control and 0.5 mM TBHP treated RBC ((1) and (2)).

SSC distributions.

3.3. (Auto) fluorescence properties of oxidized / rigidified RBCs measured by flow cytometry

RBCs exposed to an oxidized agent can be characterized by measuring fluorescence emission intensity by one- and TPEF microscopies [17,25,47]. The study by Yakimov et al. (2019) [48] revealed that RBCs fluorescence can also be detected when using flow cytometry, where low, but clearly detectable signal in all available spectral channels in their set-up was observed. In this study, we demonstrated that RBCs oxidation by 0.5 mM TBHP induced an increase in fluorescence emission in all three treated samples from healthy donors (Fig. 4a, 4b, 4c), in the spectral channel which corresponds to the following excitation and emission wavelengths: ex = 488 nm / em = 525 (40) nm. The detected autofluorescence in the control group as well, probably comes from RBCs dominant endogenous fluorophores [48–50]. The detected signal possibly came from hemoglobin degradation products, present intrinsically in low concentration in control donor RBCs. The intensified formation of heme fluorescent products can be induced by oxidation [47], laser irradiation [17,45] or in some pathophysiological states such as atherosclerotic plaques [51]. We have also demonstrated analogous findings using epifluorescence microscopy, revealing that the control group exhibits very low autofluorescence intensity, while RBCs treated with 0.5 mM TBHP show an increased fluorescence intensity (Supplementary Fig. S5).

It is underestimated that fluorescence pulse width (FlW2) can provide size information on the fluorescence-emitting particle [27], since the signals originating from individual and clustered cells are separated. In our study, fluorescence peak area was a parameter that was different between the control and TBHP treated RBCs (Fig. 5). In the TBHP treated RBCs we observed several peaks, formed as a consequence of increased fluorescence intensity and possibly the formation of RBCs clusters. However, the clustering level could vary between the samples, and autofluorescence not caused by oxidation, could affect the measurements. We observed that peaks were present in all TBHP treated RBC samples, but also in one control RBCs sample (Fig. 5b), indicating the advance of flow cytometry to detect interindividual differences in oxidative status of healthy donors. More importantly, the existence of fluorescence peaks with different areas in the population of 0.5 mM TBHP oxidized RBCs indicated that oxidation induces the appearance of RBC clusters with increased fluorescence intensity. Indirectly we have been shown clustering in TBHP treated RBCs, by using phase contrast microscopy (see Supplement Material Figs. S6, S7, S8, S9). In such a way, flow cytometric analysis allowed a clear distinction between control, untreated RBCs, oxidized RBCs, and sample containing an equal portion of oxidized and normal RBCs (Fig. 5).

3.4. Phase contrast microscopy of RBCs

Phase contrast microscopy was employed to indirectly assess the extent of aggregation in the treated RBCs and elucidate their morphological characteristics. The control RBCs sample demonstrated a homogeneous cell distribution (Fig. 6a). It becomes apparent that the RBCs sample treated with 0.5 mM TBHP exhibited aggregation, as illustrated in Fig. 6b.

Notably, areas devoid of cellular entities exhibited a considerable increase in size within the treated sample, as demonstrated in Supplementary Fig. S9. This expansion in pixel area devoid of cells can be attributed to the augmented aggregation of RBCs observed in the treated sample. Furthermore, the influence of a 0.5 mM TBHP treatment on RBCs aggregation was corroborated by complementary techniques, such as flow cytometry.

3.5. TPEF microscopy of RBCs

TPEF imaging was applied on control RBCs (Fig. 7a), the RBCs treated with 0.5 mM TBHP, and a mixture of TBHP-treated and control RBCs (Fig. 7b and 7c). The TPEF images depicted deviations from the native morphology in the 0.5 mM TBHP-treated RBCs, indicating the TPEF footprint of *in vitro* induced oxidation. We want to emphasize that the TPEF signal observed in the RBCs membrane in 0.5 mM treated RBCs was not uniform across all RBCs in the sample. Individual variability in the TPEF signal spatial distribution among treated RBCs suggests varying degrees of tolerance to oxidation within the pool of RBCs. Notably, TPEF microscopy revealed potential interactions between oxidized hemoglobin and RBCs membrane components, as evidenced by the fluorescence signal confined to the RBCs membranes (Fig. 7b). This result follows our and other previous studies on femtosecond laser interaction with hemoglobin molecules extracellularly or within RBCs [17,52], as well as documented discrepancies in SSC histograms between control and oxidized RBCs, reflecting internal properties of the cell such as refractive index change. Overall, this can provide a possible differentiation between oxidized and control RBCs in the mixed suspension (Fig. 7c, where the green arrow points to control RBCs and the red arrow points to the 0.5 mM treated RBCs). However, TPEF imaging of oxidized RBCs should be more explored since the inter-individual differences between RBCs of a single donor can affect the distribution of TPEF within RBCs.

Previous reports showed that the membrane-attached hemoglobin is one of the determining factors of RBCs deformability, i.e., when an RBCs contains more membrane-attached hemoglobin molecules, its ability to deform worsens [16]. In this study, we demonstrated that it is more likely that membrane-attached hemoglobin photoproduct and/or degradation/oxidation is responsible for the TPEF signal (Fig. 7) since it was especially pronounced in the sample of RBCs rigidified with 0.5 mM TBHP, with already confirmed lower deformability (Fig. 1). In this way,

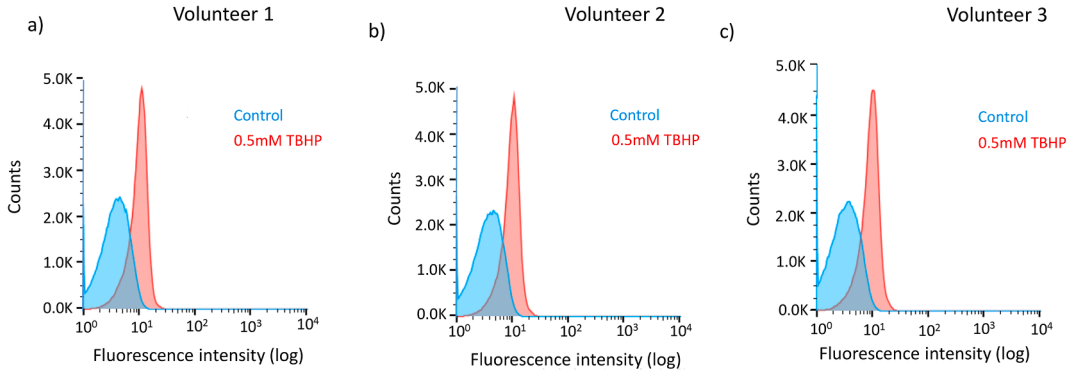

Fig. 4. Autofluorescence intensity of 0.5 mM TBHP treated and control, untreated RBCs of three healthy donors.

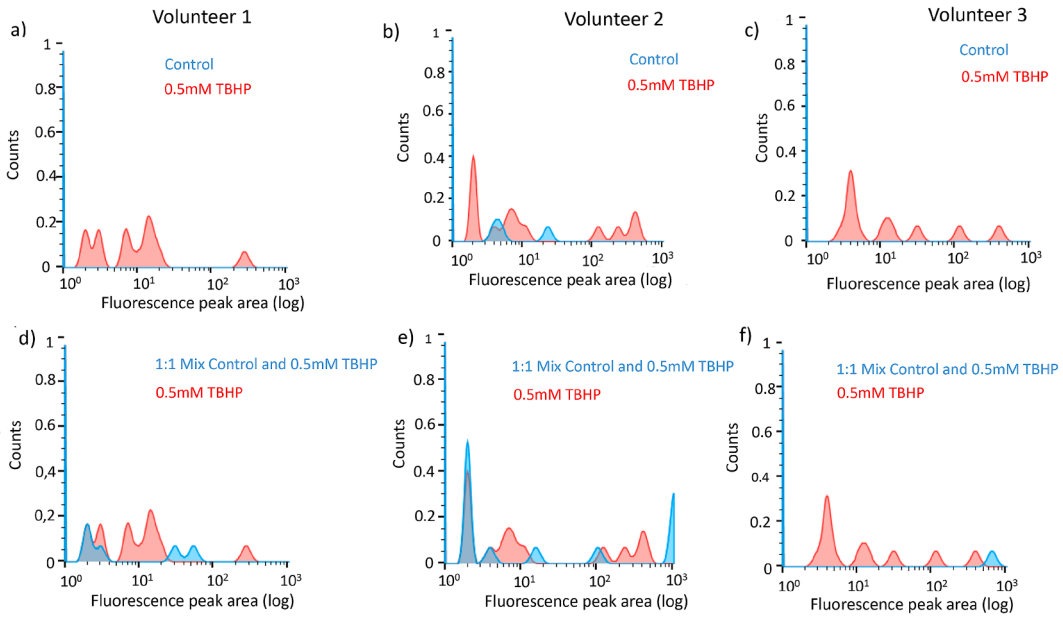

Fig. 5. Fluorescence peak area of oxidized RBCs. a), b, and c) Fluorescence peak area from control, untreated, and 0.5 mM THBP treated RBCs of three healthy donors. Peaks were not observed in control RBCs samples of donors 1 and 3. d), e) and f) 1:1 mix of control and 0.5 mM THBP treated RBCs of the same three healthy donors.

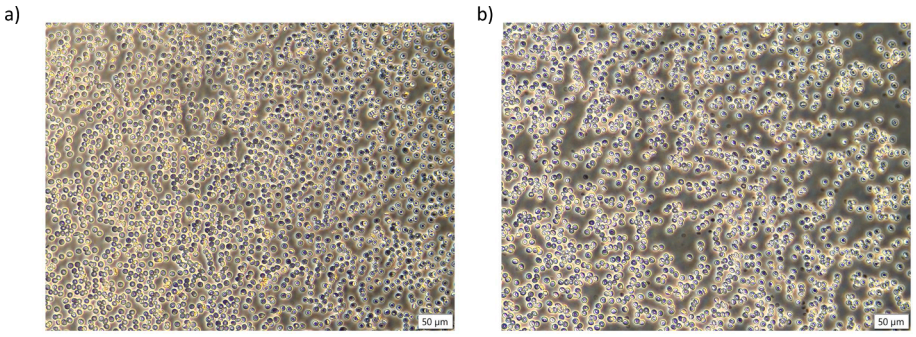

Fig. 6. Phase contrast microscopy of a) control RBCs and b) RBCs treated with 0.5 mM TBHP.

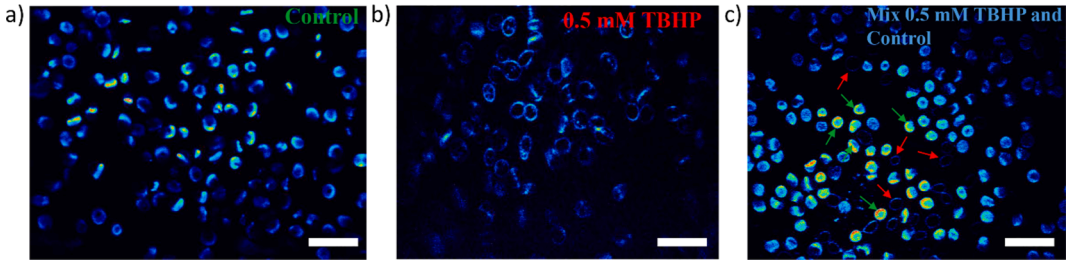

Fig. 7. TPEF imaging of a) Control, healthy donor's untreated RBCs; b) 0.5 mM TBHP treated RBCs of the same donor, c) Mixture of Control (green arrow) 0.5 mM treated RBCs (red arrow). Scale bar 20 µm.

based on the obtained results with a sample containing two subpopulations equally represented, normal and less deformable oxidized RBCs, we demonstrated that the presented TPEF microscopy set-up can indirectly serve as a technique for monitoring the quality of stored RBCs for transfusion purposes, as already proposed by Saytashev and coworkers (2016) [53].

4. Conclusion

In conventional ektacytometry, differences in RBC subpopulations deformability are often obscured due to the averaging measurement process. To address this limitation, this study introduces an approach that integrates label-free optics-based techniques such as flow cytometry, phase-contrast, and two-photon excitation fluorescent microscopy with ektacytometry. The aim was to evaluate subpopulations that exhibit decreased RBCs deformability upon an *in vitro* oxidation using 0.5 mM TBHP as a low-level oxidative agent.

The study found that flow cytometry can easily detect rigidified subpopulations based on FSC/SSC light distribution, RBCs fluorescence intensity, and peak area. The latter are most likely originating from

hemoglobin photo and/or degradation products, as we demonstrated in our recent study [17] Phase-contrast microscopy confirmed clustering in rigidified RBCs that was demonstrated by flow cytometry. Moreover, single-photon excitation microscopy confirmed increased fluorescence intensity in 0.5 mM oxidized RBCs population.

Additionally, two-photon excitation fluorescence microscopy proved altered morphology and spatial location of fluorescence intensity signal near the membrane of oxidized RBCs compared to control RBCs, indicating a link with the reduced deformability.

The proposed label-free optics-based methodology approach, which combines established techniques (ektacytometry and flow cytometry) with more sophisticated microscopy (two-photon excitation fluorescence microscopy), emerges as a promising tool for detecting mechano-biological changes in different RBC subpopulations induced by oxidative stress. The findings suggest potential applications in clinical practice for monitoring pathological conditions influenced by physical or environmental stress and as a quality control measure for stored RBCs. Overall, our study contributes to understanding the effects of oxidative stress on RBCs biomechanics, morphology, and fluorescence properties.

Ethics approval

The collection of venous blood from healthy blood donors at the Institute for Transfusiology and Hemobiology, Military Medical Academy, Belgrade, Serbia was approved by the Institutional Ethical Review Board (No 9/2021).

7. Consent for publication

All authors of the manuscript agree to its submission and publication.

Funding

This work was supported by the Science Fund of the Republic of Serbia [program PROMIS, project HEMMAGINERO, grant number 6066079]. The authors acknowledge funding provided by the Institute of Physics Belgrade and the Institute for Medical Research University of Belgrade, National Institute of the Republic of Serbia through a grant by the Ministry of Science Technological Development and Innovation of the Republic of Serbia (contract No. 451-03-66/2024-03/200015). The authors also acknowledge funding provided by the Project Advanced Biophysical Methods for Soil Targeted Fungi-Based Biocontrol Agents -BioPhysFUN [Grant number 4545] from the Green program of cooperation between science and industry, Science Fund of the Republic of Serbia.

Declaration of competing interest

The authors declare that they have no known competing financial interests or personal relationships that could have appeared to influence the work reported in this paper.

Appendix A. Supplementary data

Supplementary data to this article can be found online at https://doi.org/10.1016/j.saa.2024.125420.

Data availability

Data will be made available on request.

References

[1] M.J. McAteer, L.J. Dumont, J. Cancelas, N. Rugg, R. Vassallo, P. Whitley, S. Graminske, K. Friedman, Multi-institutional randomized control study of haemolysis in stored red cell units prepared manually or by an automated system, Vox Sang. 99 (1) (2010) 34–43, https://doi.org/10.1111/j.1423-0410.2010.01313.x.

[2] Anderson, H. L., Brodsky, I. E., & Mangalmurti, N. S. (2018). The Evolving Erythrocyte: Red Blood Cells as Modulators of Innate Immunity. Journal of immunology (Baltimore, Md.: 1950), 201(5), 1343–1351. doi: 10.4049/jimmunol.1800565.

[3] S. Chien, Physiological and pathophysiological significance of hemorheology, in: Clinical Hemorheology: Applications in Cardiovascular and Hematological Disease, Diabetes, Surgery and Gynecology, Springer, Netherlands, Dordrecht, 1987, pp. 125–164.

[4] L. Kuck, J.N. Peart, M.J. Simmonds, Active modulation of human erythrocyte mechanics, Am. J. Physiol. Cell Physiol. 319 (2) (2020) C250–C257, https://doi.org/10.1152/ajpcell.00210.2020.

[5] V. Pretini, M.H. Koenen, L. Kaestner, M.H.A.M. Fens, R.M. Schiffelers, M. Bartels, R. Van Wijk, Red Blood Cells: Chasing Interactions, Front. Physiol. 10 (2019) 945, https://doi.org/10.3389/fphys.2019.00945.

[6] J.C. Kuo, M.J. Paszek, Glycocalyx curving the membrane: forces emerging from the cell exterior, Annu. Rev. Cell Dev. Biol. 37 (2021) 257–283, https://doi.org/10.1146/annurev-cellbio-120219-054401.

[7] G. Bartosz, Erythrocyte aging: physical and chemical membrane changes, Gerontology 37 (1–3) (1991) 33–67, https://doi.org/10.1159/000213251.

[8] A. Catan, C. Turpin, N. Diotel, J. Patche, A. Guerin-Dubourg, X. Debussche, E. Bourdon, N. Ah-You, N. Le Moullec, M. Besnard, R. Veerapen, P. Rondeau, O. Meilhac, Aging and glycation promote erythrocyte phagocytosis by human endothelial cells: Potential impact in atherothrombosis under diabetic conditions, Atherosclerosis 291 (2019) 87–98, https://doi.org/10.1016/j.atherosclerosis.2019.10.015.

[9] V.M. Barodka, E. Nagababu, J.G. Mohanty, D. Nyhan, D.E. Berkowitz, J.M. Rifkind, J.J. Strouse, New insights provided by a comparison of impaired deformability with erythrocyte oxidative stress for sickle cell disease, Blood Cell Mol. Dis. 52 (4) (2014) 230–235, https://doi.org/10.1016/j.bcmd.2013.10.004.

[10] R. Huisjes, A. Makhro, E. Llaudet-Planas, L. Hertz, P. Petkova-Kirova, L. P. Verhagen, S. Pignatelli, M.A.E. Rab, R.M. Schiffelers, E. Seiler, W.W. van Solinge, J.V. Corrons, L. Kaestner, M. Mañú-Pereira, A. Bogdanova, R. van Wijk, Density, heterogeneity and deformability of red cells as markers of clinical severity in hereditary spherocytosis, Haematologica 105 (2) (2020) 338–347, https://doi.org/10.3324/haematol.2018.188151.

[11] M. Leo, D.I.F. Giacinto, M. Nardini, A. Mazzini, C. Rossi, E. Porceddu, M. Papi, A. Grieco, D.E.M. Spirito, G. Ciasca, Erythrocyte viscoelastic recovery after liver transplantation in a cirrhotic patient affected by spur cell anaemia, J. Microsc. 280 (3) (2020) 287–296, https://doi.org/10.1111/jmi.12958.

[12] N.Z. Piety, J. Stutz, N. Yilmaz, H. Xia, T. Yoshida, S.S. Shevkoplyas, Microfluidic capillary networks are more sensitive than ektacytometry to the decline of red blood cell deformability induced by storage, Sci. Rep. 11 (1) (2021) 604, https://doi.org/10.1038/s41598-020-79710-3.

[13] I. Doh, W.C. Lee, Y.H. Cho, A.P. Pisano, F.A. Kuypers, Deformation measurement of individual cells in large populations using a single-cell microchamber array chip, Appl. Phys. Lett. 100 (17) (2012) 173702–1737023, https://doi.org/10.1063/1.4704923.

[14] Y.J. Kang, S. Serhrouchni, A. Makhro, A. Bogdanova, S.S. Lee, Simple assessment of red blood cell deformability using blood pressure in capillary channels for effective detection of subpopulations in red blood cells, ACS Omega 7 (43) (2022) 38576–38588, https://doi.org/10.1021/acsomega.2c04027.

[15] M. Gutierrez, M.B. Fish, A.W. Golinski, O. Eniola-Adefeso, Presence of rigid red blood cells in blood flow interferes with the vascular wall adhesion of leukocytes, Langmuir 34 (6) (2018) 2363–2372, https://doi.org/10.1021/acs.langmuir.7b03890.

[16] X.Q. Mi, J.Y. Chen, L.W. Zhou, Effect of low power laser irradiation on disconnecting the membrane-attached hemoglobin from erythrocyte membrane, J. Photochem. Photobiol. B Biol. 83 (2) (2006) 146–150, https://doi.org/10.1016/j.jphotobiol.2005.12.018.

[17] M.D. Radmilović, I.T. Drvenica, M.D. Rabasović, V.L. Ilić, D. Pavlović, S. Oasa, V. Vukojević, M. Perić, S.N. Nikolić, A.J. Krmpot, Interactions of ultrashort laser pulses with hemoglobin: Photophysical aspects and potential applications, Int. J. Biol. Macromol. 244 (2023) 125312, https://doi.org/10.1016/j.ijbiomac.2023.125312.

[18] M.J. Chen, M.P. Sorette, D.T. Chiu, M.R. Clark, Prehemolytic effects of hydrogen peroxide and t-butylhydroperoxide on selected red cell properties, BBA 1066 (2) (1991) 193–200, https://doi.org/10.1016/0005-2736(91)90186-c.

[19] J.G. Mohanty, E. Nagababu, J.M. Rifkind, Red blood cell oxidative stress impairs oxygen delivery and induces red blood cell aging, Front. Physiol. 5 (2014) 84, https://doi.org/10.3389/fphys.2014.00084.

[20] T. Maruyama, M. Hieda, S. Mawatari, T. Fujino, Rheological Abnormalities in Human Erythrocytes Subjected to Oxidative Inflammation, Front. Physiol. 13 (2022) 837926, https://doi.org/10.3389/fphys.2022.837926.

[21] J. Gienger, H. Gross, V. Ost, M. Bär, J. Neukammer, Assessment of deformation of human red blood cells in flow cytometry: measurement and simulation of bimodal forward scatter distributions, Biomed. Opt. Express 10 (9) (2019) 4531–4550, https://doi.org/10.1364/BOE.10.004531.

[22] D.H. Tycko, M.H. Metz, E.A. Epstein, A. Grinbaum, Flow-cytometric light scattering measurement of red blood cell volume and hemoglobin concentration, *Appl. Opt.* 24 (9) (1985) 1355–1365, https://doi.org/10.1364/AO.24.001355.

[23] I. Drvenica, S. Mojsilović, A. Stančić, D. Marković, M. Kovačić, I. Maslovarić, I. Rapajić, D. Vučetić, V. Ilić, The effects of incubation media on the assessment of the shape of human erythrocytes by flow cytometry: a contribution to mathematical data interpretation to enable wider application of the method,

European Biophysics Journal: EBJ 50 (6) (2021) 829–846, https://doi.org/10.1007/s00249-021-01527-3.
[24] Steinkamp, J. A. (1984). Flow cytometry. Review of scientific instruments, 55(9), 1375-1400. doi: 10.1063/1.1137948.
[25] E. Nagababu, F.J. Chrest, J.M. Rifkind, Hydrogen-peroxide-induced heme degradation in red blood cells: the protective roles of catalase and glutathione peroxidase, Biochimica et Biophysica Acta (BBA)-General Subjects 1620 (1–3) (2003) 211–217, https://doi.org/10.1016/S0304-4165(02)00537-8.
[26] R. Fedr, Z. Kahounová, J. Remšík, M. Reiterová, T. Kalina, K. Souček, Variability of fluorescence intensity distribution measured by flow cytometry is influenced by cell size and cell cycle progression, Sci. Rep. 13 (1) (2023) 4889, https://doi.org/10.1038/s41598-023-31990-1.
[27] K. Kang, S.B. Lee, J.H. Yoo, C.W. Nho, Flow cytometric fluorescence pulse width analysis of etoposide-induced nuclear enlargement in HCT116 cells, Biotechnol. Lett 32 (8) (2010) 1045–1052, https://doi.org/10.1007/s10529-010-0277-x.
[28] M. Brujić, J. Grujić-Milanović, Z. Miloradović, D.j. Jovović, L. Živković, N. Mihailović-Stanojević, D. Karanović, B. Spremo-Potparević, DNA, protein and lipid oxidative damage in tissues of spontaneously hypertensive versus normotensive rats, Int. J. Biochem. Cell Biol. 141 (2021) 106088, https://doi.org/10.1016/j.biocel.2021.106088.
[29] S. Shin, Y. Ku, M.S. Park, J.S. Suh, Slit-flow ektacytometry: laser diffraction in a slit rheometer, Cytometry B Clin. Cytom. 65 (1) (2005) 6–13, https://doi.org/10.1002/cyto.b.20048.
[30] https://www.bdbiosciences.com/content/dam/bdb/marketing-documents/BD_FACSCalibur_instructions.pdf.
[31] M.D. Rabasović, D.V. Pantelić, B.M. Jelenković, S.B. Ćurčić, M.S. Rabasović, M. D. Vrbica, V.M. Lazovic, B.P. Ćurčić, A.J. Krmpot, Nonlinear microscopy of chitin and chitinous structures: a case study of two cave-dwelling insects, J. Biomed. Opt. 20 (1) (2015) 016010, https://doi.org/10.1117/1.JBO.20.1.016010.
[32] K. Bukara, S. Jovanic, I.T. Drvenica, A. Stancic, V. Ilic, M.D. Rabasovic, D. Pantelic, B. Jelenkovic, B. Bugarski, A.J. Krmpot, Mapping of hemoglobin in erythrocytes and erythrocyte ghosts using two photon excitation fluorescence microscopy, J. Biomed. Opt. 22 (2) (2017) 26003, https://doi.org/10.1117/1.JBO.22.2.026003.
[33] L.M. Snyder, N.L. Fortier, J. Trainor, J. Jacobs, L. Leb, B. Lubin, D. Chiu, S. Shohet, N. Mohandas, Effect of hydrogen peroxide exposure on normal human erythrocyte deformability, morphology, surface characteristics, and spectrin-hemoglobin cross-linking, J. Clin. Invest. 76 (5) (1985) 1971–1977, https://doi.org/10.1172/JCI112196.
[34] N. Shaklai, B. Frayman, N. Fortier, M. Snyder, Crosslinking of isolated cytoskeletal proteins with hemoglobin: a possible damage inflicted to the red cell membrane, BBA 915 (3) (1987) 406–414, https://doi.org/10.1016/0167-4838(87)90027-6.
[35] P.J. Bronkhorst, E. Nijhof, J.J. Sixma, Parametrization of the deformation curve as a tool for standardization and interpretation of ektacytometric measurements, Clin. Hemorheol. Microcirc. 15 (1995) 803–816, https://doi.org/10.3233/CH-1995-15602.
[36] O.K. Baskurt, M.R. Hardeman, M. Uyuklu, P. Ulker, M. Cengiz, N. Nemeth, S. Shin, T. Alexy, H.J. Meiselman, Parameterization of red blood cell elongation index–shear stress curves obtained by ektacytometry, Scand. J. Clin. Lab. Invest. 69 (7) (2009) 777–788, https://doi.org/10.3109/00365510903266069.
[37] J. Kim, H. Lee, S. Shin, Advances in the measurement of red blood cell deformability: a brief review, J. Cell. Biotechnol. 1 (1) (2015) 63–79, https://doi.org/10.3233/JCB-15007.
[38] Gibaud, E. (2015) Numerical simulation of red blood cells flowing in a blood analyzer. Hematology. PhD thesisis, Université Montpellier, 2015. English. NNT: 2015MONTS135.
[39] R.E. Waugh, M. Narla, C.W. Jackson, T.J. Mueller, T. Suzuki, G.L. Dale, Rheologic properties of senescent erythrocytes: loss of surface area and volume with red blood cell age, Blood 79 (5) (1992) 1351–1358.
[40] M.J. McVey, W.M. Kuebler, A. Orbach, D. Arbell, O. Zelig, G. Barshtein, S. Yedgar, Reduced deformability of stored red blood cells is associated with generation of extracellular vesicles, Transfus. Apher. Sci. 59 (5) (2020) 102851, https://doi.org/10.1016/j.transci.2020.102851.
[41] B.G. de Grooth, L.W. Terstappen, G.J. Puppels, J. Greve, Light-scattering polarization measurements as a new parameter in flow cytometry, Cytometry 8 (6) (1987) 539–544, https://doi.org/10.1002/cyto.990080602.
[42] E. Henry, S.H. Holm, Z. Zhang, J.P. Beech, J.O. Tegenfeldt, D.A. Fedosov, G. Gompper, Sorting cells by their dynamical properties, Sci. Rep. 6 (2016) 34375, https://doi.org/10.1038/srep34375.
[43] C. Ahlgrim, T. Pottgiesser, T. Sander, Y.O. Schumacher, M.W. Baumstark, Flow cytometric assessment of erythrocyte shape through analysis of FSC histograms: use of kurtosis and implications for longitudinal evaluation, PLoS One 8 (3) (2013) e59862.
[44] B.W. Silverman Density Estimation for Statistics and Data Analysis 1986 Chapman and Hall New York 10.1201/9781315140919.
[45] J.W. Tukey, Exploratory Data Analysis, Addison-Wesley, Reading, MA, 1977.
[46] B.H. Erickson, T.A. Nosanchuk, Understanding Data, Second Edition, Open University Press, Buckingham, 1992.
[47] E. Nagababu, S. Ramasamy, J.M. Rifkind, Y. Jia, A.I. Alayash, Site-specific cross-linking of human and bovine hemoglobins differentially alters oxygen binding and redox side reactions producing rhombic heme and heme degradation, Biochemistry 41 (23) (2002) 7407–7415, https://doi.org/10.1021/bi0121048.
[48] B.P. Yakimov, M.A. Gogoleva, A.N. Semenov, S.A. Rodionov, M.V. Novoselova, A. V. Gayer, A.V. Kovalev, A.I. Bernakevich, V.V. Fadeev, A.G. Armaganov, V. P. Drachev, D.A. Gorin, M.E. Darvin, V.I. Shcheslavskiy, G.S. Budylin, A. V. Priezzhev, E.A. Shirshin, Label-free characterization of white blood cells using fluorescence lifetime imaging and flow-cytometry: molecular heterogeneity and erythrophagocytosis, Biomedical Optics Express 10 (8) (2019) 4220–4236, https://doi.org/10.1364/BOE.10.004220.
[49] M. Monici, Cell and tissue autofluorescence research and diagnostic applications, Biotechnol. Annu. Rev. 11 (2005) 227–256, https://doi.org/10.1016/S1387-2656(05)11007-2.
[50] W. Zheng, D. Li, Y. Zeng, Y. Luo, J.Y. Qu, Two-photon excited hemoglobin fluorescence, Biomed. Opt. Express 2 (1) (2011) 71–79, https://doi.org/10.1364/BOE.2.000071.
[51] N.M. Htun, Y.C. Chen, B. Lim, T. Schiller, G.J. Maghzal, A.L. Huang, K.D. Elgass, J. Rivera, H.G. Schneider, B.R. Wood, R. Stocker, K. Peter, Near-infrared autofluorescence induced by intraplaque hemorrhage and heme degradation as marker for high-risk atherosclerotic plaques, Nat. Commun. 8 (1) (2017) 75, https://doi.org/10.1038/s41467-017-00138-x.
[52] R. Zhu, T. Avsievich, X. Su, A. Bykov, A. Popov, I. Meglinski, Hemorheological alterations of red blood cells induced by 450-nm and 520-nm laser radiation, J. Photochem. Photobiol. B Biol. 230 (2022) 112438, https://doi.org/10.1016/j.jphotobiol.2022.112438.
[53] I. Saytashev, R. Glenn, G.A. Murashova, S. Osseiran, D. Spence, C.L. Evans, M. Dantus, Multiphoton excited hemoglobin fluorescence and third harmonic generation for non-invasive microscopy of stored blood, Biomed. Opt. Express 7 (9) (2016) 3449–3460, https://doi.org/10.1364/BOE.7.003449.

Microscopy Research and Technique

WILEY

MICROSCOPY RESEARCH & TECHNIQUE

RESEARCH ARTICLE

Development of Structured Illumination Microscope Using Transmission Diffraction Grating Obtained by Analog Microfilming Method

Aleksa Denčevski[1] | Jovana Z. Jelić[1] | Ana Senkić[2] | Aleksandar J. Krmpot[1] | Mihailo D. Rabasović[1]

[1]Institute of Physics Belgrade, University of Belgrade, National Institute of the Republic of Serbia, Belgrade, Serbia | [2]Centre for Advanced Laser Techniques, Institute of Physics Zagreb, Zagreb, Croatia

Correspondence: Aleksa Denčevski (dencevski@ipb.ac.rs)

Received: 10 April 2024 | **Revised:** 13 June 2024 | **Accepted:** 16 November 2024

Review Editor: Alberto Diaspro

Funding: This study was supported by the Institute of Physics Belgrade, through a grant by the Ministry of Education, Science, and Technological Development of the Republic of Serbia.

Keywords: diffraction grating | resolution measurement | structured illumination microscopy | super-resolution microscopy

ABSTRACT

We present the development of a custom-built structured illumination microscope (SIM) featuring a specially designed transmission diffraction grating. Employing the analog microfilming method, we fabricated transmission diffraction gratings suited to the specific requirements of our system. This robust and cost-effective method allows for the fabrication of diffraction gratings with customized constants, ensuring excellent transmission in both the visible and near-infrared spectra. Additionally, to assess the performance of our system, we measured the resolution in both epifluorescent and super-resolution imaging modalities by applying two independent methods: the conventional resolution measurement using fluorescent beads and the knife-edge technique applied on the MoS_2 monolayer flakes. Both methods confirmed enhancement in the resolution of SIM over the epifluorescent imaging modality. Furthermore, we have successfully demonstrated the capabilities of our microscope by imaging fluorescently labeled astrocytes, specifically targeting the vimentin filament protein within these cells. The super-resolution images reveal fine structures of the vimentin cytoskeleton that remain unresolved in the epifluorescent image.

1 | Introduction

Fluorescent microscopy is one of the most widely used methods for visualizing biological samples. However, its resolution is fundamentally limited by diffraction. The diffraction limit, commonly defined by Abbe or Rayleigh criteria, depends on the excitation wavelength and numerical aperture of the objective lens (Mondal and Diaspro 2013). In recent years, novel methods have been developed to exceed the diffraction limit and enable the recording of the fine structures of biological samples (Hess, Girirajan, and Mason 2007; Hell and Wichmann 1994; Schmidt et al. 2021). Among these techniques, a simple optical configuration of a structure illumination microscope emerged as a powerful approach that enables the enhancement of resolution up to two times compared to the diffraction limit (Diaspro and Van Zandvoort 2016; Gustafsson 2000; Heintzmann and Huser 2017; Wu and Shroff 2018).

All structured illumination microscope (SIM) setups utilize a regular illumination pattern to excite fluorescent samples. Microscopes might be regarded as low-pass spatial frequency filters. Specifically, the pattern enables the inclusion of high-frequency components of the sample structure within the frequency range that can be recorded. By recording

Summary

- We fabricated transmission diffraction gratings suited to the specific requirements of our system.
- We have successfully demonstrated the capabilities of our microscope by imaging fluorescently labeled astrocytes.

multiple images at various angles and phases of the pattern, it becomes possible to achieve an image resolution surpassing the diffraction limit by reconstruction (Diaspro and Van Zandvoort 2016).

Several methods have been developed for generating the illumination pattern in SIM. Commonly, diffraction gratings are employed to generate the pattern on the sample, whereas two diffraction orders interfere in the focal plane of the objective (Heintzmann and Cremer 1999; Gao et al. 2011; Wang, Pitter, and Somekh 2011; Gustafsson et al. 2008; Matsuzaki et al. 2024). In many applications, the beam is shaped using diffractive optical elements (DOE) (Liu et al. 2022), a spatial light modulator (SLM) (Förster et al. 2014), or a digital micromirror device (DMD) (Dan, Yao, and Lei 2014; Calisesi et al. 2022). The fiber coupler method has also been utilized to generate two (Hu et al. 2019) or three beams (Helle et al. 2020; Calvarese et al. 2022) that interfere with the sample plane, effectively producing the pattern. While these approaches allow for the rapid generation of complex patterns, they are considerably more expensive and technically challenging compared to the use of diffraction gratings.

To surpass the diffraction limit and achieve higher-resolution imaging, it is necessary to perform reconstruction using the recorded images and remove the pattern generated by any of the aforementioned methods. Various software tools have been developed for image reconstruction, with notable examples including FairSIM (Müller et al. 2016) and SIMToolbox (Křižek et al. 2015; Pospisil et al. 2018). In recent years, novel software solutions have emerged to enable image reconstruction using only three recorded images without changing the pattern phase (Ingaramo et al. 2014; Ströhl and Kaminski 2015). On the other hand, applications utilizing three-beam interference allow for sample recording without pattern rotation (Calvarese et al. 2022; Schropp, Seebacher, and Uhl 2017; Schropp and Uhl 2014).

In this study, we will present the development of a custom-built SIM microscope as well as the measurement of the resolution of two imaging modalities by several independent methods. Also, we will present the recording of biological samples to present the capabilities of our custom-built setup.

Due to critical limitations with commercially available options, we have developed a method for the fabrication of transmission diffraction gratings suited to the specific requirements of our system. The primary drawback of commercial gratings for SIM setups is the lack of symmetry in optical power distribution between ± 1 diffraction orders. On the contrary, the developed method enabled us to fabricate diffraction gratings with preferred constants, suitable for both visible and near-infrared spectra. Also, we developed a mechanism for rotating the diffraction grating and adjusting its position. By rotating the grating just three times and changing the phase three times, we can record nine images for subsequent reconstruction.

Our system allows for imaging in both epifluorescent (EPI) and super-resolution (SIM) modalities using a single setup, facilitated by a rapid and straightforward mode-switching mechanism. To minimize sample exposure to laser radiation, the entire system is hardware-trigger-controlled. We have implemented an Arduino microcontroller for easy synchronization and activation of all system components.

For data analysis, we employed the OS-SIM and MAP-SIM algorithms from the SIMToolbox software, an open-source tool available at (SIMToolbox n.d.). To control the entire system, we have developed user-friendly software that not only enables simple operation but also ensures reliable and selective data storage.

2 | Methods

2.1 | 2D SIM Setup

We have built a custom-made 2D SIM, Figure 1, based on the arrangement presented in (Gustafsson 2000). The mechanical foundation of our system is provided by a microscopic frame (ICM405, Zeiss, Germany), from which the original optical components were removed. Through the meticulous design of mechanical elements, we reconfigured the microscopic frame and positioned optical components such as the dichroic mirror (DM) and tube lenses (TL) in both excitation and emission, aligning them according to the requirements of our system.

For the excitation, a laser diode (SHD4850MG, Roithner Lasertechnik GmbH, Austria) at 488 nm is used, providing an elliptical beam with a maximum output power of 50 mW. Laser diode current and power levels are controlled by a laser driver (LDC205C, Thorlabs, USA). Ellipticity correction is achieved using a beam expander (BE) with two cylindrical lenses (f_1,f_2). A second BE, consisting of two plano-convex lenses (f_3,f_4), is employed for beam expansion. Since the laser diode operates in a multimodal transversal mode, a 30 μm pinhole is positioned at the common focal plane of the lens (f_3) and (f_4) for additional spatial filtering. The absence of higher mode artifacts is confirmed by measuring the beam profile before and after correction. Power losses of approximately 20 % are attributed to spatial beam filtering.

The collimated and filtered beam is directed onto a specially developed transmission diffraction grating with a constant of 40.1 μm. The properties and design of the diffraction grating are discussed in detail in chapter 3.1. The diffraction grating is mounted on a rotational-translational stage, originally designed according to (Nilsson, Dahlberg, and Andersson 2021). This grating can be rotated by the preferred angle in the plane perpendicular to the direction of beam propagation. The stage also facilitates precise translation movement of the grating, allowing for control of the phase of the illumination pattern in the focal plane of the objective. Details of this precision stage are

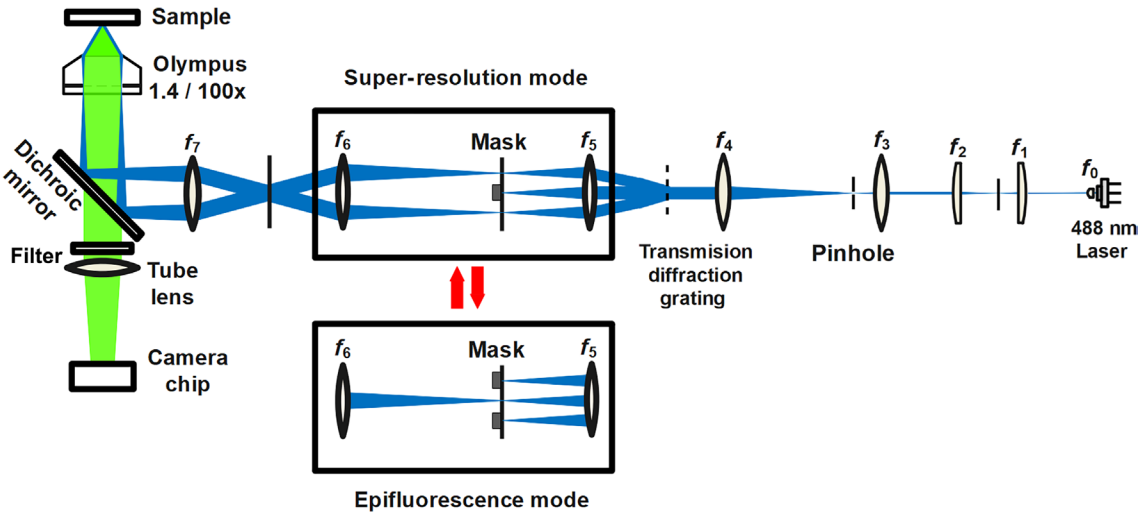

FIGURE 1 | 2D SIM experimental setup. A laser diode at a wavelength of 488 nm is used for excitation. A system consisting of two BEs and a pinhole aperture is used for beam cleaning and expansion, enabling the expanded beam to reach the diffraction grating. In the EPI imaging modality, all orders except zero are cutoff. In the super-resolution SIM imaging modality, only ± 1 diffraction orders are allowed to pass. We use this mode to record images for subsequent reconstruction. The fluorescent signal passes through an objective lens, a DM, and an emission filter before being focused onto the camera chip using a tube lens.

described in the next chapter. The grating is positioned in the focal plane of the lens (f_5), which, together with the next lens (f_6), forms a BE with an expansion factor of 1.5. The BE enables the use of a somewhat coarser diffraction grating, significantly facilitating its production, while also allowing for more precise control of the pattern's phase change.

A mode-switching mechanism consisting of two masks mounted on a specially designed turret is positioned in the focal plane of the lens (f_5). This setup allows for operation in two distinct modes: epifluorescent and super-resolution. The first mask selectively filters out all orders except the zero-order, facilitating work in epifluorescent mode. The second mask blocks all orders except − 1 and 1, providing structured illumination in super-resolution mode. A mode-switching mechanism ensures consistent positioning for efficient order filtering and a smooth transition between microscope operating modes.

Following this beam expansion, the beam(s) is (are) directed onto the TL (f_7), an achromatic lens with a focal length of 200 mm. Importantly, the focal plane of the TL aligns with the back focal plane of the objective. The entire optical system is designed to complement the objective (UPLSAPO100XO/1.4, Olympus, Japan). In the super-resolution mode, the − 1 and 1 diffraction orders reach the edges of the back aperture, achieving the finest pattern in the sample plane with a pattern period of 272 nm.

The aforementioned DM (DMLP490R, Thorlabs, USA) was used to separate the excitation light from the emission light. The emission branch of our setup is designed to incorporate as few optical components as possible to minimize the losses in the fluorescence signal. Fluorescence collected by the objective is directed onto a DM and a TL (TTL 200, Throlabs, USA). For detection, we use a camera (CS2100M—USB, Thorlabs, USA) mounted on a translational stage, enabling precise adjustment of its position along the optical axis. The camera features a chip with dimensions of 1920×1080 pixels and a pixel size of 5.04 μm. Each pixel on the camera corresponds to an area of 45.3×45.3 nm in the sample plane. Spectral filtering is implemented in both the excitation (FELH0500, Thorlabs, USA) and emission (MF530-43, Thorlabs, USA) arms.

2.2 | Control System

The board (TSI-IOBOB2, Thorlabs, USA) functions as a shield for the Arduino microcontroller and monitors the camera's activity. It enables the triggering of the camera by detecting either the rising or falling edge of the trigger signal. Stepper motors (NEMA 17, Stepperonline), controlled via a driver (TB6600, Stepperonline), handle the rotation and translation of the diffraction grating. The system is synchronized so that the laser diode is active only during the camera exposure. The rotation of the diffraction grating and pattern's phase shift take place only when the laser diode is turned off to reduce the phototoxicity and photobleaching of biological samples.

The entire setup is controlled using user-friendly software developed in the Python programming language. The software enables the selection of parameters such as the rotation angle of the diffraction grating, the number of phases, and the exposure time. It provides precise control of the laser diode power levels using the digital-to-analog converter, directly controlled by the same microcontroller. Moreover, the control software allows for a seamless selection of operating modes for a rapid transition between epifluorescent and super-resolution imaging modalities. The software automatically generates appropriate folders to store recorded images and important information regarding measurement conditions, such as laser power, camera exposure time, objective type, and the size of the field of view. The Arduino code, as well as the Python code of the software controlling the entire system, with all corresponding files for hardware triggering, can be found in the repository (Denčevski 2024).

2.3 | Image Reconstruction Software

The recorded images were used for reconstruction using the open-source software SIMToolbox (SIMToolbox n.d.), which offers a range of algorithms for image reconstruction. Specifically, we employed two algorithms: OS-SIM, which allows for the resolution improvement up to a maximum of 1.4 times (Karadaglić and Wilson 2008), and MAP-SIM, capable of potentially reducing artifacts caused by refractive index mismatching within the samples and illumination imperfections. We opted for this software due to its ability for manual recognition of peaks in Fourier space using different filters. While reconstruction typically involves a calibration file (SIMToolbox n.d.), our developed setup does not support such calibration.

3 | Results

3.1 | Fabrication and Characterization of Diffraction Gratings

The core component of the SIM setup is the system responsible for generating an interference pattern in the sample plane. This system features a specially designed diffraction grating mounted on a stage, facilitating both translational and rotational motion of the grating. This capability allows for precise manipulation of the interference pattern within the sample plane. We fabricated transmission diffraction gratings using the microfilming method (Minton 1994). Initially, a grating pattern generated by a matrix of pixels was printed. The size of this matrix was determined by the dimensions of the paper used for printing and the printing resolution. Specifically, we utilized 300×200 mm photo matte paper with a printing resolution of 300 dpi, resulting in a matrix of 3452 rows by 2362 columns. Subsequently, we populated the matrix with zeros and units, where a unit represented a black-colored pixel on the paper, and a zero indicated transparent pixel. We ensured that each row of the matrix contained alternating segments of zeros and units, maintaining an equal width of transparent and non-transparent stripes in the grating. By comparing the paper size to the number of pixels, we determined the printed grating pixel size to be approximately 85×85 μm. We obtained printed gratings with constants ranging from 170 to 2040 μm. Subsequently, we used an analog microfilming device, with a maximum scanning resolution of 640 dpi. The resulting transmission diffraction gratings are 10 mm wide and have a constant range from 13.3 to 89.5 μm. The resolution of the microfilming device limits the finest possible diffraction grating constant we can achieve. The finest usable diffraction grating we generated has a constant of 13.3 μm.

Additionally, we determined the constant of each obtained diffraction grating using two approaches. First, we recorded the bright-field images of the diffraction gratings with our microscope, Figure 2a. The grating constants were then calculated using these images and the prior knowledge of the pixel size. The second method involved conventional measurement of the angle of diffraction orders. The results obtained by these methods are in agreement. For example, the diffraction grating used in this setup has a constant of 40.1 μm. With the second method, a constant of 38.7 μm was measured. For all diffraction gratings listed in the table, the second method gives slightly lower values; however, the deviation between these methods did not exceed 4 % in any case.

Furthermore, we examined the transmission properties of the foil used for microfilming, as well as the transmission characteristics of the coating. The transmission curves, Figure 2b, illustrate certain losses on the foil material. However, diffraction gratings fabricated in this manner can be used in both the visible and near-infrared parts of the spectrum. Even though the analog microfilming method is known as a permanent method for data storage, there is a lack of information regarding the potential effects of the high-intensity radiation on the microfilm foil, to the best of our knowledge. Hence, we investigated the photostability of the produced gratings through regular usage over a 2-year timeframe. The average power density applied to the diffraction grating was approximately 0.2 Wcm^{-2}. Our observations revealed no degradation of the grating over time.

In addition to the appropriate diffraction grating constant, the second requirement for SIM grating is to have a symmetrical power distribution between ± 1 orders to achieve high contrast. We measured the power distribution across different orders and confirmed that the variation in power distribution between ± 1 orders is approximately 5% or less. Table 1 provides an overview of the produced transmission diffraction gratings, outlining the constants of the printed gratings used in the production of corresponding diffraction gratings, as well as the power distribution between ± 1 and 0 diffraction orders relative to laser power measured immediately after the diffraction grating.

Table 1 indicates specific losses associated with each grating, all of which remain below 20%. These losses result from the presence of higher diffraction orders, which occur due to the non-sinusoidal transmission of the grating. This limitation is inherent to the analog microfilming method. The presence of higher diffraction orders does not affect the interference image due to the implementation of a mask. This mask effectively removes the higher diffraction orders, ensuring a rapid transition between microscope imaging modalities.

To facilitate adjustments in both the pattern phase and rotation angle, we developed a specialized mechanical translational-rotation system. This system involves securing the mount of the transmission diffraction grating to a timing pulley, enabling rotation around a free axis. This arrangement enables the rotation of the grating in a plane perpendicular to the direction of laser beam propagation. The aforementioned timing pulley is linked to a smaller pulley via a timing belt. The smaller pulley is then linked to the axis of a stepper motor, which is controlled via a driver. The reduction ratio between these two timing pulleys allows for a rotation of the grating by 120° when the motor axis completes a 360° rotation. Therefore, our system operates independently of the driver's micro-stepping. The entire assembly is mounted on a differential translator, similarly controlled by a stepper motor-driver setup. This arrangement ensures the consistent rotation of the diffraction grating and adjustment of the phase

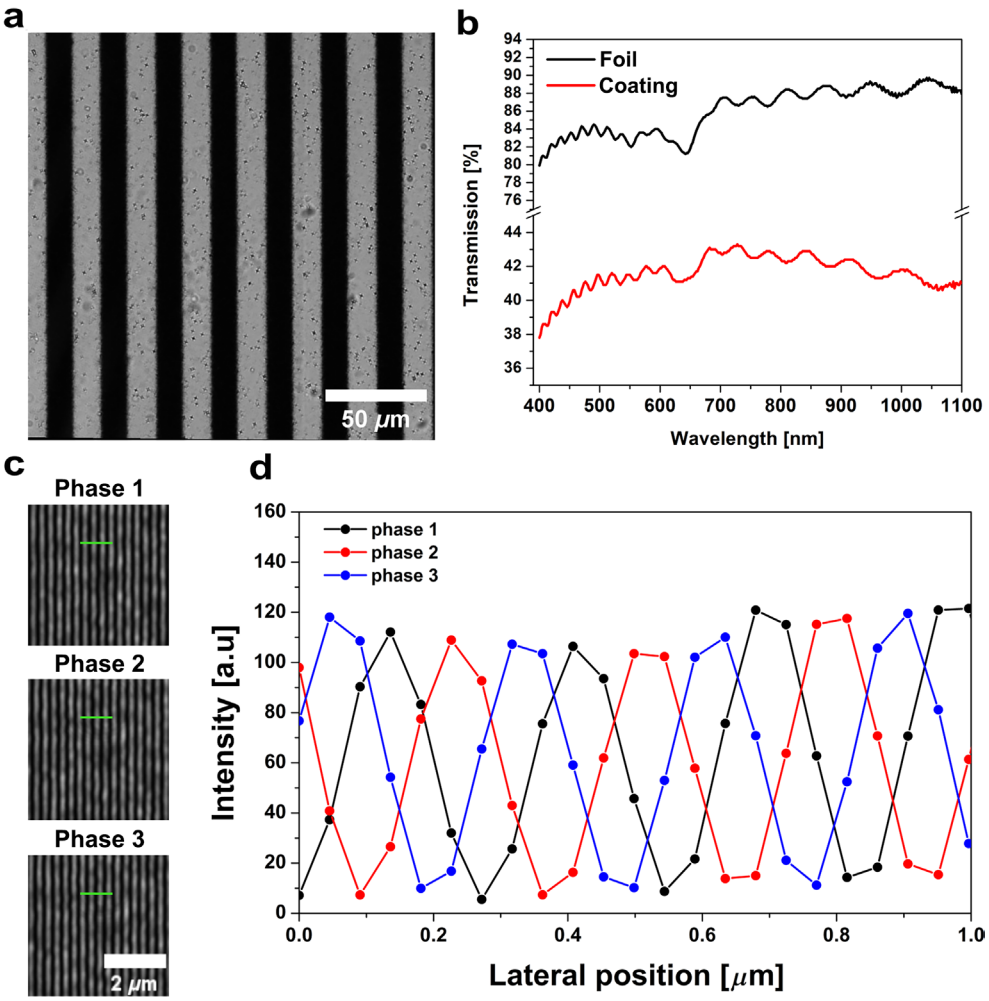

FIGURE 2 | Illustration of diffraction grating characteristics and phase control. (a) Bright-field image of the transmission diffraction grating. (b) Transmission of both the microfilm foil and coating. (c) The interference patterns in the sample plane shifted by one-third of the diffraction grating constant were recorded as a demonstration of phase control. (d) The intensity profiles extracted at the marked position (green line) on the corresponding interference patterns.

TABLE 1 | Overview of produced transmission diffraction gratings. The matrices employed to fabricate these gratings had varying periods, resulting in a range of constants for both printed and microfilmed versions. Additionally, the table outlines the power distribution among the zeroth, ± 1 orders of diffraction, offering insights into the performance of the gratings.

Matrix's period [pixel]	Printed grating constant [μm]	Diffraction grating constant [μm]	P_{-1} [%]	P_0 [%]	P_{+1} [%]
4	340	13.3	18	44	19
6	510	22.5	19	44	17
8	680	27.4	19	44	19
10	850	33.9	24	43	24
12	1020	40.1	23	41	23
14	1190	47.9	22	41	22
16	1360	54.2	24	43	24
18	1530	61.4	22	43	21

for the preferred displacement. Typically, the diffraction grating is shifted by an nth fraction of the grating constant. In our setup, we commonly rotate the grating by 120° and shift the diffraction grating three times by a third of the grating constant. However, this mechanism allows for arbitrary rotation angles and grating displacements as needed.

Given the variety of diffraction gratings produced via the microfilming method, we selected a specific grating where the ± 1 diffraction orders, upon passing through a segment of the optical system, align on the periphery of the back aperture of the objective. This allows for obtaining the finest interference pattern in the sample plane. To investigate the period of the pattern in the sample plane as well as the change in the phase of the pattern, we removed the emission filter and recorded the reflection of the laser. Following this, we analyzed the intensity profiles extracted from the resulting interference images and determined the distance between the maxima of the pattern perpendicular to its propagation. Based on the prior knowledge of the camera's pixel size in the sample plane, we determined the pattern's period to be 272 nm. The finest period of the pattern is limited by the numerical aperture of the objective lens as well as by the pixelization of the printing and the resolution of the analog microfilming method.

Figure 2c illustrates the variations in the interference pattern as the diffraction grating undergoes controlled translation. Additionally, Figure 2d shows the intensity distribution of the interference pattern for one angle of the diffraction grating and three different phases. We evaluated the contrast of the interference pattern using modulation contrast (Calvarese et al. 2022). We calculated the M modulation contrast of the pattern profile in Figure 2d by averaging the peak and valley values. For all three phases, we obtained $C = 0.8$, where 1 is the theoretical maximum of contrast.

The diffraction grating affects the polarization, as noted in (Palmer 2020). Additionally, the performance of the DM is influenced by polarization. Since our laser diode is linearly polarized, the observed 20 % reduction in modulation contrast compared to the theoretical value is likely due to this polarization effect. However, even without polarization control, our modulation contrast is comparable to, or higher than, other custom SIM setups (Calvarese et al. 2022). An ideal solution for our system would be to develop a half-wave plate similar to the azimuthal polarizer described in (Lu-Walther et al. 2015). Another, although slower, solution would be to rotate half-wave plates simultaneously with the diffraction grating to keep the polarization consistent. The influence of the DM on the polarization can be reduced by adding two identical DMs at an angle of 90 to each other or by replacing the DM with a 30: 70 beam splitter (Calvarese et al. 2022).

The interference pattern is shifted by one-third of a grating constant, Figure 2c,d. To ensure that the grating shifts by the *n*th part of the grating constant, we first determined the number of stepper motor steps required to move the grating for the grating constant. This allowed us to establish the relationship between the rotation of the stepper motor and the phase of the pattern. This information helped us determine the number of steps needed to shift the grating when positioned at an arbitrary angle relative to the direction of motion of the differential translator used for phase shifting. The same interference image was used to investigate the rotation of diffraction grating. Consecutive images of grating rotated by 120° were recorded. A fast Fourier transform (FFT) of all images was performed and the rotation angle was compared to the software-selected rotation angle. A deviation of 0.2° was observed after three consecutive rotations of the diffraction grating by 120°. This information was used for correction in the software.

We have investigated the properties of the rotation and translation system of the diffraction grating in detail, focusing in particular on the repeatability and the influence of the direction and speed of the motor rotation. To check the repeatability of the rotation of the diffraction grating, we rotated the motor shaft by 360°, 30 times in succession. After a total rotation of the diffraction grating by 360°, we checked the position of the grating in relation to the previous position. This test simulates the rotation of the diffraction grating during a real image acquisition. At speeds of less than 2000 steps / s, the deviation in the position of the diffraction grating does not exceed 0.1 %.

With regard to the reproducibility of the translation of the diffraction grating, it is important to move the grating by one-third of its constant during image acquisition. Although the translational position of the grating between two acquisitions is not a critical parameter, we made sure to move the grating in the opposite direction after each image acquisition. This precaution prevents the support of the grating from obstructing the laser beam after several acquisitions.

We examined potential deviations in both the direction and speed of rotation of the motor, but no significant deviations were observed. Calibration of the pattern's phase and correction for deviations in the position of the diffraction grating during rotation are key components of the control system we developed.

The microfilming method is a widely used technique for storing large amounts of data. This method allows for the production of a substantial quantity of microfilms in a short time, making it suitable for the mass production of diffraction gratings. We examined the reproducibility of manufacturing diffraction gratings using the microfilming method. The characteristics of the diffraction gratings produced in the first series are shown in Figure 2 and Table 1. We produced a new series of gratings, with the diffraction grating used in this experiment having a constant of 40.1 μm. The mean value of the grating constants from the second series is 40.9 μm, and the deviation of the constants within the series does not exceed 5 %.

We also compared the transmission characteristics of the diffraction gratings from the two series. At a wavelength of 488 nm, the maximum deviation between two diffraction gratings, regardless of the manufacturing series, does not exceed 3 %. Given the importance of the power distribution of the ± 1 diffraction orders, we examined the deviation in the power distributions of these two orders. As previously mentioned, the power difference of these two orders does not exceed 5 %, which was confirmed for both series of diffraction gratings.

Due to all the above factors, analog microfilming can be used to make transmission diffraction gratings not only for laboratory purposes but also for mass production. This method is currently less common due to modern data storage techniques. A

disadvantage of this method of producing diffraction gratings is the inability to achieve sinusoidal transmission, resulting in losses associated with the presence of higher diffraction. Our cost for making these diffraction gratings is about $\$5 - \$7$ per piece, which is approximately $10 - 20$ times cheaper than off-the-shelf DOEs. If we consider the microfilming method as a custom, cost-free method, the production cost of these gratings is up to several 100 times lower than custom DOEs.

3.2 | Assessment of the SIM Resolution

The resolution enhancement of SIM over the EPI imaging modality was confirmed through two distinct measurement approaches. Initially, a conventional technique involving the imaging of fluorescent beads was employed. Intensity profiles of individual beads were extracted from the recorded images. Approximately 30 intensity profiles were extracted and fitted with a Gaussian function. The resolution was subsequently determined as the mean value of the FWHM values obtained from the processed intensity profiles.

Second, we applied the knife-edge technique on transition-metal dichalcogenides, specifically on MoS_2 monolayer flakes. Due to their sub-nanometer thickness (Park et al. 2015), MoS_2 monolayer flakes provide sharp edges suitable for resolution measurements using the knife-edge technique (Mylonakis et al. 2024). Intensity profiles over the edge of the monolayer flake were extracted at approximately 30 positions along the edge and then fitted with the error function (which represents the integral of a Gaussian function). As in the conventional technique, the resolution was calculated as the mean of the FWHM parameters obtained from the processed intensity profiles. These procedures were performed for both EPI and SIM imaging modalities.

3.2.1 | Conventional Resolution Assessment

For conventional resolution measurement, we used the TetraSpeck Fluorescent Microspheres Size Kit (Invitrogen, Thermo Fisher Scientific). This kit contains fluorescent microspheres, often referred to as beads, arranged in six viewing regions on a single microscopic slide. Each region contains beads of specific nominal sizes: 0.1, 0.2, 0.5, 1.0, or 4.0 μm, as well as a mixture of all sizes. For our resolution measurements, we specifically used the 0.1 μm beads. Each bead is fluorescently labeled with four distinct fluorescent dyes, one of which corresponds to excitation at the wavelength of 488 nm. For spectral filtering, we used a filter (MF530-43, Thorlabs, USA) to complement the emission spectra of the fluorescent label.

First, we recorded an image in EPI modality, Figure 3a. Afterward, nine images were recorded (for three different phases at each of three distinct orientations of the diffraction grating) in the SIM modality. The reconstruction performed by the MAP-SIM algorithm of the SIMToolbox software resulted

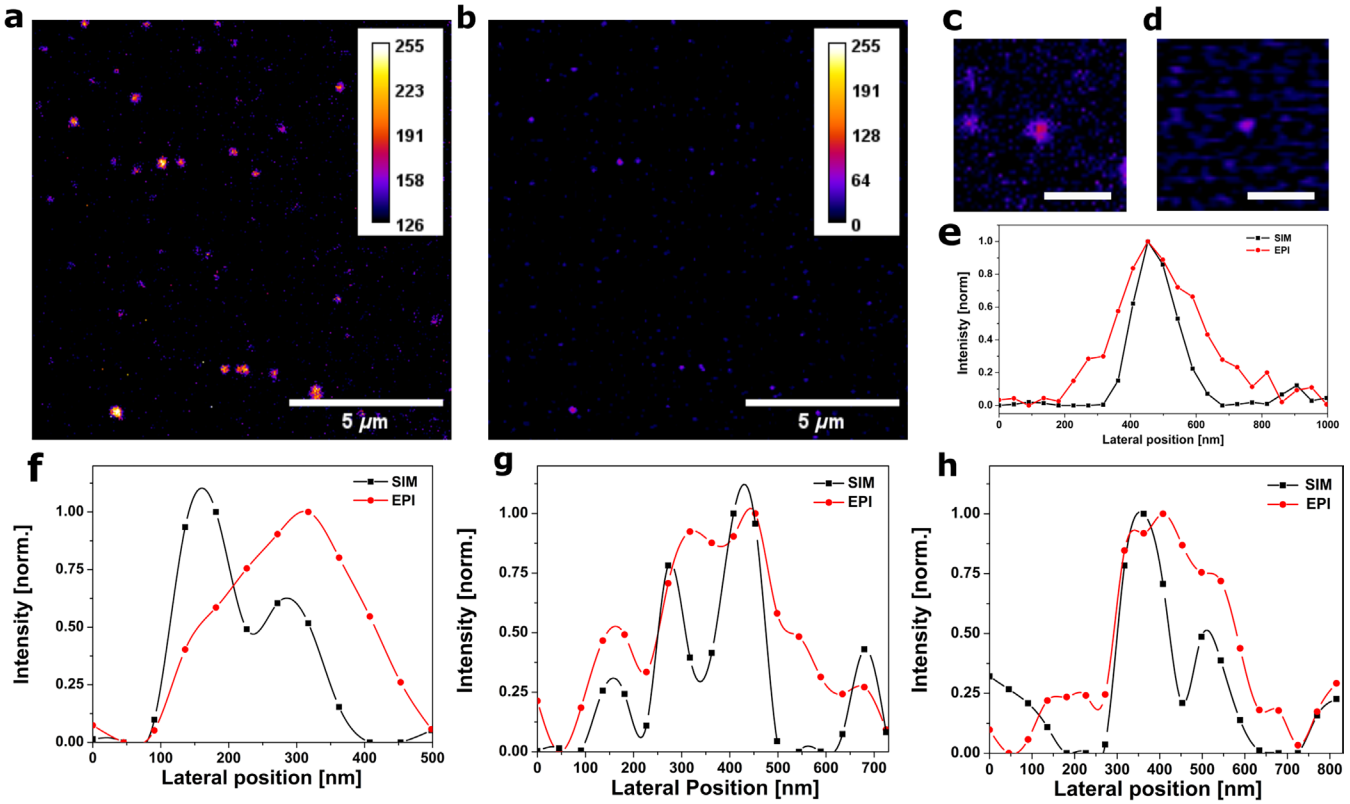

FIGURE 3 | Conventional resolution measurement technique using 0.1 μm fluorescent beads. (a) The EPI image. (b) Reconstructed SIM image obtained by the application of the MAP-SIM algorithm of the SIMToolbox software. The insets show single beads recorded in the EPI (c) and SIM (d) imaging modalities. Scale bar is 2 μm. (e) Comparison of single bead intensity profiles extracted from corresponding insets. (f–h) Intensity profiles of observed two-bead systems showing continuous distribution in the EPI image and two beads at the distance of around 135 nm, resolved in the reconstructed SIM image.

in the SIM image, Figure 3b. The insets, Figure 3c,d, show a single bead recorded in the EPI and SIM imaging modalities, respectively. Since the same sample area was imaged in both modalities, intensity profiles were extracted at the same position within the images and compared, Figure 3e. The extracted intensity profiles were further used for resolution assessment. The resolution measurement on the image recorded in EPI mode resulted in a resolution of (243 ± 9) nm. The same procedure applied to the profiles extracted from the SIM image yielded a mean FWHM value of (163 ± 6) nm. The displayed errors represent the errors of the mean. Given the anticipated resolution and bead size, a deconvolution method must be applied for a more accurate resolution measurement.

The systems consisting of two beads at distances comparable to their sizes were observed in different positions within the sample. Figure 3f–h shows intensity distributions of those two-bead systems recorded in both imaging modalities of our microscope. The difference between the continuous intensity distribution extracted from the EPI images and the resolved distribution (according to the Abbe criteria) obtained on the reconstructed SIM images is evident, showing two beads at a distance of approximately 135 nm. A more precise determination of the resolution is limited by the pixelization of the camera (Pawley 2006), with one pixel corresponding to the area of 45.3×45.3 nm in the sample plane.

Given that the MAP-SIM reconstruction algorithm depends on two parameters, spectral merging and cutoff, we tested variations in the image reconstruction for different values of these parameters. We used reconstructed images of 0.5 μm fluorescent beads and then extracted the intensity profiles of those beads and fitted them with the Gaussian function. Our objective was to find the parameter values for which we obtained bead sizes smaller than their nominal size value. This process helped us to limit the range of parameter values used for the reconstruction. As for the cut-off parameter, we estimated it based on the FFT of the epifluorescent image recorded before the recording of nine images used for reconstruction.

3.2.2 | Resolution Assessment Using the Knife-Edge Technique

For resolution assessment using the knife-edge technique, we used MoS_2 monolayer flakes synthesized via the chemical vapor deposition technique, described in detail in (Senkić et al. 2023). To achieve resolutions approaching the theoretical limit, glycerin was applied on top of the monolayers and secured with a coverglass. Excitation of the sample was performed at a wavelength of 488 nm. The emission filter (FBH 650–40, Thorlabs, USA) was used for spectral filtering, as these monolayers exhibit a photoluminescent signal at wavelengths above 600 nm (Zeng et al. 2017). Initially, we recorded an image of the monolayer flake in EPI imaging modality, Figure 4a. Subsequently, intensity profiles were extracted over the monolayer-substrate boundary, Figure 4b, at approximately 30 positions along the edge of the monolayer flake and then fitted using the error function, Figure 4c. The FWHM parameter of the corresponding Gaussian distribution was determined for each processed intensity profile. The obtained resolution of (212 ± 4) nm in the EPI imaging modality presents the mean value of FWHM values, with the error corresponding to the standard error of the mean.

To determine the resolution in SIM imaging modality, we recorded a set of nine images (for three different phases at each of three distinct orientations of the diffraction grating) of the MoS_2 monolayer flake. The reconstructed image, Figure 4d, was generated using the MAP-SIM algorithm within the SIMToolbox software. We followed the same data analysis procedures as for EPI imaging to evaluate resolution in SIM modality. The MAP-SIM reconstruction yielded a mean FWHM value of (134 ± 8) nm, indicating an enhanced resolution compared to EPI imaging. The obtained resolution is consistent with the distances between two beads observed in intensity profiles displayed in Figure 3f–h. By comparing the resolution between the EPI and SIM imaging modalities, we estimate a resolution enhancement of 1.58 times. This is consistent with other custom SIM setups that use different methods for generating interference image in the sample plane, as reported in (Calvarese et al. 2022; Sandmeyer et al. 2019), where the resolution enhancements are 1.5 and 1.62, respectively. Also, the resolution of our SIM imaging modality is consistent with the results reported by (Cainero et al. 2021). Furthermore, we investigated the resolution of the image reconstructed by the OS-SIM algorithm. The obtained resolution of (153 ± 5) nm corresponds to the maximum expected improvement of 1.4 times compared to EPI imaging modality (Karadaglić and Wilson 2008). The granulation of the monolayer flake present in the reconstructed image is most likely a consequence of the material growth.

Through the microfilming method, we have successfully developed diffraction gratings capable of generating fine patterns in the sample plane, leading to noticeable improvements in resolution. This enhancement is apparent when comparing the resolution of epifluorescence images with those obtained through super-resolution SIM. Moreover, this method allows us to fabricate diffraction gratings with preferred constants, ensuring excellent transmission in both the visible and near-infrared spectra. This versatility enables the development of linear SIM systems for a range of excitation wavelengths, all without significant modifications to the optical setup. However, there are limitations to consider. Recording using diffraction grating fabricated by the microfilming method is slower compared to SIM setups that utilize SLMs. Also, microfilming only enables the fabrication of black-and-white patterns without gray shades. Nonetheless, the cost-effectiveness of production of these gratings is significantly higher—up to a 100 times—compared to commercial alternatives such as DOE and SLM (Hannebelle et al. 2023).

The photoluminescent signal obtained from MoS_2 monolayers results in a relatively high signal-to-noise ratio and no-photobleaching effect, making them convenient for the resolution measurement of different microscopic systems. To confirm their photostability, we extracted a 100×100 pixel area within each image from a set of nine images of the monolayer flake and calculated the mean photoluminescent signal intensity. The mean intensity of the signal in this area remains relatively constant, with a maximum deviation of about 5 % across

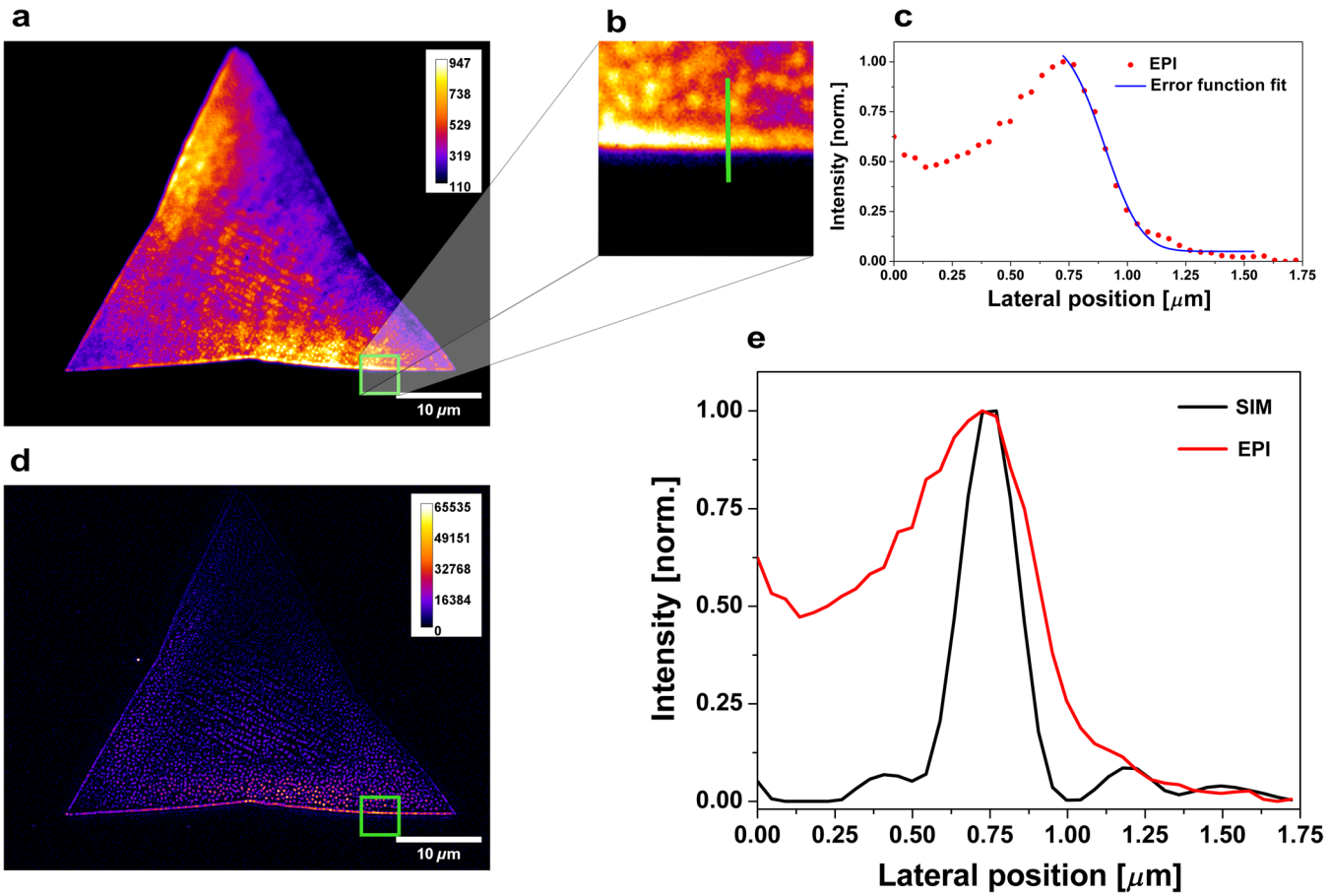

FIGURE 4 | The application of the knife-edge technique on MoS_2 monolayers. (a) The EPI image of the MoS_2 monolayer flake. (b) Shows the extraction of the intensity profile over the edge of the MoS_2 monolayer, followed by fitting using the error function as presented in (c). (d) The super-resolution SIM image. (e) Comparison between the intensity profiles obtained at the marked position of both EPI and SIM images.

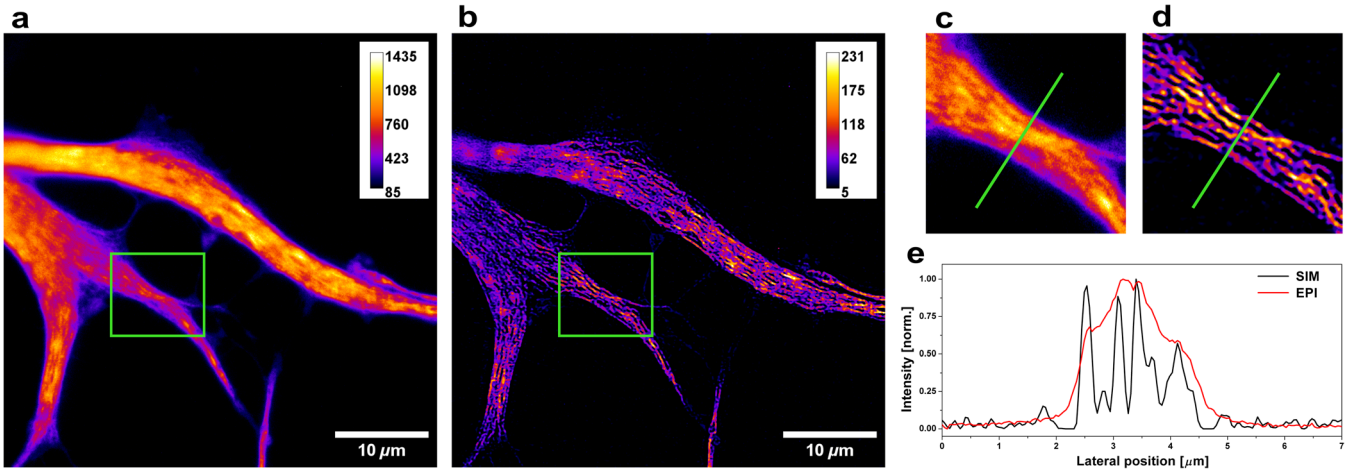

FIGURE 5 | Super-resolution Imagining of fluorescently labeled Astrocytes. (a) The EPI image. (b) The super-resolution SIM image. The insets show enlarged areas of the sample marked on the EPI image (c) and super-resolution SIM image (d). (e) The intensity profiles extracted across the marked areas of the corresponding insets show an improvement in the resolution of SIM over the EPI imaging modality.

the set of images. Additionally, the sub-nanometer thickness of MoS_2 monolayer flakes (Park et al. 2015) makes them suitable for evaluating the quality of the illumination pattern in the sample plane and for additional system alignment purposes. Furthermore, we investigated if the sample plane is plan-parallel to the diffraction grating's plane by tilting the grating. The observed deviations in the average intensity were over 20 %, confirming that our system was well-aligned.

3.3 | Imaging of Biological Samples Using Custom-Made SIM

As the primary application of the SIM setup is the imaging of biological samples, we demonstrated the capabilities of our custom-made SIM microscope by imaging fluorescently labeled astrocytes. A laser diode emitting at the wavelength of 488 nm was used for excitation of the fluorescently labeled vimentin filament protein within these cells (Wu et al. 2022). The emission filter (MF530-43, Thorlabs, USA) was used for spectral filtering. Figure 5a presents the sample recorded in the EPI imaging modality. Subsequently, we recorded a total of nine images, for three different phases at each of three distinct orientations of the diffraction grating. The super-resolution SIM image, Figure 5b, was obtained by reconstructing these nine images using the MAP-SIM algorithm of the SIMToolbox software. The insets, Figure 5c,d, show the same sample region recorded in EPI and SIM imaging modalities, respectively. These insets illustrate the enhanced resolution achieved with SIM imaging. To confirm the resolution improvement, we extracted intensity profiles across the marked region on the insets, for both EPI and SIM images. The intensity profile, Figure 5e, obtained from the super-resolution SIM image reveals fine structures of the vimentin cytoskeleton that remain unresolved in the EPI image.

4 | Conclusion

We have developed a method to fabricate the transmission diffraction gratings suited to the specific requirements of our system. From a variety of gratings produced via the microfilming method, we implemented the one providing the finest pattern in the sample plane, characterized by a period of 272 nm. The variation in power distribution between ± 1 orders is approximately 5 % or less. The losses associated with the presence of higher diffraction orders (which remain below 20 %) arise due to the non-sinusoidal transmission of the grating, a limitation inherent to the analog microfilming method. We examined the photostability of the produced gratings over a two-year period, which revealed no degradation of the grating over time. We examined the reproducibility of manufacturing diffraction gratings using the analog microfilming method and confirmed that this method is not limited to laboratory use. It is well optimized for mass production, both due to the quality characteristics of the manufactured gratings and the cost-effectiveness of the process.

We employed two distinct measurement approaches to evaluate the resolution enhancement achieved by implementing this grating. Initially, we utilized a conventional resolution measurement technique involving the imaging of sub-resolution-sized fluorescent beads. In the EPI modality, the resolution measurement resulted in (243 ± 9) nm. Following the same protocol for the SIM modality, we obtained the resolution of (163 ± 6) nm. For a more accurate resolution measurement, a deconvolution method must be applied, given the anticipated resolution and bead size. Following this, we applied the knife-edge technique on transition-metal dichalcogenides, specifically on the sharp edges of MoS_2 monolayer flakes. The obtained resolution in the EPI imaging modality is (212 ± 4) nm. The reconstructed image generated using the MAP-SIM algorithm yielded a mean FWHM value of (134 ± 8) nm, indicating an enhanced resolution compared to EPI imaging. Furthermore, we investigated the resolution of the image reconstructed by the OS-SIM algorithm. The obtained resolution of (153 ± 5) nm corresponds to the maximum expected improvement of 1.4 times relative to the EPI imaging modality.

To conclude, we have successfully developed a method to fabricate transmission diffraction gratings capable of generating fine illumination patterns in the sample plane of our custom-made SIM setup. Moreover, this method allows us to fabricate diffraction gratings with preferred constants, ensuring excellent transmission in both the visible and near-infrared spectra. Consequently, these gratings are well-suited for the development of near-infrared SIM setups. However, the recording using diffraction grating fabricated by the microfilming method is slower compared to SIM setups that utilize SLMs. Nonetheless, the cost-effectiveness of production of these gratings is significantly higher—up to a 100 times—compared to commercial alternatives such as DOE and SLM. We have successfully demonstrated the capabilities of our microscope by imaging fluorescently labeled astrocytes, specifically the vimentin filament protein within these cells. The SIM images reveal fine structures of the vimentin cytoskeleton that remain unresolved in the EPI image.

Author Contributions

Aleksa Denčevski: conceptualization, investigation, funding acquisition, writing – original draft, writing – review and editing, visualization, validation, methodology, software, formal analysis. **Jovana Z. Jelić:** conceptualization, investigation, funding acquisition, validation, visualization, writing – review and editing, formal analysis, writing – original draft. **Ana Senkić:** validation, data curation, writing – review and editing. **Aleksandar J. Krmpot:** writing – review and editing, project administration. **Mihailo D. Rabasović:** conceptualization, investigation, funding acquisition, writing – review and editing, visualization, validation, methodology, formal analysis, data curation, supervision, resources.

Acknowledgments

The research was supported by the Move For The Science project, granted by Philip Morris. Special thanks to Milan Minić for his invaluable technical assistance and support. Our gratitude is extended to the Laboratory for Biology at the Petnica Research Center for providing a sample of fluorescently labeled astrocytes. We would like to thank prof. Vladana Vukojević from Karolinska Insitute in Stockholm, Sweden for providing fluorescent beads. Additionally, we appreciate the support provided by Lid d.o.o. company for microfilming. The authors acknowledge funding provided by the Institute of Physics Belgrade, through the grant by the Ministry of Education, Science, and Technological Development of the Republic of Serbia.

Conflicts of Interest

The authors declare no conflicts of interest.

Data Availability Statement

The data that support the findings of this study are available from the corresponding author upon reasonable request.

References

Cainero, I., E. Cerutti, M. Faretta, et al. 2021. "Measuring Nanoscale Distances by Structured Illumination Microscopy and Image

Cross-Correlation Spectroscopy (SIM-ICCS).” *Sensors* 21: 21. https://doi.org/10.3390/s21062010.

Calisesi, G., D. Ancora, C. Tacconi, et al. 2022. “Enlarged Field of View in Spatially Modulated Selective Volume Illumination Microscopy.” *Microscopy and Microanalysis* 28: 1–10.

Calvarese, M., P. Paiè, A. Candeo, et al. 2022. “Integrated Optical Device for Structured Illumination Microscopy.” *Optics Express* 30: 30246–30259.

Dan, D., B. Yao, and M. Lei. 2014. “Structured Illumination Microscopy for Super-Resolution and Optical Sectioning.” *Chinese Science Bulletin* 59: 1291–1307.

Denčevski, A. 2024. “Software for Controlling Custom Structured Illumination Microscope (SIM).” https://github.com/aleksa98/SIM-.git.

Diaspro, V., and M. A. Van Zandvoort. 2016. “Super-Resolution Imaging in Biomedicine.” https://doi.org/10.1201/9781315372884.

Förster, R., H.-W. Lu-Walther, A. Jost, M. Kielhorn, K. Wicker, and R. Heintzmann. 2014. “Simple Structured Illumination Microscope Setup With High Acquisition Speed by Using a Spatial Light Modulator.” *Optics Express* 22: 20663–20677.

Gao, L., N. Bedard, N. Hagen, R. T. Kester, and T. S. Tkaczyk. 2011. “Depth-Resolved Image Mapping Spectrometer (IMS) With Structured Illumination.” *Optics Express* 19: 17439–17452.

Gustafsson, M. 2000. “Surpassing the Lateral Resolution Limit by a Factor of Two Using Structured Illumination Microscopy.” *Journal of Microscopy* 198: 82–87.

Gustafsson, M., L. Shao, P. Carlton, et al. 2008. “Three-Dimensional Resolution Doubling in Wide-Field Fluorescence Microscopy by Structured Illumination.” *Biophysical Journal* 94: 4957–4970.

Hannebelle, M. T., E. Raeth, S. M. Leitao, et al. 2023. “OpenSIM: Open Source Microscope Add-on For Structured Illumination Microscopy.” https://doi.org/10.1101/2023.06.16.545316.

Heintzmann, R., and C. Cremer. 1999. “Laterally Modulated Excitation Microscopy: Improvement of Resolution by Using a Diffraction Grating.” *Proceedings of SPIE—The International Society for Optical Engineering* 3568: 185–196.

Heintzmann, R., and T. Huser. 2017. “Super-Resolution Structured Illumination Microscopy.” *Chemical Reviews* 117: 13890–13908. https://doi.org/10.1021/acs.chemrev.7b00218.

Hell, S., and J. Wichmann. 1994. “Breaking the Diffraction Resolution Limit by Stimulated Emission: Stimulated-Emission-Depletion Fluorescence Microscopy.” *Optics Letters* 19: 780–782.

Helle, Ø., F. Dullo, M. Lahrberg, J.-C. Tinguely, O. Hellesø, and B. Ahluwalia. 2020. “Structured Illumination Microscopy Using a Photonic Chip.” *Nature Photonics* 14: 1–8.

Hess, S., T. Girirajan, and M. Mason. 2007. “Ultra-High Resolution Imaging by Fluorescence Photoactivation Localization Microscopy.” *Biophysical Journal* 91: 4258–4272.

SIMToolbox. n.d. “The SIMToolbox Project.” https://simtoolbox.github.io/.

Hu, S., L. Liu, Y. Huang, et al. 2019. “Compact and Low-Cost Structured Illumination Microscopy Using an Optical Fiber Coupler.” *Optics Communications* 436: 227–231.

Ingaramo, M., A. York, E. Hoogendoorn, M. Postma, H. Shroff, and G. Patterson. 2014. “Richardson-Lucy Deconvolution as a General Tool for Combining Images With Complementary Strengths.” *Chemphyschem: A European Journal of Chemical Physics and Physical Chemistry* 15: 794–800. https://doi.org/10.1002/cphc.201300831.

Karadaglić, D., and T. Wilson. 2008. “Image Formation in Structured Illumination Wide-Field Fluorescence Microscopy.” *Micron* 39: 808–818.

Křižek, P., T. Lukes, M. Ovesny, K. Fliegel, and G. Hagen. 2015. “SIMToolbox: A MATLAB Toolbox for Structured Illumination Fluorescence Microscopy.” *Bioinformatics* 32: 318–320. https://doi.org/10.1093/bioinformatics/btv576.

Liu, G., N. Xu, H. Yang, Q. Tan, and G. Jin. 2022. “Miniaturized Structured Illumination Microscopy With Diffractive Optics.” *Photonics Research* 10: 1317–1324.

Lu-Walther, H.-W., M. Kielhorn, R. Förster, A. Jost, K. Wicker, and R. Heintzmann. 2015. “FastSIM: A Practical Implementation of Fast Structured Illumination Microscopy.” *Methods and Applications in Fluorescence* 3: 014001.

Matsuzaki, T., R. Kawamura, A. Yamamoto, et al. 2024. “Advanced Interferometry With 3-D Structured Illumination Reveals the Surface Fine Structure of Complex Biospecimens.” *Journal of Physical Chemistry Letters* 15: 1097–1104.

Minton, C. R. 1994. *Handbook of Microfilm Technology and Procedures*. Bradford, UK: Association of Records Managers Administrators (ARMA).

Mondal, P., and A. Diaspro. 2013. *Fundamentals of Fluorescence Microscopy: Exploring Life with Light*, 1–218. Dordrecht, the Netherlands: Springer Dordrecht.

Müller, M., V. Mönkemöller, S. Hennig, W. Hübner, and T. Huser. 2016. “Open-Source Image Reconstruction of Super-Resolution Structured Illumination Microscopy Data in ImageJ.” *Nature Communications* 7: 10980.

Mylonakis, M., G. J. Tserevelakis, G. Vlachos, et al. 2024. “Bimodal Optical and Optoacoustic Multiview Microscope in the Frequency-Domain.” *Optics Letters* 49: 462–465.

Nilsson, D. P. G., T. Dahlberg, and M. Andersson. 2021. “Step-by-Step Guide to 3D Print Motorized Rotation Mounts for Optical Applications.” *Applied Optics* 60: 3764–3771.

Palmer, C. 2020. *Diffraction Grating Handbook*. 8th ed. New York: Richardson Gratings™ MKS Instruments, Inc.

Park, J., N. Choudhary, J. Smith, G. Lee, M. Kim, and W. Choi. 2015. “Thickness Modulated MoS2 Grown by Chemical Vapor Deposition for Transparent and Flexible Electronic Devices.” *Applied Physics Letters* 106: 012104.

Pawley, J. 2006. *Handbook of Biological Confocal Microscopy*. Vol. 236, 59–79. Wisconsin, US: Springer Science & Business Media.

Pospisil, J., T. Lukes, J. Bendesky, K. Fliegel, K. Spendier, and G. Hagen. 2018. “Imaging Tissues and Cells Beyond the Diffraction Limit With Structured Illumination Microscopy and Bayesian Image Reconstruction.” *GigaScience* 8: giy126. https://doi.org/10.1093/gigascience/giy126.

Sandmeyer, A., M. Lachetta, H. Sandmeyer, W. Hübner, T. Huser, and M. Müller. 2019. “DMD-Based Super-Resolution Structured Illumination Microscopy Visualizes Live Cell Dynamics at High Speed and Low Cost.” https://doi.org/10.1101/797670.

Schmidt, R., T. Weihs, C. Wurm, et al. 2021. “MINFLUX Nanometer-Scale 3D Imaging and Microsecond-Range Tracking on a Common Fluorescence Microscope.” *Nature Communications* 12: 12. https://doi.org/10.1038/s41467-021-21652-z.

Schropp, M., C. Seebacher, and R. Uhl. 2017. “XL-SIM: Extending Superresolution into Deeper Layers.” *Photonics* 4: 33. https://doi.org/10.3390/photonics4020033.

Schropp, M., and R. Uhl. 2014. “Two-Dimensional Structured Illumination Microscopy.” *Journal of Microscopy* 256: 23–36. https://doi.org/10.1111/jmi.12154.

Senkić, A., J. Bajo, A. Supina, B. Radatović, and N. Vujicic. 2023. “Effects of CVD Growth Parameters on Global and Local Optical Properties of MoS2 Monolayers.” *Materials Chemistry and Physics* 296: 127185.

Ströhl, F., and C. Kaminski. 2015. "A Joint Richardson-Lucy Deconvolution Algorithm for the Reconstruction of Multifocal Structured Illumination Microscopy Data." *Methods and Applications in Fluorescence* 3: 014002. https://doi.org/10.1088/2050-6120/3/1/014002.

Wang, L., M. C. Pitter, and M. G. Somekh. 2011. "Wide-Field High-Resolution Structured Illumination Solid Immersion Fluorescence Microscopy." *Optics Letters* 36: 2794–2796.

Wu, H., Y. Shen, S. Sivagurunathan, et al. 2022. "Vimentin Intermediate Filaments and Filamentous Actin Form Unexpected Interpenetrating Networks That Redefine the Cell Cortex." *Proceedings of the National Academy of Sciences* 119: e2115217119.

Wu, Y., and H. Shroff. 2018. "Faster, Sharper, and Deeper: Structured Illumination Microscopy for Biological Imaging." *Nature Methods* 15: 1011–1019. https://doi.org/10.1038/s41592-018-0211-z.

Zeng, Y., X. Li, W. Chen, J. Liao, J. Lou, and Q. Chen. 2017. "Highly Enhanced Photoluminescence of Monolayer MoS2 with Self-Assembled Au Nanoparticle Arrays." *Advanced Materials Interfaces* 4: 1700739. https://doi.org/10.1002/admi.201700739.

Application of the Knife-Edge Technique on Transition Metal Dichalcogenide Monolayers for Resolution Assessment of Nonlinear Microscopy Modalities

Jovana Z Jeli, Marta Bukumira, Aleksa Denevski, Ana Senki, Livio Žuži, Borna Radatovi, Nataša Vujii, Tanja Paji, Mihailo D Rabasovi, Aleksandar J Krmpot

Microscopy and Microanalysis, 2024, **00**, 1–10
https://doi.org/10.1093/mam/ozae061

Original Article

Microscopy AND Microanalysis

Application of the Knife-Edge Technique on Transition Metal Dichalcogenide Monolayers for Resolution Assessment of Nonlinear Microscopy Modalities

Jovana Z. Jelić[1], Marta Bukumira[1], Aleksa Denčevski[1], Ana Senkić[2], Livio Žužić[3], Borna Radatović[4], Nataša Vujičić[2], Tanja Pajić[5], Mihailo D. Rabasović[1], and Aleksandar J. Krmpot[1,*]

[1]*Institute of Physics Belgrade, University of Belgrade, National Institute of the Republic of Serbia, Pregrevica 118, Belgrade 11080, Serbia*
[2]*Centre for Advanced Laser Techniques, Institute of Physics Zagreb, Bijenička cesta 46, Zagreb 10000, Croatia*
[3]*Department of Physics, University of Zagreb, Bijenička cesta 32, Zagreb 10000, Croatia*
[4]*Materials Science Factory, Instituto de Ciencia de Materiales de Madrid (ICMM-CSIC), Sor Juana Ines de la Cruz 3, Madrid 28049, Spain*
[5]*Department for General Physiology and Biophysics, Faculty of Biology, University of Belgrade, Studentski trg 16, Belgrade, 11158, Serbia*

***Corresponding author:** Aleksandar J. Krmpot, E-mail: krmpot@ipb.ac.rs

Abstract

We report application of the knife-edge technique at the sharp edges of WS_2 and MoS_2 monolayer flakes for lateral and axial resolution assessment in all three modalities of nonlinear laser scanning microscopy: two-photon excited fluorescence (TPEF), second- and third-harmonic generation (SHG, THG) imaging. This technique provides a high signal-to-noise ratio, no photobleaching effect and shows good agreement with standard resolution measurement techniques. Furthermore, we assessed both the lateral resolution in TPEF imaging modality and the axial resolution in SHG and THG imaging modality directly via the full-width at half maximum parameter of the corresponding Gaussian distribution. We comprehensively analyzed the factors influencing the resolution, such as the numerical aperture, the excitation wavelength and the refractive index of the embedding medium for the different imaging modalities. Glycerin was identified as the optimal embedding medium for achieving resolutions closest to the theoretical limit. The proposed use of WS_2 and MoS_2 monolayer flakes emerged as promising tools for characterization of nonlinear imaging systems.

Key words: knife-edge technique, nonlinear laser scanning microscopy, resolution measurement, second/third harmonic generation, WS_2 and MoS_2 monolayers

Introduction

Nonlinear laser scanning microscopy (NLSM) is a specialized microscopy technique that uses localized nonlinear excitation to excite fluorescence only within a thin raster-scanned plane. In NLSM, two-photon excited fluorescence (TPEF) is typically detected and used for imaging (Masters & So, 2009; Tserevelakis et al., 2012; Rohrbacher et al., 2017). In addition to TPEF, other imaging techniques include three-photon excited fluorescence, and second- and third-harmonic generation (SHG, THG) (Zipfel et al., 2003; Tserevelakis et al., 2010).

Every optical system has a fundamental limitation of resolution due to diffraction which causes the image to spread in both lateral and axial directions. The diffraction pattern (light intensity distribution) of a point-like light source in the lateral (x,y) and axial (z) dimensions is referred to as a point-spread function (PSF) (Cole et al., 2011). According to the Houston criterion for resolution (van den Bos & den Dekker, 2001), two point sources are considered resolved if the full-width at half maximum (FWHM) of their PSFs no longer overlap. In microscopy, resolution depends on many factors such as numerical aperture (NA) of the objective lens, wavelength, refractive index of the embedding medium, coverglass thickness, distance between the object and coverglass, etc. (Kozubek, 2001).

The standard technique for evaluating resolution is based on the imaging of nanospheres, often referred to as beads. Beads can be used directly to assess lateral resolution, or to determine the PSF by applying the deconvolution method (using bead images and prior knowledge of the actual bead size). Although this method is practical, it does have certain limitations. As bead size decreases, the signal-to-noise ratio (SNR) deteriorates, making it challenging to obtain reliable measurements. Deconvolution, on the other hand, can be severely affected by noise. With axial resolution, the stack image of the beads must be recorded. This is challenging in practice as the beads are prone to photobleaching. Consequently, the measurement of axial resolution results in a relatively small number of data points which affects the quality of the assessment. Furthermore, due to the coherent nature of the SHG signal, its PSF is a contentious issue, as pointed out in Chen et al. (2012). Accordingly, imaging of common polystyrene beads by SHG microscopy is not widely used and has been reported only in terms of the material nonlinear response characterization, with no resolution assessment (Hou & Labarthet, 2018). Similarly, sparse THG imaging of similar objects for resolution measurement was demonstrated in Masihzadeh et al. (2009). Several inorganic nanocrystals of noble metals or metal oxides arranged in a noncentrosymmetric crystal structure

Received: February 5, 2024. **Revised:** June 19, 2024. **Accepted:** June 23, 2024

(such as $KTiOPO_4$) have been used as point-like SHG signal sources in NLSM (Mahou et al., 2017), in a manner similar to beads. In contrast to fluorescence, SHG is theoretically an achromatic phenomenon which can be obtained at arbitrary wavelengths covering the entire range of tunable NIR lasers. This makes such crystal structures suitable for NLSM resolution evaluation.

Due to the lack of techniques for assessing resolution of all three modalities of NLSM (TPEF, SHG, and THG) within a single microscopic system, we were inspired to conduct a more in-depth investigation into this matter. Here, we propose application of the knife-edge technique to monolayers of transition metal dichalcogenides (TMDs), in particular WS_2 and MoS_2, for evaluation of lateral resolution. In their single-layer form, TMDs have a D_{3h} symmetry where the lack of inversion symmetry allows for an unusually strong SHG signal. This effect is very sensitive to layer thickness, crystalline orientation, and layer stacking (Kumar et al., 2013; Yin et al., 2014; Rosa et al., 2018). The thickness of our samples (<1 nm) (Radisavljevic et al., 2011) and their efficient SHG production (Woodward et al., 2016) and THG (Wang et al., 2013) signals also allow direct measurement of axial resolution. The intensity profiles obtained at the monolayer-substrate boundary are free from artifacts typically associated with thicker samples. Although a similar approach was reported by Mehravar et al. (2020), the absence of axial resolution results in their study can be attributed to excessive thickness of the samples used. Other 2D materials (2DMs) such as hBN have been reported as a test material in resolution assessment of a confocal focus-engineered coherent anti-Stokes Raman scattering (cFE-CARS) microscope (Lee et al., 2023). However, h-BN exhibits an SHG signal that is an order of magnitude lower than that of the MoS_2 monolayer (Li et al., 2013). SHG and THG signals obtained by WS_2 and MoS_2 monolayers both result in a relatively high SNR and no photobleaching effect.

While the knife-edge technique is commonly used for laser beam profile determination (Araújo et al., 2009), its application in resolution assessment of various microscopic techniques (Chu et al., 2005; Wachulak et al., 2017; Mennel et al., 2018; Mylonakis et al., 2024) has generally been limited and auxiliary. The knife-edge technique is a method of assessing resolution by analyzing the transition zone across a boundary formed by sharp-edged objects. By extracting intensity profiles across the edge and measuring the width and slope, one can determine the resolution of an optical system. A sharper and narrower transition generally indicates a higher resolution, while a wider transition indicates a lower resolution. In this study, we present the measurement of resolution in different imaging modalities of our custom-built nonlinear laser scanning microscope (Rabasovic et al., 2015) utilizing two distinct approaches.

Here, we report application of the knife-edge technique on WS_2 and MoS_2 (for lateral resolution assessment in SHG and THG modalities). We also evaluated both lateral (in TPEF modality) and axial resolution (in SHG and THG modalities) directly via the FWHM parameter of the corresponding Gaussian distribution. Our study includes a comprehensive analysis of how the resolution varies with the NA of the objective lens, excitation wavelengths, refractive index of the embedding medium, and imaging modality of the microscope. In addition, the obtained PSF (FWHM) values were employed in deconvolution of the image, resulting in significant improvement in image resolution.

Materials and Methods

NLSM Experimental Setup

Our custom-made NLSM system [detailed information can be found in Pajić et al. 2022] enables precise control of power levels and motorized positioning of the sample in the axial direction with a minimum step-size of 0.25 μm. For TPEF and SHG imaging, a tunable (700–1,000 nm) Kerr lens mode-locked femtosecond Ti: Sapphire laser (Mira 900, Coherent Inc., CA, USA) with a repetition rate of 76 MHz and pulse duration of 160 fs was used. Femtosecond pulses were also obtained from a SESAM mode-locked Yb:KGW laser (Time-Bandwidth Products AG, Time-Bandwidth Yb GLX; Zurich, Switzerland) at a fixed wavelength of 1,040 nm with a pulse duration of 200 fs and a repetition rate of 83 MHz. After being expanded 3.75 times with a Keplerian telescope (obtained by AC254-040-A and AC254- 150-A lenses, both from Thorlabs, Inc.), the laser beams are directed toward the objective lens via a main dichroic mirror (MDM; FF700-SDi01-25x36, Semrock). Beam raster scanning over the sample is achieved using a galvo scanner (6,215H, Cambridge Technologies). A National Instruments USB-6351 card was used for signal acquisition and control of the galvo scanner with a sampling rate of 1.2 M sample/s.

SHG and TPEF signals were collected in back reflection by an objective lens, passed through the MDM, filtered with appropriate filters (depending on the excitation wavelengths used and imaging modality), and then focused onto a photomultiplier tube (PMT) (RCA, PF10006). In SHG modality, we used several narrow bandpass filters (FBH370-10, FBH400-10, FBH420-10, and FB520-10, all from Thorlabs, Inc.). In the TPEF modality, the signal was filtered with a shortpass filter (FESH0700, Tholarbs, Inc.). In THG imaging, the signal was detected in the forward direction (transmission arm) after being reflected by two harmonic beam splitters (HBSY13, Thorlabs, Inc.) to reduce reflection of laser light. Finally, the residual laser light was filtered out by two filters (FGUV11M, Thorlabs, Inc. and FSR-U340, Newport). After filtering, the THG signal was focused onto the entrance window of the PMT (H7422, Hamamatsu, Japan).

Fluorescent Beads

To measure lateral resolution in TPEF modality, we used a TetraSpeck Fluorescent Microspheres Size Kit (Invitrogen, Thermo Fisher Scientific Inc.) which was specially developed for the calibration of microscopes. The slide contains six viewing areas, each of which contains nanospheres of a specific (nominal) size: 0.1 μm, 0.2 μm, 0.5 μm, 1.0 μm, or 4.0 μm and a mixture of all sizes. Each nanosphere is stained with four different fluorescent dyes: 365/430 nm, 505/515 nm, 560/580 nm, and 660/680 nm. This makes them suitable for applications that require a broad spectral range. For the purpose of resolution measurements, the optimal SNR was obtained for 0.2 μm fluorescent beads. The profile extracted from the recorded images of the beads was fitted by the Gaussian function. The lateral resolution was directly assessed through the FWHM parameter of the Gaussian fit.

WS_2 and MoS_2 Monolayers

Synthesis

MoS_2 samples were synthesized using a chemical vapor deposition (CVD) technique, described in detail in Senkić et al. (2023). Samples were grown on two substrates: c-cut sapphire

and Si/SiO_2, each with a 290 nm oxide layer thickness. The synthesis procedure is the same as described in Senkić et al. (2023), with a growth temperature, T_G, equal to 875°C. The thickness of monolayers was determined using atomic force microscopy (AFM), and was determined to be 0.8 nm Senkić et al. (2023).

Similar to the MoS_2 growth, DI water-based solutions were used for WS_2. As a growth promotor, a 5 ppm concentration of NaOH solution was used, whereas the tungsten source was a 100 ppm concentration of ammonium metatungstate hydrate $(NH_4)_6H_2W_{12}O_{40} \cdot H_2O$ (99.99% Sigma Aldrich). These solutions were mixed in equal parts, and the 10 μL droplet of this mixture was dropcast onto the cleaned substrate, which were then placed on a hot plate at 120°C until the droplet dried. The Si/SiO_2 substrate was first cleaned with argon gas, and then in an O_2 plasma chamber for 10 min. Before loading the substrate with the deposited metal precursor, the CVD furnace was heated to 500°C under argon flow ($\zeta = 200$ sccm). When the substrate was loaded, the furnace temperature was raised to the growth temperature of 850°C. The sulfur temperature was set to 140°C, and argon flow to 100 sccm. When both temperatures reached their target value, the argon flow was decreased to 75 sccm and the synthesis process was started. After 5 min, the furnace was then quickly cooled to 775°C using compressed air with the argon flow set to 50 sccm, whereas the sample remained in the furnace. Then, the argon flow was stopped ($\zeta = 0$ sccm), the furnace further cooled to 500°C, and the sample was completely removed from the CVD furnace.

Transfer

MoS_2 and WS_2 were moved from the Si wafer by using polydimethylsiloxane (PDMS) transfer (Niehues et al., 2018). The first step is a pickup, in which 2DMs are moved from the growth substrate on the PDMS sheet. In this step, the PDMS sheet (160 μm thick) purchased from GEL-PAK company was cut into a rectangle slightly larger than the Si/SiO_2 substrate and positioned on top of the Si/SiO_2 surface with 2DMs. To increase the separation speed in the following phase, PDMS is left without contact on one of the edges of the Si/SiO_2 substrate, which was ensured by placing a carbon fiber or any similar object on the substrate edge before placing PDMS on top. Subsequently, the PDMS/2DM/substrate is placed on top of a DI (deionized) water and ammonia solution (1,000:1 ratio), which is gently stirred to ensure the flow of the solution. The solution slowly intercalates between the PDMS and Si/SiO_2 substrate, separating 2DM from the Si/SiO_2 substrate. After complete separation in a few minutes, the Si/SiO_2 substrate sinks into the solution, and PDMS with 2DM are left floating on top of the solution. PDMS with 2DM is additionally rinsed with DI water and dried with nitrogen flow to remove residual water from the surface.

For placing 2DMs from PDMS on sapphire, PDMS with 2DM is positioned on top of the sapphire and gently pressed with an Q-tip to ensure adequate adhesion over the whole surface. PDMS with 2DM is fixed on a z-axis manipulator with which the separation of PDMS and sapphire can be controlled. To ensure that the 2DM has higher adhesion with sapphire, PDMS is slowly separated in small steps with a z-axis manipulator. The front of the adhesion is monitored with an optical microscope to increase separation speed in areas of no interest and reduce it in regions with 2DM flakes. After the controlled and complete separation of PMDS, 2DM is left on the sapphire surface. For detailed information about this process, see Castellanos-Gomez et al. (2013).

Sample Preparation

The MoS2 and WS2 substrate monolayers were placed on a microscopic slide and fixed with a coverslip, leaving the layer of air between the two glass surfaces. In addition, we introduced various media with different refractive indices to the monolayers. A small amount of glycerin, with a refractive index of $n = 1.47$ was directly applied on top of the monolayers and then fixed with a coverslip. Distilled water was also used as an embedding medium, but without a coverslip as we employed a "water-dipping" objective lens for this type of samples. During the recording in different embedding media, no degradation of monolayer flakes was observed, so samples prepared in this way can be used several times. This approach allowed us to systematically examine how different embedding media influence resolution assessment.

Objective Lenses

We used a range of objective lenses (see Table 1) to investigate how resolution assessment is affected by different measurement conditions. A variety of different objective lenses was used, taking into account their different NA's, magnifications and using different immersion media. For samples embedded in distilled water, we employed the water-dipping objective lens, specifically W Plan-APOCHROMAT. This type of objective lens is designed to be used without a coverslip, with the tip submerged into the embedding medium.

Theoretical Limit Calculation

The theoretical limits for the lateral and axial resolutions under the different measurement conditions given in this paper were calculated using the following equations (Squier &

Table 1. Overview of Objective Lenses Used (All from Zeiss)

Objective lens	Magnification	Numerical aperture	Immersion	Working distance (mm)	Chromatic aberration correction	Spherical aberration correction
EC Plan-NEOFLUAR	40×	1.30	Oil	0.21	Red and blue; green close	Blue, green
W Plan-APOCHROMAT	40×	1.00	Water-dipping	2.50	Deep blue, blue, green and red	Deep blue and blue
Plan-APOCHROMAT	20×	0.80	—	0.55	Deep blue, blue, green and red	Deep blue and blue
GF Planachromat	40×	0.65	—	0.53	Red and blue	Green

Müller, 2001; van den Bos & den Dekker, 2001; Masters & So, 2009; Farahi, 2015):

$$\mathrm{FWHM}_{\mathrm{lat}} = \frac{1}{\sqrt{N}} \frac{0.51 \cdot \lambda}{\mathrm{NA}} \quad (1)$$

$$\mathrm{FWHM}_{\mathrm{ax}} = \frac{1}{\sqrt{N}} \frac{1.77 \cdot n \cdot \lambda}{\mathrm{NA}^2} \quad (2)$$

with λ representing excitation wavelength, n is the index of refraction of respective embedding media, and N is the nonlinearity order ($N = 2$ for TPEF and SHG, $N = 3$ for THG). We should emphasize that the magnitude for NAs used in all calculation throughout the paper were from the specifications of the objective lenses given by the manufacturer. This can be considered as the best possible approximation as the exact magnitude is only valid under certain conditions (refractive index of the sample/embedding medium and proximity to the coverslip surface) and may vary with different settings/conditions. In other words, if the embedding medium is changed, the refractive index changes and so does the NA which depends on the refractive index. This change cannot be measured or estimated, so the value from the objective specification is used in the calculations for all settings/conditions.

Results

Lateral Resolution in TPEF Modality

WS_2 and MoS_2 monolayers can generate photoluminescence when excited in the 520–640 nm and 610–670 nm ranges (Rigosi et al., 2015). Therefore, they can be used for resolution assessment of fluorescence microscopy modalities in general. However, due to the spectral range of our lasers, it was not possible to obtain a TPEF signal from these monolayers. Therefore, we opted to use 0.2 μm fluorescent spheres to access lateral resolution. The inset in Figure 1 shows the fluorescent spheres recorded in the TPEF modality using the 40 × 1.3 objective lens. By fitting the extracted intensity profile using a Gaussian function, we determined the lateral resolution to be (320 ± 20) nm. The data points for fitting were chosen to include the feature of interest (i.e., peak), while expanding the range did not affect the fitting parameters. The result corresponds to the FWHM of the obtained intensity distribution, with the error representing the fitting error. The lateral resolution in the TPEF modality was only successfully determined at an excitation wavelength of 730 nm. The theoretical limit for lateral resolution in the TPEF modality, which was calculated under the same conditions according to the equation (1), is 203 nm. Excitation at higher wavelengths resulted in insufficient SNR for the resolution measurement. It was not possible to record a stacked image of satisfactory quality for axial resolution assessment due to pronounced photobleaching. It is also important to note that the fluorescent spheres used in this case cannot be considered as point-like sources due to their size and expected resolution. In contrast, the use of TMD monolayers does not lead to photobleaching and eliminates the need for deconvolution due to their subnanometer thickness. Consequently, the application of knife-edge technique to TMD monolayers provides a reliable measurement of both lateral and axial resolution.

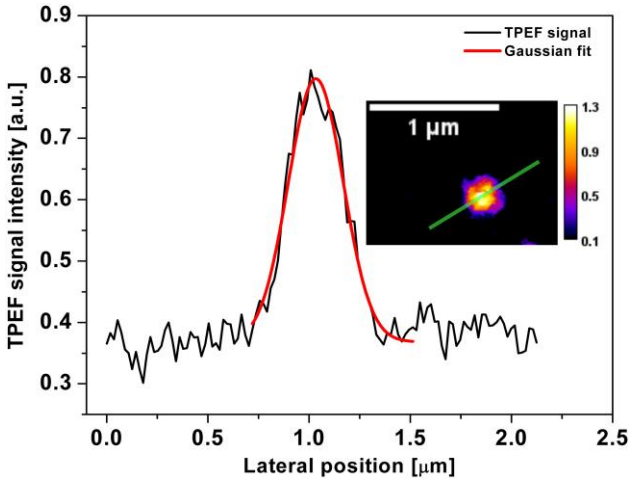

Fig. 1. TPEF signal of a fluorescent bead with a nominal size of 0.2 μm. The individual intensity profile was extracted from the labeled position on the inset. The profile was fitted using a Gaussian function with a quality indicator for the fit of $R^2 = 97.5\%$. The sample was recorded using a 40 × 1.3 objective lens at the excitation wavelength of 730 nm.

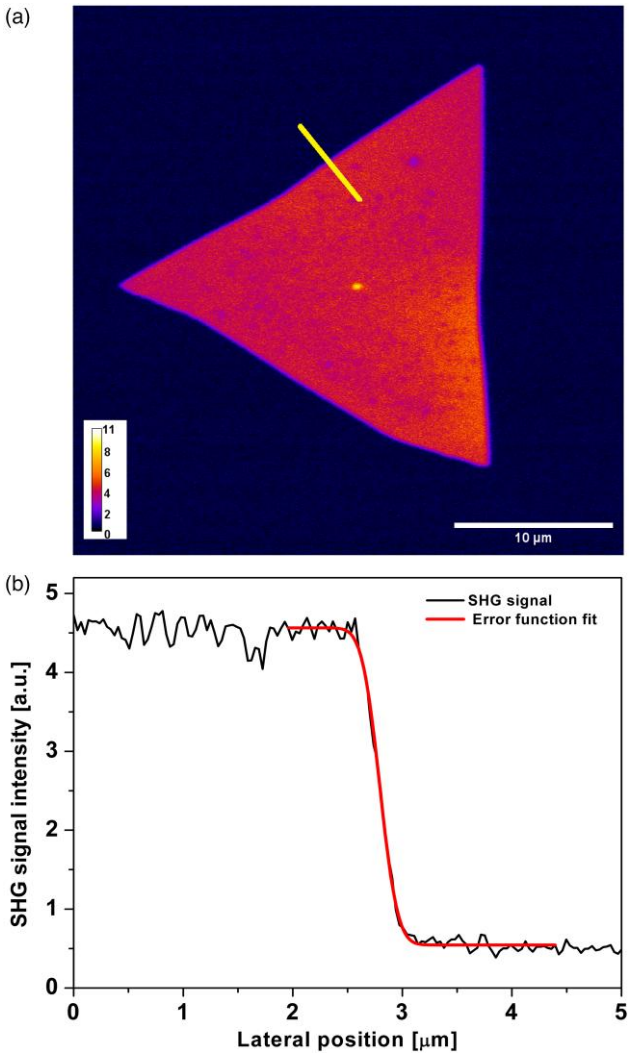

Fig. 2. (**a**) SHG image of a MoS_2 flake. The image was recorded at an excitation wavelength of 800 nm using a 40 × 1.3 objective lens with glycerin as the embedding medium. The marker (line) indicates the position along the edge of the monolayer flake from which the intensity profile was extracted. (**b**) Typical intensity profile extracted at the edge of the MoS_2 monolayer flake. The profile was fitted using the error function, with the parameter for the quality of fit $R^2 = 99.8\%$.

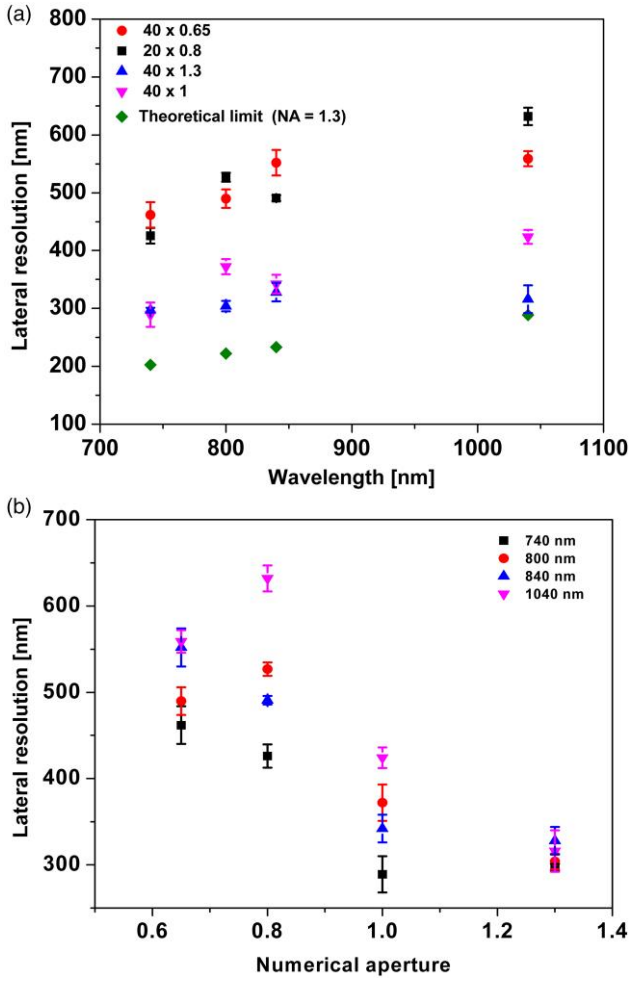

Fig. 3. Dependence of the lateral resolution on (**a**) the excitation wavelength for various objective lenses and (**b**) the numerical aperture for various excitation wavelengths. The results were obtained for a MoS_2 monolayer in the SHG modality.

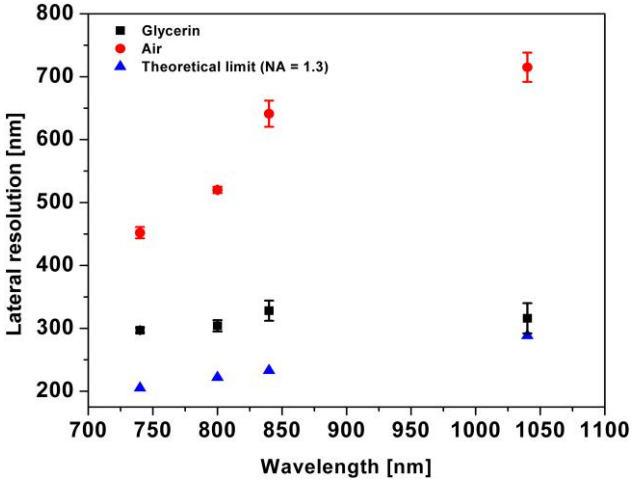

Fig. 4. Dependence of the lateral resolution on the excitation wave length for two embedding media, air, and glycerin. The graph shows the results obtained with a 40 × 1.3 objective lens and the theoretical limit for the lateral resolution under the same measurement conditions. The results were obtained for a MoS_2 monolayer in the SHG modality.

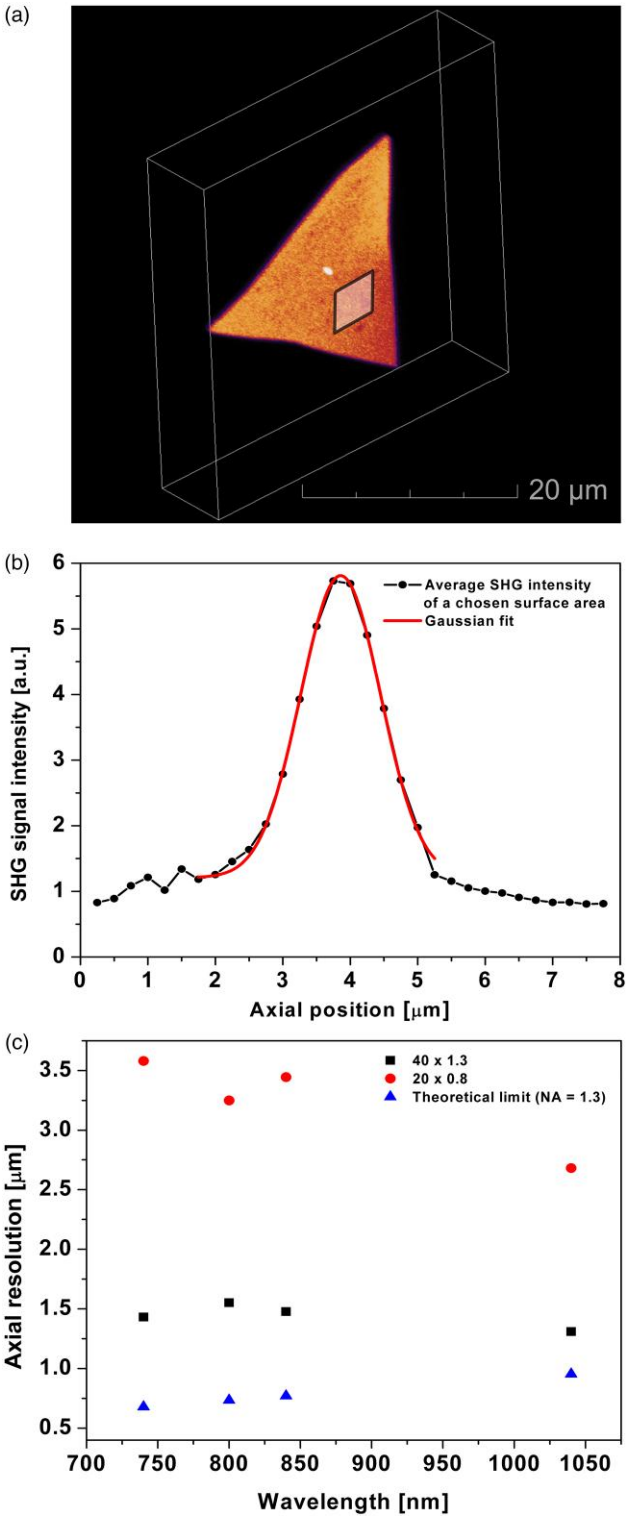

Fig. 5. (**a**) Calibrated 3D model of the MoS_2 monolayer flake with labeled surface from which the average intensity was calculated. (**b**) Intensity profile obtained by averaging the intensity of a chosen surface area of 100 × 100 pixels for each image of the flake in the stack. The *x*-axis represents the axial position of the image plane. The fitting was performed using Gaussian fit, with the quality parameter $R^2 = 99.7\%$. (**c**) Dependence of the axial resolution on the excitation wavelengths in the SHG modality for 40 × 1.3 and 20 × 0.8 objective lenses.

Resolution Assessment in SHG Modality

MoS_2 and WS_2 monolayers were used for resolution measurement in the SHG modality. No significant differences in the resolution assessment were found between these two materials. The typical image of a monolayer flake is shown in Figure 2a. These flakes exhibit distinct and well-defined edges, suitable for lateral resolution assessment using the knife-edge technique. To determine lateral resolution, we extracted intensity profiles over the edge and performed fits using the error function (which is the integral of the Gaussian function) (Davis & Brown, 2002), as shown in Figure 2b. The data points for the fit were chosen to include features of interest (the slope), while further expansion of the range did not affect the fit parameters. The intensity profiles of the monolayer-substrate boundary were analyzed at typically ten different positions along the edge, resulting in a total of 800 processed profiles. The lateral resolution was then calculated based on the mean value of the parameter w (the half-width at $\frac{1}{e^2}$ of the corresponding Gaussian distribution) obtained for each processed monolayer flake, with the error corresponding to the standard error of the mean. The resolution is presented as FWHM of the Gaussian distribution corresponding to the data obtained, where FWHM is calculated as $w/0.85$.

The axial resolution was determined based on the recorded stack, a series of consecutive images taken in equidistant sample planes, of a thin monolayer. A homogeneous surface of approximately 100 × 100 pixels was selected within the monolayer. The same surface was analyzed on all images of the stack. The average value of the pixel intensity of the observed surface was determined. The dependence of the average intensity of the chosen surface area on the corresponding axial position of the image plane was fitted by the Gaussian function. The FWHM parameter of the Gaussian fit was read directly as the axial resolution of the microscope under the specified conditions, with the error corresponding to the fitting error.

Both lateral and axial resolutions were presented as the FWHM values, all in accordance with the Houston criterion for resolution. An identical data analysis procedure was applied for resolution assessment in THG modality.

Table 2. Comparison of Axial Resolutions in SHG Modality between Different Embedding Media and Objective Lenses, along with the Theoretical Limits Provided in Brackets.

SHG	740 nm	800 nm
Glycerin	1.4 μm (0.81 μm)	1.6 μm (0.87 μm)
Air	5.9 μm (0.55 μm)	6.7 μm (0.59 μm)

The theoretical limits were calculated using the equations (1) and (2) with the refractive indices of glycerin and air: $n = 1.47$ and $n = 1$, respectively.

Lateral Resolution in SHG Modality

To investigate wavelength-dependent variation in lateral resolution of the microscope, we recorded SHG signal of the monolayer flake at four different excitation wavelengths: 740 nm, 800 nm, 840 nm, and 1,040 nm, using glycerin as the embedding medium. The dependence of the resolution on wavelength for different NA's of objective lenses is shown in Figure 3a. The graph illustrates the theoretical limit of lateral resolution for the objective lens with a numerical aperture of 1.3 at different wavelengths. The experimental results align with expectations and show a deterioration of resolution with increasing wavelength for the specific objective lens. A lower value indicates better resolution and vice versa. An exception was noted at 800 nm, where better resolution was achieved with a lower NA objective lens (0.8 versus 0.65). A similar apparent exception was also observed at 740 nm (1.0 versus 1.3), which is within the experimental margin of error. Additionally, the obtained values are above the theoretical limit at all wavelengths. Figure 3b shows the dependence of the lateral resolution on the NA of the corresponding objective lenses for different wavelengths. The results are generally in line with expectations, with two exceptions observed for objective lenses with NA values of 0.8 and 1.0, where better resolution was achieved at 840 nm compared to 800 nm. The aforementioned exceptions might be attributed to the fact that the objective lenses used in this study are not designed for infrared light but for visible light (see Table 1), resulting in suboptimal focusing. This may vary from case to case (for different objectives, at different wavelengths). The lateral resolution for the 40 × 1.3 objective lens exhibits weak wavelength dependence, which agrees well with the theoretical limit shown in Figure 3a. As the monolayer flakes are significantly thinner than the expected resolution, deconvolution is not required. Notably, no photobleaching of the samples was observed at any wavelength during monolayer imaging.

In addition to the factors already mentioned, resolution is further influenced by the order of interaction. While TPEF

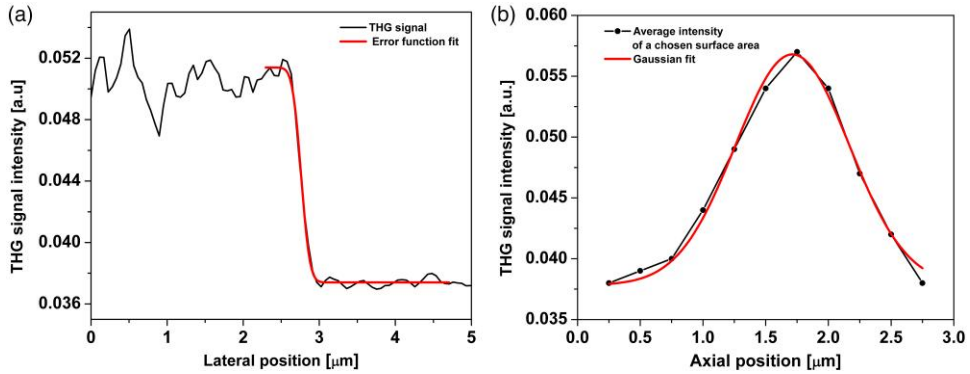

Fig. 6. (**a**) Typical intensity profile extracted at the edge of the WS_2 monolayer flake in THG modality for a 40 × 1.3 objective lens. The profile was fitted using the error function, with the quality of fit parameter $R^2 = 99.6\%$. (**b**) Intensity distribution obtained by averaging the intensity of a chosen area of 60 × 60 pixels for each image in the stack. The *x*-axis represents the axial position of the image plane. Fitting was performed using the Gaussian function, with the quality parameter of fit $R^2 = 99\%$.

and SHG are conceptually distinct processes, both involve two-photon interactions, suggesting that the resolutions obtained for the corresponding imaging modalities should be closely aligned. This implies that the theoretical limit will be the same for both imaging modalities at a given wavelength. Despite the slightly higher excitation wavelength of 740 nm used for the resolution measurement in the SHG modality, the measured resolution of (300±10) nm exceeds that of the TPEF modality (320±20) nm obtained at 730 nm. However, this statement is not conclusive as the measurements are within the margin of error. Both measurements were performed using a 40 × 1.3 objective lens. The fluorescent beads utilized in our study do not serve as ideal point-like sources for resolution measurement. In contrast, monolayer flakes due to their extensive thinness, offer a better approximation when combined with the knife-edge technique.

Using the same method, we also investigated the influence of the embedding medium on the lateral resolution of the SHG modality. We recorded images of monolayer flakes at various excitation wavelengths using a 40 × 1.3 objective lens, with one sample embedded in glycerin and the other in air. Figure 4 illustrates the lateral resolution for the two specified embedding media. It is shown that the resolution is closer to the theoretical limit when glycerin is present at all excitation wavelengths used, indicating a more appropriate utilization of the objective lens.

Axial Resolution in SHG Modality

In addition to assessing lateral resolution, we also investigated axial resolution using the same samples. The SHG signal of glycerin-embedded monolayer flakes was recorded at various excitation wavelengths. For each wavelength, a stack of typically 30 images was acquired, with a slice spacing of 0.25 μm. To determine the axial resolution at a specific wavelength, we selected a homogeneous surface area from each image of the stack. Figure 5a displays the calibrated 3D model of the monolayer flake and provides an example of the surface used to derive parameters for axial resolution assessment. The resolution was determined based on the dependence of average intensity of the chosen surface area on the corresponding axial position of the image plane in the stack. This is shown in Figure 5b. This dependence was fitted with a Gaussian function and the FWHM was determined as a measure of resolution. The measurement involved two objective lenses with distinct NA values with an aim to investigate how the resolution varies with the NA for different wavelengths. The corresponding results are shown in Figure 5c together with the theoretical resolution limit in the case of an objective lens with an NA value of 1.3. Although the obtained resolution is above the theoretical limit, the observed trend deviates from expectations and indicates an improvement in resolution with increasing wavelength, which is particularly evident for the 20 × 0.8 objective lens. A similar trend can be seen for the 40 × 1.3 objective lens. As expected, superior results were consistently obtained with the higher NA objective lens.

We also investigated how axial resolution is affected by the embedding medium. The SHG signal of MoS_2 monolayer flakes was recorded using a 40 × 1.3 objective lens at excitation wavelengths of 740 nm and 800 nm, using glycerin and air as embedding media. A comparison between the axial resolutions obtained for different embedding media is provided in Table 2. Significantly poorer results were obtained when air was used as the embedding medium.

Table 3. Comparison of Lateral and Axial Resolution in THG Modality between Different Embedding Media and Objective Lenses, along with the Theoretical Limits Provided in Brackets.

THG (1,040 nm)	Lateral Resolution (μm)		Axial Resolution (μm)
	20 × 0.8	40 × 1.3	40 × 1.3
Glycerin	0.44 (0.39)	0.27 (0.24)	1.10 (0.92)
Air	0.75 (0.39)	0.43 (0.24)	5.90 (0.63)

The theoretical limits were calculated using the equations (1) and (2) with the refractive indices of glycerin and air: $n = 1.47$ and $n = 1$, respectively.

Resolution Assessment in THG Modality

We measured both lateral and axial resolution of the microscope in the THG modality using WS_2 monolayer flakes immersed in glycerin with an excitation wavelength of 1,040 nm and a 40 × 1.3 objective lens. Figure 6a shows a typical intensity profile extracted from the edge of the monolayer flake. This profile was fitted with the error function, resulting in a lateral resolution of (270 ± 10) nm. Figure 6b shows the distribution of the average intensities of the selected surface area from each image of the stack (slice separation of 0.25 μm) over the axial position of the image plane. Using this profile, we were able to determine the axial resolution to be (1.07 ± 0.06) μm. We investigated how both the lateral and axial resolution in THG modality vary between different embedding media and objective lenses. An overview of the results is displayed in Table 3, which quantifies the effect of embedding media with different refractive indices on image

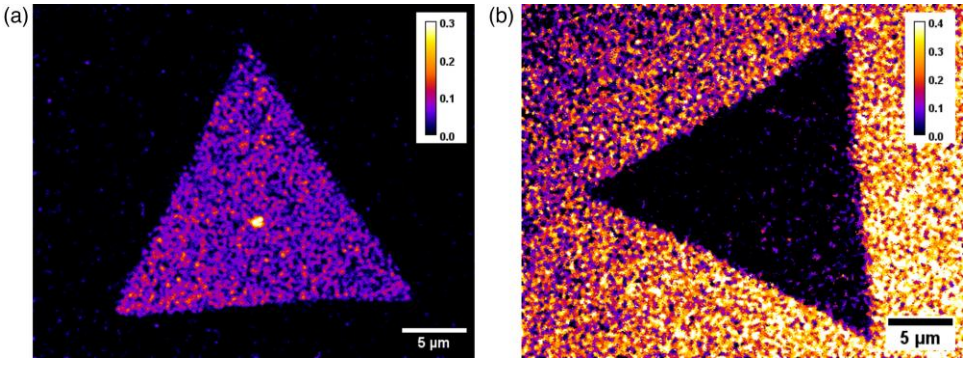

Fig. 7. (**a**) MoS_2 monolayer flake with glycerin as the embedding medium. (**b**) MoS_2 monolayer flake with air as embedding medium. The figure clearly shows decreasing of the THG signal in air.

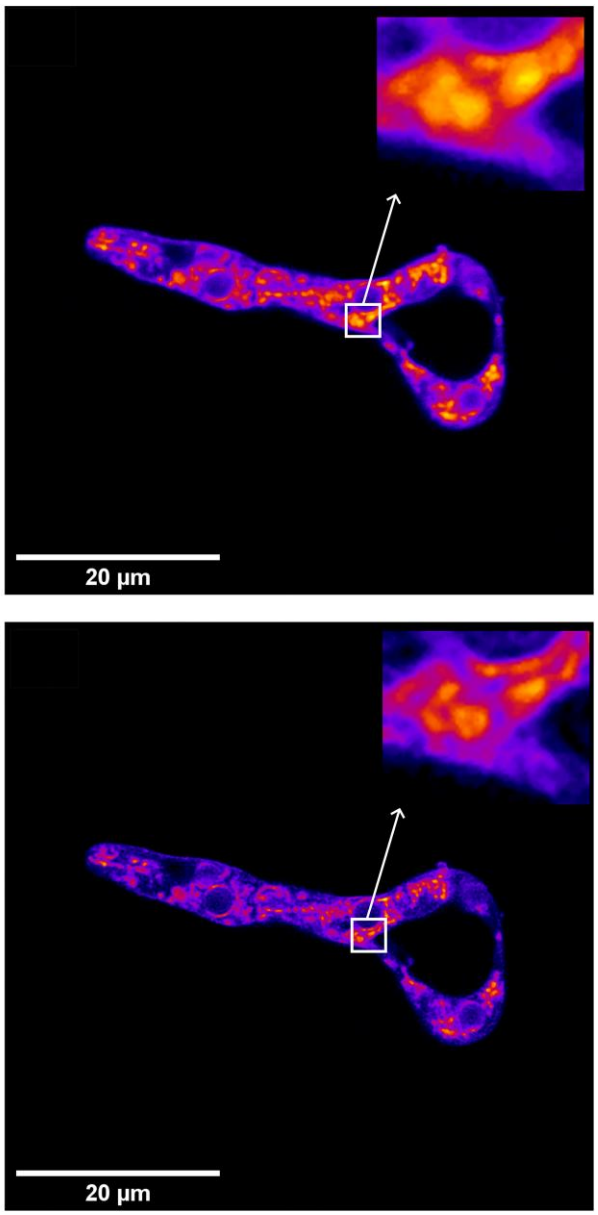

Fig. 8. TPEF signal of *Phycomyces blakesleeanus* hyphae, stained with the vital mitochondrial dye Rhodamine123, excitation wavelength 800 nm, laser power 2 mW, emission filters: VIS (400–700 nm) bandpass filter (from EOS50D camera, Canon), and 530/43 bandpass filter (MF530-43, Thorlabs, Inc.). (**a**) Original, unprocessed image. (**b**) Image deconvoluted using the Richardson–Lucy algorithm in MATLAB software. Deconvolution was performed using the Gaussian distribution with a FWHM equivalent to the FWHM of the PSF measured under identical experimental conditions. The insets show that smaller mitochondria can be resolved when the image is deconvoluted.

resolution. Here, too, significantly poorer results were achieved for the resolution in air.

An interesting observation is that the THG signal of MoS_2 monolayer flakes in glycerin differs from that in air. More specifically, the MoS_2 monolayer flake exhibits a dominant THG signal in glycerin over the substrate-glycerin interface, whereas the same monolayer flake in air suppresses the THG signal. Figure 7a shows the THG signal of MoS_2 immersed in glycerin is presented, whereas Figure 7b demonstrates how the THG signal from the sapphire substrate dominates over the THG signal of the MoS_2 monolayer flake. It is known from the literature that the $\chi^{(3)}$ values of 2DMs depend on the excitation wavelengths (Autere et al., 2018, and references therein; Wang et al., 2013) as well as other parameters such as strain, defects, doping, substrates, and chemical treatment (Autere et al., 2018, and references therein). Here, the only difference between these two systems is the interface, which causes the increase in the nonlinear optical response through phenomenological surface-enhanced THG discussed in Tsang (1995). Although a detailed explanation of this effect is beyond the scope of this discussion, it is worth noting that even in this case, an inverted edge emerges that allows resolution assessment using the knife-edge technique. There is no difference in the assessment of SHG resolution when either material is used.

Image Resolution Improvement by Deconvolution

The PSF full-width values presented in this paper can be used as input data for deconvolution to improve the resolution of images acquired with this NLSM setup. Deconvolution is particularly important for improving image quality when dealing with samples containing structures whose dimensions are very close to the resolution limit, as it enables them to be visualized as distinct and separate objects. Figure 8 shows a representative image before (a) and after (b) deconvolution, highlighting a significant improvement in the efficiency of discerning and identifying small objects within the sample. In Figure 8, the image was deconvoluted using the Richardson–Lucy algorithm in MATLAB software. The deconvolution was performed using a Gaussian distribution with a FWHM equivalent to the FWHM of PSF measured under identical experimental conditions.

Conclusion

We have presented measurements of resolution for all imaging modalities (TPEF, SHG, and THG) of our custom-built NLSM using two distinct approaches. We performed a direct assessment of both lateral (using fluorescent nanospheres in the TPEF modality) and axial resolution (in the SHG and THG modalities). The assessment of lateral resolution in the SHG and THG modalities was performed using the knife-edge technique on WS_2 and MoS_2 monolayers. The lateral technique offers a higher SNR, no photobleaching effect and shows good agreement with the conventional resolution measurement technique using fluorescent nanospheres. Assessing SHG and THG imaging resolution by the knife-edge method overcomes the coherence problem encountered when probing with small (point-like) objects. The obtained results, namely the PSF FWHM values, were employed in image processing by deconvolution, for resolution enhancement.

In addition, we performed a comprehensive analysis of how the resolution varies with numerical aperture of the objective lens, excitation wavelength and refractive index of the embedding medium. The results closest to the theoretical limit were obtained when glycerin was used as the embedding medium at all wavelengths, for both SHG and THG imaging modalities and all objective lenses examined. The latter implies that various embedding media can significantly influence resolution and thus the quality of acquired images. The use of a suitable medium might lead to significantly better imaging results, as objective lenses are usually designed for biological samples embedded in media with a refractive index above 1. As a side note, the intensity of the THG signal from TMD

monolayers strongly depends on the substrate- monolayer-medium combination and can either be enhanced or suppressed. For example, MoS_2 monolayer flakes show a pronounced THG signal in glycerin over the substrate-glycerin interface, while the same monolayer flakes in air suppress the THG signal.

In conclusion, the proposed use of WS_2 and MoS_2 monolayers has emerged as a promising tool for the characterization not only of nonlinear imaging systems in terms of lateral and axial resolution, but also of various microscopic systems.

Availability of Data and Materials

The authors have declared that no datasets apply for this piece.

Acknowledgments

We would like to thank Milan Minić for indispensable technical help and support. We thank Professor Michael Pravica from University of Nevada, Las Vegas (UNLV) for reviewing the manuscript.

Author Contributions Statement

J.Z.J. drafted the manuscript, processed the data and reviewed the literature, M.B. performed the measurements, processed the data and reviewed the literature, A.D. sorted out and processed the data and reviewed the literature, A.S. synthesized the MoS_2 monolayer flakes, L.Ž. synthesized the WS_2 monolayer flakes, B.R. performed the PDMS transfer, N.V. supervised the synthesis, T.P. grown the fungi and prepare the sample, M.D.R and A.J.K. built the instrument, performed measurements, processed the data, conceptualized and supervised the research. All authors reviewed the manuscript. J.Z.J., M.B., and A.D. contributed equally to this work. This paper will be the part of midterm check point in their PhD studies.

Financial Support

This research was supported by the Science Fund of the Republic of Serbia, Grant No. 4545, project "Advanced Biophysical Methods for Soil Targeted Fungi-Based Biocontrol Agents" - BioPhysFUN; and the Institute of Physics Belgrade, through the grant by the Ministry of Science, Technological Development and Innovations of the Republic of Serbia. A.S., B.R., and N.V. acknowledge the support of Croatian Science Foundation, Grant No. UIP-2017-05-3869, Centre of Excellence for Advanced Materials and Sensing Devices, ERDF Grant No. KK.01.1.1.01.0001 and Centre for Advanced Laser Techniques, ERDF Grant KK.01.1.1.05.

Conflict of Interest

The authors declare that they have no competing interest.

References

Araújo M, Silva R, Lima E, Pereira D & De Oliveira P (2009). Measurement of Gaussian laser beam radius using the knife-edge technique: Improvement on data analysis. *Appl Opt* **48**, 393–396. https://doi.org/10.1364/AO.48.000393

Autere A, Jussila H, Dai Y, Wang Y, Lipsanen H & Sun Z (2018). Nonlinear optics with 2D layered materials. *Adv Mater* **30**(24), e1705963. https://doi.org/10.1002/adma.201705963

Castellanos-Gomez A, Buscema M, Zant H & Steele G (2013). Deterministic transfer of two-dimensional materials by all-dry viscoelastic stamping. *2D Mater* **1**, 011002. https://doi.org/10.1088/2053-1583/1/1/011002

Chen X, Nadiarynkh O, Plotnikov S & Campagnola P (2012). Second harmonic generation microscopy for quantitative analysis of collagen fibrillar structure. *Nat Protoc* **7**(4), 654–669. https://doi.org/10.1038/nprot.2012.009

Chu S-W, Tai S-P, Ho C-L, Lin C-H & Sun C-K (2005). High-resolution simultaneous three-photon fluorescence and third-harmonic-generation microscopy. *Microsc Res Tech* **66**(4), 193–197. https://doi.org/10.1002/(ISSN)1097-0029

Cole R, Jinadasa T & Brown C (2011). Measuring and interpreting point spread functions to determine confocal microscope resolution and ensure quality control. *Nat Protoc* **6**(12), 1929–1941. https://doi.org/10.1038/nprot.2011.407

Davis B & Brown G (2002). Diffraction by a randomly rough knife edge. *IEEE Trans Antenn Propag* **50**(12), 1769–1778. https://doi.org/10.1109/TAP.2002.804019

Farahi N. (2015). Resolution analysis of films with embedded spheres for imaging of nanoplasmonic arrays. Thesis. ProQuest LLC, Ann Arbor, MI. Available at https://www.proquest.com/openview/bea17cff0074a8c98f01910ec4d90533/1?pq-origsite=gscholar&cbl=18750

Hou R & Labarthet F (2018). Second harmonic generation microscopy from non-centrosymmetric gold half-coated polystyrene spheres. *Surf Sci* **676**, 46–50. https://doi.org/10.1016/j.susc.2018.01.014

Kozubek M (2001). Theoretical versus experimental resolution in optical microscopy. *Microsc Res Tech* **53**(2), 157–166. https://doi.org/10.1002/jemt.1080

Kumar N, Najmaei S, Cui Q, Ceballos F, Ajayan P, Lou J & Zhao H (2013). Second harmonic microscopy of monolayer MoS_2. *Phys Rev B* **87**(16), 161403. https://doi.org/10.1103/PhysRevB.87.161403

Lee G, Jyothsna K, Park J, Lee J, Raghunathan V & Kim H (2023). Confocal nonlinear optical imaging on hexagonal boron nitride nanosheets. *PhotoniX* **4**(1), 27. https://doi.org/10.1186/s43074-023-00103-6

Li Y, Rao Y, Mak K, You Y, Wang S, Dean C & Heinz T (2013). Probing symmetry properties of few-layer MoS_2 and h-BN by optical second-harmonic generation. *Nano Lett* **13**(7), 3329–3333. https://doi.org/10.1021/nl401561r

Mahou P, Malkinson G, Chaudan É., Gacoin T, Beaurepaire E & Supatto W (2017). Metrology of multiphoton microscopes using second harmonic generation nanoprobes. *Small* **13**, 1701442. https://doi.org/10.1002/smll.201701442

Masihzadeh O, Schlup P & Bartels R (2009). Enhanced spatial resolution in third-harmonic microscopy through polarization switching. *Opt Lett* **34**, 1240–1242. https://doi.org/10.1364/OL.34.001240

Masters B & So P (2009). Handbook of biomedical nonlinear optical microscopy. *J Biomed Opt* **14**, 019901. https://doi.org/10.1117/1.3077566

Mehravar S, Cromey B & Kieu K (2020). Characterization of multiphoton microscopes by nonlinear knife-edge technique. *Appl Opt* **59**(22), G219–G224. https://doi.org/10.1364/AO.391881

Mennel L, Furchi MM, Wachter S, Paur M, Polyushkin DK & Mueller T (2018). Optical imaging of strain in two-dimensional crystals. *Nat Commun* **9**(1), 516. https://doi.org/10.1038/s41467-018-02830-y

Mylonakis M, Tserevelakis G, Vlachos G, Fanouraki E, Pavlopoulos A, Pavlidis M & Zacharakis G (2024). Bimodal optical and optoacoustic multiview microscope in the frequency-domain. *Opt Lett* **49**(3), 462–465. https://doi.org/10.1364/OL.510384

Niehues I, Blob A, Stiehm T, Schmidt R, Jadriško V, Radatović B, Čapeta D, Kralj M, Michaelis de Vasconcellos S & Bratschitsch R (2018). Strain transfer across grain boundaries in MoS_2 monolayers grown

by chemical vapor deposition. *2D Mater* **5**(3), 031003. https://doi.org/10.1088/2053-1583/aaba9a

Pajić T, Todorovic N, Živić M, Nikolic S, Rabasović M, Clayton A & Krmpot A (2022). Label-free third harmonic generation imaging and quantification of lipid droplets in live filamentous fungi. *Sci Rep* **12**(1), 18760. https://doi.org/10.1038/s41598-022-23502-4

Rabasovic M, Pantelic D, Jelenkovic B, Ćurčić S, Rabasovic M, Vrbica M, Lazovic V, Curcic B & Krmpot A (2015). Nonlinear microscopy of chitin and chitinous structures: A case study of two cave-dwelling insects. *J Biomed Opt* **20**(1), 016010–016010. https://doi.org/10.1117/1.JBO.20.1.016010

Radisavljevic B, Radenovic A, Brivio J, Giacometti V & Kis A (2011). Single-layer MoS_2 transistors. *Nat Nanotechnol* **6**, 147–150. https://doi.org/10.1038/nnano.2010.279

Rigosi AF, Hill HM, Li Y, Chernikov A & Heinz TF (2015). Probing interlayer interactions in transition metal dichalcogenide heterostructures by optical spectroscopy: MoS_2/WS_2 and $MoSe_2/WSe_2$. *Nano Lett* **15**(8), 5033–5038. https://doi.org/10.1021/acs.nanolett.5b01055

Rohrbacher A, Olarte OE, Villamaina V, Loza-Alvarez P & Resan B (2017). Multiphoton imaging with blue-diode-pumped SESAM-modelocked Ti:sapphire oscillator generating 5 nJ 82 fs pulses. *Opt Express* **25**(9), 10677–10684. https://doi.org/10.1364/OE.25.010677

Rosa H, Wei H, Verzhbitskiy I, Rodrigues M, Taniguchi T, Watanabe K, Eda G, Pereira V & Gomes J (2018). Characterization of the second- and third-harmonic optical susceptibilities of atomically thin tungsten diselenide. *Sci Rep* **8**(1), 10035. https://doi.org/10.1038/s41598-018-28374-1

Senkić A, Bajo J, Supina A, Radatović B & Vujičić N (2023). Effects of CVD growth parameters on global and local optical properties of MoS2 monolayers. *Mater Chem Phys* **296**, 127185. https://doi.org/10.1016/j.matchemphys.2022.127185

Squier J & Müller M (2001). High resolution nonlinear microscopy: A review of sources and methods for achieving optimal imaging. *Rev Sci Instrum* **72**(7), 2855–2867. https://doi.org/10.1063/1.1379598

Tsang TY (1995). Optical third-harmonic generation at interfaces. *Phys Rev A* **52**(5), 4116–4125. https://doi.org/10.1103/PhysRevA.52.4116

Tserevelakis G, George F, Krmpot A, Vlachos M, Fotakis C & Tavernarakis N (2010). Imaging *Caenorhabditis elegans* embryogenesis by third-harmonic generation microscopy. *Micron* **41**, 444–447. https://doi.org/10.1016/j.micron.2010.02.006

Tserevelakis G, Psycharakis S, Resan B, Brunner F, Gavgiotakis E, Weingarten K & George F (2012). Femtosecond laser nanosurgery of sub-cellular structures in HeLa cells by employing Third Harmonic Generation imaging modality as diagnostic tool. *J Biophotonics* **5**, 200–207. https://doi.org/10.1002/jbio.201100055

van den Bos A & den Dekker A (2001). Resolution reconsidered-conventional approaches and an alternative. In *Advances in Imaging and Electron Physics*, Peter H (Ed.), vol. **117**, pp. 241–360. Amsterdam: Elsevier.

Wachulak PW, Torrisi A, Bartnik A, Wegrzyński Ł, Fok T & Fiedorowicz H (2017). A desktop extreme ultraviolet microscope based on a compact laser-plasma light source. *Appl Phys B* 123, 1–5. https://doi.org/10.1007/s00340-016-6595-5

Wang R, Chien H-C, Kumar J, Kumar N, Chiu H-Y & Zhao H (2013). Third-harmonic generation in ultrathin films of MoS_2. *ACS Appl Mater Interfaces* **6**(1), 314–318. https://doi.org/10.1021/am4042542

Woodward R, Murray R, Phelan C, Oliveira R, Runcorn T, Kelleher E, Li S, de Oliveira E, Fechine GJM, Eda G & de Matos C (2016). Characterization of the second- and third-order nonlinear optical susceptibilities of monolayer MoS_2 using multiphoton microscopy. *2D Mater* **4**(1), 011006. https://doi.org/10.1088/2053-1583/4/1/011006

Yin X, Ye Z, Chenet D, Ye Y, O'Brien K, Hone J & Zhang X (2014). Edge nonlinear optics on a MoS_2 atomic monolayer. *Science* **344**(6183), 488–490. https://doi.org/10.1126/science.1250564

Zipfel W, Williams R & Webb W (2003). Nonlinear magic: Multiphoton microscopy in the biosciences. *Nat Biotechnol* **21**(11), 1369–1377. https://doi.org/10.1038/nbt899

Optical and Quantum Electronics (2024) 56:1225
https://doi.org/10.1007/s11082-024-06973-9

Elongation index derivative as a potential hemorheological parameter in a diffraction analysis of diabetes mellitus patients' erythrocytes

Mihajlo D. Radmilović[1] · Vesna Lj. Ilić[2] · Drenka Trivanović[2] · Ana Petakov[3] · Katarina Lalić[3,4] · Mihailo D. Rabasović[1] · Aleksandar J. Krmpot[1] · Ivana T. Drvenica[2]

Received: 29 December 2023 / Accepted: 15 April 2024 / Published online: 19 June 2024

Abstract
Comparative analysis of erythrocyte deformability in individuals with Diabetes Mellitus (DM) and healthy individuals (Control) was represented, focusing on the Elongation index (EI) calculation based on diffraction images. While no statistically significant differences in EI values were observed between the groups, we determined specific points along the deformability curve and revealed the first derivative of deformability curve (dEI / dSS) as a potential metric for quantifying erythrocyte response to deformation, where SS represents shear stress in Pa (Pascal). Statistically significant differences in dEI / dSS at the half maximum value of the deformability curve were identified, suggesting a slower erythrocyte response to shear stress in DM patients. Scatter plot analysis demonstrated a linear declining trend in dEI / dSS index with an increase in shear stress, indicating decaying erythrocyte responsiveness to higher shear stress values, particularly pronounced in DM patients. Although pilot, this study suggests that dEI / dSS can provide valuable insights into the hemorheological aspects of DM pathology and contribute to a comprehensive understanding of erythrocyte mechanobiological behavior in response to varying shear stress levels. Correlations between the proposed measure of RBC mechanical properties and established clinical markers of DM and its complications (serum cholesterol, creatinine, and urea level) are obtained to get preliminary insight into dEI / dSS application for better diagnosis and/or patient management.

Keywords Erythrocyte deformability · Diabetes mellitus · Ektacytometry · Laser diffraction

1 Introduction

Erythrocyte deformability plays a pivotal role in blood flow through the small capillaries (Mokken et al. 1992). Understanding how erythrocytes behave when they are exposed to increased pressures is an important biophysical aspect of microcirculation (Maeda et al.

Extended author information available on the last page of the article

1996; Kobayashi et al. 2022; Pretorius et al. 2018). Erythrocytes that have reduced deformability by obstructing capillary blood flow may induce the metabolic stress of the tissues (Cho et al. 2014). Diseases such as Diabetes mellitus (DM) (especially type 2) are sensitive to the change in deformability of erythrocyte membrane (Shin et al. 2007; Sokolova et al. 2017; Babu et al. 2021). Studies which include a large number of individuals across the globe estimated that world prevalence of DM will increase 7.7%, affecting 439 million adults by 2030 (Shaw et al. 2010). In the year 2015, it was approximated that there existed 415 million individuals (with an uncertainty range of 340 to 536 million) aged between 20 and 79 who had diabetes (Ogurtsova et al. 2017). Diabetes was responsible for causing 5.0 million fatalities, and the total global healthcare spending related to DM reached an estimated amount of 673 billion US dollars (Ogurtsova et al. 2017). Low - and middle - income countries have higher probability for the increasing trend of citizen with DM (Rabi et al. 2006). Projections indicated that the number of individuals aged 20 to 79 with diabetes would escalate to 642 million (with an uncertainty range of 521 to 829 million) by the year 2040 (Ogurtsova et al. 2017). Since DM represent a modern age disease with pandemic tendencies and erythrocytes mechanical and rheological properties are affected with DM complications (Wang et al. 2021; Lee et al. 2015), we tried to expand hemorheological parameters diagnostic potential in DM patients. It is postulated that hemorheological determinants, such as calculated Elongation index (EI) have influence in the pathogenesis of diabetic organ complications, particularly retinopathy, nephropathy, and neuropathy (Schut et al. 1993; Jensen et al. 1989; Lee et al. 2015; Chung et al. 2018). Reduction in erythrocyte EI in DM is connected to escalated levels of glycosylated hemoglobin, higher sorbitol content, and increased level of oxidized hemoglobin that can be bound to the inner side of the erythrocyte membrane, all of which may disrupt the erythrocyte surface-to-volume ratio (Malandrino et al. 2012; Mawatari et al. 2004; Schut et al. 1993; Ercan et al. 2002). Moreover, there has been shown a direct correlation between microvascular complications and reduced erythrocytes deformability (Kobayashi et al. 2022). Thus, EI represent important hemorheological parameter applied in clinical studies (Baskurt et al. 2004, Baskurt et al. 2009).

Nevertheless, a degree of discordance is present in the available scientific literature related to the calculation of EI of diabetic erythrocytes. It's not established a unique standard methodology for determining EI (Baskurt et al. 2009). For comparison of EI curves between different experimental groups, it's often necessary to standardize and parametrize measurements (Bronkhorst et al. 1995), methodological diversity is present, encompassing a spectrum of investigative techniques, such as filtration, ektacytometry, micropipette aspiration, viscosity assessments of erythrocyte suspensions, as well as osmotic gradient ektacytometry (Schut et al. 1993; Musielak et al. 2009).

We investigated erythrocyte deformability in DM patients by calculating EI and its first derivative to shear stress (SS) (dEI / dSS) in a ½ maximal value of deformability curve. In this way, we aimed to determine the rate of erythrocyte deformation change by introducing a new hemorheological parameter dEI / dSS, which is beyond standard diffraction optical measurements. We have shown that dEI / dSS is directly correlated with serum cholesterol level (s – cholesterol) and inversely correlated with ½ EI. Thus, we indicate that dEI / dSS can be potentially used as a deformability parameter in clinical practice for better management of DM patients.

2 Materials and methods

2.1 Blood samples

Venous blood samples were taken in K_2EDTA vacutainers (BD, United States), by puncture of the forearm vein of both type I ($n=7$) and type II ($n=6$) diabetic patients, undergoing regular check-ups in the Clinic for Endocrinology, Diabetes and Metabolic Diseases of the University Clinical Center of Serbia. Before sample collection, the patients signed an informed consent as an obligatory procedure within obtained ethical approval No 1332/VII-5 from 7th July 2020 issued by the Faculty of Medicine at University of Belgrade. We tried to ensure homogeneity of the diabetic patients by designing inclusion and exclusion criteria and by matching number of male and female individuals. For DM group inclusion criteria were: individuals diagnosed with DM, age between 18 and 75 years, stable diabetic condition, defined as no significant changes in medication regimen within the past three months. Exclusion criteria for DM group were: pregnant individuals, coexisting medical conditions that could significantly impact glucose metabolism (e.g., pancreatic disorders, malignancies), current use of investigational drugs or participation in other clinical trials involving diabetes management. For control, blood from 11 healthy age- and sex-matched donors (individuals having no systematic disease) were obtained, the inclusion criteria were: individuals without a diagnosis of DM, age-matched to the diabetic group (between 18 and 75 years), no current use of medications known to affect glucose metabolism. The exclusion criteria for control group were: individuals with a history of impaired glucose tolerance, pregnancy, any chronic medical condition that could affect glucose metabolism (e.g., polycystic ovary syndrome, Cushing's syndrome), current use of medications known to affect glucose metabolism. The pseudo-anonymized samples were stored at 4 °C (no longer than 1 h after blood collection) until transport and processing at the Institute for Medical Research University of Belgrade was performed.

2.2 Erythrocyte isolation

Whole blood (10 mL) underwent centrifugation at 1811 × *g* for 20 min at 4 °C using the Megafuge 1.0R equipment from Heraeus centrifuge (Germany). The resulting supernatant, containing leukocytes in plasma, was carefully aspirated, and discarded. The precipitated erythrocytes were reconstituted in an isotonic saline solution (0.9% NaCl, specifically Natrii chloridi infundibile 9 g/L from Hemofarm (Serbia)) at a volumetric ratio of 1:4. The suspension was homogenized by a twisting motion applied to the test tube. Residual plasma proteins were separated from the erythrocyte suspension via centrifugation at 1257 × *g* for 10 min at 4 °C. These procedures were repeated thrice. Finally, the packed erythrocytes were reconstituted in an isotonic phosphate-buffered saline solution (PBS; 0.8% saline buffered with 10 mM sodium phosphate, pH 7.2–7.4, EuroClone (Italy) at the same volumetric ratio of 1:4.

2.3 Ektacytometry measurements

Ektacytometry, also recognized as laser diffraction ektacytometry, is a non-invasive and highly sensitive technique for assessing erythrocyte deformability. This method employs

laser light scattering patterns generated by erythrocytes under controlled SS, enabling a quantitative evaluation of deformability through diffraction image Fig. 1a, b. Erythrocytes were isolated as described above (Material and Methods Sect. 2.2.), and then suspension of 6 µl of packed erythrocytes in 600 µl of polyvinylpyrrolidone (PVP) were prepared, and deformability measurements were performed by utilizing the RheoSCAN-AnD300 ektacytometer (RheoMeditech, Korea). Specifically, 500 µL of this PVP-packed erythrocyte solution was introduced into the microchannel cuvette and placed in the ektacytometer. The microchannel width was set at 200 µm. For any specific pressure, a diffraction image was recorded Fig. 1a and b. The acquisition time for the one diffraction image was 1s. From every image (recorded on specific pressure) EI was calculated (Eq. 1). One measurement on different pressures requires 100 diffraction images for effective deformability curve construction. After 90 images (recorded per one measurement), EI values do not change too much with pressure and converge to some value, and because of that, 100 diffraction images were used per one measurement. Deformability curve represents mechanical characteristics of erythrocytes through change deformation in different externally applied SS. They are fitted using Hill function family curve (Baskurt et al. 2009). For the EI estimation from the raw data Lineweaver – Burk Plot can be used (Baskurt et al. 2009), which represents double linear form of Hill function which is based on. However, the double reciprocal plot distorts the error structure of the data fit and, therefore, is not the most accurate tool for representing kinetics (Greco et al. 1979) or any other processes, From the fitted deformability curves all parameters such as: SS at one half maximal value of deformability curve (½ SS), value of EI at one half maximum of deformability curve (½ EI), value of EI at the pressure of 3 Pa and dEI / dSS also at one half maximal value of deformability curve was determined. The definition of EI is given in Eq. 1. (Shin et al. 2005a). EI is calculated from the diffraction images at the specific SS. dEI / dSS at the specific SS is calculated using the finite difference method; this calculation is performed on the fitted deformability curves. The individual values of determined hemorheological parameters for all examined DM patients and controls are given in Table S1 (Supplementary material).

$$EI = \frac{a - b}{a + b} \tag{1}$$

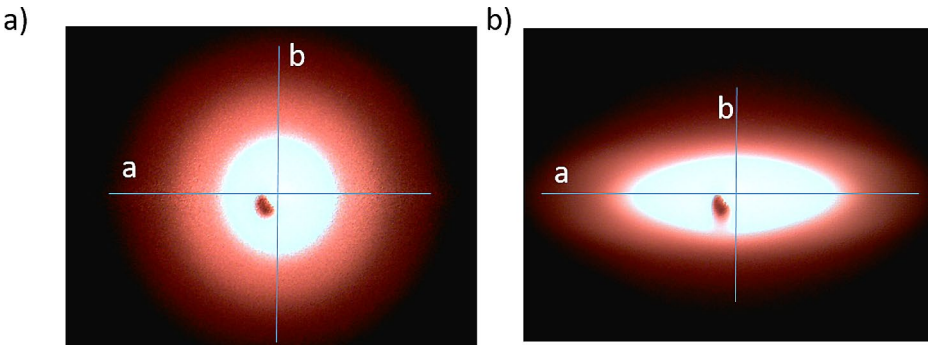

Fig. 1 Diffraction images of erythrocyte population recorded on the ektacytometer RheoScan-D300, (**a**) without SS, undeformed erythrocyte, (**b**) maximal shear stress (18 Pa), maximally deformed erythrocytes. "a" and "b" represents deformation axis. More specifically, deformation axis are lengths of diffraction pattern recorded on ektacytometer camera, represented as pixel number

2.4 Statistical analysis

Statistical analysis of the results was done using R Software for statistical computing (R version 4.3.2). The results are expressed as mean ± standard deviation. The normality of distribution was determined with the Shapiro–Wilk test. The statistical significance of differences between the groups was determined with a two-tailed t-test or a two-tailed t-test or the Mann–Whitney U test, depending on the distribution's normality. Differences with p values of < 0.05 were considered significant. For correlation analysis, correlated variables that have $p < 0.05$ were only considered in further analysis and discussion. The association between two parameters was determined, depending on the normality of their distributions, by Pearson product-moment correlation or Spearman rank-order correlation test. Descriptive statistics is given as Table S2 in the Supplementary material.

3 Results and discussion

Impaired deformability, as a typical hemorheological index has been associated with several pathological conditions, including certain hematological disorders, malaria, cardiovascular diseases, and metabolic disorders, such as highly prevalent DM (Huisjes al 2020, Di Giacinto et al. 2020). Glucose is a main substrate for energetic metabolism of erythrocytes, and it is well known that in the presence of long-lasting hyperglycemia in DM, the morphology, metabolism, and function of erythrocytes are inevitably subject to a series of changes that further affect hemorheology and microcirculation (Zhou et al. 2018; Sprague et al. 2006). Nevertheless, DM still represents an example of "covertly abnormal" blood rheology (Schmid-Schönbein, 1987, Brun et al. 2022) since it cannot be always determined by commercially available point-of-care (POC) devices within clinical environment. Ektacytometry, a laser diffraction technique, is the primary method for evaluating the deformability of erythrocytes in both research and clinical settings (Piety et al. 2021), based on the calculated EI from the diffraction images recorded on different shear stresses. However, since ektacytometry measures average deformability in bulk erythrocyte populations and does not provide information on the deformability of single cell, the reports on deformability in DM patients are still contradictory, i.e., the EI in DM have still not been validated as a clinical utile rheological biomarker, while the prognostic importance of EI for complications predictions in the case of sickle cell disease has been confirmed (Franck et al. 2022). Motivated by the previously mentioned, we aimed to represent erythrocyte deformability measurement by extracting a new hemorheological parameter and its fluctuations in DM patients.

The obtained deformability curves, presented in Fig. 2a, illustrate the comparative analysis of erythrocytes between control samples (blue curve) and DM samples (red curve). While control exhibits slightly elevated EI values compared to DM, no statistically significant differences in EI values are found between the two groups. The inherent variability among healthy donors and DM patients probably contributes to subtle distinctions in deformability that are challenging to quantify. Furthermore, our analysis indicates a lack of statistical differences in EI values at the half maximum of deformation curve and at 3 Pa between these two conditions, as illustrated in Fig. 2b.

Considering this, our focus shifts towards discerning specific physiologically relevant points along the deformability curve, such as EI at the half maximum value and EI values

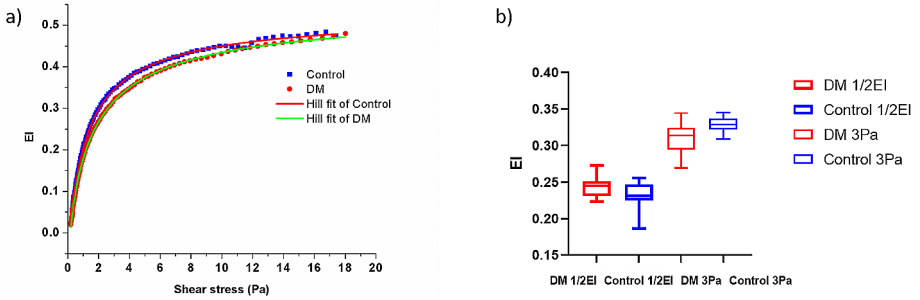

Fig. 2 (**a**) Deformability curve of healthy volunteer (blue curve) and DM patient (red curve). Raw data are fitted using Hill function, where EI=x^n / (½ SS ^*n*+x^n), x represent Shear stress (Pa), ½ SS represent value of SS at half maximum of the curve, n is Hill coefficient, in control sample parameters are: ½ SS=1.53, *n*=0.86 and in DM patients: ½ SS=1.32, *n*=0.93. (**b**) EI measured on 3 Pa and on the EI half maximum value on control (number of individuals=11) and DM patients (number of individuals=12)

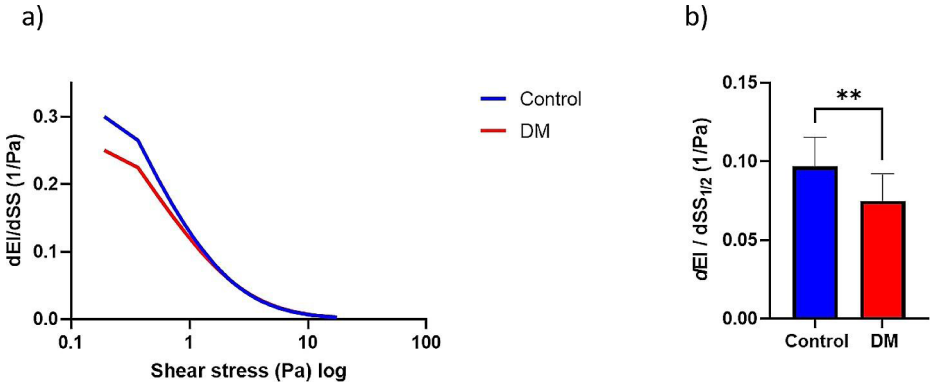

Fig. 3 (**a**) Derivation of deformability curves from Fig. 2a), blue (Control), red (DM patients) abscissa is presented on log scale for better observation of differences in dEI / dSS; (**b**) Change in dEI / dSS at the half maximum value of the derivation curve between erythrocytes of healthy donors (control) and DM patients

at 3 Pa. The calculation of the first derivative at these points is established as a metric for assessing EI alterations.

The derivative curves in Fig. 3 reveal that dEI/ dSS emerges as a suitable metric for quantifying erythrocyte deformation, particularly in assessing erythrocyte responsiveness to shear stress, compared to regular EI.

Our investigation has revealed statistically significant differences in the values of dEI / dSS at the half maximum deformability curve between the healthy donor group and individuals diagnosed with DM (depicted in Fig. 3b, where the blue bar corresponds to the control sample and the red bar represents the DM sample).

Here we indicate a non-clearly observable disparity in erythrocyte response to stress between DM patients and the control group, where DM erythrocytes exhibited a comparatively slower response. This insight underscores the potential clinical relevance of dEI / dSS

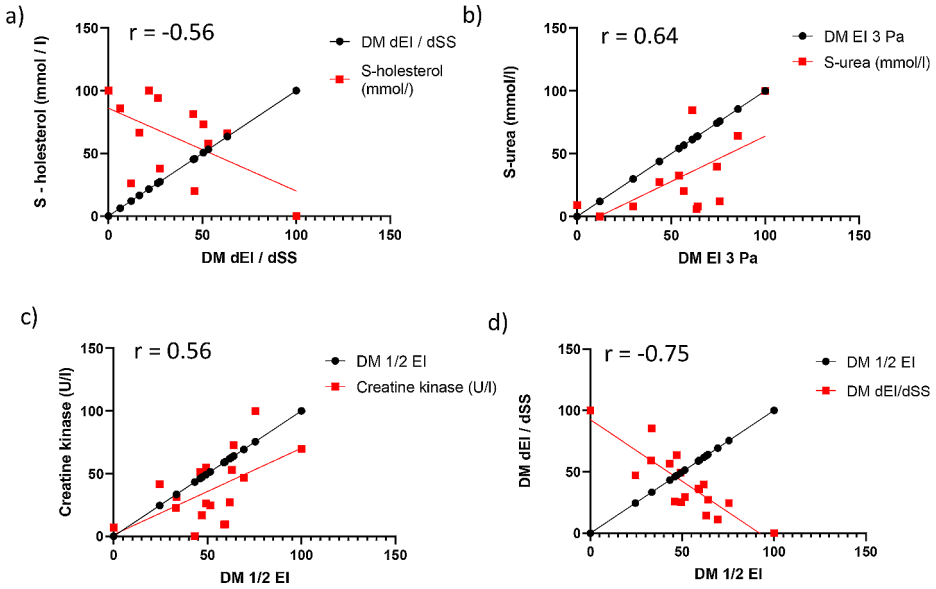

Fig. 4 Multiple correlation analysis of hemorheological parameter with clinical data of DM patients. r – Pearson coefficient. (**a**) Correlation plot of DM dEI / dSS and S – cholesterol ($p<0.05$), (**b**) correlation plot of DM EI 3 Pa and S – urea ($p<0.05$), (**c**) correlation plot of DM ½ EI and creatine kinase ($p<0.05$, (**d**) correlation plot of DM ½ EI and DM dEI / dSS ($p<0.05$)

as a valuable metric in characterizing erythrocyte deformability and provides better understanding on the altered physiological dynamics in DM patients. For better characterization of erythrocyte mechanical properties between control and DM patients, we separated DM group to Diabetes mellitus type1 (DMT1) and Diabetes mellitus type 2 (DMT2) patients. We observe significant difference on EI 3 Pa between DMT1 group and control (Supplement material Fig S1a). We didn't observe any differences between the patients' groups and control in ½ EI parameter (Supplement material Fig S1b). However, we have shown that dEI / dSS is more sensitive hemorheological parameter than EI 3 Pa, by observing differences between DMT1 group and control with stronger statistical significance (Supplement material Fig S1c), although we are aware of small group size at the moment.

The connection between the mechanical properties of red blood cells and various physiological processes can provide valuable insights. For instance, when examining parameters EI 3 Pa, ½ EI, and the rate dEI / dSS in relation to clinical factors as depicted in Fig. 4, we gain a deeper understanding of their interplay.

An interesting observation emerged when comparing dEI / dSS with serum cholesterol levels, indicating a statistically significant correlation ($p<0.05$), as shown in Fig. 4a. This finding aligns with existing literature, which suggests that higher cholesterol levels lead to increased rigidity of cell membranes (Subczynski et al. 2017; Chen et al. 1997). Conversely, while no significant correlation was found between EI 3 Pa and cholesterol, a direct relationship was noted between EI 3 Pa and serum urea levels (Fig. 4b). Urea plays a role in maintaining the osmotic stability of erythrocytes (Macey 1984), hence the correlation with EI 3 Pa.

Additionally, the parameter ½ EI exhibited a positive correlation with creatine kinase enzyme levels (Fig. 4c). Studies suggest that both liver and blood cells are involved in clearing creatine kinase from circulation (Pan et al. 2023). Moreover, previous research has highlighted a strong correlation between serum creatine levels and erythrocyte deformability in patients with diabetic nephropathy (Brown et al. 2005).

Considering diabetic nephropathy, it was anticipated that the dEI / dSS in diabetic patients would inversely correlate with half-maximal deformation force (½ EI), as depicted in Fig. 4d.

To understand the relationship between dEI / dSS and the ½ SS, we employed a scatter plot analysis as shown in Fig. 5. Both experimental groups exhibit a linear declining trend, indicating a decrement in dEI / dSS with an increment in ½ SS. This observation underscores a mechanical phenomenon wherein erythrocyte responsiveness to mechanical stress diminishes with higher shear stress values and conversely increases with lower shear stress values.

Specifically, the erythrocytes from DM individuals manifest a more pronounced and rapid alteration in dEI /dSS (depicted by the red line in Fig. 5 with a slope of -0.03) compared to those in the control group (represented by the blue line in Fig. 5 with a slope of -0.015). This discrepancy suggests that erythrocytes from DM patients exhibit a constrained range of membrane deformation control, indicative of an altered mechanical response to shear stress.

However, it is important to acknowledge that at lower shear stress values, the fluctuation of EI in both groups is subject to random variations in EI. This is attributed to the absence of established laminar flow of erythrocytes in the microchannel under such conditions (Shin et al. 2005b; McNamee et al. 2020). The results shown in the Fig. 5 elucidate the differential mechanical behavior of erythrocytes in response to varying shear stress levels, contributing to an understanding of underlying biophysical mechanism of erythrocyte deformability in the context of DM pathology. Diffraction signal intensity of the erythrocyte population

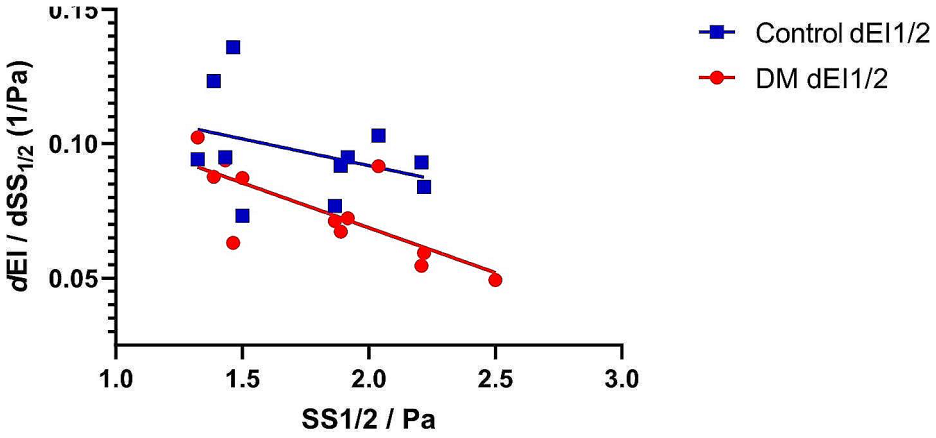

Fig. 5 Linear regression model of dEI / dSS at the half-maximal value of the deformability curve change in relation to ½ SS, control represented as blue line (R Squared=0.129) and DM represented as the red line (R Squared=0.568). Data was presented for each individual patient (DM) and healthy volunteer (Control)

also depends on hemoglobin and glucose concentration (Streekstra et al. 1994) which can be determined by standard biochemical, but also different optical techniques (Biswas et al. 2020; Cherkasova et al. 2016). Thus, our future studies will still include the correlation of dEI / dSS with the clinic-demographic data such age, sex, level of HbA1c, DM type, therapy, BMI, and other clinically established biomarkers of the disease in large-scale studies, since we identified small sample size in each group as a limitation of the present work.

Ektacytometry is a widely used method to measure the deformability of erythrocytes, but it only provides an average measure and doesn't account for variations in individual cells. This is where optical tweezers and microfluidic devices can find applications since recent studies have shown that these methods are more sensitive in assessing the progressive impairment of erythrocyte deformability than ektacytometry (Kim et al. 2015; Piety et al. 2021; Kang et al. 2022). The presence of rigid erythrocytes in blood flow can have a significant impact on the immune response as well. A recent study has found that the adhesion of leukocytes to the vascular wall gets disrupted by the presence of rigid erythrocytes (Gutierrez et al. 2018). This is where monitoring erythrocytes with impaired deformability on an individual level becomes crucial. Motivated by the findings of this study, our future research will include some other optics-based techniques, such as flow-cytometry, in combination with ektacytometry to better distinguish between populations of healthy and rigid erythrocytes from patients with DM, as one of the most frequent modern-age diseases.

There is paramount interest in finding the new metric as a potential prognostic marker for the prevalent clinical complications in DM patients, and our upcoming experiments will include the validation of the clinical utility of dEI / dSS in DM patients with specific micro- and macrovascular complications as well.

4 Conclusion

The dEI / dSS at the half maximum value of the deformability curve emerges as a particular metric for quantifying erythrocyte deformation response.

The statistically significant differences ($p<0.05$) observed in dEI / dSS at the half maximum of deformability curve between the control group and DM patients underscore the potential clinical relevance of this parameter. Moreover, no statistical differences were found in EI values at the half maximum value of deformability curve and at 3 Pa between the two conditions, highlighting the specificity of dEI / dSS in capturing alterations associated with DM pathology.

The scatter plot analysis further reveals a certain linear declining trend in both groups, indicating a decrement in dEI / dSS with an increment in shear stress. Importantly, erythrocytes from DM individuals exhibit a more pronounced and rapid alterations in dEI / dSS compared to the control group, suggesting a constrained range of membrane deformation control, and altered mechanical response to shear stress in DM patients. By exploration of the mechanical properties of red blood cells in conjunction with various physiological parameters we have uncovered significant associations between dEI / dSS and serum cholesterol levels ($p<0.05$). This finding supports existing literature indicating that elevated cholesterol levels contribute to increased rigidity of cell membranes. Conversely, although no direct correlation was found between EI 3 Pa and cholesterol, a clear relationship emerged between EI 3 Pa and serum urea levels, with urea playing a crucial role in main-

taining erythrocyte osmotic stability. Furthermore, the positive correlation between ½ EI and creatine kinase enzyme levels highlights the involvement of both liver and blood cells in the clearance of creatine kinase from circulation, having particular importance in patients with diabetic nephropathy. Considering diabetic nephropathy, our anticipation of an inverse correlation between dEI / dSS and ½ EI was confirmed, indicating potential implications for understanding the mechanical characteristics of erythrocytes in diabetic patients. Future work is needed to provide better understanding of dEI / dSS in prediabetic stage or in complication caused by DM. Moreover, oxidative stress of erythrocytes and its correlation with dEI / dSS should be the topic for future studies.

Overall, our findings support the notion that dEI / dSS should be considered as a potent biophysical parameter with the perspective of long-term clinical applications, offering valuable insights into the altered mechanical behavior of erythrocytes in individuals with DM and their future management. However, we need to emphasize that application of dEI / dSS in clinical practice needs large scale studies providing more deformability data to be processed and analyzed.

Supplementary Information The online version contains supplementary material available at https://doi.org/10.1007/s11082-024-06973-9.

Author contributions M. R. (Mihajlo Radmilović): Writing – original draft, Data curation, Formal analysis, V. I.: Investigation, Visualization, Conceptualization, Supervision, Writing – review & editing, D.T.: Data curation, Formal analysis, M. R. (Mihailo Rabasović): Writing – review & editing, A. P.: Resources, K. L.: Resources, A. K.: Writing – review & editing, Supervision, Project administration, I. D.: Investigation, Conceptualization, Validation, Writing – review & editing, Project administration.

Funding This work was supported by the Science Fund of the Republic of Serbia [program PROMIS, project HEMMAGINERO, grant number 6066079]. The authors acknowledge funding provided by the Institute of Physics Belgrade, through the grant by the Ministry of Education, Science and Technological Development of the Republic of Serbia and the Institute for Medical Research University of Belgrade, National Institute of the Republic of Serbia, through the contract No. 451-03-66/2024-03/200015. The authors acknowledge funding provided also by the Project Advanced Biophysical Methods for Soil Targeted Fungi-Based Biocontrol Agents -BioPhysFUN [Grant number 4545] from the Program DEVELOPMENT – Green program of cooperation between science and industry, Science Fund of the Republic of Serbia.

Data availability The data that support the findings of this study are not openly available, but will be available from the corresponding author upon reasonable request.

Code availability Not applicable.

Declarations

Ethics approval Before sample collection for this study, the patients signed an informed consent as an obligatory procedure within obtained ethical approval No 1332/VII-5 from 7th July 2020 issued by the Faculty of Medicine at University of Belgrade.

Consent to participate Not applicable for this study.

Consent for publication All authors of the manuscript agree to its submission and publication.

Competing interests The authors declare no competing interests.

References

Babu, N.: Hemorheological study on erythrocyte aggregation in patients with type 2 diabetes mellitus without cholesterol and with hypercholesterol. Thromb. Updat. **5**, 100085 (2021). https://doi.org/10.1016/j.tru.2021.100085

Baskurt, O.K., Meiselman, H.J.: Analyzing shear stress–elongation index curves: Comparison of two approaches to simplify data presentation. Clin. Hemorheol Microcirc. **31**, 23–30 (2004). PMID: 15272150

Baskurt, O.K., Hardeman, M.A.X.R., Uyuklu, M., Ulker, P., Cengiz, M., Nemeth, N., Shin, S., Alexy, T., Meiselman, H.J.: Parameterization of red blood cell elongation index – shear stress curves obtained by ektacytometry. Scand. J. Clin. Lab. Invest. **69**, 777–788 (2009). https://doi.org/10.3109/00365510903266069

Biswas, U., Kumar, J.: Detection and analysis of hemoglobin concentration in blood with the help of photonic crystal based micro ring resonator structure. Opt. Quantum Electron. 1–16 (2020). https://doi.org/10.1007/s11082-020-02566-4

Bronkhorst, P.J., Nijhof, E.J., Sixma., J.J.: Parametrization of the deformation curve as a tool for standardization and interpretation of ektacytometric measurements. Clin. Hemorheol Microcirc. **15**, 803–816 (1995). https://doi.org/10.3233/CH-1995-15602

Brown, C.D., Ghali, H.S., Zhao, Z., Thomas, L.L., Friedman, E.A.: Association of reduced red blood cell deformability and diabetic nephropathy. Kidney Int. **67**, 295–300 (2005). https://doi.org/10.1111/j.1523-1755.2005.00082.x

Brun, J.-F., Varlet-Marie, E., Myzia, J., de Mauverger, E.R., Pretorius, E.: Metabolic influences modulating erythrocyte deformability eryptosis metabolites. **12**, 4 (2022). https://doi.org/10.3390/metabo12010004

Chen, Z., Rand, R.P.: The influence of cholesterol on phospholipid membrane curvature and bending elasticity. Biophys. J. **73**, 267–276 (1997)

Cherkasova, O., Nazarov, M., Shkurinov, A.: Noninvasive blood glucose monitoring in the terahertz frequency range. Opt. Quantum Electron. **1–12** (2016). https://doi.org/10.1007/s11082-016-0490-5

Cho, M., Shin, S., Moon, H., Chung, H.: Effect of clinical and RBC hemorheological parameters on myocardial perfusion in patients with type 2 diabetes mellitus. Biorheology. **51**, 215–226 (2014). https://doi.org/10.3233/BIR-140659

Chung, S.M., Oh, J.H., Moon, J.S., Kim, Y.K., Yoon, J.S.: Critical shear stress is associated with diabetic kidney disease in patients with type 2 diabetes. Sci. Rep. 1–7 (2018). https://doi.org/10.1038/s41598-018-19274-5

Ercan, M., Konukoğlu, D., Erdem, T., Önen, S.: The effects of cholesterol levels on hemorheological parameters in diabetic patients. Clin. Hemorheol. Microcirc. 26 257–263 PMID: 12122231 (2002)

Franck, P., Buijs, P., Meenhuis, A., Dane, M., Postma, C., Spaans, A., Gijsbertha, N., Kuypers, F.A., Hudig, C., Kerkhoffs, J.L.: The ektacytometric elongation Index (EI) of erythrocytes, validation of a prognostic, rheological biomarker for patients with sickle cell disease. Eur. J. Haematol. 1–10 (2022). https://doi.org/10.1111/ejh.13748

Di Giacinto, F., Tartaglione, L., Nardini, M., Mazzini, A., Romanò, S., Rizzo, G.E., Papi, M., Spirito, M., Pitocco, D., Ciasca, D.: Searching for the mechanical fingerprint of pre-diabetes in T1DM: A case report study. Front. Bioeng. Biotechnol. **8**, 569978 (2020). https://doi.org/10.3389/fbioe.2020.569978

Greco, W.R., Hakala, M.T.: Evaluation of methods for estimating the dissociation constant of tight binding enzyme inhibitors. J. Biol. Chem. **254**, 12104–12109 (1979). https://doi.org/10.1016/S0021-9258(19)86435-9

Gutierrez, M., Fish, M.B., Golinski, A.W., Eniola-Adefeso, O.: Presence of rigid red blood cells in blood flow interferes with the vascular wall adhesion of leukocytes. Langmuir. **34**(6), 2363–2372 (2018). https://doi.org/10.1021/acs.langmuir.7b03890

Huisjes, R., Makhro, A., Llaudet-planas, E., Hertz, L., Verhagen, L.P., Pignatelli, S., Rab, M.A.E., Schiffelers, R.M., Seiler, E., Solinge, W.W., Van, Corrons, V., Kaestner, L., Mañú-pereira, M., Bogdanov, A., Wijk, R.: Van.: Red cells as markers of clinical severity in hereditary spherocytosis. Haematologica. 105, 338–347 (2020). https://doi.org/10.3324/haematol.2018.188151

Jensen, T., Feldt-Rasmussen, B.O., Bjerre-Knudsen, J., Deckert, T.: Features of endothelial dysfunction in early diabetic nephropathy. Lancet. **75**, 461–463 (1987). https://doi.org/10.1016/s0140-6736(89)91365-2

Kang, Y.J., Serhrouchni, S., Makhro, A., Bogdanova, A., Lee, S.S.: Simple assessment of red blood cell deformability using blood pressure in capillary channels for effective detection of subpopulations in red blood cells. ACS Omega. **7**(43), 38576–38588 (2022). https://doi.org/10.1021/acsomega.2c04027

Kim, J., Lee, H., Shin, S.: Advances in the measurement of red blood cell deformability: A brief review. J. Cell. Biotechnol. **1**, 63–79 (2015). https://doi.org/10.3233/JCB-15007

Kobayashi, J., Ohtake, K., Murata, I., Sonoda, K.: Nitric oxide nitric oxide bioavailability for red blood cell deformability in the microcirculation: A review of recent progress. Nitric Oxide. **129**, 25–29 (2022). https://doi.org/10.1016/j.niox.2022.09.004

Lee, S., Lee, M.Y., Nam, J.S., Kang, S., Park, J.S., Shin, S., Ahn, C.W., Kim, K.R.: Hemorheological approach for early detection of chronic kidney disease and diabetic nephropathy in type 2 diabetes. Diabetes Technol. Ther. **17**, 1–8 (2015). https://doi.org/10.1089/dia.2014.0295

Macey, R.I.: Transport of water and urea in red blood cells. Am. J. Physiol. Cell. Physiol. **246**, C195-C203 (1984). https://doi.org/10.1152/ajpcell.1984.246.3.C195

Maeda, N.: Erythrocyte rheology in microcirculation. Jpn J. Physiol. **46**, 1–14 (1996). https://doi.org/10.2170/jjphysiol.46.1

Malandrino, N., Wu, W.C., Taveira, T.H.: Association between red blood cell distribution width and macrovascular and microvascular complications in diabetes. Diabetologia. 226–235 (2012). https://doi.org/10.1007/s00125-011-2331-1

Mawatari, S., Saito, K., Murakami, K., Fujino, T.: Absence of correlation between glycated hemoglobin and Lipid Composition of Erythrocyte Membrane in type 2 Diabetic patients. Front. Physiol. 123–127 (2004). https://doi.org/10.1016/j.metabol.2003.07.016

McNamee, A.P., Fitzpatrick, T., Tansley, G.D., Simmonds, M.J.: Sublethal supraphysiological shear stress alters erythrocyte dynamics in subsequent low-shear flows. Biophys. J. **119**, 2179–2189 (2020). https://doi.org/10.1016/j.bpj.2020.10.022

Mokken, F.C., Kedaria, M., Henny, C.P., Hardeman, M.R., Gelb, A.W.: The clinical importance of erythrocyte deformability, a hemorrheological parameter. Ann. Hematol. **64**, 113–122 (1992). https://doi.org/10.1007/BF01697397

Musielak, M.: Red blood cell-deformability measurement: Review of techniques. Clin. Hemorheol Microcirc. **42**, 47–64 (2009). https://doi.org/10.3233/CH-2009-1187

Ogurtsova, K., da Rocha Fernandes, J.D., Huang, Y., Linnenkamp, U., Guariguata, L., Cho, N.H., Cavan, D., Shaw, J.E., Makaroff, L.E.: IDF diabetes atlas: Global estimates for the prevalence of diabetes for 2015 and 2040. Diabetes Res. Clin. Pract. **128**, 40–50 (2017). https://doi.org/10.1016/j.diabres.2017.03.024

Pan, N., Wu, Y., Yang, B., Zhang, M., He, Y., Wang, Z., Zhang, L.: The liver and blood cells are responsible for creatine kinase clearance in blood circulation: A retrospective study among different human diseases. Clin. Chim. Acta. **544**, 117335 (2023). https://doi.org/10.1016/j.cca.2023.117335

Piety, N.Z., Stutz, J., Yilmaz, N., Xia, H., Yoshida, T.: Microfluidic capillary networks are more sensitive than ektacytometry to the decline of red blood cell deformability induced by storage. Sci. Rep. 1–11 (2021). https://doi.org/10.1038/s41598-020-79710-3

Pretorius, E.: Erythrocyte deformability and eryptosis during inflammation, and impaired blood rheology. Clin. Hemorheol Microcirc. **69**, 545–550 (2018). https://doi.org/10.3233/CH-189205

Rabi, D.M., Edwards, A.L., Southern, D.A., Sargious, P.M., Norton P., Larsen, E.T., Ghali, W.A.: Association of socio-economic status with diabetes prevalence and utilization of diabetes care services. BMC Health Serv. Res. **124** (2006). https://doi.org/10.1186/1472-6963-6-124

Schmid-Schönbein, Teitel, P.: In vitro assessment of covertly abnormal blood rheology: Critical appraisal ofpresently available microrheological methodology. A review focusing on diabetic retinopathy as a possible consequence of rheological occlusion. Clin. Hemorheol Microcirc. **7**, 203–238 (1987). https://doi.org/10.3233/CH-1987-7206

Schut, N.H., Arkel, E.C., Van, Hardeman, M.R., Bilo, H.J.G., Michels, R.P.J., Vreeken, J.: No decreased erythrocyte deformability in type 1 (insulin-dependent) diabetes, either by filtration or by ektacytometry. Acta Diabetol. 89–92 (1993). https://doi.org/10.1007/BF00578220

Shaw, J.E., Sicree, R.A., Zimmet, P.Z.: Global estimates of the prevalence of diabetes for 2010 and 2030. Diabetes Res. Clin. Pract. **87**, 4–14 (2010). https://doi.org/10.1016/j.diabres.2009.10.007

Shin, S., Ku, Y., Park, M.S., Suh, J.S.: Deformability of red blood cells: A determinant of blood viscosity. J. Mech. Sci. Technol. **19**, 216–223 (2005a). https://doi.org/10.1007/BF02916121

Shin, S., Ku, Y., Park, M.S., Suh, J.S.: Slit-flow ektacytometry: Laser diffraction in a slit rheometer. Cytometry. **65B**, 6–13 (2005b). https://doi.org/10.1002/cyto.b.20048

Shin, S., Ku, Y., Babu, N., Singh, M.: Erythrocyte deformability and its variation in diabetes mellitus. Indian J. Exp. Biol. 45, 121–128 PMID: 17249336 (2007)

Sokolova, I.A., Kachalova, A.V., Fabrichnova, A.A., Kovaleva, Y.A., Shahnazarov, A.A., Koshelev, V.B.: Hemorheological properties in patients with type-1 and type-2 diabetes mellitus. J. Biomed. Photonics Eng. **51**, 457–459 (2017). https://doi.org/10.18287/JBPE17.03.030402

Sprague, R.S., Stephenson, A.H., Bowles, E.A., Stumpf, M.S., Lonigro, A.J.: Reduced expression of G(i) in erythrocytes of humans with type 2 diabetes is associated with impairment of both cAMP generation and ATP release. Diabetes. **55**, 3588–3593 (2006). https://doi.org/10.2337/db06-0555

Streekstra, G.J., Hoekstra, A.G., Heethaar, R.M.: Anomalous diffraction by arbitrarily oriented ellipsoids: Applications in ektacytometry. Appl. Opt. **33**, 7288–72896 (1994). https://doi.org/10.1364/AO.33.007288

Subczynski, W.K., Mainali, L., Raguz, M., O'Brien, W.J.: Organization of lipids in fiber-cell plasma membranes of the eye lens. Exp. Eye Res. **156**, 79–86 (2017). https://doi.org/10.1016/j.exer.2016.03.004

Wang, Y., Yang, P., Yan, Z., Liu, Z., Ma, Q., Zhang, Z., Su, Y.: The relationship between erythrocytes and diabetes mellitus. J. Diabetes Res. ID. **6656062** (2021). https://doi.org/10.1155/2021/6656062

Zhou, Z., Mahdi, A., Tratsiakovich, Y., Zahorán, S., Kövamees, O., Nordin, F., Uribe Gonzalez, A.E., Alvarsson, M., Östenson, C.G., Andersson, D.C., Hedin, U., Hermesz, E., Lundberg, J.O., Yang, J., Pernow, J.: Erythrocytes from patientswith type 2 diabetes induce endothelial dysfunction via arginase I. J. Am. Coll. Cardiol. **72**, 769–780 (2018). https://doi.org/10.1016/j.jacc.2018.05.052

Authors and Affiliations

Mihajlo D. Radmilović[1] · Vesna Lj. Ilić[2] · Drenka Trivanović[2] · Ana Petakov[3] · Katarina Lalić[3,4] · Mihailo D. Rabasović[1] · Aleksandar J. Krmpot[1] · Ivana T. Drvenica[2]

✉ Ivana T. Drvenica
ivana.drvenica@imi.bg.ac.rs

Mihajlo D. Radmilović
mihajlor@ipb.ac.rs

Vesna Lj. Ilić
vesnai@imi.bg.ac.rs

Drenka Trivanović
drenka.trivanovic@imi.bg.ac.rs

Ana Petakov
anapetakov@gmail.com

Katarina Lalić
katarina.s.lalic@gmail.com

Mihailo D. Rabasović
rabasovic@ipb.ac.rs

Aleksandar J. Krmpot
krmpot@ipb.ac.rs

[1] Institute of Physics Belgrade, University of Belgrade, Pregrevica 18, Belgrade, Serbia

[2] Institute for Medical Research, National Institute of Republic of Serbia, University of Belgrade, Dr. Subotića 4, Belgrade, Serbia

[3] Clinic for Endocrinology, Diabetes and Metabolic Diseases, University Clinical Center of Serbia, Dr. Subotića 13, Belgrade 11000, Serbia

[4] Faculty of Medicine, University of Belgrade, Dr. Subotića 8, Belgrade 11000, Serbia

Pajić et al. *Microsystems & Nanoengineering* (2024)10:47
https://doi.org/10.1038/s41378-024-00664-x

Microsystems & Nanoengineering
www.nature.com/micronano

ARTICLE Open Access

In vivo femtosecond laser nanosurgery of the cell wall enabling patch-clamp measurements on filamentous fungi

Tanja Pajić[1]✉, Katarina Stevanović[1], Nataša V. Todorović[2], Aleksandar J. Krmpot[3], Miroslav Živić[1], Svetlana Savić-Šević[3], Steva M. Lević[4], Marina Stanić[5], Dejan Pantelić[3], Brana Jelenković[3] and Mihailo D. Rabasović[3]✉

Abstract

Studying the membrane physiology of filamentous fungi is key to understanding their interactions with the environment and crucial for developing new therapeutic strategies for disease-causing pathogens. However, their plasma membrane has been inaccessible for a micron-sized patch-clamp pipette for pA current recordings due to the rigid chitinous cell wall. Here, we report the first femtosecond IR laser nanosurgery of the cell wall of the filamentous fungi, which enabled patch-clamp measurements on protoplasts released from hyphae. A reproducible and highly precise (diffraction-limited, submicron resolution) method for obtaining viable released protoplasts was developed. Protoplast release from the nanosurgery-generated incisions in the cell wall was achieved from different regions of the hyphae. The plasma membrane of the obtained protoplasts formed tight and high-resistance (GΩ) contacts with the recording pipette. The entire nanosurgical procedure followed by the patch-clamp technique could be completed in less than 1 hour. Compared to previous studies using heterologously expressed channels, this technique provides the opportunity to identify new ionic currents and to study the properties of the ion channels in the protoplasts of filamentous fungi in their native environment.

Introduction

Filamentous fungi are an extremely diverse cosmopolitan group with great importance to the functioning of the biosphere. Together with bacteria, fungi represent the most important group of decomposers in almost all ecosystems, and mycorrhizal fungi form symbiotic associations with nearly 80% of land plants[1]. Moreover, the biodiversity of mycorrhizal fungi in soil has a critical impact on maintaining plant and ecosystem biodiversity[2]. In addition, some fungi are pathogenic and cause diseases in animals or plants[3], and fungi that threaten human health have enormous biomedical importance[4]. Ion channels are known or expected to play important roles in fungal physiology[5], including ion and nutrient uptake[6], signal transduction[7], and response to osmotic stress[8]. In contrast to animal and plant cells, little is known about the function of the ion channels in fungi. To date, only a handful of channels in filamentous fungi have been cloned and/or characterized by electrophysiological techniques; this has been performed mainly by heterologous expression of the channel proteins identified by screening for homologs of known yeast, animal or plant proteins[9–19]. The main reason for the near-complete lack of studies on native membranes is the rigid, chitinous cell wall that blocks access to the patch-clamp pipette. The cell wall makes it impossible to use the patch-clamp method; the gold standard for ion current measurements. For the membrane to be accessible by the glass

Correspondence: Tanja Pajić (tpajic@bio.bg.ac.rs) or
Mihailo D Rabasović (rabasovic@ipb.ac.rs)
[1]Institute of Physiology and Biochemistry "Ivan Djaja", Faculty of Biology, University of Belgrade, Studentski trg 16, 11158 Belgrade, Serbia
[2]Institute for Biological Research "Siniša Stanković", University of Belgrade, National Institute of the Republic of Serbia, Bulevar Despota Stefana 142, 11000 Belgrade, Serbia
Full list of author information is available at the end of the article

pipette for the patch-clamp method, all or part of the wall must be removed. The naked protoplast (cellular cytoplasm whose entire contents are enclosed by the plasma membrane) would then be released through the opening in the hyphal wall to enable access with the patch-clamp pipette. The formation of a high-resistance contact ("seal") between the tip of the glass pipette and the membrane is a prerequisite for the patch-clamp technique and is only possible if the membrane is clean[20].

There are several ways to remove the cell wall: mechanically, enzymatically and by laser cell surgery[21,22]. Mechanical dissection of tissue to release a small number of protoplasts has never been successful in filamentous fungi, while this method is used in plant tissues to avoid the deleterious effects of enzymatic treatment on the plasma membrane[23]. Enzymatic removal of the cell wall was successful in plants[24,25] but did not produce positive results in the filamentous fungi *Neurospora*[26] and *Saprolegnia*[27]. Contacts with resistances greater than 200 and 500 MΩ were not possible to attain. These results were in contrast to plant findings and occurred because the fungal cell wall is structurally and molecularly distinct from the cellulose-based plant cell wall.

However, a small localized portion of the fungal cell, such as a tiny cell wall section, is possible to remove using the laser ablation technique[28] while leaving the bulk of the wall intact. In this way, the polarity of the fungal cells is preserved, and a portion of the plasma membrane is accessible for patch-clamp measurements. Laser removal of the cell wall combined with patch-clamp recording has previously been used in some algae and plants[21,29–32] and only in two filamentous fungi[10,33]. However, these experiments were conducted more than twenty years ago with UV lasers and did not evolve into a routine protocol. The UV lasers used in these studies operated with nanosecond (ns) laser pulses, which are known to cause photothermal and photomechanical damage to samples[34–36]. Recent developments in laser technology and microscopy, especially ultrafast femtosecond (fs) lasers, enable operations with extremely high precision. The main advantage of fs lasers is that they produce negligible thermal effects compared to ns lasers because their pulses are shorter than the thermal diffusion time (picoseconds to nanoseconds)[37]. Due to the non-thermal nature of the fs laser interacting with the cellular material, the material is mainly ablated[28,34,35,38], causing minimal damage to the surrounding cellular material. In addition, the pulse energy for fs laser ablation is in the sub-nJ range, which is well below the pulse energies of UV-ns lasers. In addition, the wavelengths of fs lasers used for cell surgery are in the NIR range, which is not as harmful to the cell as UV wavelengths are; this aspect is particularly important for stray radiation during surgery.

Femtosecond lasers emit ultrashort laser pulses that allow a significant reduction in dissection size compared to ns lasers[34,35,38]. Thus, they are ideal for precise cell surgery at the nanoscale to microscale. In fs laser cell nanosurgery, a laser beam is focused down to the diffraction-limited focal spot/volume by a high numerical aperture (NA) objective lens on the cell wall or membrane[28,35,38]. In addition, the surgical process achieved with fs lasers enables the removal of very small amounts of material with high precision, creating a small incision on the cell wall/membrane or other cell structures. The high peak intensities of the fs laser pulses induce multiphoton interaction processes and provide a lower energy threshold for cell wall/membrane removal[28,35,38]. The typical peak intensity for fs laser ablation is on the order of 10^{12} W/cm^2 [39,40]. Briefly, ultrashort laser pulses with relatively low energy enable more precise submicrometer surgical incisions than ns lasers[34,35,38,41].

Laser nanosurgery has become an important tool in many biological fields because of its precision, noninvasiveness, and versatility. This technique has been used as a microdissection tool for studying the function of microtubules, mitochondria and other organelles in cultured cells, tissues, and whole organisms, as well as for optotransfection and other forms of laser-based molecular delivery[42]. Other potential applications of this technology include developmental biology studies of cell mechanics, intracellular transport, and cell signaling, as well as the development of new therapies for diseases such as cancer and genetic disorders. In the context of fungi, fs laser nanosurgery could be used to selectively remove portions of the cell wall. The combination of laser ablation and localized patch clamping allows the measurement of ionic currents through the plasma membrane while retaining information about the location of the membrane from which recordings were made. This approach enables the detection of the asymmetric distribution of the ion channels along hyphae and the exploration of the ion channel involvement in the fungal cell polarity establishment, signal integration, and hyphal tropism; all of these play key roles in establishing fungal virulence[43] and interactions with surrounding organisms or the environment[44,45]. Thus, we were motivated to develop and optimize a protocol that allows high-quality recording of currents via the patch-clamp method on the plasma membrane of fungal protoplasts released from the wall by subcellular nanosurgery using a fs titanium-sapphire (Ti:Sa) laser. Therefore, to the best of our knowledge, we present the first successful application of fs laser nanosurgery to access the plasma membrane of filamentous fungal hyphae for patch-clamp recording. We demonstrated that the released protoplasts could successfully form high-resistance contacts with a patch-clamp pipette. The incisions produced by the fs laser were smooth-edged, protoplasts were released from those incisions, and the probability of protoplast release was a

function of the incision size and was modified by the presence of a high Ca^{2+} concentration. The method could be readily used for the selective release and subsequent recording of protoplasts from different regions (tip, middle, and side branches) of the fungal hyphae. Finally, we provided the first electrophysiological snapshot obtained on filamentous fungal protoplasts after cell wall removal by fs laser nanosurgery and showed that the protoplast membrane was characterized by a number of different types of ionic currents, predominantly anionic.

Results

In vivo two-photon imaging, cell wall laser nanosurgery and patch-clamp recording

A nonlinear laser scanning microscope (NLSM) using fs laser pulses is the necessary prerequisite for the application of precision laser ablation. The NLSM system also enables in vivo imaging of single cells and cellular structures using two-photon excitation fluorescence (TPEF) before and after laser nanosurgery. We successfully created laser-generated incisions in cell wall sections of the filamentous fungus *Phycomyces blakesleeanus* using tightly focused, 160 fs, near-infrared (NIR) laser pulses (Fig. 1). To remove a small portion of the cell wall in a specific area of the hyphae, the cell wall must be visualized and distinguished from the plasma membrane and other cell structures. Since the cell wall and the plasma membrane are in close contact[46], hyphae were plasmolyzed and kept in hyperosmotic solution to retract the cytoplasm before the procedure, as shown in Fig. 1a. The plasmolyzed hyphae stained with calcofluor white (CFW) and treated with an exocytosis inhibitor and a respiratory inhibitor (sodium azide) to prevent cell wall regeneration were subjected to nanosurgery. We selected for the nanosurgery the section where the hyphal protoplast was retracted from the cell wall and placed the spot-wise pattern on the selected section (Fig. 1b). The laser-generated incision is clearly visible in the TPEF images (Fig. 1c) and in the bright-field images. The cell viability after nanosurgery was regularly verified by bright-field microscopy. The protoplast enveloped by the plasma membrane exited through the incision in the cell wall without deforming or bursting (Fig. 1d). Thus, the released round protoplasts were viable for up to several hours during the electrophysiological measurements. Representative patch-clamp current recordings obtained from the released protoplasts in the "outside-out" and "whole-cell" configurations are shown in Fig. 1f and g, respectively.

We obtained 79 fungus-released protoplasts in the patch-clamp microscopy chamber that were sufficiently large (larger than 7 μm) and spatially accessible to the patch pipette. Membrane contact with high resistance (greater than GΩ resistance) was obtained on 22 released protoplasts (28%). Eight protoplasts (10%) were very stable and allowed multiple successful pipette approaches which resulted in the formation of multiple GΩ-resistance contacts and patch excisions. A total of 36 giga-ohm seal contacts were obtained. All patch-clamp configurations were used for the recording. The current family obtained from the entire protoplast membrane in the "whole cell" configuration had a typical appearance (Fig. 1f). The single-channel currents recorded from the excised patches in the inside-out or outside-out configurations were more diverse. We used solutions with asymmetric ion concentrations to identify the general type of ion basis for selectivity (K^+, Cl^-, glutamate$^-$, or Ca^{2+}) for each recorded channel current based on the reversal potential (V_{rev}) (Fig. 1g).

Laser nanosurgery procedure—the main steps and key factors

The main steps for successful fs laser nanosurgery of the fungal cell wall to obtain viable protoplasts for patch-clamp analysis are shown in Fig. 2. The first important step was to decrease the osmolarity of the growth media to acclimate the fungi to conditions with lower osmolarity and increase their sensitivity to the plasmolysis solution. This approach ensured faster plasmolysis during the preparation phase of nanosurgery. By reducing the osmolarity of the growth medium by 30%, the plasmolysis time (in minutes) was decreased from 30 ± 10 to 5 ± 2. The introduction of two-stage plasmolysis and the increase in the Ca^{2+} concentration in the hyperosmotic solution followed, and these were considered the most important, key factors for successful surgery and the recovery of viable, patchable, released protoplasts. The Ca^{2+} concentration was increased to accelerate plasmolysis (<1 min) and stabilize the protoplasts[33]. The step before plasmolysis reduced the physiological shock that would occur if the fungi were transferred directly from the medium to a hyperosmotic solution (450 mOsm difference). This was achieved by staining the fungi with diluted dye in a standard isoosmotic solution.

To achieve precision and enable successful nanosurgery and imaging, the fungal hyphae were immobilized on the coverslip. A number of substrate-coating materials were tested (Supplementary Table 1), and a collagen coating was found to provide better immobilization of the fungal hyphae while allowing for the patch-pipette approach.

The cell wall of the filamentous fungus *Phycomyces blakesleeanus* is weakly autofluorescent and can be visualized by excitation at 730 nm, presumably as a signal from the chitin-containing (chitin and chitosan) component of the cell wall[47,48]. The removal of the cell wall by the laser nanosurgical procedure was not efficient enough on the native hyphae. After staining the cell wall with

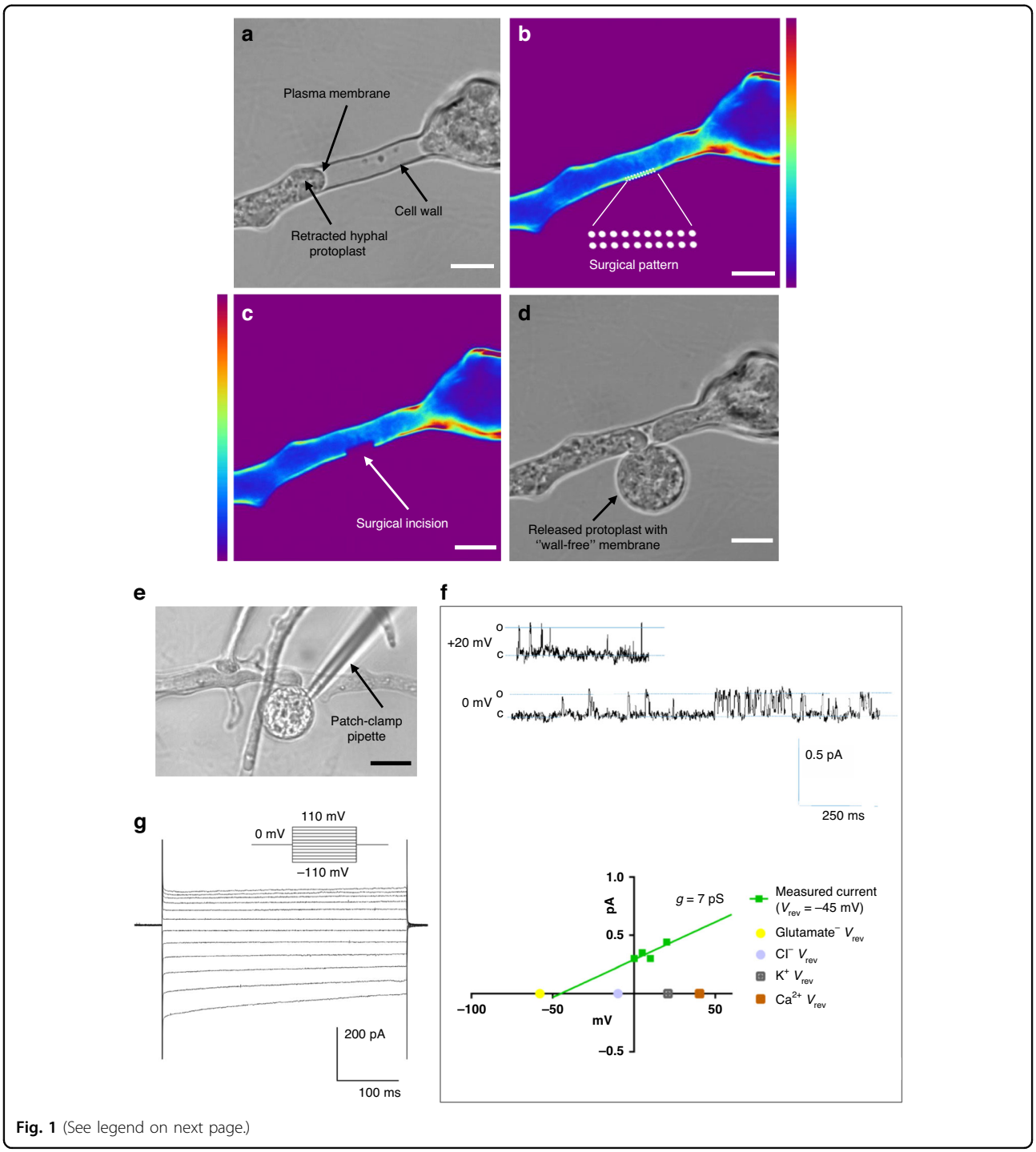

Fig. 1 (See legend on next page.)

CFW, the surgery was almost 100% successful. All nanosurgical procedures presented were performed with a cell wall stained with CFW to improve the absorption of laser energy. CFW has a high affinity for cell wall components (chitin and other polysaccharides), and the absorption maximum is at 345 nm under single-photon excitation conditions[49].

Two-photon imaging of the cell wall was performed with a very low average laser power of 0.5 mW and a pulse energy of 0.007 nJ at the sample plane. A wavelength of 730 nm was used for both multiphoton imaging and nanosurgery, bypassing the time required to change wavelengths. A diameter of hyphae (<15 μm) poses a major challenge for successfully cutting off a portion of

(see figure on previous page)

Fig. 1 In vivo laser nanosurgery of the cell wall of the filamentous fungus *Phycomyces blakesleeanus* using fs laser pulses and patch-clamp recording of the released fungal protoplast membrane current activity after the surgical procedure. a Bright-field and **b** TPEF image of the plasmolyzed and labeled hypha before surgery. A 20×2 spot-wise pattern was positioned on the cytoplasm-free section of the cell wall. The average laser power in the sample plane for imaging was 1.1 mW (dwell time 2.5 µs) at 730 nm. **c** TPEF image of the same hypha after surgery. The surgical incision is indicated by the arrow. The laser power at the sample plane for the surgery was 6.1 mW (dwell time 1 s) at 730 nm. The color intensity bars for the TPEF signal are as follows: violet/blue, lowest TPEF signal; and dark red, highest TPEF signal. The color intensity bar is linear and covers the entire range of the data. Scale bar: 10 µm. **d** Bright-field image of the same hypha with the protoplast released through the surgical incision after laser cutting. **e** Bright-field image of the patch-clamp pipette in contact with the membrane of the protoplast released through the surgical incision. Scale bar: 20 µm. All images were taken with a Zeiss 40× 1.3 oil objective. **f** Top: Representative single-channel current recordings obtained from the released protoplast at V_h of +20 mV and 0 mV. o: open channel current level; c: closed channel current level. The calibration bar is on the right side. Bottom: current-voltage (IV) dependency of the recording shown above. On the abscissa, the reversal potentials of the main ions in the bath and pipette solutions are shown, indicating that the current is carried mainly by glutamate. The obtained conductance (g) is given above the linear fit through the measured points. Recorded in SolB. **g** Representative current recorded from the entire protoplast membrane in the whole-cell configuration. The cells were recorded in SolA with a low-chloride pipette solution. The voltage stimulation protocol used to obtain the recordings is shown in the inset. The calibration bar is at the bottom

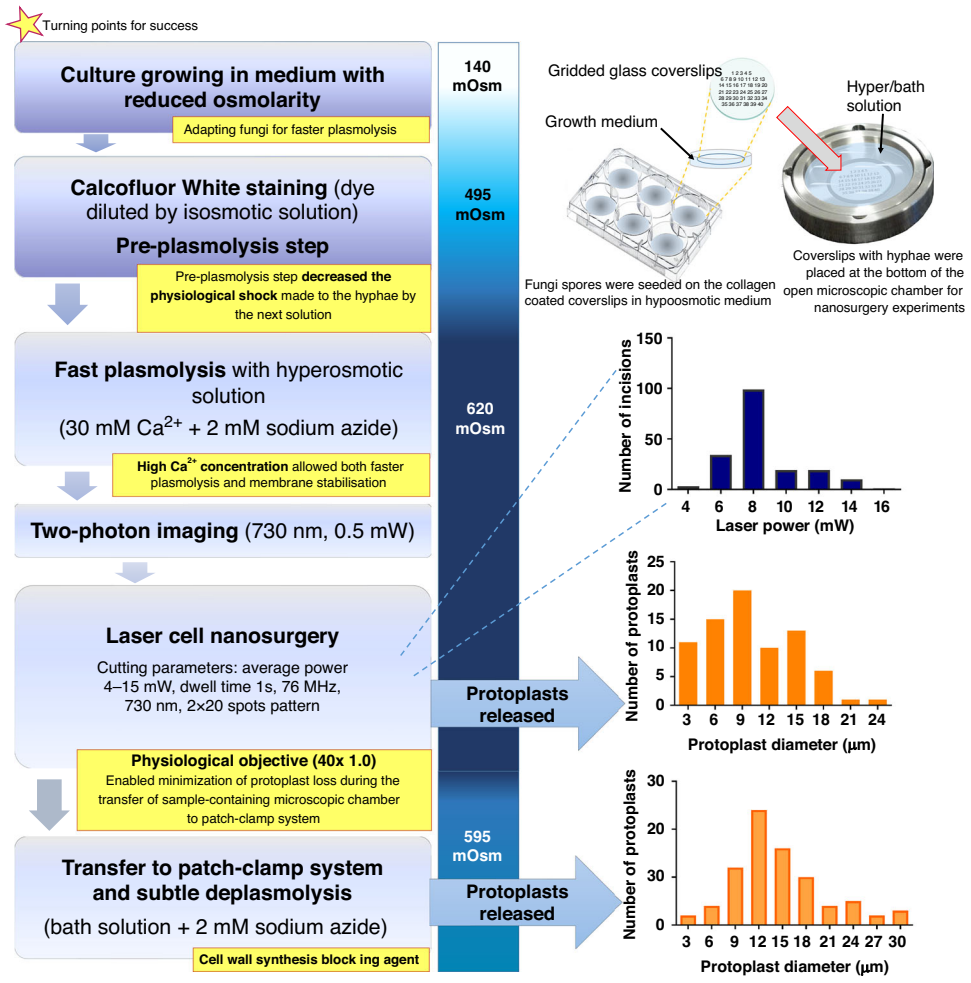

Fig. 2 Laser nanosurgery procedure main steps and turning points for successful removal of the *Phycomyces blakesleeanus* hyphae cell wall. The osmolarity of the extracellular solution at each step of the procedure is indicated on the blue gradient strip. A detailed description of the procedure can be found in the Materials and Methods section. The distribution of the average laser power used for nanosurgery of *P. blakesleeanus* cell walls is shown in the upper graph, and the distributions of the sizes of the protoplasts released in the two consecutive steps (bottom) are shown as histograms with the upper bin boundary on the abscissa

the cell wall without endangering the rest of the cell. After optimizing the surgical procedure, we selected a 2 × 20 spot-wise pattern positioned on the cytoplasm-free section of the cell wall in the TPEF image. Depending on the degree of plasmolysis, i.e., the length of the site available for cutting, the 2 × 20 dot pattern was scaled (adjusted: scale, angle, and position) for surgery to the size that would cut off as much of the wall as possible without critically approaching the plasma membrane. Based on the selected pattern length, cell wall thickness, and proximity to the protoplast, the cutting power was selected in the drawing mode of the software. We were able to control the parameters of surgery: dwell time per point, laser power and wavelength. The surgical procedure was automated, started "on click" and lasted approximately 20 s. Prior to the surgical experiments, tests were performed to determine the average laser power required to cut a small portion of the cell wall, and the damage threshold was determined. The damage threshold was approximately 3.5 mW (using a 40× 1.0 physiological objective). The overall distribution of laser powers at the sample plane used for nanosurgery is shown in the upper graph in Fig. 2; the lower power range was used in the majority of the operations. Laser powers of 6 to 12 mW were used in 90% of the cell wall operations. The dwell time of 1 s per point was maintained at the same value during the surgical procedure for all hyphae. Femtosecond pulses (160 fs) at a 76 MHz repetition rate and very low pulse energies (0.05-0.20 nJ) at the specimen plane ensured successful wall cutting with high spatial resolution of the surgical incisions.

Subsequently, subtle deplasmolysis was performed to stimulate the protoplast release without overstretching the membrane to interact with the pipette. To avoid hypoosmotic stress and maintain the integrity of the protoplast plasma membrane, the osmolarity of the solution in the microscopic chamber was reduced by only a few tens of mOsm such that slightly hyperosmotic conditions were present. The optimized concentration of sodium azide for inhibiting cell wall production was consistently present in all solutions, and its presence was an indispensable factor for success. Respiration and growth of *Phycomyces blakesleeanus* under the conditions used for nanosurgery are shown in Suppl. Fig. S1.

Because the nanosurgery (using an upright nonlinear microscope) and patch-clamp (using an inverted microscope) systems are separate, the physiological objective played a key role. Since a dip-in objective is normally used without a top coverslip, it was possible to approach the sample above and completely immerse the objective tip in the solution surrounding the sample. Consequently, there was no need for removal of the coverslip, which would otherwise lead to possible loss of the emerged protoplasts. On the other hand, the gridded coverslips on which the fungi were grown and placed at the bottom of the open microscopic chamber allowed the precise localization of the hyphae subjected to nanosurgery.

As expected, the size of the patch pipette influenced the success of giga-ohm sealing. For our purposes, the best pipettes for the fungal protoplast patch-clamp were between 10 MΩ and 15 MΩ. Smaller and larger pipettes were two times less likely to achieve good-quality contact. The protoplast size was also an important factor in the success of high membrane-pipette contact formation. When contact was successful, the released protoplasts were significantly ($p = 0.016$) larger (18 ± 6 μm) than those where contact (15 ± 5 μm) could not be achieved. Potentially, with further practice, the success rate of achieving contact with the gigaohmic seal could be significantly improved for these smaller released protoplasts. To estimate the success rate of patch-clamp contact on released protoplasts that were sufficiently large and accessible to the pipette, we divided the number of giga-ohm contacts obtained by the number of patch-pipette contacts attempted on "patchable" protoplasts. Overall, the success rate was 55%, with 23 successful contacts out of 42 pipette approaches. The entire process (cell surgery + patch clamping) was quite complex, and certain steps needed to be precisely followed for a high success rate and reproducibility. The concentration of chemicals, osmolarity of the solutions, timing and cutting parameters needed to also be kept within a specified narrow range.

Electron microscopic imaging of the surgical incision in the cell wall and released protoplast

To verify the appearance of the edges of the incisions in the plasmolyzed hyphal cell wall, we imaged the fungus subjected to nanosurgery using a scanning electron microscope (SEM).

As shown in Fig. 3, SEM images revealed crack-free precision cuts, with smooth edges of the slit in the hyphal cell wall made with the femtosecond laser ($n = 11$ incisions at 10 images). The released protoplast membrane had no large masses of remaining or deposited material ($n = 2$) (Fig. 3f). The surgical parameters used allowed localized removal of the cell wall with an average thickness of 30 nm (Fig. 3e), sometimes even at extremely short distances from the plasma membrane (0.5–3 μm), leaving the released protoplast viable. The mean length of the incisions measured from TPEF images was 6.7 ± 2.9 μm ($n = 185$), whereas mean length of the incisions measured from the SEM images was 9.3 ± 4.4 μm ($n = 6$). The width of the incisions measured from the SEM images was 2.2 ± 0.2 μm ($n = 3$).

Protoplast release parameters

After successful creation of the surgical incision in the cell wall, the release of protoplasts into the surrounding

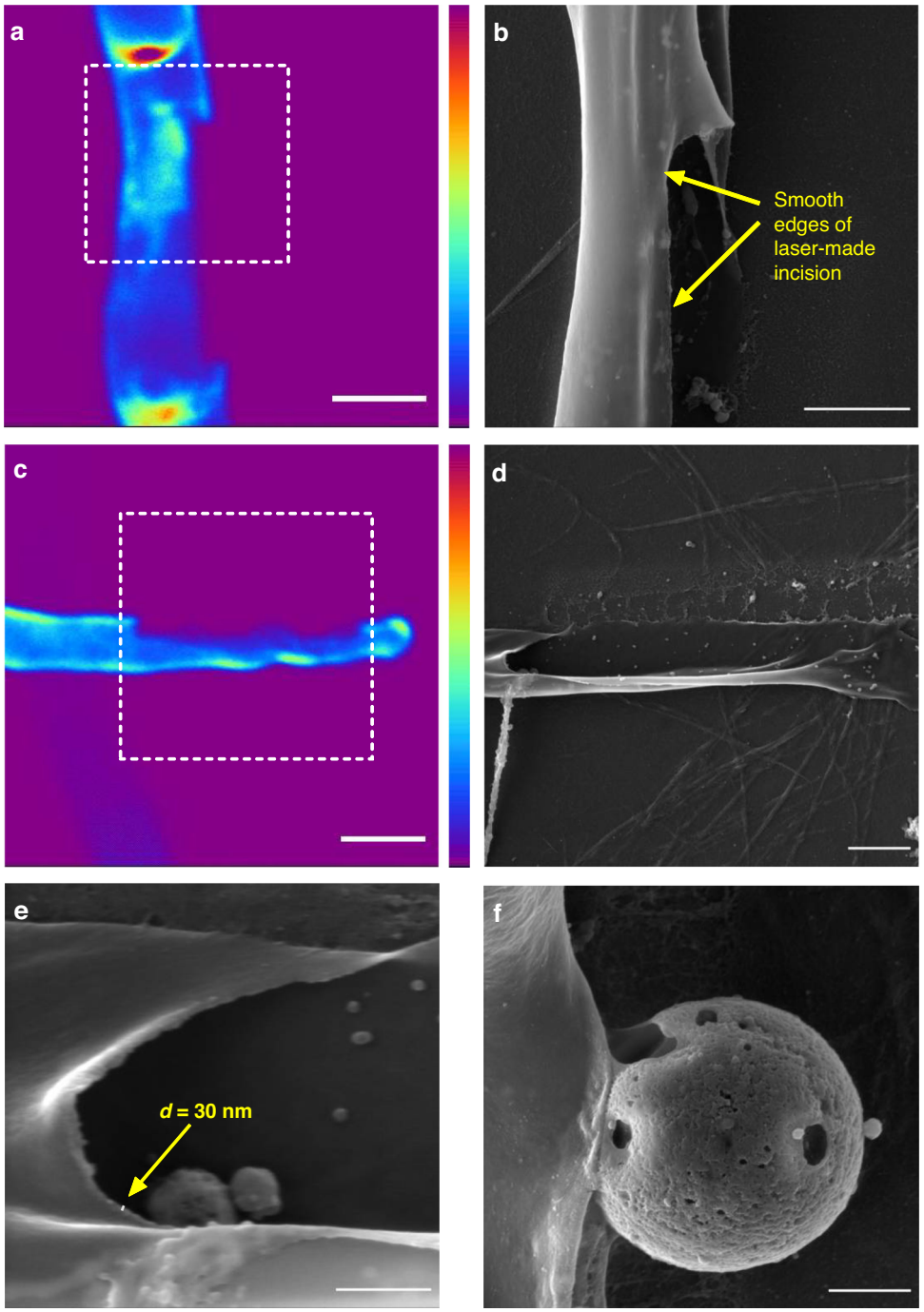

Fig. 3 SEM images of the *Phycomyces blakesleeanus* cell wall after the femtosecond laser nanosurgery. a TPEF image of the fs laser-generated incision in the hyphal cell wall. The average laser power in the sample plane was 1.0 mW for imaging (dwell time 2.5 µs) and 7.5 mW for surgery (dwell time 1 s). Scale bar: 5 µm. **b** SEM image of the same laser-generated incision shown in a. Scale bar: 2 µm. **c** TPEF image of the fs laser-made incision. The average laser power in the sample plane was 1.0 mW for imaging (dwell time 2.5 µs) and 7.6 mW for surgery (dwell time 1 s). Scale bar: 5 µm. All TPEF images were acquired with a Zeiss 40× 1.3 oil objective. The color intensity bars for the TPEF signal are as follows: violet/blue, lowest TPEF signal; and dark red, highest TPEF signal. The color intensity bar is linear and covers the entire range of the data. **d** SEM image of the entire laser-generated incision, same as that shown in c. Scale bar: 2 µm. **e** Hyphal cell wall thickness (*d*) of the incision shown in d. Scale bar: 0.5 µm. **f** Released protoplast through a laser incision made with 6.7 mW average power at 730 nm. Scale bar: 1 µm

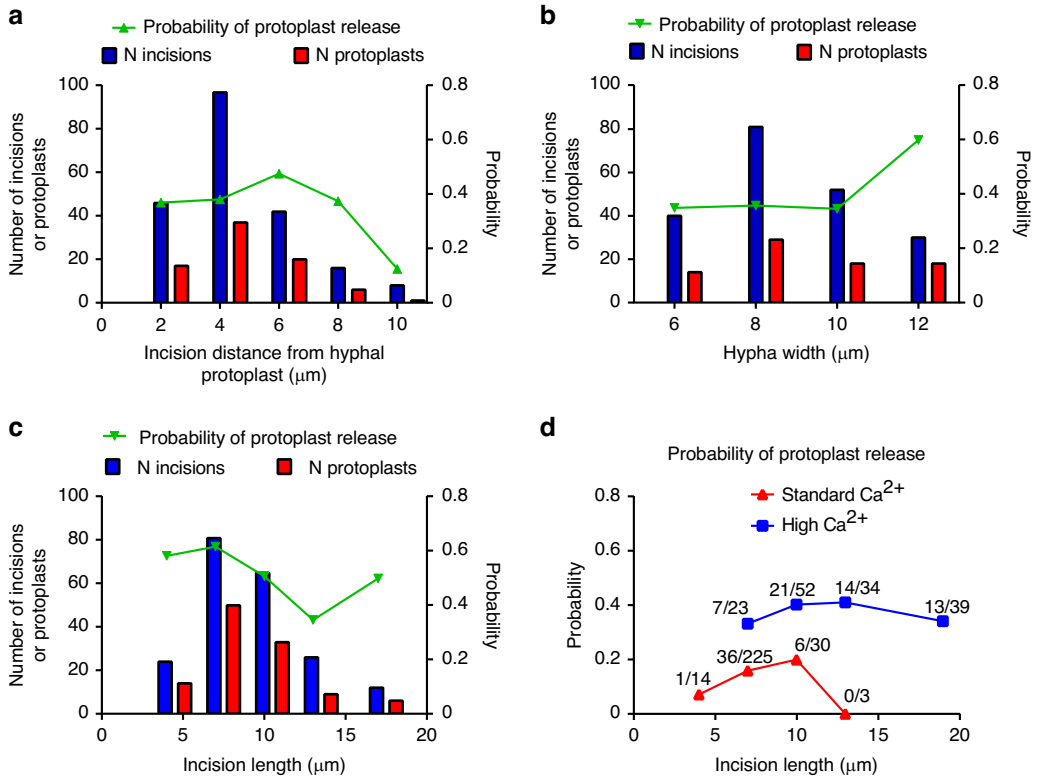

Fig. 4 Parameters affecting the probability of protoplast release. Probability of protoplast release from the nanosurgery-produced incision, superimposed on the corresponding histogram bin of parameter values. **a** Distance of the laser incision from the hyphal protoplast during nanosurgery: distribution and dependence of the probability of protoplast release. **b** Hyphal width at the site of nanosurgery: distribution and dependence of the probability of protoplast release. **c** Length of surgical incision: distribution and dependence of the probability of protoplast release. **d** In a separate series of experiments, the effect of increased calcium concentration on the probability of protoplast release was measured as a function of incision length in the nanosurgical phase of the procedure, without subsequent steps of deplasmolysis. High [Ca^{2+}]: 30 mM, as used in the surgical protocol. The hyperosmotic solution used was 600-617 mOsm throughout the protoplast release period. Standard [Ca^{2+}]: 3 mM and 1 mM (pooled data). The hyperosmotic solution used was 555-560 mOsm throughout the protoplast release time. For each 3 μm incision size bin in the histogram, the corresponding number of protoplasts obtained divided by the number of surgical sections performed is shown above the probability curve. In all graphs, the abscissa represents the upper limit of the bin. For **a**–**c**: n_{tot}(incisions) = 203 (**a**); 209 (**b**); 208 (**c**). n_{tot}(protoplast) = 71(**a**), 81(**b**), 112 (**c**). For **d**: n_{tot}(incisions) = 272 (Standard Ca^{2+}); 148 (High Ca^{2+}). n_{tot}(protoplast) = 43 (Standard Ca^{2+}); 55 (High Ca^{2+})

medium was observed. Not all incisions released protoplasts. We found that several factors influenced the probability of protoplast release (Pr = number of protoplasts/number of incisions). The distance of the laser cut from the protoplast in the hypha during the procedure influenced how many protoplasts could be recovered. As shown in Fig. 4a, when the protoplast in the hypha was more than 6 μm from the incision site, the probability of protoplast release decreased from approximately 0.4 and was lowest at the largest distances tested. This result further confirmed that the protoplasts were not damaged in our protocol, even when the site of nanosurgery was in close proximity to the retracted hyphal protoplast. The width of the hyphae (w_h), which reflected the overall size of the hyphae, did not appear to affect the possibility of obtaining released protoplasts for $w_h < 10$ μm. Wider hyphae ($w_h > 10$ μm) were more favorable for protoplast release with a Pr of 0.6, while for smaller hyphae, Pr was 0.35 (Fig. 4b). Finally, the size of the incision also affected the release probability, with smaller incisions releasing more protoplasts. As shown in Fig. 4c, the probability decreased with increasing incision length, from $Pr = 0.62$ at an incision length of 5.5 ± 1.5 μm to $Pr = 0.35$ at an incision length of 11.5 ± 1.5 μm. We are confident that all hyphae were viable after the nanosurgical procedures because they retained their characteristic cytoplasmic streaming and healthy appearance and were deplasmolyzed when transferred to less hyperosmotic conditions. Thus, the dependence of Pr on incision size was caused by the influence of underlying physiological or mechanical aspects controlling protoplast release. We also noted a slightly better protoplast yield in the plasmolyzed hyphae that exhibited a cytoplasmic bridge across the "empty" region near the incision site than in those whose hyphal

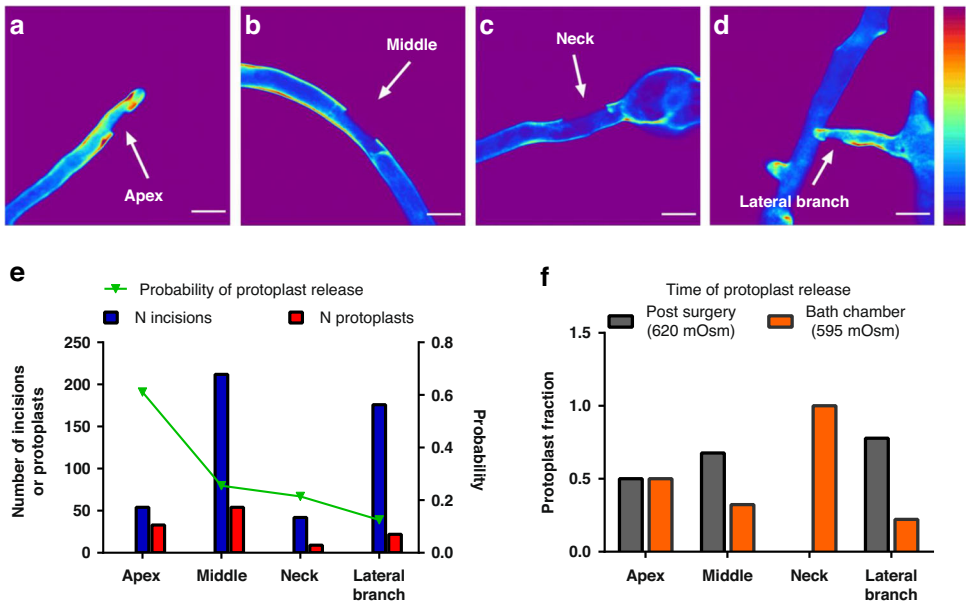

Fig. 5 Nanosurgery applied to different sites on the hyphae. TPEF images of the hyphae with a laser surgical incision at different locations: **a** apex, **b** middle, **c** "neck" and **d** lateral branch of the labeled hypha. The white arrows indicate a laser-made incision in the hyphal cell wall. All images were taken with a Zeiss 40× 1.3 oil objective. The color intensity bars for the TPEF signal are as follows: violet/blue, the lowest TPEF signal; and dark red, the highest TPEF signal. The color intensity bar is linear and covers the entire range of the data. Scale bar: 10 µm. **e** Probability of the protoplast release at each site (apex, middle, neck and lateral branch), with the corresponding number of incisions obtained. **f** Osmotic conditions during the protoplast release at the different sites are shown as fractions of the total number of protoplasts released at each site in each of the solutions used: "postsurgery"= 620 mOsm; "bath chamber" = 595 mOsm

protoplasts were completely separated (Pr = 0.44 and 0.36, respectively).

In a separate set of experiments on nanosurgery, we examined protoplast release immediately after nanosurgery, without a deplasmolysis step, under slightly different plasmolysis and surgical conditions, as explained in the Methods section. We investigated whether the high calcium concentration used throughout the procedure affected protoplast release (Fig. 4d). We compared protoplast release at a high Ca^{2+} concentration (30 mM) with protoplast release at a standard Ca^{2+} concentration (1 and 3 mM, merged). At standard Ca^{2+} concentrations, the probability of protoplast release was clearly dependent on the size of the incision and was quite low (< 0.2). Increasing [Ca^{2+}] to 30 mM increased the probability of obtaining the protoplast for the same incision size to 0.4. The calcium dependence of the probability of protoplast release indicated that a physiological mechanism was involved in the process of expelling protoplasts from the hyphal wall through a surgically made incision.

Laser nanosurgery of the cell wall at different sites along the hyphae

Since hyphae are polarized cells, selective sampling from different hyphal regions would be highly desirable. We exploited the precision and flexibility of the nanosurgical method to perform incisions and obtain protoplasts from the localized portions of the following hyphal regions ("compartments"): 1. The tip (apex), which represents the fast-growing portion of the hyphae (Fig. 5a); 2. The middle (Fig. 5b); 3. The "neck", which represents the base of the hyphae, just below the spore (Fig. 5c); And 4. The lateral branch (Fig. 5d). The average laser power used for the cuts in the different compartments did not vary, while the distance of the incision from the hyphal protoplast at the time of nanosurgery needed to be adjusted due to the narrower space in the side branch compartment; the distance of the incision from the hyphal protoplast was shorter in the lateral branch compartment than in the middle compartment: $p = 0.0220$; compared to the tip compartment: $p = 0.0003$. Figure 5e shows the number of incisions with their Pr values for each site. The Pr was highest in the apical region (0.6) but rather low in the lateral branches (0.13). Interestingly, the protoplasts were released from the different regions under different osmotic conditions (Fig. 5f). For example, protoplasts from the neck did not appear in the hyperosmotic solution used for surgery, with 100% of protoplasts obtained from the neck were released during deplasmolysis in the bath chamber; however, protoplasts from the hyphal tip were released equally well in both

hyperosmotic and deplasmolysis solutions. The success in achieving giga-ohm contact was highest for protoplasts from lateral branches (55%), while it was 25-30% for protoplasts from other regions.

Registered currents of protoplasts obtained by nanosurgery

The excised patch currents measured from protoplasts obtained by nanosurgery were predominantly anionic. Only in one case did the measured current have a reversal potential corresponding to calcium ions. Approximately one-third (35%) of the registered currents belonged to the group mediated by nonselective anionic channels that transport both chloride ions and organic acids ("anionic unselective"), whereas 44% of the currents were mediated by channels that are highly selective for chloride ("Cl^- selective") (Fig. 6a). Some of the currents recorded (17%) were mediated by channels highly permeable to glutamate ("organic acids permeable"). These currents had a reversal potential close to the calculated V_{rev} for glutamate. Figure 6b shows the total conductance range (g) for each group, along with typical excised patch current recordings. Most frequently, Cl^- selective currents had short openings and closings at depolarized potentials ($n = 7$) (Fig. 6b bottom trace), whereas glutamate-permeating currents alternated between two modes: (I) infrequent and relatively short openings and (II) several hundred ms long openings with sub-conductance levels interspersed with very short closed states ($n = 4$). Figure 6b middle trace shows the current that started in mode I and then abruptly transitioned to mode II. Nonselective currents exhibited a wide range of conductances and likely represent a heterogeneous group. Top trace in Fig. 6b shows the most frequently recorded current activity, bursts of current accompanied by very short needle-like openings ($n = 7$).

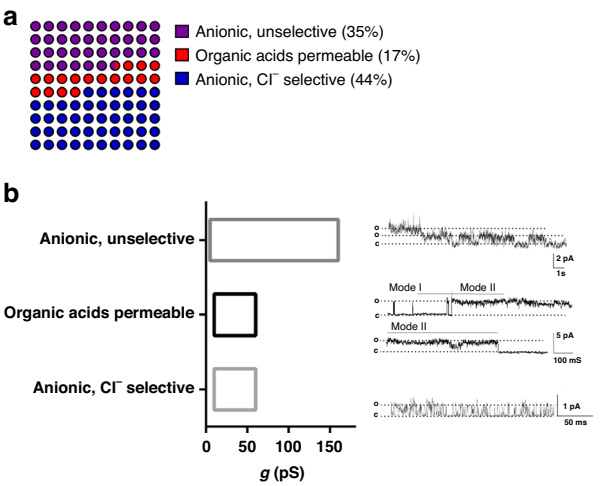

Fig. 6 Summary of the properties of the obtained currents. **a** Major types of currents present in the protoplast membrane categorized according to ion permeability. Ion permeability was determined from IV plots under asymmetric conditions, as shown in the bottom panel of Fig. 1g. **b** Conductance ranges determined for major protoplast types of ion currents, with representative current recordings shown on the right. Unselective anionic current recording, inside-out, $V_h = +80$ mV, bath solution with high glutamate content (solB), $g = 15$ pS; Organic acid-carried current, outside-out, $V_h = +30$ mV, bath solution with nitrate (solA), $g = 40$ pS, activity modes indicated above current recording. Cl^- -selective current, outside-out, $V_h = +80$ mV, solB, $g = 12$ pS. o: open channel current level; c: closed channel current level. The calibration bar for each recording is presented on the right side

Discussion

In this study, we described a highly reproducible laser-based technique for the nanodissection of the fungal cell walls to obtain released viable fungal protoplasts whose plasma membrane was suitable for patch-clamp electrophysiology. Similar approaches were reported long ago using ns-UV laser pulses but were not further developed[10,33]. Compared with ns lasers, fs lasers can target specific regions with high accuracy without damaging the out-of-focus region, resulting in better surgical outcomes. They can produce clean and precise incisions with minimal thermal or mechanical damage. The high precision of fs laser ablation enabled the cutting of a small piece of cell wall without endangering the plasma membrane of the protoplast; this cut was only a few micrometers away from the protoplast or even closer. Another advantage of fs IR lasers over ns UV lasers is the wavelength used. IR lasers have longer wavelengths than UV lasers; thus, they can penetrate deeper into tissues due to nonlinear two-photon absorption that occurs only in the focal volume[38]. UV lasers that emit shorter wavelengths have more energy, increasing the susceptibility to cellular DNA damage[50] and inducing oxidative stress and cell death[51]. Another advantage of this method is the use of the same fs IR nanosurgical laser for two-photon imaging of live hyphae to mark the desired cell wall area for surgery. Compared to previous studies in which bright-field images were used to mark and section the cell wall, in the present study, we used two-photon fluorescence of the cell wall from TPEF images. The ability to select a region on the TPEF images for cutting contributed greatly to the accuracy and precision of the overall cell surgery method[38]. We did not observe any vaporization, cavitation, or carbonization on the TPEF or BF images recorded after the surgical procedure. Imaging the specimen by either modality during the surgical action was not possible. Additionally, in the SEM images, we did not observe fragments of the removed cell wall. The processes that potentially occurred during surgery and the possible transformations of the ablated/ejected materials are described in detail in Vogel and Venugopalan 2003[52]. The nanosurgery method presented here could lead to

successful patch-clamp recording only if the conditions for each step were kept within the optimal range, as many factors influenced the biological aspects of the procedure.

Fungi exhibit a cell wall integrity response; this is a signaling pathway activated by cell wall stress or damage involving fungal-specific kinases[53] and is the basic survival mechanism. The cell wall integrity pathway is involved in the response to osmotic stress[54], fungal morphogenesis, and fungal pathogenicity. The respiratory inhibitor azide was used throughout the protocol because it is the only respiratory chain inhibitor capable of almost complete inhibition of classical respiration for prolonged periods (unlike cyanide[55]) without significant induction of alternative respiration (unlike antimycin[55]); its use resulted in a long-term reduction in total respiration to 20% while maintaining viability. Under conditions of this pronounced metabolic suppression, all intracellular signaling pathways that depended on kinase activity and therefore required ATP, including the cell wall integrity response, were assumed to be suppressed.

Prevention of new wall formation was one of the key elements in the procedure's success because when azide was omitted, the hyphal protoplasts remained in the hyphae. In rare cases, when a protoplast was released without an applied azide due to the vigorous hypoosmotic swelling immediately after producing the wall incision, the contact between the patch pipette and the protoplasts was not achieved. The high concentration of calcium used throughout the procedure could account for the complete absence of potassium permeating currents in our system. The fungal-specific tandem pore outwardly rectifying K^+ channels (TOKs) are found in the genome of filamentous fungi, and heterologous expression shows that they form functional K^+ channels that may be present in the plasma membrane of filamentous fungi[12,56]. The TOK channels are blocked by Ca^{2+} on the extracellular side of the membrane[12]. Therefore, the almost absolute dominance of anionic currents (96% of all recorded currents) could be a result of the experimental conditions. Furthermore, the hyperosmotic conditions during the procedure could influence the activation or properties of the registered ionic currents. Notably, the osmolarity of the extracellular solutions used during patch-clamp seal formation and electrophysiological recordings was approximately isosmotic (with respect to the cytoplasm) because the protoplasts were optimally "inflated"; otherwise, the membrane would not be suitable for sealing. Filamentous fungi are organisms adapted to a wide range of different environmental conditions, such as the osmolarity of the surrounding environment; therefore, the possible change in physiology caused by a shift in osmolarity is likely to be the biologically relevant physiological state[57].

Immediately after surgery, protoplast release was frequently observed, and the probability of protoplast release was higher when the wall incision was made in close proximity to the hyphal protoplast. Turgor pressure-induced release of protoplasts could not be ruled out as part of the explanation for this phenomenon since the pressure relative to the cell wall in intact hyphae is 500 kPa greater, providing turgor to the cell[58,59]. However, under hyperosmotic conditions, turgor pressure is lower[58], and an additional cellular process, likely mediated by the cytoskeleton, could be involved in the protoplast release, since an increased calcium concentration enhanced the protoplast release from the incision. The more successful formation of sealing contacts in the protoplasts released from side branches was potentially due to the favorable interaction with the young plasma membrane, as is often the case with enzymatically derived plant protoplasts[24]. Notably, the close proximity of protoplasts to the laser incisions during nanosurgery had no detrimental effect on the health of the plasma membrane; this was reflected by the ability of the protoplasts to make high-resistance contact with the patch pipette, further demonstrating that the protocol presented in this study could produce consistently healthy released protoplasts from versatile locations. Our finding that numerous anionic conductances are present on the plasma membrane of filamentous fungi is consistent with the data from a limited number of available cloned ion channels[13,15] revealing the presence of CLC-like and Bestrophin-like channels. Additionally, unidentified ion channels could be present on these membranes. The prospects for further applications of the presented method include the discovery and identification of ion currents in the native protoplast membrane that have remained undetected to date because of the low homology of the underlying channels with animal or plant counterparts. These advances would further the understanding of the physiology of filamentous fungi.

Phycomyces blakesleeanus, the filamentous fungal model system used in this work, is a member of the order Mucorales (representative of the phylum Mucoromycota); members of this order form mycorrhizal symbiotic relationships with plants[60], while other members are serious human pathogens[61] whose prevalence is increasing[62,63]. The recently published WHO recommendation[64] identifies Mucorales as a high-priority group for monitoring, researching, and developing new drug targets. Therefore, the discovery and characterization of the membrane currents of *Phycomyces blakesleeanus* involved in the physiological responses of hyphae could lead to the identification of much-needed novel drug targets to combat human pathogens[65], as well as to better protect or exploit the mycorrhyzal symbiosis with plants in ecosystems and agriculture[66]. Further modifications of the described method may be required in the future to expand its application to other filamentous fungal phyla. The

potential applications of this technique span the entire range of fungal biology applications.

Materials and methods

Culture and growth conditions

A wild-type strain of the filamentous fungus *Phycomyces blakesleeanus* (Burgeff) [NRRL 1555(-)] was used in this study. The spores were seeded at a concentration of 10^6 spores/mL in standard liquid minimal medium (SLM)[67] at pH 4–5 containing the following per liter: 2 g L-asparagine·H_2O, 5 g KH_2PO_4, 500 mg $MgSO_4·7H_2O$, and microelements (28 mg $CaCl_2$, 1 mg thiamine hydrochloride, 2 mg citric acid·H_2O, 1.8 mg $Fe(NO_3)_3·9H_2O$, 1 mg $ZnSO_4·7H_2O$, 300 µg $MnSO_4·H_2O$, 50 µg $CuSO_4·5H_2O$, and 50 µg $Na_2MoO_4·2H_2O$), with half the glucose concentration (10 g D (+)-glucose) (1/2glucSLM) to reduce the osmolarity of the growth medium. The osmolarity was additionally decreased by diluting the medium by 10% from 210 to 140 mOsm to adapt the fungus to lower osmolarity conditions and ensure faster plasmolysis during the preparatory phase of nanosurgery. Fungi were grown in illuminated stationary open 100 mm Petri dishes at 21-22 °C.

Sample preparation

For cell nanosurgery experiments, the fungi were grown on glass coverslips ($d = 15$ mm) coated with a thin layer of 50% type I collagen as an immobilizer and placed on the bottom of 6-well plates. The collagen was previously polymerized at room temperature for 24 hours. The collagen-coated coverslips were inoculated with 15 µL of spore suspension from a Petri dish culture with an additional 50 µL of diluted 1/2glucSLM medium (to prevent the sample from drying out); the sample was allowed to stand for 1 hour to allow the spores to adhere/anchor to the collagen. After 1 hour, 2 mL of diluted 1/2glucSLM medium was added to the wells. This method proved to be the best in terms of hyphal adherence and growth. The experiment was always performed with fungi from the exponential growth phase (19-30 hours old). Most of the fungal hyphae were simple, elongated cells with a "spore "head" still visible, although some hyphae had just begun to form side branches.

Previously, we performed hyphal adhesion experiments on the following substrate-coating materials and coverslip surface modifications: gelatin, silicone, laminin, poly-L-lysine, concanavalin A, collagen type I, and plasma treatment (Supplementary Table S1). The hyphae adhered to and grew best on collagen type I. The optimal collagen thickness was then determined and found to be 10 µL of working collagen solution on a 15 mm diameter coverslip. Half-millimeter numbers were engraved on the coverslips (with a diamond scribe pencil) before the collagen treatment. Mapping of the culture coverslips was necessary to accurately determine the positions of the fungal hyphae before and after surgery because the surgery itself and the electrophysiology were performed on two separate microscopes.

Before the experiments, a coverslip containing the immobilized hyphae was placed on the bottom of the microscopic chamber and filled with the appropriate amount of hyperosmotic solution.

Staining of the cell wall

Live hyphae from the exponential growth phase (19-30 h) were incubated with 1% Calcofluor White (CFW; Sigma Aldrich) dye in isosmotic solution (495 mOsm) for 10 min at 20 °C. Then, 10 µM brefeldin A was added to the isosmotic dye solution. After incubation, the hyphae were washed three times in minimal media.

Preparation of solutions

The isosmotic solution for the CFW step contained (in mM) 60 KCl, 65 K-glutamate, 2 $MgCl_2$, 1 $CaCl_2$, and 10 HEPES (pH 7) supplemented with sucrose to produce 495 mOsm.

The hyperosmotic extracellular solutions (hyperECSs) used for plasmolysis and during nanosurgery contained the following (in mM): 60 KCl, 65 K-glutamate, 2 $MgCl_2$, 30 $CaCl_2$, and 10 HEPES at pH 7 supplemented with sorbitol to achieve the desired osmolarity (620 mOsm). In some experiments, slightly more hyperosmotic conditions were used (hyperECS: 680 mOsm, bath solution: 640 mOsm). Of the 13 attempts at the pipette approach, only 2 were successful using these conditions.

In a subset of experiments, the solution was modified to match the ion content of the patch-clamp bath solution and to investigate the ion basis of the recorded currents. For experiments with nitrate-based solution, hyperECS was modified by replacing $CaCl_2$ with $Ca(NO_3)_2$. For experiments with glutamate-based solutions, the ratio of KCl to K-glutamate in hyperECS was changed to 1:4 or 1:0, while the sum of the concentration remained at 125 mM.

For the experiment on the effect of Ca^{2+} on protoplast release, solutions with the following composition were used (in mM): standard [Ca^{2+}] solution (1 mM and 3 mM; data were pooled) - 60 KCl, 65 K-glutamate, 2 $MgCl_2$, 10 HEPES, 1 or 3 $CaCl_2$, pH 7, supplemented with sorbitol to 555-560 mOsm.

The high [Ca^{2+}] solution had the same ionic composition as the standard Ca^{2+} solution; the only differences were $CaCl_2$ (30 mM) with an osmolarity of 600-617 mOsm.

Patch-clamp recording solutions

The osmolarity of the chamber bath solution was 595 ± 10 mOsm; this solution was 25 mOsm hyperosmotic

than the pipette solution (570 mOsm). During the deplasmolysis step with a solution change, appropriate solutions were used to alter the ion composition of the final solutions to the following: nitrate solution (SolA) (in mM): 82.75 Cl^-, 125 K^+, 48.75 glutamate, 23.75 Ca^{2+}, 45 NO_3^-, 2 Mg^{2+}, 10 HEPES; and high-glutamate solution (SolB) (in mM): 70.25 Cl^-, 125 K^+, 106.25 glutamate, 23.75 Ca^{2+}, 2 Mg^{2+}, and 10 HEPES. The patch pipette solutions contained the following (in mM): solution combined with SolA: 125 KCl, 5 $CaCl_2$, 2 $MgCl_2$, and 10 HEPES; low chloride solution: 50 KCl, 5 K-glutamate, 1 $CaCl_2$, 2 $MgCl_2$, and 10 HEPES. The following patch pipette solution was used in combination with SolB: 125 KCl, 5 K-glutamate 1 $CaCl_2$, 2 $MgCl_2$, and 10 HEPES. All solutions were sterile-filtered at pH 7.

Hyphal plasmolysis and deplasmolysis

Plasmolysis was performed in two steps. In the pre-plasmolysis step (10 min incubation), hyphae were transferred from hypoosmotic growth medium to an isosmotic solution (495 mOsm) containing the cell wall dye. This step prior to plasmolysis served to facilitate the transition of the hyphae into the hyperosmotic solution used during imaging and nanosurgery. The hyperosmotic solution (HoS) (620 mOsm, except for one subset in which 680 mOsm was used) contained a high concentration of calcium (30 mM) in the form of $CaCl_2$ or $Ca(NO_3)_2$. A high Ca^{2+} content enabled faster plasmolysis and stabilization of the membrane by increasing the ionic strength of the hyperosmotic solution.

The onset of plasmolysis was considered the time at which hyphal protoplast withdrawal was observed at two or more sites along the hyphae in at least 25-30% of the hyphae in the field of view. Retraction from the tip was not used as a criterion for measuring plasmolysis time. After the nanosurgical procedure, the gentle deplasmolysis step was performed. We carefully removed ¼ of the hyperosmotic solution and slowly added 520 mOsm solution in the same volume, which decreased the osmolarity of the solution in the microscopic chamber to 595 ± 10 mOsm. A difference of 25 ± 10 mOsm between hyperECS and the bath solution allowed protoplasts to exit in some cases. However, in the majority (64%) of the experiments, protoplasts exited the hyphal wall through the laser-generated incision while still in the hyperosmotic solution.

Fungi were treated with an exocytosis inhibitor (10 µM brefeldin A) added before the plasmolysis step and a respiration inhibitor (2 mM sodium azide) to prevent cell wall regeneration during the procedure. Sodium azide was continuously present in all solutions (except during CFW staining). The addition of enzymes (chitinases and chitosanase cocktail) that would breakdown cell wall residues, which we hypothesized might be present at the cut site, was tested; however, these enzymes were found to have no effect and were not used under the optimized conditions.

Measurement of the biomass yield and oxygen consumption

To measure the biomass yield, *P. blakesleeanus* mycelia were grown in Petri dishes for 16 hours in 500 (control), 760 and 860 mOsm solutions. The biomass was measured after 30 and 90 minutes for both the control and treatment groups. The yield gain was determined for each culture as the biomass at each time point reduced by the average biomass of the control at the beginning of growth. The growth inhibition percentage was calculated as follows: (yield gain/average of control) *100. Oxygen consumption by *P. blakesleeanus* mycelia was measured using a Clark-type oxygen electrode (Qubit Systems). The mycelial suspension was diluted in fresh liquid minimal medium to an appropriate concentration (oxygen consumption between 15-25 µmol/L × min) and aerated for 1 minute before measurement. Two milliliters of the suspension ($n = 3$) was transferred to a 4 mL electrode chamber and maintained at a constant temperature of 25 °C. The long-term effect of incubation in 5 mM NaN_3 was measured using a 28-hour-old culture.

Graphs can be found in the Supplemental material (Fig. S1).

Measurement of the effect of calcium on the protoplast release

The effect of Ca^{2+} on the probability of protoplast release from nanosurgical incisions was measured using images taken immediately after the incisions were made. An oil immersion objective was used for this series of experiments. Nanosurgery and imaging were performed in standard Ca^{2+} or high Ca^{2+} solutions without subsequent patch-clamp recording.

NLSM experimental setup for TPEF imaging and nanosurgery

Laser nanosurgery and TPEF imaging of live hyphae were performed via a custom-built nonlinear laser-scanning microscope (Fig. 7) based on the Jenaval upright microscope frame. Previously described in references[47] and[68]. A femtosecond tunable (700–1000 nm) mode-locked Ti:Sa laser (Mira 900, Coherent, Inc., CA, USA), which generates 160 fs, 30 nJ pulses at a 76 MHz repetition rate, was used. Power control for nanosurgery and imaging was achieved using a motorized variable neutral density filter (VNDF) and fast mechanical shutter (Sh) for blocking or transmitting the laser beam. After passing through the VNDF and shutter, the laser beam was raster scanned over the sample using two galvanometer mirrors (Cambridge Technologies, 6215H; Bedford, Massachusetts, USA). A high numerical aperture

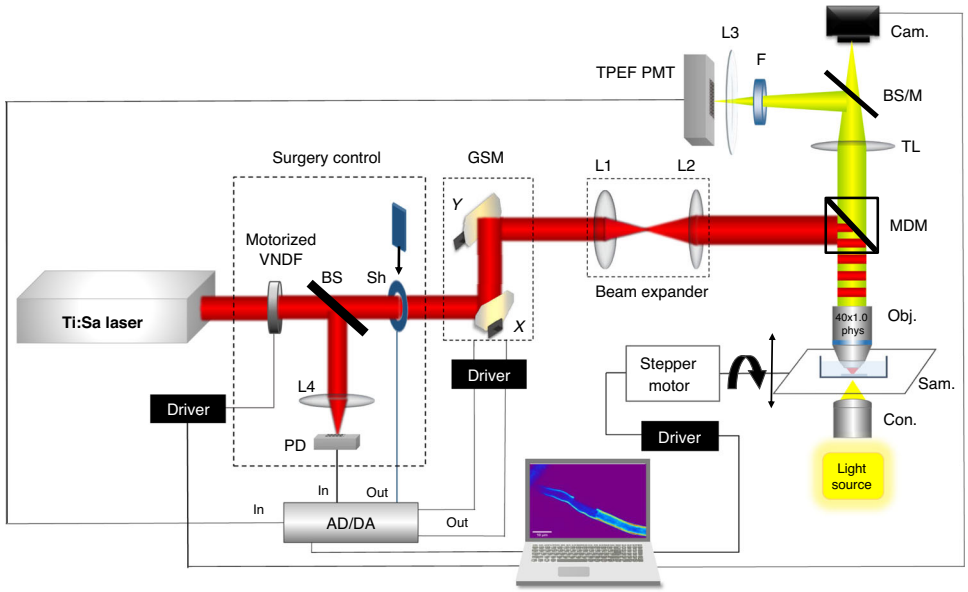

Fig. 7 Schematic drawing of the NLSM setup for nanosurgery and cell wall imaging. Ti:Sa fs laser for cell surgery and TPEF imaging, VNDF motorized variable neutral density filter, Sh shutter, GSM galvanometer-scanning mirrors, L1 and L2 - beam expander, MDM main dichroic mirror (cutoff 700 nm), Obj. microscopic objective 40 × 1.0 physiological, Sam. sample, Con. aspheric condenser lens, TL tube lens, BS/M beam splitter or mirror toggle, Cam. camera, F VIS filter 400–700 nm for CFW fluorescence, L3, L4 focusing lens, TPEF PMT photomultiplier tube for TPEF signal, PD photodiode, AD/DA acquisition card

(NA) physiological (dip-in) objective lens (Carl Zeiss W Plan-Apochromat 40X, NA = 1.0) was used for tight focusing of the laser beam into the sample. On some occasions, to obtain higher-quality images, we used an oil-immersion high-NA objective lens (Carl Zeiss, EC Plan-Neofluar 40X, NA = 1.3). In this case, the hyphal culture was placed under an additional coverslip on top to enable the use of an oil immersion objective. The physiological objective worked in the same microscopic chamber during laser surgery and patch-clamp procedures on two separate systems. The patch-clamp recordings were performed on a separate system with an inverted microscope that allows the measuring pipette to access the sample from above. A physiological objective lens was used for imaging and surgery on a nonlinear system to perform both procedures of surgery and patch-clamp on the exact same hypha in the same chamber. This process ensured faster transfer from the nonlinear system to the patch system and prevented sample perturbation and possible loss of the obtained protoplast when the upper coverslip was removed. To determine the position for surgery on the hyphal chitin cell wall, it was necessary to visualize the cell wall and ensure that there was sufficient absorption of the laser beam at the wavelength intended for surgery. The intrinsic autofluorescence of chitin enabled imaging of the cell wall. Nevertheless, the hyphae were stained to increase the absorption of the laser beam and consequently reduce the value of the laser power required for sample imaging and nanosurgery. TPEF was used to scan hyphal cell walls stained with CFW dye using the same wavelength as that used for the surgery (730 nm). The fluorescent signal was collected using back reflection by an objective lens, filtered through a visible (400–700 nm) bandpass filter and detected via a photomultiplier tube (PMT) (RCA, PF1006). The steering of the galvo mirrors, the TPEF signal acquisition and shutter were controlled by a USB-6351 National Instrument card at a sampling rate of 1.2 MHz. The power regulation and stage axial position were controlled by a microcontroller. The sample (a coverslip with immobilized hyphae at the bottom of the open microscopic chamber) was placed on the motorized translation stage. The motorized stage was powered by a stepper motor that could translate the sample along the z-axis with 0.3 µm resolution. This approach was essential for accurately targeting the middle of longitudinal sections of the cell wall.

A custom-made add-on to the imaging software was used for the surgical procedure. This approach enabled arbitrary pattern inscription onto the TPEF image, where the dwell time and the average power of the laser beam could be controlled. The surgical procedure was as follows: first, the TPEF image of the hyphae was recorded; second, the pattern (usually the BMP image) was imported and superimposed onto the TPEF image; and third, the scale, exact position and rotation angle were adjusted. Afterward, the average laser power and the dwell time

were defined. The shutter was opened at the beginning and closed at the end of the surgical procedure, and then the laser power and the software were automatically set back to the imaging mode. During surgery, the laser beam was moved from point to point for a time (<μs) much shorter than the dwell time (order of 1 s).

Bright-field images were taken by a Canon EOS 50D digital camera (Tokyo, Japan) whose CMOS sensor was placed at the image plane of the tube lens. The BS/M Toggle switch enabled the utilization of either a camera for bright-field or TPEF PMT for fluorescence imaging.

Scanning electron microscopy (SEM)

The characterization of the laser made incision and the released protoplast was performed using a high-resolution field emission gun scanning electron microscope (FEG-SEM-Mira3, TESCAN). The samples were prepared for SEM according to the standard protocol with paraformaldehyde fixation followed by drying in a critical point drying chamber (K850, Quorum Technologies, Laughton, UK) as previously described in ref. [69]. The samples were sputter-coated with 10 nm of gold/palladium using a Quorum sputter coater to make them conductive for SEM analysis.

Patch-clamp setup and method

The microscopic chamber was mounted on an inverted microscope (Zeiss Axiovert 10, Germany) with a Luis & Newman micromanipulator system. Currents were measured with an EPC8 amplifier (HEKA), digitized at 10 kHz using an Instrutec 1600 interface (HEKA); the currents were low-pass filtered at 3 kHz, recorded, and processed with Pulse software (HEKA). The pipettes used for on-cell and inside-out patch recordings had a resistance of 10-20 MΩ, while those used for whole-cell and out-out recordings were in the range of 5–10 MΩ. The pipettes were pulled from thick-walled borosilicate glass with filament on a Flaming-Brown P97 pipette puller (Sutter Instruments) and polished with a microforge (L/MCPZ 101, List Medical-Elektronic).

The contact resistance between the pipette and the membrane was monitored by continuous testing with square-wave voltage pulses. Prior to immersion in the bath, the pipette was pressurized to approximately 60 mbar to ensure that any debris between the pipette and the membrane was washed away prior to contact. After contact with the membrane, which resulted in an increase in the resistance of several MΩ, the release of positive pressure was often not sufficient for a tight seal, and a slight negative pressure was also applied to pull the membrane into the pipette; this was then released again to prevent the protoplast from being completely sucked into the pipette. Seal formation typically took a few seconds to half a minute. Giga-seal contact was reached when the contact resistance reached or exceeded 1 GΩ. Recording "on cell" was rarely used because it did not provide satisfactory voltage control. The excision of the membrane patch was achieved by moving the pipette rapidly away from the protoplast in the horizontal direction. The membrane current activity in the inside-out or outside-out configuration was recorded in the gap-free mode of the voltage clamp with the range of holding voltages (V_h) to measure the amplitude of the active channels and to generate IV plots. Alternatively, the standard voltage clamp protocol was applied when entering the whole-cell configuration: V_h of −50 mV, followed by a series of steps in 20 mV increments, from −110 mV to +110 mV. The duration of each step sequence was 500 ms, with a rest period of 0.5–1 s. Series resistances were not compensated. All experiments were performed at 20 °C.

Data analysis and statistics

Image analysis

Bright-field image analysis of the extruded protoplasts and cell wall incision lengths was performed using ImageJ (W. Rasband, National Institute of Health, Maryland, USA; http://imagej.nih.gov/ij/).

Current analysis

The current data analysis was performed using the Pulse and Clampfit software packages (Molecular Devices, USA). The reversal potentials (V_{rev}) for each ion were calculated using the calculator available at https://www.physiologyweb.com/calculators/nernst_potential_calculator.html. The conductance g (pS) was extracted as the slope of the current-voltage dependence for each detectable single-channel current recorded at three or more different V_h. The current V_{rev} was extrapolated from the linear IV plot. In rare cases where the current was rectified (nonlinear IV relationship), the nonrectified portion of the IV plot was used for extrapolation. Care was taken to design the solutions such that the V_{rev} for each of the ions was sufficiently separated from the others to allow rough typing of the currents based on the ion with the largest contribution to the V_{rev} (defined as the ion whose V_{rev} was close to the V_{rev} of the recorded single-channel current).

Statistics

Graphing and statistical comparisons were made using Graph Pad Prism software. Boxes of the box and whisker plots are enclosed by the 25th and 75th percentile ranges, respectively, with the line representing the median; whiskers extend to the minimum and maximum values, respectively. Histograms of the incision length and distance of the hyphal protoplasts from the incision were generated from all values in each group with 3 μm binning and plotted with the upper bin boundary on the x-axis.

One-way ANOVA with multiple comparisons and Holm-Sidac correction and the unpaired two-tailed *t*-test with Welch's correction for unequal variances were used to calculate statistical significance. The confidence intervals for statistical significance were 0.05 (*), 0.01 (**), 0.005 (***), and 0.0001 (****). The release probabilities were calculated from all available data. Throughout the manuscript, the data are presented as the mean ± SD.

Acknowledgements
This work was supported by the Ministry of Science, Technological Development and Innovations, Republic of Serbia [contract numbers: 451-03-47/2023-01/200178 and 451-03-47/2023-01/200007]; the Project Advanced Biophysical Methods for Soil Targeted Fungi-Based Biocontrol Agents - BioPhysFUN [Grant number 4545] from the Program DEVELOPMENT – Green program of cooperation between science and industry, Science Fund of the Republic of Serbia; the Project HEMMAGINERO [Grant number 6066079] from the Program PROMIS, Science Fund of the Republic of Serbia; and the Institute of Physics Belgrade through grants from the Ministry of Science, Technological Development and Innovations of the Republic of Serbia. We would like to thank Vladimir Lazović for his valuable technical help with some TPEF imaging and nanosurgery experiments with unlabeled hyphae. Additionally, we would like to thank Milan Minić for indispensable technical help and support.

Author details
[1]Institute of Physiology and Biochemistry "Ivan Djaja", Faculty of Biology, University of Belgrade, Studentski trg 16, 11158 Belgrade, Serbia. [2]Institute for Biological Research "Siniša Stanković", University of Belgrade, National Institute of the Republic of Serbia, Bulevar Despota Stefana 142, 11000 Belgrade, Serbia. [3]Institute of Physics Belgrade, University of Belgrade, National Institute of the Republic of Serbia, Pregrevica 118, 11080 Belgrade, Serbia. [4]University of Belgrade, Faculty of Agriculture, Nemanjina Street 6, 11080 Belgrade, Serbia. [5]Institute for Multidisciplinary Research, University of Belgrade, Kneza Višeslava 1, 11030 Belgrade, Serbia

Author contributions
M.Ž., N.V.T., B.J. and D.P. conceptualized the initial study plan. M.Ž, N.V.T., A.J.K., M.D.R., T.P. and K.S. designed the final study concept. T.P. conducted all laser nanosurgeries, performed the TPEF imaging, maintained the fungal culture and prepared the samples. K.S. conducted all patch-clamp experiments. T.P. and K.S. conducted the plasmolysis/deplasmolysis experiments. N.V.T. and K.S. designed the patch-clamp protocols. N.V.T. supervised the patch-clamp and plasmolysis/deplasmolysis experiments and performed the data analysis. The solution design for patch-clamp was performed by K.S. and N.V.T., and the design of the hyperosmotic solutions for plasmolysis by T.P. and M.Ž. A.J.K. and M.D.R. designed and developed the NLSM set up and supervised the nanosurgery and imaging experiments and TPEF image processing/analysis. M.D.R., A.J.K. and T.P. designed the laser nanosurgery protocols. M.Ž. supervised the biological part of the research. M.S. performed the oxygen consumption measurements and analysis. T.P. and M.S. performed the biomass yield measurements. S.S-Š. performed the SEM imaging. S.M.L. conducted the sample drying procedure in the critical point dryer. T.P., K.S. and N.V.T. prepared the samples for critical point drying and SEM analysis. D.P. wrote the software for TPEF imaging and nanosurgery. T.P. performed the TPEF and BF image analysis. N.V.T. performed the current analysis and statistics. T.P., N.V.T., M.D.R., A.J.K., and M.Ž. prepared the manuscript. All authors participated in the manuscript revision and approved the submitted version.

Data availability
All data needed to evaluate the conclusions in the paper are presented in the paper and/or the Supplementary Materials. Additional data related to this paper may be requested from the corresponding authors.

Conflict of interest
The authors declare no competing interests.

Supplementary information The online version contains supplementary material available at https://doi.org/10.1038/s41378-024-00664-x.

Received: 20 September 2023 Revised: 1 December 2023
Accepted: 19 December 2023
Published online: 07 April 2024

References

1. Genre, A., Lanfranco, L., Perotto, S. & Bonfante, P. Unique and common traits in mycorrhizal symbioses. *Nat Rev Microbiol* **18**, 649–660 (2020).
2. Van Der Heijden, M. G. A. et al. Mycorrhizal fungal diversity determines plant biodiversity, ecosystem variability and productivity. *Nature* **396**, 69–72 (1998).
3. Fisher, M. C. et al. Emerging fungal threats to animal, plant and ecosystem health. *Nature* **484**, 186–194 (2012).
4. Gow, N. A. R. et al. The importance of antimicrobial resistance in medical mycology. *Nat Commun* **13**, 5352 (2022).
5. Prole, D. L. & Taylor, C. W. Identification and analysis of cation channel homologues in human pathogenic fungi. *PLoS One* **7**, 42404 (2012).
6. Liu, M., Du, P., Heinrich, G., Cox, G. M. & Gelli, A. Cch1 mediates calcium entry in Cryptococcus neoformans and is essential in low-calcium environments. *Eukaryot Cell* **5**, 1788–1796 (2006).
7. Zhang, X. et al. Heat stress modulates mycelium growth, heat shock protein expression, ganoderic acid biosynthesis, and hyphal branching of ganoderma lucidum via cytosolic Ca2+. *Appl Environ Microbiol* **82**, 4112–4125 (2016).
8. Lew, R. R. & Nasserifar, S. Transient responses during hyperosmotic shock in the filamentous fungus Neurospora crassa. *Microbiology* **155**, 903–911 (2009).
9. Zhou, X. L., Stumpf, M. A., Hoch, H. C. & Kung, C. A Mechanosensitive Channel in Whole Cells and in Membrane Patches of the Fungus Uromyces. *Science* **253**, 1415–1417 (1991).
10. Roberts, S. K., Dixon, G. K., Dunbar, S. J. & Sanders, D. Laser ablation of the cell wall and localized patch clamping of the plasma membrane in the filamentous fungus Aspergillus: Characterization of an anion-selective efflux channel. *N Phytol* **137**, 579–585 (1997).
11. Silverman-Gavrila, L. B. & Lew, R. R. An IP3-activated Ca2+ channel regulates fungal tip growth. *J Cell Sci* **115**, 5013–5025 (2002).
12. Roberts, S. K. TOK homologue in Neurospora crassa: First cloning and functional characterization of an ion channel in a filamentous fungus. *Eukaryot. Cell* **2**, 181–190 (2003).
13. Oddon, D. M., Diatloff, E. & Roberts, S. K. A CLC chloride channel plays an essential role in copper homeostasis in Aspergillus nidulans at increased extracellular copper concentrations. *Biochim. Biophys. Acta - Biomembr.* **1768**, 2466–2477 (2007).
14. Živić, M., Popović, M., Todorović, N. & Vučinić, Ž. Outwardly rectifying anionic channel from the plasma membrane of the Fungus Phycomyces blakesleeanus. *Eukaryot. Cell* **8**, 1439 (2009).
15. Roberts, S. K., Milnes, J. & Caddick, M. Characterisation of AnBEST1, a functional anion channel in the plasma membrane of the filamentous fungus, Aspergillus nidulans. *Fungal Genet Biol* **48**, 928–938 (2011).
16. Malvezzi, M., Chalat, M., Janjusevic, R. et al. Ca^{2+}-dependent phospholipid scrambling by a reconstituted TMEM16 ion channel. *Nat Commun* **4**, 2367 (2013).
17. Križak, S. et al. Osmotic swelling activates a novel anionic current with VRAC-like properties in a cytoplasmic droplet membrane from Phycomyces blakesleeanus sporangiophores. *Res Microbiol* **166**, 162–173 (2015).
18. Zhao, C. & Tombola, F. Voltage-gated proton channels from fungi highlight role of peripheral regions in channel activation. *Commun Biol* **4**, 261 (2021).
19. Dionysopoulou, M., Yan, N., Wang, B., Pliotas, C. & Diallinas, G. Genetic and cellular characterization of MscS-like putative channels in the filamentous fungus Aspergillus nidulans. *Channels* **16**, 148–158 (2022).
20. Sperelakis, N. *Cell Physiology Source Book: Essentials of Membrane Biophysics*. (Elsevier, 2011). https://doi.org/10.1016/C2010-0-66479-0
21. Henriksen, G. H. & Assmann, S. M. Laser-assisted patch clamping: A methodology. *Pflug Arch Eur J Physiol* **433**, 832–841 (1997).
22. Shakoor, A., Gao, W., Zhao, L., Jiang, Z. & Sun, D. Advanced tools and methods for single-cell surgery. *Microsyst Nanoeng* **8**, 1–21 (2022).
23. Sun, S., Furtula, V. & Nothnagel, E. A. Mechanical release and lectin labeling of maize root protoplasts. *Protoplasma* **169**, (Springer-Verlag, 1992).

24. Elzenga, J. T. M., Keller, C. P. & Van Volkenburgh, E. Patch clamping protoplasts from vascular plants method for the quick isolation of protoplasts having a high success rate of gigaseal formation. *Plant Physiol* **97**, 1573–1575 (1991).
25. Fairley, K., Laver, D. & Walker, N. A. Whole-cell and single-channel currents across the plasmalemma of corn shoot suspension cells. *J Membr Biol* **121**, 11–22 (1991).
26. Levina, N. N., Lew, R. R., Hyde, G. J. & Heath, I. B. The roles of Ca2+ and plasma membrane ion channels in hyphal tip growth of Neurospora crassa. *J Cell Sci* **108**, 3405–3417 (1995).
27. Garrill, A., Jackson, S. L., Lew, R. R. & Heath, I. B. Ion channel activity and tip growth: tip-localized stretch-activated channels generate an essential Ca2+ gradient in the oomycete Saprolegnia ferax. *Eur J Cell Biol* **60**, 358–365 (1993).
28. Ronchi, P., Terjung, S. & Pepperkok, R. At the cutting edge: Applications and perspectives of laser nanosurgery in cell biology. *Biol Chem* **393**, 235–248 (2012).
29. Taylor, A. R. & Brownlee, C. Localized patch clamping of plasma membrane of a polarized plant cell: Laser Microsurgery of the Fucus spiralis rhizoid cell wall. *Plant Physiol* **99**, 1686–1688 (1992).
30. De Boer, A. H. et al. Laser microsurgery: a versatile tool in plant (electro) physiology. *Protoplasma* **178**, 1–10 (1994).
31. Henriksen, G. H., Taylor, A. R., Brownlee, C. & Assmann, S. M. Laser microsurgery of higher plant cell walls permits patch-clamp access. *Plant Physiol* **110**, 1063–1068 (1996).
32. Miedema, H., Henriksen, G. H. & Assmann, S. M. A laser microsurgical method of cell wall removal allows detection of large-conductance ion channels in the guard cell plasma membrane. *Protoplasma* **209**, 58–67 (1999).
33. Véry, A. A. & Davies, J. M. Laser microsurgery permits fungal plasma membrane single-ion-channel resolution at the hyphal tip. *Appl Environ Microbiol* **64**, 1569–1572 (1998).
34. Oraevsky, A. A. et al. Plasma mediated ablation of biological tissues with nanosecond-to-femtosecond laser pulses: Relative role of linear and nonlinear absorption. *IEEE J Sel Top. Quantum Electron* **2**, 801–809 (1996).
35. Gabel, C. V. Femtosecond lasers in biology: Nanoscale surgery with ultrafast optics. *Contemp Phys* **49**, 391–411 (2008).
36. Uchugonova, A. Nanosurgery of cells and chromosomes using near-infrared twelve-femtosecond laser pulses. *J Biomed Opt* **17**, 101502 (2012).
37. Kohli, V., Elezzabi, A. Y. & Acker, J. P. Cell nanosurgery using ultrashort (femtosecond) laser pulses: Applications to membrane surgery and cell isolation. *Lasers Surg Med* **37**, 227–230 (2005).
38. Vogel, A., Noack, J., Hüttman, G. & Paltauf, G. Mechanisms of femtosecond laser nanosurgery of cells and tissues. *Appl Phys B: Lasers Opt* **81**, 1015–1047 (2005).
39. Tserevelakis, G. J. et al. Femtosecond laser nanosurgery of sub-cellular structures in HeLa cells by employing Third Harmonic Generation imaging modality as diagnostic tool. *J Biophotonics* **5**, 200–207 (2012).
40. de Medeiros, G. et al. Cell and tissue manipulation with ultrashort infrared laser pulses in light-sheet microscopy. *Sci. Rep.* **10**, 1–12 (2020).
41. Chung, S. H. & Mazur, E. Surgical applications of femtosecond lasers. *J Biophotonics* **2**, 557–572 (2009).
42. Heinemann, D., Zabic, M., Terakawa, M. & Boch, J. Laser-based molecular delivery and its applications in plant science. *Plant Methods* **18**, 82 (2022).
43. Pérez-Martín, J., Bardetti, P., Castanheira, S., de la Torre, A. & Tenorio-Gómez, M. Virulence-specific cell cycle and morphogenesis connections in pathogenic fungi. *Semin. Cell Dev Biol* **57**, 93–99 (2016).
44. Gutjahr, C. & Parniske, M. Cell and developmental biology of arbuscular mycorrhiza symbiosis. *Annu Rev Cell Dev Biol* **29**, 593–617 (2013).
45. Bassilana, M., Puerner, C. & Arkowitz, R. A. External signal–mediated polarized growth in fungi. *Curr Opin Cell Biol* **62**, 150–158 (2020).
46. Knepper, C., Savory, E. A. & Day, B. Arabidopsis NDR1 is an integrin-like protein with a role in fluid loss and plasma membrane-cell wall adhesion. *Plant Physiol* **156**, 286–300 (2011).
47. Rabasović, M. D. et al. Nonlinear microscopy of chitin and chitinous structures: a case study of two cave-dwelling insects. *J Biomed Opt* **20**, 1 (2015).
48. Chung, L. Y. et al. Biocompatibility of potential wound management products: Fungal mycelia as a source of chitin/chitosan and their effect on the proliferation of human F1000 fibroblasts in culture. *J Biomed Mater Res* **28**, 463–469 (1994).
49. Maeda, H. & Ishida, N. Specificity of binding of hexopyranosyl polysaccharides with fluorescent brightener. *J Biochem* **62**, 276–278 (1967).
50. Niemz, M. H. *Laser-tissue Iteractions: Fundamentals and Applications*. (Springer-Verlag, 2004).
51. Tirlapur, U. K. & König, K. Femtosecond near-infrared laser pulses as a versatile non-invasive tool for intra-tissue nanoprocessing in plants without compromising viability. *Plant J* **31**, 365–374 (2002).
52. Vogel, A. & Venugopalan, V. Mechanisms of pulsed laser ablation of biological tissues. *Chem Rev* **103**, 577–644 (2003).
53. Yoshimi, A., Miyazawa, K., Kawauchi, M. & Abe, K. Cell wall integrity and its industrial applications in filamentous fungi. *J Fungi* **8**, 435 (2022).
54. Fuchs, B. B. & Mylonakis, E. Our paths might cross: the role of the fungal cell wall integrity pathway in stress response and cross talk with other stress response pathways. *Eukaryot Cell* **8**, 1616–1625 (2009).
55. Stanić, M. et al. Effect of long-term cyanide exposure on cyanide-sensitive respiration and phosphate metabolism in the fungus phycomyces blakesleeanus. *Arch Biol Sci* **66**, 847–857 (2014).
56. Ketchum, K. A., Joiner, W. J., Sellers, A. J., Kaczmarek, L. K. & Goldstein, S. A. N. A new family of outwardly rectifying potassium channel proteins with two pore domains in tandem. *Nature* **376**, 690–695 (1995).
57. Duran, R., Cary, J. W. & Calvo, A. M. Role of the osmotic stress regulatory pathway in morphogenesis and secondary metabolism in filamentous fungi. *Toxins* **2**, 367 (2010).
58. Lew, R. R. How does a hypha grow? the biophysics of pressurized growth in fungi. *Nat Rev Microbiol* **9**, 509–518 (2011).
59. Lew, R. R., Levina, N. N., Shabala, L., Anderca, M. I. & Shabala, S. N. Role of a mitogen-activated protein kinase cascade in ion flux-mediated turgor regulation in fungi. *Eukaryot Cell* **5**, 480–487 (2006).
60. Mansfield, T. M., Albornoz, F. E., Ryan, M. H., Bending, G. D. & Standish, R. J. Niche differentiation of Mucoromycotinian and Glomeromycotinian arbuscular mycorrhizal fungi along a 2-million-year soil chronosequence. *Mycorrhiza* **33**, 139–152 (2023).
61. Lax, C. et al. Genes, pathways, and mechanisms involved in the virulence of mucorales. *Genes* **11**, 317 (2020).
62. Walther, G., Wagner, L. & Kurzai, O. Outbreaks of Mucorales and the Species Involved. *Mycopathologia* **185**, 765–781 (2020).
63. Pasrija, R. & Naime, M. Resolving the equation between mucormycosis and COVID-19 disease. *Mol Biol Rep* **49**, 3349–3356 (2022).
64. World Health Organization. *WHO fungal priority pathogens list to guide research, development and public health action*. *Licence: CC BY-NC-SA 3.0 IGO* **1**, (2022).
65. Fisher, M. C. et al. Tackling the emerging threat of antifungal resistance to human health. *Nat Rev Microbiol* **20**, 557–571 (2022).
66. Mohan, J. E. et al. Mycorrhizal fungi mediation of terrestrial ecosystem responses to global change: Mini-review. *Fungal Ecol* **10**, 3–19 (2014).
67. Sutter, R. P. Mutations Affecting Sexual Development in Phycomyces blakesleeanus (car mutants/defined medium). *Proc Natl Acad Sci USA* **72**, 127–130 (1975).
68. Bukara, K. et al. Mapping of hemoglobin in erythrocytes and erythrocyte ghosts using two photon excitation fluorescence microscopy. *J Biomed Opt* **22**, 1 (2017).
69. Žižić, M. et al. Biotransformation of selenium in the mycelium of the fungus Phycomyces blakesleeanus. *Anal Bioanal Chem* **414**, 6213–6222 (2022).

analytical chemistry

pubs.acs.org/ac
Article

Mapping the Direction of Nucleocytoplasmic Transport of Glucocorticoid Receptor (GR) in Live Cells Using Two-Foci Cross-Correlation in Massively Parallel Fluorescence Correlation Spectroscopy (mpFCS)

Stanko N. Nikolić,[‖] Sho Oasa,[‖] Aleksandar J. Krmpot,[‖] Lars Terenius, Milivoj R. Belić, Rudolf Rigler,[⊥,#] and Vladana Vukojević*[,⊥]

Cite This: *Anal. Chem.* 2023, 95, 15171−15179

ABSTRACT: Nucleocytoplasmic transport of transcription factors is vital for normal cellular function, and its breakdown is a major contributing factor in many diseases. The glucocorticoid receptor (GR) is an evolutionarily conserved, ligand-dependent transcription factor that regulates homeostasis and response to stress and is an important target for therapeutics in inflammation and cancer. In unstimulated cells, the GR resides in the cytoplasm bound to other molecules in a large multiprotein complex. Upon stimulation with endogenous or synthetic ligands, GR translocation to the cell nucleus occurs, where the GR regulates the transcription of numerous genes by direct binding to glucocorticoid response elements or by physically associating with other transcription factors. While much is known about molecular mechanisms underlying GR function, the spatial organization of directionality of GR nucleocytoplasmic transport remains less well characterized, and it is not well understood how the bidirectional nucleocytoplasmic flow of GR is coordinated in stimulated cells. Here, we use two-foci cross-correlation in a massively parallel fluorescence correlation spectroscopy (mpFCS) system to map in live cells the directionality of GR translocation at different positions along the nuclear envelope. We show theoretically and experimentally that cross-correlation of signals from two nearby observation volume elements (OVEs) in an mpFCS setup presents a sharp peak when the OVEs are positioned along the trajectory of molecular motion and that the time position of the peak corresponds to the average time of flight of the molecule between the two OVEs. Hence, the direction and velocity of nucleocytoplasmic transport can be determined simultaneously at several locations along the nuclear envelope. We reveal that under ligand-induced GR translocation, nucleocytoplasmic import/export of GR proceeds simultaneously but at different locations in the cell nucleus. Our data show that mpFCS can characterize in detail the heterogeneity of directional nucleocytoplasmic transport in a live cell and may be invaluable for studies aiming to understand how the bidirectional flow of macromolecules through the nuclear pore complex (NPC) is coordinated to avoid intranuclear transcription factor accretion/abatement.

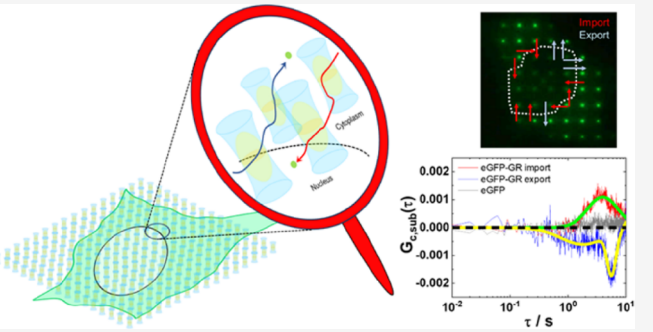

The concentration of transcription factors in the cell nucleus is a key determinant of the kinetics of gene transcription, through which cell identity and function are eventually conferred.[1,2] It is dynamically controlled in live cells by means of transcription factor import/export into/out of the cell nucleus via the nuclear pore complex (NPC), which is accomplished through two basic mechanisms: passive diffusion and active directional transport.[3,4] While our understanding of the energetics of the nucleocytoplasmic transport and the biochemical composition and overall organization of the NPC, which is the sole bidirectional gateway through which molecules pass in/out of the cell nucleus, is continuously improving,[5,6] the spatial organization of directionality of nucleocytoplasmic transport in a single cell remains less well characterized and it is not well understood how the bidirectional nucleocytoplasmic flow of macromolecules is coordinated. The main obstacle to progress is the limited number of analytical methods that can quantitatively characterize the directionality of nucleocytoplasmic transport in live cells at multiple spots simultaneously.

To date, time-resolved fluorescence microscopy imaging and correlation spectroscopy techniques have been shown to be

Received: April 2, 2023
Accepted: September 15, 2023
Published: October 2, 2023

https://doi.org/10.1021/acs.analchem.3c01427
Anal. Chem. 2023, 95, 15171−15179

well suited to address this problem in live cells. For example, fluorescence recovery after photobleaching (FRAP), Förster resonance energy transfer (FRET), single-molecule imaging/single particle tracking microscopy, and other related methods have been indispensable for this purpose, as they made it possible to quantify the dynamics of nucleocytoplasmic shuttling and characterize intranuclear reactions and retention.[7−13] Fluorescence correlation spectroscopy (FCS) and FCS-based methods have enabled us to simultaneously measure with single-molecule and particle sensitivity local translational diffusion coefficients and the local velocities and directions of transport. The value of conventional single-beam FCS for flow measurements was realized already at the inception of FCS when the theoretical background was developed, and a first successful application was demonstrated.[14] Subsequent studies have shown that conventional FCS is suitable even for more complex applications, such as hydrodynamic flow profiling in microchannel structures,[15] that the dynamic range of flow velocities that can be measured by FCS is wide, ranging over 4 orders of magnitude,[16] and that FCS is suitable for involved applications using microfluidic devices[17] or to characterize cerebral blood flow.[18] However, these studies have also revealed the limitations of conventional FCS for characterizing molecular transport, most notably the fact that it cannot determine the direction of flow. Hence, dual-focus FCS was developed to overcome this limitation and used to measure the velocity and direction of flow by cross-correlation analysis of signals in two foci.[19,20] In addition, more specialized FCS-based methods have also developed. For example, interferometric fluorescence cross-correlation spectroscopy (iFCCS) was applied to quantitatively characterize flow and diffusion transport in 2D and 3D;[21] and multipoint holographic FCS (MP-hFCS), where a spatial light modulator (SLM) was used to generate 8 independent foci, was applied in live cells to quantitatively characterize the nuclear import of the glucocorticoid (GR) receptor via cross-correlation analysis between two independent foci.[22] While these approaches were invaluable for measuring the velocity and direction of molecular transport, they provided this information for a limited region only. To overcome the limited overview and characterize molecular transport in a wider area, methods that use spatiotemporal correlation analysis of fluorescence fluctuations within an image/series of images were developed, such as two-photon image correlation and cross-correlation spectroscopy,[23] spatiotemporal image correlation spectroscopy (STICS),[24] and spatiotemporal image correlation of structured illumination microscopy data.[25] In addition, imaging FCS methods, such as imaging total internal reflection (ITIR)-FCS[26] and single-plane illumination microscopy-based FCS (SPIM-FCS),[27,28] were developed and used to characterize heterogeneity in diffusion and the direction and velocity of transport in multiple positions simultaneously. However, these methods also have some drawbacks that limit their suitability for characterizing the spatial heterogeneity of diffusion and the velocity and direction of transport in live cells. For example, the accuracy and precision of STICS-based methods depends, in addition to the dependence on the concentration and brightness of fluorescent molecules and the point spread function (PSF) of the microscope, on image settings in terms of scanning speed (pixel dwell time, time between the scan lines, and time between images), pixel size, the size of the region of interest (ROI) defined by the number of pixels that it contains, number of frames, and signal acquisition time,[29] and averaging over a relatively large number of pixels (>64) is needed to allow an accurate characterization of diffusion/motion. This leads to averaging out of spatial heterogeneity of diffusion and the direction and velocity of transport. STICS-based methods also encounter problems when analyzing heterogeneous samples since the presence of bright speckles significantly deforms the autocorrelation curve (ACC). In imaging FCS methods, such as ITIR-FCS and SPIM-FCS, pixel binning and cross-correlation between distant, nonoverlapping pixel areas are necessary to avoid large errors that arise due to crosstalk when cross-correlating the signals from areas that overlap.[26]

We have recently developed massively parallel FCS (mpFCS) in which geometrically independent multiple excitation foci are formed in the specimen and demonstrated its value for quantitative scanning-free confocal fluorescence microscopy imaging and characterization of fast dynamic processes in live cells.[30,31] Here, we present how this new FCS-based imaging modality can be used to map the spatial organization of directionality of nucleocytoplasmic transport in live cells using, as a model system, live HEK cells expressing the GR fused at the N-terminal end with the enhanced green fluorescent protein (eGFP-GR). The GR is a hormone-dependent receptor that belongs to the nuclear receptor superfamily of transcriptional regulatory factors.[32] It is indispensable for maintaining homeostasis under normal physiology and under stress. In unstimulated cells, the GR resides in the cytoplasm, bound into a large multiprotein complex.[33,34] Upon stimulation with endogenous or synthetic ligands[35] and their binding to the cytoplasmic GR, ligand-induced GR translocation to the cell nucleus occurs. In the cell nucleus, GR regulates the transcription of numerous genes—it is estimated that glucocorticoid-responsive genes probably represent 3−10% of the human genome,[36] acting either as an activator or repressor of genes across the genome by direct binding of GR oligomeric forms (dimers or tetramers[37−42]) to glucocorticoid response elements (GREs) on the genome DNA and/or by physically associating with other transcription factors (e.g., NF-κB). The GR concentration in the cell nucleus is dynamically regulated through a complex, perpetually ongoing bidirectional nucleocytoplasmic shuttling of GR.[43] Despite being extensively studied,[10,11,44,45] little is known about how bidirectional flow of GR is spatially organized and coordinated in a live cell to avoid collision of inward/outward shuttling GR and its intranuclear accretion/abatement.

EXPERIMENTAL SECTION

Cell Culture and Pharmacological Treatment. HEK cells (ATCC) were grown in 25 mL cell culture flasks with filter caps (T-25, Sarstedt) in Dulbecco's modified Eagle medium (DMEM; Gibco) supplemented with 10% fetal bovine serum (FBS; Gibco) and 1% penicillin−streptomycin (Gibco), 100 U/mL final concentration penicillin, and 100 μg/mL streptomycin and maintained in a humidified atmosphere containing 5% CO_2 at 37 °C.

One day before transfection, HEK cells were seeded in Lab-Tek 8-well chambered coverglass (Thermo Fisher Scientific), with a seeding density of 1.0×10^4 cells per well (volume of 400 μL). The cells were transfected with 100 ng of peGFP-C1 or peGFP-GR-C1 plasmids for expression of the enhanced green fluorescent protein (eGFP) or wild-type human GR α fused with eGFP, respectively, using 0.2 μL of Lipofectamine 2000 (Thermo Fisher Scientific). Twenty-four hours after

https://doi.org/10.1021/acs.analchem.3c01427
Anal. Chem. 2023, 95, 15171−15179

transfection, the cell culture medium was replaced as described below, and the cells were subjected to further analysis.

To induce GR translocation into the nucleus, the synthetic ligand dexamethasone (Dex; Sigma-Aldrich) was used. For pharmacological treatment, a 2 mM Dex stock solution prepared by dissolving Dex in dimethyl sulfoxide (DMSO) was diluted to 500 nM in phenol red-free medium FluoroBrite DMEM (Gibco) and the cell culture medium was replaced. In control experiments, the phenol red-free medium FluoroBrite DMEM (Gibco) was used.

Chemicals. Yellow-green fluorescence (Ex/Em: 505/515) carboxylate-modified polystyrene nano/microspheres of different nominal diameters, d = 100 nm ($D_{fs,100}$ = 4.4 × 10^{-12} m^2 s^{-1}) or 2.0 μm (FluoSpheres Size Kit #2), and carboxylate-functionalized quantum dot nanocrystals, d = 20 nm, with emission maxima at 525 nm (Qdot 525 ITK Carboxyl Quantum Dots; Molecular Probes, Life Technologies Corporation, USA) were used for mpFCS instrument calibration and performance characterization. Thirty min of sonication was applied to minimize the agglomeration of quantum dots/fluospheres.

For fFMI instrument alignment, a uniform thin layer of Rh6G was prepared by squeezing 1 μL of concentrated Rh6G solution in water between a microscopic slide and a cover glass (no. 1.5 thickness, 22 × 40 mm) and allowed to dry.

Confocal Laser Scanning Microscopy (CLSM) Imaging. Time-lapse CLSM imaging was performed using the LSM880 system (Carl Zeiss), equipped with the VIS-laser module comprising the Ar-ion laser (458, 488, and 514 nm), C-Apochromat 40×/1.2 N.A. W objective, and gallium arsenide phosphide (GaAsP) detector. eGFP was excited using a 488 nm Ar-ion laser line. Fluorescence was detected in the 493−630 nm range. Following treatment with 500 nM Dex, time-lapse confocal images were acquired at 1 min intervals for 35 min.

Optical Setup for Massively Parallel Fluorescence Correlation Spectroscopy (mpFCS). The optical setup for mpFCS is described in detail in our previous work[30,31] and the Supporting Information (Section SI1, Figure S1). Briefly, the instrument was built using an inverted epi-fluorescence microscope Axio Observer D1 frame equipped with a C-Apochromat 63×/1.2 W Corr objective lens (Carl Zeiss, Germany). A continuous wavelength (CW) 488 nm frequency-doubled diode laser Excelsior 488 (Spectra-Physics, France) was used as the excitation light source. A Diffractive Optical Element (DOE; Holoeye, Germany) was used to precisely create a spot-wise illumination pattern that matches the distribution of single-photon avalanche diodes (SPADs) on the Single Photon Counting SPC2 or the SPC3 camera (Micro Photon Devices MPD, Italy).[46] To enable fast sample localization, an 18.0 megapixel digital single-lens reflex (DSLR) camera EOS 600D (pixel size of 18.5 μm^2 and pixel pitch of 4.3 μm; Canon Inc., Japan) was coupled to the side port of the microscope opposite to the SPC2/SPC3 camera, and the light path between the two camera ports was manually switched.

mpFCS Data Acquisition. For mpFCS data acquisition in aqueous suspension of fluospheres or quantum dots, an instrumental setup comprising a 32 × 32 DOE and the SPC2 camera was used.[30] Here, the photosensitive area of the chip consists of 32 × 32 circular SPADs that are 20 μm in diameter, and the distance between adjacent diodes along a row/column, i.e., the pitch of the camera, is 100 μm. A total of 131,000 frames were acquired every 20.74 μs, yielding 1024 fluorescence intensity fluctuation traces recorded over 2.71 s. The data was stored in the internal memory of the SPC2 camera during signal acquisition and then transferred to a Dell Precision Fixed Workstation T5600 Xeon E5−2620 2 GHz equipped with an NVIDIA GeForce GTX 780 graphic card containing 2304 Compute Unified Device Architecture (CUDA) for fast data analysis by two-foci cross-correlation as described in Data Processing.

For mpFCS measurements in live cells, the more sensitive SPC3 camera with significantly reduced afterpulsing was used; here, the photosensitive area of the chip consists of 64 × 32 circular SPADs that are 30 μm in diameter, and the distance between adjacent diodes along a row/column, i.e., the pitch of the camera, is 150 μm. In addition, a spot-wise, 16 × 16 illumination was applied and every other SPAD in the centrally positioned 16 × 16 SPADs of the SPC3 camera was used for signal detection.[31] Fifteen minutes after treatment with 500 nM Dex, 1,048,570 frames were acquired at a temporal resolution of 100 μs/frame, yielding 256 fluorescence intensity fluctuation traces recorded over 104.85 s. During signal acquisition, the data was stored in the internal memory of the SPC3 camera and then transferred to a PC for further analysis using the Origin Data Analysis and Graphing software (OriginLab), as described in Data Processing.

Data Processing. To calculate the two-foci cross-correlation curve (tfCCC) for arbitrary pixels a and b of the SPAD camera, the following definition applies:

$$G_{ab}^{(2)}(\tau) = \frac{\langle F_a(t)F_b(t+\tau)\rangle}{\langle F_a(t)\rangle\langle F_b(t)\rangle} = \frac{\langle n_a(t)n_b(t+\tau)\rangle}{\langle n_a(t)\rangle\langle n_b(t)\rangle} \quad (1)$$

where $F_a(t)$ and $F_b(t)$ are fluorescence intensities that are directly proportional to the number of emitted photons $n_a(t)$ and $n_b(t)$ at time t for pixels a and b, respectively, the angular brackets indicate a time average, and τ is the lag time, also called correlation time. However, for the fast, real-time, and highly precise computation of the auto- and cross-correlation functions, a multitau algorithm was developed. Explanation of the multitau procedure can be found in the literature.[31,32,47,48]

For *in vitro* mpFCS measurements in dilute suspensions of fluospheres or quantum dots, the multitau algorithm was used to analyze the raw photon counts directly, and the following formula was used for the calculation of the tfCCCs:

$$G_{ab}^{(2)}(\tau_i) = \frac{\frac{1}{M-m}\sum_{k=1}^{M-m} n_a(k\Delta\tau_i)\cdot n_b(k\Delta\tau_i + m\Delta\tau_i)}{M_{a,dir}\cdot M_{b,del}} \quad (2)$$

Briefly, in eq 2, τ_i is the lag time and $\Delta\tau_i$ is the sampling time for channel i (ith value of the auto- or cross-correlation function). The bin width for the first group is $\Delta\tau_1$ = 20.74 μs. Numbers m and M are integers defined as $m = \tau_i/\Delta\tau_i$ and $M = T/\Delta\tau_i$, where T is the total measurement time. The number of photons counted over a time interval $[(k-1)\Delta\tau_i, k\Delta\tau_i]$ is denoted as $n(k\Delta\tau_i)$. One can see that the correlation analysis boils down to obtaining the sum of the products $n(k\Delta\tau_i)\cdot n(k\Delta\tau_i + m\Delta\tau_i)$ of the counted photons at time $k\Delta\tau_i$ and $m\Delta\tau_i$ later. In eq 1, $n_a(k\Delta\tau_i)$ and $n_b(k\Delta\tau_i)$ denote photon counts at time $k\Delta\tau_i$ for pixels indicated by the subscript, while $M_{a,\mathrm{dir}}$ and $M_{b,\mathrm{del}}$ are so-called direct and delayed monitor for pixels a and b, respectively. They are computed using the following equations:

https://doi.org/10.1021/acs.analchem.3c01427
Anal. Chem. 2023, 95, 15171−15179

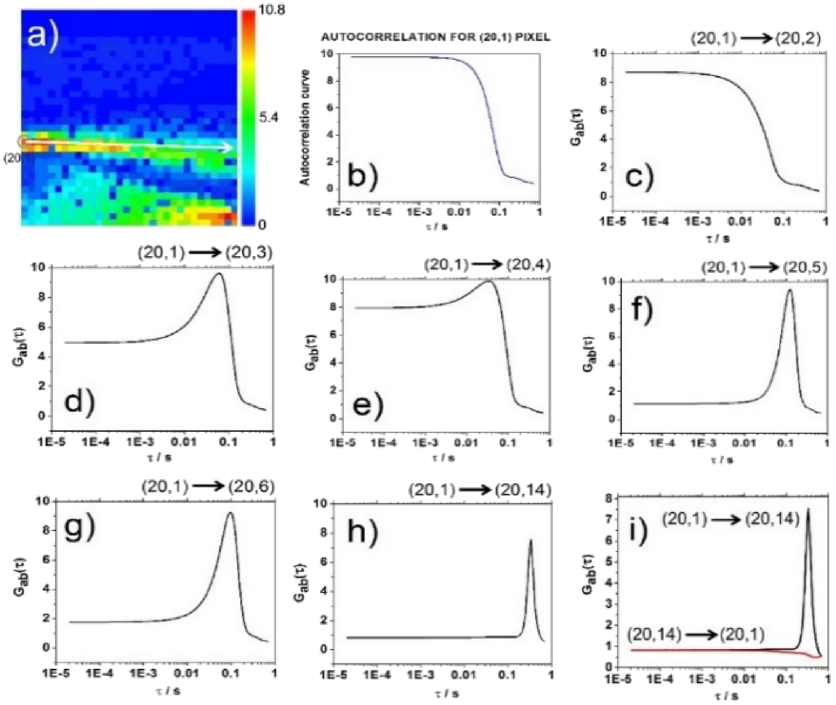

Figure 1. Two-foci cross-correlation analysis of directional particle motion in a diluted suspension of 2 μm fluospheres. (a) $G(0)$ map showing amplitudes of temporal ACCs at lag time τ = 20.74 μs in the 32 × 32 SPAD array. The upper trail, starting at the referent SPAD a = (20,1), is encircled. The white arrow indicates the path along which two-foci cross-correlation analysis is performed. (b) The two-foci ACC at the referent SPAD a = (20,1) was calculated using eq 2 when $a = b$. (c–h) Two-foci cross-correlation curves (tfCCCs) between the referent pixel a = (20,1) and pixels b = (20,2) (c), b = (20,3) (d), b = (20,4) (e), b = (20,5) (f), b = (20,6) (g), and b = (20,14) (h). (i) $tfCCC_{ab}$ between a = (20,1) and b = (20,14) (black; shown in panel h) and the corresponding $tfCCC_{ba}$ between b = (20,14) and a = (20,1) (red). The absence of a peak in $tfCCC_{ba}$ clearly indicates that the direction of particle motion is from (20,1) toward (20,14) and not from (20,14) toward (20,1).

$$M_{a,\mathrm{dir}} = \frac{1}{M-m}\sum_{k=1}^{M-m} n_a(k\Delta\tau_i) \tag{3}$$

$$M_{b,\mathrm{del}} = \frac{1}{M-m}\sum_{k=m}^{M} n_b(k\Delta\tau_i) \tag{4}$$

It is important to note that $G_{ab}^{(2)}(\tau_i) \neq G_{ba}^{(2)}(\tau_i)$. Thus, for each pair of pixels, there are two tfCCCs that are different in the case of directed molecular/particle motion, hence providing information about the direction of movement. Notably, a two-foci autocorrelation function is obtained when $a = b$ in eqs 1 and 2.

For measurements in live cells, Origin Data Analysis and Graphing software (OriginLab) was used to compute cross-correlation curves between foci in the cytoplasm and nucleus. As a first step, Origin Data Analysis and Graphing software (OriginLab) was used to post acquisition account for photobleaching in individual time series. To this aim, data compression was first applied by binning the data into 10 ms bins, and a fourth-order polynomial function was used to fit the fluorescence intensity traces that are decaying due to photobleaching:[49,50]

$$F_c(t) = \frac{F(t)}{\sqrt{\frac{f(t)}{f(0)}}} + f(0)\cdot\left(1 - \sqrt{\frac{f(t)}{f(0)}}\right) \tag{5}$$

Here, $F(t)$ and $F_c(t)$ are fluorescence intensities of raw and corrected data at time t, respectively, and $f(0)$ and $f(t)$ denote values of the fourth-order polynomial function at time 0 and t, respectively. We then employed eq 2, substituting raw photon intensities (counts) with the fourth-order polynomial functions from eq 5. The forward, cytoplasm to nucleus, and backward, nucleus to cytoplasm, translocation cross-correlation curves are respectively defined as follows:

$$G_c^{\mathrm{cyt,nuc}}(\tau) = \frac{\langle F_c^{\mathrm{cyt}}(t)\cdot F_c^{\mathrm{nuc}}(t+\tau)\rangle}{\langle F_c^{\mathrm{cyt}}(t)\rangle\cdot\langle F_c^{\mathrm{nuc}}(t)\rangle} \tag{6}$$

$$G_c^{\mathrm{nuc,cyt}}(\tau) = \frac{\langle F_c^{\mathrm{nuc}}(t)\cdot F_c^{\mathrm{cyt}}(t+\tau)\rangle}{\langle F_c^{\mathrm{nuc}}(t)\rangle\cdot\langle F_c^{\mathrm{cyt}}(t)\rangle} \tag{7}$$

where $F_c^{\mathrm{nuc}}(t)$ and $F_c^{\mathrm{cyt}}(t)$ are photobleaching-corrected fluorescence intensity time series recorded in the selected pixels in the nucleus and cytoplasm, respectively.

To readily visualize the translocation direction between two foci, the tfCCC in the direction of nucleus to cytoplasm ($G_c^{\mathrm{nuc,cyt}}(\tau)$) is subtracted from the tfCCC in the direction of cytoplasm to nucleus ($G_c^{\mathrm{cyt,nuc}}(\tau)$):

$$G_{c,\mathrm{sub}}(\tau) = G_c^{\mathrm{cyt,nuc}}(\tau) - G_c^{\mathrm{nuc,cyt}}(\tau) \tag{8}$$

In this way, a positive peak in $G_{c,\mathrm{sub}}(\tau)$ signifies nuclear import, whereas a negative peak indicates nuclear export. We refer to $G_{c,\mathrm{sub}}(\tau)$ as the subtracted cross-correlation curve.

RESULTS

Theoretical Results. Theoretical background and results of numerical simulations of fluorescent fluosphere motion are presented in the Supporting Information (Section SI2, Figures S2–S5).

https://doi.org/10.1021/acs.analchem.3c01427
Anal. Chem. 2023, 95, 15171−15179

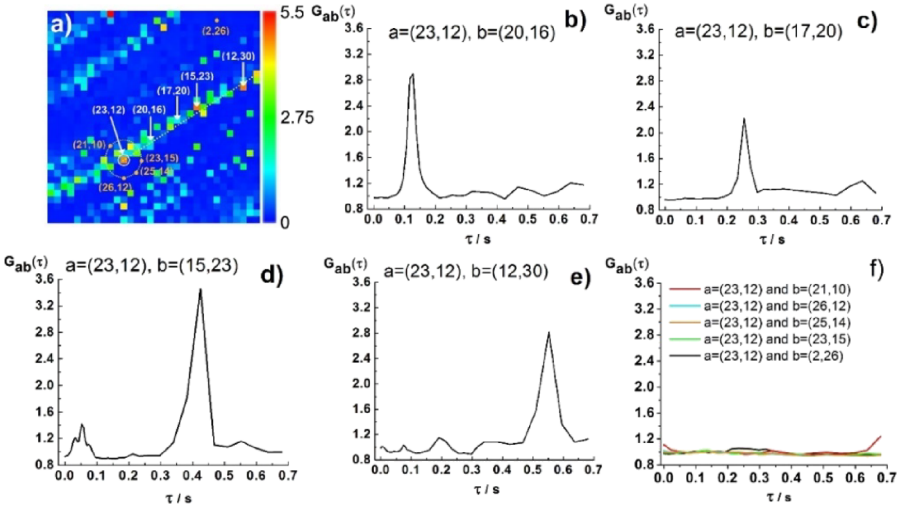

Figure 2. Two-foci cross-correlation analysis of directional particle motion in a 20 nM suspension of 100 nm fluospheres. (a) $G(0)$ map showing amplitudes of temporal ACCs at lag time τ = 20.74 μs in the 32 × 32 SPAD array. To guide the eye, the trail of fluosphere motion, including the referent SPAD a = (23,12), is highlighted (white dotted line). (b–e) tfCCCs between the referent SPAD a = (23,12) and on-trajectory SPADs (white) b = (20,16), b = (17,20), b = (15,23), or b = (12,30). (f) tfCCCs between the referent SPAD a = (23,12) and selected off-trajectory SPADs (orange-marked).

Proof-of-Concept Results Using Immobilized q-Dots and a Motorized Stage with Nanometer Positioning Precision. Results of proof-of-concept measurements using a precisely controllable motorized stage to move the sample are presented in the Supporting Information (Section SI3, Figures S6 and S7).

In Vitro Experimental Results. Here, we demonstrate using dilute suspensions of fluospheres of different diameters, d = 2 μm (Figure 1) and d = 100 nm (Figure 2), that the projection of particles' motion in the focal plane can be traced using two-foci cross-correlation analysis in mpFCS.

To begin with, a dilute suspension of large, d = 2 μm, and bright fluospheres is analyzed, where particle motion could readily be observed by temporal autocorrelation analysis of fluorescence intensity fluctuations acquired using the mpFCS system (Figure 1). As can be seen from the map of amplitudes of the temporal ACCs for lag time τ = 20.74 μs, the so-called $G(0)$ map, high $G(0)$ values are observed along paths reflecting fluosphere movement (Figure 1a). To ascertain that these traces indeed reflect particle motion, two-foci cross-correlation analysis is performed between selected pixels along the upper trail (Figure 1a, white arrow), and the thus-obtained two-foci cross-correlation curves (tfCCCs) are shown in Figure 1b–i.

The ACC in pixel (20,1) shown in Figure 1b is calculated for the referent SPAD a = (20,1) using eq 2 when a = b. The tfCCCs between two adjacent pixels a = (20,1) and b = (20,2) resemble the ACC shown in Figure 1b and lack the characteristic narrow peak that is characteristic of tfCCCs shown in Figure 1c–h. This is because of the large bead diameter, which exceeds the distance between the neighboring SPADs in the focal plane; the distance between the centers of two adjacent volume elements is Δl = 1.6 μm. Thus, fluorescence signals from the same particle are simultaneously measured in both SPADs. tfCCCs containing features of both the ACC and tfCCC features are observed for b = (20,3) and b = (20,4) (Figure 1d,e). When the distance between two pixels is sufficiently large (Figure 1f–h), a sharp peak is observed, as expected. Importantly, one can see that the greater the distance between a and b, the longer the lag time of the cross-correlation peak. From the lag times of the cross-correlation peak, one can estimate the two-dimensional (2D) velocity. Projection of the three-dimensional (3D) fluosphere trajectory as it traverses the focal plane onto the 2D image plane divided by the lag time yields the 2D velocity. The 2D velocity at which the fluorescent particle is moving from pixel a = (20,1) is first 50 μm/s, then increases to 80 μm/s, and then decreases to 60 μm/s. Given that we have neither controlled the direction nor the velocity of fluosphere motion but rather observed its movement under spontaneous, convection or pipet aspiration/dispensing-driven fluid flow, the observed difference could reflect local changes in fluosphere velocity due to heterogeneities in the fluid flow and/or apparent differences in fluosphere 2D velocity arising because 3D paths of different lengths may give the same 2D projection in the image plane. Finally, the direction of fluosphere motion in the focal plane could be determined (denoted by the white arrow in Figure 1a) from the results shown in Figure 2i. Here, a sharp peak is observed when the tfCCC is calculated in the direction from a = (20,1) to b = (20,14) (Figure 2i, black). However, when the calculation is performed in the opposite direction, from b = (20,14) to a = (20,1), the peak disappears (Figure 2i, red). This in turn means that the direction of fluosphere motion is from a = (20,1) to b = (20,14).

Sensitivity of the mpFCS instrument is further tested using a diluted suspension of small fluospheres, d = 100 nm (Figure 2).

As can be seen from the $G(0)$ map (Figure 2a) and the tfCCCs between the reference point a = (23,12) and pixels b = (20,16), b = (17,20), b = (15,23), or b = (12,30), robust peaks can be observed in the tfCCCs, confirming that these points are on the trajectory and in the direction of 100 nm fluosphere movement (Figure 2b–e). The greater the distance between pixels a and b, the longer the lag time at which the peak in the tfCCC is observed (Figure 2b–e). As before (Figure 1i), tfCCCs calculated from b to a (data not shown) showed no peaks, confirming that the direction of 100 nm fluosphere motion is from point a = (23,12) toward the set of white-

https://doi.org/10.1021/acs.analchem.3c01427
Anal. Chem. 2023, 95, 15171–15179

marked *b* points along the indicated trajectory (Figure 2a, white dotted line). Moreover, from the lag times of the peaks in the tfCCCs (Figure 2b–e), the projection of mean velocity in the focal plane could be estimated, yielding an approximate mean velocity of the directed motion of 30 μm/s between pixels (23,12) and (22,13) and 60 μm/s thereafter. We next prove that two-foci cross-correlation analysis can be used as a "radar" for detecting the direction of particle motion. In Figure 2a, we depict a circle centered at the reference pixel a = (23,12) with pixels (21,10), (26,12), (25,14), and (23,15) at its rim (Figure 2a, orange-marked). In addition, the distant pixel (2,26) is also included in this analysis as an off-trajectory example (Figure 2a, orange-marked). tfCCCs between a = (23,12) and these pixels, which are not positioned along the particle trajectory, clearly show no peaks (Figure 2f). Thus, this 360° sweeping procedure can discern the direction of the particle motion. To further corroborate this analysis, we show in the Supporting Information (Section SI4, Figures S8–S10) that two-foci cross-correlation analysis yields no tfCCCs when pure diffusion is observed (Figures S8 and S9) and that it is more powerful than classical temporal autocorrelation analysis for discerning free diffusion from directional motion when the flow is slow (Figure S10).

Nucleocytoplasmic Translocation of Glucocorticoid Receptor in the Live Cell. Finally, we applied our method to characterize in live cells the translocation of the glucocorticoid receptor tagged with enhanced green fluorescent protein (eGPFP-GR; Figure 3).

As can be seen, eGFP-GR is localized in the cytoplasm in untreated HEK cells (Figure 3a, top, 0 min). Dex (500 nM) treatment induced eGFP-GR relocation to the cell nucleus (Figure 3a, top, 30 min), whereas it did not change eGFP intracellular distribution (Figure 3a, bottom, 0 and 30 min). Over time, a 4-fold increase in nuclear fluorescence intensity following 500 nM Dex treatment was observed in eGFP-GR-expressing HEK cells (Figure 3b, dots), while no change was observed in the eGFP-expressing HEK cells (Figure 3b, circles). eGFP-GR nuclear translocation half time, defined as the time needed for fluorescence intensity in the cell nucleus to reach half of its highest value, was determined to be $t_{1/2}^{nuc}$ = 15 min (Figure 3b, red). Hence, mpFCS measurements of directional transport were performed in eGFP-GR-expressing HEK cells 15 min after the treatment with 500 nM Dex.

Nuclear/cytoplasmic positions of eGFP-GR in an untreated HEK cell expressing eGFP-GR are visualized using spot-wise illumination and the DSLR camera attached to the side-port of the mpFCS system (Figure 3c; nuclear localization is inside the white dotted contour). tfCCCs, $G_c^{cyt,nuc}(\tau)$ and $G_c^{nuc,cyt}(\tau)$, and corresponding $G_{c,sub}(\tau)$ are calculated at distinct positions along the nuclear envelope (Figure 3c, 1–13). Our data showed that the direction of nuclear import/export is location-specific, with nuclear import being observed at sites 1, 2, 3, 8, 9, 10, 12, and 13 (Figure 3c, red), whereas nuclear export was observed at sites 4, 5, 6, 7, and 11 (Figure 3c, faint blue).

Representative $G_{c,sub}(\tau)$, color-coded to indicate the direction of eGFP-GR nucleocytoplasmic transport, nuclear import (red) and nuclear export (blue), are shown in Figure 3d$_1$,d$_2$, respectively. $G_{c,sub}(\tau)$ for all 13 sites are shown in the Supporting Information (Section SI5, Figure S11a). Average $G_{c,sub}(\tau)$ for three different cells, showing similar results, are presented in Figure S11b$_1$–b$_3$.

We further computed the nucleocytoplasmic translocation times (Figure 3e$_1$) by fitting the $G_{c,sub}(\tau)$ by using a Gaussian

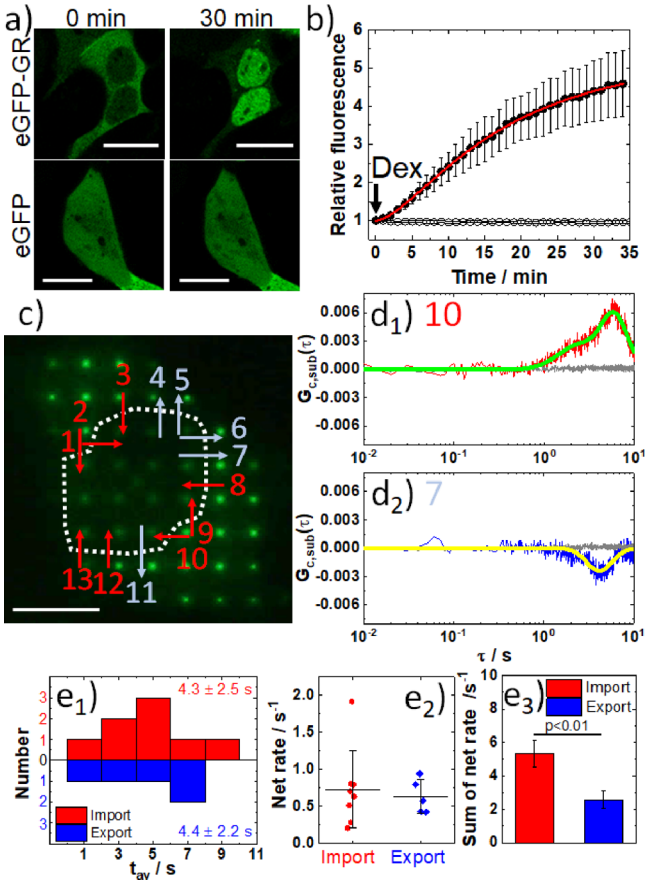

Figure 3. Spatial mapping of the direction and extent of nucleocytoplasmic transport of eGFP-GR in live cells using two-foci cross-correlation in mpFCS. (a) CLSM images of HEK cells expressing eGFP-GR (top) or eGFP (bottom; control) at 0 min (untreated) and 30 min after treatment with 500 nM Dex. Scale bars: 20 μm. (b) Relative change in nuclear fluorescence intensity over time following Dex treatment in cells expressing eGFP-GR (dots) or eGFP (circles). The arrow indicates the time of Dex addition to a concentration of 500 nM. Logistic function was used to fit the S-shaped relative fluorescence growth curve recorded in cells expressing eGFP-GR (red line). (c) Fluorescence image showing eGFP-GR distribution in an untreated cell acquired by using the DSRL Canon camera coupled to the side port of the mpFCS system. Arrows show the directions of eGFP-GR; nuclear translocation: import (red) and export (blue). Scale bar: 10 μm. (d$_1$, d$_2$) $G_{c,sub}(\tau)$ at an import-active (red, d$_1$) and export-active site (blue, d$_2$). Translocation time is determined by Gaussian distribution fitting to $G_{c,sub}(\tau)$ (green/yellow). (e$_1$) Histogram of import (red) and export (blue) translocation time. (e$_2$) Net rate of nucleocytoplasmic transport calculated as the ratio of the tfCCC amplitude over import/export time. (e$_3$) Sum net rate in a single cell. All values are shown as the average ± standard deviation (SD). SD was calculated from three independent measurements in three cells. Statistical significance was assessed using a two-tail Student's *t* test.

distribution function (Figure 3d$_1$,d$_2$, green and yellow, respectively). On the average, the nucleocytoplasmic translocation times were t_{av}^{imp} = (4.3 ± 2.5) s for nuclear import and t_{av}^{exp} = (4.4 ± 2.2) s for nuclear export (Figure 3e$_1$). By dividing the amplitude of the fitted Gaussian distribution function with the corresponding nucleocytoplasmic translocation time, the net rate of nucleocytoplasmic translocation could be estimated at independent sites (Figure 3e$_2$) and summed at all analyzed sites (Figure 3e$_3$).

https://doi.org/10.1021/acs.analchem.3c01427
Anal. Chem. 2023, 95, 15171–15179

This analysis, corroborated by theoretical calculations (Section SI5, Figures S12−S14), showed that on average, net rate of nucleocytoplasmic translocation at different sites along the nuclear envelope was not significantly different between nuclear import and export sites (Figure 3e$_2$). However, given that the number of sites at which nuclear import was observed is larger than the number of sites where nuclear export occurred, the total import net rate was twice the total export net rate (Figure 3e$_3$), consistent with the net eGFP-GR translocating into the cell nucleus.

DISCUSSION

In this work, we have theoretically and experimentally shown that two-foci cross-correlation analysis in mpFCS enables us to characterize the directional motion of fluospheres/molecules in solution/live cells. This is exemplified here for fluospheres of different sizes, d = 2 μm, which is larger than the distance between two adjacent pixels in the mpFCS instrument (Figure S1), and d = 100 nm, which is smaller, in dilute aqueous suspension (Figures 1 and 2 and Figures S2−S5), for immobilized q-dots precisely moved using a translation stage with nanometer step size (Figures S6 and S7), and for ligand-induced eGFP-GR nuclear translocation in live cells (Figure 3 and Figure S11).

Using dilute suspension of fluorescent particles, we demonstrated theoretically and experimentally that by calculating tfCCCs between a referent pixel and different adjacent pixels in the focal plane, we could identify the direction in which the particle is moving since a sharp peak is observed only in the tfCCC that is calculated along the projection of the 3D path of particle motion onto the 2D image plane as it traverses the focal plane and in the direction of particle movement from an earlier to a later particle position (Figures 1 and 2). Moreover, we showed that the tfCCC peak is observed at the lag time that corresponds to the transit time between the two foci positions, demonstrating that our technique can be used not only to trace the projection of the 3D particle trajectory onto the 2D image plane as the particle traverses the focal plane but also to map the forward/backward direction of its motion and the 2D velocity.

We further showed using ligand-induced eGFP-GR nuclear translocation as an example that two-foci cross-correlation analysis can characterize in live cells the cellular dynamics of fluorescently tagged proteins. Most notably, our study showed that by calculating tfCCCs, we could map the direction of ligand-induced eGFP-GR nucleocytoplasmic translocation along the nuclear envelope contour in the focal plane (Figure 3). This further revealed that eGFP-GR nuclear import and export occurred simultaneously at different locations along the nuclear envelope and with similar nucleocytoplasmic translocation times, t_{av}^{imp} = (4.3 ± 2.5) s for nuclear import and t_{av}^{exp} = (4.4 ± 2.2) s for nuclear export (Figure 3e$_1$), and that the net effect at the macroscopic level is determined by the number of sites through which import/export occurs (Figure 3e$_1$−e$_3$). We thus confirmed a previous finding by multipoint holographic fluorescence correlation spectroscopy (MP-hFCS)[22] showing that under ligand-induced eGFP-GR nuclear translocation, the actual passing through of nuclear pores is faster than the macroscopic change in fluorescence intensity that is observed by time-lapse confocal fluorescence microscopy imaging. We, however, took the understanding of mechanisms underlying acute, strong-binding ligand-induced eGFP-GR translocation one step further by showing that import/export processes occur simultaneously at different locations, which was not shown by MP-hFCS, and that the net change in eGFP-GR concentration at the macroscopic level is determined by the number of sites through which eGFP-GR import/export occurs and not by differences in the actual eGFP-GR translocation time (Figure 3e$_1$−e$_3$). Having said this, we underline here that this conclusion is valid only for acute, strong-binding ligand-induced eGFP-GR nuclear translocation at the time of the highest net change in eGFP-GR nuclear concentration and does not necessarily apply for other conditions, such as under stimulation with endogenous or synthetic weakly binding GR-specific ligands or upon withdrawal of GR ligand.[51−54]

In conclusion, two-foci cross-correlation in mpFCS is a versatile tool for characterization of both direction and 2D velocity of active transport in live cells and may be useful for understanding how the bidirectional traffic of macromolecules is spatially organized and coordinated in live cells to achieve controlled local accretion/abatement of molecules of interest. In addition, directional fluorescent particle motion in fluids can be characterized in detail, enabling us not only to characterize local heterogeneities in fluid flow but also to investigate the essential role of the fluid phase for long-range material transport and the emergence of large-scale synergy in biological systems.[55]

ASSOCIATED CONTENT

Supporting Information

The Supporting Information is available free of charge at https://pubs.acs.org/doi/10.1021/acs.analchem.3c01427.

SI1: optical setup; SI2: theoretical background and numerical simulations of directional particle motion; SI3: proof-of-concept measurements using a piezo-based linear stage with nanometer positioning precision for controlled translation of immobilized quantum dots; SI4: comparison between auto- and two-foci cross-correlation analysis of diffusion and flow in dilute aqueous solution and nanoparticles in suspension; SI5: glucocorticoid receptor nucleocytoplasmic translocation in live cells (PDF)

AUTHOR INFORMATION

Corresponding Author

Vladana Vukojević − *Department of Clinical Neuroscience (CNS), Center for Molecular Medicine (CMM), Karolinska Institute, 17176 Stockholm, Sweden;* orcid.org/0000-0003-0873-5653; Email: Vladana.Vukojevic@ki.se

Authors

Stanko N. Nikolić − *Department of Clinical Neuroscience (CNS), Center for Molecular Medicine (CMM), Karolinska Institute, 17176 Stockholm, Sweden; Institute of Physics Belgrade, University of Belgrade, 11080 Belgrade, Serbia; Division of Arts and Sciences, Texas A&M University at Qatar, Doha, Qatar*

Sho Oasa − *Department of Clinical Neuroscience (CNS), Center for Molecular Medicine (CMM), Karolinska Institute, 17176 Stockholm, Sweden;* orcid.org/0000-0003-3800-590X

Aleksandar J. Krmpot − *Department of Clinical Neuroscience (CNS), Center for Molecular Medicine (CMM), Karolinska Institute, 17176 Stockholm, Sweden; Institute of Physics*

Belgrade, University of Belgrade, 11080 Belgrade, Serbia; Division of Arts and Sciences, Texas A&M University at Qatar, Doha, Qatar; orcid.org/0000-0003-2751-7395

Lars Terenius − *Department of Clinical Neuroscience (CNS), Center for Molecular Medicine (CMM), Karolinska Institute, 17176 Stockholm, Sweden;* orcid.org/0000-0003-2880-9576

Milivoj R. Belić − *Division of Arts and Sciences, Texas A&M University at Qatar, Doha, Qatar*

Rudolf Rigler − *Department of Clinical Neuroscience (CNS), Center for Molecular Medicine (CMM), Karolinska Institute, 17176 Stockholm, Sweden*

Complete contact information is available at: https://pubs.acs.org/10.1021/acs.analchem.3c01427

Author Contributions

[‖]S.N.N., S.O., and A.J.K. contributed equally to this work.

Author Contributions

[⊥]R.R. and V.V. equally contributed to this work as senior authors.

Author Contributions

[#]We regretfully inform that our esteemed colleague and FCS pioneer R.R. has passed away on Oct 5th 2022.

Author Contributions

V.V. and R.R. designed the study. A.J.K. designed and built-up the experimental setup, and performed the experiments with S.O. S.N.N. wrote the mpFCS data acquisition, analysis, and presentation program and performed numerical simulations. M.R.B. supervised the numerical simulations. All authors analyzed and interpreted the data, contributed to manuscript writing, and have given approval to the final version of the manuscript.

Notes

Research reported in this publication was supported by the National Institute on Alcohol Abuse and Alcoholism of the National Institutes of Health under award number R01AA028549. The content is solely the responsibility of the authors and does not necessarily represent the official views of the National Institutes of Health. The funding agencies had no influence on the study design, methods, data collection, analyses, or the manuscript writing. All data are available in the main text or the Supporting Information.

The authors declare no competing financial interest.

■ ACKNOWLEDGMENTS

We thank Prof. Masataka Kinjo, Hokkaido University, Sapporo, Japan, for providing the expression plasmid of eGFP-GR. Financial support from Institute of Physics Belgrade through the grant by the Ministry of Science, Technological Development and Innovation of the Republic of Serbia, Swedish Research Council (2018-05337 and 2022-03402), Olle Engkvists Foundation (199-0480), Magnus Bergvall Foundation (2020-04043), Karolinska Institutet's Research Foundation Grants (2020-02325), Swedish Foundation for Strategic Research (SBE13-0115), NIH/NIAAA (R01AA028549), Strategic Research Program in Neuroscience (StratNeuro), ERASMUS+: European Union Programme for Education, Training, Youth and Sport to AJK and SNN, Qatar National Research Fund (PPM 04-0131-200019), and Science Fund of the Republic of Serbia (project HEMMAGINERO under PROMIS call, grant no. 6066079) is gratefully acknowledged.

■ REFERENCES

(1) Lambert, S. A.; Jolma, A.; Campitelli, L. F.; Das, P. K.; Yin, Y.; Albu, M.; Chen, X.; Taipale, J.; Hughes, T. R.; Weirauch, M. T. *Cell* **2018**, *172* (4), 650−665.
(2) Spitz, F.; Furlong, E. *Nat. Rev. Genet.* **2012**, *13* (9), 613−626.
(3) Bressloff, P. C.; Newby, J. M. *Rev. Mod. Phys.* **2013**, *85*, 135−196.
(4) Timney, B. L.; Raveh, B.; Mironska, R.; Trivedi, J. M.; Kim, S. J.; Russel, D.; Wente, S. R.; Sali, A.; Rout, M. P. *J. Cell. Biol.* **2016**, *215* (1), 57−76.
(5) Lin, D. H.; Hoelz, A. *Annu. Rev. Biochem.* **2019**, *88*, 725−783.
(6) Hampoelz, B.; Andres-Pons, A.; Kastritis, P.; Beck, M. *Annu. Rev. Biophys.* **2019**, *48*, 515−536.
(7) Qian, H.; Sheetz, M. P.; Elson, E. L. *Biophys. J.* **1991**, *60* (4), 910−921.
(8) Middeler, G.; Zerf, K.; Jenovai, S.; Thulig, A.; Tschödrich-Rotter, M.; Kubitscheck, U.; Peters, R. *Oncogene* **1997**, *14* (12), 1407−1417.
(9) Keminer, O.; Siebrasse, J. P.; Zerf, K.; Peters, R. *Proc. Natl. Acad. Sci. U.S.A.* **1999**, *96* (21), 11842−11847.
(10) Gebhardt, J. C. M.; Suter, D. M.; Roy, R.; Zhao, Z. W.; Chapman, A. R.; Basu, S.; Maniatis, T.; Xie, X. S.; et al. *Nat. Methods* **2013**, *10* (5), 421−426.
(11) Groeneweg, F. L.; van Royen, M. E.; Fenz, S.; Keizer, V. I. P.; Geverts, B.; Prins, J.; de Kloet, E. R.; Houtsmuller, A. B.; Schmidt, T. S.; Schaaf, M. J. M.; Tuckermann, J. P. *PLoS ONE* **2014**, *9*, 3e90532.
(12) Zhang, J.; Roggero, V. R.; Allison, L. A. *Vitam. Horm.* **2018**, *106*, 45−66.
(13) Sallaberry, I.; Luszczak, A.; Philipp, N.; Navarro, G. S. C.; Gabriel, M. V.; Gratton, E.; Gamarnik, A. V.; Estrada, L. C. *Sci. Rep.* **2021**, *11* (1), 24415.
(14) Magde, D.; Webb, W. W.; Elson, E. L. *Biopolymers* **1978**, *17* (2), 361−376.
(15) Gosch, M.; Blom, H.; Holm, J.; Heino, T.; Rigler, R. *Anal. Chem.* **2000**, *72* (14), 3260−3265.
(16) Brister, P. C.; Kuricheti, K. K.; Buschmann, V.; Weston, K. D. *Lab Chip.* **2005**, *5* (7), 785−791.
(17) Kunst, B. H.; Schots, A.; Visser, A. J. W. G. *Anal. Chem.* **2002**, *74* (20), 5350−5357.
(18) Fu, X.; Sompol, P.; Brandon, J. A.; Norris, C. M.; Wilkop, T.; Johnson, L. A.; Richards, C. I. *Nano Lett.* **2020**, *20* (8), 6135−6141.
(19) Brinkmeier, M.; Dörre, K.; Riebeseel, K.; Rigler, R. *Biophys. Chem.* **1997**, *66* (2−3), 229−239.
(20) Brinkmeier, M.; Dörre, K.; Stephan, J.; Eigen, M. *Anal. Chem.* **1999**, *71* (3), 609−616.
(21) Saha, I.; Saffarian, S.; Abraham, T. *PLOS ONE* **2019**, *1412*, No. e0225797.
(22) Yamamoto, J.; Mikuni, S.; Kinjo, M. *Biomed. Opt. Express.* **2018**, *9* (12), 5881−5890.
(23) Wiseman, P. W.; Squier, J. A.; Ellisman, M. H.; Wilson, K. R. *J. Microsc.* **2000**, *200* (Pt 1), 14−25.
(24) Hebert, B.; Costantino, S.; Wiseman, P. W. *Biophys. J.* **2005**, *88* (5), 3601−3614.
(25) Ashdown, G. W.; Cope, A.; Wiseman, P. W.; Owen, D. M. *Biophys. J.* **2014**, *107* (9), L21−L23.
(26) Sankaran, J.; Manna, M.; Guo, L.; Kraut, R.; Wohland, T. *Biophys. J.* **2009**, *97* (9), 2630−2639.
(27) Wohland, T.; Shi, X.; Sankaran, J.; Stelzer, E. H. K. *Opt. Express* **2010**, *18* (10), 10627−10641.
(28) Sankaran, J.; Shi, X.; Ho, L. Y.; Stelzer, E. H. K.; Wohland, T. *Opt. Express* **2010**, *18* (25), 25468−25481.
(29) Longfils, M.; Smisdom, N.; Ameloot, M.; Rudemo, M.; Lemmens, V.; Fernández, G. S.; Röding, M.; Lorén, N.; Hendrix, J.; Särkkä, A. *Biophys. J.* **2019**, *117* (10), 1900−1914.
(30) Krmpot, A. J.; Nikolić, S. N.; Oasa, S.; Papadopoulos, D. K.; Vitali, M.; Oura, M.; Mikuni, S.; Thyberg, P.; Tisa, S.; Kinjo, M.; Nilsson, L.; Terenius, L.; Rigler, R.; Vukojević, V. *Anal. Chem.* **2019**, *91* (17), 11129−11137.

(31) Oasa, S.; Krmpot, A. J.; Nikolić, S. N.; Clayton, A. H. A.; Tsigelny, I. F.; Changeux, J. P.; Terenius, L.; Rigler, R.; Vukojević, V. *Anal. Chem.* **2021**, *93* (35), 12011−12021.
(32) Nicolaides, N. C.; Chrousos, G.; Kino, T. *Glucocorticoid Receptor. Comprehensive Free Online Endocrinology Book*. Feingold, K. R.; Anawalt, B.; Boyce, A. et al., Eds. MDText.com, Inc.: South Dartmouth (MA); 2000-. PMID: 25905394.
(33) Mazaira, G. I.; Echeverria, P. C.; Galigniana, M. D. *J. Cell Sci.* **2020**, *133* (12), jcs238873.
(34) Noddings, C. M.; Wang, R.Y-R.; Johnson, J. L.; Agard, D. A. *Nature* **2022**, *601* (7893), 465−469.
(35) Frew, A. J. Glucocorticoids. in *Clinical Immunology* (5ed.), Eds.: Robert R., Rich, Thomas A., Fleisher, William T., Shearer, Harry W., Schroeder, Anthony J., Frew, Cornelia M., Weyand, Elsevier, 2019, 1165−1175.e1 (ISBN 9780702068966).
(36) Nicolaides, N. C.; Chrousos, G.; Kino, T. *Glucocorticoid Receptor. Comprehensive Free Online Endocrinology Book*. Feingold, K. R.; Anawalt, B.; Boyce, A., et al. Eds. MDText.com, Inc.: South Dartmouth (MA); 2000-. https://www.ncbi.nlm.nih.gov/books/NBK279171/.
(37) Presman, D. M.; Ganguly, S.; Schiltz, R. L.; Johnson, T. A.; Karpova, T. S.; Hager, G. L. *Proc. Natl. Acad. Sci. U.S.A.* **2016**, *113* (29), 8236−8241.
(38) Presman, D. M.; Hager, G. L. *Transcription* **2017**, *8* (1), 32−39.
(39) Paakinaho, V.; Johnson, T. A.; Presman, D. M.; Hager, G. L. *Genome Res.* **2019**, *29* (8), 1223−1234.
(40) Johnson, T. A.; Paakinaho, V.; Kim, S.; Hager, G. L.; Presman, D. M. *Nat. Commun.* **2021**, *12* (1), 1987.
(41) Robertson, S.; Rohwer, J. M.; Hapgood, J. P.; Louw, A.; Chang, A. Y. W. *PLoS ONE* **2013**, *8*, 5e64831.
(42) Tiwari, M.; Oasa, S.; Yamamoto, J.; Mikuni, S.; Kinjo, M. *Sci. Rep.* **2017**, *7* (1), 4336.
(43) Mazaira, G. I.; Piwien Pilipuk, G.; Galigniana, M. D. *Trends in Endocrinol. Metabol.* **2021**, *32* (10), 827−838.
(44) McNally, J. G.; Müller, W. G.; Walker, D.; Wolford, R.; Hager, G. L. *Science* **2000**, *287* (5456), 1262−1265.
(45) Morisaki, T.; Müller, W. G.; Golob, N.; Mazza, D.; McNally, J. G. *Nat. Commun.* **2014**, *5*, 4456.
(46) Vitali, M.; Bronzi, D.; Krmpot, A. J.; Nikolic, S. N.; Schmitt, F.; Junghans, C.; Tisa, S.; Friedrich, T.; Vukojevic, V.; Terenius, L.; Zappa, F.; Rigler, R. *IEEE J. Sel. Top. Quantum Electron.* **2014**, *20* (6), 344−353.
(47) Wohland, T.; Rigler, R.; Vogel, H. *Biophys. J.* **2001**, *80* (6), 2987−2999.
(48) Brinkmeier, M.; Rigler, R. *Exp. Techn. Phys.* **1995**, *41*, 205−210.
(49) Ries, J.; Chiantia, S.; Schwille, P. *Biophys. J.* **2009**, *96* (5), 1999−2008.
(50) Macháň, R.; Foo, Y. H.; Wohland, T. *Biophys. J.* **2016**, *111* (1), 152−161.
(51) Robertson, S.; Hapgood, J. P.; Louw, A. *Steroids* **2013**, *78* (2), 182−194.
(52) Vandevyver, S.; Dejager, L.; Libert, C. *Traffic* **2012**, *13* (3), 364−374.
(53) Stavreva, D. A.; Wiench, M.; John, S.; Conway-Campbell, B. L.; McKenna, M. A.; Pooley, J. R.; Johnson, T. A.; Voss, T. C.; Lightman, S. L.; Hager, G. L. *Nat. Cell Biol.* **2009**, *11* (9), 1093−1102.
(54) Nicolaides, N. C.; Chrousos, G.; Kino, T.n[Updated 2020 Nov 21]. In: *Glucocorticoid Receptor*; Feingold, K. R.; Anawalt, B.; Blackman, M. R.; et al., Editors. Available from:https://www.ncbi.nlm.nih.gov/books/NBK279171/.
(55) Jingjing, F.; Zexin, Z.; Xiaodong, W.; Jianfeng, X.; Yan, He *iScience* **2019**, *22*, 123−132.

https://doi.org/10.1021/acs.analchem.3c01427
Anal. Chem. 2023, 95, 15171−15179

International Journal of Biological Macromolecules 244 (2023) 125312

Contents lists available at ScienceDirect

International Journal of Biological Macromolecules

journal homepage: www.elsevier.com/locate/ijbiomac

Interactions of ultrashort laser pulses with hemoglobin: Photophysical aspects and potential applications

Mihajlo D. Radmilović [a], Ivana T. Drvenica [b], Mihailo D. Rabasović [a], Vesna Lj. Ilić [b], Danica Pavlović [a], Sho Oasa [c], Vladana Vukojević [c], Mina Perić [d,e], Stanko N. Nikolić [a,f], Aleksandar J. Krmpot [a,f,*]

[a] Institute of Physics Belgrade, University of Belgrade, Belgrade, Serbia
[b] Institute for Medical Research, National Institute of Republic of Serbia, University of Belgrade, Belgrade, Serbia
[c] Department of Clinical Neuroscience, Karolinska Institutet, Stockholm, Sweden
[d] Faculty of Biology, University of Belgrade, Belgrade, Serbia
[e] Institute of Molecular Genetics and Genetic Engineering, University of Belgrade, Belgrade, Serbia
[f] Division of Arts and Sciences, Texas A&M University at Qatar, Doha, Qatar

ARTICLE INFO

Keywords:
Erythrocytes
Two-photon excitation fluorescence
Hemoglobin photoproduct
Femtosecond laser
Protoporphyrin IX

ABSTRACT

Hemoglobin (Hb), a life-sustaining and highly abundant erythrocyte protein, is not readily fluorescent. A few studies have already reported Two-Photon Excited Fluorescence (TPEF) of Hb, however, the mechanisms through which Hb becomes fluorescent upon interaction with ultrashort laser pulses are not completely understood. Here, we characterized photophysically this interaction on Hb thin film and erythrocytes using fluorescence spectroscopy upon single-photon/two-photon absorption, and UV-VIS single-photon absorption spectroscopy. A gradual increase of the fluorescence intensity, ending up with saturation, is observed upon prolonged exposure of Hb thin layer and erythrocytes to ultrashort laser pulses at 730 nm. When compared to protoporphyrin IX (PpIX) and oxidized Hb by H_2O_2, TPEF spectra from a thin Hb film and erythrocytes showed good mutual agreement, broad peaking at 550 nm, supporting hemoglobin undergoes degradation and that same fluorescent specie(s) originating from the heme moiety are generated. The uniform square shaped patterns of the fluorescent photoproduct exhibited the same level of the fluorescence intensity even after 12 weeks from the formation, indicating high photoproduct stability. We finally demonstrated the full potential of the formed Hb photoproduct with TPEF scanning microscopy towards spatiotemporally controlled micropatterning in HTF and single human erythrocyte labelling and tracking in the whole blood.

1. Introduction

Human adult hemoglobin (Hb) is an iron-containing metalloprotein in erythrocytes, the primary function of which is to transport oxygen from the lungs to all other organs and tissues. It is made up of two α- and two β-polypeptide chains, each associated with one hem prosthetic group [1]. While the absorption spectrum of oxyhemoglobin (oxyHb) shows several bands, as the intense Soret or B band in the region of 370 nm - 450 nm and the so-called Q-band in the region of 500 nm – 650 nm in the porphyrin ring [2], the conventional single-photon excitation fluorescence (SPEF) of Hb is not or hardly detectable due to the fast non-radiative decay that dominates over spontaneous fluorescence emission [3–5]. In contrast, the intense two-photon absorptivity of Hb in the near-infrared range [6] followed by strong fluorescence emission, have made Two-Photon Excited Fluorescence (TPEF) imaging possible [4] and applicable in a number of studies: for erythrocytes imaging [7,8], analysis of residual Hb distribution in empty erythrocytes membranes (i.e., erythrocyte ghosts) [9], in vivo imaging of microvasculature [10–12], and even time-resolved diagnostic imaging [13]. Of note, Hb excitation through a two-photon absorption process, which is governed by significantly different selection rules than single photon absorption, is described in detail in [3,5], while the corresponding single and two photon absorption spectra are given in [6].

Due to high absorptivity of Hb in the VIS and near infrared (NIR) region, erythrocytes are also readily imaged using absorption-based techniques, such as photo-acoustic microscopy [14]. Photo-acoustic

* Corresponding author: Institute of Physics Belgrade, University of Belgrade, Belgrade, Serbia, Pregrevica 118, Belgrade 11080, Serbia.
E-mail address: krmpot@ipb.ac.rs (A.J. Krmpot).

https://doi.org/10.1016/j.ijbiomac.2023.125312
Received 21 March 2023; Received in revised form 16 May 2023; Accepted 8 June 2023
Available online 10 June 2023

microscopy is an imaging technique that leverages the non-radiative decay of Hb, which happens to be the most frequently used contrast agent for this modality [15–17]. Another type of label free imaging techniques, used for erythrocytes imaging is the nonlinear Third Harmonic Generation (THG) microscopy. This method has demonstrated efficacy in imaging erythrocytes contained within transfusion bags. [18].

The significance of photochemical manipulation of proteins is especially boosted by the discoveries of their optogenetics, photobiomodulation and bioimaging applications in recent years [19,20]. Understanding the photophysical and photochemical processes during the interaction of Hb with ultrashort laser pulses is of great importance for the development of functional imaging aimed for the assessment of erythrocytes functional status [21], where hemoglobin is the main intracellular protein of these cells. Besides, a better understanding of the interaction of Hb with ultrashort laser pulses could contribute to the development of new methods for the characterization and tracking of extracellular Hb presence. This implies extracellular Hb from endogenous sources due to hemolysis (in all diseases where in common feature is hemoglobinemia, such retinopathy, neuropathy, nephropathy and brain hemorrhages) [22], or exogenous sources, such in the cases of use of hemoglobin-based oxygen carriers [23] and hemoglobin-based drug delivery system, which have great potential in cancer therapy [22,24,25]. So far it was only shown that upon ultrashort laser pulses interaction with Hb, there is relation between TPEF spectra of heme and hemoglobin, as stated in [3].

However, despite already established, as well as emerging applications of Hb-based TPEF microscopy, the origin of generated fluorescence still needs to be completely understood. While it was initially proposed that the origin of the observed Soret fluorescence (420–460 nm) with a fluorescence emission peak at 438 nm originates from Hb [3], it was shown that TPEF does not directly originate from Hb, but rather from a photoproduct created upon the interaction of ultrashort laser pulses used in this nonlinear imaging technique with Hb [26]. This lack of basic understanding motivated us to deeper study ultrashort laser pulses interaction with Hb, with a particular focus on characterizing the durability of the Hb photoproduct and experimental conditions under which it is being formed. Since we efficiently demonstrated utility of TPEF microscopy to image the erythrocytes, the ultrashort laser pulses interaction with Hb was further photophysically characterized on thin Hb films using fluorescence spectroscopy upon two-photon absorption, UV-VIS single-photon absorption spectroscopy, and spectral fluorescent imaging. To examine whether degradation of the heme moiety occurs when ultrashort laser pulses used in TPEF microscopy imaging interact with Hb, spectroscopic properties of heme precursor protoporphyrin IX (PpIX), a heterocyclic organic compound that consists of four pyrrole rings, were analyzed. In addition, photophysical properties of the Hb photoproduct were compared to photophysical properties of compound (s) formed under Hb oxidation with hydrogen peroxide (H_2O_2) [27,28] to determine whether there are differences in the optical response of products formed under chemically induced Hb degradation. Finally, we examined the potential of the Hb photoproduct to be used for micropatterning and single erythrocyte tracking.

2. Materials and methods

2.1. Sample collection and processing

Venous blood from healthy human volunteer was collected at the Institute for Transfusiology and Hemobiology, Military Medical Academy, Belgrade, Serbia. The protocol was approved by the Institutional Ethical Review Board (No 9/2021). In conformance with the World Medical Association Declaration of Helsinki, informed consent was obtained from potential participants. The blood was drawn using vacutainer tubes (10 mL plastic vacutainer (BD Vacutainer® EDTA Tubes) with BD Hemogard™ lavender closure containing 18 mg K2EDTA). To prepare slides for direct TPEF microscopy imaging of erythrocytes, 10 μL of whole blood was diluted in isotonic saline solution (0.9 % NaCl, Natrii chloridi infundibile 9 g/L, Hemofarm, Serbia) in the volume: volume ratio 1:30. 3 μL of diluted whole blood sample was smeared onto a microscope slide, covered by a No. 1.5 coverslip and sealed.

2.2. Hb isolation

To isolate hemoglobin, human erythrocytes were precipitated by whole blood centrifugation. To this aim, 10 mL of whole blood was centrifuged at 1811 $\times g$ for 20 min at 4 °C (Megafuge 1.0R, Heraus centrifuge, Langenselbold, Germany). The supernatant, consisting of leucocytes in plasma, was carefully removed by aspiration and discarded. The precipitated erythrocytes were resuspended in isotonic saline solution (0.9 % NaCl, Natrii chloridi infundibile 9 g/L, Hemofarm, Serbia) in a volume:volume ratio of 1:4 and the suspension was homogenized by fine twisting the test tube. The remaining plasma proteins were removed by centrifugation of the erythrocyte suspension at 1257 $\times g$ for 10 min at 4 °C. These steps were repeated three times. Finally, the precipitated erythrocytes (packed) were resuspended in the isotonic phosphate buffered saline solution (PBS; 0.8 % saline buffered with 10 mM sodium phosphate, pH 7.2–7.4) in the volume: volume ratio of 1:4.

The hemolysis of erythrocytes suspension was performed using hypotonic 5 mM sodium phosphate buffer, pH 7.2, at 4 °C. Specifically, in 1 mL of erythrocytes suspension in PBS, 9 mL of 5 mM sodium phosphate buffer was added, and the tube was slightly mixed and then left at 4 °C for 1 h. The suspension was centrifuged at 3220 $\times g$ for 40 min at 4 °C. After centrifugation, the supernatant fluid containing released Hb molecules was collected, and the aliquots were filtered through 0.2 μm syringe filter. If not used immediately, the samples of Hb were aliquoted and stored at −20 °C for future use. Just before the experiment, a Hb aliquot would be thawed, and its concentration checked. Only one freeze-thaw cycle was allowed so the aliquots were discarded after experiment performed. All tests were done with Hb stored for less than two years from Hb isolation, since our previous results showed that it remains intact-undecomposed and non-aggregated under these storage conditions [29].

2.3. Hb thin film preparation for TPEF microscopy imaging

Thin Hb films were prepared by smearing 5 μL of Hb on the microscope slide, air-drying for 3 min and covered by No. 1.5 coverslip and sealed. The film thickness was <50 μm, as measured by confocal laser scanning microscopy, i.e., scanning along the z-axis. The smallest step of motorized the microscope stage stepper motor was 0.3 μm.

2.4. Protoporphyrin IX (PpIX) thin film preparation for TPEF microscopy imaging

Protoporphyrin IX (PpIX) in the form of a disodium salt was purchased from Sigma Aldrich (USA) and used without further purification. 20 μM stock solution of PpIX was prepared by dissolving 0.1 g of PpIX in 1 M HCl to the total volume of 50 mL. The stock solution was stored at 25 °C protected from light, to minimize photo-induced degradation of PpIX. To prepare slides for TPEF spectroscopy and spectral imaging, the PpIX stock solution was diluted in 1 × PBS (Sigma Aldrich, 140 mM NaCl, 10 mM phosphate buffer, and 3 mM KCl, pH 7.4) to the final concentration of 5 μM. 5 μL of this solution was placed on a microscope slide and treated in the same way as for Hb thin film preparation described above.

2.5. TPEF imaging of Hb treated with H_2O_2

The 22.5 M H_2O_2 was diluted using PBS (Sigma Aldrich, 140 mM NaCl, 10 mM phosphate buffer, and 3 mM KCl, pH 7.4) to a concentration of 250 μM. Further, 1 mL of Hb at a concentration of 22.3 g/L,

was incubated with 0.5 mL of 250 μM H_2O_2 for 30 min at room temperature (≈ 21 °C). After incubation, 5 μL of this mixture was placed on a microscope slide, smeared, dried, covered by a #1.5 coverslip and sealed.

2.6. TPEF scanning microscopy, micropatterning, and micro-spectroscopy

The experimental setup and home built TPEF microscope have been previously reported [30,31]. In this work, we upgraded it for micropatterning and micro-spectroscopic experiments. Schematic drawing of the experimental setup is shown in Fig. 1. The Ti:Sapphire laser (Coherent, Mira 900-F), pumped by a frequency-doubled Nd:YVO4 laser (Coherent, Verdi V10), was used to generate ultrashort laser pulses with the repetition rate of 76 MHz and pulse duration of 160 fs. Galvo-scanning mirrors (Cambridge Technology) are used for raster scanning and micropatterning. Two microscope objectives were used in this study: EC Plan-NEOFLUAR 40× /1.3 N.A. oil (Carl Zeiss) for erythrocyte imaging and Plan-Apochromat 20× /0.8 N.A. air (Carl Zeiss) for Hb micropattering. The laser beam was expanded to fulfill the back aperture of the objective lens. A short-pass dichroic mirror was used to reflect the laser beam towards the objective lens and transmit the signal to the 15.1-megapixel digital single-lens reflex (DSLR) camera (Canon, EOS 50D) and the Photomultiplier Tube (PMT) (RCA, PF1006). The DSLR camera was used for taking bright-field images. We removed the infrared filter from the camera to see the back reflection of the laser beam from the cover glass for the purpose of system alignment and to facilitate axial positioning of the thin Hb layer. Band pass filters (VIS and/or 450 nm short pass) were placed in front of the PMT to collect Hb photoproduct fluorescence. A 700 nm long pass filter was used to remove parasitic laser lines shorter than 700 nm. A short pass 700 nm filter was placed in front of the PMT detector to additionally remove back scattered laser light. The Hb photoproduct formation and erythrocytes imaging were performed at 730 nm ultrashort laser pulses. This wavelength is chosen as optimal according to the optical setup and properties of Hb molecule, whilst details are given in our previous study [9].

In addition, we were able to record in situ TPEF emission spectra of the Hb photoproduct and erythrocytes using fiber-coupled, thermo-electrically (TE) cooled charge-coupled device (CCD) spectrometer with reduced thermal noise (Glacier X, BWTEK). To collect the TPEF emission from arbitrary chosen excitation point, the fiber was attached to the adapter plate (Thorlabs, S1SMA) mounted on the precise translation stage (Thorlabs, ST1XY-D/M). Henceforth, we refer to the in situ acquisition of TPEF emission spectra from an arbitrarily chosen point in

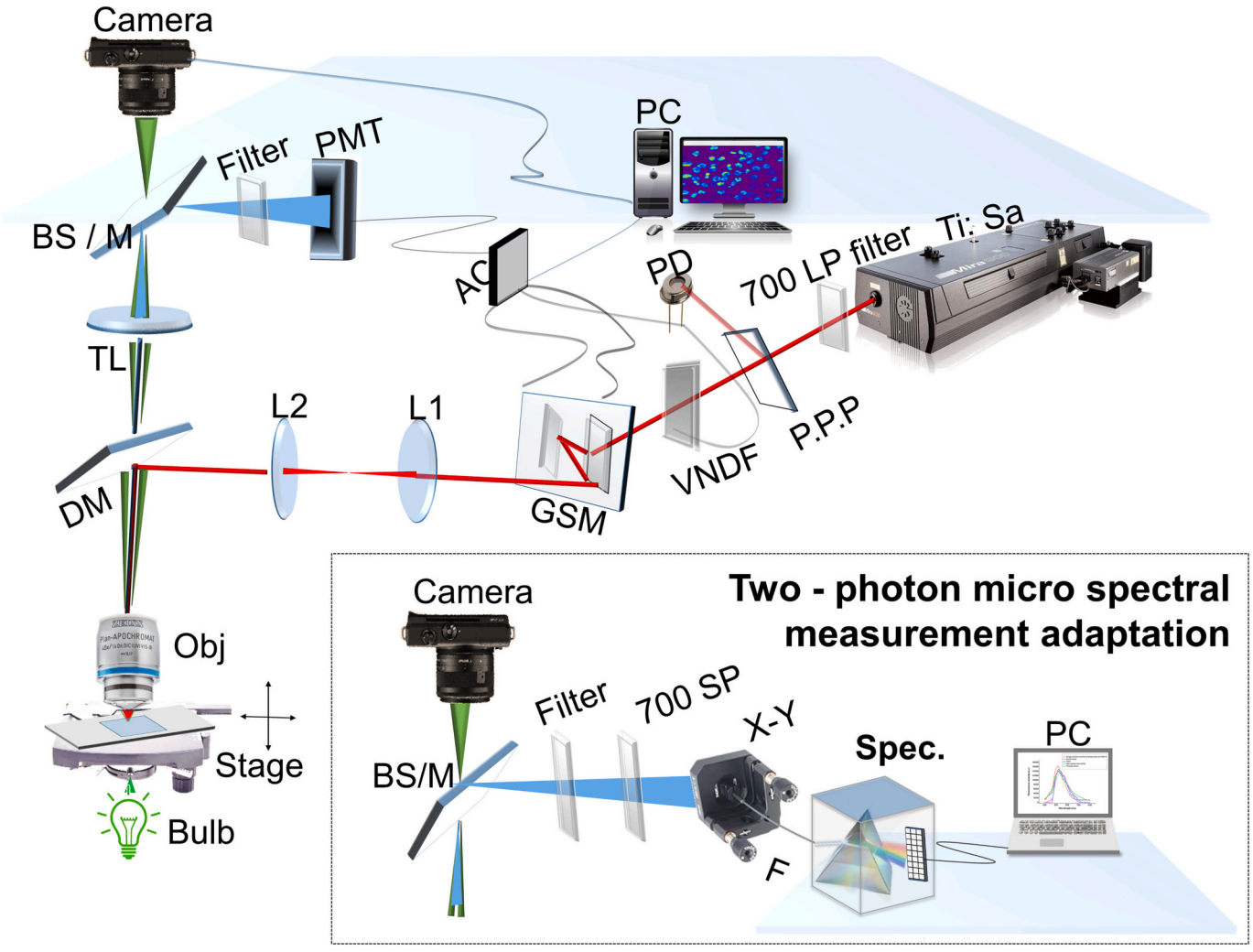

Fig. 1. Schematic 3D drawing of the home-built TPEF microscope with specific adaptations for in situ emission spectra measurement (inset). The TPEF microscope comprising the: Ti:Sa, Ti:Sapphire laser; 700 LP filter, 700 nm long pass filter; P.P.P., plan parallel plate; PD, photo-diode; VNDF, variable neutral density filters; GSM, galvo scanning mirrors; L1 and L2 lenses; AC, acquisition card; DM, dichroic mirror (short pass); Bulb, bulb for bright-field imaging; TL, tube lens; BS/M, beam splitter or mirror; PMT, photomultiplier tube. Inset: The module for micro spectral measurements comprises: 700 SP filter, 700 nm short pass filter; X-Y F, functional X-Y stage controller, Spec, compact high-performance CCD spectrometer with TE cooling.

the sample as micro-spectroscopy. Square-shaped TPEF emission patterns were inscribed by raster-scanning of the sample, whereas arbitrary patterns were inscribed by scanning the beam along a corresponding line. The latter is enabled by a specially written program that recognizes arbitrary figures in both vector, and bitmap formats, and controls the dwell time, power and writing speed of the fs laser beam.

2.7. Single-photon excitation fluorescence (SPEF) and confocal laser scanning microscopy (CLSM)

Hb photoproduct lastingness was assessed by single-photon excitation fluorescence (SPEF) using a confocal laser scanning microscope (LSM 510, Carl Zeiss), equipped with an Ar multi-line (458 nm, 488 nm, and 514 nm) laser and a Plan Apochromat 40 × 1.3 N.A. oil-immersion objective (Carl Zeiss). Optical slice thickness was set to <4.3 μm, by choosing the pinhole diameter of 5.65 Airy units, to collect as much as possible fluorescence light from the photoproduct and to increase Signal to noise ratio (SNR). The best signal-to-noise-ratio in the SPEF images of the Hb photoproduct in the square-shaped patterns was at 488 nm excitation wavelength. Emission was collected using the main dichroic beam splitter, HFT 488 nm and long pass filter LP 505 nm.

2.8. Absorption spectra measurements

Absorption spectra of Hb and TPEF irradiated Hb in the intact thin film were measured using the Beckman Coulter DU700 spectrophotometer. A special aluminum holder was designed to hold the microscope slide with Hb specimen, to mimic a cuvette for the spectrophotometer. The dimensions of the holder were 45 mm × 10 mm × 10 mm. The mask with the round hole was placed over the cover glass with Hb layer and photoproduct square pattern. The hole matches the Hb photoproduct enabling the portion of incident light from the spectrophotometer to pass only through the region where the Hb photoproduct is. Prior to the absorption measurements, necessary calibration was performed for the overall transmission.

2.9. Spectral imaging

Spectral confocal Laser Scanning Microscopy (CLSM) imaging was performed using an LSM880 (Carl Zeiss) instrument, equipped with several lasers: three diode lasers (543 nm and 633 nm), and an Ar-ion laser (lines: 458 nm, 488 nm and 514 nm); objective lens (Plan-Apochromat 20×/0.8 N.A.); and gallium arsenide phosphide (GaAsP) spectral array detector. The pinhole size was adjusted to 33 μm (1 Airy unit at 488 nm). The fluorescence (single-photon excitation fluorescence (SPEF)) was spectrally split by a diffraction grating and detected in the 418 nm - 723 nm range with a 3 nm wavelength resolution using the GaAsP spectral array detector. For all wavelengths, the laser power was 9.4 μW at the objective lens. SPEF emission spectra are displayed only for wavelengths that are longer than the wavelength of the excitation laser.

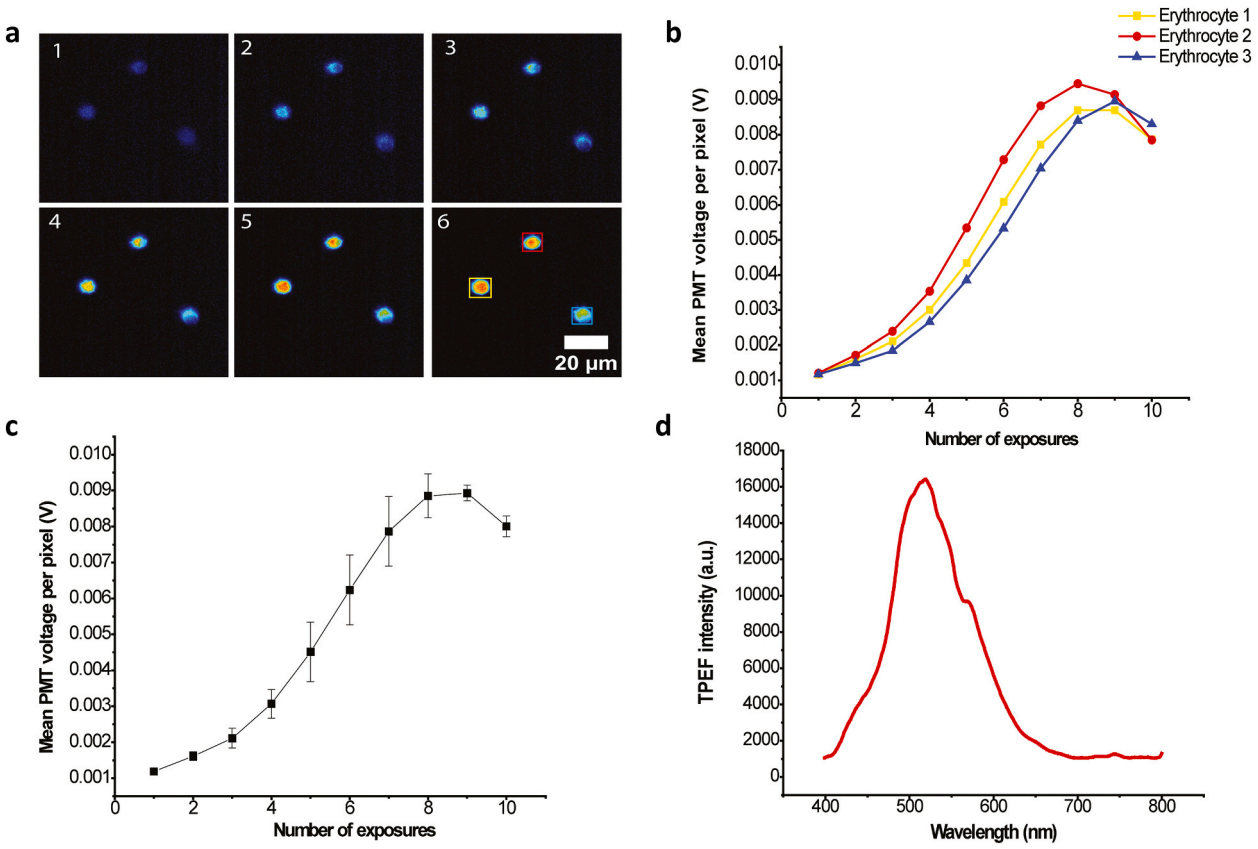

Fig. 2. TPEF microscopy enables both selective erythrocyte photolabeling and imagining in the whole blood. (a) Label-free TPEF microscopy images (6 out of 10) of erythrocytes. The image pixel size is 1024 × 1024 pixels; it is averaged out from 30 scans with the pixel dwell time is 8.53 e^{-4} s. In total, each image took 26.1 s to be recorded, which represents a single unit of exposure. The image intensity is represented by pseudocolor code of PMT voltage values for each pixel (dark blue – lowest TPEF signal, red – highest TPEF signal); (b) Mean pixel values of PMT voltage proportional to the TPEF intensity for each ROI (yellow, red and blue square box) shown in (a)), presented with the curve of the corresponding colour. Mean pixel values were calculated from region of interest (ROI), (yellow, red and blue squares) and for each image, the square size is 100 × 100 pixels; (c) Black curve is average of three erythrocytes shown in (b), standard error was presented for the ordinate (voltage); (d) TPEF spectrum recorded in an arbitrarily selected point in a single erythrocyte, using micro-spectral measurement adaptation. (For interpretation of the references to colour in this figure legend, the reader is referred to the web version of this article.)

3. Results and discussion

3.1. Photo-labeling of erythrocytes using TPEF microscopy and micro-spectroscopy analysis of erythrocytes fluorescence emission

To confirm already demonstrated feasibility of TPEF microscopy for erythrocytes imaging [8,9], we initially performed an analysis on diluted human whole blood. The blood was diluted in order to get sparse erythrocytes that are not stacked to each other and clearly distinguishable at the image. TPEF microscopy allowed us to selectively photo-label individual erythrocytes in a whole blood specimen. Here, photo-labeling refers to the process of rendering fluorescent individual erythrocytes using ultrashort 730 nm laser pulses. The gradual increase of TPEF from the irradiated erythrocytes as the laser beam scans over them is shown in Fig. 2a. This result was in accordance with the already demonstrated increase of the fluorescence intensity in the erythrocytes upon illumination with ultrashort laser pulses and formation of a so called Hb photoproduct [26]. Herein, the increase of TPEF signal has been proven through the PMT voltage dependence on the number of exposures (Fig. 2b), since PMT voltage is directly proportional to the fluorescence intensity. The abscissa shows the number of exposures whereat one exposure refers to a series of 30 consecutive image frames acquired by raster laser scanning, the acquisition of which lasted ~26.1 s. The ordinate shows the mean PMT voltage *per* exposure per pixel of the rectangular regions given in the last image (no.6) at Fig. 2a. The average PMT voltage i.e., fluorescence intensity curve is presented in Fig. 2c. In addition, the TPEF emission spectrum was acquired (Fig. 2d) using a CCD array fiber optic spectrometer mounted on the nonlinear microscope (Fig. 1 inset).

3.2. Hb photoproduct formation using 730 nm ultrashort laser pulses

To ascertain that the observed increase in TPEF intensity comes solely from the Hb photoproduct that was formed upon erythrocytes illumination with ultrashort 730 nm laser pulses, but not from other molecules, we performed experiments using isolated Hb. To this aim, square-shaped patterns were inscribed in the thin Hb film in a spatio-temporally controlled manner: 1024 × 1024 pixels at average laser power of 20 mW (Fig. 3a). Both SPEF (Fig. 3b) and TPEF images (Fig. 3c) were acquired. The acquisition procedure was repeated 10 times

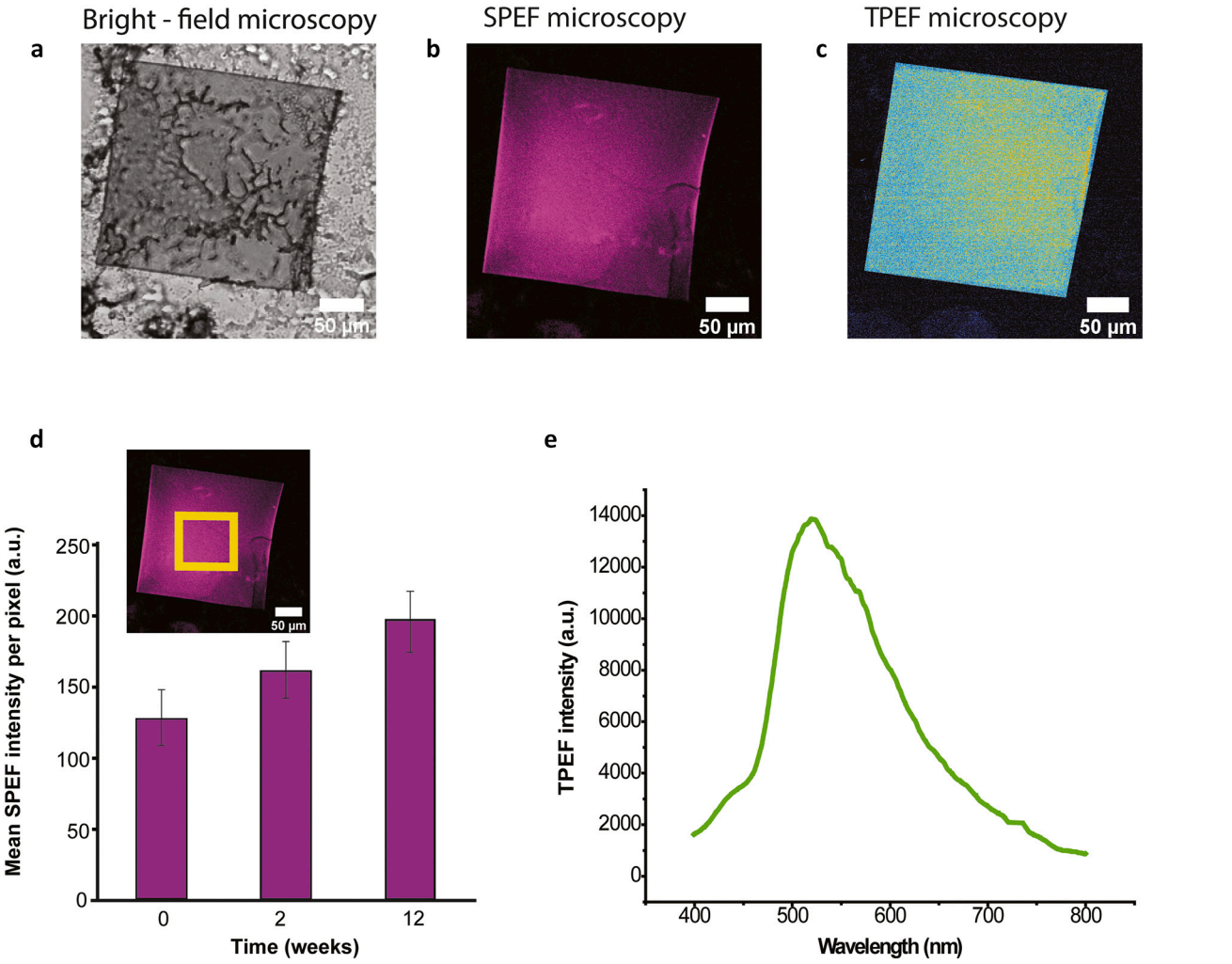

Fig. 3. SPEF spectra of the Hb photoproduct formed upon Hb thin film exposure to ultrashort 730 nm laser pulses. (a) Bright-field microscopy image of the specimen shown reveals that the Hb photoproduct (dark grey square) is less optically translucent than Hb (light grey surrounding); (b) Single-photon excitation fluorescence (SPEF) emission image of the specimen shown in (a) reveals that Hb photoproduct SPEF can be excited at 488 nm (plum square) whereas Hb cannot (black surrounding); (c) Representative TPEF microscopy image showing intense emission in the yellow-green square-shaped area where the Hb photoproduct was formed, in comparison to the non-fluorescent Hb in the surrounding (black); (d) The Hb photoproduct is lasting and its SPEF emission properties are preserved over extended time, as evident from the mean SPEF intensity per pixel (measured in the yellow rectangular area in the inset); (e) TPEF spectrum of the Hb photoproduct recorded in an arbitrarily selected point in the thin layer. (For interpretation of the references to colour in this figure legend, the reader is referred to the web version of this article.)

(number of exposures) after 8 scanning times the maximum TPEF intensity was reached, after that the TPEF intensity started to decrease due to photobleaching (see Fig. 2b). To demonstrate that strong TPEF emission is observed only from the region that was exposed to ultrashort 730 nm laser pulses, the field of view, i.e., the scanned region was expanded, the average laser power was lowered down to 2.5 mW and a TPEF image was acquired (Fig. 3c). In addition, bright field imaging clearly showed that transmission properties of the extensively illuminated square-shaped area have become less transparent (Fig. 3a). Finally, using single-photon excitation at 488 nm, we detected SPEF emission from the Hb photoproduct formed only in the region exposed to ultrashort 730 nm laser pulses, but not in the surrounding region (Fig. 3b, plum). Here, it is worth reminding that Hb is not naturally fluorescent [26], which is obvious from the dark region around the fluorescent square (Fig. 3a and c). The photoproduct formation depends on exposure time and laser average power, among other parameters that are fixed in our experiment (wavelength, repetition rate, pulse duration etc.). The fluorescence intensity signal starts to increase even after the first exposure. For Hb isolated as stated in previous Section 2.2, TPEF intensity of the Hb photoproduct becomes detectable at a laser excitation power of approximately 10 mW after the first exposure, which corresponds to the deposited energy of 261 mJ on the square area 62,500 μm^2.

Similarly, to erythrocytes, the increase in fluorescence intensity was gradual with the number of scanning times (i.e., number of exposures) across the square area which is proportional to the total absorbed dose/energy (plot is equivalent to the plot shown in (Fig. 2b). This suggests that ultrashort laser pulses interact directly with Hb to form photoproduct in the erythrocyte. Longitudinal SPEF recordings showed that the Hb photoproduct is stable over a considerably long time (Fig. 3d). The TPEF spectrum of the Hb photoproduct in the thin film showed maximum at (550 ± 2) nm (Fig. 3e), the same to the TPEF emission spectrum recorded from a single erythrocyte (Fig. 2c). This observation suggests that ultrashort laser pulses interact solely with Hb in the erythrocytes from the whole blood, forming the same photoproduct. Or, at least, one could say that the interaction of the ultrashort laser pulses with other molecular species in erythrocytes is negligible, at the given conditions. The dynamic of Hb photoproduct formation is also the same in erythrocytes and Hb thin film: gradual increase of the fluorescence intensity with number of exposures that end up with saturation plateau. We might anticipate that interaction of ultrashort laser pulses with Hb is mainly followed up with an intensive Hb degradation, due to the increasing fluorescence intensity over time and the eventual saturation of the fluorescence when the majority of Hb in focal volume is degraded.

3.3. UV-VIS absorption spectroscopy of TPEF irradiated and non-irradiated thin Hb layer

To characterize the single-photon absorption spectra of Hb and the TPEF irradiated Hb in the intact thin film, measurements were performed outside and inside the illuminated square-shaped region (Fig. 3a-c), respectively. The term irradiated Hb was used because of the measurement procedure of the absorption spectra. Since photoproduct was formed in a thin layer of Hb film so that both Hb and the photoproduct are on the same optical path. In addition, some Hb remains unconverted into the photoproduct even in the treated volume. That's why the recorded absorption spectrum is not solely from the photoproduct, but from both, photoproduct and Hb together.

As expected, the UV-VIS absorption spectrum of Hb thin film showed spectral bands that are characteristic of oxyHb: an absorption band in the UV region with a maximum at $\lambda_{max}^{UV} \approx$ 275 nm due to $\pi \rightarrow \pi^*$ transitions; and several absorption bands, such as the λ_{max}^{His} 350 nm attributed to the absorption of the non-covalent bond between iron and histidine in the Hb protein part; the Soret or B band λ_{max}^{Soret}at (410 ± 2) nm and the Q band with two transitions, the $\lambda_{max}^{Q\beta}\beta$ band at 539 nm and $\lambda_{max}^{Q\alpha}\alpha$ band at 577 nm [32] (Fig. 4, blue line). Similarly, the UV-VIS absorption spectrum of the TPEF irradiated Hb thin film showed the same bands, but clear differences in band intensity and/or peak position were noted (Fig. 4, red line). The observed differences and important relations between them are summarized in Table 1.

A 7 nm bathochromic shift of the Soret band was noted in the irradiated Hb with a significant decrease in Soret band intensity (Fig. 4, Table 1). The bands in the VIS part of the Hb absorption spectrum originate from the heme group, and changes in their positions and intensities are indicators of displacements along the normal coordinates of the porphyrin ring [33]. The ratio of $\Delta\alpha/\Delta\beta$ was <1 for both Hb and Hb after irradiation with fs laser pulses (Fig. 4, Table 1). Still, this ratio in irradiated Hb was significantly lower than untreated Hb indicating the degradation of Hb upon the interaction with fs laser pulses. The mentioned 7 nm bathochromic shift of the Soret peak in the irradiated Hb, indicates the transformation of oxygenated to oxidized Hb species [33–35]. Reduced ratio A_{max}^{Soret}/A_{560} ratios of irradiated Hb in comparison to intact Hb indicate free heme presence and breakdown of Hb molecule [33].

3.4. Single-photon excitation fluorescence (SPEF) emission spectra of thin film Hb photoproduct by confocal microscopy spectral imaging

The Hb photoproduct square shape patterns are imaged using single-photon excitation confocal microscopy (Fig. 5a), and square shape patterns (Fig. 5b) were formed previously by the exposure to the ultrashort laser pulses as explained in Section 2.9. SPEF emission spectra were recorded for different excitation wavelengths (Fig. 5c) from the Hb region of interest 1 (ROI1, dashed circle) and from the photoproduct region of interest (ROI 2, solid circle). Excitation efficiency dependence was constructed by extracting emission maxima at different excitation wavelengths (Fig. 5d). The SPEF emission spectrum acquired using the shortest excitation wavelength, λ_{exc} = 458 nm, showed a fluorescence emission maximum at λ_{em} = 550 nm and a broad emission band (red curve), being good agreement with TPEF emission spectrum (Fig. 3e). The emission spectra acquired using excitation wavelengths longer than 458 nm, λ_{exc} > 458 nm, showed emission maxima that are slightly red shifted to one another, possibly suggesting that the Hb photoproduct may comprise several spectrally distinct molecules. The existence of more than one molecular species is confirmed by the absorption spectroscopy (Section 3.3) and it is in accordance with the results given in

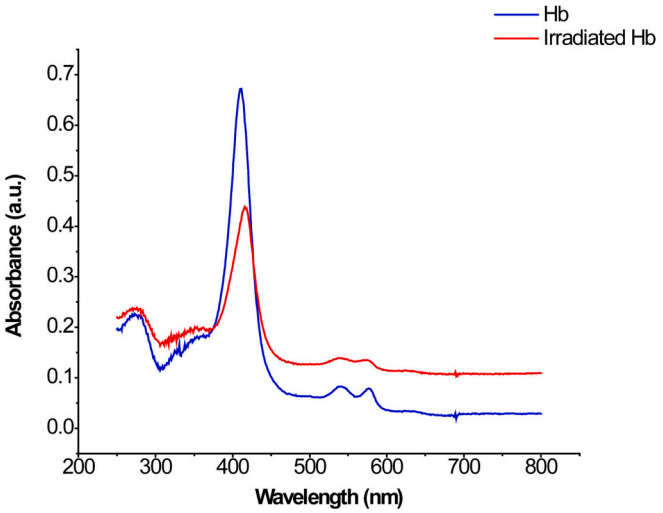

Fig. 4. Absorption spectra of Hb and the irradiated Hb thin layers. UV-VIS absorption spectra of intact Hb thin layer (blue) and irradiated Hb that contains the photoproduct (red line). All characteristics of absorption spectra are given in Table 1. (For interpretation of the references to colour in this figure legend, the reader is referred to the web version of this article.)

Table 1
Characteristics of Hb and Hb photoproduct UV-VIS absorption spectra. The mean and standard deviation of four separate absorbance measurements is represented.

Absorption band maximum position / intensity	Hb	Irradiated Hb region containing the photoproduct
λ_{max}^{UV} / nm	273 ± 2	272 ± 2
λ_{max}^{His} / nm	351 ± 2	351 ± 2
λ_{max}^{Soret} / nm	410 ± 2	417 ± 2
$\lambda_{max}^{Q\beta}$ / nm	539 ± 2	538 ± 2
$\lambda_{max}^{Q\alpha}$ / nm	577 ± 2	576 ± 2
A_{max}^{UV}	0.226 ± 0.003	0.237 ± 0.001
A_{max}^{His}	0.179 ± 0.008	0.200 ± 0.002
A_{max}^{Soret}	0.671 ± 0.002	0.438 ± 0.001
$A_{max}^{Q\beta}$	0.082 ± 0.007	0.139 ± 0.003
$A_{max}^{Q\alpha}$	0.079 ± 0.001	0.134 ± 0.003
A_{560}	0.063 ± 0.002	0.132 ± 0.005
$\Delta A_{Q\alpha}/\Delta A_{Q\beta} = (A_{max}^{Q\alpha} - A_{560})/(A_{max}^{Q\beta} - A_{560})$	0.804 ± 0.027	0.371 ± 0.014
$A_{max}^{Soret} / A_{max}^{Q\alpha}$	8.506 ± 0.046	3.254 ± 0.007
$A_{max}^{Soret} / A_{max}^{UV}$	2.962 ± 0.042	1.848 ± 0.014

[33–35]. In addition, excited by the different wavelengths one molecular species would give just the change in the fluorescence intensity while keeping the position of the spectral maximum fixed.

3.5. TPEF emission of PpIX

To characterize the Hb iron ion role in Hb photoproduct formation, TPEF spectra of PpIX were investigated. The obtained TPEF emission spectrum of PpIX (Fig. 6a black line) shows both distinctions and similarities to TPEF spectrum of the Hb photoproduct (Fig. 3e). Most notably, unlike Hb, PpIX is easily excited and TPEF emission is readily observed even at low irradiation intensities (Fig. 6a, black curve). However, the TPEF emission observed at low irradiation intensities originated predominantly from unaltered PpIX molecules, as evident from previously published data [36]. When using higher laser power (e.g., 16.5 mW), the TPEF emission spectrum of PpIX is considerably changed: becoming broader and with a maximum peak around 550 nm (Fig. 6a, blue curve), resembling the TPEF emission spectrum of the Hb photoproduct (Fig. 3e). This, in turn, suggests that intense irradiation of PpIX leads to the generation of PpIX photoproduct that is similar to the Hb photoproduct, so that iron atom is not necessary for the formation of Hb photoproduct.

3.6. TPEF emission of Hb treated with H_2O_2

It has been shown that Hb treatment with H_2O_2 also leads to the formation of a fluorescent product [27,28]. To determine whether similar photoproducts are formed under Hb treatment with H_2O_2 as upon its interaction with 730 nm ultrashort laser pulses, we compared how the TPEF intensity changed when increasing the exposure time (Fig. 6b) and TPEF spectra (Fig. 6c). Unlike for Hb thin film, where increase of fluorescence intensity and saturation were eventually observed (Fig. 6b, light green squares), the fluorescence of the H_2O_2-treated Hb shows a high TPEF emission intensity immediately upon excitation, even at the first exposure (Fig. 6b, olive dots). The increase of fluorescence in Hb film (Fig. 6b, light green) has the same trend as in erythrocytes (Fig. 2b). The slight discrepancy is due to different number of graph points and concentration of Hb in erythrocytes and thin Hb film. Moreover, the observed TPEF intensity was independent on the number of exposures, i.e., absorbed dose, of 730 nm ultrashort laser pulses. This confirms the hypothesis of the photodegradation of Hb involved in the photoproduct formation, since interaction between Hb and a 10 (or more) fold excess H_2O_2 leads to Hb degradation according to the [28]. Finally, the TPEF spectrum of H_2O_2-treated Hb thin film showed very good agreement with the TPEF spectra of Hb thin film treated with ultrashort laser pulses, the erythrocytes and the PpIX layer under high laser power, 16.5 mW (Fig. 6c).

Taken together, this suggests that upon Hb reaction with H_2O_2 and in the photochemical interaction of ultrashort laser pulses with Hb, the Hb photoproduct shows, at least with regard to TPEF emission, similar features. The overlap between the TPEF emission spectra of PpIX and Hb thin film suggests that heme, i.e., porphyrin rings photoexcitation playing a significant role in the Hb photoproduct formation. This could even include heme degradation, as already demonstrated within diseased so-called Köln erythrocytes', where observed fluorescence does not resemble that of porphyrins, chelated or otherwise, but does reveal some characteristics of dypirolic compound spectra [37]. Since dipyrrolic urinary pigments in patients with unstable hemoglobin disease are characterized and support the previous assumption regarding fluorescent Koln erythrocytes, it is more likely that under ultrashort laser pulses the heme's porphyrin ring breakage is enhanced. Importantly, fluorescent heme degradation products are already recognized as markers of red blood cell (RBC) oxidative stress [38], based on the original work of Nagababu and Rifkind, 1998, who have found that even small portion of the non-neutralized hydrogen peroxide in erythrocytes degrades the protoporphyrin and produce stable fluorescent heme degradation products. Nagababu and Rifkind 1998 reported two heme degradation products, one with an excitation wavelength of 321 nm and emission wavelength in the region of 465 nm and the second one with the excitation wavelength of 460 nm and emission wavelength in the region of 525 nm, based on the results that the same fluorescent bands were obtained after hydrogen peroxide treatment of heme or hemin. The broad emission spectra of a Hb photoproduct obtained in our study indicates that there are probably more than one Hb photoproduct species as well. The same authors [39] revealed that the mechanism for the generation of heme degradation products needs an initial reaction with hydrogen peroxide, producing Fe (IV) ferrylhemoglobin (ferrylHb) species, which further reacts with the second molecule of hydrogen peroxide producing superoxide radical, that can be retained longer in heme pocket than the superoxide formed during Hb autoxidation, and consequently initiating degradation of heme [28]. Namely, even in physiological conditions, RBCs are continuously exposed to both endogenous and exogenous sources of reactive oxygen species (ROS) (i.e., superoxide and hydrogen peroxide (H_2O_2)), which are mainly neutralized by the RBC antioxidant system. However, the autoxidation of Hb bound to the membrane is unavailable to the RBC antioxidant system which is mostly cytosolic. This process is especially pronounced when Hb is partially oxygenated, resulting in an increased rate of autoxidation and increased affinity for the RBC membrane, eventually affecting RBC deformability [38]. Even in fresh RBC samples heme degradation products can be found, and the amount of heme degradation increases in older RBCs [38]. Taking all these findings together, the interaction of ultrashort laser pulses with hemoglobin more likely accelerates the deoxygenation of hemoglobin and generation of superoxide radical, which affects heme, inducing the formation of stable fluorescent photoproduct.

3.7. Applications

3.7.1. Selective photo-labeling and live tracking of photo-labeled erythrocytes

Thanks to the high stability of the Hb photoproduct obtained upon interaction of the 730 nm ultrashort laser pulses with Hb molecules (Fig. 3d) and high spatiotemporal selectivity of our TPEF scanning microscope, we performed live tracking of individually labeled erythrocyte

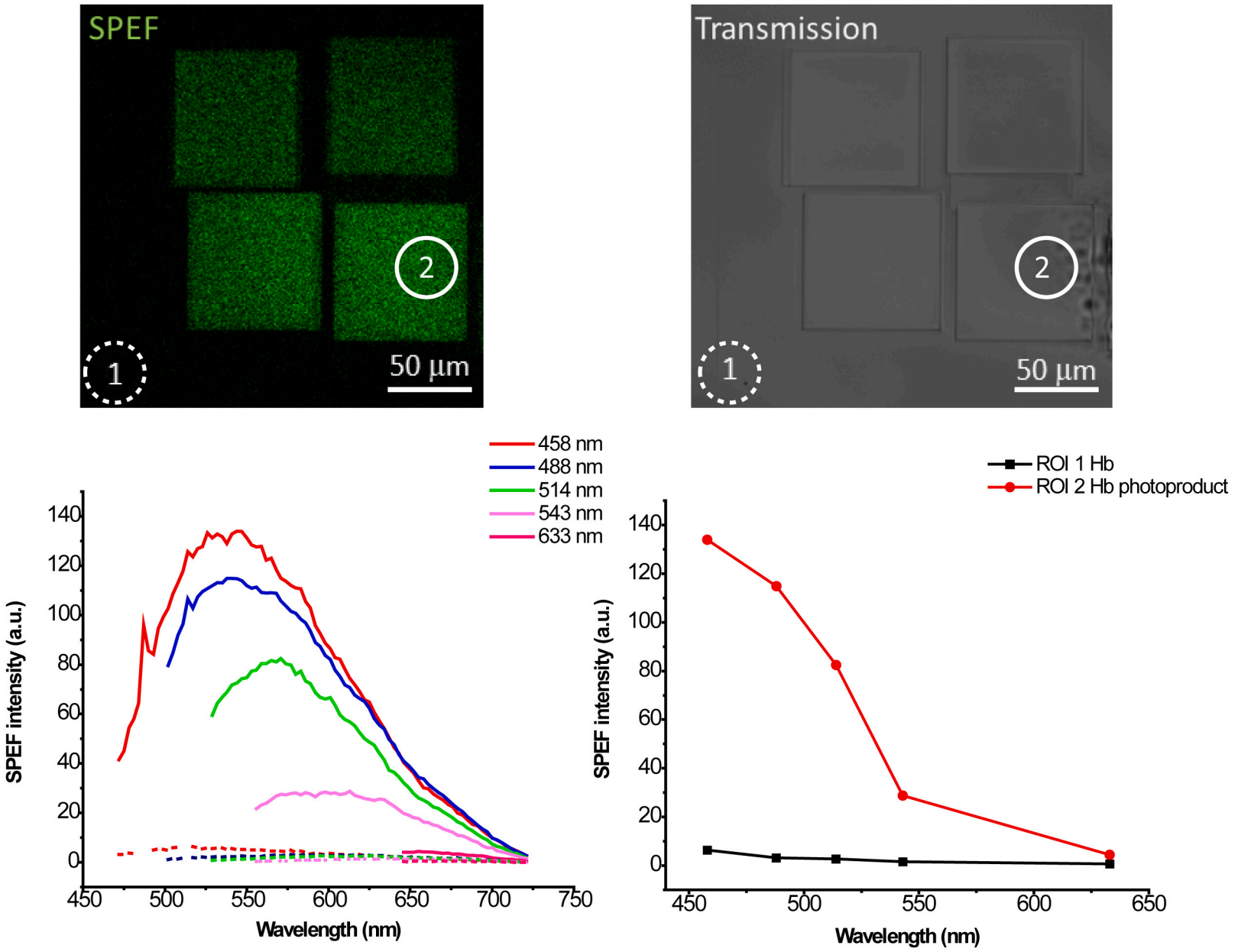

Fig. 5. Spectral imaging of Hb photoproduct patterns. (a) Single-photon excitation (SPEF) fluorescent image of the Hb photoproduct patterns recorded at 458 nm excitation, dashed circle represents region of interest (ROI 1) which is not irradiated by ultrashort pulsed laser beam under conditions needed for photoproduct formation, and solid circle represents ROI 2 which is irradiated by ultrashort pulsed laser beam, and it's clearly separate by photoproduct fluorescence emission, (b) Corresponding Bright-field image; (c) Single-photon excitation fluorescence spectra, read-out from ROI 1 (dashed line) for different excitation wavelengths and from ROI 2 (solid line); (d) Excitation efficiency: the emission intensity maxima at the different excitation wavelengths from ROI 1 Hb (untreated Hb) and ROI 2 (Hb photoproduct).

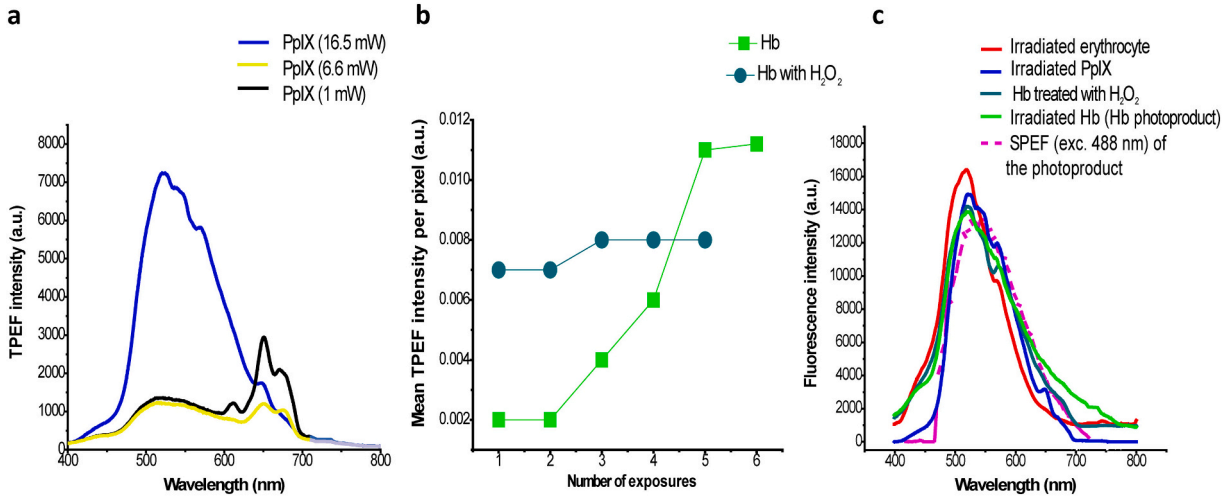

Fig. 6. TPEF spectra of PpIX and H_2O_2-treated Hb. (a) TPEF spectra of PpIX irradiated using different ultrashort pulsed laser powers (1.0 mW, black; 6.6 mW, yellow; 16.5 mW, dark blue); (b) Dependence of TPEF intensity vs. number of exposures in Hb thin film and H_2O_2-treated Hb thin film; (c) Overlapped TPEF spectra of Hb photoproduct (obtained in thin layer of Hb, green), the erythrocyte (red), thin layer PpIX under the laser power conditions (16.5 mW, blue), H_2O_2-treated Hb thin layer (cobalt blue) and Hb photoproduct SPEF spectrum (dashed purple). (For interpretation of the references to colour in this figure legend, the reader is referred to the web version of this article.)

(s) in vitro in the whole blood (Fig. 7 a-d). We present four timelapse images from the video (Supplemental Information) in which one erythrocyte is labeled by focused fs laser beam and then traced during its random motion. This was inspired by [11] where flow of the erythrocytes was shown in the vasculature of a whole, live animal but only with statical images, while we bring the dynamics of movement (Fig. 7 and corresponding video). Although the photo-labeling and tracking were performed in vitro, this method based on TPEF microscopy will enable to track with long-term period individual erythrocyte in a tissue [40] and blood vessel in laboratory animals, for instance in zebra fish [11] or even in mouse brain vasculature [41 – 43]. According to [41 – 43], where shadows of erythrocytes were traced in the blood flow in live animals through the cranial window using TPEF imaging, erythrocytes could be fluorescently activated by a fs laser beam and tracked through the vessels. In addition to selective photo-labeling of solely and deliberately chosen erythrocytes, that can be achieved by spatiotemporal control of the laser beam, but not by bulk H_2O_2 treatment, there are some more advantages of the presented method. Namely, treating the erythrocytes with H_2O_2 is rather uncontrollable in terms of targeted transformation of Hb only into the fluorescent molecule(s). H_2O_2 interact with other molecules in the erythrocytes' membrane and other structures which might be damaged or altered. Also, erythrocytes' morphology and related Hb distribution would be altered. Using the method of the laser photo-labeling presented in this work, only Hb molecules would be affected, and the erythrocytes would preserve their original morphology as well as its original Hb distribution which was already shown in [9]. The erythrocytes morphology and internal Hb distribution are one of key markers indicating the cell adaptation to physiological processes and their response to pathological conditions [9]. Eventually, the proposed method might have application for erythrocytes tracing in the blood vessels of the live animals even in imaging of highly bloodied and low transparent organs such as kidneys, since TPEF microscopy is extensively used nowadays for those purposes [41]. Prior investigations have unequivocally demonstrated that the morphology of erythrocytes can be studied using Two-Photon Excitation Fluorescence (TPEF) imaging, which enables examination of their oxygenation status [15], as well as distribution of Hb [9]. However, it is unclear whether the ultrashort laser pulses interferes with Hb's ability to perform its primary function of binding and releasing oxygen. In our present study, we establish that Hb undergoes alterations as a result of such interaction.

Having in mind the relationship of oxidative stress and hemoglobin, hemoglobin-based TPEF methodology is an emerging platform for the assessment of redox status of erythrocytes and their deformability under both physiological and pathophysiological conditions and even a broader spectrum of diseases that share the common feature of the appearance of extracellular hemoglobin or early cancer progression in means of neoangiogenesis. In this respect, photo acoustic microscopy can be employed for tracking of erythrocytes as suggested in [11] but with higher repetition rate lasers. Also, this technique can be used for investigation of oxygen saturation in the blood vessels [15].

3.7.2. *Pattern inscription (micropatterning) in Hb layer*

The long–term stability of the Hb photoproduct, its fluorescence and spatial precision of TPEF emission microscopy, enabled one more application – micro patterning of the Hb layer (Fig. 8). The inscribed patterns can stay fluorescent even for several months after being inscribed. In Fig. 8 a-d simple, spot-wise, patterns are presented in addition to the uniform square area. The spots were obtained from the diffraction limited focal volume and demonstrate the method limitation in terms of the spatial resolution. At each figure, a new spot-wise pattern was added, while the previous ones are still clearly visible. To demonstrate possibility and versatility of the method, as well as potential applications, we further wrote the letters “HEMMAGINERO” (dimensions 60 μm × 6 μm) in the Hb layer (Fig. 8e).

In terms of optical and spectroscopic response to the treatment with ultrashort laser pulses all mammalian [4,9,12,44,45] or even other vertebrates [46] Hb and erythrocytes are the same [47]. On the other hand, the slaughterhouses mammalian blood is a waste material from which Hb can be isolated in relatively low cost and relatively simple technological processes [48,49]. This might be a starting point for utilization of the Hb as the material for optical memories [50], hemoglobin-based therapeutics [51], intravital microscopy [52], conversion of micro fluorescent information into the document security or mass production of calibration samples in fluorescent microscopy [53–55]. Microscopic slides with fluorescent patterns are already commercially available [56] and broadly used for calibration and resolution measurements. While the fluorescence durability of the patterns in the existing materials remains unknown, we suggest Hb as a material for long lasting fluorescent patterns. In addition, the utilization of Hb from wasted slaughterhouse blood as the widely available material will be nature friendly since this material is considered to be severe pollutant [49].

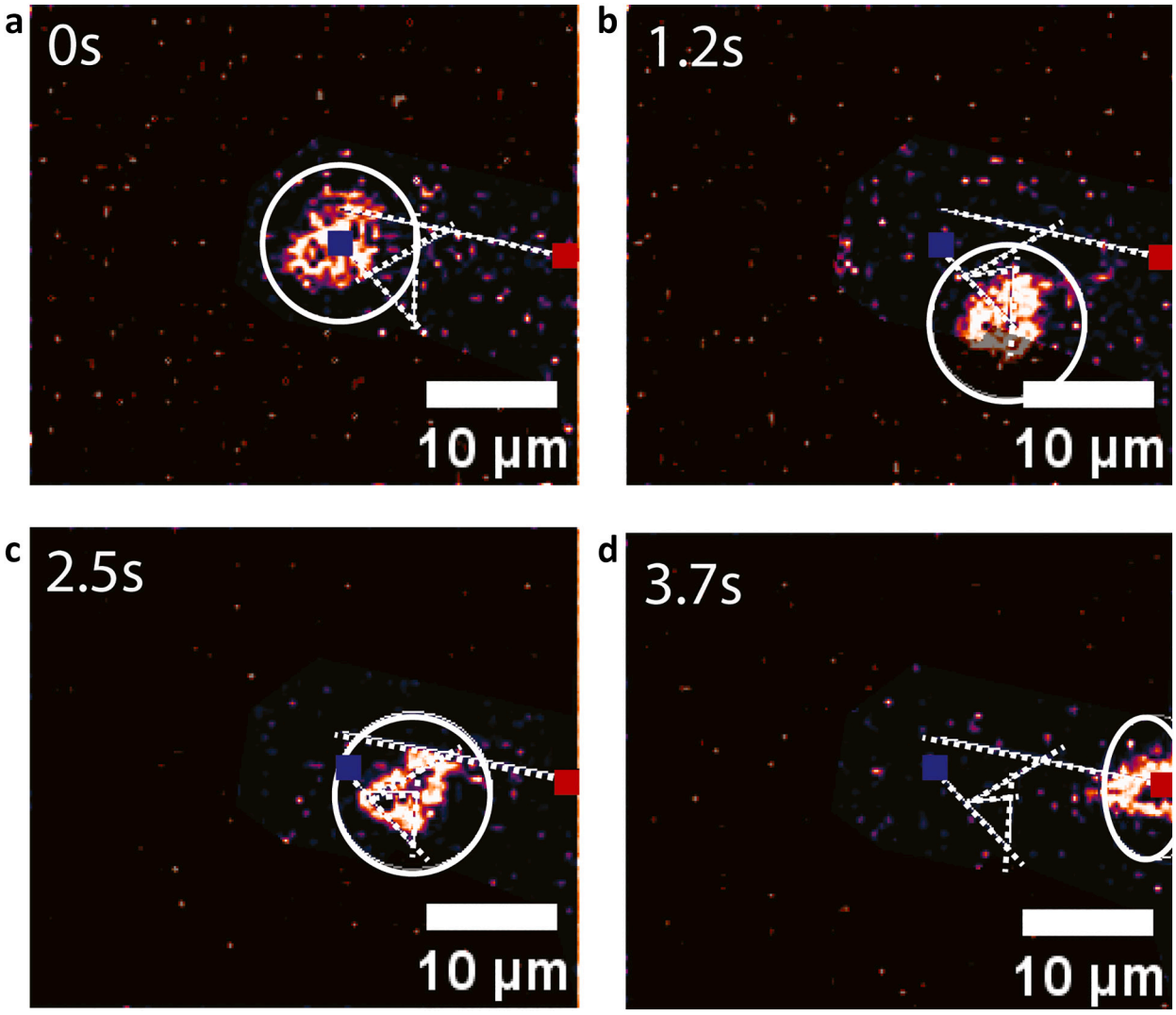

Fig. 7. Timelapse TPEF emission images of a single erythrocyte (encircled white). (a-d) Photo-labeled erythrocyte tracking in whole blood. The white dashed lines represent erythrocyte's trajectory with starting position (blue square) and final position (red square). (For interpretation of the references to colour in this figure legend, the reader is referred to the web version of this article.)

4. Conclusion

Using different spectroscopic techniques, in this study, we presented a novel insight into the photophysical properties of the fluorescent product emerged after exposure of Hb to 730 nm ultrashort laser pulses (hence Hb photoproduct) and its possible applications. We suggest that the interaction of the Hb with the ultrashort laser pulses in NIR region leads to the degradation of the Hb molecules and release of the iron, ending up with iron-free fluorescent species comparable to those emerged from the interaction of Hb with H_2O_2. Unlike the chemical interaction of Hb with H_2O_2 that occurs in bulk solution, using the tightly focused ultrashort pulsed laser beam the Hb photoproduct can be formed in spatiotemporal controllable manner without interaction with other molecules and erythrocytes structures (e.g. membrane). In other words, we can irradiate selected erythrocytes solely, and the laser pulses will alter primarily Hb, but not the other molecules. We inscribed sub-micrometer fluorescent patterns on a Hb thin film by the spatiotemporal control, of ultrashort pulsed laser beam. We have also induced the Hb photoproduct formation in a single human healthy erythrocyte making them fluorescent in the sample of whole blood and track their movement in space and time. The present study could contribute towards understanding photophysical properties of photoproduct, formed by the interaction of ultrashort laser pulses with Hb and erythrocytes, establishing a foundation for the future progress in the field of bio-derived biomaterials.

Supplementary data to this article can be found online at https://doi.org/10.1016/j.ijbiomac.2023.125312.

CRediT authorship contribution statement

M. Radmilović prepared the samples, performed TPEF imaging, TPEF spectra measurements and absorption spectra measurements, erythrocytes tracking, Hb micro-patterning, and prepared all the images; I. Drvenica prepared the samples and supervised Hb and erythrocytes isolation, managed the research; M. Rabasović constructed the TPEF experimental setup, supervised the TPEF imaging and spectra measurements, managed the research; V. Ilić supervised sample preparation, managed the research; D. Pavlović prepared the samples and imaged the erythrocytes by TPEF microscopy and measured absorption spectra; S. Oasa performed spectral imaging; V. Vukojević supervised spectral imaging; M. Perić performed confocal imaging; S. Nikolić maintained TPEF experimental setup and modified the imaging software; A. Krmpot constructed the TPEF experimental setup, supervised the measurements, managed the research. All the authors wrote and reviewed the

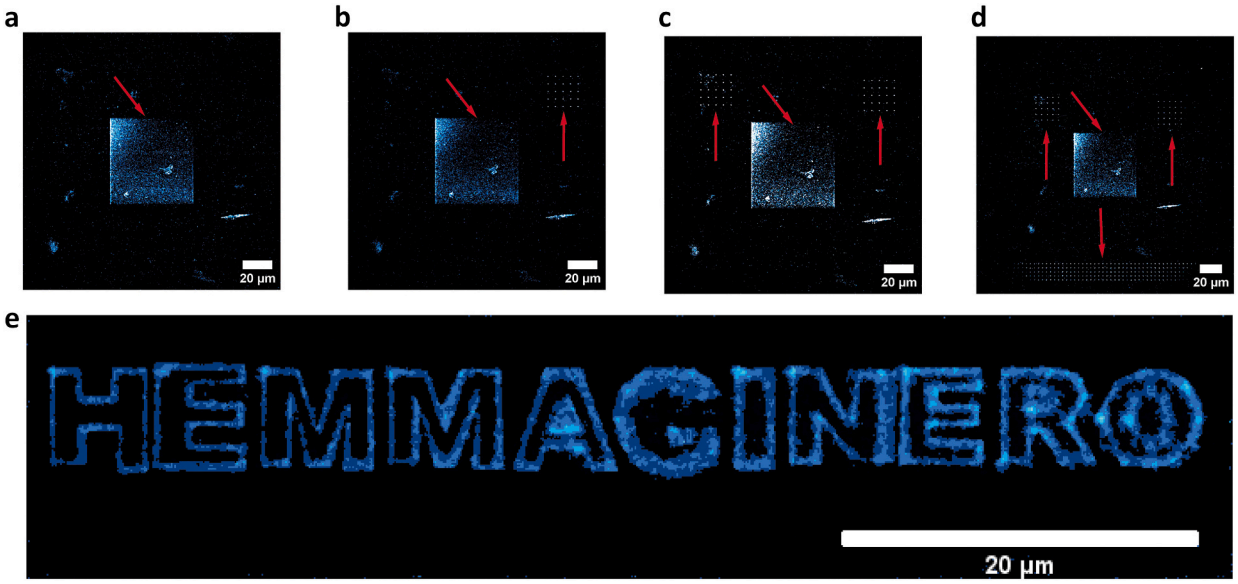

Fig. 8. Micropattering in Hb layer by fs laser pulses. (a-d) Arbitrary uniform and spot-wise patterns (red arrow pointed) inscribed in the thin Hb film by ultrashort laser pulses. The patterns exhibit increased TPEF signal (marked by red arrows). (e) Fluorescent Hb photoproduct in the form of letters pattern. (For interpretation of the references to colour in this figure legend, the reader is referred to the web version of this article.)

manuscript. This article is a part of M. Radmilović's PhD thesis.

Declaration of competing interest

The authors declare that they have no known competing financial interests or personal relationships that could have appeared to influence the work reported in this paper.

Data availability

Data will be made available on request.

Acknowledgement

We would like to thank to Milan Minić, Institue of Physics Belgrade for the technical support and to the staff of the Center for Laser Microcopy, Faculty of Biology, University of Belgrade, Serbia. This work was supported by the Science Fund of the Republic of Serbia [program PROMIS, project HEMMAGINERO, grant number 6066079] and Qatar National Research Fund [grant number PPM 04-0131-200019]. The authors acknowledge funding provided by the Institute of Physics Belgrade, through the grant by the Ministry of Education, Science and Technological Development of the Republic of Serbia and the Institute for Medical Research University of Belgrade, National Institute of the Republic of Serbia, through the contract No. 451-03-47/2023-01/200015.

References

[1] L. Kiger, C. Vasseur, E. Domingues-Hamdi, G. Truan, M.C. Marden, V. Baudin-Creuza, Dynamics of α-Hb chain binding to its chaperone AHSP depends on heme coordination and redox state, Biochim. Biophys. Acta - Gen. Subj. 2014 (1840) 277–287, https://doi.org/10.1016/j.bbagen.2013.09.015.
[2] M. Weissbluth, Hemoglobin, Springer, Berlin, 1974, pp. 10–26.
[3] Q. Sun, W. Zheng, J. Wang, Y. Luo, J.Y. Qu, Mechanism of two-photon excited hemoglobin fluorescence emission, J. Biomed. Opt. 20 (2015) 105014, https://doi.org/10.1117/1.JBO.20.10.105014.
[4] W. Zheng, D. Li, Y. Zeng, Y. Luo, J.Y. Qu, W.R. Zipfel, R.M. Williams, R. Christie, A. Y. Nikitin, B.T. Hyman, W.W. Webb, Two-photon excited hemoglobin fluorescence, Biomed. Opt. Express 2 (2011) 71–79, https://doi.org/10.1364/BOE.2.000071.
[5] G.O. Clay, A.C. Millard, C.B. Schaffer, J. Aus-der-Au, P.S. Tsai, J.A. Squier, D. Kleinfeld, Spectroscopy of third-harmonic generation: evidence for resonances in model compounds and ligated hemoglobin, J. Opt. Soc. Am. B. 23 (2006) 932, https://doi.org/10.1364/josab.23.000932.
[6] G.O. Clay, C.B. Schaffer, D. Kleinfeld, Large two-photon absorptivity of hemoglobin in the infrared range of 780-880 nm, J. Chem. Phys. 126 (2007) 01B609, https://doi.org/10.1063/1.2404678.
[7] N.L. Garrett, A. Lalatsa, I. Uchegbu, A. Schätzlein, J. Moger, Exploring uptake mechanisms of oral nanomedicines using multimodal nonlinear optical microscopy, J. Biophotonics 5 (2012) 458–468, https://doi.org/10.1002/jbio.201200006.
[8] G.D. Vigil, S.S. Howard, Photophysical characterization of sickle cell disease hemoglobin by multi-photon microscopy, Biomed. Opt. Express 6 (2015) 4098–4104, https://doi.org/10.1364/boe.6.004098.
[9] K. Bukara, S.Z. Jovanić, I.T. Drvenica, A. Stančić, V. Ilić, M.D. Rabasović, D. V. Pantelić, B.M. Jelenković, B. Bugarski, A.J. Krmpot, Mapping of hemoglobin in erythrocytes and erythrocyte ghosts using two photon excitation fluorescence microscopy, J. Biomed. Opt. 22 (2017) 026003, https://doi.org/10.1117/1.jbo.22.2.026003.
[10] D. Li, W. Zheng, Y. Zeng, Y. Luo, J.Y. Qu, Two-photon excited hemoglobin fluorescence provides contrast mechanism for label-free imaging of microvasculature in vivo, Opt. Lett. 36 (2011) 834–836, https://doi.org/10.1364/OL.36.000834.
[11] Y. Zeng, J. Xu, D. Li, L. Li, Z. Wen, J.Y. Qu, Label-free in vivo flow cytometry in zebrafish using two-photon autofluorescence imaging, Opt. Lett. 37 (2012) 2490–2492, https://doi.org/10.1364/OL.37.002490.
[12] D. Li, W. Zheng, S.K. Teh, Y. Zeng, Y. Luo, J.Y. Qu, Time-resolved detection enables standard two-photon fluorescence microscopy for in vivo label-free imaging of microvasculature in tissue, Opt. Lett. 36 (2011) 2638–2640, https://doi.org/10.1364/OL.36.002638.
[13] R. Podlipec, J. Mur, J. Petelin, J. Štrancar, R. Petkovšek, Two-photon retinal theranostics by adaptive compact laser source, Appl. Phys. A Mater. Sci. Process. 126 (2020) 1–9, https://doi.org/10.1007/s00339-020-03587-2.
[14] R.L. Shelton, S.P. Mattison, B.E. Applegate, Volumetric imaging of erythrocytes using label-free multiphoton photoacoustic microscopy, J. Biophotonics 7 (2014) 834–840, https://doi.org/10.1002/jbio.201300059.
[15] Y. Wang, S. Hu, K. Maslov, Y. Zhang, Y. Xia, L.V. Wang, In vivo integrated photoacoustic and confocal microscopy of hemoglobin oxygen saturation and oxygen partial pressure, Opt. Lett. 36 (2011) 1029, https://doi.org/10.1364/ol.36.001029.
[16] J.J. Yao, L.V. Wang, Photoacoustic microscopy, Laser Photonics Rev. 7 (2013) 758–778.
[17] G.J. Tserevelakis, M. Pavlidis, A. Samaras, G.D. Barmparis, K.G. Mavrakis, I. Draganidis, A. Oikonomou, E. Fanouraki, G.P. Tsironis, G. Zacharakis, Hybrid confocal fluorescence and photoacoustic microscopy for the label-free investigation of melanin accumulation in fish scales, Sci. Rep. 12 (2022) 1–14, https://doi.org/10.1038/s41598-022-11262-0.
[18] I. Saytashev, R. Glenn, G.A. Murashova, S. Osseiran, D. Spence, C.L. Evans, M. Dantus, Multiphoton excited hemoglobin fluorescence and third harmonic generation for non-invasive microscopy of stored blood, Biomed. Opt. Express 7 (2016) 3449–3460, https://doi.org/10.1364/boe.7.003449.
[19] M.E. Reinhard, M.W. Mara, T. Kroll, H. Lim, R.G. Hadt, R. Alonso-Mori, M. Chollet, J.M. Glownia, S. Nelson, D. Sokaras, K. Kunnus, T.B. van Driel, R.W. Hartsock, K. S. Kjaer, C. Weninger, E. Biasin, L.B. Gee, K.O. Hodgson, B. Hedman, U. Bergmann,

E.I. Solomon, K.J. Gaffney, Short-lived metal-centered excited state initiates iron-methionine photodissociation in ferrous cytochrome c, Nat. Commun. 12 (2021) 1–8, https://doi.org/10.1038/s41467-021-21423-w.
[20] https://www.ncbi.nlm.nih.gov/pmc/articles/PMC3822757/.
[21] J.G. Mohanty, E. Nagababu, J.M. Rifkind, Red blood cell oxidative stress impairs oxygen delivery and induces red blood cell aging, Front. Physiol. 5 (2014) 1–6, https://doi.org/10.3389/fphys.2014.00084.
[22] S. Sun, A. Lv, S. Li, C. Zhao, Q. Chen, Z. Li, Y. Wang, A. Wu, H. Lin, Biomolecule-based stimuli-responsive nanohybrids for tumor-specific and cascade-enhanced synergistic therapy, Acta Biomater. 152 (2022) 484–494, https://doi.org/10.1016/j.actbio.2022.08.038.
[23] A.I. Alayash, Oxygen therapeutics: can we tame haemoglobin? Nat. Rev. Drug Discov. 3 (2004) 152–159, https://doi.org/10.1038/nrd1307.
[24] D. Chakraborty, S. Sarkar, P.K. Das, Blood dots: hemoglobin-derived carbon dots as hydrogen peroxide sensors and pro-drug activators, ACS Sustain. Chem. Eng. 6 (2018) 4661–4670, https://doi.org/10.1021/acssuschemeng.7b03691.
[25] S. Li, W. Sun, M. Ouyang, B. Yu, Y. Chen, Y. Wang, D. Zhou, Hemoglobin-related biomaterials and their applications, Adv. NanoBiomed Res. 2200103 (2022) 1–12, https://doi.org/10.1002/anbr.202200103.
[26] E.A. Shirshin, B.P. Yakimov, S.A. Rodionov, N.P. Omelyanenko, A.V. Priezzhev, V. V. Fadeev, M.E. Darvin, Formation of hemoglobin photoproduct is responsible for two-photon and single photon-excited fluorescence of red blood cells, Laser Phys. Lett. 15 (2018), 075604, https://doi.org/10.1088/1612-202X/aac003.
[27] E. Nagababu, J.M. Rifkind, Formation of fluorescent heme degradation products during the oxidation of hemoglobin by hydrogen peroxide, Biochem. Biophys. Res. Commun. 247 (1998) 592–596, https://doi.org/10.1006/bbrc.1998.8846.
[28] E. Nagababu, J.M. Rifkind, Reaction of hydrogen peroxide with ferrylhemoglobin: superoxide production and heme degradation, Biochemistry. 39 (2000) 12503–12511, https://doi.org/10.1021/bi992170y.
[29] A.Z. Stančić, I.T. Drvenica, H.N. Obradović, B.M. Bugarski, V.L. Ilić, D.S. Bugarski, Native bovine hemoglobin reduces differentiation capacity of mesenchymal stromal cells in vitro, Int. J. Biol. Macromol. 144 (2020) 909–920, https://doi.org/10.1016/j.ijbiomac.2019.09.167.
[30] M.D. Rabasović, D.V. Pantelić, B.M. Jelenković, S.B. Ćurčić, M.S. Rabasović, M. D. Vrbica, V.M. Lazović, B.P.M. Ćurčić, A.J. Krmpot, Nonlinear microscopy of chitin and chitinous structures: a case study of two cave-dwelling insects, J. Biomed. Opt. 20 (2015) 016010, https://doi.org/10.1117/1.jbo.20.1.016010.
[31] T. Lainović, J. Margueritat, Q. Martinet, X. Dagany, L. Blažić, D. Pantelić, M. D. Rabasović, A.J. Krmpot, T. Dehoux, Micromechanical imaging of dentin with Brillouin microscopy, Acta Biomater. 105 (2020) 214–222, https://doi.org/10.1016/j.actbio.2020.01.035.
[32] N.S. Selim, S.M. El-marakby, Radiation-induced changes in the optical properties of hemoglobin molecule, Spectrochim. Acta A Mol. Biomol. Spectrosc. 76 (2010) 56–61, https://doi.org/10.1016/j.saa.2010.02.046.
[33] E.K. Hanson, J. Ballantyne, A blue spectral shift of the hemoglobin soret band correlates with the age (time since deposition) of dried bloodstains, PLoS One 5 (2010) 1–11, https://doi.org/10.1371/journal.pone.0012830.
[34] I.T. Drvenica, A.Z. Stančić, A.M. Kalušević, S.B. Marković, J.J. Dragišić Maksimović, V.A. Nedović, B.M. Bugarski, V.L. Ilić, Maltose-mediated, long-term stabilization of freeze- and spray-dried forms of bovine and porcine hemoglobin, J. Serb. Chem. Soc. 84 (2019) 1105–1117, https://doi.org/10.2298/JSC190513067D.
[35] C. Bonaventura, R. Henkens, A.I. Alayash, S. Banerjee, A.L. Crumbliss, Molecular controls of the oxygenation and redox reactions of hemoglobin, Antioxid. Redox Signal. 18 (2013) 2298–2313, https://doi.org/10.1089/ars.2012.4947.
[36] H. Lu, F. Floris, M. Rensing, S. Andersson-Engels, Fluorescence spectroscopy study of protoporphyrin IX in optical tissue simulating liquid phantoms, Materials (Basel) 13 (2020) 7–16, https://doi.org/10.3390/ma13092105.
[37] S.M. Waugh, P.S. Low, Hemichrome binding to band 3: nucleation of Heinz bodies on the erythrocyte membrane, Biochemistry. 24 (1) (1985) 34–39, https://doi.org/10.1021/bi00322a006.
[38] J.G. Mohanty, E. Nagababu, J.M. Rifkind, Red blood cell oxidative stress impairs oxygen delivery and induces red blood cell aging, Front. Physiol. 5 (2014) 1–6, https://doi.org/10.3389/fphys.2014.00084.
[39] E. Nagababu, S. Ramasamy, J.M. Rifkind, Y. Jia, A.I. Alayash, Site-specific cross-linking of human and bovine hemoglobins differentially alters oxygen binding and redox side reactions producing rhombic heme and heme degradation, Biochemistry. 41 (2002) 7407–7415, https://doi.org/10.1021/bi0121048.
[40] U.N. Shroff, I.M. Schiessl, G. Gyarmati, A. Riquier-Brison, J. Peti-Peterdi, Novel fluorescence techniques to quantitate renal cell biology, Methods Cell Biol. 154 (2019) 85–107, https://doi.org/10.1016/bs.mcb.2019.04.013.
[41] D. Sardella, A.M. Kristensen, L. Bordoni, H. Kidmose, A. Shahrokhtash, D. S. Sutherland, S. Frische, I.M. Schiessl, Serial Intravital 2-photon Microscopy and Analysis of the Kidney Using Upright Microscopes, 2023, pp. 1–17, https://doi.org/10.3389/fphys.2023.1176409.
[42] E. Gutiérrez-jiménez, H. Angleys, P.M. Rasmussen, M.J. West, L. Catalini, N. K. Iversen, M.S. Jensen, S. Frische, L. Østergaard, Disturbances in the control of capillary flow in an aged APPswe/PS1ΔE9 model of Alzheimer's disease, Neurobiol. Aging 62 (2018) 82–94, https://doi.org/10.1016/j.neurobiolaging.2017.10.006.
[43] E. Gutiérrez-jiménez, C. Cai, I.K. Mikkelsen, P.M. Rasmussen, H. Angleys, M. Merrild, K. Mouridsen, S.N. Jespersen, J. Lee, N.K. Iversen, S. Sakadzic, L. Østergaard, Effect of electrical forepaw stimulation on capillary transit-time heterogeneity (CTH), J. Cereb. Blood Flow Metab. 36 (2016) 2072–2086, https://doi.org/10.1177/0271678X16631560.
[44] T. Wu, J. Liao, J. Yu, Y. Gao, H. Li, J. Wu, X. Xia, K. Shi, W. Zheng, In vivo label-free two-photon excitation autofluorescence microscopy of microvasculature using a 520 nm femtosecond fiber laser, Opt. Lett. 45 (2020) 2704–2707, https://doi.org/10.1364/OL.394242.
[45] S. He, C. Ye, Q. Sun, C.K.S. Leung, J.Y. Qu, Label-free nonlinear optical imaging of mouse retina, Biomed. Opt. Expr. 6 (2015) 2459–2465, https://doi.org/10.1364/BOE.6.001055.
[46] Y. Zeng, J. Xu, D. Li, L. Li, Z. Wen, J.Y. Qu, Label-free in vivo flow cytometry in zebrafish using two-photon autofluorescence imaging, Opt. Lett. 37 (2012) 2490–2492, https://doi.org/10.1364/OL.37.002490.
[47] J.F. Ortas, P. Mahou, S. Escot, C. Stringari, N.B. David, L. Bally-Cuif, N. Dray, M. Négrerie, W. Supatto, E. Beaurepaire, Label-free imaging of red blood cells and oxygenation with color third-order sum-frequency generation microscopy, Light Sci. Appl. 12 (2023), https://doi.org/10.1038/s41377-022-01064-4.
[48] I.T. Kostić, V.L. Ilić, V.B. Dordević, K.M. Bukara, S.B. Mojsilović, V.A. Nedović, D. S. Bugarski, D.N. Veljović, D.M. Mišić, B.M. Bugarski, Erythrocyte membranes from slaughterhouse blood as potential drug vehicles: isolation by gradual hypotonic hemolysis and biochemical and morphological characterization, Colloids Surf. B Biointerfaces. 122 (2014) 250–259, https://doi.org/10.1016/j.colsurfb.2014.06.043.
[49] C.S.F. Bah, A.E.D.A. Bekhit, A. Carne, M.A. Mcconnell, Slaughterhouse blood: an emerging source of bioactive compounds, Compr. Rev. Food Sci. Food Saf. 12 (2013) 314–331, https://doi.org/10.1111/1541-4337.12013.
[50] L.A. Frolova, Y. Furmansky, A.F. Shestakov, N.A. Emelianov, P.A. Liddell, D. Gust, I. Visoly-Fisher, P.A. Troshin, Advanced nonvolatile organic optical memory using self-assembled monolayers of porphyrin-fullerene dyads, ACS Appl. Mater. Interfaces 14 (2022) 15461–15467, https://doi.org/10.1021/acsami.1c24979.
[51] P. Charoenphol, K. Oswalt, C.J. Bishop, Therapeutics incorporating blood constituents, Acta Biomater. 73 (2018) 64–80, https://doi.org/10.1016/j.actbio.2018.03.046.
[52] W. Choe, A.P. Acharya, B.G. Keselowsky, B.S. Sorg, Intravital microscopy imaging of macrophage localization to immunogenic particles and co-localized tissue oxygen saturation, Acta Biomater. 6 (2010) 3491–3498, https://doi.org/10.1016/j.actbio.2010.03.006.
[53] I. Begemann, A. Viplav, C. Rasch, M. Galic, Stochastic micro-pattern for automated correlative fluorescence - scanning electron microscopy, Nat. Publ. Gr. (2015) 1–12, https://doi.org/10.1038/srep17973.
[54] L. Benedetti, E. Sogne, S. Rodighiero, D. Marchesi, P. Milani, M. Francolini, Customized patterned substrates for highly versatile correlative light-scanning electron microscopy, Sci. Rep. 4 (2014) 7033, https://doi.org/10.1038/srep07033.
[55] A.D. Corbett, M. Shaw, A. Yacoot, A. Jefferson, L. Schermelleh, T. Wilson, M. Booth, P.S. Salter, Microscope Calibration Using Laser Written Fluorescence 26, 2018, pp. 21887–21900, https://doi.org/10.1364/OE.26.021887.
[56] https://www.psfcheck.com/psfcheck-slides.

scientific reports

Check for updates

OPEN

Label-free third harmonic generation imaging and quantification of lipid droplets in live filamentous fungi

Tanja Pajić[1], Nataša V. Todorović[2], Miroslav Živić[1], Stanko N. Nikolić[3], Mihailo D. Rabasović[3], Andrew H. A. Clayton[4] & Aleksandar J. Krmpot[3]✉

We report the utilization of Third-Harmonic Generation microscopy for label-free live cell imaging of lipid droplets in the hypha of filamentous fungus *Phycomyces blakesleeanus*. THG microscopy images showed bright spherical features dispersed throughout the hypha cytoplasm in control conditions and a transient increase in the number of bright features after complete nitrogen starvation. Colocalization analysis of THG and lipid-counterstained images disclosed that the cytoplasmic particles were lipid droplets. Particle Size Analysis and Image Correlation Spectroscopy were used to quantify the number density and size of lipid droplets. The two analysis methods both revealed an increase from 16×10^{-3} to 23×10^{-3} lipid droplets/μm^2 after nitrogen starvation and a decrease in the average size of the droplets (range: 0.5–0.8 μm diameter). In conclusion, THG imaging, followed by PSA and ICS, can be reliably used for filamentous fungi for the in vivo quantification of lipid droplets without the need for labeling and/or fixation. In addition, it has been demonstrated that ICS is suitable for THG microscopy.

Third harmonic generation (THG) microscopy as a label-free nonlinear imaging technique is a powerful tool for visualization of various cells and tissue structures[1]. THG has been mainly applied to imaging animal cell structures[1–7] and tissues[1,4,6,8–14], as well as the dynamics of cellular processes (functional imaging)[1,6,12,15]. Also, THG microscopy has been used to study human and fossil vertebrate teeth[16], 3D engineered human adipose tissue[17], and small organisms (Drosophila melanogaster, zebrafish, Xenopus laevis, early mouse embryos[8,18–20] and C. elegans[21,22]). In addition to animal specimens, THG microscopy has also been applied to plants[11,23–27], algae[26,27] and yeast[2,28]. To the best of our knowledge, there is a paucity of THG studies on filamentous fungi.

The THG phenomenon is a nonlinear coherent scattering process induced by structures with specific properties. In THG, the joint energy of three photons is converted into one photon. As THG is a third-order process, ultra-short laser pulses with high peak power densities at the optical focus are required to ensure sufficient signal. Contrast in THG microscopy is generated at interfaces where there is a large change in refractive index or third-order non-linear susceptibility[29,30]. Due to higher index of refraction of lipids (R.I.(lipids) = 1.46–1.48 at 1100–480 nm)[31] with respect to the cytoplasm (R.I. = 1.360–1.390 at 633 nm)[32], the THG signal is efficiently produced at the interface between the aqueous phase and by lipid-rich structures[33–35]. These include cellular membranes and lipid droplets (LDs).

Lipid droplets are dynamic cellular organelles which play a key role in lipid homeostasis and energy in eukaryotic cells. Studies of lipid droplet physiology in fungi are still in their infancy but their quantitation has relevance to issues in biomedicine, agriculture, industrial waste and the energy crisis. As mentioned above, THG microscopy is a particularly suitable technique for lipid droplet physiology studies[11,35,36]. The advantages of THG microscopy are it is non-invasive, produces inherently confocal images, doesn't require fixation or external labelling-similar to Raman-based[37–42], differential interference contrast (DIC)[43] and light sheet microscopy[37], and is minimally phototoxic allowing for in vivo studies. A point of difference between Raman-based techniques and

[1]Faculty of Biology, Institute of Physiology and Biochemistry, University of Belgrade, Studentski trg 16, Belgrade 11158, Serbia. [2]Institute for Biological Research "Siniša Stanković", University of Belgrade, National Institute of the Republic of Serbia, Bulevar Despota Stefana 142, Belgrade 11000, Serbia. [3]Institute of Physics Belgrade, University of Belgrade, National Institute of the Republic of Serbia, Pregrevica 118, Belgrade 11080, Serbia. [4]Department of Physics and Astronomy, Optical Sciences Centre, School of Science, Computing and Engineering Technologies, Swinburne University of Technology, Melbourne, VIC 3122, Australia. ✉email: krmpot@ipb.ac.rs

THG microscopy is the simpler excitation scheme and minimal risk of aberration artefacts in THG microscopy. Combining THG with fluorescence microscopy is useful to identify the molecular source of the THG-generated signals (i.e. lipophilic fluorescent dyes to target LDs)[4,7,36]. Once THG-associated structures are identified they can be followed using THG microscopy in situ.

Quantitation of images containing LDs can be challenging. The desired parameters include LD number, density, size and morphology. Readily-available image analysis software and programming languages for this purpose are ImageJ, Cell Profiler, Imaris, AMIRA, Volocity, MATLAB, D programming, for both fluorescent images[44–47] and for lipid droplet images taken by label-free[11,17,20] techniques. Automated quantitation of lipid droplets uses either thresholding of the images (threshold-based) or watershed methods (morphology-based)[48], and are usually optimized for a specific cell line. It would be desirable to have a more general image analysis platform that does not require extensive cell-line specific thresholding. In this regard, Image Correlation Spectroscopy (ICS) is a promising method because it is based on measuring spatially-correlated fluctuations. ICS has been applied to confocal images where it measures the spatial variation of fluorescence intensity fluctuations, which can be further related to particle density and aggregation state[49]. On the other hand, ICS has been rarely used for nonlinear techniques, only for two photon excitation fluorescence (TPEF)[50] or recently for second harmonic generation imaging (SHG)[51].

The filamentous fungi[52] are ubiquitous organisms that contribute profoundly to a wide range of ecosystem processes, including decomposition of organic carbon, carbon storage and nutrient transfer. As an invisible and often overlooked part of carbon cycle, filamentous fungi as saprophytes and plant symbionts (mycorrhizal fungi) create a sink for plant organic carbon and distribute it to below-ground hyphal biomass[53]. The oleaginous filamentous fungi have the ability to accumulate large amount of carbon in the form of lipids, more than 20% of their biomass[54,55] under appropriate conditions. These lipids are considered to be a valuable alternative resource for various biotechnological applications (biodiesel production, high-value chemicals, food/feed additives, and efficient bioremediation of wastewaters)[56,57], in a bio-based economy. Additionally, the lipid accumulations have been implicated in the resistance of fungi to toxins[58] and virulence of pathogenic fungi[59]. Moreover, yeast cells modified to lack the lipid droplets entirely, are extremely vulnerable to a variety of stresses[60] altogether demonstrating that LD studies could potentially lead to novel antifungal treatments. We have chosen for the THG imaging study of LDs the well-known model species *Phycomyces blaekseneanus*, oleaginous fungi from the order Mucorales with very rapid growth (from the spores, through exponential growth phase, to stationary phase in under 36 h). The challenge of utilizing THG imaging for filamentous fungi is that the LDs in filamentous fungi are of rather small dimensions (< 1.5 μm) unlike e.g. in white adipocyte cells where LDs dimensions can reach 100 μm[61]. Our aim is to show that THG microscopy is highly suited for imaging the density and size of LDs in live filamentous fungi. To this end, we will use filamentous fungi in the baseline control condition, with sporadic and small LDs, corresponding to low lipid content conditions[62], and fungi with denser LDs brought upon by nitrogen starvation-induced autophagy response[63], the conserved cellular mechanism of molecular recycling[64]. In addition to label-free THG imaging of LDs in fungi, we also present two methods for LDs quantification and analysis. The first method is based on ImageJ/Fiji open source platform, particle analysis tool, which provides measurements of the size, shape and number of LDs. The second method is called Image Correlation Spectroscopy (ICS)[65], which provides measurements of density and size of particles through spatial autocorrelation analysis.

Our aim is to show that ICS is a good method for quantification of LDs in THG images.

Materials and methods

Filamentous fungus strain and growth conditions. A wild-type strain of oleaginous Zygomycetous fungus *Phycomyces blakesleeanus* (Burgeff) [NRRL 1555(-)] was used as the model cell system in this study. For optimal growth of the mycelium, spores at concentration of the order 10^7 spores/ml were plated on 100 mm Petri dishes at 21–23 °C. Standard liquid minimal (SLM) medium for cultivation contained per liter: 20 g of D (+)-glucose (carbon source), 2 g of L-asparagine·H_2O (nitrogen source), 5 g KH_2PO4, 500 mg $MgSO_4{\cdot}7H_2O$, and microelements/"trace stock" (28 mg $CaCl_2$, 1 mg thiamine hydrochloride, 2 mg citric acid·H_2O, 1.8 mg $Fe(NO_3)_3{\cdot}9H_2O$, 1 mg $ZnSO_4{\cdot}7H_2O$, 300 μg $MnSO_4{\cdot}H_2O$, 50 μg $CuSO_4{\cdot}5H_2O$, and 50 μg $Na_2MoO_4{\cdot}2H_2O$). The glucose was autoclaved separately, and the final pH of the medium was 4.5. The osmolarity was about 200 mOsm.

For the nitrogen starvation experiments, the fungi were first grown in the SLM medium and after 22 h were divided into two groups. Group 1 was the control group and group 2 was the nitrogen starved group (N-starved). Fungi from control group 1 were collected by centrifugation (10 min) and resuspended in SLM medium. For group 2, fungal cells were centrifuged (10 min) and resuspended in nitrogen-free medium (SLM medium without L-asparagine) (Fig. 1). The age-matched fungal cultures were imaged at different time points after nitrogen starvation (3, 4.5, 6 h and > 6 h (up to 8.5 h)) at room temperature. All fungal cultures used for imaging were in exponential growth phase (total time from seeding was in the range 24–30.5 h). Data collected from the 6–8.5 h time-points were pooled and represented the group in prolonged nitrogen starvation (labelled 6 h on the graphs).

Lipid staining. Live fungal cells were stained without chemical fixation. To stain the fungal cells, hyphae in exponential growth phase (26 h) were incubated with 40 ng/mL of Nile Red dye (Acros Organics) for 10 min at 20 °C.

Nonlinear laser scanning microscopy (NLSM) experimental setup and hyphae imaging. The images of live unstained fungal cells were obtained using a bespoke nonlinear laser-scanning microscope, previously described in references[66,67], but modified for THG imaging (Fig. 2). For third harmonic generation (THG) imaging of hyphae the following experimental setup, based on significantly modified Zeiss Jenaval upright microscope, was used: Infrared femtosecond pulses were provided by a SESAM mode-locked Yb:KGW laser (Time-

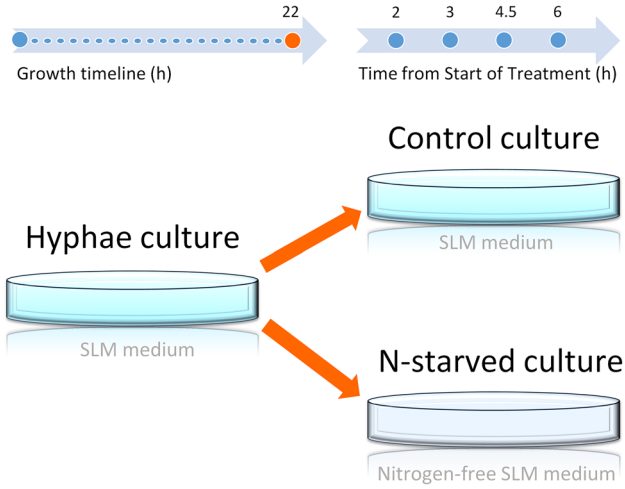

Figure 1. The outline of experimental design of nitrogen starvation. Hyphae cultures are grown in control conditions (Control culture) or in nitrogen-depleted medium (N-starved culture). Time points of sampling are marked as blue dots.

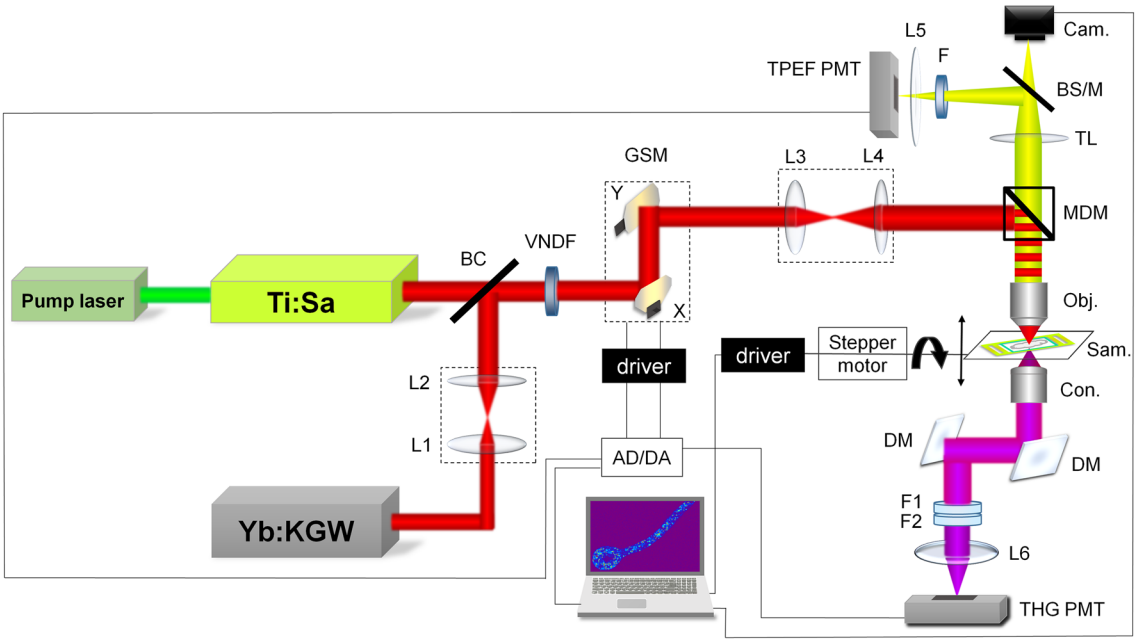

Figure 2. NLSM setup. Ti:Sa—laser for TPEF imaging, Yb:KGW—laser for TPEF and THG imaging, BC—beam combiner, L1 and L2—lenses of 1:1 beam expander for recollimation, VNDF—variable neutral density filter, GSM—galvanometer-scanning mirrors, L3 and L4—lenses of 1:3.75 beam expander for imaging, MDM—main dichroic mirror (cut-off 700 nm), Obj.—microscopic objective 40 × 1.3, Sam.—sample, Con.—aspheric condenser lens, DM—dichroic mirrors reflective for THG (347 nm) and transmissive for Yb laser (1040 nm), F1—Hoya glass UV filter, peak transmission 340 nm, F2—bandpass filter 275–375 nm, L6—focusing lens, THG PMT—photomultiplier tube for THG signal, TL—tube lens, BS/M—beam splitter or mirror toggle, Cam.—camera, F—VIS filter 400–700 nm for autofluorescence or VIS + 570 nm long pass for Nile Red fluorescence, L5—focusing lens, TPEF PMT—photomultiplier tube for TPEF signal, AD/DA—acquisition card. The scheme was created in Microsoft Power Point 2016 (https://www.microsoft.com/en-us/microsoft-365/powerpoint).

Bandwidth Products AG, Time-Bandwidth Yb GLX; Zurich, Switzerland, wavelength 1040 nm, pulse duration 200 fs and repetition rate 83 MHz). The laser wavelength was chosen so that THG signal whose wavelength is 3 times shorter (347 nm) is still in the range of conventional air UV optics. The laser light was first passed through a collimating 1:1 beam expander (L1 and L2) for divergence compensation, and then combined (at BC) with the Ti: Sa laser beam used for TPEF imaging. After that, both beams pass the motorized variable neutral density filter (VNDF) for power regulation and the mechanical shutter. The beams were raster scanned over the sample

using two galvanometer mirrors (Cambridge Technologies, 6215H; Bedford, Massachusetts, USA) and a 1:3.75 beam expander (L3 and L4) was used to fill the back aperture of the objective lens and to achieve 4f. configuration. The beams were further directed onto the sample by a short-pass main dichroic mirror (MDM, cut-off at 700 nm) through the high numerical aperture (NA) oil immersion objective lens (Carl Zeiss, EC Plan-Neofluar 40X, NA 1.3). The THG signal was detected in the forward direction (transmission arm), parallel to the direction of laser propagation. First, the signal was collected by high NA aspheric lens (condenser). Then, it was reflected by two dichroic mirrors (DM) that reflect 347 nm but transmit 1040 nm to prevent the laser beam from reaching the detector. Further on, the signal was filtered out from the rest of the laser photons by a bandwidth filter 275–375 nm (Thorlabs FGUV11M) and a Hoya glass UV filter (Newport FSR-U340) with a maximum transmission at 340 nm. The THG signal was detected using a photomultiplier tube (PMT) (Hamamatsu, H7422, Japan), after being focused by a 50 mm focal length lens (L6) onto the entrance window of the PMT.

For the (auto)TPEF imaging a tunable (700–900 nm) Kerr lens mode locked Ti:Sa laser (Mira 900, Coherent Inc. CA, USA) was used, pumped by CW (continuous-wave) frequency doubled Nd:YVO4 laser at 532 nm (VERDI V10, Coherent Inc. CA, USA). The wavelength of the Ti:Sa laser was set to 730 nm for auto TPEF imaging since most of the endogenous fluorophores (NADH, flavins, etc.) can be excited at this wavelength[68] on the one hand, and because of the technical limitation (laser tunability range and dichroic mirror cut off) on the other hand. The fluorescent signal was collected in back reflection by the objective lens, passed the MDM, tube lens (TL) and filtered out by VIS (400–700 nm) band pass filter (Canon, taken from the camera EOS50D) for the detection of the autofluorescence excited by Ti:Sa laser. Additionally, 570 nm long pass filter (colored glass, unknown vendor) was used for Nile Red fluorescence which is excited by Yb: KGW laser and detected simultaneously by THG signal. TPEF signals were detected after being focused by 50 mm focal length lens (L5) onto the entrance window of the TPEF PMT.

The acquisition was performed by National Instrument card USB-6351 at the rate of 1.2 M sample/s. This enabled high enough frame rate at low resolution for live monitoring, for instance 3 frames per second at 256 × 256 pixels with 6 averages. For high resolution images, it takes 30 s for 1024 × 1024 image with 30 averages. The lateral and axial resolution of the microscope with 40 × 1.3 objective lens were estimated to be 300 nm and 1000 nm, respectively.

Bright field images were taken with a Canon EOS 50D digital camera (Tokyo, Japan) whose CMOS sensor was placed at the image plane of the tube lens. Toggle switch BS/M enables utilization either of camera for bright field or TPEF PMT for fluorescence imaging.

A specially designed sample holder was used, that enables hyphae with the growing medium to be placed between two coverslips in order meet the criteria for the best NA of the objective lens, but also to avoid losses of the UV THG signal by thick deck glass (Supplementary Figs. S1 and S2 show different imaging conditions of hyphae that were tested in order to find the best one). The #1.5 coverslips (170 µm thickness) were used. 20 µl of hyphae suspension was used to keep the hyphae alive. The holder was placed between objective lens and the aspheric condenser on the motorized table that can be translated in steps of 0.3 µm along the beam propagation direction (z axis) for optical slicing of the sample and 3D imaging.

In control versus N-starved group imaging, time points were gathered sequentially. Using a label-free imaging technique, such as THG, enabled us to take images of samples with minimal delay after taking fungi from the culture. The overall time a sample culture was kept under the microscope to acquire at least 3 THG images of live hypha was between 25 and 37 min. Effectively, time points for control and treatment were offset for 30–40 min on one experimental day and on the next day, offset in opposite direction to the other. The exact ranges of time of growth (mean and standard deviation) for all hypha included in experimental groups are collected in Supplemental Fig. S4.

Image analysis. THG image analysis of lipid droplets in 2D was performed using ImageJ (W. Rasband, National Institute of Health, Maryland, USA, http://imagej.nih.gov/ij/). Algorithms written in MATLAB (in-house-created code) and VolView software were used for 3D and 4D image processing. Two methods for image analysis were used to quantify LDs number and size, Particle Size Analysis (PSA) and Image Correlation Spectroscopy (ICS). Details of both procedures are in the Supplementary Information.

Statistics. For quantitative image analysis, images of individual hypha under control conditions (n = 44) and after nitrogen starvation (n = 17) were obtained from 6 independently grown cultures. GraphPad Prism was used for graphing and statistical comparisons. The boxes of the box and whisker plots are enclosed by the 25th and 75th percentile range with the line representing the median; the whiskers are extending to the minimal and maximal value, respectively. Histograms of number of LDs were generated from all LD diameters in each group with 0.3 µm binning and each bin value was divided with the sum of hypha areas in the group. Errors in histograms of Number of LDs/hypha area were calculated as: Relative Error (binned N/area) = Relative Error (Number of LDs/hypha area) + Relative Error (Area), and Relative Error (binned N/area) was multiplied by value of Number of LDs/hypha area for that bin. Two-way ANOVA with multiple comparisons and Holm-Sidac correction and unpaired two tailed t test with Welch's correction for unequal variances, were used for the calculation of statistical significances. Where appropriate, unpaired two-sided Mann–Whitney test with was used instead. Confidence level for statistical significance was: 0.05 (*), 0.01 (**), 0.005 (***), 0.0001 (****).

Results

THG images, one slice (2D) and 3D reconstruction, of unstained live *P. blakesleeanus* hyphae in exponential growth phase are shown in Fig. 3a,b, respectively. The THG signal at the cell circumference originates from chitinous cell wall and plasma membrane which follow the cell wall shape. In the cytoplasm, various entities that

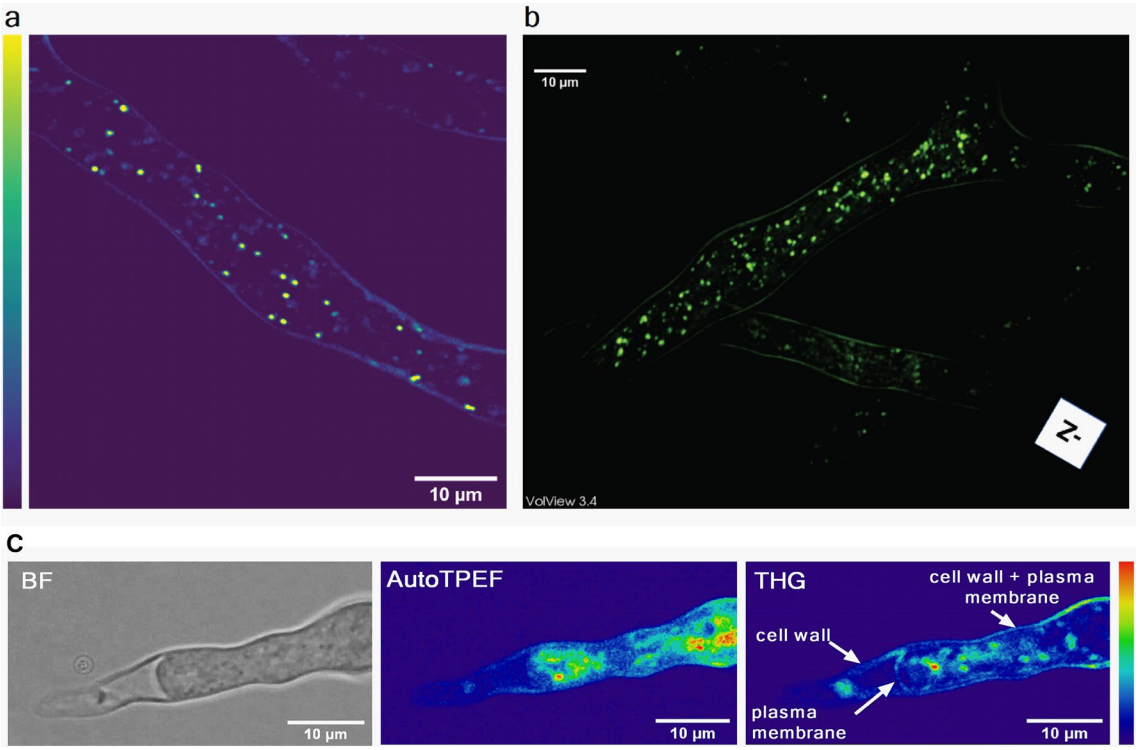

Figure 3. Label-free imaging of *Phycomyces blakesleeanus* hyphae from the exponential phase in SLM. (**a**) one THG slice; (**b**) 3D model built out of 23 THG slices 0.9 µm apart. The average laser power at sample plane was 23–26 mW. (**c**) Multimodal imaging: bright field (BF) (left), autoTPEF (middle) and THG (right) images of the same live unlabeled hypha. The hypha was plasmolyzed and the retracted plasma membrane is solely visible in the THG image. The average laser power at sample plane was 2.7 mW (TPEF) and 55 mW (THG). Color intensity bar for both, TPEF and THG signals: deep blue—the lowest signal, red the highest signal. All the images were taken with Zeiss 40 × 1.3 oil objective lens.

produce THG signal are visible. The hyphae were placed in the liquid growth medium between two coverslips. The high resolution of the microscopic system (diffraction limited), the thickness of the hyphae (ca 10 µm) and transparency of the medium make possible the whole hyphae to be optically sectioned and a 3D model to be reconstructed (Fig. 3b and Supplementary Video S1 in the Supplementary Information). It is obvious that strong THG signal features are prominent among all the entities in the cytoplasm. According to the literature these are most likely lipid droplets since they have a large index of refraction in comparison with the rest of cytoplasm. In addition, the power dependence of the THG signal originating from LDs is provided in Supplementary Material (Fig. S3).

The cell wall and plasma membrane are separated by a very small distance which is not resolvable in the images of native hyphae obtained by diffraction limited techniques (resolution of approximately 250 nm). To visualize the cell wall and the plasma membrane separately, we plasmolyzed the hyphae so the plasma membrane was retracted from the cell wall at a resolvable distance (Fig. 3c). The retracted cytoplasm is clearly visible in bright-field (Fig. 3c left) and autoTPEF images (Fig. 3c middle), but the plasma membrane can be solely distinguished only in the THG image (Fig. 3c right) since its refractive index is different from the cytoplasm.

There is no significant overlap of AutoTPEF and THG signal in the hyphae. While THG imaging is not necessarily specific for LDs, because the THG signal is produced by any refractive index change, LDs still produce significantly higher THG signal in comparison with other structures in the cytoplasm of a cell like *P. blakesleeanus*. This fact can be used to extract LDs in a cell, over a broad but still much lower signal range than other cytoplasm entities. As the very first step toward the confirmation that high THG signal features in unlabeled live *P. blakesleeanus* are LDs, we performed the imaging of the same hyphae by detecting auto fluorescence signal upon two photon excitation at 730 nm (Fig. 4a left). In order to ensure that high THG signal entities (Fig. 4a right) are not artifacts that might be caused by e.g. high laser intensity damage, we merged the two images, THG and autoTPEF (Fig. 4a middle) showing clearly there is no significant increase of TPEF signal at the same locations. The hyphae were in exponential growth phase, as in Fig. 3.

Colocalization of lipid droplets signal imaged by TPEF and THG. Whilst many label-free imaging studies on various biological samples have shown that strong THG contrast in the cytoplasm arises mostly from LDs[11,35,36], in the case of *Phycomyces blaekseneanus* THG imaging has never been applied to this type of organism.

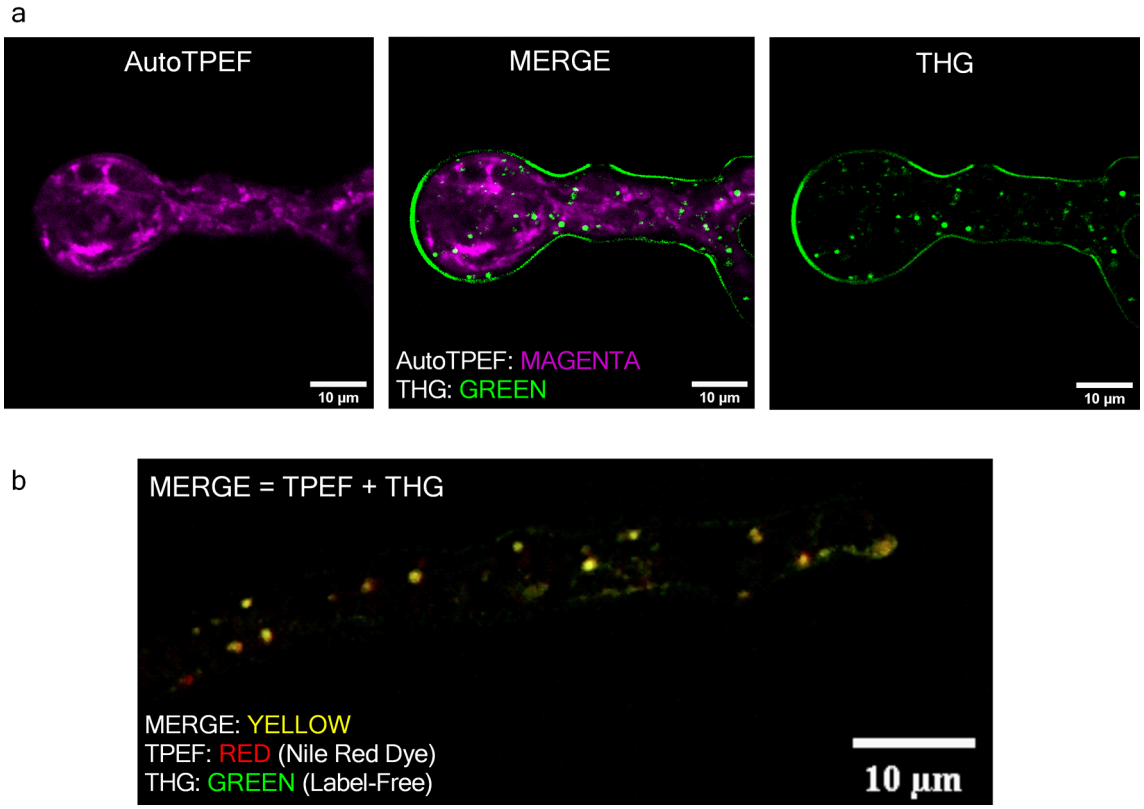

Figure 4. TPEF and THG images of *Phycomyces blakesleeanus* exponential growth phase hyphae in standard liquid medium show that the predominant source of spot wise THG signal are lipid droplets. (**a**) Merged autoTPEF and THG images of same unlabeled live hypha showing that there is no overlap of autoTPEF and THG signal. The average laser power at sample plane was 28 mW at 1040 nm (for THG) and 3.4 mW at 730 nm (autoTPEF). (**b**) In vivo colocalization of stained LDs imaged by TPEF and LDs imaged by THG modality. Average laser power at sample plane was 32 mW for both THG and TPEF at 1040 nm. Pearson's correlation coefficient $R_{total} = 0.844$ (ImageJ, The Colocalization Threshold plugin). All images were taken with Zeiss 40 × 1.3 oil objective lens.

To prove firmly that the cytoplasmic puncta in THG images of hyphae are LDs we performed colocalization experiments (Fig. 4b). The hyphae were stained by Nile Red dye which is considered as a standard for lipids[69]. The TPEF of Nile Red dye was excited by the same laser used for THG and the TPEF signal was collected through 400–700 nm band pass and 570 nm long pass filters, which effectively isolates the fluorescence signal to the 570–700 nm spectral region. The laser beam was focused with the Zeiss Plan Neofluar 40 × 1.3 objective lens, and both, TPEF and THG signals were detected simultaneously. Before the measurement, a very small volume of the sample (10 µl of fungi suspension) was added between two coverslips. This enables hyphae to stay alive during the imaging but also to be immobilized as close as possible to the coverslip thus achieving the best possible resolution.

The quantitative comparison of the TPEF and THG images (colocalization analysis) was performed based on Pearson's correlation coefficient and Image Cross-Correlation Spectroscopy (ICCS). Pearson's correlation coefficient was in the range $0.74 < R_{total} < 0.88$ (ImageJ, The Colocalization Threshold plugin). According to the ICCS analysis, the fraction of THG-detected clusters interacting with the TPEF-detected clusters was 0.89 indicating a high degree of spatial correlation between fluctuations generated from the lipid probe and THG signal. The degree of colocalization obtained in our work is in accordance or higher with those obtained in label-free imaging on live and in some fixed samples[7,70].

Based on the colocalization experiment (Fig. 4b) and the results shown in Fig. 4a one might consider that most round bright features in THG images of *Phycomyces blaekseneanus* are the lipid droplets.

THG image analysis and quantification of lipid droplets. For the quantification of LDs, we analyzed a small set of THG images by Particle Size Analysis and Image Correlation Spectroscopy (both available in ImageJ). To test and compare the two methods we used hyphae cultures grown in completely nitrogen-depleted media (N–starved) and their age-matched sister cultures from the same batch grown in standard media as a control. Nitrogen limitation is known to cause autophagy in filamentous fungi[71], leading to alterations in lipid metabolism and an increase in the number of LDs[72,73]. We performed THG imaging on hyphae in exponential growth phase, alternating between control (Fig. 5a) and N-starved (Fig. 5b) age matched hypha batches. From Fig. 5 it is obvious, even by the bare eye, that there is significant increase in LD number after nitrogen starvation

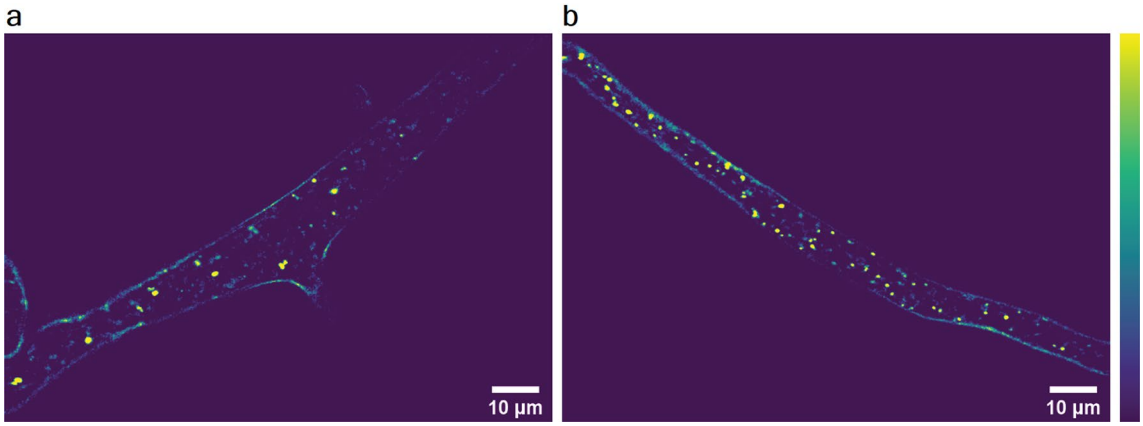

Figure 5. THG images of N-starved hyphae. (**a**) control hyphae; (**b**) N-starved (4.5 h duration of growth in nitrogen-depleted conditions). Both images were taken with Zeiss 40 × 1.3 objective lens whilst average laser power at sample plane was 24 mW (in A) and 20 mW (in B). Violet-lowest THG signal, yellow—highest THG signal.

for 4.5 h. Once we confirmed that we obtained the expected increase of LD number, we went ahead to test the two methods of quantification and the sensitivity of THG imaging for LDs detection.

For the PSA method (available in ImageJ as "Analyze particles") the raw THG image (Fig. 6a left) was thresholded and converted to an 8-bit mask, upon which the program automatically counted the number of "particles" representing LDs in images analyzed (Fig. 6a middle). In addition to the number of particles, the diameter and area were quantified as well.

Because of the thresholding and limited resolution of the image (pixel size), the PSA might be insensitive to very small or weak signal entities. As the result, some emerging LDs might be omitted and not shown in the final results. To resolve this issue, we performed ICS which extracts the information on particle properties (number and size) based on the spatial fluctuations of the signal intensity in the images. ICS is also applicable to images that are diffuse.

Due to the morphology of the hyphae, it was necessary to pre-process THG images before applying the ICS analysis. Cell wall of hyphae was removed from the image since it hinders the correlation analysis (producing the pedestal at the G curve) because of the sharp discontinuity in intensity at the periphery of the hyphae along the whole circumference. We applied multiple subtractions of the background (average pixel intensity of ROI outside the hypha) until the wall disappears[74]. The latter procedure is depicted in Fig. 6a right and it is obvious that the THG signal from the majority of LDs is much more intense than the signal from the wall (approx. > 10x).

After removal of the cell wall, image correlation procedure was performed in Image J. As the result one obtains a spatial autocorrelation image from which the G curve is extracted by taking an intensity profile through the center of the image. An example of a G curve is shown in Fig. 6b. The number of LDs was calculated using the following formula:

$$N_{LD} = \frac{N_{pix} \cdot N_{pix}}{r^2 \pi \cdot G(0)}$$

where N_{pix} is the pixel size of the $2^n \times 2^n$ image (where n is an integer), r is mean radius of LDs taken as half of the FWHM of the G curve, and G (0) is maximal value of the G curve. r and G (0) are extracted from the Lorentzian fit of the G curve (Fig. 6b insert). It should be noted that the morphology of the LDs differs substantially from the morphology of the clusters which are usually examined by ICS analysis. Thus, in our case, multiple subtractions of the background do not lead to the flattening of the curve G versus number of subtractions as might be expected[74]. The flattening of the G curve shown in the reference 74 is used as criterion how many times the background has to be subtracted before ICS is applied. Our criteria for the number of background subtraction were: (a) cessation of a significant reduction in the number of LDs after each subsequent subtraction (Fig. 6c, black squares), (b) approximate matching of the number of LDs per hyphae with PSA and (c) experience (the cell wall disappears from the image observed by the eye). Upon examination of tens of images, both control and treated hyphae, we concluded that, on average (depending on initial image quality), 20 consecutive subtractions were sufficient for reliable ICS analysis.

To check whether the extra removal of the cell wall would give different number of LDs, we performed manual removal of the cell wall solely. It was done by delineation and cropping prior to the multiple background subtractions. After 20 consecutive background subtractions, this method does not give substantially different results in the number of LDs compared to images where the cell wall was not manually cropped (illustrated by the graph in Fig. 6c).

LDs analysis by PSA and ICS. A comparison of LD number and size obtained by ICS and PSA is in Table 1. The number of LDs per area of hyphae is approximately the same on average, but mean diameter obtained by ICS

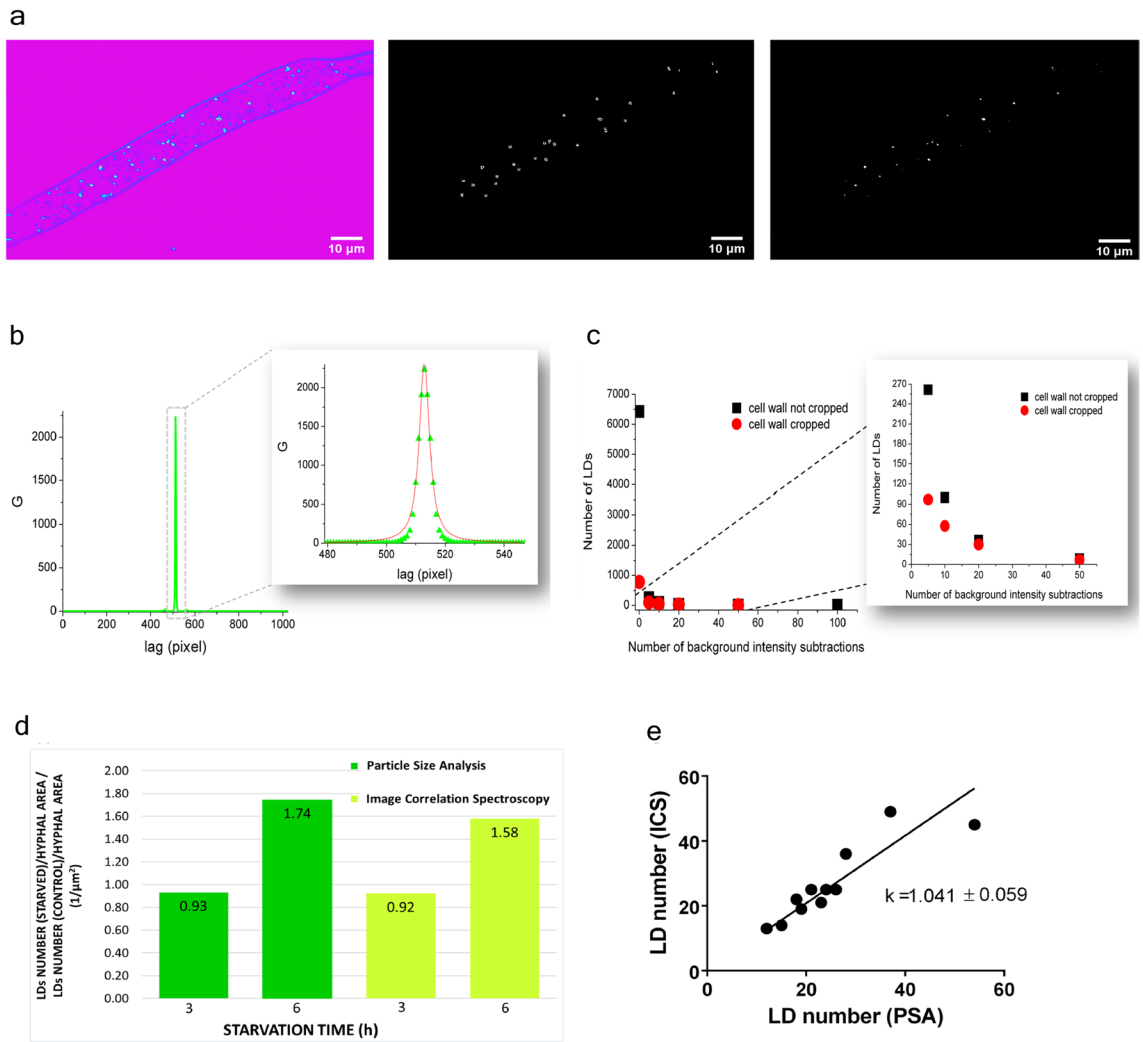

Figure 6. Image Correlation Spectroscopy (ICS) and Particle Size Analysis (PSA) on THG images. (**a**) Processing for PSA and ICS analysis of the same THG image. Left: The unprocessed THG image of *Phycomyces blakesleeanus* exponential growth phase hyphae in standard liquid medium; middle: 8-bit mask obtained in Particle size analysis; right: background subtracted image for ICS analysis. The image from left (unprocessed THG image) was processed by applying 20 × background subtractions. Both images are displayed at full dynamic range (8 bits). THG image was taken with Zeiss 40 × 1.3 objective lens, while average laser power at sample plane was 27 mW. (**b**) ICS analysis: The autocorrelation function (G curve) taken as the plot through the center of intensity correlated THG image of a live and unlabeled hyphae. The autocorrelation curve was fit to a Lorentzian function to extract FWHM value as described in Methods section. (**c**) ICS analysis, the effect of the cell wall removal: The number of LDs obtained from the G curves after each background subtraction for the THG image where the cell wall was manually cropped (red circles) and for the same THG image where cell wall was not cropped prior to the background subtractions (black squares). (**d**) Comparison of ICS- and PSA—derived data obtained from the same set of THG images of cultures N-starved for 3 h and 6 h and their age-matched controls (n = 3 for each group). The ratio of the number of LDs per unit hyphal area, in N-starved hypha to the number of LDs per unit hypha area in age- matched controls. (**e**) The agreement of LD number quantification obtained by ICS and PSA. For each image, ICS-obtained LD number is plotted against PSA-obtained LD number for that image. Data for both graphs were obtained from label-free THG images, whose analysis is presented in Table 1.

is slightly lower. This discrepancy might be explained because of different definitions for the object size used in those two methods.

To estimate the change of LD number in treated hyphae, we calculated the ratio of LD number per area in treated hyphae in respect to control ones (Fig. 6d). The total number of LDs after 3 h of starvation shows no significant change. With longer starvation time the number of LDs increases by more than 50%.

Using ICS analysis, number of features counted was 80 ± 12% of the LD number that was found by visual inspection (n = 12) and in close correlation with the data obtained by PSA. When numbers of obtained LDs by both methods are plotted for each individual image as a separate point (Fig. 6e), the regression line has a slope close to 1, confirming that ICS is equally reliable as PSA method in detecting and counting LDs. The coefficient of regression R^2 was approximately 0.8.

Control/Treatment	Image correlation spectroscopy		Particles size analysis	
	Number of LDs/hyphae area (1/μm^2) × 10^{-3} (mean ± SE)	Mean LDs diameter (μm) (mean ± SE)	Number of LDs/hyphae area (1/μm^2) × 10^{-3} (mean ± SE)	Mean LDs diameter (μm) (mean ± SE)
Control cells for 3 h N-starvation	16 ± 1	0.56 ± 0.06	16 ± 2	0.74 ± 0.02
3 h N-starved cells	15 ± 5	0.60 ± 0.10	15 ± 6	0.74 ± 0.03
Control cells for 6 h N-starvation	15 ± 4	0.52 ± 0.08	13 ± 3	0.78 ± 0.02
6 h N-starved cells	24 ± 3	0.46 ± 0.02	22 ± 4	0.74 ± 0.04

Table 1. A comparison of the number and size of lipid droplets obtained by the quantification analysis of the two methods, ICS and PSA. n = 3 for each group presented.

Nitrogen starvation induced changes in lipid droplet number and size, as quantified from THG images. To fully use THG imaging (exposure time for an image takes maximum 30 s for 1024 × 1024 pixels image with 30 averages) and subsequent analysis as a LD assay, we performed a set of imaging and measurements across time, from filamentous fungi cultures, grown in nitrogen-depleted and control conditions. Fungi cultures were imaged after growing at least 2 h post start of the treatment (nitrogen starvation or control), precautionary step to avoid possible effects of manipulation during preparation for the start of treatment (e.g. centrifugation).

The number of LDs per unit cell area (Number of LDs/hypha area) in all imaged hypha in fungi cultures grown in nitrogen depleted media (N-starved) was significantly larger compared to the entire group of control culture hypha (Control) (Fig. 7a). To elucidate the time course of observed induction of increase in LD number, the Control and N-starved groups are broken down to duration-from-start-of-treatment groups each, and values of Number of LDs/hypha area plotted across time (Fig. 7b). The Number of LDs/hypha area in Controls remained almost the same during the time of observation, with the slight, not significant, trend of increase towards the later growth time points (Fig. 7b). N-starved had similar Number of LDs/hypha area to corresponding Control only at the 3 h of treatment time point. We detected twofold increase of Number of LDs/hypha area after 4.5 h treatment, compared to corresponding Control. Significant increase of Number of LDs/hypha area in N-starved hypha, compared to corresponding Control hypha, persisted at longer times of treatment (Fig. 7b).

The average diameter of LDs was significantly reduced in N-starved cultures, compared to controls, when entire groups were compared regardless of treatment time (Fig. 7c). As it can be seen from the time course graph (Fig. 7d), average LD diameters were approximately the same from the 2 h treatment time to the longest treatment time in Controls. They were also same in 3 h and 4.5 h N-starved hypha and their corresponding Controls. The effect of N-starvation on average LD size becomes clear only after 6 h or more of treatment (Fig. 7d).

The histograms of LD diameters, graphed as Number of LDs/hypha area (Fig. 7e) for the 4.5 h and 6 h time-of-treatment groups, reveal that LDs smaller than 1.6 μm are more numerous in N-starved groups than in corresponding Controls for 4.5 h time point, while at 6 h, only the number of LDs smaller than 1 μm is increased. LD average diameter change between 4.5 and 6 h N-starvation groups seems to be a result of significant loss of population of LDs larger than 0.6 μm during prolonged growth in N-starving conditions. To summarize, the overall change in LDs during growth without available nitrogen is found to be an increase in number of LDs between 3 and 4.5 h time point, followed with the loss of population of larger-than-average LDs during prolonged starvation.

Discussion

Once considered to be passive lipid storage agglomerations, lipid droplets are now recognized as dynamic cellular organelles, serving as ubiquitous central hubs of energy and lipid homeostasis in eukaryotic cells[75]. Studies of lipid droplet physiology in fungi, although still scarce[76], harbor promise of providing novel solutions for a number of important issues: mitigation and modulation of fungal resistance to fungicides and stress, securing the food safety, better understanding how to use fungi as a crucial component of sustainable organic waste reuse and conversion to energy source, to name a few. *Phycomyces blakesleeanus*, model fungus used in our study, belongs to *Mucormycota,* the phylogenetic group of fungi able of forming arbuscular mycorrhiza and other mutually beneficial symbiosis[77] with terrestrial plants[78]. During fungi-plant mutually beneficial interaction, a fungi transports nitrogen to a plant, and receives up to 30% of organic C compounds synthesized by a plant[78] in return. It is known that organic molecules sent from plant to fungi are lipids[79,80], and that lipid droplets form in large amounts in hypha adjacent to the area of contact with the plant[81]. Similar to *Phycomyces*, arbuscular mycorrhizal fungi can accumulate significant amount of acquired organic carbon in the form of lipid droplets[82]. THG imaging of LDs as described here is a method that could be directly applied to living mycorrhizal fungi related to *Phycomyces*, without the need for any modification of the protocol, or other staining.

The fungi culturing conditions used in our study resulted in a fairly modest accumulation of lipid droplets, as expected[62]. THG imaging analysis enabled us to watch and quantify changes in lipid droplet number, brought upon by complete removal of nitrogen, from such low density/diameter baseline. As expected, complete omission of nitrogen induced only a transient increase in number of lipid droplets, followed by lipid turnover[83]. THG imaging analysis detected the significant decline of lipid reserve at late stages of growth. Altogether, this shows the usefulness of THG imaging approach for broader exploration of LD in filamentous fungi under various living conditions.

Optical imaging techniques are commonly used to study lipid droplets in vivo, but lipids usually have to be labeled with various dyes. On the other hand, prolonged imaging using fluorescent dyes can be phototoxic to

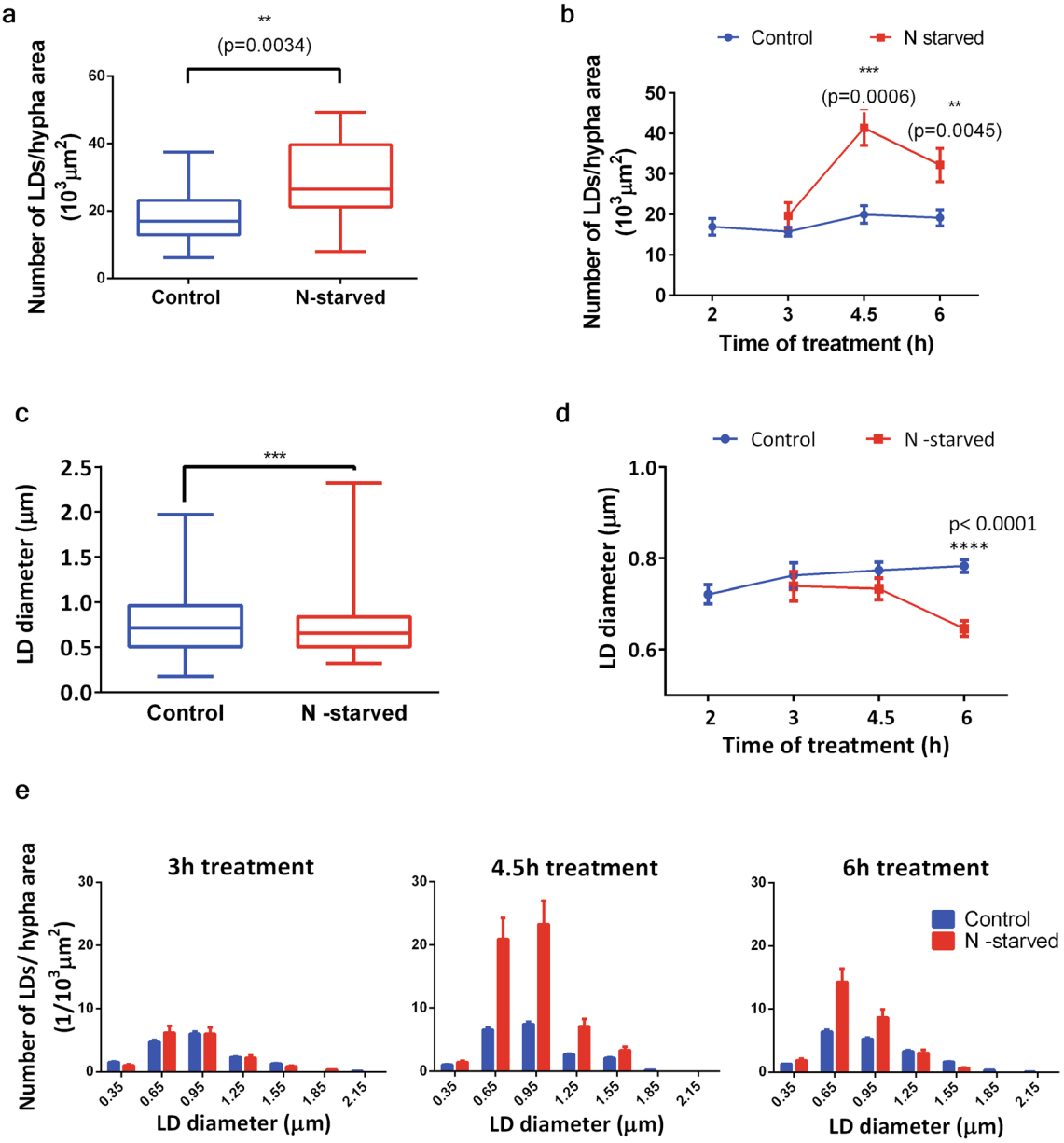

Figure 7. Quantification of LDs from THG images of *Phycomyces blaekseneanus* hypha. Hypha were cultured without nitrogen or in standard liquid media for 2–6 h (or longer up to 8 h) after the start of treatment. Obtained THG images of LDs were analyzed by PA. n = 6 independent cultures. (**a**) N-starvation increases number of LDs per unit area. LD number obtained from the individual hypha is normalized to hypha area (in 10^3 µm^2). Control (n = 44), N-starved group (n = 17). The box and whisker plots, enclosed by the 25th and 75th percentile range, median line with whiskers extending minimal to maximal value. Unpaired t test with Welch's correction, two tail, $p = 0.0038$. (**b**) Time course of LD number/unit area, showing that the increase of LD number by N-starvation is significant at 4.5 h ($p = p = 0.0006$) and later times ($p = 0.0045$), compared to corresponding control. Two-way ANOVA, with Holm-Sidac correction. Mean ± SE, $n_{(Control)} = 8$; 7; 11; 21 for time points (in h), respectively: 2; 3; 4.5; 6. $n_{(N\text{-}starved)} = 6$; 3; 7 for time points (in h), respectively: 3; 4.5; 6. (**c**) N-starvation decreases diameter of LDs. LD diameters from Control (n = 1205) and N-starved group (n = 431). The box and whisker plots, enclosed by the 25th and 75th percentile range, median line with whiskers extending minimal to maximal value. Mann–Whitney ($p = 0.0008$), two-tailed. (**d**) Time course of LD diameter changes, showing that the decrease by N-starvation is significant only at long starvation times. Two-way ANOVA, Holm-Sidac correction ($p < 0.0001$), compared to corresponding control. Mean ± SE, $n_{(Control)} = 176$; 124; 302; 571 for time points (in h), respectively: 2; 3; 4.5; 6. $n_{(N\text{-}starved)} = 100$; 118; 214 for time points (in h), respectively:3; 4.5; 6. (**e**) Differential distribution of increased number of LDs after 4.5 h and 6 h N-starvation. The largest LDs are lost at longest starvation times. Histograms of LD diameter distributions, 0.3 µm binning, for Control and N-starved group. Number of LDs in each bin of the histogram is divided by sum of hypha area of the appropriate group. Errors are calculated as stated in Methods section. Numbers on x axes represent the upper bin limit.

cells and may perturb metabolic processes, including lipid metabolism. Hence, label-free imaging methods, are advantageous for the study of living cells[84–86].

THG imaging, a label-free method we have applied to live hyphae of oleaginous fungi *Phycomices blakesleeanus*, generated images with the characteristic spots of high THG signal intensity attributed to lipid droplets as the products of normal and stressed cellular physiology. Several lines of evidence support this attribution. First, the steep change of refractive index between lipids at the interface of lipid droplets and the rest of the cytoplasm generates high intensity THG signal, according to literature[11]. Second, to exclude possible laser-damaged spots that would produce high THG signal, we performed TPEF imaging of unstained hyphae showing that autoTPEF images are devoid of any prominent spots, present on a THG image of the same hypha. Third, we have performed colocalization experiments where the hyphae were stained with lipid specific dye and imaged by both, TPEF and THG method. The spots at the both images were mostly overlapped which verifies that the spots contained lipids. In addition, following the same logic of steep changes of refractive index, we have shown that the cell wall and the cell membrane in label-free hyphae can be imaged and distinguished by THG method.

There are a number of caveats to be discussed regarding the imaging of lipid stains. Because of the simultaneous detection of both (TPEF and THG) signals restricted number of dyes for live imaging could be used. In this study fixation was not a choice since it alters the structure of LDs[87]. The dye used in this study, Nile Red, might be not so specific for LDs and it can bind to other bodies and structures in the cell[88]. The signal originating from other structures than LDs can bleed into the detection band which eventually might affect the colocalization degree. In addition, the degree of colocalization is further deteriorated by the strong THG signal from the cell wall. The THG imaging requires significantly higher laser powers in comparison to the TPEF imaging. Because of that, one has to make a trade-off in terms of applied laser power when detecting both signals simultaneously. The price paid for this trade-off is the loss of some structures (e.g. small LDs, otherwise visible at higher laser powers) in THG images and appearance of weak, blurry TPEF signal from out of focus LDs (otherwise not visible at lower laser powers).

To extract quantitative data from THG images, two methods for image analysis were applied, Particle Size Analysis (PSA) and Image Correlation Spectroscopy (ICS). Both methods can quantify the number of lipid droplets and their average size (diameter). Since ICS was primarily developed for fluorescent images and cluster analysis and to the best of our knowledge it was not used so far for THG images, we have tested it by comparing the results to the PSA. The test was performed on the images of the hyphae under normal and stressed (nitrogen starvation) circumstances. The nitrogen starvation is known to cause increased number of lipid droplets[72,73] which was confirmed by both methods and the agreement between numbers obtained by both methods was good.

Overall, the proposed imaging method (THG) and the method of image analysis (ICS) was shown to be suitable for label-free in vivo studies of lipid droplets of oleaginous fungi. Application of THG method to future studies of lipid droplet dynamics in fungi could help to advance basic understanding of fungi cellular physiology, and then, of processes involved in the cycling of carbon in nature.

Data availability

The data available upon a reasonable request to the corresponding author.

Received: 23 June 2022; Accepted: 1 November 2022
Published online: 05 November 2022

References

1. Weigelin, B., Bakker, G. J. & Friedl, P. Third harmonic generation microscopy of cells and tissue organization. *J. Cell Sci.* **129**, 245–255 (2016).
2. Yelin, D. & Silberberg, Y. Laser scanning third-harmonic-generation microscopy in biology. *Opt. Express* **5**(8), 169–175 (1999).
3. Barzda, V. *et al.* Visualization of mitochondria in cardiomyocytes. *Opt. Express* **13**, 8263 (2005).
4. Witte, S. *et al.* Label-free live brain imaging and targeted patching with third-harmonic generation microscopy. *Proc. Natl. Acad. Sci. U. S. A.* **108**, 5970–5975 (2011).
5. Tsai, C.-K. *et al.* Imaging granularity of leukocytes with third harmonic generation microscopy. *Biomed. Opt. Express* **3**, 2234 (2012).
6. Weigelin, B., Bakker, G.-J. & Friedl, P. Intravital third harmonic generation microscopy of collective melanoma cell invasion. *IntraVital* **1**, 32–43 (2012).
7. Gavgiotaki, E. *et al.* Third Harmonic Generation microscopy as a reliable diagnostic tool for evaluating lipid body modification during cell activation: The example of BV-2 microglia cells. *J. Struct. Biol.* **189**, 105–113 (2015).
8. Oron, D. *et al.* Depth-resolved structural imaging by third-harmonic generation microscopy. *J. Struct. Biol.* **147**, 3–11 (2004).
9. Sun, C.-K. *et al.* Multiharmonic-generation biopsy of skin. *Opt. Lett.* **28**, 2488 (2003).
10. Aptel, F. *et al.* Multimodal nonlinear imaging of the human cornea. *Investig. Ophthalmol. Vis. Sci.* **51**, 2459–2465 (2010).
11. Débarre, D. *et al.* Imaging lipid bodies in cells and tissues using third-harmonic generation microscopy. *Nat. Methods* **3**, 47–53 (2006).
12. Farrar, M. J., Wise, F. W., Fetcho, J. R. & Schaffer, C. B. In vivo imaging of myelin in the vertebrate central nervous system using third harmonic generation microscopy. *Biophys. J.* **100**, 1362–1371 (2011).
13. Genthial, R. *et al.* Label-free imaging of bone multiscale porosity and interfaces using third-harmonic generation microscopy. *Sci. Rep.* **7**, 1–16 (2017).
14. Gavgiotaki, E. *et al.* Third Harmonic Generation microscopy distinguishes malignant cell grade in human breast tissue biopsies. *Sci. Rep.* **10**, 1–13 (2020).
15. Canioni, L. *et al.* Imaging of Ca^{2+} intracellular dynamics with a third-harmonic generation microscope. *Opt. Lett.* **26**, 515–517 (2001).
16. Chen, Y.-C. *et al.* Third-harmonic generation microscopy reveals dental anatomy in ancient fossils. *Opt. Lett.* **40**, 1354 (2015).
17. Chang, T. *et al.* Non-invasive monitoring of cell metabolism and lipid production in 3D engineered human adipose tissues using label-free multiphoton microscopy. *Biomaterials* **34**, 8607–8616 (2013).
18. Débarre, D. *et al.* Velocimetric third-harmonic generation microscopy: micrometer-scale quantification of morphogenetic movements in unstained embryos. *Opt. Lett.* **29**, 2881 (2004).

19. Sun, C. K. *et al.* Higher harmonic generation microscopy for developmental biology. *J. Struct. Biol.* **147**, 19–30 (2004).
20. Watanabe, T. *et al.* Characterisation of the dynamic behaviour of lipid droplets in the early mouse embryo using adaptive harmonic generation microscopy. *BMC Cell Biol.* **11**(1), 1–11 (2010).
21. Tserevelakis, G. J. *et al.* Imaging Caenorhabditis elegans embryogenesis by third-harmonic generation microscopy. *Micron* **41**, 444–447 (2010).
22. Aviles-Espinosa, R. *et al.* Cell division stage in C. elegans imaged using third harmonic generation microscopy. In *Biomedical Optics and 3-D Imaging (2010), Paper BTuD78 BTuD78* (The Optical Society, Washington, 2013).
23. Yu, M. M. L. *et al.* In situ analysis by microspectroscopy reveals triterpenoid compositional patterns within leaf cuticles of Prunus laurocerasus. *Planta* **227**, 823–834 (2008).
24. Prent, N. *et al.* Applications of nonlinear microscopy for studying the structure and dynamics in biological systems. *Photonic Appl. Nonlinear Opt. Nanophotonics Microw. Photonics* **5971**, 597106 (2005).
25. Tokarz, D. *et al.* Molecular organization of crystalline β-carotene in carrots determined with polarization-dependent second and third harmonic generation microscopy. *J. Phys. Chem. B* **118**, 3814–3822 (2014).
26. Cisek, R. *et al.* Optical microscopy in photosynthesis. *Photosynth. Res.* **102**, 111–141 (2009).
27. Barzda, V. *Non-Linear Contrast Mechanisms for Optical Microscopy* 35–54 (Springer, Dordrecht, 2008).
28. Segawa, H. *et al.* Label-free tetra-modal molecular imaging of living cells with CARS, SHG, THG and TSFG (coherent anti-Stokes Raman scattering, second harmonic generation, third harmonic generation and third-order sum frequency generation). *Opt. Express* **20**, 9551 (2012).
29. Barad, Y., Eisenberg, H., Horowitz, M. & Silberberg, Y. Nonlinear scanning laser microscopy by third harmonic generation. *Appl. Phys. Lett.* **70**, 922–924 (1997).
30. Boyd, R. W. *Nonlinear Optics* (Academic Press, New York, 2008).
31. Iy, Y., En, L. & Vv, T. Refractive index of adipose tissue and lipid droplet measured in wide spectral and temperature ranges. *Appl. Opt.* **57**, 4839 (2018).
32. Liu, P. Y. *et al.* Cell refractive index for cell biology and disease diagnosis: past, present and future. *Lab Chip* **16**, 634–644 (2016).
33. Chen, Y.-C., Hsu, H.-C., Lee, C.-M. & Sun, C.-K. Third-harmonic generation susceptibility spectroscopy in free fatty acids. *J. Biomed. Opt.* **20**, 095013 (2015).
34. Small, D. M. *et al.* Label-free imaging of atherosclerotic plaques using third-harmonic generation microscopy. *Biomed. Opt. Express* **9**, 214 (2018).
35. Bautista, G. *et al.* Polarized thg microscopy identifies compositionally different lipid droplets in mammalian cells. *Biophys. J.* **107**, 2230–2236 (2014).
36. Tserevelakis, G. J. *et al.* Label-free imaging of lipid depositions in C. elegans using third-harmonic generation microscopy. *PloS One* **9**(1), e84431 (2014).
37. Siddhanta, S., Paidi, S. K., Bushley, K., Prasad, R. & Barman, I. Exploring morphological and biochemical linkages in fungal growth with label-free light sheet microscopy and Raman spectroscopy. *ChemPhysChem* **18**, 72–78 (2017).
38. Zhang, C., Li, J., Lan, L. & Cheng, J.-X. Quantification of lipid metabolism in living cells through the dynamics of lipid droplets measured by stimulated Raman scattering imaging. *Anal. Chem.* **89**, 4502–4507 (2017).
39. Brackmann, C. *et al.* CARS microscopy of lipid stores in yeast: The impact of nutritional state and genetic background. *J. Raman Spectrosc.* **40**, 748–756 (2009).
40. Zhang, C. & Boppart, S. A. Dynamic signatures of lipid droplets as new markers to quantify cellular metabolic changes. *Anal. Chem.* **92**, 15943–15952 (2020).
41. Dong, P. T. *et al.* Polarization-sensitive stimulated Raman scattering imaging resolves amphotericin B orientation in Candida membrane. *Sci. Adv.* **7**, 1–11 (2021).
42. Yasuda, M., Takeshita, N. & Shigeto, S. Inhomogeneous molecular distributions and cytochrome types and redox states in fungal cells revealed by Raman hyperspectral imaging using multivariate curve resolution-alternating least squares. *Anal. Chem.* **91**, 12501–12508 (2019).
43. Kurian, S. M., Pietro, A. . Di. & Read, N. D. Live-cell imaging of conidial anastomosis tube fusion during colony initiation in Fusarium oxysporum. *PLoS One* **13**, e0195634 (2018).
44. Adomshick, V., Pu, Y. & Veiga-Lopez, A. Automated lipid droplet quantification system for phenotypic analysis of adipocytes using Cell Profiler. *Toxicol. Mech. Methods* **30**, 378–387 (2020).
45. Jüngst, C., Klein, M. & Zumbusch, A. Long-term live cell microscopy studies of lipid droplet fusion dynamics in adipocytes. *J. Lipid Res.* **54**, 3419–3429 (2013).
46. Exner, T. *et al.* Lipid droplet quantification based on iterative image processing. *J. Lipid Res.* **60**, 1333–1344 (2019).
47. Rambold, A. S., Cohen, S. & Lippincott-Schwartz, J. Fatty acid trafficking in starved cells: Regulation by lipid droplet lipolysis, autophagy, and mitochondrial fusion dynamics [Developmental Cell 32 (2015) 678–692]. *Dev. Cell* **32**, 678–692 (2015).
48. Dejgaard, S. Y. & Presley, J. F. New automated single-cell technique for segmentation and quantitation of lipid droplets. *J. Histochem. Cytochem.* **62**, 889–901 (2014).
49. Nohe, A. & Petersen, N. O. Image correlation spectroscopy. *Sci. STKE* **2007**, (2007).
50. Wiseman, P. W., Squier, J. A., Ellisman, M. H. & Wilson, K. R. Two-photo image correlation spectroscopy and image cross-correlation spectroscopy. *J. Microsc.* **200**, 14–25 (2000).
51. Slenders, E. *et al.* Image Correlation spectroscopy with second harmonic generating nanoparticles in suspension and in cells. *J. Phys. Chem. Lett.* **9**, 6112–6118 (2018).
52. Bahram, M. & Netherway, T. Fungi as mediators linking organisms and ecosystems. *FEMS Microbiol. Rev.* **46**, 1–16 (2022).
53. Parihar, M. *et al.* The potential of arbuscular mycorrhizal fungi in C cycling: A review. *Arch. Microbiol.* **202**, 1581–1596 (2020).
54. Ratledge, C. Regulation of lipid accumulation in oleaginous microorganisms. *Biochem. Soc. Trans.* **30**, A101–A101 (2002).
55. Cerdá-Olmeda, E. & Avalos, J. Oleaginous fungi: Carotene-rich from Phycomyces. *Prog. Lipid Res.* **33**, 185–192 (1994).
56. Passoth, V. Lipids of yeasts and filamentous fungi and their importance for biotechnology. *Biotechnol. Yeasts Filamentous Fungi* https://doi.org/10.1007/978-3-319-58829-2_6 (2017).
57. Mhlongo, S. I. *et al.* The potential of single-cell oils derived from filamentous fungi as alternative feedstock sources for biodiesel production. *Front. Microbiol.* **12**, 57 (2021).
58. Chang, W. *et al.* Trapping toxins within lipid droplets is a resistance mechanism in fungi. *Sci. Rep.* **51**(5), 1–11 (2015).
59. Liu, N. *et al.* Lipid droplet biogenesis regulated by the FgNem1/Spo7-FgPah1 phosphatase cascade plays critical roles in fungal development and virulence in Fusarium graminearum. *New Phytol.* **223**, 412–429 (2019).
60. Petschnigg, J. *et al.* Good fat, essential cellular requirements for triacylglycerol synthesis to maintain membrane homeostasis in yeast. *J. Biol. Chem.* **284**, 30981–30993 (2009).
61. Suzuki, M., Shinohara, Y., Ohsaki, Y. & Fujimoto, T. Lipid droplets: Size matters. *J. Electron Microsc.* **60**, S101–S116 (2011).
62. Nand, K. & Mohrotra, B. S. Mycological fat production in India. II. Effect of hydrogen-ion concentration on fat synthesis. *Sydowia* **24**, 144–152 (1971).
63. Pollack, J. K., Harris, S. D. & Marten, M. R. Autophagy in filamentous fungi. *Fungal Genet. Biol.* **46**, 1–8 (2009).
64. Jaishy, B. & Abel, E. D. Lipids, lysosomes, and autophagy. *J. Lipid Res.* **57**, 1619–1635 (2016).
65. Petersen, N. O., Höddelius, P. L., Wiseman, P. W., Seger, O. & Magnusson, K. E. Quantitation of membrane receptor distributions by image correlation spectroscopy: Concept and application. *Biophys. J.* **65**, 1135–1146 (1993).

66. Bukara, K. *et al.* Mapping of hemoglobin in erythrocytes and erythrocyte ghosts using two photon excitation fluorescence microscopy. *J. Biomed. Opt.* **22**, 026003 (2017).
67. Despotović, S. Z. *et al.* Altered organization of collagen fibers in the uninvolved human colon mucosa 10 cm and 20 cm away from the malignant Tumor. *Sci. Rep.* **101**(10), 1–11 (2020).
68. Huang, S., Heikal, A. A. & Webb, W. W. Two-photon fluorescence spectroscopy and microscopy of NAD (P) H and flavoprotein. *Biophys. J.* **82**(5), 2811–2825 (2002).
69. Greenspan, P., Mayer, E. P. & Fowler, S. D. Nile red: A selective fluorescent stain for intracellular lipid droplets. *J. Cell Biol.* **100**, 965 (1985).
70. Yi, Y.-H. *et al.* Lipid droplet pattern and nondroplet-like structure in two fat mutants of Caenorhabditis elegans revealed by coherent anti-Stokes Raman scattering microscopy. *J. Biomed. Opt.* **19**, 011011 (2013).
71. Chen, Y. *et al.* Nitrogen-starvation triggers cellular accumulation of triacylglycerol in Metarhizium robertsii. *Fungal Biol.* **122**, 410–419 (2018).
72. Weng, L. C. *et al.* Nitrogen deprivation induces lipid droplet accumulation and alters fatty acid metabolism in symbiotic dinoflagellates isolated from Aiptasia pulchella. *Sci. Rep.* **4**, 1–8 (2014).
73. Aguilar, L. R. *et al.* Lipid droplets accumulation and other biochemical changes induced in the fungal pathogen Ustilago maydis under nitrogen-starvation. *Arch. Microbiol.* **199**, 1195–1209 (2017).
74. Rocheleau, J. V., Wiseman, P. W. & Petersen, N. O. Isolation of bright aggregate fluctuations in a multipopulation image correlation spectroscopy system using intensity subtraction. *Biophys. J.* **84**, 4011–4022 (2003).
75. Olzmann, J. A. & Carvalho, P. (2018) Dynamics and functions of lipid droplets. *Nat. Rev. Mol. Cell Biol.* **203**(20), 137–155 (2018).
76. Yu, Y. *et al.* The role of lipid droplets in Mortierella alpina aging revealed by integrative subcellular and whole-cell proteome analysis. *Sci. Rep.* **71**(7), 1–12 (2017).
77. Bonfante, P. & Venice, F. Mucoromycota: going to the roots of plant-interacting fungi. *Fungal Biol. Rev.* **34**, 100–113 (2020).
78. Smith, S. & Read, D. *Mycorrhizal Symbiosis* (Academic Press, New York, 2008).
79. Luginbuehl, L. H. *et al.* Fatty acids in arbuscular mycorrhizal fungi are synthesized by the host plant. *Science* **356**, 1175–1178 (2017).
80. Jiang, Y. *et al.* Plants transfer lipids to sustain colonization by mutualistic mycorrhizal and parasitic fungi. *Science* **356**, 1172–1173 (2017).
81. Keymer, A. *et al.* Lipid transfer from plants to arbuscular mycorrhiza fungi. *Elife* **6**, e29107 (2017).
82. Deka, D., Sonowal, S., Chikkaputtaiah, C. & Velmurugan, N. Symbiotic associations: Key factors that determine physiology and lipid accumulation in oleaginous microorganisms. *Front. Microbiol.* **11**, 555312 (2020).
83. Athenaki, M. *et al.* Lipids from yeasts and fungi: Physiology, production and analytical considerations. *J. Appl. Microbiol.* **124**, 336–367 (2018).
84. Fujita, K. & Smith, N. I. Label-free molecular imaging of living cells. *Mol. Cells OS* 530–535 (2008).
85. Knaus, H., Blab, G. A., van Jerre Veluw, G., Gerritsen, H. C. & Wösten, H. A. B. Label-free fluorescence microscopy in fungi. *Fungal Biol. Rev.* **27**, 60–66 (2013).
86. Borile, G., Sandrin, D., Filippi, A., Anderson, K. I. & Romanato, F. Label-free multiphoton microscopy: Much more than fancy images. *Int. J. Mol. Sci.* **22**, 2657 (2021).
87. Martins, A. S., Martins, I. C. & Santos, N. C. Methods for lipid droplet biophysical characterization in flaviviridae infections. *Front. Microbiol.* **9**, 1951 (2018).
88. Nile Red. Available at: https://www.thermofisher.com/order/catalog/product/N1142.

Acknowledgements

We thank Dunja Stefanović for invaluable help with growing of some cultures, and Marina Stanić for help with Nile red staining and many useful discussions. Also, we would like to thank Milan Minić for technical help and support.

Author contributions

T.P. conducted all the experiments, processed the images, and prepared the samples. N.T. designed the protocols and supervised the sample preparation and treatments. M.Ž. supervised the biological part of research. S.N. designed the acquisition and improved the software for imaging. M.R. designed the optical setup, supervised the imaging experiments and image analysis. A.C. supervised image processing, particularly LD quantification. A.K. designed the study, designed the optical setup, and supervised the experiments. All authors took participation in the manuscript preparation and revision.

Funding

This work was supported by the Ministry of Education, Science and Technological Development, Republic of Serbia [contract numbers: 451-03-68/2022-14/200178 and 451-03-68/2022-14/200007]; the Project HEMMAGINERO [Grant number 6066079] from Program PROMIS, Science Fund of the Republic of Serbia; and the Institute of Physics Belgrade, through the grant by the Ministry of Education, Science and Technological Development of the Republic of Serbia.

Competing interests

The authors declare no competing interests.

Additional information

Supplementary Information The online version contains supplementary material available at https://doi.org/10.1038/s41598-022-23502-4.

Correspondence and requests for materials should be addressed to A.J.K.

analytical chemistry

pubs.acs.org/ac Article

Dynamic Cellular Cartography: Mapping the Local Determinants of Oligodendrocyte Transcription Factor 2 (OLIG2) Function in Live Cells Using Massively Parallel Fluorescence Correlation Spectroscopy Integrated with Fluorescence Lifetime Imaging Microscopy (mpFCS/FLIM)

Sho Oasa,[¶] Aleksandar J. Krmpot,[¶] Stanko N. Nikolić,[¶] Andrew H. A. Clayton, Igor F. Tsigelny, Jean-Pierre Changeux, Lars Terenius, Rudolf Rigler,* and Vladana Vukojević*

Cite This: *Anal. Chem.* 2021, 93, 12011−12021 Read Online

ACCESS | Metrics & More | Article Recommendations | Supporting Information

ABSTRACT: Compartmentalization and integration of molecular processes through diffusion are basic mechanisms through which cells perform biological functions. To characterize these mechanisms in live cells, quantitative and ultrasensitive analytical methods with high spatial and temporal resolution are needed. Here, we present quantitative scanning-free confocal microscopy with single-molecule sensitivity, high temporal resolution (~10 μs/frame), and fluorescence lifetime imaging capacity, developed by integrating massively parallel fluorescence correlation spectroscopy with fluorescence lifetime imaging microscopy (mpFCS/FLIM); we validate the method, use it to map in live cell location-specific variations in the concentration, diffusion, homodimerization, DNA binding, and local environment of the oligodendrocyte transcription factor 2 fused with the enhanced Green Fluorescent Protein (OLIG2-eGFP), and characterize the effects of an allosteric inhibitor of OLIG2 dimerization on these determinants of OLIG2 function. In particular, we show that cytoplasmic OLIG2-eGFP is largely monomeric and freely diffusing, with the fraction of freely diffusing OLIG2-eGFP molecules being $f^{cyt}_{D,free}$ = (0.75 ± 0.10) and the diffusion time $\tau^{cyt}_{D,free}$ = (0.5 ± 0.3) ms. In contrast, OLIG2-eGFP homodimers are abundant in the cell nucleus, constituting ~25% of the nuclear pool, some $f^{nuc}_{D,bound}$ = (0.65 ± 0.10) of nuclear OLIG2-eGFP is bound to chromatin DNA, whereas freely moving OLIG2-eGFP molecules diffuse at the same rate as those in the cytoplasm, as evident from the lateral diffusion times $\tau^{nuc}_{D,free} = \tau^{cyt}_{D,free}$ = (0.5 ± 0.3) ms. OLIG2-eGFP interactions with chromatin DNA, revealed through their influence on the apparent diffusion behavior of OLIG2-eGFP, $\tau^{nuc}_{D,bound}$ (850 ± 500) ms, are characterized by an apparent dissociation constant $K^{OLIG2\text{-}DNA}_{d,app}$ = (45 ± 30) nM. The apparent dissociation constant of OLIG2-eGFP homodimers was estimated to be $K^{(OLIG2\text{-}eGFP)2}_{d,app} \approx 560$ nM. The allosteric inhibitor of OLIG2 dimerization, compound NSC 50467, neither affects OLIG2-eGFP properties in the cytoplasm nor does it alter the overall cytoplasmic environment. In contrast, it significantly impedes OLIG2-eGFP homodimerization in the cell nucleus, increasing five-fold the apparent dissociation constant, $K^{(OLIG2\text{-}eGFP)2}_{d,app,NSC50467} \approx 3$ μM, thus reducing homodimer levels to below 7% and effectively abolishing OLIG2-eGFP specific binding to chromatin DNA. The mpFCS/FLIM methodology has a myriad of applications in biomedical research and pharmaceutical industry. For example, it is indispensable for understanding how biological functions emerge through the dynamic integration of location-specific molecular processes and invaluable for drug development, as it allows us to quantitatively characterize the interactions of drugs with drug targets in live cells.

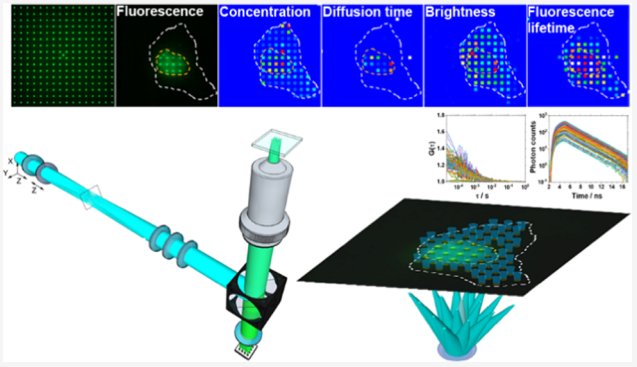

The intracellular environment is a complex and crowded, spatially heterogeneous medium the organization of which is bestowed and dynamically maintained through innumerable reaction-diffusion processes.[1,2] While strong interactions (bond dissociation energies D_0 > 20 kJ/mol) are important determinants of cellular physiology as they confer specificity and selectivity,[3] it is well established that weak, nonspecific interactions (D_0 < 20 kJ/mol), such as hydrogen bonding and interactions between permanent and transient

Received: May 21, 2021
Accepted: August 9, 2021
Published: August 24, 2021

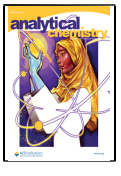

https://doi.org/10.1021/acs.analchem.1c02144
Anal. Chem. 2021, 93, 12011−12021

dipoles, are equally important despite being so weak that they can be broken with energies that are within the range of thermal fluctuations. At the molecular level, weak interactions define macromolecular configuration and conformation, and hence, their function.[4] At the cellular level, they are critical determinants of the overall organization of the cellular interior and significantly contribute to compartmentalization, i.e., the formation of distinct local environments (often called membrane-less organelles), where particular interactions between relevant biomolecules are enabled to efficiently proceed.[5−7] The evolution of mechanisms that harness weak cooperative interactions was recently shown to render living organisms more capable of robustly undergoing evolutionary changes, and it appears that such mechanisms have been repeatedly positively selected during the evolution of increasingly complex organisms.[8] The quest to deploy weak cooperative interactions is also of relevance for designing new drugs, in particular for the development of so-called allosteric drugs.[9−11] Allosteric drugs exploit a fundamental mechanism, initially identified in multisubunit/multimeric proteins,[12−14] which was later observed also in monomeric, intrinsically disordered proteins.[15] They bind to a distant binding site, inducing rearrangements in the network of weak cooperative interactions that propagate across comparatively long distances, eventually rendering the active site more/less amenable for orthosteric ligand/drug binding.[16] Efforts to develop allosteric drugs focus on understanding the function of natural molecules that act as allosteric modulators,[17] rely on the use of computational approaches to identify allosteric binding sites that can be specifically targeted,[18,19] and are inseparable from the advancement of experimental techniques to understand detailed molecular mechanisms that underlie allostery[20] and to characterize the effects of prospective allosteric drug candidates.[21] Experimental techniques designed to probe these processes in the cellular milieu need to be sensitive over a range of timescales (nanoseconds-to-seconds) and length scales (nanometers to microns).

Fluorescence correlation spectroscopy (FCS) and its dual-color variant fluorescence cross-correlation spectroscopy (FCCS) are the only presently available techniques that can nondestructively measure the concentration, diffusion, and binding of fluorescent/fluorescently labeled molecules in live cells with single-molecule sensitivity and high, sub-microsecond, temporal resolution.[22] However, the same feature of FCS/FCCS that enables the ultimate, single-molecule sensitivity—the possibility to probe a minute observation volume element, thereby significantly reducing the background and improving the signal-to-background-ratio, confers also a serious limitation. Thus, conventional FCS/FCCS is of limited overview, i.e., measurements are restricted to a single-point location, probing in the cell a tiny volume of $(0.2-2) \times 10^{-15}$ l.[23−26] To overcome this limitation, FCS was "amalgamated" with imaging-based methods, yielding new experimental techniques, such as temporal image correlation spectroscopy (TICS)[27] and raster image correlation spectroscopy (RICS),[28,29] which rely on raster scanning of the laser beam to illuminate a larger area; and single-plane illumination microscopy-based FCS (SPIM-FCS)[30−33] and massively parallel FCS (mpFCS),[34−36] which deploy different illumination strategies to cover a larger area. While these new techniques enable location-specific mapping of molecular concentration and diffusion in cells, they also entail some limitations. For example, the temporal and spatial resolution of TICS are inversely related and one is improved at the expense of the other—spatial resolution of TICS increases when the temporal resolution is in the millisecond range, due to long image plane acquisition time by raster scanning. This renders TICS either ill-suited for the study of fast processes or confers low spatial resolution.[27] Similarly, RICS sacrifices spatial resolution to determine the diffusion and the number of molecules,[28,29,37] as averaging over a relatively large number of pixels (>64) is needed to allow an accurate spatial correlation analysis. It also has significant problems when analyzing heterogeneous samples since the presence of bright speckles significantly deforms the autocorrelation curve. SPIM-FCS, which relies on the use of light-sheet illumination and a 2D camera to examine larger areas, can achieve high temporal resolution—recently reaching 6 μs for a reasonably short ($\approx$100 s) measurement duration using the Swiss single-photon avalanche diode array (CHSPAD) camera.[32,38] SPIM-FCS is, however, inherently hampered by the nonuniform thickness of the light sheet, which widens toward the edges, thus forming larger observation volume elements. Furthermore, scattering of the light sheet in heterogeneous environments and the presence of opaque compounds within the specimen alter the light-sheet intensity and can even completely block the incident light, which is recognized by the appearance of dark stripes in SPIM images. In SPIM-FCS, this translates to nonuniform illumination and hence a nonuniform signal-to-noise (SNR) ratio across the image. mpFCS relies on the spatial modulation of the incident laser beam by a diffractive optical element (DOE) to generate a large number of illumination spots, and a matching SPAD camera to detect in a confocal arrangement of the fluorescence intensity fluctuations from a large number (1024 in a 32 × 32 arrangement) of observation volume elements, providing single-molecule sensitivity and high spatial (~250 nm) and temporal (21 μs) resolution.[34,35,39,40] mpFCS was shown to be widely applicable, for the analysis of fast diffusion processes of eGFP-fused functional biomolecules in live cells[35] and in live tissue *ex vivo*.[39] The broad applicability of the mpFCS for functional fluorescence microscopy imaging (fFMI) was a motivation for us to go a step further and develop a new fFMI modality, mpFCS integrated with fluorescence lifetime imaging microscopy (mpFCS/FLIM). The fluorescence lifetime of a fluorophore or a fluorescently labeled macromolecule provides information on the environment local to the fluorophore (e.g., refractive index, polarity, pH, PO_2, Ca^{2+}). It can provide complementary insights into nanoscale (1−10 nm) macromolecular interactions or conformations via Förster resonance energy transfer (FRET) and dynamic quenching on the nanosecond timescale.

Here, we present an integrated massively parallel FCS and FLIM system (mpFCS/FLIM) on the same microscope frame. This enables massively parallel measurements to quantitatively characterize the location-specific concentration, mobility and interactions (via FCS), and local properties of the immediate surrounding of biomolecules (via fluorescence lifetime). We demonstrate the capabilities of mpFCS/FLIM for quantitative live cell biochemistry and cellular pharmacology by characterizing the effect of test compound NSC 50467 on oligodendrocyte transcriptional factor 2 (OLIG2) dimerization. OLIG2, a basic helix−loop−helix transcription factor in the central nervous system, plays an important role in neuronal cell differentiation during development,[41] adult neurogenesis,[42] and glioblastoma development.[43] Substances that target

https://doi.org/10.1021/acs.analchem.1c02144
Anal. Chem. 2021, 93, 12011−12021

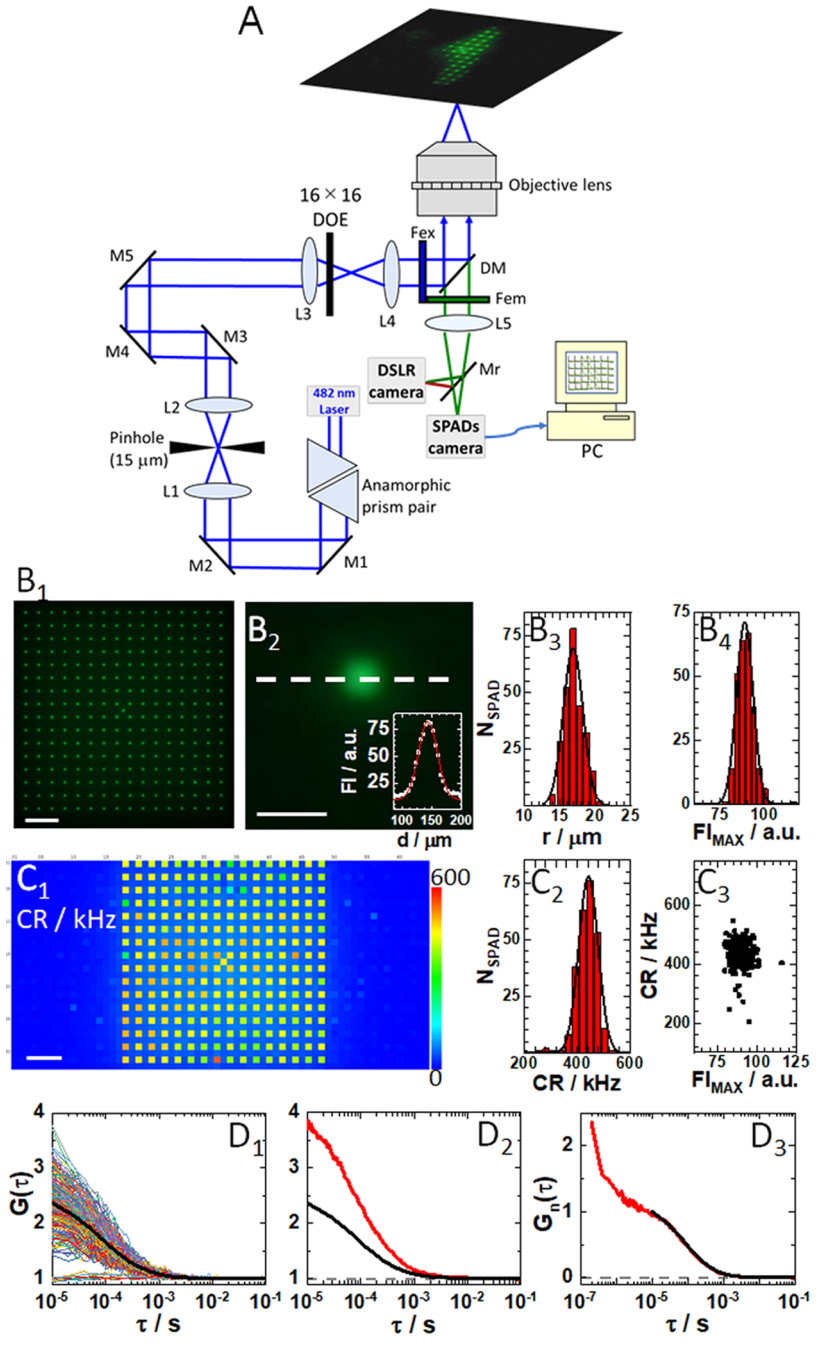

Figure 1. Optical setup for mpFCS/FLIM. (A) Schematic drawing of the mpFCS/FLIM optical setup. The 482 nm laser beam with elliptical cross-section is transformed into a circular beam using an anamorphic prism pair and expanded using a Kepler telescope setup (L1 and L2) with a pinhole in its focus. The expanded circular laser beam is focused by the focusing lens (L3) mounted on an *xyz* translation stage, which is positioned in front of the diffractive optical element (DOE) that can be translated along and rotated around the *z*-axis. The illumination matrix consisting of 16 × 16 (256) spots, which are generated in the image plane of the back port of the microscope, is imaged by the microscope relay optics (L4) and the objective lens to the object plane. Fluorescence is detected by a single-photon avalanche diode (SPAD) camera that can be translated along the *z*-axis and tilted at two angles (pitch and yaw) or a digital single-lens reflex (DSLR) camera. (B_1) Image of the illumination matrix visualized by the DSLR camera using a thin fluorescence layer as a specimen. (B_2) Enlarged image of a single illumination spot shown in (B_1). Inset: Fluorescence intensity (FI) distribution through the center of the spot (white dashed line) and the best-fit Gaussian curve (red solid line). Spot roundness, assessed by measuring the spot radius in different directions: horizontal (0°; white dashed line), 45, 90, and 135°, showed that the ratio of spot radius over the spot radius at 0° was 1.00, 1.02, 0.96, and 1.04, respectively. (B_3) Histogram of spot radii for all 256 spots in the confocal image of the illumination matrix is shown in (B_1). The average spot radius, r_{spot} = (17 ± 2) μm, was determined from a half of the full width at half-maximum (FWHM) of the best-fit Gaussian curve. (B_4) Histogram of peak fluorescence intensity for all spots in the confocal image of the illumination matrix is shown in (B_1). The average peak fluorescence intensity, FI_{MAX} = (90 ± 5) au. (C_1) Scanning-free confocal image of the same specimen as in (B_1) acquired using the SPC^3 SPAD camera. Here, each SPAD in addition to being a photodetector also acts as a 30 nm pinhole. Of note, every other SPAD in the centrally positioned 32 × 32 SPADs of the 64 × 32 SPC^3 SPAD camera was used. Unilluminated SPADs (dark blue), on the sides and in-between the illuminated ones (yellow−red ones), are clearly distinguishable by fluorescence intensity. (C_2) Histogram of fluorescence intensity, i.e., photon count rates (CR) measured in all illuminated SPADs shown in (C_1). The average fluorescence intensity was

https://doi.org/10.1021/acs.analchem.1c02144
Anal. Chem. 2021, 93, 12011−12021

Figure 1. continued

determined, CR = (440 ± 35) kHz. (C_3) Scatter plot showing spot peak intensity measured using the SPC^3 SPAD camera (C_1) as compared to the spot intensity measured using the DSLR camera (B_1). While a unimodal distribution is observed, six SPADs with disparate values were identified. (D_1) 256 single-SPAD autocorrelation curves (ACCs) recorded in an aqueous buffer solution of eGFP, c_{eGFP} = 4 nM, with the corresponding average ACC (black). (D_2) ACCs acquired in the same solution as in D_1 by mpFCS (black; same as in D_1) and spFCS ACC (red). The dashed gray line shows $G(\tau) = 1$. (D_3) ACCs shown in D_2 normalized to the same amplitude, $G(10\ \mu s) = 1$ at $\tau = 10\ \mu s$, acquired using the spFCS (red) and the mpFCS (black) systems. The dashed gray line shows $G_n(\tau) = 0$. In all images, scale bar is 10 μm.

OLIG2 are attractive candidates for the development of therapeutic agents for glioblastoma.[44] However, identification of such molecules is not trivial due to the large and complex surface through which OLIG2 interacts with itself and other partners, which is uncharacteristic and with no hydrophobic pockets.[18,19] The NSC 50467 compound was identified *in silico* using the so-called "combined pharmacophore approach" and was predicted to act as an allosteric inhibitor of OLIG2 homodimerization[45−47] thus impeding OLIG2 homodimer binding to the enhancer box (E-box), which is the canonical bHLH transcription factor binding site.[45−47]

EXPERIMENTAL SECTION

Optical Setup for Massively Parallel Fluorescence Correlation Spectroscopy Integrated with Fluorescence Lifetime Imaging Microscopy (mpFCS/FLIM). The optical design of the mpFCS/FLIM system and important features are shown in Figure 1A−C_3. Information about optical alignment, calibration, data acquisition, analysis, image rendering, and fitting of temporal autocorrelation curves (ACCs) using eq S1 is provided in the Supporting Information (Section S1, Figures S1−S5).

Software for mpFCS/FLIM. mpFCS/FLIM data acquisition, analysis, and graphical presentation were carried out using our own software, into which the Micro Photon Device (MPD) software for running the 2D SPAD array was integrated. The software was written in Embaracadero C++ Builder 10.2 (Embarcadero Technologies). Detailed information about data acquisition, analysis, and image rendering are given for mpFCS in Section S1b and for FLIM in Section S1c. Phasor plot analysis is presented in Section S1d.

Cell Culture and Transfection. Procedures for cell culturing and transfection for mpFCS/FLIM measurements (Section S2a), pharmacological treatment of cells (Section S2b), and cell culture for FRET-FLIM measurements (Section S2c) can be found in the indicated sections in the Supporting Information.

Dissociation Constant Assessment. Procedures for calculating the apparent dissociation constants of OLIG2-eGFP dimers (Section S3) and Olig2-eGFP−DNA complexes (Section S4) can be found in the indicated sections in the Supporting Information.

Standard Solutions for mpFCS/FLIM Calibration. Relevant information about standard solutions used for mpFCS/FLIM system calibration can be found in Section S5.

Statistical Analysis. All values are presented as mean ± standard deviation (SD). Two-tailed Student's *t*-test was used to compare two groups. The correlation analyses were reported using the probability value (*p*-value). Differences between two groups were considered to be significant when $p < 0.05$. Pearson's sample correlation coefficient *r* was used to assess the strength of a linear association between two variables. Statistical analysis was performed using the Origin 2018 program for interactive scientific graphing and data analysis and/or Excel. During data analysis, data from a few pixels (<5%) were disregarded due to the extremely high background in these SPADs. The results were replicated in three independent experiments, starting from cell transfection, culturing, treatment, and measurement. Similar trends were observed in all three experiments. Figures show representative data acquired in a single cell.

RESULTS

Validation of mpFCS/FLIM System Performance for FCS. The sensitivity and temporal resolution of the mpFCS/FLIM system are unprecedented, enabling us to perform measurements in a buffered aqueous solution of the enhanced Green Fluorescent Protein (eGFP; Figure 1D_1−D_3). Of note, the amplitude of the average ACC acquired by mpFCS is half the amplitude of the ACC acquired using conventional single-point FCS (spFCS), largely due to a higher background in the mpFCS system than in the spFCS system (Figure 1D_2). In contrast, normalized autocorrelation curves nicely overlap (Figure 1D_3), revealing that the observation volume elements (OVEs) in the mpFCS and the spFCS systems are of similar size. We also show that the ACC can be fitted with the acceptable signal to noise using eq S1, $\alpha = 1$, $i = 1$, $T = 0$ (Figure S4A,B) and that the axial ratio is not diverging ($s = \omega_z/\omega_{xy} = 4.6$), which indicates that the assumption of a 3D-ellipsoidal Gaussian OVE is applicable. Finally, we show by *z*-stack imaging that the fluorescence intensity profile in the axial direction is Gaussian with a half width at half-maximum, HWHM = (1.15 ± 0.09) μm (Figure S4C).

Validation of mpFCS/FLIM System Performance for FLIM. To characterize the performance of the mpFCS/FLIM system for fluorescence lifetime (τ_f) measurements, the instrument response function (IRF) was measured and single-exponential decay fitting of FLIM curves was compared to convolution fitting with the IRF (Figure S6); effects of the gate width and the step size between gates on τ_f were examined (Figure S7); the precision with which τ_f of pure species can be determined was assessed using solutions of molecules with known fluorescence lifetimes (Figures 2 and S8); and the ability of our system to resolve two lifetimes using measurements at a single frequency was evaluated using a series of two-component solutions with different relative contributions of the two component (Figures 2 and S9). The most important results are summarized in Figure 2.

Briefly, Figure 2A_1 shows 256 simultaneously recorded fluorescence decay curves in a phosphate buffer solution of eGFP. Analysis using the single-exponential decay model (eq S2) yielded a histogram of fluorescence lifetimes from which eGFP fluorescence lifetime was determined, $\tau_{f,eGFP}$ = (2.5 ± 0.02) ns (Figure 2A_2). This value agrees well (i.e., to within 10%) with the values obtained in other laboratories.[48−50]

Using a 2.0 ns gate width and a 0.2 ns gate step time, τ_f was measured for several standards in solution, covering a τ_f range from 1 to 10 ns (Figure 2B_1,B_2). The agreement between

https://doi.org/10.1021/acs.analchem.1c02144
Anal. Chem. 2021, 93, 12011−12021

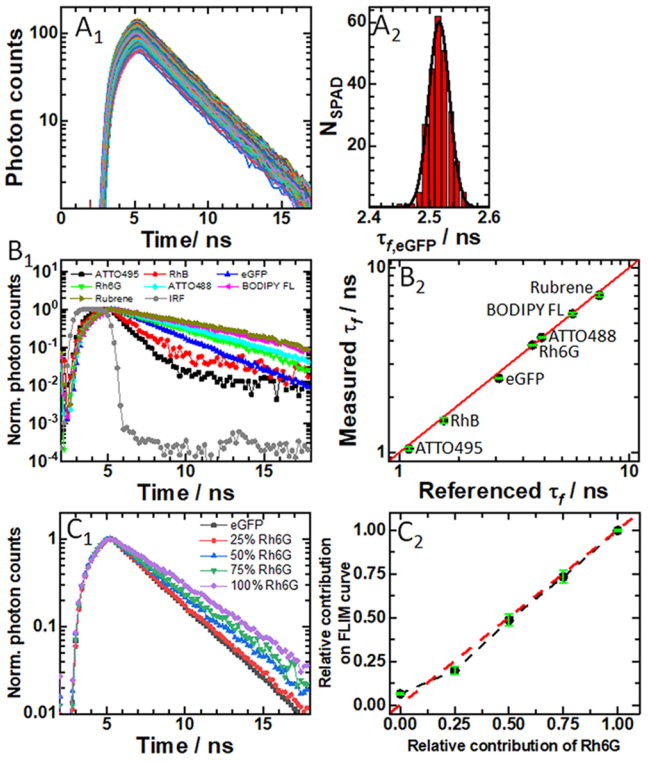

Figure 2. Fluorescence lifetime imaging microscopy (FLIM) using the integrated mpFCS/FLIM system. (A_1) 256 simultaneously recorded eGFP fluorescence decay curves in aqueous phosphate buffer. (A_2) Corresponding histogram of fluorescence lifetimes obtained using a one-component exponential decay model to fit the fluorescence decay curves. From a best-fit Gaussian curve, the fluorescence lifetime was determined, $\tau_{f,eGFP}$ = (2.50 ± 0.02) ns. (B_1) Fluorescence decay curves recorded in aqueous solutions of different fluorescent dyes: ATTO495 (black), Rhodamine B (RhB; red), eGFP (blue), Rhodamine 6G (Rh6G; green), ATTO488 (cyan), BODIPY FL (magenta), Rubrene (dark yellow), and the Instrumental Response Function (IRF; gray), all acquired using the same SPAD in the SPC3 camera. (B_2) Comparison of fluorescence lifetimes measured using the mpFCS/FLIM system with literature values. Pearson's correlation indicated that there was a significant positive association between the measured and literature values ($r(7) = 0.999$, $p < 0.001$). The red line indicates perfect agreement. (C_1) Normalized fluorescence decay curves for Rh6G, eGFP, and their mixtures made so that a specified number of photons originates from Rh6G, e.g., 50% Rh6G indicates that 50% of photons are from Rh6G: eGFP (0% Rh6G; dark gray), 25% Rh6G (red), 50% Rh6G (blue), 75% Rh6G (green), and 100% Rh6G (violet). (C_2) Comparison of the relative contribution of Rh6G, as determined from fluorescence lifetime measurements using a two-component exponential decay fitting model with fixed fluorescence lifetimes: $\tau_{f,eGFP}$ = 2.5 ns and $\tau_{f,Rh6G}$ = 3.8 ns (black dots), with its actual concentration in a two-component mixture. Pearson's correlation indicated that there was a significant positive association between the measured τ_f and values found in the literature ($r(5) = 0.995$, $p < 0.01$).

expected and measured fluorescence lifetimes, which can be gleaned from Figure $2B_2$, is excellent ($r = 0.999$, $p < 0.001$).

Given that τ_f can be considered a "molecular fingerprint," allowing detection and discrimination between multiple species that emit fluorescence over the same spectral window, we tested the capability of our instrument to distinguish fluorophores that emit in the same spectral region and have discernible lifetimes, Rhodamine 6G (Rh6G), $\tau_{f,Rh6G}$ = (3.80 ± 0.04) ns, and eGFP, $\tau_{f,eGFP}$ = (2.50 ± 0.02) ns. To this aim, we mixed Rh6G and eGFP solutions at different proportions (Figure $2C_1,C_2$). As expected, the total τ_f increased as the proportion of the species with the longer τ_f (here Rh6G) was increased (Figure $2C_1$). A fit of the data to an exponential decay function by two processes (eq S3; with τ_f for eGFP and Rh6G fixed and amplitudes floated) yielded relative amplitudes that matched well the calculated relative contribution of the components in the mixture (Figure $2C_2$).

Since attempts to fit the data with a two-component-exponential decay model with free-floating τ_f and their relative contributions did not lead to extraction of the correct component lifetimes and their relative amounts (Figure $S9A_1,A_2$), phasor analysis[51−53] was used to analyze the simultaneously acquired fluorescence decay curves, assuming that two lifetime components were common to all of the curves. By deploying phasor analysis, which uses the Fourier transform to decompose experimentally measured fluorescence decay curves into complex-valued functions of the modulus (m) and the phase angle (θ_{tot}) (eqs S4−S21), global analysis of a two-component system is reduced to algebraic calculations in the phasor space (Figure $S9B_3$). Following calibration experiments (Figure S8), we computed by phasor analysis τ_f and components' fractions with dramatically improved accuracy and precision (Figure $S9B_1,B_2$).

Spatial Mapping of Fluorescence Lifetime in a Fixed Specimen. To demonstrate spatial mapping of τ_f, a fixed plant specimen, the acridine orange stained section through the rhizome of the lily of the valley (*Convallaria majalis*) was used (Figure 3).

Fluorescence images acquired using a spot-wise, 16×16, illumination and the DSLR camera (Figure $3A,B_1$) show cells in the central parenchyma made visible owing to the fluorescence signal from the cell wall. The fluorescence image of the same cell as in Figure $3B_1$ acquired using the SPC[3] SPAD camera is shown in Figure $3B_2$. Fluorescence decay curves simultaneously recorded in 256 individual SPADs (Figure S10), exemplified in Figure 3C, when fitted using a two-component exponential decay model (Figure $3D_1$), yielded a short, $\tau_{f,wall1}$ = (0.6 ± 0.1) ns (Figure $3D_2$) and a long fluorescence lifetime component, $\tau_{f,wall2}$ = (2.9 ± 0.2) ns (Figure $3D_3$). Importantly, the thus determined τ_f provided significant image contrast (Figure $3E_1,E_2$), and even a "ratiometric" image could be obtained revealing the relative contribution of the component with the short fluorescence lifetime (Figure $3E_3$).

Spatial Mapping of Concentration, Diffusion, and Fluorescence Lifetime in Live Cells. To demonstrate spatial mapping of the concentration, diffusion, and lifetime in live cells (Figure S11), we first performed measurements on fluorescent proteins, eGFP (Figures 4 and S12) or eGFP tetramer ($eGFP_{tet}$; Figures S13 and S14), as nonreactive molecular probes.

Our data show that for similar eGFP concentrations in the cell, $c_{eGFP} \approx 20$ nM, and in the aqueous buffer solution, $c_{eGFP} \approx 4$ nM, the mean diffusion time of eGFP was about 2.5 times longer in the cell than in the aqueous buffer, $\tau_{D,eGFP,cell}$ = (260 ± 60) μs vs $\tau_{D,eGFP,buffer}$ = (110 ± 10) μs, consistent with previous studies,[54] whereas the molecular brightness and fluorescence lifetimes were similar $CPSM_{eGFP,cell}$ = (1.0 ± 0.3) kHz and $CPSM_{eGFP,buffer}$ = (1.0 ± 0.2) kHz, $\tau_{f,eGFP,cell}$ = (2.50 ± 0.05) ns and $\tau_{f,eGFP,buffer}$ = (2.50 ± 0.02) ns. However, the relative standard deviations (RSD) of all measured variables were higher in the living cell (Figure $4B_2,C_2,D_2,E_2$) than those

https://doi.org/10.1021/acs.analchem.1c02144
Anal. Chem. 2021, 93, 12011−12021

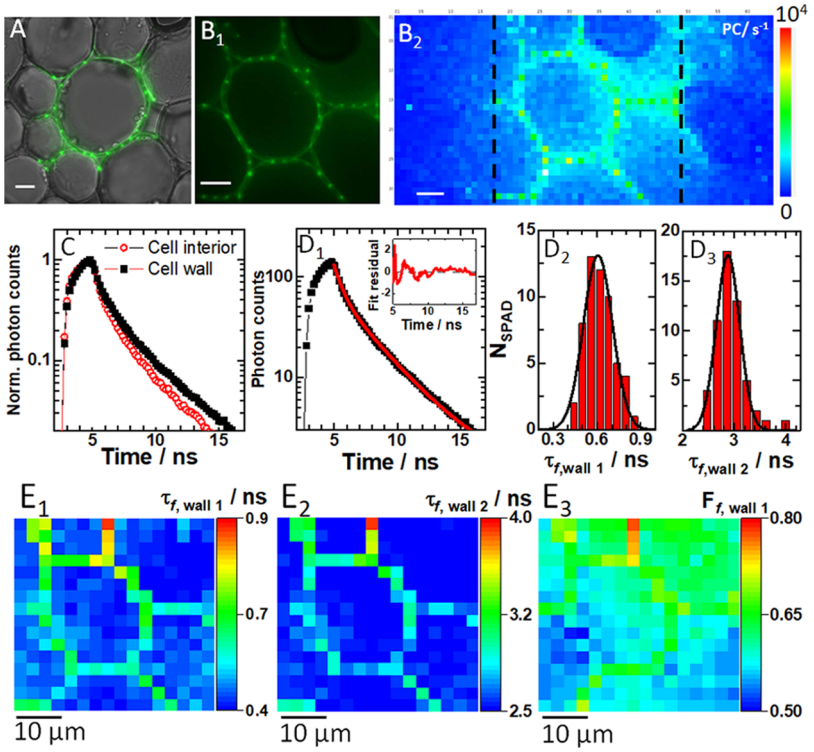

Figure 3. Spatial distribution of fluorescence lifetime in a fixed section of the rhizome of lily of the valley (*C. majalis*). (A) Fluorescence image of a spot-wise, 16 × 16, illuminated cell (green) overlaid on a wide-field transmission image (gray) of a region in the central parenchyma recorded using the DSLR camera. (B_1) Zoomed fluorescence image of a spot-wise illuminated cell in the central parenchyma recorded using the DSLR camera. (B_2) Fluorescence image of the same cell as in (B_1) acquired using the SPC^3 SPAD camera. Fluorescence intensity is given in photon counts (PC), exposure time 46 ms. (C) Fluorescence decay curves recorded in individual SPADs at distinct intracellular locations: cell wall (black squares) and inside the cell (red circles). All fluorescence decay curves are shown in Figure S10. (D_1) A fluorescence decay curve recorded in an individual SPAD at the cell wall (black squares) fitted using a two-component exponential decay model (eq S3, red line). Inset: Corresponding residuals. (D_2) Histogram of the short fluorescence lifetime component in the plasma membrane and the best-fit Gaussian curve yield $\tau_{f,wall1}$ = (0.6 ± 0.1) ns. (D_3) Histogram of the long fluorescence lifetime component in the plasma membrane and the best-fit Gaussian curve yield $\tau_{f,wall2}$ = (2.9 ± 0.2) ns. (E_{1-3}) FLIM images of the cell in (B_2) rendered visible by mapping the: short (E_1) and long (E_2) fluorescence lifetime component and the relative contribution of the short component (E_3). In all images, the scale bar is 10 μm.

in the homogenous solution (Figure S3B–E), indicating that the cell environment presents a spatial variation in local concentration, local diffusion processes (Figure S15), and local excited-state decay (environment). Correlation maps (Figure S16) showed that no correlation was observed between the concentration (number of eGFP), molecular brightness, and lifetime, ruling out any spatially dependent concentration quenching in the fluorescence lifetime and absence of diffusion-influenced lifetime quenching. Taken together, these results are largely consistent with the view of eGFP being a biochemically inert, monomeric protein, able to roam largely unimpeded inside the cellular milieu. The broadened distribution functions observed here (relative to homogenous aqueous buffer) reveal that the cellular interior is not uniform and that eGFP is not totally confined to the cytosol but is also found in cytoplasmic organelles.

In contrast to eGFP, which can access the entire cell, a fluorescence image of a HEK cell-expressing $eGFP_{tet}$ reveals distinctive fluorescence intensities in the cytoplasm and the cell nucleus (Figures S11B and S13A). Furthermore, the large RSD of the diffusion time for $eGFP_{tet}$ in the cytoplasm is of particular note, as it is ten-fold larger than the corresponding value for the monomeric eGFP in the cytoplasm. Because the $eGFP_{tet}$ is 4 times larger than eGFP (4 nm long axis dimension), this suggests that obstacles in the size range of 10 nm or more in the cellular environment affect $eGFP_{tet}$ dynamics, as revealed using the anomalous diffusion model (eq S1, $\alpha \neq 1$)[55−57] to fit the experimentally derived ACCs and determine the anomalous diffusion exponent (α; Figure S15B). Furthermore, and in contrast to the diffusion time, the fluorescence lifetime was homogeneous in cells expressing $eGFP_{tet}$ (Figure S13E_1). FLIM curves in the nucleus showed lower photon counts but revealed similar decay rates (Figure S14C_{1-3}). The histogram of fluorescence lifetime quantified $\tau_{f,eGFPtet}$ = (2.4 ± 0.05) ns in the cytoplasm and similarly in the nucleus (Figure S13E_2).

Spatial Mapping of Transcription Factor OLIG2-eGFP in Live Cells Before and After Treatment with Compound NSC 50467: an Allosteric Inhibitor of OLIG2 Dimerization. To demonstrate spatial mapping of the concentration, diffusion, and lifetime of interacting molecules in live cells, intracellular localization and dynamics of OLIG2 was characterized (Figures 5, S11C,D, and S17–S25).

OLIG2 is known to bind as a homodimer to the enhancer box (E-box), the canonical bHLH transcription factor binding site.[45−47] It is predominantly localized in the cell nucleus (Figures 5A_1 and S11C), but is known to shuttle between the nucleus and the cytoplasm (Figure S11D), with the actual localization pattern emerging from a dynamic equilibrium that is predominantly governed by the nuclear export signal.[58] Spatial mapping of the number of OLIG2-eGFP in untreated

https://doi.org/10.1021/acs.analchem.1c02144
Anal. Chem. 2021, 93, 12011−12021

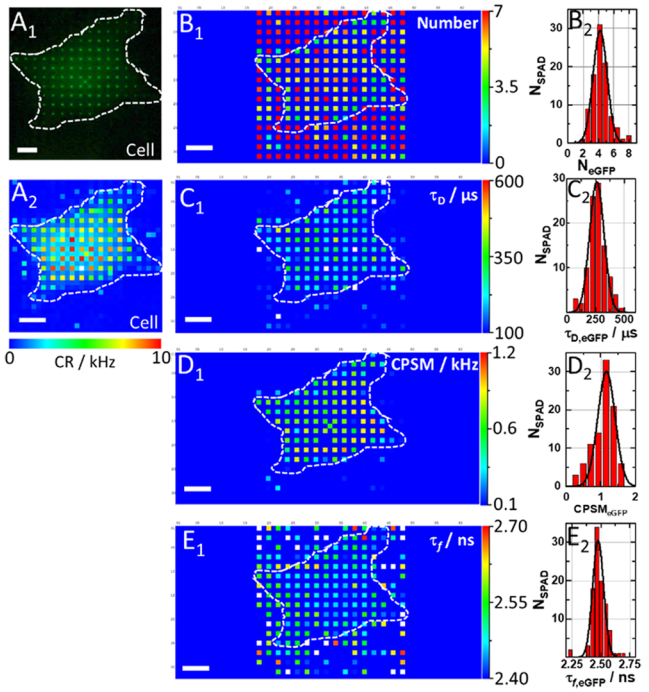

Figure 4. Spatial map of eGFP concentration, diffusion, brightness, and fluorescence lifetime in a live HEK cell. (A_1) Fluorescence image of an eGFP-expressing HEK cell acquired using a spot-wise, 16 × 16, illumination and a DSLR camera. The hand-drawn dashed line highlights the cell border visualized by transmission light imaging. (A_2) Count rate map. Corresponding ACCs and FLIM curves are shown in Figure S12. (B_1) Spatial map of the average N_{eGFP} in the OVE. Of note, the apparently high average number of molecules in the cell surrounding is an artifact of the near-zero amplitude of the ACCs in the cell culture medium (see Figure S12A_2). (B_2) Histogram corresponding to B_1. The best-fit Gaussian curve yields N_{eGFP} = (4.22 ± 0.92), corresponding to $c_{eGFP} \approx 20$ nM. (C_1) Spatial map of $\tau_{D,eGFP}$. (C_2) Histogram corresponding to (C_1) yields the average eGFP diffusion time, $\tau_{D,eGFP}$ = (260 ± 60) μs. (D_1) Spatial map of eGFP brightness as reflected by counts per second per molecule (CPSM). (D_2) Histogram corresponding to (D_1) yields average $CPSM_{eGFP}$ = (1.0 ± 0.3) kHz. (E_1) Spatial map of eGFP fluorescence lifetimes. (E_2) Histogram corresponding to (E_1) yields the average eGFP fluorescence lifetime, $\tau_{f,eGFP}$ = (2.50 ± 0.05) ns.

cells revealed that the concentration of OLIG2-eGFP in the cell nucleus is higher than in the cytoplasm (Figure 5A_2); the diffusion time, determined from the full width of the ACC at half maximum, is significantly longer in the cell nucleus than in the cytoplasm, τ_D^{nuc} = (250 ± 300) ms vs τ_D^{cyt} = (0.9 ± 1.5) ms (Figure 5A_3,E), and the fluorescence lifetime map revealed a significantly longer lifetime states in the cell nucleus, fluorescence lifetime, $\tau_{f,OLIG2\text{-}eGFP}^{nuc}$ = (3.0 ± 0.3) ns vs $\tau_{f,OLIG2\text{-}eGFP}^{cyt}$ = (2.7 ± 0.2) ns (Figure 5F), reflecting differences in the local environment surrounding the eGFP probe of OLIG2-eGFP in these cellular locations (Figure 5A_4). Given the unexpectedly large experimental errors for diffusion times, we further examined ACCs. This analysis revealed two characteristic decay times in both, the cytoplasm (Figures 5C_1 and S18B_1,C_1) and the cell nucleus (Figures 5C_2 and S18B_2,C_2), with the fast-decaying components being, within the experimental error, indistinguishable between these compartments, $\tau_{D,free}^{cyt}$ = $\tau_{D,free}^{nuc}$ = (0.5 ± 0.3) ms, while the relative amplitude and the diffusion time of the second component were larger and much longer in the cell nucleus than in the cytoplasm, $f_{D,bound}^{nuc}$ = (0.65 ± 0.10) vs $f_{D,bound}^{cyt}$ = (0.25 ± 0.10) and $\tau_{D,bound}^{nuc}$ = (850 ± 500) ms vs $\tau_{D,bound}^{cyt}$ = (60 ± 30) ms, respectively. (Of note, fluorescence intensity time series (Figure S18A_1,A_2) show that the signal intensity is unchanged over time and is not distorted by photobleaching. Rather, the ACCs recorded in the cell nucleus do not settle at 1 because the decay time of the second component is comparable to the signal acquisition time length (20 s).) Finally, OLIG2-eGFP molecular brightness in the cytoplasm, $CPSM_{OLIG2\text{-}eGFP}^{cyt}$ = (1.0 ± 0.7) kHz (Figure 5G), was within the experimental error indistinguishable from that of eGFP in live cells, $CPSM_{eGFP}$ = (1.0 ± 0.3) kHz, measured under the same conditions, suggesting that OLIG2-eGFP is monomeric in the cytoplasm. In the nucleus, average molecular brightness is higher, $CPSM_{OLIG2\text{-}eGFP}^{nuc}$ = (1.4 ± 0.7) kHz (Figure 5G and Table S1), suggesting that a dynamic equilibrium between OLIG2-eGFP monomers and dimers exists.

Treatment with the allosteric inhibitor of OLIG2 dimerization did neither change the concentration, nor the diffusion time, nor the fluorescence lifetime, and nor the molecular brightness of OLIG2-eGFP residing in the cytoplasm; $p > 0.05$ for all measurements (Figures 5C_1, D−G, S17A_{1-3} and S19A_{1-4}). However, it significantly perturbed the motions and the local environment of OLIG2-eGFP in the cell nucleus, causing, on the average, a decrease in the diffusion time by 4 times (from 850 to 200 ms; Figures 5C_2,E and S19B_2, $p = 5 \times 10^{-3}$), and reduced the fluorescence lifetime (Figure 5F, $p = 1.5 \times 10^{-8}$) and the molecular brightness (Figures 5G, S17B_3 and S19B_4, $p = 7 \times 10^{-3}$), while leaving the overall OLIG2-eGFP concentration unchanged, as reflected by the number of OLIG2-eGFP molecules (Figures 5D and S17B_1, $p > 0.05$). Moreover, the positive correlation between local OLIG2-eGFP molecular brightness and the local diffusion, which was strong in the cell nuclei of untreated cells, was significantly reduced (Figure S19$B_{2\text{-}2,3\text{-}2}$).

Finally, mpFCS measurements enabled us to assess the value of the apparent dissociation constants for OLIG2-eGFP binding to chromatin DNA before, $K_{d,app}^{OLIG2\text{-}DNA}$ = (45 ± 30) nM, and after treatment, $K_{d,NSC50467}^{OLIG2\text{-}DNA}$ = (130 ± 40) nM (Figure S19C_{1-3}). Also, mpFCS measurement of OLIG2-eGFP concentration and molecular brightness revealed that in untreated cells about 25% of OLIG2-eGFP molecules are homodimers and that treatment with NSC 50467 effectively reduced OLIG2-eGFP homodimer levels to below 7% (Table S1). This, in turn, enabled us also to infer apparent OLIG2-eGFP homodimer dissociation constants in untreated cells $K_{d,app}^{(OLIG2-eGFP)2} \approx 560$ nM, which upon treatment becomes $K_{d,app,NSC50467}^{(OLIG2\text{-}eGFP)2} \approx 3$ μM.

Taken together, the mpFCS data indicate that treatment with the allosteric modulator NSC 50467 does not significantly alter OLIG2-eGFP properties in the cytoplasm, whereas in the cell nucleus OLIG2-eGFP dimers are not efficiently formed in the presence of NSC 50467 and OLIG2-eGFP binding to the chromatin DNA is significantly abolished.

We then used Förster resonance energy transfer (FRET) via FLIM (FRET-FLIM), to further characterize NSC 50467 effects on OLIG2-eGFP dimer formation. To this aim, cells expressing OLIG2-eGFP, with eGFP acting as a FRET donor, and dark yellow fluorescent protein ShadowY tagged OLIG2 molecules (OLIG2-ShY), with ShY acting as FRET acceptor, were used. For a positive FRET control, a tandem dimer of eGFP and ShadowY (eGFP-ShY) was transfected into cells. As expected, robust FRET was observed with the positive FRET

https://doi.org/10.1021/acs.analchem.1c02144
Anal. Chem. 2021, 93, 12011−12021

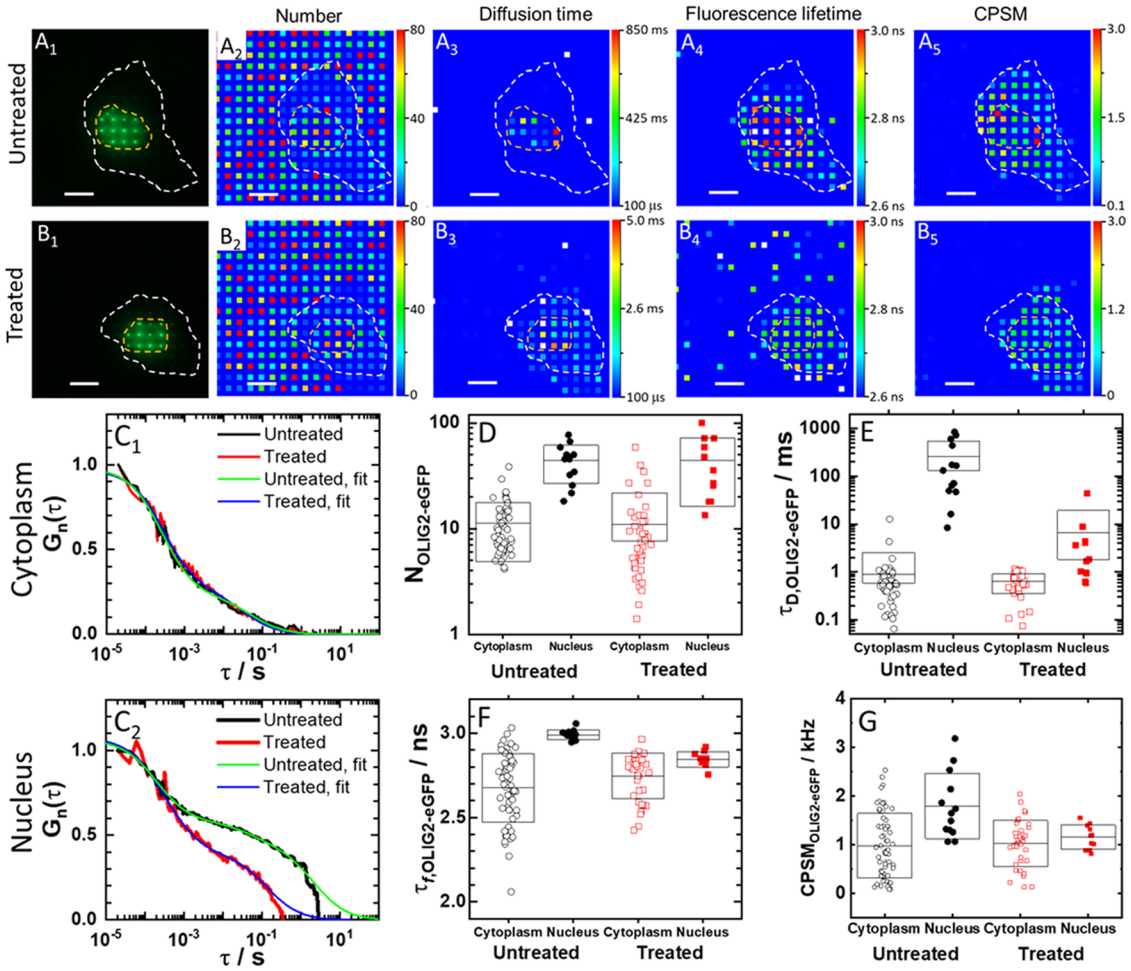

Figure 5. Spatial map of OLIG2-eGFP concentration, diffusion, brightness, and fluorescence lifetime in a live HEK cell before and after treatment with NSC 50467. (A_1, B_1) Fluorescence images of an untreated (A_1) and a treated (B_1) HEK cell-expressing OLIG2-eGFP, acquired using a spot-wise, 16 × 16, illumination and a DSLR camera. The hand-drawn dashed lines that highlight the cell border (white) and the cell nucleus (orange) were visualized by transmission light microscopy. Corresponding fluorescence intensity fluctuation time series and ACCs are shown in Figure S18. (A_2, B_2) Spatial map of the average number of OLIG2-eGFP molecules in an OVE, recorded in an untreated (A_2) and a treated (B_2) cell. (A_3, B_3) Spatial map of OLIG2-eGFP diffusion times recorded in an untreated (A_3) and a treated (B_3) cell. (A_4, B_4) Spatial map of fluorescence lifetimes recorded in an untreated (A_4) and a treated (B_4) cell. Corresponding FLIM curves are shown in Figure S18. (A_5, B_5) Spatial map of OLIG2-eGFP brightness (CPSM) recorded in an untreated (A_5) and a treated (B_5) cell. (C_1, C_2) Single-pixel ACCs normalized to the same amplitude, $G(20\ \mu s) = 1$ at $\tau = 20\ \mu s$, recorded in the same pixel in the cytoplasm (C_1) and the same pixel in the cell nucleus (C_2) before (black) and after (red) treatment. Two-component 3D free diffusion model fitting to the ACCs recorded in the cell nucleus and the cytoplasm in the untreated (green) and the treated (blue) cell. (D–G) Effect of treatment on the number of molecules (D), diffusion time (E), average fluorescence lifetime (F), and average molecular brightness (G).

control probe, with a FRET efficiency of 55% (as determined by phasor analysis of the FLIM data, Figure S20). Phasor plots recorded in cells expressing OLIG2-eGFP and OLIG2-ShadowY showed evidence of emission from a mixture of FRET and non-FRET states including the FRET contribution from the OLIG2 dimer (Figure S21A). In the context of a FRET/non-FRET state model (involving donor, acceptor, and FRET states), our analysis delivered an amplitude fraction of FRET to be (0.3 ± 0.1) in the absence of allosteric inhibitor, which decreased to (0.07 ± 0.06) upon treatment with the inhibitory compound, also observable at other cells (Figure S21B,E,F). As expected, the decrease in the FRET fraction was accompanied by an increase in the contribution of non-FRET states. This data provides evidence for the efficient inhibition of OLIG2 dimer formation by the inhibitory compound. Since the RSD of the amplitude of the FRET fraction of OLIG2 without compound is larger than that of the tandem dimer of fluorescent proteins (eGFP-ShY), we can conclude that OLIG2 dimerization in the nucleus was in addition to OLIG2 dimerization inhibition also affected by the nuclear environment (e.g., genome DNA structure).

DISCUSSION

In this work, we present two important achievements, the development of a new functional fluorescence microscopy imaging (fFMI) modality attained by integrating massively parallel fluorescence correlation spectroscopy with fluorescence lifetime imaging microscopy (mpFCS/FLIM) and demonstrate its use to characterize the action of a compound with potential therapeutic effects that target OLIG2.

Our instrument is a quantitative scanning-free confocal fluorescence microscope with single-molecule sensitivity; it has similar confocal volume elements with single-point FCS and 10 μs/frame temporal resolution and can map fluorescence

https://doi.org/10.1021/acs.analchem.1c02144
Anal. Chem. 2021, 93, 12011−12021

lifetimes from 1 to 10 ns. The instrument builds on our previous work,[35] but we have now improved to longer signal acquisition duration, ∼10 s from previous 2.7 s, with a higher temporal resolution, ∼10 μs/frame from previous ∼21 μs/frame, toward tracking faster dynamic processes. In addition, the SNR was dramatically improved. In particular, the number of particles ratio against spFCS reduced 10 times, from 50 to 5 for fluorospheres (d = 100 nm). Also, single-pixel autocorrelation curves in eGFP and QD525 in water agree to within 10% with spFCS. Importantly, the system integrated with FLIM enabled us to perform mpFCS and FLIM at the same position in the cell. This is a significant improvement compared to current practice, where considerable time lags are introduced when moving the specimen from one microscope to the other. At the same time, the time needed for finding the same cell after moving the specimen from one microscope to the other is entirely abolished. Our dedicated software provides mono- and two-component exponential decay fitting for all 256 SPADs nearly instantly, rendering a fluorescence lifetime image in a few seconds. Implementation of phasor analysis makes multicomponent analysis in FLIM easily achieved without the need to fit multicomponent exponential decay curves.

In comparison with other presently available 2D FCS instruments, such as FCS based on total internal reflection (TIR-FCS[59−62]) and single plane illumination microscopy (SPIM-FCS[30−33]), our approach is more versatile. The main limitation of TIR-FCS is its restriction to an investigation of processes at the basal plasma membrane. SPIM-FCS, on the other hand, enables us to visualize the inside of cells and perform measurements there, but it is hampered by an inhomogeneous illumination and is characterized by a relatively larger observation volume ($\sim 1 \times 10^{-15}$ l). Advantages of our approach are optical sectioning, homogenous illumination and detection, and small confocal volume elements ($\sim 0.35 \times 10^{-15}$ l), which is particularly important since larger observation volume elements average local differences in concentration, mobility, and intermediate surrounding of molecules in a live cell. Thus, the integrated mpFCS/FLIM system uniquely enables us to map with great precision the molecular numbers and mobility via mpFCS and characterize the local environment immediately surrounding fluorescent/fluorescently labeled molecules via FLIM. Instrument performance was stringently assessed in a series of validation experiments using well-characterized samples. Most notably, we have demonstrated that we could measure the concentration and diffusion of eGFP in a dilute aqueous solution (c_{eGFP} = 4 nM, Figure 1D_1−D_3) and showed that it is uniform (Figures S3 and S15). We have also shown that noninteracting molecules smaller than 5 nm, e.g., eGFP, diffuse without significant hindrance through the entire cell (Figures 4 and S15), while molecules/molecular complexes that are larger than 10 nm, such as $eGFP_{tet}$, largely reside in the cytoplasm where their diffusion is hindered by internal membranes in the cytoplasm (Figures S13 and S15). These findings are in line with experimental findings reported in the literature and with theoretical findings showing that the cytoplasm behaves to a very large extent as a liquid phase for length scales shorter than 100 nm and as a dynamically structured macromolecular matrix for longer length scales.[63] They are also important for the validation of our instrument performance.

Importantly, the integrated mpFCS/FLIM system enabled us to characterize in live cells the heterogeneous reaction-diffusion landscape of transcription factor OLIG2-eGFP and provided important new insights into its intracellular organization. It also enabled us to characterize in great detail the effects of the allosteric inhibitor NSC 50467 on OLIG2-eGFP homodimerization and interactions with chromatin DNA. The possibility to quantitatively characterize in live cells location-specific differences in transcription factor concentration, homodimerization, and DNA binding and the effect of pharmacological agents on these determinants of transcription factor function opens transcription factors to experimental therapeutics. Here, we have shown that the therapeutic compound NSC 50467 targeting OLIG2 homodimerization efficiently abolishes OLIG2-eGFP binding to chromatin DNA. We have also shown that this compound does not affect OLIG2-eGFP levels in the cytoplasm and its distribution in cytoplasmic organelles/membrane-less microdomains. The possibility to perform such detailed, previously intractable measurements may significantly facilitate new therapeutic discoveries.

In conclusion, the methodology presented here is a versatile tool with myriads of applications in biomedical research. In its current realization with 256 (16 × 16) OVEs, simultaneous sampling in cellular organelles is limited to a handful of locations. This, however, can be improved using another DOE (e.g., (32 × 32), as we have previously shown[35,39]). Also, while we have demonstrated the application of our method for studies in live tissue *ex vivo*,[35,39] our approach is better suited for studies in cell cultures, where the background from scattered fluorescence is lower than in tissues/small organisms. Despite these limitations, the strength of our approach lies in the user-friendly instrument design and the capacity of our methods to characterize both, compartmentalization of molecular processes, by measuring local excited-state decay via FLIM, and their dynamic integration, by measuring diffusion/active transport using mpFCS. Compartmentalization and dynamic integration of molecular processes are opposed yet coexisting and intertwined principles essential for normal cellular physiology as they enable location-specific processing of information and integral whole-cell response. Our methodology is thus paving the way to better understanding how biological functions emerge from underlying spatially confined chemical processes.

■ ASSOCIATED CONTENT

Supporting Information

The Supporting Information is available free of charge at https://pubs.acs.org/doi/10.1021/acs.analchem.1c02144.

S1: Optical setup for mpFCS/FLIM, data analysis, and image rendering; S2: Cell culture and transfection procedures; S3: Determining the apparent dissociation constant of OLIG2-eGFP homodimers; S4: Determining the apparent dissociation constant for OLIG2-eGFP binding to chromatin DNA by FCS; and S5: Standard solutions for mpFCS/FLIM system calibration (PDF)

■ AUTHOR INFORMATION

Corresponding Authors

Rudolf Rigler − *Department of Medical Biochemistry and Biophysics (MBB), Karolinska Institutet, 17177 Stockholm, Sweden; Department of Clinical Neuroscience (CNS), Center for Molecular Medicine (CMM), Karolinska Institutet, 17176 Stockholm, Sweden*; Email: Rudolf.Rigler@ki.se

https://doi.org/10.1021/acs.analchem.1c02144
Anal. Chem. 2021, 93, 12011−12021

Vladana Vukojević − *Department of Clinical Neuroscience (CNS), Center for Molecular Medicine (CMM), Karolinska Institutet, 17176 Stockholm, Sweden;* orcid.org/0000-0003-0873-5653; Email: Vladana.Vukojevic@ki.se

Authors

Sho Oasa − *Department of Clinical Neuroscience (CNS), Center for Molecular Medicine (CMM), Karolinska Institutet, 17176 Stockholm, Sweden;* orcid.org/0000-0003-3800-590X

Aleksandar J. Krmpot − *Institute of Physics Belgrade, University of Belgrade, 11080 Belgrade, Serbia; Department of Clinical Neuroscience (CNS), Center for Molecular Medicine (CMM), Karolinska Institutet, 17176 Stockholm, Sweden*

Stanko N. Nikolić − *Institute of Physics Belgrade, University of Belgrade, 11080 Belgrade, Serbia; Department of Clinical Neuroscience (CNS), Center for Molecular Medicine (CMM), Karolinska Institutet, 17176 Stockholm, Sweden*

Andrew H. A. Clayton − *Optical Sciences Centre, Department of Physics and Astronomy, School of Science, Swinburne University of Technology, Melbourne, Victoria 3122, Australia;* orcid.org/0000-0002-6182-3049

Igor F. Tsigelny − *Department of Neurosciences, University of California San Diego, La Jolla, California 92093-0819, United States*

Jean-Pierre Changeux − *Department of Neuroscience, Unité Neurobiologie Intégrative des Systèmes Cholinergiques, Institut Pasteur, F-75724 Paris 15, France*

Lars Terenius − *Department of Clinical Neuroscience (CNS), Center for Molecular Medicine (CMM), Karolinska Institutet, 17176 Stockholm, Sweden*

Complete contact information is available at: https://pubs.acs.org/10.1021/acs.analchem.1c02144

Author Contributions

¶S.O., A.J.K., and S.N.N. contributed equally. The manuscript was written through the contributions of all authors. All authors have given approval to the final version of the manuscript.

Notes

The authors declare no competing financial interest.

Research reported in this publication was supported by the National Institute on Alcohol Abuse and Alcoholism of the National Institutes of Health under Award Number R01AA028549. The content is solely the responsibility of the authors and does not necessarily represent the official views of the National Institutes of Health. The funding agencies had no influence on the study design, methods, data collection, analyses, or the manuscript writing. The authors declare no competing financial interest. All data are available in the main text or the supporting materials.

■ ACKNOWLEDGMENTS

The authors thank Dr. Hideji Murakoshi, Supportive Center for Brain Research, National Institute for Physiological Sciences, Aichi, Japan, for providing the ShadowY and eGFP-ShadowY expression plasmids. Test compounds were obtained through the National Cancer Institute Chemotherapeutic Agents Repository, Bethesda, MD. Financial support by the Swedish Research Council (2018-05337); Olle Engkvists Foundation (199-0480); Magnus Bergvall Foundation (2019-03381, 2020-04043); Karolinska Institutet's Research Foundation Grants (2020-02325); Swedish Foundation for Strategic Research (SBE13-0115); NIH/NIAAA (R01AA028549); Nakatani Foundation for Advancement of Measuring Technologies in Biomedical Engineering; Strategic Research Program in Neuroscience (StratNeuro); Yoshida Foundation for Science and Technology; ERASMUS+: European Union Programme for Education, Training, Youth, and Sport; Qatar National Research Foundation (PPM 04-0131-200019); and Science Fund of the Republic of Serbia (call PROMIS, Grant no. 6066079) is gratefully acknowledged.

■ REFERENCES

(1) Rivas, G.; Minton, A. P. *Trends Biochem. Sci.* **2016**, *41*, 970−981.
(2) Baum, M.; Erdel, F.; Wachsmuth, M.; Rippe, K. *Nat. Commun.* **2014**, *5*, No. 4494.
(3) Helm, C. A.; Knoll, W.; Israelachvili, J. N. *Proc. Natl. Acad. Sci. U.S.A.* **1991**, *88*, 8169−8173.
(4) Johnson, E. R.; Keinan, S.; Mori-Sánchez, P.; Contreras-García, J.; Cohen, A. J.; Yang, W. *J. Am. Chem. Soc.* **2010**, *132*, 6498−6506.
(5) Alberti, S.; Gladfelter, A.; Mittag, T. *Cell* **2019**, *176*, 419−434.
(6) Wheeler, R. J.; Hyman, A. A. *Philos. Trans. R. Soc. B* **2018**, *373*, No. 20170193.
(7) Hyman, A. A.; Weber, C. A.; Jülicher, F. *Annu. Rev. Cell Dev. Biol.* **2014**, *30*, 39−58.
(8) Gao, A.; Shrinivas, K.; Lepeudry, P.; Suzuki, H. I.; Sharp, P. A.; Chakraborty, A. K. *Proc. Natl. Acad. Sci. U.S.A.* **2018**, *115*, E11053−E11060.
(9) Nussinov, R.; Tsai, C. J. *Curr. Pharm. Des.* **2012**, *18*, 1311−1316.
(10) Amor, B. R.; Schaub, M. T.; Yaliraki, S. N.; Barahona, M. *Nat. Commun.* **2016**, *7*, No. 12477.
(11) Huang, W.; Nussinov, R.; Zhang, J. *Methods Mol. Biol.* **2017**, *1529*, 439−446.
(12) Monod, J.; Wyman, J.; Changeux, J. P. *J. Mol. Biol.* **1965**, *12*, 88−118.
(13) Koshland, D. E., Jr.; Némethy, G.; Filmer, D. *Biochemistry* **1966**, *5*, 365−385.
(14) Kirschner, K.; Eigen, M.; Bittman, R.; Voigt, B. *Proc. Natl. Acad. Sci. U.S.A.* **1966**, *56*, 1661−1667.
(15) Gunasekaran, K.; Ma, B.; Nussinov, R. *Proteins* **2004**, *57*, 433−443.
(16) Cui, Q.; Karplus, M. *Protein Sci.* **2008**, *17*, 1295−1307.
(17) Bruder, M.; Polo, G.; Trivella, D. B. B. *Nat. Prod. Rep.* **2020**, *37*, 488−514.
(18) Tsigelny, I. F.; Mukthavaram, R.; Kouznetsova, V. L.; Chao, Y.; Babic, I.; Nurmemmedov, E.; Pastorino, S.; Jiang, P.; Calligaris, D.; Agar, N.; Scadeng, M.; Pingle, S. C.; Wrasidlo, W.; Makale, M. T.; Kesari, S. *Oncotarget* **2017**, *8*, 22370−22384.
(19) Wodak, S. J.; Paci, E.; Dokholyan, N. V.; Berezovsky, I. N.; Horovitz, A.; Li, J.; Hilser, V. J.; Bahar, I.; Karanicolas, J.; Stock, G.; Hamm, P.; Stote, R. H.; Eberhardt, J.; Chebaro, Y.; Dejaegere, A.; Cecchini, M.; Changeux, J. P.; Bolhuis, P. G.; Vreede, J.; Faccioli, P.; Orioli, S.; Ravasio, R.; Yan, L.; Brito, C.; Wyart, M.; Gkeka, P.; Rivalta, I.; Palermo, G.; McCammon, J. A.; Panecka-Hofman, J.; Wade, R. C.; Di Pizio, A.; Niv, M. Y.; Nussinov, R.; Tsai, C. J.; Jang, H.; Padhorny, D.; Kozakov, D.; McLeish, T. *Structure* **2019**, *27*, 566−578.
(20) Motlagh, H. N.; Wrabl, J. O.; Li, J.; Hilser, V. J. *Nature* **2014**, *508*, 331−339.
(21) Oasa, S.; Vukojević, V.; Rigler, R.; Tsigelny, I. F.; Changeux, J. P.; Terenius, L. *Proc. Natl. Acad. Sci. U.S.A.* **2020**, *117*, 2683−2686.
(22) Rigler, R.; Elson, E. S. Fluorescence Correlation Spectroscopy. In *Theory and Applications*; Springer: Berlin, 2001; Vol. *65*.
(23) Vukojević, V.; Papadopoulos, D. K.; Terenius, L.; Gehring, W. J.; Rigler, R. *Proc. Natl. Acad. Sci. U.S.A.* **2010**, *107*, 4093−4098.
(24) Mikuni, S.; Pack, C.; Tamura, M.; Kinjo, M. *Exp. Mol. Pathol.* **2007**, *82*, 163−168.
(25) Ries, J.; Schwille, P. *BioEssays* **2012**, *34*, 361−368.

(26) Tiwari, M.; Oasa, S.; Yamamoto, J.; Mikuni, S.; Kinjo, M. *Sci. Rep.* **2017**, *7*, No. 4336.
(27) Kolin, D. L.; Costantino, S.; Wiseman, P. W. *Biophys. J.* **2006**, *90*, 628−639.
(28) Hendrix, J.; Dekens, T.; Schrimpf, W.; Lamb, D. C. *Biophys. J.* **2016**, *111*, 1785−1796.
(29) Brown, C. M.; Dalal, R. B.; Hebert, B.; Digman, M. A.; Horwitz, A. R.; Gratton, E. *J. Microsc.* **2008**, *229*, 78−91.
(30) Wohland, T.; Shi, X.; Sankaran, J.; Stelzer, E. H. *Opt. Express* **2010**, *18*, 10627−10641.
(31) Ng, X. W.; Teh, C.; Korzh, V.; Wohland, T. *Biophys. J.* **2016**, *111*, 418−429.
(32) Buchholz, J.; Krieger, J.; Bruschini, C.; Burri, S.; Ardelean, A.; Charbon, E.; Langowski, J. *Biophys. J.* **2018**, *114*, 2455−2464.
(33) Singh, A. P.; Galland, R.; Finch-Edmondson, M. L.; Grenci, G.; Sibarita, J. B.; Studer, V.; Viasnoff, V.; Saunders, T. E. *Biophys. J.* **2017**, *112*, 133−142.
(34) Vitali, M.; Bronzi, D.; Krmpot, A. J.; Nikolić, S. N.; Schmitt, F.; Junghans, C.; Tisa, S.; Friedrich, T.; Vukojević, V.; Terenius, L.; Zappa, F.; Rigler, R. *IEEE J. Sel. Top. Quantum Electron.* **2014**, *20*, 344−353.
(35) Krmpot, A. J.; Nikolić, S. N.; Oasa, S.; Papadopoulos, D. K.; Vitali, M.; Oura, M.; Mikuni, S.; Thyberg, P.; Tisa, S.; Kinjo, M.; Nilsson, L.; Terenius, L.; Rigler, R.; Vukojević, V. *Anal. Chem.* **2019**, *91*, 11129−11137.
(36) Gösch, M.; Serov, A.; Anhut, T.; Lasser, T.; Rochas, A.; Besse, P. A.; Popovic, R. S.; Blom, H.; Rigler, R. *J. Biomed. Opt.* **2004**, *9*, 913−921.
(37) Scipioni, L.; Di Bona, M.; Vicidomini, G.; Diaspro, A.; Lanzanò, L. *Commun. Biol.* **2018**, *1*, No. 10.
(38) Buchholz, J. Evaluation of Single Photon Avalanche Diode Arrays for Imaging Fluorescence Correlation Spectroscopy: FPGA-Based Data Readout and Fast Correlation Analysis on CPUs, GPUs and FPGAs. Dissertation, Heidelberg University, 2015.
(39) Papadopoulos, D. K.; Krmpot, A. J.; Nikolić, S. N.; Krautz, R.; Terenius, L.; Tomancak, P.; Rigler, R.; Gehring, W. J.; Vukojević, V. *Mech. Dev.* **2015**, *138*, 218−225.
(40) Krmpot, A. J.; Nikolic, S. N.; Vitali, M.; Papadopoulos, D. K.; Oasa, S.; Thyberg, P.; Tisa, S.; Kinjo, M.; Nilsson, L.; Gehring, W. J.; Terenius, L.; Rigler, R.; Vukojevic, V. In *Quantitative Confocal Fluorescence Microscopy of Dynamic Processes by Multifocal Fluorescence Correlation Spectroscopy*, Advanced Microscopy Techniques IV; and Neurophotonics II SPIE Proceedings, Optical Society of America, 2015; p 953600.
(41) Dennis, D. J.; Han, S.; Schuurmans, C. *Brain Res.* **2019**, *1705*, 48−65.
(42) Buffo, A.; Vosko, M. R.; Ertürk, D.; Hamann, G. F.; Jucker, M.; Rowitch, D.; Götz, M. *Proc. Natl. Acad. Sci. U.S.A.* **2005**, *102*, 18183−18188.
(43) Franceschi, E.; Minichillo, S.; Brandes, A. A. *CNS Drugs* **2017**, *31*, 675−684.
(44) Kosty, J.; Lu, F.; Kupp, R.; Mehta, S.; Lu, Q. R. *Cell Cycle* **2017**, *16*, 1654−1660.
(45) Edwards, A. L.; Meijer, D. H.; Guerra, R. M.; Molenaar, R. J.; Alberta, J. A.; Bernal, F.; Bird, G. H.; Stiles, C. D.; Walensky, L. D. *ACS Chem. Biol.* **2016**, *11*, 3146−3153.
(46) Meijer, D. H.; Kane, M. F.; Mehta, S.; Liu, H.; Harrington, E.; Taylor, C. M.; Stiles, C. D.; Rowitch, D. H. *Nat. Rev. Neurosci.* **2012**, *13*, 819−831.
(47) Sagner, A.; Gaber, Z. B.; Delile, J.; Kong, J. H.; Rousso, D. L.; Pearson, C. A.; Weicksel, S. E.; Melchionda, M.; Mousavy Gharavy, S. N.; Briscoe, J.; Novitch, B. G. *PLoS Biol.* **2018**, *16*, No. e2003127.
(48) Pepperkok, R.; Squire, A.; Geley, S.; Bastiaens, P. I. *Curr. Biol.* **1999**, *9*, 269−272.
(49) Sarkisyan, K. S.; Goryashchenko, A. S.; Lidsky, P. V.; Gorbachev, D. A.; Bozhanova, N. G.; Gorokhovatsky, A. Y.; Pereverzeva, A. R.; Ryumina, A. P.; Zherdeva, V. V.; Savitsky, A. P.; Solntsev, K. M.; Bommarius, A. S.; Sharonov, G. V.; Lindquist, J. R.; Drobizhev, M.; Hughes, T. E.; Rebane, A.; Lukyanov, K. A.; Mishin, A. S. *Biophys. J.* **2015**, *109*, 380−389.
(50) Boens, N.; Qin, W.; Basaric, N.; Hofkens, J.; Ameloot, M.; Pouget, J.; Lefevre, J. P.; Valeur, B.; Gratton, E.; vandeVen, M.; Silva, N. D., Jr.; Engelborghs, Y.; Willaert, K.; Sillen, A.; Rumbles, G.; Phillips, D.; Visser, A. J.; van Hoek, A.; Lakowicz, J. R.; Malak, H.; Gryczynski, I.; Szabo, A. G.; Krajcarski, D. T.; Tamai, N.; Miura, A. *Anal. Chem.* **2007**, *79*, 2137−2149.
(51) Vallmitjana, A.; Dvornikov, A.; Torrado, B.; Jameson, D. M.; Ranjit, S.; Gratton, E. *Methods Appl. Fluoresc.* **2020**, *8*, No. 035001.
(52) Clayton, A. H.; Hanley, Q. S.; Verveer, P. J. *J. Microsc.* **2004**, *213*, 1−5.
(53) Weber, G. *J. Phys. Chem. A* **1981**, *85*, 949−953.
(54) Dauty, E.; Verkman, A. S. *J. Mol. Recognit.* **2004**, *17*, 441−447.
(55) Feder, T. J.; Brust-Mascher, I.; Slattery, J. P.; Baird, B.; Webb, W. W. *Biophys. J.* **1996**, *70*, 2767−2773.
(56) Weiss, M.; Hashimoto, H.; Nilsson, T. *Biophys. J.* **2003**, *84*, 4043−4052.
(57) Schwille, P.; Haustein, E. Fluorescence Correlation Spectroscopy: An Introduction to its Concepts and Applications. https://pages.jh.edu/~iic/resources/ewExternalFiles/FCS-Schwille.pdf (accessed May 17, 2019).
(58) Setoguchi, T.; Kondo, T. *J. Cell Biol.* **2004**, *166*, 963−968.
(59) Thompson, N. L.; Burghardt, T. P.; Axelrod, D. *Biophys. J.* **1981**, *33*, 435−454.
(60) Ohsugi, Y.; Kinjo, M. *J. Biomed. Opt.* **2009**, *14*, No. 014030.
(61) Hassler, K.; Leutenegger, M.; Rigler, P.; Rao, R.; Rigler, R.; Gosch, M.; Lasser, T. *Opt. Express* **2005**, *13*, 7415−7423.
(62) Veerapathiran, S.; Wohland, T. *Methods* **2018**, *140*−*141*, 140−150.
(63) Kwapiszewska, K.; Szczepański, K.; Kalwarczyk, T.; Michalska, B.; Patalas-Krawczyk, P.; Szymański, J.; Andryszewski, T.; Iwan, M.; Duszyński, J.; Hołyst, R. *J. Phys. Chem. Lett.* **2020**, *11*, 6914−6920.

https://doi.org/10.1021/acs.analchem.1c02144
Anal. Chem. 2021, 93, 12011−12021

electronic reprint

JOURNAL OF SYNCHROTRON RADIATION

ISSN: 1600-5775
journals.iucr.org/s

Photon diagnostics at the FLASH THz beamline

Rui Pan, Ekaterina Zapolnova, Torsten Golz, Aleksandar J. Krmpot, Mihailo D. Rabasovic, Jovana Petrovic, Vivek Asgekar, Bart Faatz, Franz Tavella, Andrea Perucchi, Sergey Kovalev, Bertram Green, Gianluca Geloni, Takanori Tanikawa, Mikhail Yurkov, Evgeny Schneidmiller, Michael Gensch and Nikola Stojanovic

J. Synchrotron Rad. (2019). **26**, 700–707

JOURNAL OF SYNCHROTRON RADIATION

ISSN 1600-5775

Received 17 October 2018
Accepted 11 March 2019

Edited by M. Yabashi, RIKEN SPring-8 Center, Japan

[1] This article will form part of a virtual special issue on X-ray free-electron lasers.

Keywords: FLASH; intense THz; THz diagnostic; electro-optic; FTIR.

Photon diagnostics at the FLASH THz beamline[1]

Rui Pan,[a] Ekaterina Zapolnova,[a] Torsten Golz,[a] Aleksandar J. Krmpot,[b] Mihailo D. Rabasovic,[b] Jovana Petrovic,[c,d] Vivek Asgekar,[e] Bart Faatz,[a] Franz Tavella,[f] Andrea Perucchi,[g] Sergey Kovalev,[h] Bertram Green,[h] Gianluca Geloni,[i] Takanori Tanikawa,[i] Mikhail Yurkov,[a] Evgeny Schneidmiller,[a] Michael Gensch[j,k] and Nikola Stojanovic[a]*

[a]Deutsches Elektronen-Synchrotron (DESY), Notkestrasse 85, D-22607 Hamburg, Germany, [b]Institute of Physics Belgrade, Pregrevica 118, 11080 Belgrade, Serbia, [c]Vinca Institute of Nuclear Sciences, Belgrade, Serbia, [d]Center for Free-Electron Laser Science, Deutsches Elektronen-Synchrotron (DESY), Notkestrasse 85, D-22607 Hamburg, Germany, [e]Department of Physics, S. P. Pune University, Pune, India, [f]SLAC National Accelerator Laboratory, Menlo Park, California, USA, [g]Elettra – Sincrotrone Trieste SCpA, 34149 Basovizza, Trieste, Italy, [h]Helmholtz-Zentrum Dresden-Rossendorf (HZDR), Bautzner Landstraße 400, 01328 Dresden, Germany, [i]European XFEL, Holzkoppel 4, 22869 Schenefeld, Germany, [j]German Aerospace Center (DLR), Institute of Optical Sensor Systems, Rutherfordstraße 2, 12489 Berlin, Germany, and [k]Institute of Optics and Atomic Physics, Technical University of Berlin, Strasse des 17 Juni 135, 10623 Berlin, Germany. *Correspondence e-mail: nikola.stojanovic@desy.de

The THz beamline at FLASH, DESY, provides both tunable (1–300 THz) narrow-bandwidth (∼10%) and broad-bandwidth intense (up to 150 uJ) THz pulses delivered in 1 MHz bursts and naturally synchronized with free-electron laser X-ray pulses. Combination of these pulses, along with the auxiliary NIR and VIS ultrashort lasers, supports a plethora of dynamic investigations in physics, material science and biology. The unique features of the FLASH THz pulses and the accelerator source, however, bring along a set of challenges in the diagnostics of their key parameters: pulse energy, spectral, temporal and spatial profiles. Here, these challenges are discussed and the pulse diagnostic tools developed at FLASH are presented. In particular, a radiometric power measurement is presented that enables the derivation of the average pulse energy within a pulse burst across the spectral range, jitter-corrected electro-optical sampling for the full spectro-temporal pulse characterization, spatial beam profiling along the beam transport line and at the sample, and a lamellar grating based Fourier transform infrared spectrometer for the on-line assessment of the average THz pulse spectra. Corresponding measurement results provide a comprehensive insight into the THz beamline capabilities.

1. Introduction

FLASH, the free-electron laser (FEL) in Hamburg at DESY, provides ultrafast XUV and soft X-ray radiation for users to perform pump–probe experiments. FLASH has two independent FEL undulator beamlines (Faatz *et al.*, 2016): FLASH1 and FLASH2. Each FEL branch ends with a dedicated experimental hall that has a number of beamlines.

FLASH1 has a unique feature, a dedicated THz undulator installed downstream of the XUV undulators. This feature allows the generation of intense THz pulses by the same electron bunch that generates XUV pulses (Stojanovic & Drescher, 2013), as shown in Fig. 1. As THz and XUV undulators are separated by empty drift space, XUV and THz pulses generated by the same electron bunch are naturally synchronized with no more than 5 fs timing jitter (Frühling *et al.*, 2009). Furthermore, THz pulses are carrier envelope phase (CEP) stable. Downstream of the THz undulator, the electron beam is deflected to ground by the so-called electron beam dump magnet (hereon referred to as the dump magnet). This

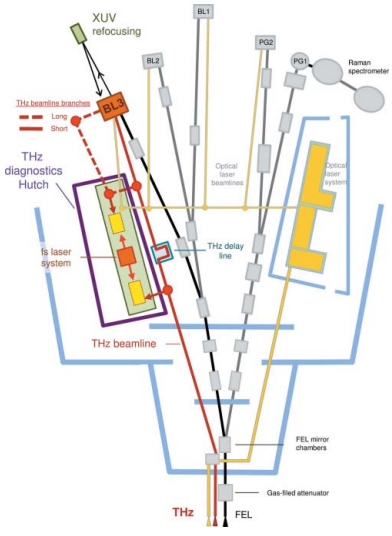

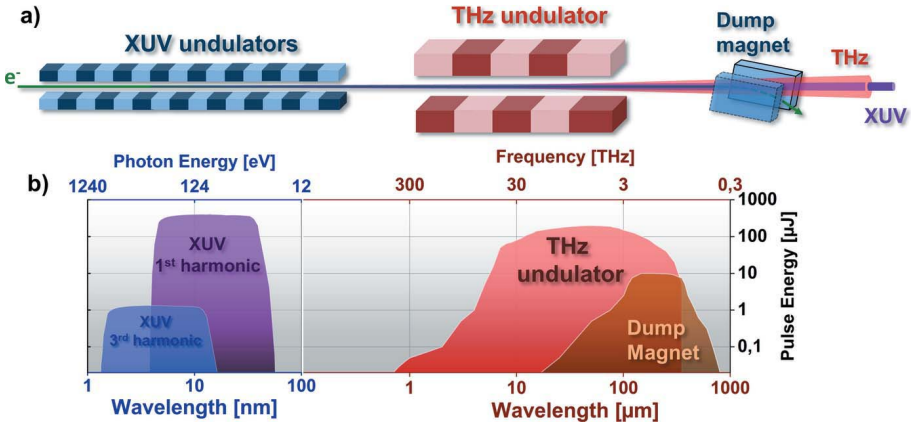

Figure 1
Scheme of the FLASH1 THz photon sources. (*a*) The THz undulator is located downstream of the XUV undulators, separated by free space. The electron beam dump magnet follows the THz undulator. (*b*) Representation of the pulse energies that can be obtained at FLASH1 from the XUV and THz sources over a wide spectral range.

stage separates the electron beam from the photon (THz and XUV) beams. The dump magnet on its own generates an intense THz transient, mainly by the edge and bending radiation process (Tavella *et al.*, 2011; Geloni *et al.*, 2009*a*,*b*). Only a fraction of the total bending radiation is collected in the THz beamline downstream (estimated to be 11.4%), as beamline design is optimized for the radiation in the forward direction, while bending radiation is created tangentially along the bend. THz and XUV beams are separated by a large flat mirror (210 mm × 140 mm) with a 10 mm aperture for the XUV beam (Gensch *et al.*, 2008). Transport of the THz beam into the experimental hall over ∼70 m requires multiple collimations and this is provided by all-reflective optics. By this unique photon generation scheme, the photon spectrum of FLASH1 is extended to the long-wavelength range. As shown in Fig. 1, FLASH1 covers the XUV range from 1.4 nm to 52 nm including harmonics (Tiedtke *et al.*, 2009), and the THz range from 1 µm to above 300 µm (300 THz to 1 THz). With an independent and synchronized near-infrared (NIR) laser (Redlin *et al.*, 2011) having a center wavelength of 800 nm, FLASH1 can provide XUV, THz and NIR laser beams for users at the same time to study photon–matter interactions.

Based on the scheme shown in Fig. 1, there are two types of intense THz sources. The first is a THz undulator (Grimm *et al.*, 2010) that generates tunable, linearly polarized (horizontally), narrow-bandwidth ($\Delta\lambda/\lambda$ = 10%) radiation. The wavelength is tunable from 1 µm to above 300 µm. The longest wavelength that can be reached depends on the electron beam energy for a given THz undulator period and peak field (see Fig. 2). Pulse energies delivered to the experiment can reach up to 150 µJ, depending on the FLASH accelerator parameters (mainly the electron bunch charge and its compression).

The second source of THz radiation is the dump magnet that generates edge and bending radiation. The edge radiation is generated by the longitudinal acceleration of the electron beam at the interface between the free space and the dump magnet magnetic field (Tavella *et al.*, 2011; Geloni *et al.*, 2009*a*,*b*). This kind of radiation has a broad spectral bandwidth (quasi single-cycle temporal profile), is radially polarized and generated in the forward direction to the electron beam propagation. Electrons also generate the bending radiation along the bending arc of the dump magnet. The dump magnet vacuum chamber acceptance angle for the bending radiation is relatively small (2.4°) compared with 21° of the complete bend that the electrons experience. Thus only a fraction of the bending radiation radiated in the forward radiation is collected into the THz beamline. Also, the bending radiation has a broad bandwidth (quasi single-cycle temporal profile) and is linearly polarized. The bending radiation is collected by the THz beamline mostly from the bending plane and is thus polarized mainly in the vertical direction, orthogonal to the THz undulator pulse polarization. Combined edge and bending dump magnet radiation can reach a pulse energy of over 10 µJ. This radiation is generated parasitically and can be used independently from the undulator radiation.

The THz beamline delivers the beam to the end-station at the end of the BL3 XUV beamline in the FLASH1 experimental hall (see Fig. 3). The THz beam can be delivered to the experiment via two branches, a short one with ultra-high-vacuum transport (10^{-9} mbar) and a long one via THz diagnostics hutch with high-vacuum transport (10^{-7} mbar). Due to the difference in optical path, the THz pulse arrives later than the XUV pulse to the end-station, 12 ns for the short branch and 21 ns for the long branch. We use two approaches to achieve temporal overlap of the XUV and THz pulses in the experiment: the first is delaying the XUV pulse by refocusing via multilayer mirrors; the second is to generate two electron bunches at the FLASH electron gun timed to achieve temporal overlap of the respective THz and XUV pulses in the experiment (Zapolnova *et al.*, 2018).

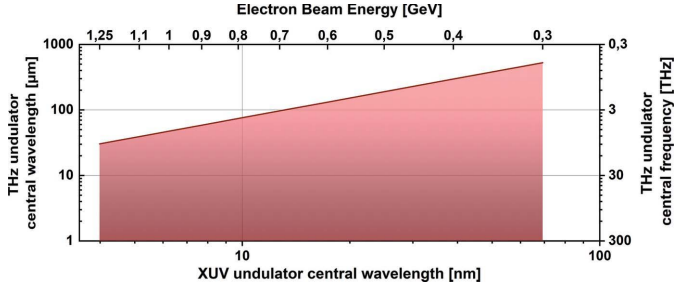

Figure 2
THz undulator spectral range. The shaded area represents the range where the fundamental frequency of the THz undulator radiation can be reached for FLASH1 as a function of the FEL XUV wavelength (lower horizontal axis) and the electron beam energy in the linac (upper horizontal axis).

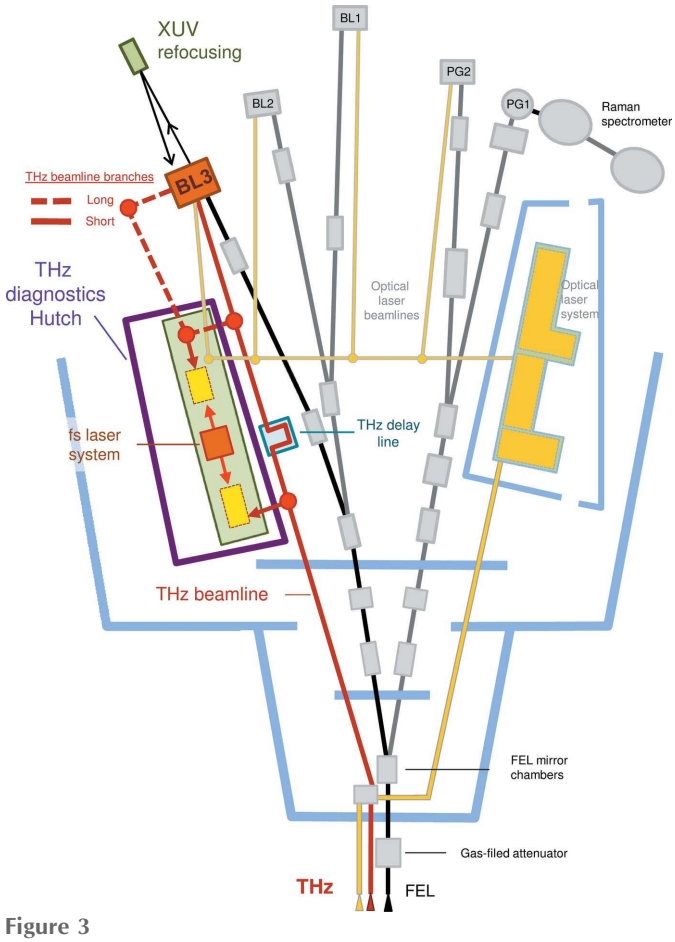

Figure 3
Scheme of the THz beamline in the FLASH1 experimental hall. THz beam is delivered to the end-station at the BL3 XUV beamline, via one of the two branches.

There are many unique applications for the CEP stable intrinsically synchronized THz pulses from the FLASH THz beamline. One important scientific area is in atomic and molecular physics. Here the THz field can act as a streak camera, allowing molecular reactions to be clocked and processes induced by the femtosecond-long XUV pulses from FLASH on a timescale of a few femtoseconds (Frühling *et al.*, 2009; Schütte *et al.*, 2012; Oelze *et al.*, 2017; Schmid *et al.*, 2019). An emerging new class of experiments at FLASH is the application of the strong THz fields for these tunable narrow-band pulses in selective excitation or selective THz control of matter [for a description of this field see, for example, Green *et al.* (2016), Buzzi *et al.* (2018), Kampfrath *et al.* (2013) and Kovalev *et al.* (2017)]. The first experiments performed at FLASH have focused on driving the magnetization dynamics in magnetic thin films by selective phonon excitation (Radu, 2019) and on the THz control of dynamic surface processes (Waltar *et al.*, 2018).

2. THz diagnostics

In a typical THz-pump/XUV-probe experiment at FLASH, determination of the properties of the driving THz pulse is of key importance. Based on the needs of the user experiments in past years, we have developed diagnostics tools to fully characterize the THz beam at the experiment. Presently, all the tools are developed in the THz diagnostics hutch at FLASH1 experimental hall and will be transferred to the end-station at BL3 beamline (see Fig. 3). In this paper we present tools for the full spectral, temporal and spatial characterization of the THz pulses and the pulse-energy measurement. Thereby we discuss some of the major challenges for diagnostics, *i.e.* the extremely broad THz spectral range of FLASH sources, 1 MHz repetition rate in 10 Hz bursts and jitter to externally synchronized lasers (Azima *et al.*, 2009; Tavella *et al.*, 2011), that can be used for THz waveform characterization.

2.1. THz power measurement

We measure the THz pulse energies using a radiometer (RM3700, head RjP-735/RF, by Laser Probe). We have cross-referenced this detector to a PTB (The National Metrology Institute of Germany) traceable 3A-P-THz, by Ophir Optronics Solutions (Green *et al.*, 2016). The radiometer detector has a cavity pyroelectric probe and it has a time constant of 1 ms. Its temporal response prevents us from resolving individual pulses of the FLASH micro-pulses within a 1 MHz burst. However, the detector time constant is well matched to the maximal duration of the 1 MHz burst (with duration of 0.8 ms, containing up to 800 pulses) defined by the FLASH accelerator. Therefore, the integration is performed over all micro-bunches in a burst, which allows for determination of the average THz pulse energy with good accuracy.

Fig. 4 depicts the THz pulse energy as a function of the central wavelength of the THz undulator. The total THz beamline transmission (from the source until the end of beamline) as a function of wavelength is depicted as well. We calculate the beamline transmission by modeling the THz source and the optical transport with the *Synchrotron Radia-*

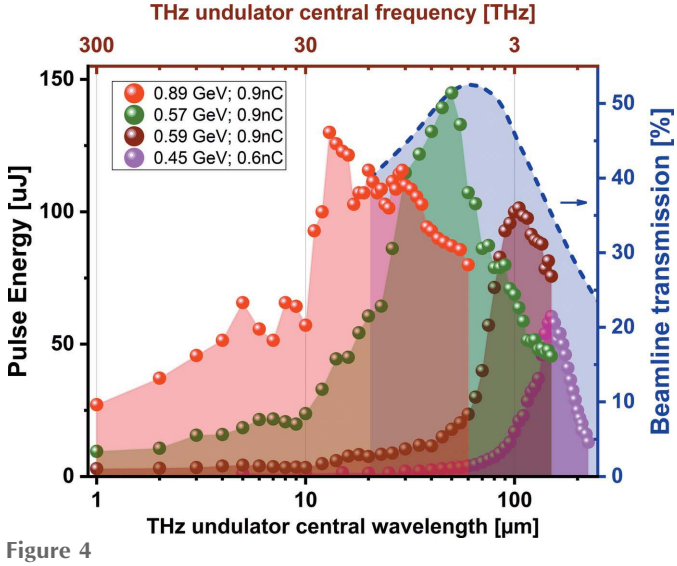

Figure 4
THz pulse energies measured at the beamline end-station for different conditions of the FLASH accelerator. The blue dashed line shows the beamline transmission, calculated using the *SRW* software package (Chubar & Elleaume, 1998).

tion Workshop (*SRW*) software package (Chubar & Elleaume, 1998). We also account for the Fresnel losses in the diamond window that separates the beamline from the accelerator vacuum (Gensch *et al.*, 2008). We present examples of four measurements taken for different electron beam settings of the FLASH accelerator. Note that the abrupt end of the THz undulator tuning range at long wavelengths relates to the maximal wavelength that can be reached at a particular electron beam energy and is determined by the maximum field (1.2 T) inside the undulator (see also Fig. 2).

2.2. THz temporal profile measurements

The THz time domain spectroscopy (TDS) via electro-optic sampling (EOS) method is a well established technique for the full characterization of the THz pulse temporal structure (Wu & Zhang, 1995; Schmuttenmaer, 2004), in a broad spectral range. The electric field of the THz pulse changes the birefringence of the EOS crystal. This transient change is sampled by an ultrashort laser pulse. By scanning the laser pulse in time, the complete THz pulse shape can be reconstructed.

At an accelerator-based light source, such as FLASH, the laser system is synchronized to the master clock of the FLASH accelerator (Schulz *et al.*, 2015). One of the main limiting factors for the use of an externally synchronized laser for EOS detection is the temporal jitter between the FEL and the laser pulses. Jitter limits the temporal resolution and subsequently the spectral bandwidth of EOS detection. We have measured the jitter of the probe laser (pulse duration 20 fs FWHM) in the THz hutch to the FLASH THz pulses to be around 100 fs RMS (∼200 fs peak-to-peak). To solve this, we chose to detect the THz pulses' arrival time on a single-shot basis using spectral decoding electro-optic detection (EOSD) (Jiang & Zhang, 1998). This technique enables single-shot THz detection by imprinting the THz pulse electric field onto a stretched probe laser pulse, thus defining the arrival time of one with respect to the other. Spectral decoding is photon efficient (for a single-shot method) and enables the arrival time detection even with femtosecond oscillator pulses, which allows for a high-repetition-rate arrival time detection scheme that can be matched to the FLASH pulse pattern. Full EO detection of the THz pulses at FLASH then comprises two main components: arrival time monitoring by spectral decoding in combination with scanning electro-optic sampling (EOS). EOS data are sorted for their arrival time and the THz pulse shape is retrieved. The complete detection setup is installed in a high-vacuum chamber (10^{-7} mbar) to avoid measurement distortions by absorption in ambient air. We achieved a temporal resolution of the arrival time sorting of 9.7 fs RMS. Most importantly, the EOS sampling has a bandwidth of 37–3000 µm (0.1–8 THz) limited by the gallium phosphide (GaP) EOS crystal (100 µm thick). The setup has been developed in collaboration with the TELBE team at HZDR and details can be found in the literature (Kovalev *et al.*, 2017; Golz, 2018).

Two typical examples of measured THz waveform profiles are shown in Figs. 5(*a*) and 5(*b*). The THz and the probing laser beam are overlapped and focused on the GaP EOS crystal, with beam sizes of 350 µm FWHM and 70 µm FWHM, respectively. The THz undulator was set to nominal wavelengths of 155 µm and 42 µm (corresponding to frequencies of 1.93 THz and 7.1 TH, respectively). For the long-wavelength example, unfiltered and spectrally filtered pulses are presented. The wire-grid THz bandpass filter used has been centered at 155 µm wavelength (1.93 THz) with 15% spectral bandwidth. For the unfiltered pulse, it is interesting to observe that the electric field and high-harmonic content increase along the pulse. This indicates the change of the electron bunch form factor (Nodvick & Saxon, 1954) inside the undulator. In the respective unfiltered THz pulse spectrum [see Fig. 5(*c*)] we clearly observe the first harmonic peaking at 169 µm (1.77 THz) and the third harmonic at 52 µm (5.68 THz), and the baseline includes the broadband spectrum from the dump magnet radiation. As expected, the measurement with the THz bandpass filter shows a strong peak around 160 µm (1.87 THz), with a small (few percent) leakage between 75 and 100 µm (3 and 4 THz). Similarly, in the spectrum of the short-wavelength pulse (tuned to 42 µm) we observe the first harmonic peaking at 43 µm (7 THz).

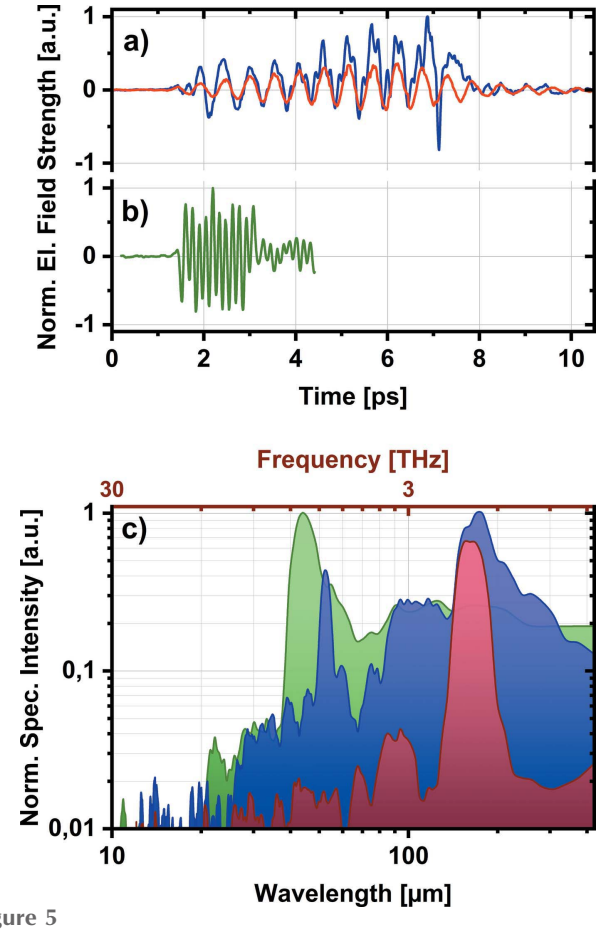

Figure 5
THz pulse waveforms measured by arrival-time-sorted time domain spectroscopy (TDS). (*a*) The THz pulse produced by the undulator set at the nominal wavelength of 155 µm (1.93 THz). The unfiltered temporal profile is shown by the blue line and the filtered by the red line, with 155 µm (1.93 THz) bandpass filter (15% bandwidth). (*b*) The unfiltered THz pulse at 43 µm (7 THz) (green line). (*c*) The corresponding THz pulse spectra.

It is worth noting that the EOSD scheme can be used as a THz arrival-time detection tool in other experiments. A recent application evaluated the timing jitter between two electron bunches with 21 ns delay timed for temporal overlap of THz and XUV pulses at the experimental end-station at BL3 (Zapolnova *et al.*, 2018).

2.3. THz beam profile

Knowledge of the transverse THz beam profile is important as it allows precise determination of the fluence (and the peak field) on the sample, as well as optimal optical design to maximize the beam transmission in the experiment. We model the THz source and the radiation transport using the *SRW* software package (Chubar & Elleaume, 1998) and observe the strong interference effects between undulator and dump magnet radiation (edge and bending radiation) at FLASH (Asgekar *et al.*, 2014).

An example of the measured THz beam profile from the dump magnet, with the THz undulator switched off, is shown in Fig. 6(*a*). An example of the THz undulator beam tuned to 88 µm (3.4 THz) is shown in Fig. 6(*b*). The beams have been imaged in the THz diagnostics hutch so that they image the plane approximately 10 m downstream of the radiation source. We perform 2D raster scanning of the beams. As a detector we employ an amplified pyroelectric detector (LME-501 from InfraTec). Both measurements have been performed with 30 µm long-pass THz spectral filter. The profiles have been reproduced by *SRW* calculation, whereby the integration of the output power was performed over the 30–300 µm (1–10 THz) spectral range to account for the filtering, and the form factor of a 50 fs RMS long electron bunch was used.

For the dump magnet, both the measurement and calculation render a half-moon-like structure that can be explained by interference of the edge radiation with the bending radiation from the dump magnet. For the THz undulator beam we observe slight asymmetry in the horizontal plane which can be explained by interference of the undulator and the dump magnet radiation (Asgekar *et al.*, 2014).

We focus both beams with an off-axis parabolic mirror of focal length 150 mm and measure the beam profile with a Pyrocam III camera from Ophir Photonics for the dump magnet and with a microbolometer camera for the undulator beam. The results are shown in Figs. 6(*c*) and 6(*d*), respectively. We observe a beam size of 600 µm FWHM for the dump magnet and 350 µm FWHM for the undulator beam.

Moreover, we follow the THz undulator beam profile evolution, by wavefront propagation in *SRW*. The undulator radiation wavelength is set to 160 µm (1.87 THz). For an experimental confirmation, we measure the beam profile in the THz diagnostics hutch at five different positions along the beam path [see Fig. 7(*a*)], using the knife-edge technique. Zero

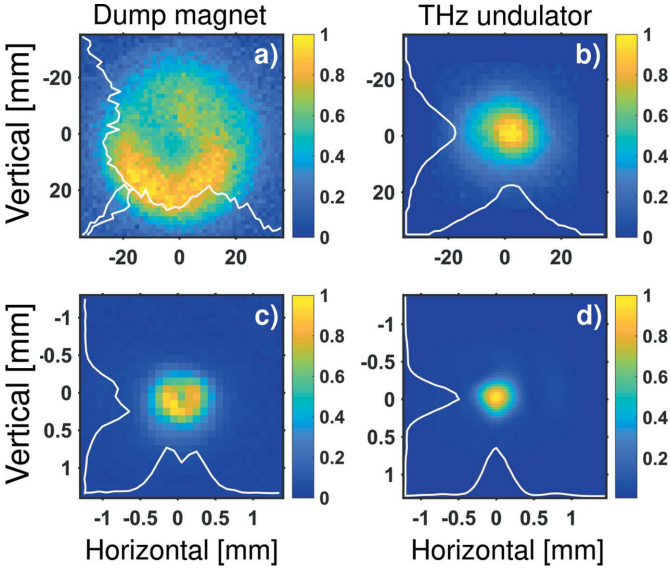

Figure 6
(Top) THz transverse beam profiles at FLASH. (*a*) Dump magnet (the THz undulator is off), and (*b*) THz undulator tuned to 88 µm (3.4 THz), unfocused beam profiles measured in the THz hutch; beam position imaged 10 m from the virtual source. Note that the undulator profile is padded with zeros to fill in the same image size. (Bottom) The same beams focused. (*c*) Dump magnet beam (600 µm FWHM), and (*d*) THz undulator beam (350 µm FWHM).

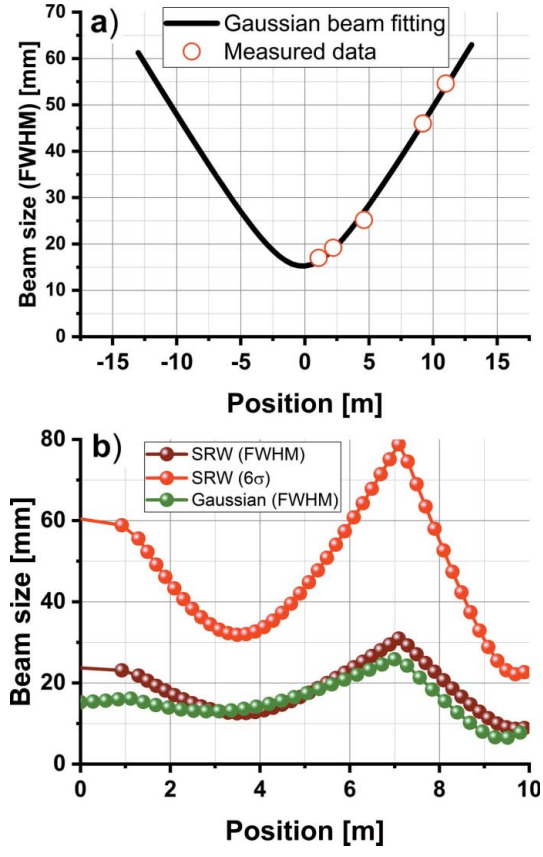

Figure 7
THz undulator beam size at 160 µm (1.87 THz) and its propagation. (*a*) Beam size measured at five different locations along the beam path (red circles) fitted by a Gaussian beam propagation. (*b*) THz beam propagation over the 10 m path, with the focusing mirrors inserted at the 1 m and 7 m position marks. The THz beam was approximated by fitted Gaussian beam (FWHM) (green curve) and calculated from the source by *SRW* (FWHM) (brown curve) and 6σ (red curve).

position denotes the THz beamline window at which the beam is extracted into the THz diagnostics station. We assume a Gaussian beam profile and obtain the beam parameters by fitting. The plot in Fig. 7(*b*) compares the beam size evolution (FWHM) calculated by *SRW* (brown curve) with the approximated Gaussian beam propagation (ABCD matrix formalism), fitted from the measured data (green curve), for the last 10 m of the THz beamline transport. Two toroidal mirrors with focal lengths of 3.8 m and 1.8 m are inserted at the 1 m and 7 m position marks, respectively. In this particular example, the goal was to couple the THz beam into an experimental chamber through a 25 mm aperture, located at the 10 m position mark, with highest possible transmission. The red curve depicts the THz beam size at the equivalent of 6σ (or 99.7% beam energy), and at the 10 m position mark we achieve the desired sub-25 mm beam size. We observe a reasonable agreement between these two numerical models, with the big advantage of the Gaussian beam propagation providing very fast and efficient evaluation of the beam sizes in the optical system.

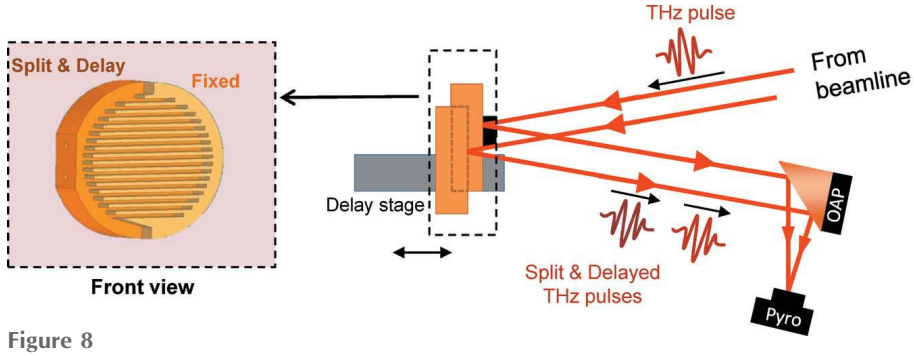

Figure 8
Scheme of the lamellar grating interferometer. OAP: off-axis parabolic mirror.

2.4. THz spectrum measurement

For a quick THz spectral characterization, when temporal pulse structure is not necessary, we have developed the variation of the Fourier transform infrared (FTIR) spectrometer based on a reflective lamellar grating. Unlike the most commonly used Michelson interferometer (based on amplitude division), the reflective lamellar grating interferometer (Richards, 1964; Bell, 1972) divides the wavefront spatially. Because of this, the reflective lamellar grating design has a key advantage: a high (close to 100%) and smooth efficiency response (*e.g.* typical Fabry–Perot interferences that plague Michelson interferometers are absent). A comparison of the efficiency of the lamellar grating and the Michelson interferometer can be found in Fig. 3 of Richards (1964). As a side note, owing to a large spectral bandwidth, the lamellar gratings have found application in extreme ultraviolet (XUV) spectroscopy and metrology (Gebert *et al.*, 2014; Usenko *et al.*, 2017).

As shown in Fig. 8, the lamellar grating spectrometer consists of two interleaved gratings, manufactured from a 100 mm-diameter gold-coated copper mirror. One is fixed and the other is mounted on the motorized stage responsible for introducing the optical delay between the split beams. For detection a pyroelectric detector (LME-501 from InfraTec) with a 2 mm × 2 mm chip size was used.

The THz beam is collimated in a way that uniformly illuminates the gratings. The period of the grating (h = 2 mm) is chosen to match the spectral range of the THz sources at FLASH. The long-wavelength limit (Bell, 1972) for lamellar gratings is $\lambda_{max} < h/2$, which is 1 mm (corresponding to 0.3 THz) in our case. For wavelengths longer than λ_{max}, a cavity effect starts decreasing the modulation depth of the THz waves, which are polarized parallel to the fringes. The high-frequency limit for this geometry is 30 µm (corresponding to 10 THz), which is determined by diffraction theory and depends on the geometry of the device (Strong & Vanasse, 1960; Naftaly *et al.*, 2008; Ferhanoglu *et al.*, 2009): $\lambda_{min} = hs/f$, where f = 130 mm is the focal length of the parabolic mirror and s = 2 mm is the width of the exit slit of the detector (defined by the detector effective aperture).

An example of the measured interferogram and the calculated spectrum is shown in Fig. 9. The THz pulse was generated by the edge radiation and filtered by a 215 µm (1.4 THz) bandpass filter. The fluctuations of the shot-to-shot THz pulse energy at FLASH can be as high as 20% RMS, depending on the FLASH accelerator settings. We split a small portion of the beam for a reference measurement that is then used to

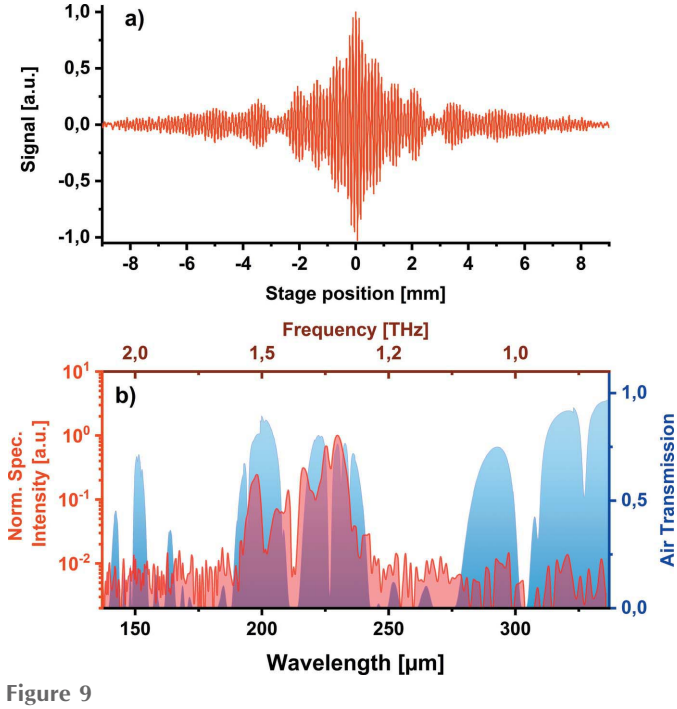

Figure 9
FTIR measurement for THz edge radiation with 215 µm (1.4 THz) THz bandpass filter. (*a*) Double-sided interferogram. (*b*) Respective spectrum (red curve) and air transmission with water vapor (in blue) show the strong absorption lines in this spectral range.

normalize the measured interferogram on a single-shot basis. The normalized interferogram in Fig. 9(*a*) was obtained during 20 min of scanning at 10 Hz repetition rate (12000 shots). Fig. 9(*b*) shows the normalized spectrum, obtained by taking a Fourier transform of the measured interferogram. We observe the spectral content as expected from the filter response with a signal-to-noise ratio exceeding 100.

Measurement has been performed in ambient air and we observe a strong modulation from the water vapor absorption lines. We are currently upgrading it to an all-in-vacuum spectrometer.

3. Conclusion

We have presented a range of THz diagnostic tools developed for THz/XUV pump–probe experiments at FLASH1, DESY. The THz pulse energy is an important parameter for optimization of the FLASH accelerator, and it reaches values from tens of μJ up to 150 μJ. The upgrade of a currently used radiometer to an online monitor is in progress. The THz temporal profile can be measured with 10 fs timing resolution and covers the spectral range from 37 to 3000 μm (0.1 to 8 THz). The ongoing development of this technique will explore the use of different EOS crystals to extend the measured bandwidth to shorter wavelengths, GaSe (Kübler *et al.*, 2005) and SiC (Naftaly *et al.*, 2016) being good candidates that should allow THz detection in the 10–40 THz and 0.1–15 THz spectral windows, respectively. To fully exploit the high THz pulse energies at FLASH, we are upgrading the single-shot EOSD THz detection technique to one via tilted laser pulse front (Teo *et al.*, 2015). This technique is free from the spectral distortions that plague EOSD (Jamison *et al.*, 2008) and allows for the full bandwidth of the pulse to be retrieved (limited only by the EOS crystal). The measurements of the transversal THz beam profile are used for the design of the beam transfer line and calibration of the peak field and intensity in the experiment. A broadband FTIR spectrometer, covering the spectral range 30–1000 μm (0.3–10 THz), based on a reflective lamellar grating is developed for spectral measurements. It will be permanently installed inside the THz beamline vacuum environment for distortion-free THz spectrum measurements, enabling quick and robust spectral studies [*e.g.* suitable for THz shaping by emerging THz meta-materials (Yen *et al.*, 2004; Monticone & Alù, 2017; Stojanović *et al.*, 2018; Polley *et al.*, 2018)].

Funding information

RP, EZ, AK, MR and NS acknowledge financial support from German Academic Exchange Service (DAAD Grant Numbers 57219839 and 57393513). NS acknowledge financial support from Bundesministerium für Bildung und Forschung (grant No. 05K12CH4). JP and AP were supported by the 'Stephenson Distinguished Visitor Programme' at DESY in Hamburg (Germany). JP, MR and AK acknowledge support from the Ministry of Education, Science and Technological Development of Serbia, under Grant No. III45010 and OI 171038 and bilateral projects 451-03-01732/2017-09/6 and 451-03-01038/2015-09/1. MG and BG acknowledge support from the European Cluster of Advanced Laser Light Sources (EUCALL) project which has received funding from the European Union's Horizon 2020 research and innovation program under grant agreement No 654220. VA acknowledges support from the Alexander von Humboldt Foundation, Germany.

References

Asgekar, V., Geloni, G., Kocharyan, V., Stojanovic, N., Michel, P. & Gensch, M. (2014). *Infrared Phys. Technol.* **64**, 26–32.

Azima, A., Düsterer, S., Radcliffe, P., Redlin, H., Stojanovic, N., Li, W., Schlarb, H., Feldhaus, J., Cubaynes, D., Meyer, M., Dardis, J., Hayden, P., Hough, P., Richardson, V., Kennedy, E. T. & Costello, J. T. (2009). *Appl. Phys. Lett.* **94**, 144102.

Bell, R. J. (1972). *Introductory Fourier Transform Infrared Spectroscopy*. New York: Academic Press.

Buzzi, M., Först, M., Mankowsky, R. & Cavalleri, A. (2018). *Nat. Rev. Mater.* **3**, 299–311.

Chubar, O. & Elleaume, P. (1998). *Proceedings of the Sixth European Particle Accelerator Conference (EPAC'98)*, 22–26 June 1998, Stockholm, Sweden, pp. 1177–1179.

Faatz, B., Plönjes, E., Ackermann, S., Agababyan, A., Asgekar, V., Ayvazyan, V., Baark, S., Baboi, N., Balandin, V., Bargen, N., Bican, Y., Bilani, O., Bödewadt, J., Böhnert, M., Böspflug, R., Bonfigt, S., Bolz, H., Borges, F., Borkenhagen, O., Brachmanski, M., Braune, M., Brinkmann, A., Brovko, O., Bruns, T., Castro, P., Chen, J., Czwalinna, M. K., Damker, H., Decking, W., Degenhardt, M., Delfs, A., Delfs, T., Deng, H., Dressel, M., Duhme, H., Düsterer, S., Eckoldt, H., Eislage, A., Felber, M., Feldhaus, J., Gessler, P., Gibau, M., Golubeva, N., Golz, T., Gonschior, J., Grebentsov, A., Grecki, M., Grün, C., Grunewald, S., Hacker, K., Hänisch, L., Hage, A., Hans, T., Hass, E., Hauberg, A., Hensler, O., Hesse, M., Heuck, K., Hidvegi, A., Holz, M., Honkavaara, K., Höppner, H., Ignatenko, A., Jäger, J., Jastrow, U., Kammering, R., Karstensen, S., Kaukher, A., Kay, H., Keil, B., Klose, K., Kocharyan, V., Köpke, M., Körfer, M., Kook, W., Krause, B., Krebs, O., Kreis, S., Krivan, F., Kuhlmann, J., Kuhlmann, M., Kube, G., Laarmann, T., Lechner, C., Lederer, S., Leuschner, A., Liebertz, D., Liebing, J., Liedtke, A., Lilje, L., Limberg, T., Lipka, D., Liu, B., Lorbeer, B., Ludwig, K., Mahn, H., Marinkovic, G., Martens, C., Marutzky, F., Maslocv, M., Meissner, D., Mildner, N., Miltchev, V., Molnar, S., Mross, D., Müller, F., Neumann, R., Neumann, P., Nölle, D., Obier, F., Pelzer, M., Peters, H., Petersen, K., Petrosyan, A., Petrosyan, G., Petrosyan, L., Petrosyan, V., Petrov, A., Pfeiffer, S., Piotrowski, A., Pisarov, Z., Plath, T., Pototzki, P., Prandolini, M. J., Prenting, J., Priebe, G., Racky, B., Ramm, T., Rehlich, K., Riedel, R., Roggli, M., Röhling, M., Rönsch-Schulenburg, J., Rossbach, J., Rybnikov, V., Schäfer, J., Schaffran, J., Schlarb, H., Schlesselmann, G., Schlösser, M., Schmid, P., Schmidt, C., Schmidt-Föhre, F., Schmitz, M., Schneidmiller, E., Schöps, A., Scholz, M., Schreiber, S., Schütt, K., Schütz, U., Schulte-Schrepping, H., Schulz, M., Shabunov, A., Smirnov, P., Sombrowski, E., Sorokin, A., Sparr, B., Spengler, J., Staack, M., Stadler, M., Stechmann, C., Steffen, B., Stojanovic, N., Sychev, V., Syresin, E., Tanikawa, T., Tavella, F., Tesch, N., Tiedtke, K., Tischer, M., Treusch, R., Tripathi, S., Vagin, P., Vetrov, P., Vilcins, S., Vogt, M., Wagner, A. Z., Wamsat, T., Weddig, H., Weichert, G., Weigelt, H., Wentowski, N., Wiebers, C., Wilksen, T., Willner, A., Wittenburg, K., Wohlenberg, T., Wortmann, J., Wurth, W., Yurkov, M., Zagorodnov, I. & Zemella, J. (2016). *New J. Phys.* **18**, 062002.

Ferhanoglu, O., Seren, H. R., Lüttjohann, S. & Urey, H. (2009). *Opt. Express*, **17**, 21289–21301.

Frühling, U., Wieland, M., Gensch, M., Gebert, T., Schütte, B., Krikunova, M., Kalms, R., Budzyn, F., Grimm, O., Rossbach, L., Plönjes, E. & Drescher, M. (2009). *Nat. Photon.* **3**, 523.
Gebert, T., Rompotis, D., Wieland, M., Karimi, F., Azima, A. & Drescher, M. (2014). *New J. Phys.* **16**, 073047.
Geloni, G., Kocharyan, V., Saldin, E., Schneidmiller, E. & Yurkov, M. (2009*a*). *Nucl. Instrum. Methods Phys. Res. A*, **605**, 409–429.
Geloni, G., Kocharyan, V., Saldin, E., Schneidmiller, E. & Yurkov, M. (2009*b*). *Nucl. Instrum. Methods Phys. Res. A*, **607**, 470–487.
Gensch, M., Bittner, L., Chesnov, A., Delsim-Hashemi, H., Drescher, M., Faatz, B., Feldhaus, J., Fruehling, U., Geloni, G., Gerth, C., Grimm, O., Hahn, U., Hesse, M., Kapitzki, S., Kocharyan, V., Kozlov, O., Matyushevsky, E., Morozov, N., Petrov, D., Ploenjes, E., Roehling, M., Rossbach, J., Saldin, E. L., Schmidt, B., Schmueser, P., Schneidmiller, E. A., Syresin, E., Willner, A. & Yurkov, M. V. (2008). *Infrared Phys. Technol.* **51**, 423–425.
Golz, T. (2018). PhD thesis, Hamburg University, Germany.
Green, B., Kovalev, S., Asgekar, V., Geloni, G., Lehnert, U., Golz, T., Kuntzsch, M., Bauer, C., Hauser, J., Voigtlaender, J., Wustmann, B., Koesterke, I., Schwarz, M., Freitag, M., Arnold, A., Teichert, J., Justus, M., Seidel, W., Ilgner, C., Awari, N., Nicoletti, D., Kaiser, S., Laplace, Y., Rajasekaran, S., Zhang, L., Winnerl, S., Schneider, H., Schay, G., Lorincz, I., Rauscher, A. A., Radu, I., Mährlein, S., Kim, T. H., Lee, J. S., Kampfrath, T., Wall, S., Heberle, J., Malnasi-Csizmadia, A., Steiger, A., Müller, A. S., Helm, M., Schramm, U., Cowan, T., Michel, P., Cavalleri, A., Fisher, A. S., Stojanovic, N. & Gensch, M. (2016). *Sci. Rep.* **6**, 22256.
Grimm, O., Morozov, N., Chesnov, A., Holler, Y., Matushevsky, E., Petrov, D., Rossbach, J., Syresin, E. & Yurkov, M. (2010). *Nucl. Instrum. Methods Phys. Res. A*, **615**, 105–113.
Jamison, S., Gillespie, W. & Phillips, P. (2008). *Signal*, **1**, 2.
Jiang, Z. & Zhang, X.-C. (1998). *Appl. Phys. Lett.* **72**, 1945–1947.
Kampfrath, T., Tanaka, K. & Nelson, K. A. (2013). *Nat. Photon.* **7**, 680.
Kovalev, S., Green, B., Golz, T., Maehrlein, S., Stojanovic, N., Fisher, A. S., Kampfrath, T. & Gensch, M. (2017). *Struct. Dyn.* **4**, 024301.
Kübler, C., Huber, R. & Leitenstorfer, A. (2005). *Semicond. Sci. Technol.* **20**, S128–S133.
Monticone, F. & Alù, A. (2017). *Rep. Prog. Phys.* **80**, 036401.
Naftaly, M., Dean, P., Miles, R. E., Fletcher, J. R. & Malcoci, A. (2008). *Quantum Electron.* **14**, 443–448.
Naftaly, M., Molloy, J., Magnusson, B., Andreev, Y. & Lanskii, G. (2016). *Opt. Express*, **24**, 2590–2595.
Nodvick, J. S. & Saxon, D. S. (1954). *Phys. Rev.* **96**, 180–184.
Oelze, T., Schütte, B., Müller, M., Müller, J. P., Wieland, M., Frühling, U., Drescher, M., Al-Shemmary, A., Golz, T., Stojanovic, N. & Krikunova, M. (2017). *Sci. Rep.* **7**, 40736.
Polley, D., Hagström, N. Z., Schmising, C. K., Eisebitt, S. & Bonetti, S. (2018). *J. Phys. B At. Mol. Opt. Phys.* **51**, 224001.
Radu, I. (2019). In preparation.
Redlin, H., Al-Shemmary, A., Azima, A., Stojanovic, N., Tavella, F., Will, I. & Düsterer, S. (2011). *Nucl. Instrum. Methods Phys. Res. A*, **635**, S88–S93.
Richards, P. L. (1964). *J. Opt. Soc. Am.* **54**, 1474–1484.
Schmid, G., Schnorr, K., Augustin, S., Meister, S., Lindenblatt, H., Trost, F., Liu, Y., Stojanovic, N., Al-Shemmary, A., Golz, T., Treusch, R., Gensch, M., Kübel, M., Foucar, L., Rudenko, A., Ullrich, J., Schröter, C. D., Pfeifer, T. & Moshammer, R. (2019). *Phys. Rev. Lett.* **122**, 073001.
Schmuttenmaer, C. A. (2004). *Chem. Rev.* **104**, 1759–1779.
Schulz, S., Grguraš, I., Behrens, C., Bromberger, H., Costello, J., Czwalinna, M., Felber, M., Hoffmann, M., Ilchen, M., Liu, H., Mazza, T., Meyer, M., Pfeiffer, S., Prędki, P., Schefer, S., Schmidt, C., Wegner, U., Schlarb, H. & Cavalieri, A. L. (2015). *Nat. Commun.* **6**, 5938.
Schütte, B., Bauch, S., Frühling, U., Wieland, M., Gensch, M., Plönjes, E., Gaumnitz, T., Azima, A., Bonitz, M. & Drescher, M. (2012). *Phys. Rev. Lett.* **108**, 253003.
Stojanović, D. B., Beličev, P. P., Gligorić, G. & Hadžievski, L. (2018). *J. Phys. D Appl. Phys.* **51**, 045106.
Stojanovic, N. & Drescher, M. (2013). *J. Phys. B At. Mol. Opt. Phys.* **46**, 192001.
Strong, J. & Vanasse, G. A. (1960). *J. Opt. Soc. Am.* **50**, 113–118.
Tavella, F., Stojanovic, N., Geloni, G. & Gensch, M. (2011). *Nat. Photon.*, **5**, 162.
Teo, S. M., Ofori-Okai, B. K., Werley, C. A. & Nelson, K. A. (2015). *Rev. Sci. Instrum.* **86**, 051301.
Tiedtke, K., Azima, A., von Bargen, N., Bittner, L., Bonfigt, S., Düsterer, S., Faatz, B., Frühling, U., Gensch, M., Gerth, C., Guerassimova, N., Hahn, U., Hans, T., Hesse, M., Honkavaar, K., Jastrow, U., Juranic, P., Kapitzki, S., Keitel, B., Kracht, T., Kuhlmann, M., Li, W. B., Martins, M., Núñez, T., Plönjes, E., Redlin, H., Saldin, E. L., Schneidmiller, E. A., Schneider, J. R., Schreiber, S., Stojanovic, N., Tavella, F., Toleikis, S., Treusch, R., Weigelt, H., Wellhöfer, M., Wabnitz, H., Yurkov, M. V. & Feldhaus, J. (2009). *New J. Phys.* **11**, 023029.
Usenko, S., Przystawik, A., Jakob, M. A., Lazzarino, L. L., Brenner, G., Toleikis, S., Haunhorst, C., Kip, D. & Laarmann, T. (2017). *Nat. Commun.* **8**, 15626.
Waltar, K., Haase, J., Lucchini, M., van Bokhoven, J. A., Hengsberger, M., Osterwalder, J. & Castiglioni, L. (2018). *Opt. Express*, **26**, 8364–8374.
Wu, Q. & Zhang, X. (1995). *Appl. Phys. Lett.* **67**, 3523–3525.
Yen, T.-J., Padilla, W., Fang, N., Vier, D., Smith, D., Pendry, J., Basov, D. & Zhang, X. (2004). *Science*, **303**, 1494–1496.
Zapolnova, E., Golz, T., Pan, R., Klose, K., Schreiber, S. & Stojanovic, N. (2018). *J. Synchrotron Rad.* **25**, 39–43.

analytical chemistry

Article

Cite This: *Anal. Chem.* XXXX, XXX, XXX−XXX

pubs.acs.org/ac

Functional Fluorescence Microscopy Imaging: Quantitative Scanning-Free Confocal Fluorescence Microscopy for the Characterization of Fast Dynamic Processes in Live Cells

Aleksandar J. Krmpot,[◆,‡] Stanko N. Nikolić,[◆,‡] Sho Oasa,[◆] Dimitrios K. Papadopoulos,[§,†] Marco Vitali,[∥] Makoto Oura,[⊥] Shintaro Mikuni,[⊥] Per Thyberg,[#] Simone Tisa,[¶] Masataka Kinjo,[⊥] Lennart Nilsson,[▽] Lars Terenius,[◆] Rudolf Rigler,[*,◆,○] and Vladana Vukojević[*,◆]

[◆]Department of Clinical Neuroscience (CNS), Center for Molecular Medicine (CMM), Karolinska Institutet, Stockholm 17176, Sweden

[‡]Institute of Physics Belgrade, University of Belgrade, Belgrade 11080, Serbia

[§]Max-Planck Institute for Molecular Cell Biology and Genetics, Dresden 01307, Germany

[∥]Sicoya GmbH, Berlin 12489, Germany

[⊥]Laboratory of Molecular Cell Dynamics, Faculty of Advanced Life Science, Hokkaido University, Sapporo, Hokkaido 001-0021, Japan

[#]Department of Applied Physics, AlbaNova University Center, Royal Institute of Technology, Stockholm 10691, Sweden

[¶]Micro Photon Devices (MPD), Bolzano 39100, Italy

[▽]Department of Biosciences and Nutrition, Karolinska Institutet, Huddinge 14183, Sweden

[○]Department of Medical Biochemistry and Biophysics (MBB), Karolinska Institutet, Stockholm 17177, Sweden

Supporting Information

ABSTRACT: Functional fluorescence microscopy imaging (fFMI), a time-resolved (21 μs/frame) confocal fluorescence microscopy imaging technique without scanning, is developed for quantitative characterization of fast reaction-transport processes in solution and in live cells. The method is based on massively parallel fluorescence correlation spectroscopy (FCS). Simultaneous excitation of fluorescent molecules in multiple spots in the focal plane is achieved using a diffractive optical element (DOE). Fluorescence from the DOE-generated 1024 illuminated spots is detected in a confocal arrangement by a matching matrix detector comprising 32 × 32 single-photon avalanche photodiodes (SPADs). Software for data acquisition and fast auto- and cross-correlation analysis by parallel signal processing using a graphic processing unit (GPU) allows temporal autocorrelation across all pixels in the image frame in 4 s and cross-correlation between first- and second-order neighbor pixels in 45 s. We present here this quantitative, time-resolved imaging method with single-molecule sensitivity and demonstrate its usefulness for mapping in live cell location-specific differences in the concentration and translational diffusion of molecules in different subcellular compartments. In particular, we show that molecules without a specific biological function, e.g., the enhanced green fluorescent protein (eGFP), exhibit uniform diffusion. In contrast, molecules that perform specialized biological functions and bind specifically to their molecular targets show location-specific differences in their concentration and diffusion, exemplified here for two transcription factor molecules, the glucocorticoid receptor (GR) before and after nuclear translocation and the Sex combs reduced (Scr) transcription factor in the salivary gland of *Drosophila* ex vivo.

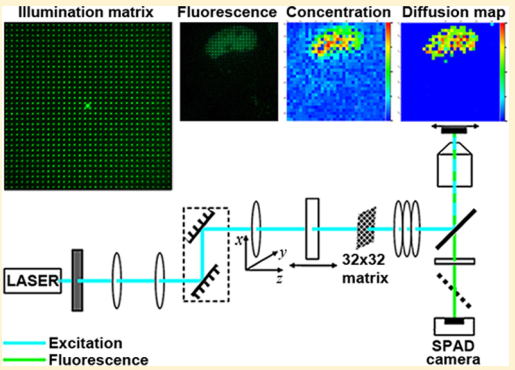

The living cell is a complex dynamic system where local concentrations and spatial distribution of molecules are perpetually changing. Living cells control the concentration and spatial distribution of biological molecules through molecular interactions and transport processes. Through reaction-transport processes, biomolecules are integrated over space and time into dynamical self-regulatory networks and perform complex, life-sustaining functions, such as gene transcription and signal transduction. To understand how these complex biological functions emerge through random motion and molecular collisions, the concentration and mobility of biological molecules need to be quantitatively characterized in live cells.[1,2]

Received: April 13, 2019
Accepted: July 31, 2019
Published: July 31, 2019

DOI: 10.1021/acs.analchem.9b01813
Anal. Chem. XXXX, XXX, XXX−XXX

So far, fluorescence microscopy techniques, confocal laser scanning microscopy (CLSM)[3−10] and fluorescence correlation spectroscopy (FCS)[11−16] in particular, have proven to be indispensable for such studies. However, despite their great versatility, CLSM and FCS also have limitations. Most notably, CLSM imaging is not directly quantitative; while fluorescence is inherently quantitative and fluorescence intensity is proportional to the number of molecules, involved calibration experiments are needed to relate the signal intensity measured using a CLSM system to the number of molecules.[17] Moreover, because of the heterogeneous chemical composition inside different subcellular compartments or because of different conditions in different cells (e.g., pH, oxidative stress, crowding), fluorescent molecules are not necessarily in the same local environment. Hence, their brightness may be different.[18] Under such circumstances, the difference in fluorescence intensity need not necessarily reflect differences in molecular numbers but may rather reflect differences in molecular brightness due to local differences in environmental conditions.

In addition, the temporal resolution of CLSM is low. In CLSM, the acquisition at the level of individual pixels is fast, in the order of microseconds, but the acquisition of an image frame is slow, lasting more than a quarter of a second for a 512 × 512 pixels image. On top of this, the signals in a CLSM image are not acquired at the same point in time, and there is always a time lag between the signals acquired in individual pixels. The temporal resolution of CLSM can be improved by scaling down the number of pixels, i.e., by reducing the area from which the signal is acquired. This, however, results in loss of overview. Classical single-point FCS (spFCS) is also hampered by limited overview, providing quantitative information in a minute observation volume element (OVE) that is typically 0.2−2.0 fl (μm^3). Hence, to acquire quantitative information from several locations in a cell using the conventional spFCS setup, spFCS measurements need to be performed successively, which is not suitable for the study of fast dynamical processes.

To overcome these limitations, specific illumination techniques are used to irradiate a larger area in the sample and the signal is simultaneously recorded from different locations using array detectors. Following the pioneering work at the beginning of this millennium,[19−22] several different experimental realizations of multiplexed FCS have been reported.[23−36] These inventions have significantly advanced our capacity to characterize the spatiotemporal dynamics of complex biological transformations and approach challenging biological problems from the holistic point of view.[24,26,28,33,35,37−45] However, further improvements are needed in order to develop instrumentation with better temporal resolution and with data acquisition and analysis software that are sufficiently robust for reliable routine application in biomedical research.

We present here a setup for quantitative, time-resolved confocal fluorescence microscopy imaging without scanning that is based on massively parallel FCS (mpFCS) measurements, where a diffractive optical element (DOE) and a matching matrix single-photon avalanche photodiode (SPAD) camera are used to achieve massively parallel confocal arrangement.[32,34,38] We show that this approach can map the local concentration and translational diffusion coefficients of molecules in live cells. Since these properties are tightly linked to biomolecular activity at functional sites and are crucial for understanding their mechanisms of action, we call this method functional fluorescence microscopy imaging (fFMI).

MATERIALS AND METHODS

fFMI Instrumental Setup. The fFMI system consists of an inverted epi-fluorescence microscope Axio Observer D1 equipped with a C-Apochromat 63×/1.2 W Corr objective and a high efficiency filter set (Filter Set 38 HE) for enhanced green fluorescent protein (eGFP) consisting of an excitation bandpass filter EX BP 470/40 nm (central wavelength/bandwidth), long pass dichroic mirror with a cutoff wavelength of 495 nm, and an emission band pass filter EM BP 525/50 (all from Carl Zeiss, Germany); a continuous wave (CW) 488 nm frequency-doubled diode laser Excelsior 488 (Spectra-Physics, France); a telescopic laser beam expander; a double filter wheel with 10 (5 + 5) uniform neutral density filters of different optical density (OD) to enable a wide range of attenuation (OD 0.2−8.0) in discrete steps (Thorlabs Inc., USA); a diffractive optical element (DOE) specially designed to split the single laser beam into 32 × 32 beams (Holoeye, Germany); a Single Photon Counting Camera SPC^2 that enables parallel single photon counting by means of a monolithic 32 × 32 array (Micro Photon Devices MPD, Italy).[32] These elements were assembled on an optical table with active vibration damping (Technical Manufacturing Corporation TMC, USA) using standard opto-mechanical components (Newport Corporation, USA, and Thorlabs Inc., USA). To enable fast sample localization, an 18.0 megapixel digital single-lens reflex (DSLR) camera Canon EOS 600D (Canon Inc., Japan) with a pixel size of 18.5 μm^2 and a pixel pitch of 4.3 μm (http://snapsort.com/compare/Canon-600d-vs-Canon_EOS_550D/specs) was coupled to the side port opposite to the SPAD camera, and the light path between the two camera ports was manually switched.

Raw data, i.e., photon counts, acquired by the SPAD camera were transferred to a Dell Precision Fixed Workstation T5600-Xeon E5-2620 2 GHz equipped with an NVIDIA GeForce GTX 780 graphic card containing 2304 compute unified device architecture (CUDA) cores that were used for fast data analysis by auto- and cross-correlation.

LSM 510 ConfoCor 3 System. An individually modified ConfoCor 3 instrument (Carl Zeiss, Germany) for laser scanning fluorescence microscopy imaging and for spFCS was used as a reference.[46] spFCS data were analyzed using the program for data analysis in the running software package and the scientific graphing and data analysis software Origin (OriginLab).

Software for fFMI. The software for data acquisition and analysis was written in Embaracadero C++ Builder XE7 (Embarcadero Technologies, USA).

RESULTS

Instrumental Design. Key elements of the instrumental design, highlighted in Figure 1a and insets a_1−a_3, describe the underlying working principle. Briefly, collimated light from the single-beam CW laser is expanded and led to an achromatic doublet lens (focal length f = 150 mm) mounted on a precise x−y−z translation stage (Figure 1a, focusing lens), which focuses the expanded and collimated laser beam on the DOE mounted on a single-axis precise translation stage (Figure 1a, DOE). By filling the aperture of the DOE, the diffraction pattern consisting of 32 × 32 well-separated illumination spots and the zeroth-order diffraction maximum in the center is formed in the focal plane of the focusing lens that coincides with the image plane of the rear port of the inverted epi-fluorescence microscope (Figure 1a, rear port image plane). Formation of the spot-wise

DOI: 10.1021/acs.analchem.9b01813
Anal. Chem. XXXX, XXX, XXX−XXX

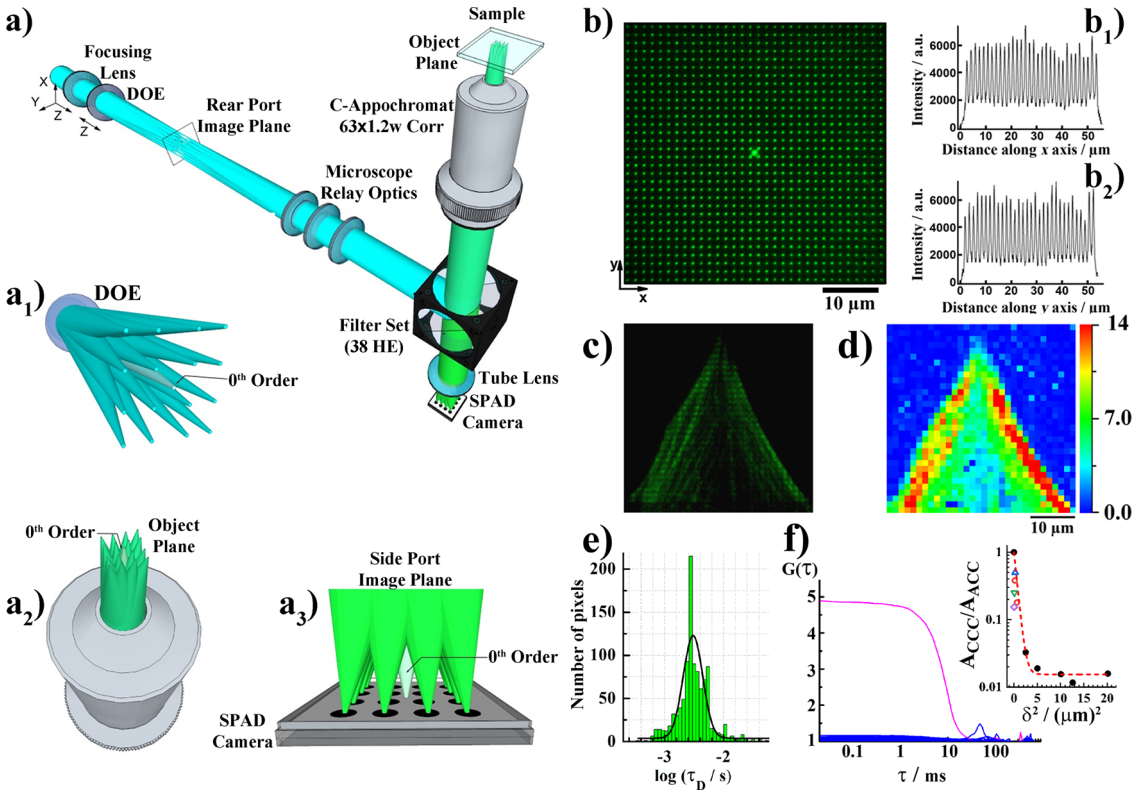

Figure 1. Instrumental setup for functional fluorescence microscopy imaging (fFMI). (a) Schematic presentation of the optical arrangement in the fFMI instrument. The expanded single laser beam is focused by the focusing lens on the diffractive optical element (DOE). The illumination matrix of 32 × 32 laser beam spots (here depicted as a 4 × 4 matrix for simplicity) is formed at the image plane of the rear port of the microscope. Inset: Formation of the ordered spotty pattern at three characteristic planes: (a_1) in the rear port image plane, (a_2) in the object plane, and (a_3) in the side port image plane. Of note, the zeroth-order diffraction peak falls exactly between 4 central pixels of the SPAD camera when the fFMI system is fully aligned and is therefore not detected by the SPAD camera. (b) Image of the illumination matrix generated in the focal plane of the microscope objective. A thin layer formed by drying of a concentrated Rhodamine 6G (Rh6G) solution was used as the sample, and the image was acquired by the 18.0 megapixel digital single-lens reflex (DSLR) camera. The zeroth-order diffraction peak is readily visible when using the pixel-dense DSLR camera. Inset: Fluorescence intensity profiles along (b_1) the *x*-axis and (b_2) the *y*-axis show that the sample is illuminated in a distinct pattern of 32 × 32 spots. The pitch (the shortest distance between two adjacent spots) of the illumination matrix in the sample plane is 1.587 μm. (c) Image of filamentous actin in fixed muntjac skin fibroblast cells acquired under spot-wise illumination using the 18.0 megapixel DSLR camera. (d) Image of the sample described in (c) acquired by the SPAD camera. Signal acquisition time = 1 ms. Fluorescence intensities ranged from 0 (dark blue) to ≥13 700 photons per second (red). The scale bar is 10 μm. (e) Distribution of diffusion times in a dilute aqueous suspension of fluospheres, d = 100 nm, recorded by the fFMI system. The average diffusion time was determined to be $\tau_D = (3 \pm 2)$ ms. (f) ACC recorded in an individual pixel, i.e., by an individual SPAD in the SPAD matrix detector (magenta). Cross-correlation curves (CCCs) derived by cross-correlating the signals recorded in this particular SPAD and its first- and second-order neighbors (blue). Inset: (f_1) Amplitude of the CCCs (blue) normalized to the amplitude of the ACC (magenta), A_{CCC}/A_{ACC}, as a function of the squared distance between neighboring OVEs (δ). As expected, the amplitudes of the CCCs decay exponentially with the distance between neighboring OVEs squared,[47] and the data from this study (black dots) agree well with results reported in the literature: Buchholz, PhD Thesis (CCC1 and CCC2, Figure 6.4; red circles),[48] Dertinger et al. (Figure 6; blue triangle),[47] Ries and Schwille (Figure 4; green inverted triangle),[49] and Ries et al. (Figure 2d; lilac diamond).[50] The relative amplitude $A_{CCC}/A_{ACC} = 1$ at OVE distance $\delta = 0$ corresponds to cross-correlation of fluorescence intensity fluctuations in the reference pixel to itself. The fitted single-exponential decay curve (red, dashed) shows that the amplitude of the CCC decays exponentially with δ^2.[47]

illumination pattern is schematically depicted in Figure 1, inset a_1, featuring for the sake of clarity an array of 4 × 4 spots with the clearly indicated zeroth-order diffraction maximum. The relay optics of the rear port of the microscope (Figure 1a, microscope relay optics), the dichroic mirror (integrated in the Filter Set 38 HE), and the objective lens project the illumination matrix from the rear port into the focal plane of the objective (Figure 1a, object plane; Figure 1, inset a_2). A uniform thin layer of dried Rh6G was used to visualize the illumination matrix. The image acquired using the pixel-dense DSLR camera shows that the sample is illuminated in a distinct spot-wise array of 32 × 32 well-separated points of similar intensity, except for the zeroth-order diffraction spot visible in the center (Figure 1b). Corresponding fluorescence intensity distribution profiles along the *x* and *y* axes are shown in Figure 1, insets b_1 and b_2, respectively.

After passing through the dichroic mirror and the emission filter integrated in the Filter Set 38 HE, the spot-wise fluorescence matrix is imaged by the objective and the tube lenses onto the SPAD camera (Figure 1a and inset a_3). The SPAD camera is attached to one of the two side ports of the microscope, with the DSLR camera being attached to the other side and used for fast sample localization using standard wide-field imaging. The SPAD camera contains a photosensitive chip and a 16-bit photon counter based on a field programmable gate array (FPGA). The photosensitive area of the chip consists of 32 × 32 circular SPADs that are 20 μm in diameter. The distance between adjacent diodes along a row/column, i.e., the pitch of

DOI: 10.1021/acs.analchem.9b01813
Anal. Chem. XXXX, XXX, XXX−XXX

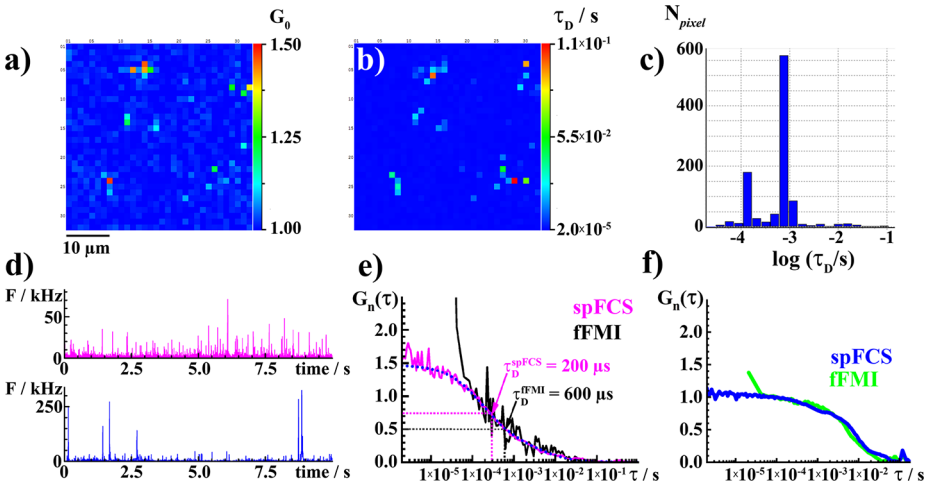

Figure 2. fFMI instrument calibration and performance characterization using a dilute aqueous suspension of quantum dots. (a) Spatial map of amplitudes (G_0) of individual ACCs at the lag time τ = 103.7 μs, acquired by fFMI. Fluorescence intensity fluctuations were recorded in a single measurement lasting 2.7 s. (b) Corresponding spatial map of translational diffusion times (τ_D). (c) Diffusion time distribution histogram corresponding to the data shown in (b). (d) Fluorescence intensity fluctuations recorded in the same sample as in (a−c) acquired using a conventional spFCS system. Fluorescence intensity bursts of different intensities (note the different scales on the ordinates) reveal that the dilute quantum dot suspension is polydisperse, containing single quantum dots (magenta) and a significantly lower amount of very bright quantum dot agglomerates that were sporadically observed (blue trace). (e) ACCs normalized to the same amplitude, $G_n(\tau)$ = 1 at lag time τ = 103.7 μs, obtained by temporal autocorrelation analysis of fluorescence intensity fluctuations reflecting diffusion of single quantum dots. The ACCs were acquired by fFMI (black) and spFCS (magenta). The black ACC is an average ACC acquired from 10 consecutive fFMI recordings of fluorescence intensity fluctuations in a single SPAD, i.e., in a single OVE/single pixel, each measurement lasting 2.7 s. The magenta ACC is acquired from the fluorescence intensity fluctuation time series of 10 s. The dotted blue line shows fitting of the magenta ACC. (f) ACCs normalized to the same amplitude, $G_n(\tau)$ = 1 at lag time τ = 103.7 μs, reflecting diffusion of sparse quantum dot agglomerates, acquired by fFMI in a single pixel and in a 2.7 s measurement (blue) and by spFCS (green).

the camera, is 100 μm. Further details on the SPAD camera design and performance can be found in refs 32 and 51−53. Since the aperture of every SPAD is a pinhole positioned in the conjugate focal plane with respect to the illumination matrix, confocal configuration is achieved for all 32 × 32 foci.

By imaging the complex spatial distribution of filamentous actin in fixed muntjac skin fibroblast cells, we could verify that there is no significant loss of information due to interspaced sampling (Figure 1c,d). Images acquired by the pixel-dense DSLR camera (Figure 1c) and the SPAD camera (Figure 1d) clearly show that the SPAD camera veritably reflects the spatial distribution of actin filaments over long distances.

In a well-aligned fFMI system, similar values for the translational diffusion time are obtained in the majority of pixels, and the distribution of diffusion times across the whole matrix is narrow, exemplified here for a measurement performed in a dilute aqueous suspension of 100 nm fluospheres (Figure 1e). The measured diffusion time, $\tau_D = (3 \pm 2)$ ms (Figure 1e), is in good agreement with the value obtained using the reference spFCS system, τ_D = (2.5 ± 0.5) ms (see fFMI Instrument Calibration and Performance Characterization for details on instrument calibration).

Finally, cross-correlation of signals recorded in a reference pixel with the signal recorded in its first- and second-order neighbors showed that there is virtually no cross-talk between neighboring SPADs, as is evident from the relatively small amplitude of the CCCs (Figure 1f, blue) that is less than 4% of the amplitude of the ACC (Figure 1f, magenta). The Supporting Information contains details of the software for data analysis, the calculation of auto- and cross-correlation curves, and image rendering (Section S1), cell culture (Section S2), instrument alignment (Section S3, Figure S1), OVE size determination (Section S4, Figure S2), and accuracy, precision, and sensitivity (Section S5, Figure S3).

fFMI Instrument Calibration and Performance Characterization. A dilute aqueous suspension of carboxylate functionalized quantum dots (2 nM) was used to compare the fFMI instrument performance with respect to the conventional spFCS system used as a reference. For this purpose, fFMI and conventional spFCS measurements were performed on the same sample (Figure 2a−f). To have similar conditions in both experiments, the illumination intensity in the conventional spFCS instrument was set to 14.8 μW at the microscope objective lens, in order to match the intensity in individual foci of the fFMI instrument, which was estimated to be 1/1024 of the intensity measured at the microscope objective (18.9 mW) reduced by 20% to account for the intensity of the zeroth-order diffraction peak.

Both fFMI and spFCS revealed that, despite prolonged sonication, the quantum dots suspension is polydisperse, being made up of individual quantum dots present in large excess (Figure 2a,b (blue pixels), Figure 2d (top), and corresponding ACCs in Figure 2e) but also containing a small amount of very bright quantum dot agglomerates of different sizes (Figure 2a,b (green-red pixels), Figure 2d (bottom), and corresponding ACCs in Figure 2f). In measurements using the conventional spFCS instrument, the presence of sparse agglomerates could be readily revealed in some but not all recordings (Figure 2d, the magenta time series exemplifies a measurement where quantum dot agglomerates were not observed), whereas fFMI revealed in a single shot that the quantum dot suspension is polydisperse and provided the spatial localization of agglomerates at the moment of measurement, as is evident from the map of ACC amplitudes, G_0, (Figure 2a, green-red pixels), the translational

DOI: 10.1021/acs.analchem.9b01813
Anal. Chem. XXXX, XXX, XXX−XXX

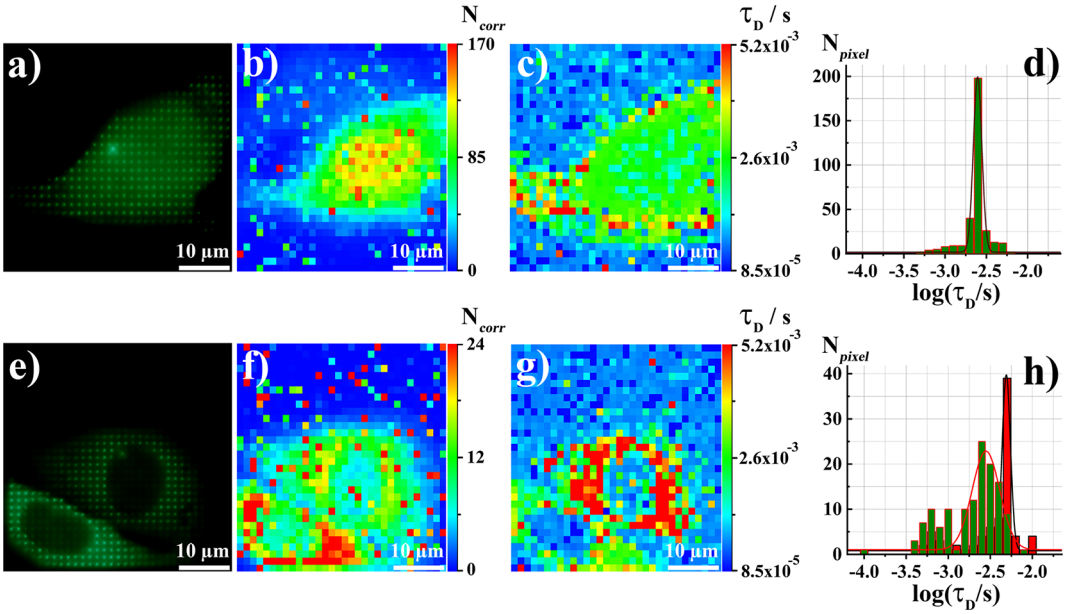

Figure 3. Spatial distribution of molecular numbers and diffusion time maps in live U-2 OS cells expressing monomeric or tetrameric eGFP. (a) 18.0 megapixel DSLR image of a spot-wise illuminated U-2 OS cell expressing monomeric eGFP. (b) Spatial distribution of molecular numbers (N_{corr}) across an optical section in the cell, with slight eGFP accumulation in the nucleus. (c) eGFP diffusion times (τ_D) across the same section as in (b). (d) The corresponding τ_D distribution histogram shows that eGFP mobility inside the cell is rather uniform, $\tau_D = (2.5 \pm 0.5)$ ms. (e) DSLR image of two cells expressing $eGFP_4$, acquired as described in (a). (f) Molecular numbers (N_{corr}) map reveals $eGFP_4$ prevalence in the cytoplasm. (g) $eGFP_4$ diffusion time map in two adjacent cells. In the upper cell, the average diffusion time, $\tau_D = (5.0 \pm 0.8)$ ms, is two times longer than the diffusion time measured for eGFP in (d). This is in agreement, within the experimental error, with the expected theoretical difference of 1.6 times. In the lower cell, where $eGFP_4$ degradation was observed, the average nuclear concentration was higher than in the upper cell, $N_{corr}^{lcell} \approx 12$ versus $N_{corr}^{lcell} \approx 6$; τ_D was the same as in cells expressing monomeric eGFP, and a wider distribution of diffusion times ((h), green histogram, versus (d)) was observed. (h) Diffusion time distribution histograms in the upper (red) and the lower (green) cell shown in (g).

diffusion time, τ_D, map (Figure 2b, green-red pixels), and the distribution of diffusion times (Figure 2c).

Both, the conventional spFCS and the fFMI system, showed marked differences in diffusion times between single quantum dots, $\tau_{D,sqd}^{spFCS} = (200 \pm 50)$ μs (Figure 2e), and quantum dot agglomerates, $\tau_{D,qda}^{spFCS} = (7 \pm 2)$ ms (Figure 2f). Importantly, the characteristic decay times of ACC obtained using the fFMI instrument and the conventional spFCS setup concurred, as is evident from the overlap of the ACCs normalized to the same amplitude, $G_n(\tau) = 1$ at $\tau = 103.7$ μs, for individual quantum dots (Figure 2e) and for quantum dot agglomerates (Figure 2f). This observation is in line with calibration measurements showing that the OVEs in the fFMI system are similar in size to that in the conventional spFCS instrument.

Of note, the average diffusion time for single quantum dots estimated from the diffusion time histogram, $\tau_{D,sqd}^{hist} = (600 \pm 100)$ μs (Figure 2c), is evidently longer than the value determined by fitting spFCS data, $\tau_{D,sqd}^{spFCS} = (200 \pm 50)$ μs (Figure 2e, magenta). This discrepancy, which is particularly pronounced for molecules/particles with short diffusion times, arises because of the comparatively low temporal resolution of the matrix SPAD detector, due to which plateauing of the ACC cannot be observed (Figure 2e). Consequently, the translational diffusion time, estimated from the full width of the ACC at its half-maximum (Figure 2e, black), will appear to be somewhat longer than what it really is (Figure 2e, magenta). Using fluospheres of different size, we could demonstrate that, the longer the translational diffusion time, the less pronounced will be this difference, and the diffusion coefficient could be correctly determined (as shown in Section S5, Figure S2).

Small Differences in Translational Diffusion Time between eGFP Monomers and Tetramers Could Be Measured in Live Cells by fFMI. In order to assess the precision of the fFMI system, its capacity to measure small differences in translational diffusion time was probed using live U-2 OS cells expressing monomeric or tetrameric eGFP, eGFP, or $eGFP_4$, respectively (Figure 3).

fFMI could also measure subtle differences in the translational diffusion between eGFP (Figure 3c,d) and $eGFP_4$ (Figure 3g,h, red pixels and bars). It showed that translational diffusion of eGFP monomers in U-2 OS cells is rather uniform across the cell, with an average diffusion time $\tau_{D,eGFP} = (2.5 \pm 0.5)$ ms (Figure 3c,d), whereas the translational diffusion time of $eGFP_4$ is about two times longer, $\tau_{D,eGFP4} = (5.0 \pm 0.8)$ ms (Figure 3g, upper cell; Figure 3h, red histogram). This difference, derived from measurements in 10 cells in each group, is in agreement with the theoretically expected value of 1.6 times.

fFMI also indicated cells where oligomeric forms containing less than four eGFP molecules prevail. Such cells (Figure 3g, lower cell) are identifiable through the shorter translational diffusion time (Figure 3h, green histogram (lower cell) versus the red histogram (upper cell)), higher average nuclear concentration of fluorescent molecules, $N_{corr}^{lcell} \approx 12$ versus $N_{corr}^{ucell} \approx 6$ (Figure 3f), and wider distribution of diffusion times (Figure 3h, green histogram, versus Figure 3d). Lower size oligomers can occur due to degradation processes. While eGFP is not efficiently degraded by proteinases, the flexible linker is, due to the specific construction of the plasmid where each eGFP sequence is preceded by an ATG start codon.

Mapping the Heterogeneous Distribution and Dynamics of Molecules in Live Cells by fFMI. Having

DOI: 10.1021/acs.analchem.9b01813
Anal. Chem. XXXX, XXX, XXX−XXX

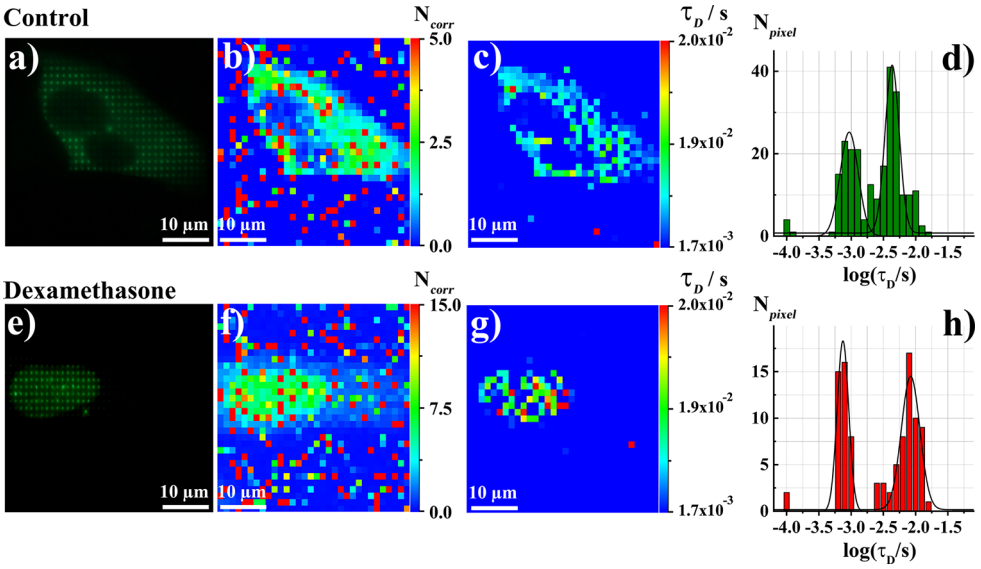

Figure 4. Spatial distribution of molecular numbers and diffusion time maps of glucocorticoid receptors (GR) before and upon ligand-induced nuclear translocation in live U-2 OS cells. (a) DSLR image of a spot-wise illuminated unstimulated U-2 OS cell expressing eGFP-GR$_{wt}$. (b) fFMI reveals the spatial distribution of eGFP-GR$_{wt}$ numbers (N_{corr}) across an optical section in the cell with their accumulation in the cytoplasm. (c) Spatial distribution of translational diffusion times (τ_D) across the same section as in (b). (d) Diffusion time distribution histogram in the cytoplasm of cells shown in (c). (e) DSLR image showing eGFP-GR$_{wt}$ translocation to the cell nucleus after stimulation with dexamethasone. (f) Spatial distribution of molecular numbers (N_{corr}) reveals eGFP-GR$_{wt}$ translocation from the cytoplasm to the cell nucleus. (g) fFMI map of eGFP-GR$_{wt}$ diffusion times (τ_D), reflecting a patchy distribution due to differences in eGFP-GR$_{wt}$ interactions with the surrounding molecules. (h) Diffusion time distribution histogram in the cell nucleus shown in (g).

established that fFMI can measure small differences in translational diffusion between cells that express uniformly diffusing molecules of different size, we assessed its capacity to map the heterogeneous distribution and nonuniform dynamic behavior of a molecule in the same cell (Figure 4). We have therefore chosen the glucocorticoid receptor (GR), a transcription factor for which the heterogeneous distribution and complex intracellular dynamics are well established and characterized by conventional spFCS.[54−56]

fFMI readily revealed the nonuniform distribution and uneven diffusion of fluorescently tagged wild type glucocorticoid receptors (eGFP-GR$_{wt}$) in the cytoplasm of untreated U-2 OS cells (Figure 4a−d), showing that eGFP-GR$_{wt}$ concentration in the periphery is lower, $N_{avg}^{pnr} \approx 1.25$, and its diffusion time is shorter, $\tau_D^{per} = \approx(0.8 \pm 0.2)$ ms, than in the perinuclear region that is enriched in intracellular membranes, $N_{avg}^{pnr} \approx 2.5$ and $\tau_D^{pnr} = (4.0 \pm 0.5)$ ms.

As expected, treatment of U-2 OS cells with the GR agonist dexamethasone (100 nM Dex) induced eGFP-GR$_{wt}$ translocation from the cytoplasm to the cell nucleus (Figure 4). In the nucleus (Figure 4e−h), eGFP-GR$_{wt}$ partitioned into different domains, showing both an uneven distribution of molecular numbers (Figure 4f) and "patchy" diffusion behavior (Figure 4g), revealing domains where eGFP-GR$_{wt}$ motility is fast and interactions with other molecules are scarce and/or nonspecific, characterized by short diffusion times, as opposed to regions where binding with higher affinities is observed; eGFP-GR$_{wt}$ motion is therefore stalled, and diffusion times are longer.

Mapping Dynamic Processes in the Plasma Membrane of Live Cells by fFMI. The capacity of the fFMI system was tested for quantitative characterization of dynamic processes in the plasma membrane. For this purpose, PC12 cells stably transformed to express a G protein-coupled receptor (GPCR), the wild type μ-opioid receptor fused at the N-terminal end with eGFP (eGFP-MOP), were used to map in live cells its spatial surface density and lateral diffusion in the plasma membrane (Figure 5). As can be seen, the plasma membrane and the perinuclear region, enriched with membranous structures of the endoplasmic reticulum and the Golgi complex, could be easily distinguished from the remaining cellular compartments and the surroundings by fluorescence intensity imaging using the DSLR camera under spot-wise illumination (Figure 5a). While the map of the average number of molecules in the OVE (N_{corr}) was noisy due to low expression levels of eGFP-MOP (Figure 5b), the translational diffusion time maps could be readily acquired, rendering the plasma membrane and the membranous structures in the perinuclear region clearly visible (Figure 5c). fFMI revealed that the eGFP-MOP diffusion in the plasma membrane (Figure 5 d, red) and in membranous structures in the perinuclear region (Figure 5d, blue) is complex, and two principal decay times were identified: $\tau_{D1} = (1.0 \pm 0.5)$ ms and $\tau_{D2} = (100 \pm 20)$ ms (Figure 5d).

Mapping ex Vivo the Heterogeneous Distribution and Dynamics of Molecules in Thick Tissue Specimen by fFMI. While we have established that crosstalk between pixels is not an issue for quantitative characterization of concentration and diffusion in dilute solutions/suspensions (Figure 1f), it is well-known that the main challenge for quantitative fluorescence microscopy imaging of a thick specimen using multifocal optical arrangement arises because out-of-focus light that originates from bright structures in remote focal planes above/below the sample plane can pass through adjacent pinholes. This increases the background signal, i.e., reduces the SNR, and gives rise to hazy images where the details that are normally observed in confocal laser scanning microscopy are obscured in spinning disk confocal microscopy.[57] In order to probe the capacity of the fFMI system to characterize dynamical processes in thick samples, the concentration and nuclear dynamics of the mCitrine-tagged Sex combs reduced (Scr) dimeric transcription factor (mCitrine-(Scr)$_2$) were investigated in salivary glands

DOI: 10.1021/acs.analchem.9b01813
Anal. Chem. XXXX, XXX, XXX−XXX

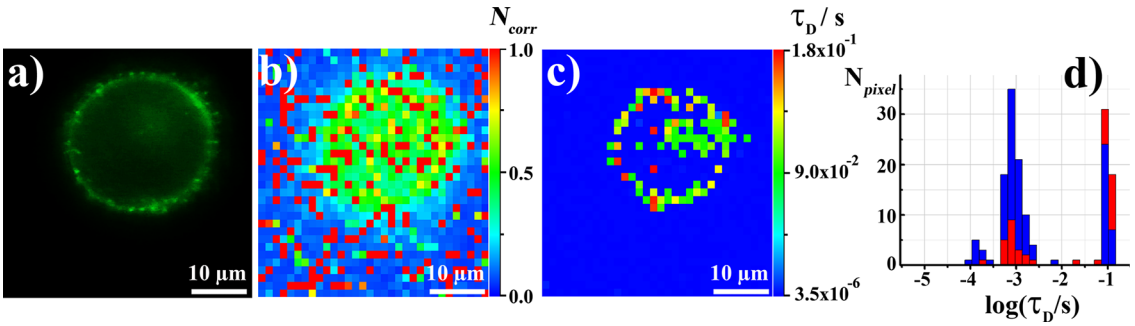

Figure 5. Dynamic lateral organization of mu-opioid receptor in the plasma membrane. (a) DSLR image of a spot-wise illuminated PC12 cell expressing eGFP-MOP. (b) Spatial distribution of eGFP-MOP numbers (N_{corr}) across an optical section in the cell. (c) Spatial distribution of diffusion times (τ_D) across the same section as in (b). (d) Corresponding diffusion time distribution histograms inside the cell (blue) and in the plasma membrane (red).

from *Drosophila* third instar larvae bearing in the genome a multimeric specific binding site of Scr (*fkh250*^{con}; see Section S2 and ref 38 for details). The results are presented in Section S6 and Figure S4.

DISCUSSION

Spatial filtering of fluorescence, which is at the heart of CLSM, is achieved by conjugate focal plane arrangement of optical elements and obstruction of out-of-focus light by detection through a pinhole. This significantly improves the SNR of fluorescence microscopy, enabling optical sectioning and fluorescence imaging with high spatiotemporal resolution and single-molecule sensitivity. Advantages for biomedical research and diagnostics brought about by confocal imaging are so numerous that it has been stated that "...confocal technology is proving to be one of the most important advances ever achieved in optical microscopy."[58] Confocal configuration was also shown to be critical for FCS;[59,60] by reducing the size of the OVE, a significantly smaller number of solvent molecules was observed, which efficiently reduced the background and enhanced the signal-to-noise ratio. This, in turn, has enabled single-molecule detection and short measurement time. The possibility to have multiplexed confocal arrangements of excitation and detection pathways is therefore essential for quantitative studies of fast dynamic processes in live cells that require high spatiotemporal resolution and single-molecule sensitivity.

Presently available state-of-the-art instruments for massively parallel FCS measurements, such as the systems described in refs 29 and 31, rely on the use of light sheet illumination and point-wise detection via an electron multiplying charge coupled device (EMCCD) camera[29] or a SPAD matrix detector.[31,36] In these arrangements, a selected plane in the sample is illuminated at a defined *z*-position by a micrometer-thin light sheet that is perpendicular to the optical axis of the detection objective lens. The advantage of light sheet illumination over a confocal arrangement comes from the specific illumination of an area that is significantly larger than the cross sectional area of the confocal volume element. The disadvantage of light sheet illumination as compared to multiplexed confocal arrangement comes from the nonuniformity of the light sheet over longer distances, which means that the area over which OVEs of the same size are obtained is restricted. In addition, structures in the specimen that absorb/scatter the excitation light distort the light sheet, and the size of the OVEs is not uniform across heterogeneous samples.[29,31] To circumvent these problems in light sheet based microscopy imaging, the sample needs to be repositioned and precisely rotated, which is a limiting factor for the study of fast dynamical processes. It also complicates sample preparation and mounting, and sample preparation procedures are considerably more complex for light sheet microscopy than for confocal imaging.[61] Such restrictions do not exist for fFMI. Here, the limit in number of focal spots is set by the intensity of the single-beam laser and the dark count of individual SPADs that comprise the matrix detector.

The advantage of the SPAD matrix detectors over EMCCD cameras primarily lies in the temporal resolution, which is inherently low in EMCCD cameras because of the slow readout and frame-transfer processes. At present, the temporal resolution of EMCCDs is in the millisecond range, at best, whereas the temporal resolution of SPADs is easily in the microsecond and even submicrosecond range. Thus, SPAD matrices hold the promise to significantly improve the temporal resolution of fluorescence microscopy imaging, allowing a 100- to 1000-times better temporal resolution. Furthermore, no analogue measurement of voltage or current is needed for SPADs, so no additional noise is added by the readout process. Finally, the SPAD detector is typically less sensitive than EMCCD to electromagnetic interference due to electromagnetic radiation generated by other equipment.

The disadvantage of SPAD matrix detectors over an EMCCD stems mainly from the variability in dark count rates between individual detectors, which gives a nonuniform SNR over an image frame (Figure 1f). This, however, is not too big a problem for fFMI; while differences in dark count rates affect the signal intensity, the outcome of temporal autocorrelation analysis is not significantly affected and the average number of molecules in the OVE and the diffusion time could still be accurately determined by autocorrelation analysis even though the SNR is not exactly the same in all foci. Of course, this is only possible when the SNR is sufficiently high in all foci. If this is not the case, the amplitude of the autocorrelation curve becomes unreliable.

Another well-known limitation associated with SPADs is related to afterpulsing.[32,62,63] In the present camera, afterpulsing is observed in the ACCs as a prominent and fast-decaying peak at lag times, $\tau < 100$ μs (Figure 2e, black; Figure 2f, green; Section S6, Figure S4g, blue). Afterpulsing is more prominently observed in measurements where low signal intensities were measured, e.g., individual quantum dots (Figure 2e, black) versus bright quantum dot agglomerates (Figure 2f, green). However, afterpulsing-related distortion of ACCs may be circumvented by cross-correlating the signals between two detectors,[32,62] by subtracting the contribution of afterpulsing from the ACCs,[63] and by SPAD design.[64]

DOI: 10.1021/acs.analchem.9b01813
Anal. Chem. XXXX, XXX, XXX−XXX

Despite the limitations of currently available technologies for massive production of SPADs, which restrain the temporal resolution and affect quantitative characterization in live cells as discussed above, the data presented here compellingly show that it is possible to achieve a massively parallel confocal arrangement and quantitative confocal imaging with single-molecule sensitivity without scanning via massively parallel FCS. This yields quantitative confocal imaging with an unprecedented temporal resolution, which in the present setup is 21 μs/frame. We have demonstrated that massively parallel analysis of fluorescence intensity fluctuations by temporal autocorrelation and spatiotemporal cross-correlation analyses can be achieved, yielding 1024 ACCs in about 4 s and about 24 000 CCCs in 45 s. The use of the graphic processing unit (GPU) is a major advantage for the calculation of CCCs, since the number of CCCs is much larger than the number of ACCs. The FPGA approach described in ref 30 calculates ACCs in real time, but the memory constraints would not allow the calculation of CCCs as well. Hence, a combination of these two approaches will likely be the best for future applications.

CONCLUDING REMARKS

The quantitative, time-resolved confocal fluorescence microscopy imaging approach developed here retains the capacity to perform optical sectioning and is empowered by the abolishment of scanning, thus allowing simultaneous data acquisition in all points in an image frame with a submillisecond temporal resolution (here 21 μs/frame). It provides, with diffraction limited spatial resolution, quantitative information about location-specific differences in the concentration and mobility of the molecules, which cannot be otherwise deduced. The possibility to characterize the fast cellular dynamics of molecules: quantitatively, nondestructively, with the ultimate sensitivity and with unprecedented temporal resolution, enables us to address how biomolecules are integrated via chemical reactions and transport processes into dynamical self-regulated networks through which emergent properties, such as gene transcription and signal transduction, arise at the higher level of organization and at longer spatio-temporal scales.

ASSOCIATED CONTENT

Supporting Information

The Supporting Information is available free of charge on the ACS Publications website at DOI: 10.1021/acs.analchem.9b01813.

Details of software for data analysis and calculation of auto- and cross-correlation curves, image rendering, cell culture, and instrument alignment along with imaging in a thick tissue specimen (PDF)

AUTHOR INFORMATION

Corresponding Authors

*E-mail: Vladana.Vukojevic@ki.se.
*E-mail: Rudolf.Rigler@ki.se.

ORCID

Aleksandar J. Krmpot: 0000-0003-2751-7395
Sho Oasa: 0000-0003-3800-590X
Dimitrios K. Papadopoulos: 0000-0003-0914-3051
Lennart Nilsson: 0000-0002-5067-6397
Lars Terenius: 0000-0003-2880-9576
Rudolf Rigler: 0000-0003-4742-0857
Vladana Vukojević: 0000-0003-0873-5653

Present Address

[†]D.K.P.: MRC Human Genetics Unit, Institute of Genetics and Molecular Medicine, University of Edinburgh, Edinburgh EH4 2XU, UK.

Author Contributions

The manuscript was written through contributions of all authors. All authors have given approval to the final version of the manuscript.

Notes

The funding agencies had no influence on the study design, methods, data collection, analyses, or the manuscript writing. The authors declare no competing financial interest.

ACKNOWLEDGMENTS

Financial support from The Knut and Alice Wallenberg Foundation (KAW 2011.0218), the Swedish Research Council (VR 2016-01922; 2018-05337), the Swedish Foundation for Strategic Research (SBE13-0115), FP7-Health-2013-Innovation-1GLORIA-602919 Project, and the Magnus Bergvall's Foundation (2016-01615; 2018-02642) is gratefully acknowledged. A.J.K. and S.N.N. gratefully acknowledge financial support from the Rajko and Maj Đermanović Fund, ERASMUS+ European Union Programme for Education, Training, Youth and Sport, and the Ministry of Education and Science of the Republic of Serbia (Grant Nos. III45016 and OI171038). S.O. gratefully acknowledges a postdoctoral fellowship by The Nakatani Foundation for Advancement of Measuring Technologies in Biomedical Engineering and a travel grant by Yoshida Foundation for Science and Technology. D.K.P. was supported by a Federation of European Biochemical Societies (FEBS) postdoctoral fellowship. We thank Milan Radosavljević, M.Sc. (Eng) for his help with hardware assembly.

REFERENCES

(1) Qian, H. *J. Stat. Phys.* **2010**, *141* (6), 990−1013.
(2) Qian, H.; Ge, H. *Mol. Cell. Biomech.* **2012**, *9* (1), 1−30.
(3) Claridge, S. A.; Schwartz, J. J.; Weiss, P. S. *ACS Nano* **2011**, *5* (2), 693−729.
(4) Diekmann, S.; Hoischen, C. *Physics of life reviews* **2014**, *11* (1), 1−30.
(5) Lock, J. G.; Stromblad, S. *Exp. Cell Res.* **2010**, *316* (8), 1438−44.
(6) Mavrakis, M.; Pourquie, O.; Lecuit, T. *Development* **2010**, *137* (3), 373−87.
(7) Owen, D. M.; Williamson, D.; Rentero, C.; Gaus, K. *Traffic* **2009**, *10* (8), 962−71.
(8) Petibois, C. *Anal. Bioanal. Chem.* **2010**, *397* (6), 2051−65.
(9) Requejo-Isidro, J. *Journal of chemical biology* **2013**, *6* (3), 97−120.
(10) Weigert, R.; Porat-Shliom, N.; Amornphimoltham, P. *J. Cell Biol.* **2013**, *201* (7), 969−79.
(11) Ries, J.; Schwille, P. *BioEssays* **2012**, *34* (5), 361−8.
(12) Elson, E. L. *Biophys. J.* **2011**, *101* (12), 2855−70.
(13) Fitzpatrick, J. A.; Lillemeier, B. F. *Curr. Opin. Struct. Biol.* **2011**, *21* (5), 650−60.
(14) Digman, M. A.; Gratton, E. *Annu. Rev. Phys. Chem.* **2011**, *62*, 645−68.
(15) Tian, Y.; Martinez, M. M.; Pappas, D. *Appl. Spectrosc.* **2011**, *65* (4), 115A−124A.
(16) Elson, E. L. *Methods* **2018**, *140−141*, 3−9.
(17) Kedziora, K. M.; Prehn, J. H.; Dobrucki, J.; Bernas, T. *J. Microsc.* **2011**, *244* (1), 101−11.
(18) Morikawa, T. J.; Fujita, H.; Kitamura, A.; Horio, T.; Yamamoto, J.; Kinjo, M.; Sasaki, A.; Machiyama, H.; Yoshizawa, K.; Ichimura, T.; Imada, K.; Nagai, T.; Watanabe, T. M. *Sci. Rep.* **2016**, *6*, 22342.

DOI: 10.1021/acs.analchem.9b01813
Anal. Chem. XXXX, XXX, XXX−XXX

(19) Blom, H.; Johansson, M.; Hedman, A. S.; Lundberg, L.; Hanning, A.; Hard, S.; Rigler, R. *Appl. Opt.* **2002**, *41* (16), 3336−42.
(20) Blom, H.; Johansson, M.; Gosch, M.; Sigmundsson, T.; Holm, J.; Hard, S.; Rigler, R. *Appl. Opt.* **2002**, *41* (31), 6614−20.
(21) Gosch, M.; Serov, A.; Anhut, T.; Lasser, T.; Rochas, A.; Besse, P. A.; Popovic, R. S.; Blom, H.; Rigler, R. *J. Biomed. Opt.* **2004**, *9* (5), 913−21.
(22) Gosch, M.; Blom, H.; Anderegg, S.; Korn, K.; Thyberg, P.; Wells, M.; Lasser, T.; Rigler, R.; Magnusson, A.; Hard, S. *J. Biomed. Opt.* **2005**, *10* (5), 054008.
(23) Michalet, X.; Colyer, R. A.; Antelman, J.; Siegmund, O. H.; Tremsin, A.; Vallerga, J. V.; Weiss, S. *Curr. Pharm. Biotechnol.* **2009**, *10* (5), 543−58.
(24) Needleman, D. J.; Xu, Y.; Mitchison, T. J. *Biophys. J.* **2009**, *96* (12), 5050−9.
(25) Colyer, R. A.; Scalia, G.; Rech, I.; Gulinatti, A.; Ghioni, M.; Cova, S.; Weiss, S.; Michalet, X. *Biomed. Opt. Express* **2010**, *1* (5), 1408−1431.
(26) Capoulade, J.; Wachsmuth, M.; Hufnagel, L.; Knop, M. *Nat. Biotechnol.* **2011**, *29* (9), 835−9.
(27) Colyer, R. A.; Scalia, G.; Villa, F. A.; Guerrieri, F.; Tisa, S.; Zappa, F.; Cova, S.; Weiss, S.; Michalet, X. *Proc. SPIE* **2011**, *7905*, 790503.
(28) Oh, D.; Zidovska, A.; Xu, Y.; Needleman, D. J. *Biophys. J.* **2011**, *101* (6), 1546−54.
(29) Bag, N.; Sankaran, J.; Paul, A.; Kraut, R. S.; Wohland, T. *ChemPhysChem* **2012**, *13* (11), 2784−94.
(30) Buchholz, J.; Krieger, J. W.; Mocsar, G.; Kreith, B.; Charbon, E.; Vamosi, G.; Kebschull, U.; Langowski, J. *Opt. Express* **2012**, *20* (16), 17767−82.
(31) Singh, A. P.; Krieger, J. W.; Buchholz, J.; Charbon, E.; Langowski, J.; Wohland, T. *Opt. Express* **2013**, *21* (7), 8652−68.
(32) Vitali, M.; Bronzi, D.; Krmpot, A. J.; Nikolic, S. N.; Schmitt, F. J.; Junghans, C.; Tisa, S.; Friedrich, T.; Vukojevic, V.; Terenius, L.; Zappa, F.; Rigler, R. *IEEE J. Sel. Top. Quantum Electron.* **2014**, *20* (6), 344.
(33) Krieger, J. W.; Singh, A. P.; Bag, N.; Garbe, C. S.; Saunders, T. E.; Langowski, J.; Wohland, T. *Nat. Protoc.* **2015**, *10* (12), 1948−74.
(34) Krmpot, A. J.; Nikolic, S. N.; Vitali, M.; Papadopoulos, D. K.; Oasa, S.; Thyberg, P.; Tisa, S.; Kinjo, M.; Nilsson, L.; Gehring, W. J.; Terenius, L.; Rigler, R.; Vukojevic, V. *SPIE Proc.* **2015**, *9536*, 95360O.
(35) Singh, A. P.; Galland, R.; Finch-Edmondson, M. L.; Grenci, G.; Sibarita, J. B.; Studer, V.; Viasnoff, V.; Saunders, T. E. *Biophys. J.* **2017**, *112* (1), 133−142.
(36) Buchholz, J.; Krieger, J.; Bruschini, C.; Burri, S.; Ardelean, A.; Charbon, E.; Langowski, J. *Biophys. J.* **2018**, *114* (10), 2455−2464.
(37) Brugues, J.; Needleman, D. *Proc. Natl. Acad. Sci. U. S. A.* **2014**, *111* (52), 18496−500.
(38) Papadopoulos, D. K.; Krmpot, A. J.; Nikolic, S. N.; Krautz, R.; Terenius, L.; Tomancak, P.; Rigler, R.; Gehring, W. J.; Vukojevic, V. *Mech. Dev.* **2015**, *138*, 218.
(39) Bag, N.; Ng, X. W.; Sankaran, J.; Wohland, T. *Methods Appl. Fluoresc.* **2016**, *4* (3), 034003.
(40) Sezgin, E.; Azbazdar, Y.; Ng, X. W.; Teh, C.; Simons, K.; Weidinger, G.; Wohland, T.; Eggeling, C.; Ozhan, G. *FEBS J.* **2017**, *284* (15), 2513−2526.
(41) Huang, S.; Lim, S. Y.; Gupta, A.; Bag, N.; Wohland, T. *Biochim. Biophys. Acta, Biomembr.* **2017**, *1859* (9 Pt A), 1483−1492.
(42) Hanley, M. L.; Yoo, T. Y.; Sonnett, M.; Needleman, D. J.; Mitchison, T. J. *Mol. Biol. Cell* **2017**, *28* (11), 1444−1456.
(43) Ng, X. W.; Teh, C.; Korzh, V.; Wohland, T. *Biophys. J.* **2016**, *111* (2), 418−429.
(44) Oh, D.; Yu, C. H.; Needleman, D. J. *Proc. Natl. Acad. Sci. U. S. A.* **2016**, *113* (31), 8729−34.
(45) Langowski, J. *Methods* **2017**, *123*, 3−10.
(46) Vukojevic, V.; Heidkamp, M.; Ming, Y.; Johansson, B.; Terenius, L.; Rigler, R. *Proc. Natl. Acad. Sci. U. S. A.* **2008**, *105* (47), 18176−81.
(47) Dertinger, T.; Pacheco, V.; von der Hocht, I.; Hartmann, R.; Gregor, I.; Enderlein, J. *ChemPhysChem* **2007**, *8* (3), 433−443.
(48) Buchholz, J. *Evaluation of single photon avalanche diode arrays for imaging fluorescence correlation spectroscopy: FPGA-based data readout and fast correlation analysis on CPUs, GPUs and FPGAs*; German Cancer Research Center (DKFZ), Helmholtz Association of National Research Centers: Heidelberg, Germany, 2015.
(49) Ries, J.; Schwille, P. *Biophys. J.* **2006**, *91* (5), 1915−1924.
(50) Ries, J.; Petrášek, Z.; García-Sáez, A. J.; Schwille, P. *New J. Phys.* **2010**, *12*, 113009.
(51) Michalet, X.; Siegmund, O. H.; Vallerga, J. V.; Jelinsky, P.; Millaud, J. E.; Weiss, S. *J. Mod. Opt.* **2007**, *54* (2−3), 239.
(52) Michalet, X.; Colyer, R. A.; Scalia, G.; Weiss, S.; Siegmund, O. H.; Tremsin, A. S.; Vallerga, J. V.; Villa, F.; Guerrieri, F.; Rech, I.; Gulinatti, A.; Tisa, S.; Zappa, F.; Ghioni, M.; Cova, S. *Proc. SPIE* **2011**, *8033*, 803316.
(53) Michalet, X.; Colyer, R. A.; Scalia, G.; Ingargiola, A.; Lin, R.; Millaud, J. E.; Weiss, S.; Siegmund, O. H.; Tremsin, A. S.; Vallerga, J. V.; Cheng, A.; Levi, M.; Aharoni, D.; Arisaka, K.; Villa, F.; Guerrieri, F.; Panzeri, F.; Rech, I.; Gulinatti, A.; Zappa, F.; Ghioni, M.; Cova, S. *Philos. Trans. R. Soc., B* **2013**, *368* (1611), 20120035.
(54) Mikuni, S.; Pack, C.; Tamura, M.; Kinjo, M. *Exp. Mol. Pathol.* **2007**, *82* (2), 163−8.
(55) Stortz, M.; Presman, D. M.; Bruno, L.; Annibale, P.; Dansey, M. V.; Burton, G.; Gratton, E.; Pecci, A.; Levi, V. *Sci. Rep.* **2017**, *7* (1), 6219.
(56) Mikuni, S.; Tamura, M.; Kinjo, M. *FEBS Lett.* **2007**, *581* (3), 389−93.
(57) Shimozawa, T.; Yamagata, K.; Kondo, T.; Hayashi, S.; Shitamukai, A.; Konno, D.; Matsuzaki, F.; Takayama, J.; Onami, S.; Nakayama, H.; Kosugi, Y.; Watanabe, T. M.; Fujita, K.; Mimori-Kiyosue, Y. *Proc. Natl. Acad. Sci. U. S. A.* **2013**, *110* (9), 3399−404.
(58) Claxton, N. S.; Fellers, T. J.; Davidson, M. W. Microscopy, confocal. In *Encyclopedia of medical devices and instrumentation*, Webster, J. G., Ed. John Wiley & Sons: Hoboken, NJ; 2006, 449−477.
(59) Rigler, R.; Mets, U.; Widengren, J.; Kask, P. *Eur. Biophys. J.* **1993**, *22* (3), 169−175.
(60) Eigen, M.; Rigler, R. *Proc. Natl. Acad. Sci. U. S. A.* **1994**, *91* (13), 5740−5747.
(61) Reynaud, E. G.; Krzic, U.; Greger, K.; Stelzer, E. H. K. *HFSP J.* **2008**, *2* (5), 266−275.
(62) Overbeck, E.; Sinn, C.; Flammer, I.; Ricka, J. *Rev. Sci. Instrum.* **1998**, *69* (10), 3515−3523.
(63) Zhao, M.; Jin, L.; Chen, B.; Ding, Y.; Ma, H.; Chen, D. Y. *Appl. Opt.* **2003**, *42* (19), 4031−4036.
(64) Ziarkash, A. W.; Joshi, S. K.; Stipcevic, M.; Ursin, R. *Sci. Rep.* **2018**, *8* (1), 5076.

DOI: 10.1021/acs.analchem.9b01813
Anal. Chem. XXXX, XXX, XXX−XXX

Journal of Biomedical Optics

BiomedicalOptics.SPIEDigitalLibrary.org

Mapping of hemoglobin in erythrocytes and erythrocyte ghosts using two photon excitation fluorescence microscopy

Katarina Bukara
Svetlana Jovanić
Ivana T. Drvenica
Ana Stančić
Vesna Ilić
Mihailo D. Rabasović
Dejan Pantelić
Branislav Jelenković
Branko Bugarski
Aleksandar J. Krmpot

SPIE.

Katarina Bukara, Svetlana Jovanić, Ivana T. Drvenica, Ana Stančić, Vesna Ilić, Mihailo D. Rabasović, Dejan Pantelić, Branislav Jelenković, Branko Bugarski, Aleksandar J. Krmpot, "Mapping of hemoglobin in erythrocytes and erythrocyte ghosts using two photon excitation fluorescence microscopy," *J. Biomed. Opt.* **22**(2), 026003 (2017), doi: 10.1117/1.JBO.22.2.026003.

Journal of Biomedical Optics 22(2), 026003 (February 2017)

Mapping of hemoglobin in erythrocytes and erythrocyte ghosts using two photon excitation fluorescence microscopy

Katarina Bukara,[a] Svetlana Jovanić,[b] Ivana T. Drvenica,[a,c] Ana Stančić,[c] Vesna Ilić,[c] Mihailo D. Rabasović,[b] Dejan Pantelić,[b] Branislav Jelenković,[b] Branko Bugarski,[a] and Aleksandar J. Krmpot[b,d,*]
[a]University of Belgrade, Department of Chemical Engineering, Faculty of Technology and Metallurgy, Belgrade, Serbia
[b]University of Belgrade, Institute of Physics Belgrade, Belgrade, Serbia
[c]University of Belgrade, Institute for Medical Research, Belgrade, Serbia
[d]Texas A&M University at Qatar, Science Program, Doha, Qatar

Abstract. The present study describes utilization of two photon excitation fluorescence (2PE) microscopy for visualization of the hemoglobin in human and porcine erythrocytes and their empty membranes (i.e., ghosts). High-quality, label- and fixation-free visualization of hemoglobin was achieved at excitation wavelength 730 nm by detecting visible autofluorescence. Localization in the suspension and spatial distribution (i.e., mapping) of residual hemoglobin in erythrocyte ghosts has been resolved by 2PE. Prior to the 2PE mapping, the presence of residual hemoglobin in the bulk suspension of erythrocyte ghosts was confirmed by cyanmethemoglobin assay. 2PE analysis revealed that the distribution of hemoglobin in intact erythrocytes follows the cells' shape. Two types of erythrocytes, human and porcine, characterized with discocyte and echinocyte morphology, respectively, showed significant differences in hemoglobin distribution. The 2PE images have revealed that despite an extensive washing out procedure after gradual hypotonic hemolysis, a certain amount of hemoglobin localized on the intracellular side always remains bound to the membrane and cannot be eliminated. The obtained results open the possibility to use 2PE microscopy to examine hemoglobin distribution in erythrocytes and estimate the purity level of erythrocyte ghosts in biotechnological processes. [DOI: 10.1117/1.JBO.22.2.026003]

Keywords: multiphoton fluorescence microscopy; ultrafast lasers; hemoglobin; label-free imaging; erythrocytes; erythrocyte ghosts.
Paper 160493RR received Jul. 14, 2016; accepted for publication Jan. 24, 2017; published online Feb. 9, 2017.

1 Introduction

Two photon excitation fluorescence (2PE) microscopy as an advanced technique offers the possibility for noninvasive, label-free high resolution imaging of living cells and deep tissues by using the fluorescence emission from the endogenous fluorescent molecules.[1–3] The near-infrared radiation generates 2PE signals of endogenous fluorophores, such as tryptophan, riboflavines, nicotinamides, collagen, elastin, and so on, and thus provides rich morphological and biochemical information of biological systems.[4–6] Less investigated and reported is the intrinsic fluorescence of hemoglobin, the main intracellular component of erythrocytes, which emits a strong Soret fluorescence with the peak at 438 nm upon two-photon excitation by femtosecond pulses in red and near-infrared region (600 to 750 nm).[7,8] Such optical properties of hemoglobin opened the possibility to use 2PE microscopy as a tool for label-free imaging of erythrocytes, even *in vivo*.[9]

In addition to the well-known physiological functions of erythrocytes, they serve as a natural blood compartment participating at the same time in biodistribution, metabolism, and action of certain drugs.[10] Furthermore, intentional usage of human and animal erythrocytes, erythrocyte membranes (i.e., ghosts), and their nanoderivatives presents modern approach in terms of prolonged and controlled drug delivery systems.[11–14] Recently, we have reported the production of drug encapsulated porcine and bovine erythrocyte ghosts by gradual hypotonic hemolysis in much higher quantities than those described in literature so far.[13] However, it was noted that after the hemolysis process a certain amount of hemoglobin remains in the final suspension of the resulting erythrocyte ghosts.[13] The fraction of this so called residual hemoglobin, which cannot be easily eliminated from the system, significantly affects subsequent encapsulation processes and encapsulated drug releasing profile.[15] Although this residual hemoglobin can be determined by the spectrophotometric method (e.g., cyanmethemoglobin method), data on spatial distribution of hemoglobin at the single cell level in erythrocytes and remaining erythrocytes ghosts are scarce. Demonstrated spatial redistribution of hemoglobin throughout intact erythrocytes in patients with vascular disorders[16] promotes the importance of this parameter monitoring in disease diagnosis as well.

Based on the aforementioned wide applicability of erythrocytes in biomedical research and diagnostic tests, it is important to have a reliable microscopy method for single cell analysis, including spatial distribution of hemoglobin. Although phase contrast microscopy traditionally represents a fast method for tracking changes of erythrocytes during the gradual hypotonic hemolysis and appearance of erythrocyte ghosts,[17,13,18] it does not provide enough information for detailed morphological analysis. Unlike the phase contrast microscopy that visualizes

*Address all correspondence to: Aleksandar J. Krmpot, E-mail: krmpot@ipb.ac.rs

1083-3668/2016/$25.00 © 2016 SPIE

all the changes of the index of refraction regardless of their origin, 2PE microscopy has high chemical selectivity, thus enabling the visualization of the distribution of certain chemical compounds. Confocal microscopy, scanning electron microscopy, transmission electron microscopy, and atomic force microscopy are considered as the most powerful tools for structural analysis of various cells, including erythrocytes. However, these methods mandatorily include cell fixation and/or labeling which might influence the fragile cell structure.[19] So far, large numbers of optical microscopic techniques have been utilized for erythrocyte imaging. Comparative study of stained cells by confocal and unstained cells by holographic microscopy has been elaborated as shown in the work of Rappaz et al.[20] Scanning microphotolysis (Scamp), also referred to as fluorescence recovery after photobleaching, has been employed for erythrocyte examination either in a linear[21] or in a two photon, i.e., nonlinear, regime.[22] Volumetric imaging of erythrocytes using photoacoustic microscopy has been described by Shelton et al.,[23] while the same method in combination with confocal microscopy is used for hemoglobin oxygen saturation measurements., as shown by Wang et al.[24] 2PE was combined with stimulated Raman scattering for hemoglobin imaging in mouse retina.[25] Even second harmonic generation (SHG) microscopy, usually accompanied with 2PE as another modality of nonlinear microscopy, has been utilized for label free imaging of human erythrocytes membrane exposed to various glucose concentrations in phosphate buffered saline (PBS).[26] In addition to demonstration of the imaging possibilities of hemoglobin by the aforementioned techniques, 2PE has recently been applied in examination of particular biomedical problems related to erythrocytes: tracking blood vessels within the tissues[27] and photophysical characterization of sickle cell disease hemoglobin.[28]

In this work, we report label-free imaging of two kinds of erythrocytes, porcine and outdated human ones, at single cell level by 2PE microscopy, with the specific aim of investigating the spatial distribution (i.e., for mapping) of hemoglobin within intact erythrocytes and residual hemoglobin in erythrocyte membranes obtained after a gradual hypotonic hemolysis process. Furthermore, the quantity of residual hemoglobin was determined by analysis of 2PE images relative to the hemoglobin concentration in intact erythrocytes. This investigation opens the possibility to use 2PE microscopy as a tool for quality assessment of erythrocytes and erythrocyte membranes as a starting material in various biotechnological processes, such as the production of erythrocyte-based drug delivery systems[13,15] or isolation of hemoglobin.[18,29] Additionally, 2PE microscopy could help in revealing the ability of erythrocyte membranes, originating from different species, to bind different amounts of hemoglobin. Since various processes require various levels of purity, this information is important for the selection of raw material.

2 Materials and Methods

2.1 *Blood Samples*

Porcine slaughterhouse blood and human outdated blood were used as starting biological materials. Porcine blood was taken from the jugular veins of Swedish Landrace swine and collected in a sterile glass bottle with 3.8% sodium-citrate as an anticoagulant, at slaughterhouse "PKB Imes" in Belgrade, Serbia. Blood samples were transported at ambient temperature and processing started 2 h after the collection. The outdated human erythrocyte concentrates were from the Institute for Transfusiology and Hemobiology, Military Medical Academy, Belgrade, Serbia. The erythrocytes were enriched by the standard procedure and preserved in saline-adenine-glucose-mannitol solution (each 100 mL contains 0.900 g dextrose monohydrate, 0.877 g sodium chloride, 0.0169 g adenine, and 0.525 g mannitol) for 42 days at 4°C. The outdated cell packs were anonymized prior to distribution, and the link to the donor was broken. If not used for the research, the cell packs would have been discarded.

2.2 *Preparation of Erythrocytes and Erythrocyte Membranes (i.e., Ghosts)*

Both porcine and human erythrocytes were precipitated by blood centrifugation at $2450 \times g$ for 20 min at 4°C. The plasma and leucocytes were carefully discarded by vacuum aspiration. The precipitated erythrocytes were resuspended in isotonic saline solution (0.9% NaCl), washed twice by centrifugation, and finally resuspended in an isotonic PBS, pH 7.2 to 7.4 (0.8% saline buffered with 10 mM sodium phosphate). Porcine and human erythrocyte ghosts were prepared by gradual hypotonic hemolysis[13,29] by using hypotonic 35-mM sodium phosphate/NaCl buffer for porcine and 5-mM sodium phosphate buffer for human erythrocytes (30 min, flow rate 150 mL/h.) After the hemolysis, the erythrocyte ghosts were precipitated by 40 min centrifugation at $3220 \times g$, at 4°C. Erythrocyte ghosts were washed out three times in the buffer solution used for hemolysis and finally in PBS solution. Concentration of hemoglobin in suspensions of erythrocytes and residual hemoglobin in erythrocyte ghosts were determined by the cyanmethemoglobin method.[30] To quantify residual hemoglobin, prior to the determination of the concentration, erythrocyte ghosts were dispersed in 1 mL of isotonic PBS containing 1% w/w of Triton X100 detergent.

2.3 *Experimental Setup for 2PE*

The homemade two-photon microscopy experimental setup is similar to that reported in our previous study.[31] The schematic of the setup is given in Fig. 1. The train of the femtosecond

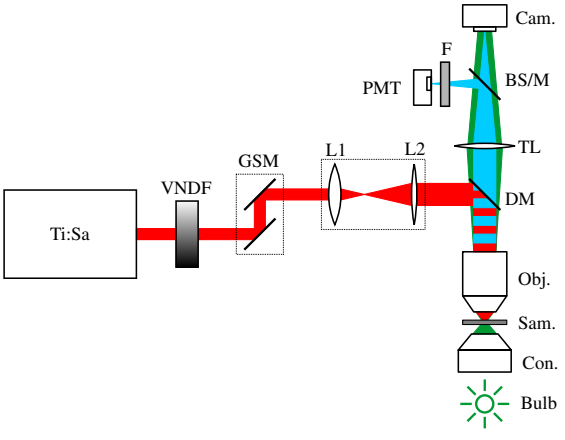

Fig. 1 Schematic of the imaging system: Ti:Sa, Ti:Sapphire laser, VNDF, variable neutral density filters, GSM, galvo scanning mirrors, L1 and L2, lenses, DM, dichroic mirror (short pass), Obj., microscope objective, Sam., sample, Con., condenser, Bulb, bulb for bright-field imaging illumination, TL, tube lens, BS/M, beam splitter or mirror, Cam., camera, F, filter, PMT, photomultiplier tube.

pulses is generated by the Ti:Sapphire laser (Coherent, Mira 900-F). The repetition rate is 76 MHz, and pulse duration is 160 fs. The galvoscanning mirrors (Cambridge Technologies, 6215H) are used to raster-scan the samples.

The laser beam is expanded in order to fill the entrance pupil of an objective (Carl Zeiss, EC Plan-NEOFLUAR, $40\times/1.3$ oil). A short-pass dichroic mirror (Thorlabs, M254H45) reflects the laser beam toward the objective, and transmits the signal toward the camera (Canon, EOS 50D) and the photomultiplier tube (PMT) (RCA, PF1006). The tube lens forms the sample image on the camera and/or PMT. The camera is used to take the bright-field image of the samples (green light in Fig. 1). The high intensity fluorescence can be seen by camera (blue light in Fig. 1). The commercial cameras usually have an infrared blocking filter. We removed this filter from our camera in order to see the backscattering/backreflection of the laser spot from the sample/cover slip which facilitated the alignment of the system. This is possible due to the fact that a small portion of the laser light leaks through the dichroic mirror (leakage of the laser is not shown in Fig. 1). A drawback of the infrared filter removing is the false coloring of the bright-field images. Thus, our bright-field images are greenish.

A beam-splitter or the mirror is used to reflect part of the signal or the complete signal to the PMT. An interference filter in front of the PMT removes scattered laser light. This filter is transparent for visible (415 to 685 nm) light, while blocking the IR and UV. Since the excitation wavelength is chosen in such a way that fluorescent signal comes predominantly from hemoglobin (Soret fluorescence), using the broadband filter ensures that all the fluorescent light will be collected, even from the wings of the fluorescent spectrum which is important in the case of relatively low excitation efficiency (see Sec. 2.4). This provides good signal-to-noise ratio and high contrast of images. Erythrocytes (hematocrit 5%, i.e., 5% suspension) and ghosts in the amount of 20 μL were allowed to settle onto a microscopic slide. Afterward, coverslips were put above settled cells and fixed to microscope slides. Imaging of erythrocytes and erythrocyte ghosts was performed at 730-nm excitation wavelength.

2.4 *Excitation Wavelength*

The excitation wavelength is of the great importance in this study and it has to be carefully selected according to its availability and the properties of the samples. Selection of the wavelength can significantly affect the chemical selectivity of the imaging, providing excitation of the specific and desired objects, and quality of the images by means of excitation efficiency and fluorescence strength. The excitation wavelength in this study is selected to be 730 nm by the following criteria:

- We have tested different excitation wavelengths within a Ti:Sapphire laser tuning range (700 to 1000 nm). Our excitation spectrum is consistent with the spectrum shown in study of Zheng et al.,[7] i.e., the excitation is the most efficient for the shortest wavelengths.
- The 2PE signal from hemoglobin at 650-nm excitation wavelength is reported to be more efficient[7] but we were not able to utilize shorter wavelengths than 700 nm due to the laser tuning range (700 to 1000 nm). Also, there is a significant leakage of the laser light to the PMT for wavelengths shorter than 730 nm. The cut-off wavelength of the dichroic mirror (hot mirror M254H45, Thorlabs, Inc.) is (700 ± 10) nm with transmission >97% for wavelengths longer than 710 nm, whereas full width at half maximum of the laser line is ~12 nm.
- The 2PE signal from glass (coverslips and microscope slides) is pronounced for wavelengths shorter than 730 nm. Thus, 730 nm is the shortest possible choice for the excitation wavelength to produce still high quality images.

3 Results and Discussion

In this study, erythrocyte membranes (ghosts) were prepared by gradual hypotonic hemolysis starting from slaughterhouse porcine and outdated human erythrocytes. During the process of gradual decrease of ionic strength of the solution surrounding erythrocytes, they swell and hemoglobin molecules leak out, leaving intact erythrocyte membranes.[13,17,18,29] Preparation of ghosts was followed by an extensive washing out procedure (to remove extracellular hemoglobin released from lysed erythrocytes). However, a small amount of hemoglobin, so called residual hemoglobin, always remains bound to membranes in resulting erythrocyte ghosts.[13]

Here, 2PE microscopy was used to quantify the relative decrease in hemoglobin's content at the end of the applied process of hemolysis and reveal its localization in the examined samples. All 2PE images are of the high quality by means of good signal-to-noise ratio, high visibility (contrast), high pixel resolution, and without or with minimal postmeasurement processing.

Bright-field microscopy images and corresponding autofluorescence 2PE images of starting porcine and human erythrocytes are presented in Figs. 2 and 3, respectively. 2PE images are acquired in 1024×1024 pixels resolution upon 30 times averaging of raw fluorescence signal. Intensity of pseudo-red color corresponds to the 2PE signal intensity.

According to image dimensions (30×30 μm^2) and physical resolution of our experiment, which is limited by diffraction and measured to be ~300 nm,[31] the minimal pixel resolution for faithful imaging of the object is set by Nyquist criterion to 200×200 pixels. In our case, 1024×1024 pixel resolution ensures that we overfill the Nyquist criterion and contribute to the high quality of the images.

As evident from Figs. 2(b) and 3(b), it is possible to notice localization of hemoglobin's content even from suspensions of

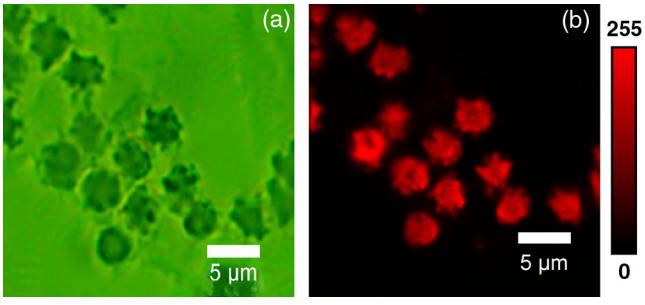

Fig. 2 Suspension of porcine erythrocytes: (a) bright-field microscopy image, (b) corresponding 2PE image revealing localization of hemoglobin; black, the lowest 2PE signal, red, the highest 2PE signal. 3-D model of examined human erythrocytes. (Video 1. MPEG, 6.16 MB [URL: http://dx.doi.org/10.1117/1.JBO.22.2.026003.1]).

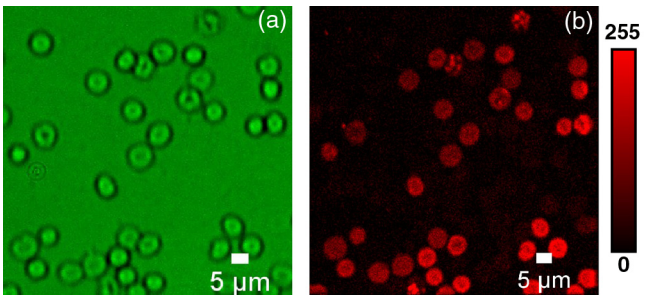

Fig. 3 Suspension of human erythrocytes: (a) bright-field microscopy image, (b) corresponding 2PE image revealing localization of hemoglobin; black, the lowest 2PE signal, red, the highest 2PE signal. Note that field of view (scale bar) is different than in a Fig. 2. It was changed because the region of interest was wider.

erythrocytes. Also, a 3-D model of examined human erythrocytes is displayed in Video 1.

Due to the presence of erythrocytes' methemoglobinreductase, hemoglobin in blood is predominately in its native ferrous form[32] which is desirable for the 2PE signal measurement. 2PE images and examination of hemoglobin distribution in a single erythrocyte for both examined types are given in Fig. 4. This result demonstrates that the resolution of the 2PE microscopy is good enough for the analysis of erythrocytes at the single cell level. As with the images in Fig. 3, these 2PE images are the results of averaging 30 individual images. Pseudocoloring corresponds to the 2PE signal intensity. No further processing of the image was performed, the data points in graphs represent the raw 2PE signal levels.

Based on the results in Fig. 4, we have confirmed that human erythrocytes have the normal morphology of biconcave discocytes,[33] whereas porcine erythrocytes have an echinocyte morphology. Such morphology of porcine erythrocytes is not a sign

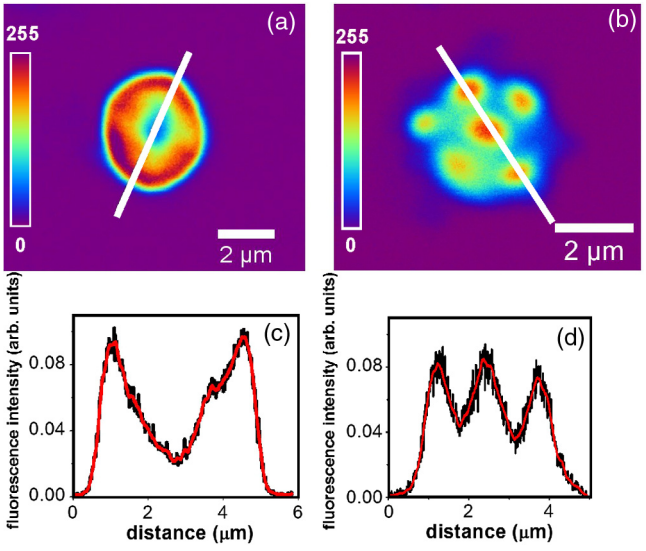

Fig. 4 Representative raw 2PE image of (a) human and (b) porcine erythrocyte. 2PE signal is presented in pseudocolor. Distribution of 2PE signals, i.e., hemoglobin concentration through the diameter of (c) human and (d) porcine erythrocyte. Black curves are raw data plot, red curves are obtained upon adjacent points averaging. Note that the two images are not recorded under the same experimental conditions; the intensities are not mutually normalized, thus they cannot be compared.

of some pathological condition but represents a common artifact in handling of porcine blood.[34]

Hemoglobin, which is the dominant component of erythrocytes, follows the cells' shape which can be easily observed by comparing the bright field and 2PE images. For human erythrocytes, its lowest density is observed to be in the central area [Fig. 4(a)], and in peripheral parts, its distribution was homogeneous. This finding is in agreement with the reported spatial distribution of hemoglobin in healthy human erythrocytes examined by confocal Raman spectroscopy[35] and atomic force microscopy.[36] On the other hand, for porcine erythrocytes, 2PE revealed a significant accumulation of hemoglobin in cells' protrusions. As shown in the study by Parshina et al.,[36] amphibian (frog) nucleated and mammalian (rat) nonnucleated healthy erythrocytes have a homogeneous distribution of cytosolic hemoglobin. Our results indicate that the deviations from the biconcave morphology of porcine erythrocytes probably affect the distribution of hemoglobin and lead to its accumulation in the cell protrusions. Taking into account that various pathological conditions are accompanied by uneven distribution of hemoglobin,[16,37] the developed method might be useful in their diagnosis. Until now it was described that isolated sickle cell disease hemoglobin (HbS) and malaria-infected red blood cells could be analyzed and photophysically characterized by multiphoton microscopy.[28,38]

The overall presence of residual hemoglobin in the final suspensions of erythrocyte ghosts was primarily determined by cyanmethemoglobin assay (Fig. 5). The concentration of residual hemoglobin was 7.21 and 1.76 g/L for the porcine and human samples, respectively. This reflects the decrease in concentrations of hemoglobin by 95% and 99% in the suspension of erythrocyte ghosts compared to the starting suspensions of porcine and outdated human erythrocytes, respectively. These amounts of residual hemoglobin in erythrocyte ghosts are consistent with the range reported in other studies.[39,40] However, the localization of residual hemoglobin in the suspension still remains unknown.

In addition to the spatial distribution of hemoglobin in intact human and porcine erythrocytes, images of residual hemoglobin in erythrocyte ghosts also can be obtained by 2PE (Figs. 6 and 7, respectively). The intensity of the 2PE signal depends on the concentration of the hemoglobin, but also on the pulse peak power, pulse duration, repetition rate, focal volume, excitation wavelength, etc. It is a nontrivial and time consuming task to quantify the dependence of the 2PE signal on hemoglobin concentration. In other words, it is almost impossible to determine

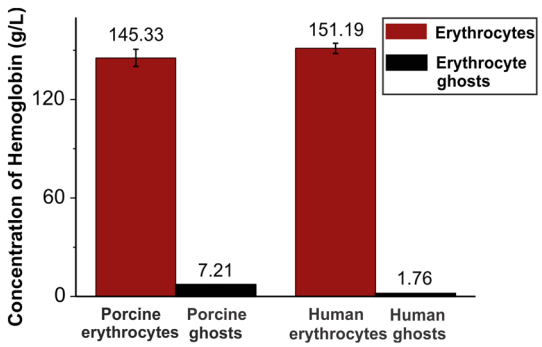

Fig. 5 Concentration of hemoglobin in erythrocytes and their ghosts obtained by gradual hemolysis. The concentration was determined by spectrophotometric cyanmethemoglobin method.

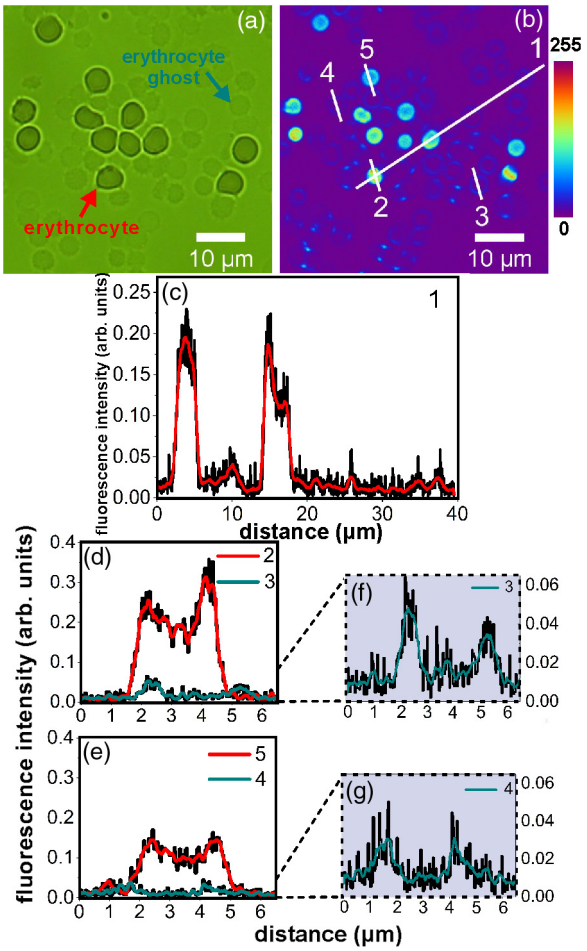

Fig. 6 Mixed suspension of human erythrocytes and resulting erythrocyte ghosts: (a) bright-field microscopy image; (b) 2PE image; (c–g) 2PE signal profiles along the corresponding lines at (b) image. Profiles 3 and 4 are given in magnified vertical scale in (f) and (g) graphs. Black curves are raw data plot, red and green curves are obtained upon adjacent points averaging.

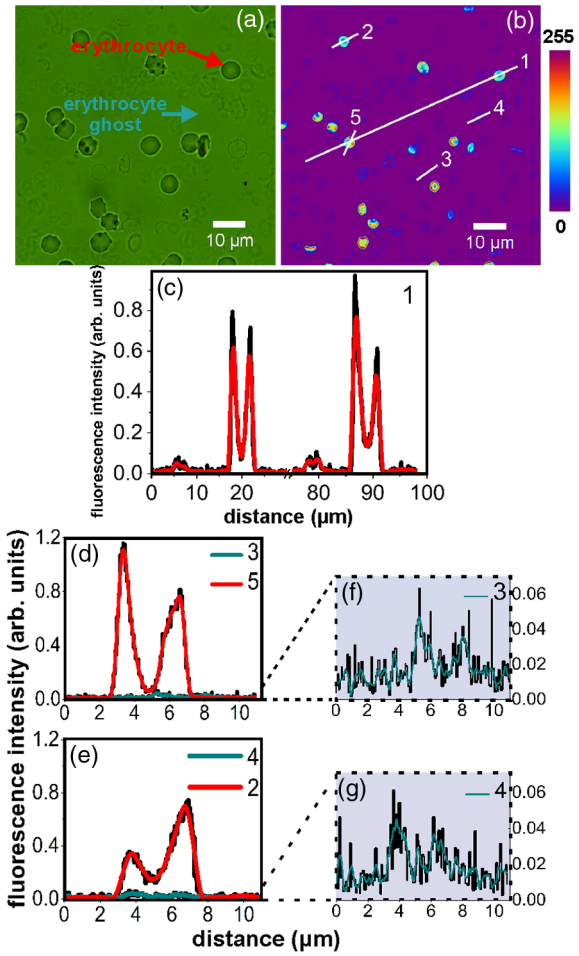

Fig. 7 Mixed suspension of porcine erythrocytes and resulting erythrocyte ghosts: (a) bright-field microscopy image; (b) 2PE image; (c–g) 2PE signal profiles along the corresponding lines at (b) image. Profiles 3 and 4 are given in magnified vertical scale in (f) and (g) graphs. Black curves are raw data plot, red and green curves are obtained upon adjacent points averaging.

absolute concentration from the 2PE signal since one has to keep all other parameters constant in separate measurements. In order to evaluate the local change (i.e., decrease) in hemoglobin content after the hemolysis, we mixed the ghosts with intact erythrocytes. In this way, we can evaluate the local content of hemoglobin, i.e., distribution of hemoglobin across erythrocytes and ghosts, and not just an average value for a whole cell or suspension. From the image data we obtained, the variation of intensity along appropriately chosen representative lines is shown in Figs. 6(b) and 7(b). The line is chosen in a way to intercept at least two erythrocytes and two ghosts which provide up to eight representative points positioned in the proximity of the membrane within the cells for comparison of 2PE signals. Note that the signals from the chosen points provide highly localized data for the comparison, opposite to the cyanmethemoglobin assay, which is intrinsically an averaging method. This ensures the same excitation parameters for both erythrocytes and erythrocyte ghosts. The above procedure ensures that the peak ratio from the 2PE intensity profile is equal to the concentration ratio in the untreated erythrocyte(s) and the ghost(s). We emphasize that this simple step enables us to determine changes in the content of residual hemoglobin in ghosts relative to the starting content of hemoglobin in intact erythrocytes, but not the absolute concentration.

There is no significant autofluorescence signal upon two photon excitation at 730 nm from any other common molecular species that can be found in erythrocytes and which could significantly affect the obtained results, except hemoglobin. Namely, lipids and saccharides are essentially nonfluorescent,[41] while aromatic amino acids as constituents of proteins, such tryptophan, phenylalanine, and tyrosine, have an absorption maximum of 280 nm[41] and cannot contribute significantly to autofluorescence generated by two-photon excitation at 730 nm. Pyridine nucleotides NADH and NADPH have an absorption maximum of 340 nm[42] and FAD has two excitation maxima at 360 and 450 nm. According to their excitation maximum, they could contribute the autofluorescence generated by two-photon excitation at 730 nm. However, their molar ratios to hemoglobin within erythrocytes (calculated based on data given in several studies)[43–45] are completely negligible.

As can be seen from Figs. 6 and 7, after the conversion of erythrocytes to empty erythrocyte membranes, fluorescence emission from hemoglobin significantly decreased, but was still detectable. Therefore, the applied process that we used allows the production of ghosts; however, a certain amount

of the hemoglobin always remains bound to the membrane. Comparing the peak values from Figs. 6(d) and 6(e) (red curves) to those in Figs. 6(f) and 6(g), one can estimate lower fluorescence emissions for both porcine and human erythrocyte ghosts in comparison to respective erythrocytes. Our results suggest that residual hemoglobin in the suspension was localized on the intracellular side of the ghost membranes. The 2PE signal in the internal volume of both, human and porcine erythrocyte ghosts, is at the noise level, thus hemoglobin content is negligible.

These results support already reported data on hemoglobin's ability to bind to erythrocyte membranes via a transmembrane protein, e.g., band 3[46] or some other cytoskeleton proteins via α globin chains.[47] This phenomenon that we have confirmed by 2PE microscopy could be used as a valuable marker of inevitable oxidative damages[48] emerged during *in vitro* storage and erythrocytes handling. The higher concentration of residual hemoglobin obtained in porcine ghosts relative to initial concentration can be explained by specific membrane lipid composition and their high susceptibility to oxidative stress induced by reactive oxygen species[49] related to a lower level of enzymes protectants against oxidative damages.[50]

Erythrocyte ghosts are extensively studied systems and have numerous potential applications. In addition to their usage as controlled drug delivery systems, they represent one of the most promising *in vitro* systems for drug partitioning studies and determination of the drug partition coefficient Kps.[51] In food science they are used for an estimation of antioxidant activity of different nutritional compounds.[52,53] Erythrocyte ghosts are suitable models for investigating membrane transport phenomena,[54] glucose translocation through biological membranes,[55] uptake and metabolism of different compounds,[56] etc. It is interesting to note that despite their widespread application, there are no studies estimating residual hemoglobin although it may significantly affect the quality of the final product. Apart from the mentioned study that suggests a positive correlation between the total content of membrane-bound hemoglobin and the level of oxidant stress,[48] it has been shown that iron from membrane-bound hemoglobin catalyzes the formation of reactive oxygen species which attack the cell membrane. This leads to peroxidation of membrane unsaturated lipids and disturbed structure and function of the membrane[57] and may directly affect the quality of the final product and/or obtained results.

In addition to using 2PE microscopy for analysis of erythrocyte ghosts as in the mentioned model or drug delivery systems, the results of this study also open a possibility of using 2PE microscopy in analysis of the spatial distribution of hemoglobin in erythrocytes in different physiological and pathological conditions. The spatial distribution of hemoglobin within erythrocytes can give information of the oxygen-transport capability and help by providing accurate diagnosis and appropriate treatment in erythrocytes disorders both in humans and animals.

4 Conclusion

In this study, we have demonstrated that 2PE microscopy can be used in analysis of the spatial distribution of hemoglobin in erythrocytes and erythrocyte ghosts, at an individual cell level. Although the maximal excitation efficiency for hemoglobin is at shorter wavelengths, high quality images can still be obtained using femtosecond pulses at 730 nm directly from a Ti:Sa oscillator. As opposed to the common spectroscopic methods such as cyanmethemoglobin assay that is intrinsically averaging, providing results for hemoglobin concentration drop after the hemolysis process in the bulk sample, 2PE microscopy gives results on hemoglobin localization and its fluorescence intensity change in randomly chosen points within the ghost-erythrocytes sample. Obtained results suggest that residual hemoglobin in erythrocyte ghosts, either human or porcine ones, is located mainly near the cell membrane rather than uniformly distributed. In addition, 2PE microscopy enables imaging of the distribution of hemoglobin in the protrusions of erythrocytes with morphology of echinocytes, thus it can be used for mapping of hemoglobin in erythrocytes morphologically different from the normal discocytes.

High-quality, label- and fixation-free visualization of hemoglobin can be achieved at 730-nm excitation wavelength. The 2PE fluorescence signal from residual hemoglobin at representative points near the cell membrane in the ghosts was reported to have lower intensity than at the corresponding points in intact erythrocytes. Obtained results suggest that residual hemoglobin in erythrocyte ghosts is located mainly near the cell membrane rather than uniformly distributed.

In such a way, through an application of 2PE microscopy hemoglobin distribution in erythrocytes together with residual hemoglobin content and distribution in the resulting erythrocyte ghosts can be directly and relatively easily estimated. The proposed method could be of significant importance for identifying different pathological or nonpathological conditions and application in material selection in biotechnological processes.

Disclosures

The authors declare no conflicts of interest.

Acknowledgments

This work has been supported by Ministry of Education, Science and Technological Development of the Republic of Serbia (Project Nos. III 46010, OI 171005, OI 171038, and III45016) and by the project NPRP 6-021-1-005 from the Qatar National Research Fund (member of the Qatar Foundation).

References

1. K. König et al., "Multiplex FISH and three-dimensional DNA imaging with near infrared femtosecond laser pulses," *Histochem. Cell Biol.* **114**(4), 337–345 (2000).
2. R. Weigert et al., "Intravital microscopy: a novel tool to study cell biology in living animals," *Histochem. Cell. Biol.* **133**(5), 481–491 (2010).
3. B. R. Masters and P. So, *Handbook of Biomedical Nonlinear Optical Microscopy*, Oxford University Press, New York (2008).
4. H. Kolesová et al., "Comparison of different tissue clearing methods and 3D imaging techniques for visualization of GFP-expressing mouse embryos and embryonic hearts," *Histochem. Cell. Biol.* **146**, 141–152 (2016).
5. L. Peralta et al., "In vivo evaluation of cervical stiffness evolution during induced ripening using shear wave elastography, histology and 2 photon excitation microscopy: insight from an animal model," *PloS One* **10**, e0133377 (2015).
6. B. G. Wang et al., "Intraocular multiphoton microscopy with subcellular spatial resolution by infrared femtosecond lasers," *Histochem. Cell Biol.* **126**(4), 507–515 (2006).
7. W. Zheng et al., "Two-photon excited hemoglobin fluorescence," *Biomed. Opt. Express* **2**, 71–79 (2010).
8. G. O. Clay, C. B. Chaffer, and D. Kleinfeld, "Large two-photon absorptivity of hemoglobin in the infrared range of 780-880 nm," *J. Chem. Phys.* **126**, 025102 (2007).

9. D. Li et al., "Time-resolved detection enables standard two-photon fluorescence microscopy for *in vivo* label-free imaging of microvasculature in tissue," *Opt. Lett.* **36**(14), 2638–2640 (2011).
10. P. H. Hinderling, "Red blood cells: a neglected compartment in pharmacokinetics and pharmacodynamics," *Pharmacol. Rev.* **49**(3), 279–295 (1997).
11. V. Leuzzi et al., "Erythrocyte-mediated delivery of recombinant enzymes," *Inherit Metab. Dis.* **39** (4), 519–530 (2016).
12. V. Bourgeaux et al., "Drug-loaded erythrocytes: on the road toward marketing approval," *Drug Des. Dev. Ther.* **10**, 665–676 (2016).
13. I. Kostić et al., "Erythrocyte membranes from slaughterhouse blood as potential drug vehicles: isolation by gradual hypotonic hemolysis and biochemical and morphological characterization," *Colloids Surf. B* **122**, 250–259 (2014).
14. R. Deak et al., "Physicochemical characterization of artificial nanoerythrosomes derived from erythrocyte ghost membranes," *Colloids Surf. B* **135**, 225–234 (2015).
15. I. T. Drvenica et al., "Biomembranes from slaughterhouse blood erythrocytes as prolonged release systems for dexamethasone sodium phosphate," *Biotechnol. Prog.* **32**, 1046–1055 (2016).
16. V. V. Revin et al., "Study of the structure, oxygen-transporting functions, and ionic composition of erythrocytes at vascular diseases," *Biomed. Res. Int.* **2015**, 973973 (2015).
17. D. Danon, "Osmotic hemolysis by a gradual decrease in the ionic strength of the surrounding medium," *J. Cell. Comp. Physiol.* **57**, 111–117 (1961).
18. R. Stojanović et al., "Isolation of hemoglobin from bovine erythrocytes by controlled hemolysis in the membrane bioreactor," *Appl. Biochem. Biotechnol.* **166**, 1491–1506 (2012).
19. E. Wisse et al., "Fixation methods for electron microscopy of human and other liver," *World J. Gastroenterol.* **16**, 2851–2866 (2010).
20. B. Rappaz et al., "Comparative study of human erythrocytes by digital holographic microscopy, confocal microscopy, and impedance volume analyzer," *Citometry* **73A**, 895–903 (2008).
21. M. Tschödrich-Rotter et al., "Optical single-channel analysis of the aerolysin pore in erythrocyte membranes," *Biophys. J.* **70**, 723–732 (1996).
22. U. Kubitschek et al., "Two-photon scanning microphotolysis for three-dimensional data storage and biological transport measurements," *J. Microsc.* **182**, 225–233 (1996).
23. R. L. Shelton, S. P. Mattison, and B. E. Applegate, "Volumetric imaging of erythrocytes using label-free multiphotonphotoacoustic microscopy," *J. Biophotonics* **7**, 834–840 (2014).
24. Y. Wang et al., "In vivo integrated photoacoustic and confocal microscopy of hemoglobin oxygen saturation and oxygen partial pressure," *Opt. Lett.* **36**, 1029–1031 (2011).
25. S. He et al., "Label-free nonlinear optical imaging of mouse retina," *Biomed. Opt. Express* **6**, 1055–1066 (2015).
26. D. Lev et al., "d-Glucose-induced second harmonic generation response in human erythrocytes," *J. Phys. Chem.* **113**, 2513–2518 (2009).
27. N. L. Garrett et al., "Exploring uptake mechanisms of oral nanomedicines using multimodal nonlinear optical microscopy," *J. Biophotonics* **5**, 458–468 (2012).
28. G. D. Vigil and S. S. Howard, "Photophysical characterization of sickle cell disease hemoglobin by multi-photon microscopy," *Biomed. Opt. Express* **6**, 4098–4104 (2015).
29. B. Bugarski and N. Dovezenski, "Hemofarm Koncern. Verfahrenzur Herstellung von Hemoglobin," Deutsches Patentamt DE 19707508 (2000).
30. O. W. Van Assendelft, A. H. Holtz, and S. M. Lewis, *Recommended Method for the Determination of the Haemoglobin Content of Blood*, I. C. S. H. Publications, World Health Organization (1984).
31. M. D. Rabasović et al., "Nonlinear microscopy of chitin and chitinous structures: a case study of two cave-dwelling insects," *J. Biomed. Opt.* **20**(1), 016010 (2015).
32. A. Mansouri and A.A. Lurie, "Concise review: methemoglobinemia," *Am. J. Hematol.* **42**, 7–12 (1993).
33. M. Diez-Silva et al., "Suresh shape and biomechanical characteristics of human red blood cells in health and disease," *MRS Bull.* **35**(5), 382–388S (2010).
34. J. D. Weiss and K. J. Wardrop, Eds., *Schalm's Veterinary Haematology*, 6th ed., pp. 144–151, Blackwell Publishing Ltd., Ames (2010).
35. L. Kang et al., "Confocal Raman microscopy on single living young and old erythrocytes," *Biopolymers* **89**, 951–959 (2008).
36. E.Y. Parshina et al., "Combined Raman and atomic force microscopy study of hemoglobin distribution inside erythrocytes and nanoparticle localization on the erythrocyte surface," *Laser Phys. Lett.* **10**, 075607 (2013).
37. J. P. Greer et al., *Wintrobe's Clinical Hematology*, 13th ed., Lippincott Williams & Wilkins, Philadelphia (2014).
38. J. Mauritz et al., "Biophotonic techniques for the study of malaria-infected red blood cells," *Med. Biol. Eng. Comput.* **48**, 1055–1063 (2010).
39. S. S. Bernstein et al., "Method for the preparation of posthemolitic residue or stroma of erythrocytes," *J. Biol. Chem.* **122**, 507–514 (1938).
40. D. Danon, A. Nevo, and Y. Marikovsky, "Preparation of erythrocyte ghosts by gradual haemolysis in hypotonic aqueous solution," *Bull. Res. Counc. Israel* **6E**, 36 (1956).
41. J. R. Lakowicz, "Protein fluorescence," Chapter 16 in *Principles of Fluorescence Spectroscopy*, 3rd ed., J. R. Lakowicz, Ed., pp. 530–578, Springer US, New York (2006).
42. H. Andersson et al., "Autofluorescence of living cells," *J. Microsc.* **191**(Pt 1), 1–7 (1998).
43. Y. Ogasawara, M. Funakoshi, and K. Ishii, "Determinationof reduced nicotinamide adenine dinucleotide phosphate concentration using high-performance liquid chromatography with fluorescence detection: ratio of the reduced form as a biomarker of oxidative stress," *Biol. Pharm. Bull.* **32**(11), 1819–1823 (2009).
44. S. Hustad et al., "Riboflavin, flavin mononucleotide, and flavinadenine dinucleotide in human plasma and erythrocytes at baseline and afterlow-dose riboflavin supplementation," *Clin. Chem.* **48**(9), 1571–1577 (2002).
45. K. J. Smock and S. L. Perkins, "Examination of the blood and bone marrow," Chapter 1 in *Wintrobe's Clinical Hematology*, J. P. Greer et al., Eds., pp. 1–64, Lippincott Williams & Wilkins, Philadelphia (2014).
46. J. Eisinger, J. Flores, and J. M. Salhany, "Association of cytosol hemoglobin with the membrane in intact erythrocytes," *Proc. Natl. Acad. Sci. U. S. A.* **79**, 408–412 (1982).
47. K. Murakami and S. Mawatari, "Oxidation of hemoglobin to methemoglobin in intact erythrocyte by a hydroperoxide induces formation of glutathionylhemoglobin and binding of alpha-hemoglobin to membrane," *Arch. Biochem. Biophys.* **417**(2), 244–250 (2003).
48. R. Sharma and B. R. Premachandra, "Membrane-bound hemoglobin as a marker of oxidative injury in adult and neonatal red blood cells," *Biochem. Med. Metab. Biol.* **46**(1), 33–44 (1991).
49. E. Brzezińska-Slebodzińska, "Species differences in the susceptibility of erythrocytes exposed to free radicals in vitro," *Vet. Res. Commun.* **27**(3), 211–217 (2003).
50. J. K. Vodela and R. R. Dalvi, "Erythrocyte glutathione-S-transferase activity in animal species," *Vet. Hum. Toxicol.* **39**, 9–11 (1997).
51. A. A. Omran, "An in vitro spectrometric method for determining the partition coefficients of non-steroidal anti-inflammatory drugs into human erythrocyte ghost membranes," *Spectrochim. Acta. A* **104**, 461–467 (2013).
52. S. Kumazawa et al., "Antioxidant activity of polyphenols in carob pods," *J. Agric. Food Chem.* **50**, 373–377 (2002).
53. S. Chaudhuri et al., "Interaction of flavonoids with red blood cell membrane lipids and proteins: antioxidant and antihemolytic effects," *Int. J. Biol. Macromol.* **41**, 42–48 (2007).
54. U. Kubitschek et al., "Two-photon scanning microphotolysis for three-dimensional data storage and biological transport measurements," *J. Microsc.* **182**, 225–233 (1996).
55. R. D. Taverna and R. G. Langdon, "Reversible association of cytochalasin B with the human erythrocyte membrane. Inhibition of glucose transport and the stoichiometry of cytochalasin binding," *Biochim. Biophys. Acta* **323**, 207–219 (1973).
56. J. Schrader, R. M. Berne, and R. Rubio, "Uptake and metabolism of adenosine by human erythrocyte ghosts," *Am. J. Physiol.* **223**, 159–166 (1972).
57. A. W. Girotti and J. P. Thomas, "Damaging effects of oxygen radicals on resealed erythrocyte ghosts," *J. Biol. Chem.* **3**, 1744–1752 (1984).

Katarina Bukara graduated from Faculty of Pharmacy, University of Belgrade. Currently, she is doing a joint PhD at University of Belgrade,

Serbia (biotechnology and biochemical engineering) and University of Antwerp, Belgium (pharmaceutical sciences). Her research concerns the development of controlled drug delivery systems for steroids and nonsteroidal anti-inflammatory drugs based on empty erythrocyte membranes and biodegradable polymers.

Svetlana Jovanić obtained her master's degee in biophysics at the University of Belgrade, Serbia. Currently, she is a junior research associate at the Institute of Physics in Belgrade and a member of the Laboratory for Biophotonics. Her PhD research is based on investigation of neurodegeneration disorders by usage of nonlinear laser scanning microscopy (two photon excitation fluorescence and second harmonic generation) on cells and tissues.

Ivana T. Drvenica is a research associate at Innovation Centre of Faculty of Technology and Metallurgy, University of Belgrade (TMF). She obtained her MSc degree in pharmaceutical sciences from the Faculty of Pharmacy, University of Belgrade, in 2009. In collaboration with Institute for Medical Research, University of Belgrade, she obtained her PhD in biotechnology at TMF in 2015 on development and characterization of erythrocyte membranes from wasted slaughterhouse blood as prolonged drug delivery vehicles.

Ana Stančić is a third-year PhD student at the Faculty of Biology, carrying out experiments for her thesis at the Institute for Medical Research, University of Belgrade. She is the stipendist of the Ministry of Education, Science and Technological Development of the Republic of Serbia. Her work is focused on *in vitro* testing of biological effects of empty erythrocyte membranes (i.e., ghosts), hemoglobin-based products and development of modern glucocorticoid derivatives.

Vesna Ilić is a molecular biologist and physiologist. She received her PhD in immunobiology. She is a head of the Group of Immunology, Institute for Medical Research, University of Belgrade. Her areas of interests include immunoglobulins and immune complexes, signaling in cells of immune and hematopoietic systems, biological effects of mesenchymal stem cells, systems for prolonged drug delivery based on erythrocytes, and heme iron formulations for prevention or treatment of anemia.

Mihailo D. Rabasović obtained his BS, MS, and PhD degrees from the physics department of the University of Belgrade in field of applied physics. His current research interests include photoacoustics, microscopy, and correlation spectroscopy. In the field of microscopy, he is interested in nonlinear and label-free techniques.

Dejan Pantelić is a research professor at the Institute of Physics in Belgrade, Serbia. His interests include holography, biophotonics, biomimetics, and microscopy. He has published more than 100 papers in refereed journals and conferences. He is a member of the Optical Society of America.

Branislav Jelenković is a research professor and head of the Photonic Center, Institute of Physics, University of Belgrade. He earned his bachelor's degree at Faculty of Electrical Engineering, University of Belgrade (1977) and PhD in physics at Faculty of physics, University of Belgrade (1985). He is a member of Serbian Academy of Science and Art, Optical Society of Serbia (copresident), American Optical Society. He won Institute of Physics Award in 2010. He has over 100 publications in peer-reviewed journals, with over 2500 citations.

Branko Bugarski obtained a PhD in 1992 at the University of Queens, Canada. Currently, he is a professor of chemical engineering at Faculty of Technology and Metallurgy, University of Belgrade, Serbia. During 1998, he was a guest professor at Oregon State University and Massachusetts Institute of Technology. The majority of his research interests are focused on immobilization, encapsulation, nanoparticles, and their application in medicine and pharmacy.

Aleksandar J. Krmpot, assistant research professor at the Institute of Physics Belgrade received his PhD in quantum optics from the University of Belgrade, Serbia. His research activities are in quantum optics (coherent optical effects) and biophotonics (microscopy and imaging). His current research activities are the development and application of nonlinear microscopy for bioimaging at Institute of Physics, Belgrade, Serbia and multifocal correlation microscopy for studies of molecular diffusion dynamics at Karolinska Institute, Stockholm, Sweden.